UNIVERSITY OF CALIFORNIA, IRVINE

Synthetic Models for Metalloenzyme Active Sites: Accessing High-Valent Bimetallic Complexes with [M–(μ-O)–M'] Cores

DISSERTATION

submitted in partial satisfaction of the requirements

for the degree of

DOCTOR OF PHILOSOPHY

in Chemistry

by

Justin L. Lee

Dissertation Committee:
Professor Andrew S. Borovik
Professor William J. Evans
Professor Alan F. Heyduk

2021

Dedications

To Mom, Dad, and Sis.

Table of Contents

List of Figures

List of Tables

List of Schemes

List of Equations

Acknowledgements

There are many people to thank for my journey through graduate school. First and foremost is my research advisor, Prof. Andy Borovik, who has taught me to always strive for perfection, be a critical thinker, and never rule out any possibilities. I have also learnt from him how to tell a good story, whether through a manuscript or in an oral presentation. Some of my most memorable moments in the research group are drawing compounds we want to synthesize and MO diagrams to explain our experimental results on the whiteboards around the peanut table. He is also instrumental in expanding my scientific toolbox and credentials, including giving me the opportunity to manage the EPR spectrometer. I am grateful for the opportunity to work with Andy in the past five years.

I would like to thank Profs. Bill Evans and Alan Heyduk, who serve as the other members of my dissertation committee. Bill was the inorganic track chair when I started at UCI and had been a helpful teacher/mentor in various courses, and Alan provided useful feedback for my progress exams. I would also like to thank the other faculty members in the chemistry department who had helped me at different points of my graduate career. Finally, I would like to thank the department for the dissertation fellowship awarded to my last summer quarter here.

"It takes a village to raise a child." This is certainly true within the Borovik group, as I had the privilege to be mentored by and/or interact with many brilliant graduate students and postdocs, including Nate, who helped me get started in the lab; Kelsey, who taught me how to properly column and loves a chat about Fe enzymes and my annual Jambalaya; and Suman, who is like a Swiss Army knife and can do anything. My mentor, Victoria, has been influential in my scientific journey; she has taught me so much, from inorganic synthesis, to everything EPR spectrometer-related, to cooking/baking. I also enjoy our 6 a.m. helium runs, and our many collaborations, from manuscripts to the EPR manual. Thanks for the support all the years, VFO, whether it came in the form of a good cheering-up or a delicious pasta dish/giant cookie/chips. Special mentions to the FOBGs (friends of the Borovik group) Alec and Andrew. It is always enlightening to have a scientific conversation with Alex at the pub, and Andrew is like an encyclopedia of all diiron chemistry for me the past few years. And to the EPR spectrometer, you have been a trooper; Meghen & Phan, keep her happy.

I would like to thank other chemistry/biochemistry laboratories in the department and the UCI instrument facilities; these resources are essential in constructing a friendly and collaborative environment that I have enjoyed for the past few years. I must acknowledge my most significant collaborators, Prof. Michael Hendrich's lab at Carnegie Mellon, for all their help that pre-dates my time at UCI. Mike taught a quantum class I was in, and former member Andrew suggested me to look into the Borovik Lab during my grad school application process. Here, I have established a fruitful collaborating relationship with Saborni, who spent years simulating spectra and trying to understand my synthetic systems. My work has greatly benefited from Mike and his team's expertise in magnetic spectroscopies.

I would like to give a shoutout to Prof. Yisong (Alex) Guo and his lab, where I performed my undergraduate research. Alex pointed me in the direction of bioinorganic chemistry, and I had

not looked back since. The non-heme Fe protein and Mössbauer spectroscopy knowledge he, Ruixi, and Jikun imparted on me was valuable to my graduate studies. I would also like to thank the many professors at Carnegie Mellon who gave me enough reasons to switch from pre-law to chemistry, which is more fun, more actions, less readings, and more pretty figures in said readings.

My inorganic cohort – what a crew! Sunny is a rascal, but I had a ton of fun pulling pranks on her the last few years, and she is always the emotional valve when I need to vent. Thanks for all the Albertson's trips for rotisserie chicken, and apologies for the 0.5 triflates. Jeff and Bronte have been good friends, both within and outside the lab. Since being roommates during our perspective visit weekend, Jeff has been a good mate to have a beer with at the pub, and an excellent sounding board for chemistry with a different perspective. Bronte is the glue to our little group, always has the latest gossips to share, and always there to listen to my concerns. And Tener being the mysterious one, but I had never felt safer than being in his Cadillac. *Viva* Bar Louie.

Outside of the lab, I have had tremendous support from my friends and family. The Quantum Lion crew – Josh, Quang, Christi, Yidan, etc. – has helped me along the entire graduate journey; I look forward to having our gigantic food adventures again. My family – Mom, Dad, and Sharon – does not understand much about chemistry, but their support is nevertheless appreciated. Finally, I would like to thank Dolores for all her love and support in the last few years; there was definitely a moment when I was not sure I would not make it through this PhD program without her being there for me. We have built a loving home with Ferric (i.e. the Pumpkinator) and the Goos, and I cannot wait to see the next chapter of our lives.

~ JLL, October 2021

"When you have eliminated the impossible,

whatever remains, *however improbable*,

must be the truth."

Sherlock Holmes

In *The Sign of The Four* by Sir Arthur Conan Doyle

Curriculum vitae

EDUCATION

University of California, Irvine (UCI), *Irvine, California* 2016 – 2021
Ph.D. Candidate in Chemistry
Dissertation Advisor: Professor A. S. Borovik
Thesis Title: Synthetic Models for metalloenzyme Active Sites: Accessing High-Valent Bimetallic with [M–(μ-O)–M'] Cores

Carnegie Mellon University (CMU), *Pittsburgh, Pennsylvania* 2012 – 2016
B.Sc. in Chemistry/Biological Chemistry with Honors
Honors Thesis Advisor: Professor Yisong Guo
Thesis Title: A Study on the Mechanism of the Epoxidation Reaction in the Biosynthesis of Viridicatin

PUBLICATIONS

Lee, J. L.; Biswas, S.; Ziller, J. W.; Hendrich, M. P.; Borovik, A. S. Preparation of a [Mn^{IV}–(μ–O)–Fe^{III}] Species: A Synthetic Model for Ribonucleotide Reductase Class Ic Active Site. *Manuscript in Preparation.*

Lee, J. L.; Biswas, S.; Hendrich, M. P.; Borovik, A. S. Binding of Divalent Late 3d Transition Metal Ions to a High-Spin Fe(IV)-Oxido Complex. *Manuscript in Preparation.*

Lee, J. L.; Biswas, S.; Sun, C.; Ziller, J. W.; Hendrich, M. P.; Borovik, A. S. Synthetic Models for Metalloenzyme Active Sites: Accessing High-Valent Non-Heme Diiron Complexes. *Manuscript in Preparation.*

Lee, J. L.; Ross, D. L.; Barman, S. K.; Borovik, A. S. C–H Bond Cleavage by Bioinspired Non-Heme Metal Complexes. *Inorg. Chem.* **2021**, *60*, 13759-13783.

Lee, J. L.; Oswald, V. F.; Biswas, S.; Hill, E. A.; Ziller, J. W.; Hendrich, M. P.; Borovik, A. S. Stepwise Assembly of Heterobimetallic Complexes: Synthesis, Structure and Physical Properties. *Dalton Trans.* **2021**, *50*, 8111-8119.

Medina, M. S.; Bretzing, K. O.; Aviles, R. A.; Chong, K.; Espinoza, A.; Garcia, C. N. G.; Katz, B. B.; Kharwa, R. N.; Hernandez, A.; **Lee, J. L.**; Lee, T. M.; Strul, M. W.; Lo Verde, C.; Wong, E. Y.; Owens, C. P. CowN sustains nitrogenase turnover in the presence of the inhibitor carbon monoxide. *J. Biol. Chem.* **2021**, *296*, 100501.

Champ, T. B.; Jang, J. H.; **Lee, J. L.**; Wu, G.; Reynolds, M. A.; Abu-Omar, M. M. Lignin-Derived Non-Heme Iron and Manganese Complexes: Catalysts for the On-Demand Production of Chlorine Dioxide in Water under Mild Conditions. *Inorg. Chem.* **2021**, *60*, 2905-2913.

Oswald, V. F.; **Lee, J. L.**; Biswas, S.; Weitz, A. C.; Mittra, K.; Fan, R.; Li, J.; Zhao, J.; Hu, M. Y.; Alp, E. E.; Bominaar, E. L.; Guo, Y.; Green, M. T.; Hendrich, M. P.; Borovik, A. S. Effects of Non-covalent Interactions on High-Spin Fe(IV)-Oxido Complexes. *J. Am. Chem. Soc.* **2020**, *142*, 11804-11817.

Li, J.; Liao, H.-J.; Tang, Y.; Huang, J.-L.; Cha, L.; Lin, T.-S.; **Lee, J. L.**; Kurnikov, I. V.; Kurnikova, M. G.; Chang, W.-c.; Chan, N.-L.; Guo, Y. Epoxidation Catalyzed by the Nonheme Iron(II)- and 2-Oxoglutarate-Dependent Oxygenase, AsqJ: Mechanistic Elucidation of Oxygen Atom Transfer by a Ferryl Intermediate. *J. Am. Chem. Soc.* **2020**, *142*, 6268-6284.

Liao, H.-J.; Li, J.; Huang, J.-L.; Davidson, M.; Kurnikov, I.; Lin, T.-s.; **Lee, J. L.**; Kurnikova, M.; Guo, Y.; Chan, N.-L.; Chang, W.-c. Insights into the Desaturation of Cyclopeptin and its C3 Epimer Catalyzed by a non-Heme Iron Enzyme: Structural Characterization and Mechanism Elucidation. *Angew. Chem. Int. Ed.* **2018**, *57*, 1831-1835.

Chang, W.-c.; Li, J.; **Lee, J. L.**; Cronican, A. A.; Guo, Y. Mechanistic Investigation of a Non-Heme Iron Enzyme Catalyzed Epoxidation in (-)-4'-Methoxycyclopenin Biosynthesis. *J. Am. Chem. Soc.* **2016**, *138*, 10390-10393.

PRESENTATIONS

J. L. Lee, C. S. Sun, S. Biswas, J. W. Ziller, M. P. Hendrich, A. S. Borovik. Synthetic Models for Metalloenzyme Active Sites: Accessing High-Valent Bimetallic Complexes with [Fe–(*μ*–O)–M] Cores. Abstracts of Papers, ACS Spring 2021, virtual, April 9, 2021. Talk.

J. L. Lee, A. S. Borovik. Synthetic Models for Metalloenzyme Active Sites: Accessing High-Valent Diiron Complexes. 2021 University of California Chemical Symposium, virtual, March 27, 2021. Talk.

J. L. Lee, S. Biswas, M. P. Hendrich, A. S. Borovik. Synthetic Models for Metalloenzyme Active Sites: Accessing High-Valent Bimetallic Complexes with [Fe–(*μ*–O)–M] Cores. UCI Student Inorganic Seminar Series, Irvine, CA, December 3, 2020. Talk.

J. L. Lee, A. S. Borovik. Effects of Lewis Acids on a Non-Heme High Spin Fe(IV)-Oxido Complex. 2020 University of California Chemical Symposium, Lake Arrowhead, CA, scheduled for March 2020. Accepted talk, canceled due to COVID-19.

J. L. Lee, A. S. Borovik. Effects of Lewis Acids on a Non-Heme High Spin Fe(IV)-Oxido Complex. SoCal Bioinorganic Conference, Los Angeles, CA, December 7, 2019. Talk.

J. L. Lee, V. F. Oswald, S. Biswas, M. P. Hendrich, A. S. Borovik. A Non-heme Fe(IV)-oxido Complex and Binding of Lewis Acids. Abstracts of Papers, ACS Fall 2019 National Meeting & Exposition, San Diego, CA, United States, August 28, 2019. Talk.

C. Sun, **J. L. Lee**, D. L. Ross, F. J. Gomez, M. E. Goulet, J. L. Kneebone, S. K. Barman, V. F. Oswald, A. S. Borovik. Bioinspired Inorganic Chemistry: Synthetic Models. SoCal Bioinorganic Conference, Pasadena, CA, December 8, 2018. Poster.

J. L. Lee, S. Biswas, M. P. Hendrich, A. S. Borovik. Modulating Intramolecular Hydrogen Bonding Networks in Non-Heme Iron Complexes to Bind Dioxygen. 5th Penn State Bioinorganic Workshop & Symposium, State College, PA, June 1-8, 2018. Poster.

J. L. Lee, S. Biswas, M. P. Hendrich, A. S. Borovik. Modulating Intramolecular Hydrogen Bonding Networks in Fe Complexes to Bind Dioxygen. Abstracts of Papers, 255th ACS National Meeting & Exposition, New Orleans, LA, United States, March 21, 2018. Talk.

V. F. Oswald, C. S. Sun, **J. L. Lee**, S. K. Barman, J. L. Kneebone, A. C. Weitz, M. P. Hendrich, A. S. Borovik. Bioinspired Inorganic Chemistry: Synthetic Tripodal Models. SoCal Bioinorganic Conference, Irvine, CA, December 2, 2017. Poster.

J. L. Lee, J. Li, Y. Guo. A Study on the Mechanism of the Epoxidation Reaction in the Biosynthesis of Viridicatin. Meeting of the Minds – Undergraduate Research Symposium, Pittsburgh, PA, May 4, 2016. Poster.

HONORS, AWARDS & PROFESSIONAL ORGANIZATIONS

Joan Rowland Award, *Department of Chemistry, UCI*	2021
Graduate Dissertation Fellowship, *Department of Chemistry, UCI*	2021
Phi Kappa Phi Honors Society	2016 – Present
Phi Kappa Phi Fellowship for Graduate/Professional Studies	2016
Phi Beta Kappa Honors Society	2016 – Present
Undergraduate Award in Inorganic Chemistry, *American Chemical Society*	2016
University Honors, *CMU*	2016
Departmental Honors, *Department of Chemistry, CMU*	2016
Dean's List, High Honors, *Mellon College of Science, CMU*	2013 – 2015
Andrew Carnegie Society Scholar	2015
Summer Undergraduate Research Fellowship, *CMU*	2015
Finalist for Student Employee of the Year, *CMU*	2015

Abstract of the Dissertation

Synthetic Models for Metalloenzyme Active Sites:
Accessing High-Valent Bimetallic Complexes with [M–(*μ*–O)–M'] Cores

By

Justin L. Lee

Doctor of Philosophy in Chemistry

University of California, Irvine, 2021

Professor Andrew S. Borovik, Chair

Metal ions are ubiquitous in biology and aid in facilitating many enzymatic transformations. For instance, high–valent iron–oxido and –hydroxido species are proposed to be key intermediates in oxidative processes catalyzed by non-heme iron proteins. A subclass of these proteins contains bimetallic sites that house either FeFe or FeM cores. To investigate the properties of both mono- and bimetallic cores, the Borovik Lab has developed a symmetric tripodal ligand framework containing phosphinic amido groups ($[poat]^{3-}$), which can stabilize high-valent metal centers, provide an auxiliary binding-site for a second metal ion, and contains a pendant arm that can provide hydrogen-bond stabilization as well as facilitate proton shuttling. The work presented in this dissertation describes my efforts to access high-valent homo-/heterobimetallic oxido and hydroxido species by a variety of synthetic routes.

Chapter 1 provides an overview of bimetallic proteins, and efforts by chemists to synthetically model the structure and function of these active sites. Previous work performed in the Borovik Lab to approach these synthetic challenges is discussed.

Chapter 2 explores the oxidation chemistry of the mononuclear complexes Fe^{II}– and Fe^{III}–hydroxido complexes in the $[poat]^{3-}$ framework, which serve as important synthons in the stepwise

assembly of subsequent bimetallic complexes. While previous members in the Borovik Lab have studied these complexes, the electrochemical properties of these compounds are reassessed in my effort to access high-valent Fe–hydroxido species.

Chapters 3 and 4 introduce the synthesis and characterization of discrete heterobimetallic complexes, with an M^{II}–OH–Fe^{III} or M^{II}–O–Fe^{IV} core (M = Zn, Cu, Ni). This stepwise assembly approach allows for the formation of dinuclear compounds in an unsymmetric framework. The Fe center is supported by the $[poat]^{3-}$ ligand, while M^{II} is supported by an N-based macrocycle. These species are compared with bimetallic complexes in similar frameworks.

Chapters 5 describes the preparation of a series of di-Fe compounds with an Fe–O–Fe or Fe–OH–Fe core. These complexes are housed within the same unsymmetric scaffold, and span across four oxidation levels, from $Fe^{II}Fe^{II}$ to $Fe^{III}Fe^{IV}$. This study illustrates the multifunctional nature of the $[poat]^{3-}$ framework, and provides useful insight into the thermodynamic parameters of proton and electron transfers in bimetallic systems. These findings have significant implications for di-Fe containing enzymes, such as ribonucleotide reductase and soluble methane monooxygenase.

Using the synthetic strategies developed in the previous chapters, Chapters 6 and 7 describe the preparation and characterization of a library of FeMn and MnFe complexes to model their biological counterparts. Their structural, electrochemical, magnetic, and reactivity properties are discussed. An Fe^{III}–O–Mn^{IV} species was trapped and studied spectroscopically, and its relevance to similar high valent FeMn active sites is biology is discussed.

Chapter 8 discusses the observation of a rare high-spin Co^{III} center in a bimetallic system *via* different spectroscopic techniques. This is an unusual finding, as most six-coordinated Co^{III} complexes adopt a low-spin configuration due to significant ligand field stabilization. A series of CoFe and CoGa complexes were prepared to probe the factors for this phenomenon, including the P=O groups in $[poat]^{3-}$ being weak field ligands, and modulation of spin exchange interactions.

Chapter 1

Introduction

Lessons from Nature

Metal ions are ubiquitous in biology and aid in facilitating enzymatic processes, including small molecule transformations, energy conversion, and electron transfer processes.[1-3] In particular, metal-catalyzed activation of dioxygen and the reversed reaction of water oxidation are essential for life.[4-10] Elucidating the various factors that control structural changes in these metal-containing active sites can improve the understanding of their functions. These metal ions are often housed deep within a protein structure to avoid undesirable reactivity. While the function of metallocofactors is mainly regulated by the ligands directly bound to the metal ions (primary coordination sphere), there are other effects from the microenvironment around the metallocofactor (secondary coordination sphere), which are usually derived from non-covalent interactions with surrounding amino acid residues.[11-14] These structural factors are best illustrated in the example of the respiratory protein myoglobin (Figure 1.1).[15-18] Its active site contains an iron/porphyrin (commonly known as heme) cofactor that reversibly binds dioxygen. In addition, hydrogen bonding (H-bonding) from a nearby histidine residue helps stabilize the Fe–O_2 adduct.[15] In the absence of this secondary coordination sphere interaction and the steric protection provided by the protein scaffold, the heme cofactor would undergo irreversible oxidation.[19-22] This demonstrates the importance of regulating function through both the primary and secondary coordination spheres of metal centers.

Bimetallic cores in Biological Systems

While the aforementioned myoglobin is one example of the heme family that represents many O_2 binding and/or activating enzymes,[4,16,18] a different class of the non-heme Fe proteins performs similar functions but does not require the prosthetic porphyrin ligand.[6,8-10,23,24] In many of

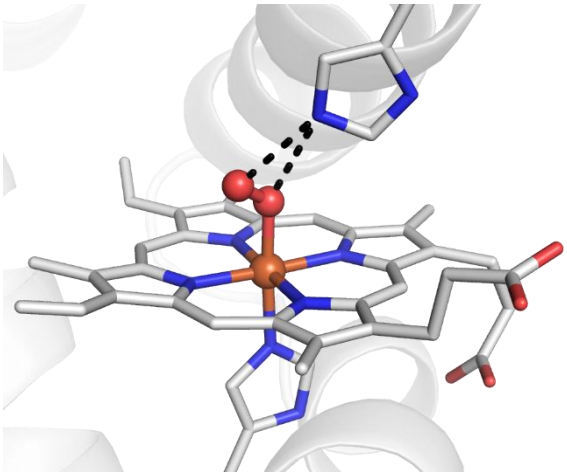

Figure 1.1. Structure of the oxymyoglobin (PDB: 1A6M). Fe is shown as an orange sphere, and O is shown as a red sphere. Dotted lines indicate H-bonds.

these non-heme active sites, such as in α-ketoglutarate dependent and Rieske enzymes, the metal center is supported by the readily available amino acid-derived ligands, and sometimes external cofactors.[25-28] Other non-heme O_2-binding/activating proteins employ a diiron center, and this is likely due to the energetics of dioxygen reduction.[4,9] Full activation of O_2 to H_2O is a 4-electron/4-proton process, but Fe ions have only been observed to access only between the +2 and +4 oxidation states under physiological conditions (i.e., a two-electron range).[20-31] Nature has evolved to circumvent these thermodynamic limitations *via* the addition of sacrificial reductants or adoption of other reaction pathways.[23,25,32,33] Another common mean is to employ a diiron site in place of a mononuclear one, as the conversion from $Fe^{II}Fe^{II}$ to $Fe^{IV}Fe^{IV}$ represents a 4-electron process that match the full activation of dioxygen.[34,35] In addition, the two metal centers can perform their functions in a cooperative manner through both structural rearrangement and electronic/magnetic exchange. These properties are best depicted in the following examples of diiron enzymes: hemerythrin, the hydroxylase component of soluble methane monooxygenase (sMMOH), and the R2 subunit of ribonucleotide reductase Class Ia (RNR R2 Ia).

Hemerythrin, a non-heme respiratory protein similar to myoglobin, binds O_2 reversibly (Figure 1.2.A).[36,37] In its resting state, two Fe^{II} ions are covalently bridged through one hydroxido and two carboxylate-based amino acids. The coordination sphere of one Fe center is completed with three histidine residues, while the other Fe is bound to only two histidines; this produces an unsymmetric core (Figure 1.2.B), in which one Fe center is coordinatively saturated (six-coordinated), and the other has one open coordination site (five-coordinated). Upon introduction of dioxygen, both Fe sites are oxidized to +3, and the reduced O_2^{2-} adduct binds to the Fe center with the open coordination site in a terminal fashion. In addition, the proton on the hydroxido bridge transfers to the distal oxygen of the peroxido ligand, and the OOH^- moiety in turns forms an intramolecular H-bond with the oxido bridge.[38,39] Notice that the H-bond stabilization found in hemerythrin is different from that in myoglobin, in which the O_2 adduct is stabilized *via* H-bonds to a histidine residue in the microenvironment of the active site (Figure 1.1).[15] In addition, hemerythrin employs both Fe centers to bind and reduce dioxygen to peroxido, while myoglobin reduces O_2 by just one-electron to superoxido.

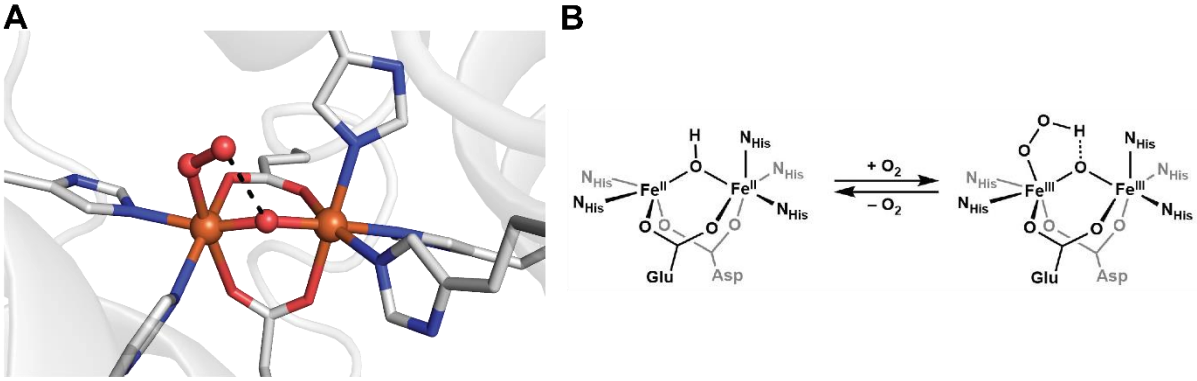

Figure 1.2. (A) Structure of the oxyhemerythrin (PDB: 1HMD). Fe is shown as an orange sphere, and O is shown as a red sphere. Dotted lines indicate H-bonds. (B) Mechanism of reversible O_2 binding in hemerythrin.

In the oxygenated form of hemerythrin, the O–O bond is partially activated but not fully cleaved; this is attributed to the N-rich coordination spheres of the Fe centers. Replacement of histidines with carboxylate-based amino acids in other diiron enzymes show significant changes to

their reactivity, as the anionic O-donors are proposed to better support high valent metal centers.[40,41] The carboxylate groups can also bind in either a mono- or bidentate fashion to one or both Fe centers, and this interchangeability allows for a flexible primary coordination sphere, in which coordination sites become available at key steps of the catalytic turnover.[42,43] In the active site of sMMOH, which converts methane to methanol, the diiron centers are bound to two histidines and four carboxylate ligands (Figure 1.3.A).[44-46] Addition of dioxygen first forms the putative Intermediate P that contains a Fe^{III}–(*μ*-1,2-peroxo)–Fe^{III} core,[47-49] and then full cleavage of the O–O bond results in a $Fe^{IV}Fe^{IV}$ intermediate termed Q (Figure 1.3.B).[44,50-52] This high valent species cleaves the strongest known aliphatic C–H bond (105 kcal mol^{-1}) in methane,[53,54] then a hydroxido group likely recombines with the methyl radical *via* a rebound mechanism to produce methanol, similar to what is observed for other non-heme and heme oxygenases.[23,25,29,55-57] Due to its unusual reactivity and the potential applications towards energy storage, the chemical structure of Q has been interrogated by a myriad of spectroscopic techniques in the past two decades, and remains controversial to this day.[34,44,58] Initially, Mössbauer spectroscopy suggested the electronic structures of the two Fe^{IV} sites are nearly equivalent, and it was believed that Q contained an $Fe^{IV}{}_2(O)_2$ "diamond" core due to a short Fe···Fe distance (2.46 Å) found in an extended X-ray absorption fine structure (EXAFS) study.[59] However, this structural assignment was inconsistent with results observed in synthetic models and computational studies on the enzyme.[60-65] Recently, the Fe···Fe distance in Q was re-evaluated to be ~ 1 Å longer than the previously reported value, which suggests the diiron site is more likely to adopt an "open" core structure.[66,67] Neese and DeBeer further correlated computational results with reported experimental data for Q, and proposed a (O=)Fe^{IV}–(*μ*-O)–Fe^{IV}(–OH) core, with the hydroxido motif in a strong H-bond interaction.[68] While the structure of Q remains ambiguous, the active site of sMMOH illustrates several important features. The bimetallic core can undergo a 4-electron process to fully reduce O_2 to two equivalents of O^{2-},

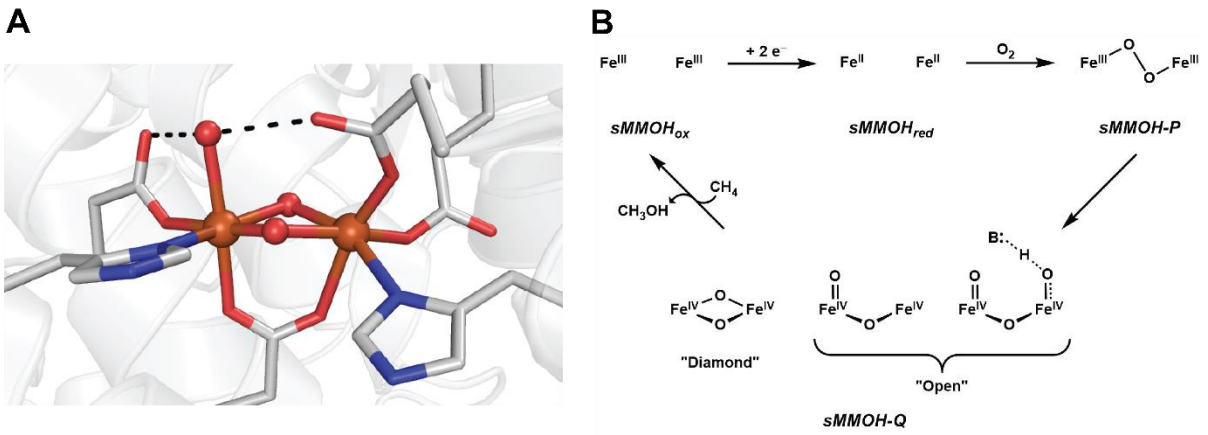

Figure 1.3. (A) Structure of the oxidized form of sMMOH (PDB: 1MHY). Fe is shown as an orange sphere, and O is shown as a red sphere. Dotted lines indicate H-bonds. (B) Proposed mechanism of O_2 activation in sMMOH. Several proposed structures of Intermediate Q are shown.

and the anionic O-donors support the Fe centers in accessing the +4 oxidation states.[59] Additionally, the flexible binding modes of the carboxylate group (mono- versus bidentate, binding to one or both metals, intramolecular H-bond) provide a dynamic coordination sphere around the dinuclear core and help facilitate reactivity, which highlight the importance of multi-functional ligands.[42,43]

The active site of RNR R2 Ia resembles to that found in sMMOH, in which a diiron core is coordinated by two histidine and four carboxylate-based ligands (Figure 1.4.A),[69,70] but they differ in function. In RNR, oxygenation first occurs at the diiron core in the R2 subunit, which initiates a long-range electron transfer (ET) that spans > 30 Å to the R1 subunit, where a ribonucleotide is reduced to a deoxynucleotide.[71-74] Another difference is the oxidation level of the key intermediate: upon reaction with dioxygen, an additional equivalent of e^- is required to form Intermediate X that is formulated as a Fe^{IV}–(μ-O)–Fe^{III} core (Figure 1.4.B), which is one valence level below sMMOH-Q.[75,76] X proceeds to cleave the O–H bond of a tyrosine residue in the microenvironment of the active site *via* a proton-coupled electron transfer (PCET) reaction, and the resultant tyrosyl radical initiates the ET process. Mutation of the tyrosine to phenylalanine suppresses the PCET and subsequent ET processes, which proved useful for the trapping and spectroscopic studies of X, but

it also eliminated the native function of the enzyme.[76-78] This represents an example of the modulation of function in the secondary coordination sphere of a dinuclear active site.

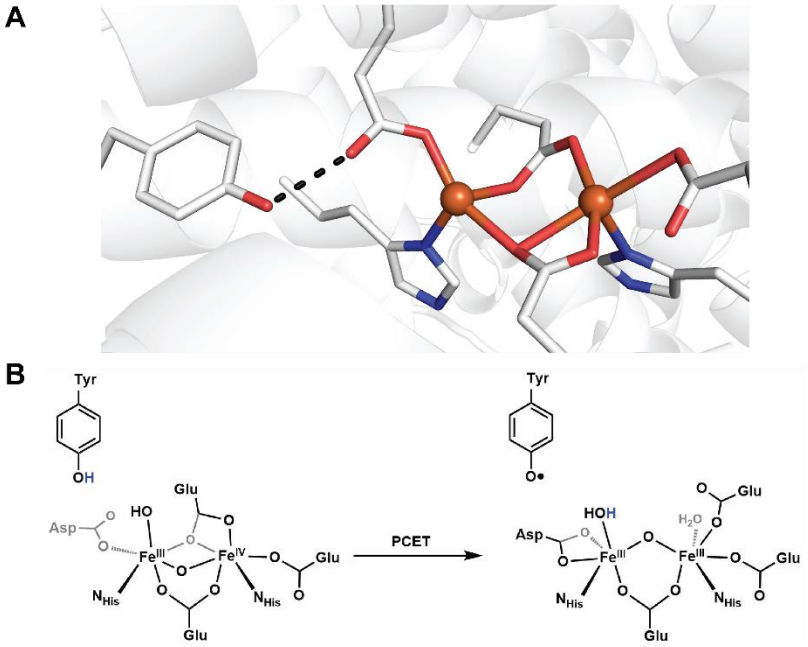

Figure 1.4. (A) Structure of the R2 subunit of class Ia RNR (PDB: 1PIY). Fe is shown as an orange sphere, and O is shown as a red sphere. Dotted lines indicate H-bonds. (B) Proposed mechanism of the tyrosine O–H bond cleavage by Intermediate X.

Three examples of diiron non-heme enzymes were described so far, and the correlations between function and the unique characteristics of their primary and secondary coordination spheres were discussed. While FeFe enzymes constitute a large fraction of bimetallic proteins, there is a growing library of other homobimetallic (e.g., MnMn) and heterobimetallic enzymes (e.g., FeMn) that perform similar functions.[79-85] For instance, the R2 subunit of RNR Class Ic and R2-like ligand-binding oxidase (R2lox) both contain an FeMn active site and activate dioxygen, but have been experimentally shown to undergoes significantly different reaction pathways than their diiron counterparts (Figure 1.5; see Chapters 6 and 7).[86-94] Much is still unknown about these active sites, and it is the goal of synthetic chemists to design inorganic complexes to model these biological cores to study their structure/function relationship.

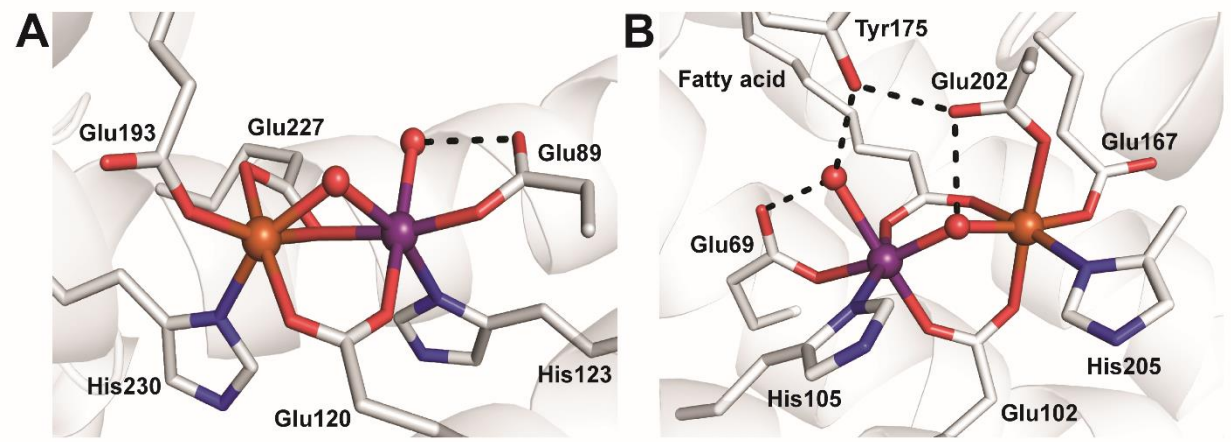

Figure 1.5. Structures of the RNR R2 Class Ic (PDB: 4M1I) and R2lox (PDB: 4HR0) active sites. Fe is shown as an orange sphere, Mn is shown as a purple sphere, and O is shown as a red sphere. Dotted lines indicate H-bonds.

Synthetic Design Principles

The non-heme biological active sites containing a dinuclear core have provided us insights into designing bimetallic model complexes. A list of synthetic design principles is considered and summarized here:

1) Regardless of the identity of the metal, a M–O–M' core is experimentally observed or proposed for the catalytically competent species in bimetallic O_2-binding/activating enzymes.[36,44,72,85,88,94-97] The O-atom can be derived from an oxido or hydroxido ligand, or even an O-atom from an amino acid residue. This single-atom bridge not only keeps the dinuclear core intact during catalysis, but also facilitates magnetic coupling and electron transfer between the two metal centers.[19,34,35,40] There are often additional single-/multiple-atom bridges, as well as terminal ligands (e.g. oxido), bound to the M–O–M' core. Flexible binding of ligands can also be important in modulating function.[42,43]
2) To perform their designated functions, the redox-active metal centers are at a low oxidation level (+2) in their resting states, and can access higher valence levels (+3, +4) during the catalytic turnover. In all non-heme enzymes, these metal sites maintain a high-

spin electron configuration at all oxidation states.[34,59] For example, the Fe^{IV} and Fe^{III} centers in RNR R2-X are experimentally verified to be $S = 2$ and 5/2, respectively.[76]

3) Biological active sites often adopt an unsymmetric scaffold to optimize their function. This is best illustrated in hemerythrin, which contains one coordinatively unsaturated Fe^{II} site that allows for the reversible binding of dioxygen.[38] It has also been observed a narrow channel from the surface of sMMOH into the diiron active site only allows for the entry of methane, but not ethane or longer alkane chains.[98-100] These findings support the notion that the complex tertiary structure of a protein dictates the reactivity of the active site within.
4) Similar to their mononuclear counterparts, bimetallic active sites utilize secondary coordination sphere interacts to modulate function. In the example of RNR Class Ia, intermediate X undergoes PCET with a tyrosine residue in the microenvironment to initiate the long range ET to the other subunit.[71-74] Mutation of the tyrosine to phenylalanine suppresses the native function of the protein.[76-78]

Synthetic Strategies of Non-heme Bimetallic Species

The prominence of bimetallic active sites in biological systems has prompted the development of synthetic models to elucidate their structure/function relationship. The preparations of discrete bimetallic compounds generally fall into three categories (Figure 1.6). The first strategy is a self-assembly approach, which relies on two mononuclear complexes that do not normally interact to bind *via* the addition of exogenous ligand(s) (Figure 1.6.A). While this strategy is synthetically straightforward, there is little selectivity over the metal and exogenous ligand binding modes, and these problems are significantly enhanced in the preparation of heterobimetallic complexes. The second method is through the usage of dinucleating ligands, which provide defined primary and

secondary coordination spheres for metal centers (Figure 1.6.B). Additionally, any remaining open coordination sites can be predicted in the original ligand design, and exogenous ligands can be systematically incorporated after metalation. These organic scaffolds are often large and pose a synthetic challenge, and, similar to the self-assembly route, provide little selectivity in binding different metal ions. The third method is a site-directed binding approach (Figure 1.6.C): one mononuclear complex contains pendant group(s)/exogenous ligand(s), which can bind to a second mononuclear complex that contains open coordination site(s). This route provides the highest binding selectivity, and is most suitable for assembly of complexes with different metals and/or ligands. These three approaches are not mutually exclusive and can overlap in synthetic preparations.

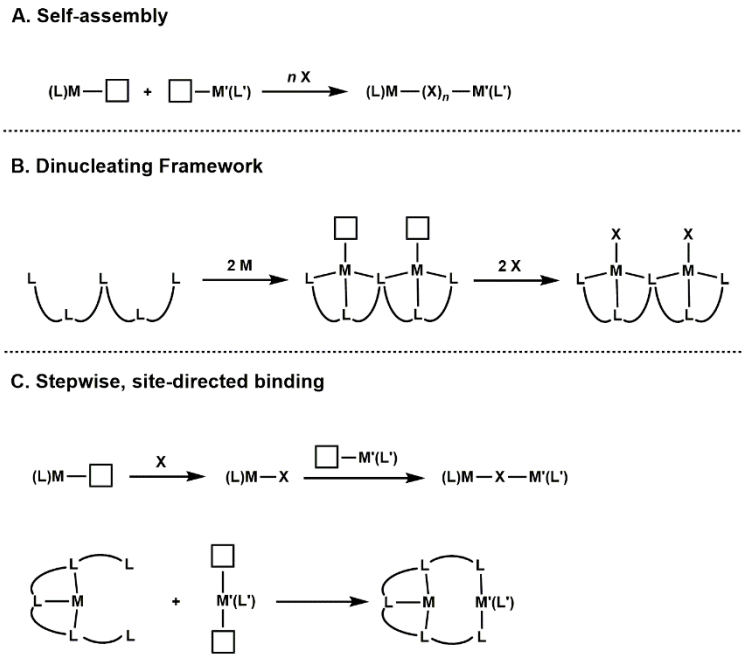

Figure 1.6. The three general approaches to assemble bimetallic complexes: (A) self-assembly, (B) dinucleating frameworks, and (C) stepwise, site-directed binding. White squares represent open coordination sites.

A large portion of bio-inspired non-heme bimetallic complexes were prepared using the self-assembly approach: this is epitomized by the development of diiron systems, largely due to the thermodynamically favorable formation of Fe^{III}–(μ-O)–Fe^{III} cores, which is the basic unit of rust. While synthetic diiron complexes have been known for decades,[101] a growing number of structural

reports of diiron proteins prompted an increase in the synthetic modeling of these active sites since the 1980s.[19] These efforts were led by the laboratories of Wieghardt and Lippard, who synthesized the first diiron compounds with an Fe^{III}–(μ-O)(μ-1,3-OAc)$_2$–Fe^{III} core that resembles the resting state of hemerythrin (Figure 1.7.A,B).[102-104] These contributions are important to the field not only due to their biological relevance, but also the systematic incorporation of different exogenous bridging ligands. The synthetic protocols for these complexes are straightforward: in a typical one-pot experiment, an Fe^{III} salt, a tridentate N-based ligand ([TACN], 1,4,7-triazacyclononane; or $[HBpz]^-$ = trispyrazolylborate), and an acetate salt are mixed in water to selectively produce the corresponding diiron complex with one bridging oxido ligand and two bridging acetate ligands. While Wieghardt expanded the library of self-assembled bimetallic complexes to include heterobimetallic species as well as unsymmetric frameworks,[105,106] Kitajima and then Lippard explored the oxygenation chemistry of the Fe/$[HBpz]^-$ system, and the latter was able to trap and crystallographically characterize an Fe^{III}–(μ-1,2-peroxo)–Fe^{III} species.[107,108] In the past ~ 20 years, the laboratory of Que made significant advances in synthetic diiron chemistry using the peroxide shunt pathway in the tris(2-methylpyridine)amine ([TPA]) and related frameworks.[34] In a seminal work, a μ-oxido diiron(III) compound was first self-assembled with Fe^{III} hydrate salts and 5-R-TPA (R = alkyl), and addition of H_2O_2 produced a high valent species;[109] structural and spectroscopic studies support the formulation of $[Fe^{IV}Fe^{III}(\mu\text{-}O)_2(5\text{-}Et\text{-}TPA)]^{3+}$ for the new complex (Figure 1.7.C), which represents the first and only crystallographically characterized Fe^{IV}–(μ-O)$_n$–Fe^{III} core.[108] Que then developed a series of high valent diiron complexes in the [TPA*] framework (tris(2-methyl-3,5-dimethyl-4-methoxypyridine)amine) that span from the (III,III) to (IV,IV) oxidation levels, and contain terminal and/or bridging (hydr)oxido ligands; these serve as useful synthetic models for the RNR R2-X and sMMO-Q intermediates.[34,111-115] Finally, it is worth highlighting the contributions of Collins, who treated the mononuclear $[Fe^{III}TAML(OH_2)]^-$ with O_2 to produce a room temperature-

stable $[Fe^{IV}_2(\mu\text{-O})(TAML)_2]^{2-}$ species (Figure 1.7.D), allowing for its crystallographic characterization;[116] the high stability of this complex can be attributed to its tetraanionic ligand field.[117] This summary highlights the crucial role of the self-assembly protocol to the development of synthetic diiron model complexes in the past three decades, as well as other homobimetallic analogs (e.g., dimanganese,[118-121] dicopper,[122,123] diruthenium,[124,125] dilanthanide,[126,127] etc). However, the dearth of heterobimetallic complexes and dinuclear complexes in unsymmetrical frameworks produced using this approach emphasizes the limitations of this method.

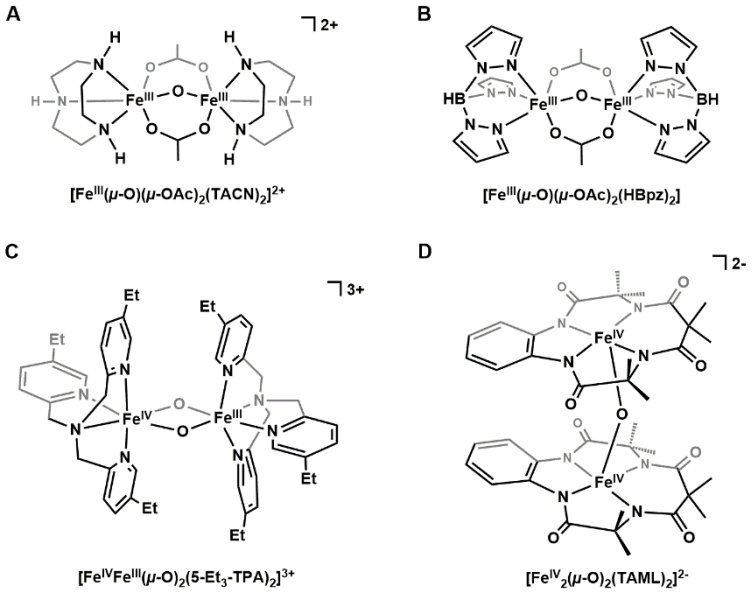

Figure 1.7. Various examples of self-assembled diiron complexes. Works of Wieghardt (A) and Lippard (B) to model the active site of hemerythrin initiated the next four decades of investigation into bioinspired synthetic diiron systems. Que and Collins structurally characterized a $Fe^{IV}Fe^{III}$ (C) and $Fe^{IV}Fe^{IV}$ (D) species, respectively.

The usage of dinucleating ligands is an attractive option to construct bimetallic complexes, as careful design of the framework can provide defined primary and secondary coordination spheres for metal centers. An example of a dinucleating ligand is [6-HPA] (1,2-bis[2-{bis(2-pyridylmethyl)aminomethyl}-6-pyridyl]ethane), which essentially is composed of two covalently-linked [TPA] ligands. Kodera prepared a $(\mu$-oxido$)Fe^{III}_2$ complex that exhibited efficient alkene epoxidation in the presence of H_2O_2,[128] and proposed some intriguing intermediates responsible for the reactivity (Figure 1.8.A). Many other groups have also adopted this approach and utilized

increasingly complex frameworks.[129-131] Suzuki isolated a Fe^{III}–(μ-1,2-peroxo)–Fe^{III} species in the [Ph-bimp] ligand (2,6-bis[bis-2-(1-methyl-4,5-diphenylimidazolyl)methylaminomethyl]-4-methylphenolate), which contains imidazole and a bridging phenolate donors;[132] this illustrates the ability to exploit metal–metal cooperativity in dinucleating ligands (Figure 1.8.B). Meyer has designed many dinucleating frameworks using a central pyrazolate bridging group,[133] and explored various small molecule transformation using homobimetallic complexes (Figures 1.8.C, D), including H_2 reduction in a dinickel system,[134,135] O_2 binding in dicopper,[136,137] and water oxidation in diruthenium,[138,139] and more.[140,141] Today, the complexity of dinucleating frameworks is truly a reflection of the advances made in organic synthesis and ligand design in the past several decades. However, these scaffolds, most of which are symmetric, are often difficult to prepare and require much synthetic efforts; developing unsymmetric dinucleating frameworks would be an additional challenge. There is also little selectivity in preparing heterobimetallic complexes, with only a few examples reported.[129,130,142]

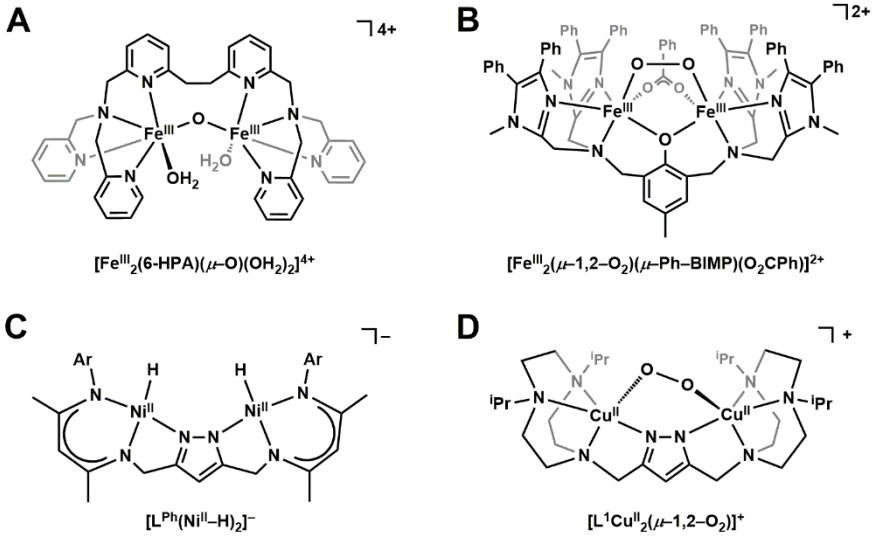

Figure 1.8. Various examples of bimetallic complexes in dinucleating frameworks, including a diiron complex that catalyzes alkene oxidation by Kodera (A), a structurally characterized μ-1,2-perixodo diiron species by Suzuki (B), and dinucleating systems using a pyrazolate linchpin group by Meyer (C and D).

The third general way to assemble bimetallic complexes is a stepwise, site-directed approach. The method requires one mononuclear complex to contain additional pendant group(s) and/or exogenous ligand(s), which can bind to a second metal ion/adduct with open coordination site(s). For instance, Nam reported the isolation of a Fe–(*μ*-O)–Sc species upon addition of $Sc^{III}(OTf)_3$ to $[(TMC)Fe^{IV}(O)]^{2+}$ ([TMC] = 1,4,8,11-tetramethyl-1,4,8,11-tetra-azacyclotetradecane).[143] Further computational studies by Swart[144] and spectroscopic studies by Que and Münck[145] support the assignment of a Fe^{III}–(*μ*-O)–Sc^{III} (Figure 1.9.A): reduction at the Fe center increases the nucleophilicity of the terminal oxido ligand, which then binds to the Sc^{III} ion. Que has since employed the same strategy to use high-valent M–oxido starting synthons and prepare a library of bimetallic complexes with a single-atom oxido-bridge.[146,147] Other groups, including Lu,[148-150] Thomas,[150-152] and Heyduk[154-155] have designed ligands that form mononuclear complexes, but these

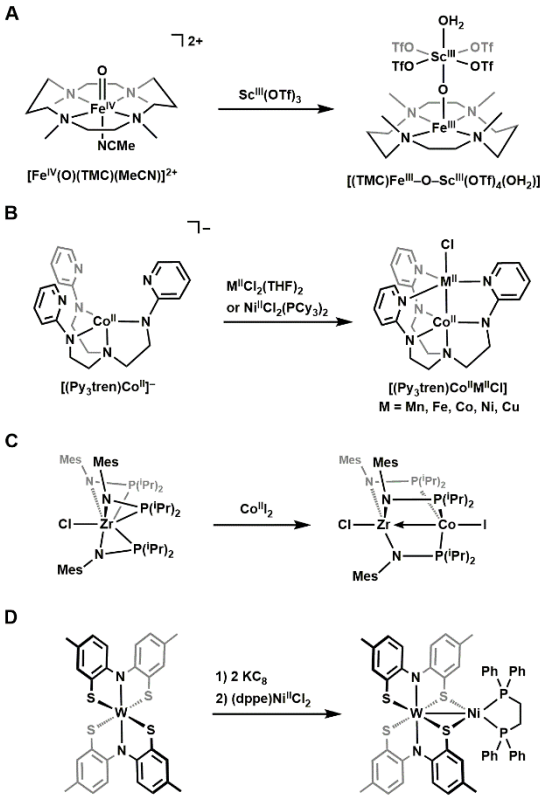

Figure 1.9. Examples of heterobimetallic complexes synthesized *via* the stepwise, site-directing binding approach. Nam and Que bound a Sc^{III} ion to $[(TMC)Fe^{IV}(O)]^{2+}$ at the exogenous oxido ligand (A), while Lu (B), Thomas (C), and Heyduk (D) incorporated pendant binding sites to assembly bimetallic compounds.

frameworks contain pendant groups that can act as an auxiliary binding site and support a second metal ion/adduct (Figures 1.9.B,C,D). The stepwise, site-directed method is highly selective, and is most commonly employed for the assembly of heterobimetallic complexes.

This section has summarized three general methods in assembling bimetallic bio-inspired synthetic complexes and provided examples of key accomplishments using each approach. While they are all important contributions to the field, many of these systems do not satisfy the design principles for model complexes for biological active sites as discussed above. For instance, many Fe^{IV}-containing complexes are intermediate spin ($S = 1$),[34,106,109-112,116] which differ from those found in biological systems: this difference is important because electronic structure is often correlated with reactivity.[156-158] Moreover, the majority of the bimetallic complexes have a symmetric ligand framework, while most biological active sites are unsymmetric to optimize key processes in the catalysis, such as substrate binding and electron transfer.[38,39,42,43,69,70] Finally, the microenvironment around a metallocofactor in proteins has been demonstrated to play a significant role in modulating reactivity.[7,11-13] While the effects of the secondary coordination sphere on mononuclear synthetic systems have been well-investigated, similar studies are rarely explored for bimetallic systems (see below). Future efforts should therefore be directed at addressing these unexplored questions.

Secondary Coordination Sphere Interactions in Synthetic Systems

Metalloenzymes have evolved to modulate the reactivity of key metal ion-containing intermediates via non-covalent interactions that are formed with the aid of amino acid residues. Although much progress has been made, establishing such microenvironments within synthetic frameworks has proven difficult. The seminal work by Collman utilized a functionalized porphyrin to stabilize an $Fe–O_2$ adduct.[159] Pendant groups containing H-bond donating pivalamide groups were installed at the *meso*-positions of the porphyrin, and the "picket fence" framework prevented

undesired irreversible oxidation of the Fe porphyrin complex and formation of a Fe^{III}–(μ-O)–Fe^{III} species (Figure 1.10). However, the pivalamide groups were too far to form any H-bond interactions with the O_2 adduct in the molecular structure (> 5 Å).[160] Replacement of one pivalamide group with the stronger H-bond donating phenylurea moiety increased the O_2 affinity of the Fe-porphyrin, but no molecular structure was reported.[161]

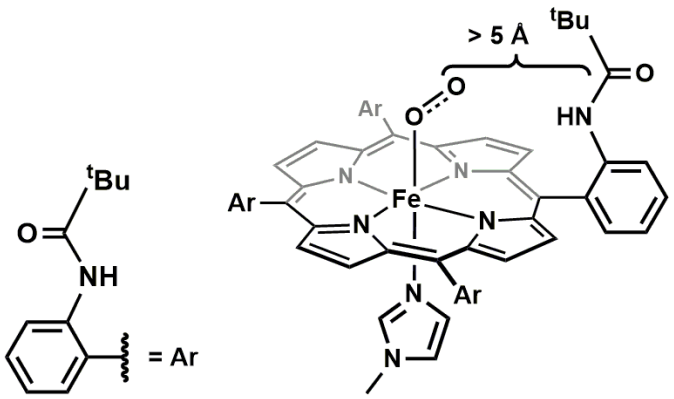

Figure 1.10. Structure of a picket fence porphyrin complex supporting an Fe–O_2 adduct.

Incorporations of H-bond interactions in synthetic non-heme mononuclear complexes have made significant progress in the past ~ 20 years, and allowed for the stabilization of many biologically relevant species, including M–O_2 adducts,[162-166] M–(hydr)oxido,[167-176] M–hydride,[177,178] and M–N_2 adducts;[179,180] several examples are illustrated in Figure 1.11. It has also been demonstrated H-bond interactions can modulate reactivity.[181] For instance, Fout varied the number of intramolecular H-bonds in a Fe^{III}–OH complex, which affects its OH–rebound reactivity towards carbon radicals (Figure 1.11.E).[182] Similarly, Jackson recently found minimal reactivity of a mononuclear Mn^{III}–OH species towards organic substrates;[183] upon the redesign of the ligand to incorporate an H-bond acceptor, the repurposed Mn^{III}–OH species exhibited significantly enhanced reactivity by up to 100-fold (Figure 1.11.F). These reports support the notion that the microenvironment around a metal site can play an important in modulating structure and function.

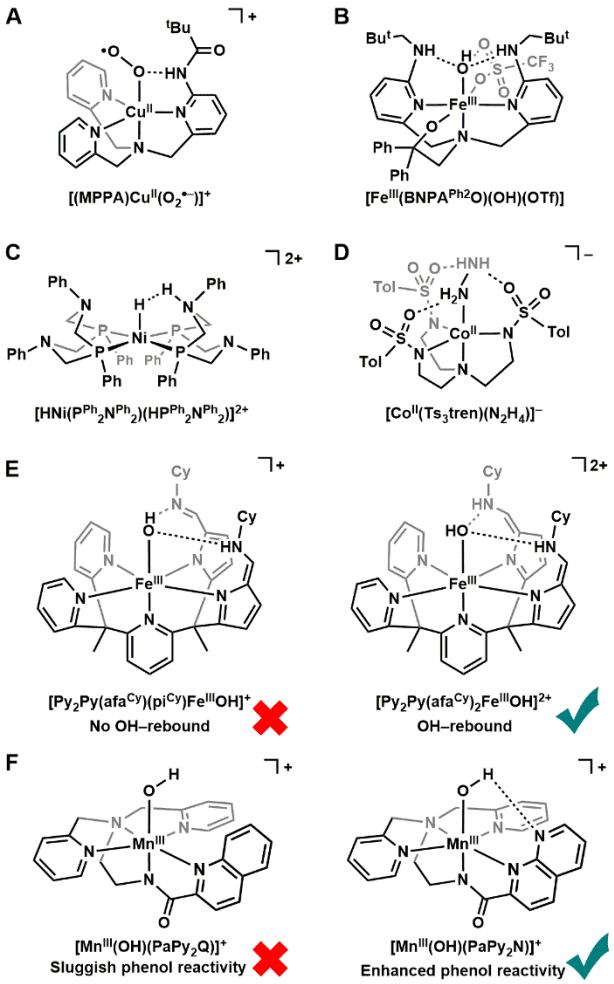

Figure 1.11. Examples of mononuclear complexes with intramolecular H-bond interactions, including Cu^{II}–superoxido (A), Fe^{III}–hydroxido (B), Ni^{II}–hydride (C), and Co^{II}–hydrazine (D). H-bond interactions have also been found to facilitate reactivity, including OH–rebound (E) and phenol O–H bond cleavage (F).

The effects of other types of secondary coordination sphere interactions have also been explored. Szymczak has incorporated various boron-containing pendant groups in his ligand frameworks, and has demonstrated the Lewis acidic boron is crucial in the capture and activation of N_2 adducts (Figure 1.12.A).[184-188] Other groups have introduced electrostatic interactions near the metal center to modulate reactivity. For instance, Yang attached a crown-ether linkage to a Mn^V(N)(salen) complex ([salen]$^{2-}$ = 2,2'-ethylenebis(nitrilomethylidene)diphenolate,*N*,*N*'-ethylenebis(salicylimine)), and found different N–N bimolecular coupling reactivity upon

introduction of redox-inactive Group I and II metal ions (Figure 1.12.B).[189] These studies show that secondary coordination sphere effects extend beyond H-bond interactions.

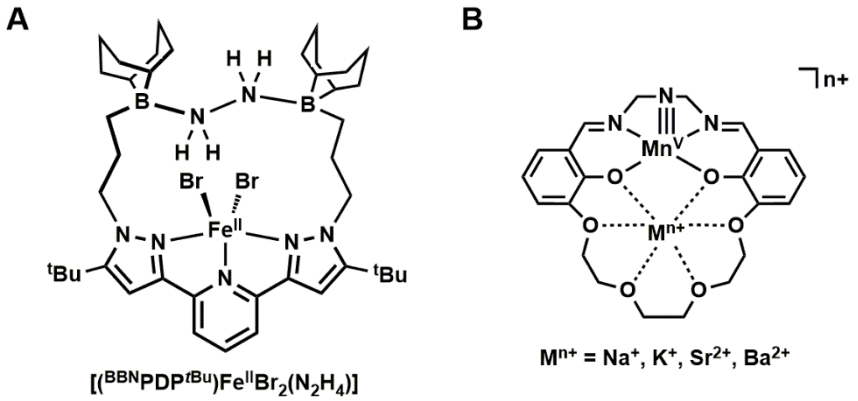

Figure 1.12. The secondary coordination sphere facilitates the function, e.g., capturing N_2H_4 for activation by an Fe complex shown by Szymczak (A), and increased bimolecular N–N coupling reactivity in a Mn^{VI}–nitrido complex in the presence of a modulated electrostatic field shown by Yang (B).

Although much progress has been made in the study of secondary coordination effects on non-heme mononuclear complexes, there are only a few examples of the bimetallic counterparts. Szymczak treated O_2/H_2O_2 to a mononuclear Cu or Zn complex in a modified [TPA] ligand that contains appended H-bond donating groups, and was able to isolate dinuclear complexes with a M–(*μ*-1,2-peroxo)–M core; the H-bond donors in the ligand are shown to be interacting with the peroxido adduct in the molecular structure (Figure 1.13.A).[190,191] In a similar self-assembly approach, Fout recently reported a diferric compound that contains a $(HO)Fe^{III}$–(*μ*-O)–$Fe^{III}(OH)$ motif, in which the terminal hydroxido ligands are H-bonded to the pendant alkyl amine groups in the [^{Py}N(afa^{Cy})] scaffold (Figure 1.13.B).[192] While further oxidative chemistry has not been reported, the diiron core and the secondary coordination sphere interactions present in this compound highly resemble the structure of Intermediate Q in sMMOH proposed by Neese and DeBeer (Figure 1.3.B),[68] and may serve as an important model complex for this enzyme in the future. There is also some success in incorporating H-bonds in dinucleating frameworks.[193] For instance, Meyer installed H-bond donating pivalyl groups in his pyrazolate-based ligands, and isolated a dinickel(II) complex

containing a terminal hydroxido and aqua ligands in an intricate H-bond network (Figure 1.13.C).[194] These reports demonstrate that incorporation of secondary coordination sphere interactions in bimetallic complexes is possible, but can prove to be a substantial synthetic challenge.

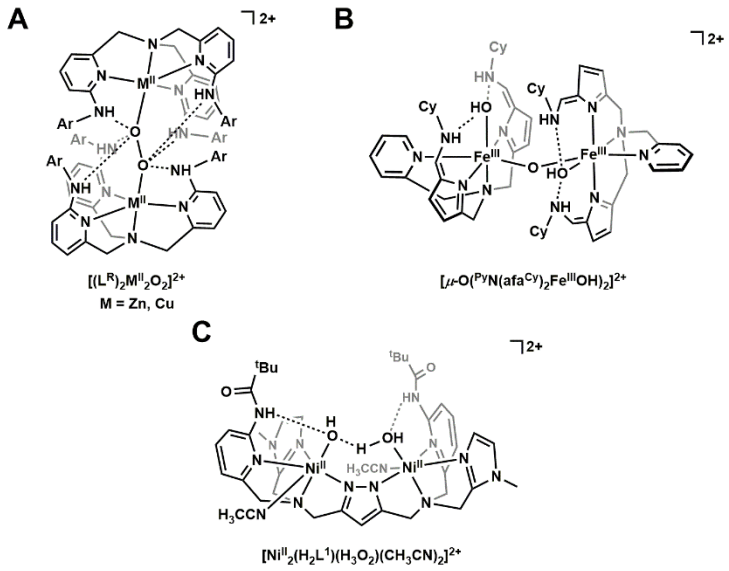

Figure 1.13. Various examples of bimetallic complexes with intramolecular H-bond interactions, including self-assembled species reported by Szymczak (A) and Fout (B), and a dinucleating system by Meyer (C).

Previous Work in Borovik Lab

The Borovik Lab has developed a large library of tripodal ligands that incorporate H-bond donors and/or acceptors to stabilize mononuclear M–OH_n (n = 0, 1, 2) species.[10-12] The prototype framework $[H_3buea]^{3-}$ (tris[(*N*'-*tert*-butylureaylato)-*N*-ethyl]aminato) demonstrates the key ligand design features: (1) it contains three anionic N-donors to support high valent metal centers (up to +5); (2) the ureate N–H groups provide H-bond interactions to stabilize an axial exogenous ligand (e.g. oxido); (3) the *tert*-butyl groups provide steric protection to avoid complex dimerization/aggregation.[195,196] The isolations of $[Fe^{III}H_3buea(O)]^{2-}$ and $[Fe^{IV}H_3buea(O)]^{-}$ are two of the many key achievements using this framework (Scheme 1.1).[196-199] However, while the features of this tripodal ligand are suitable for mononuclear complexes, high valent bi-/multi-metallic species cannot be assembled due to the steric bulk of the ethylene backbone and the *t*Bu groups.[200]

$[H_3buea]^{3-}$ was subsequently re-designed, and one of the ureate arms was removed in the tridentate $[H_21]^{2-}$ ligand (bis[(*N*'-*tert*-butylureido)-*N*-ethyl]-N-methylaminato).[201] With additional coordinate sites available in the equatorial plane, bimetallic diiron(III,III) complexes containing oxido- and imido-bridging motifs can be prepared, with the ureate arms also serving as bridging groups and H-bond donors to stabilize the bent Fe^{III}–(*μ*-O/N)–Fe^{III} core (*d*(Fe···Fe) ~ 3 Å; Scheme 1.1).[202] However, further oxidation chemistry of these complexes was not accessible.

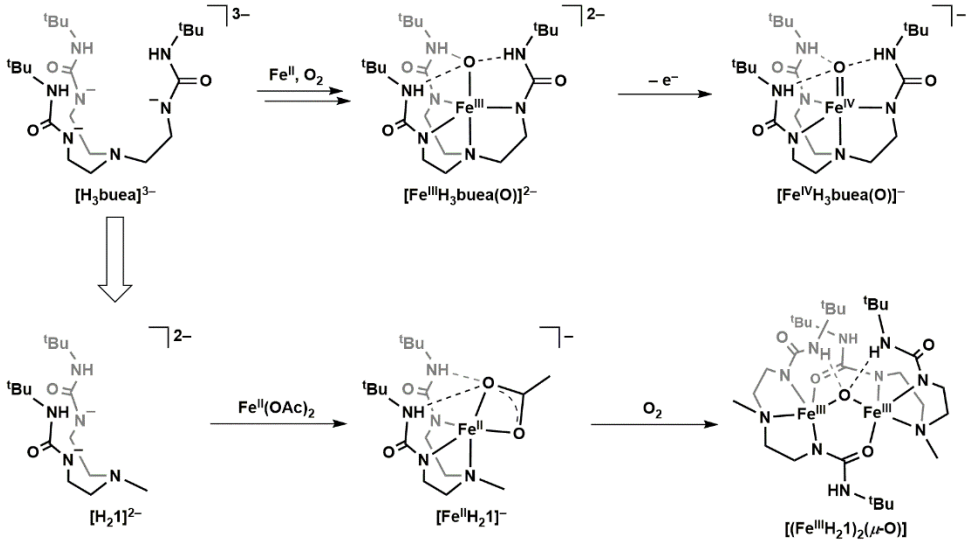

Scheme 1.1. The $[H_3buea]^{3-}$ ligand supports mononuclear Fe–oxido complexes, while the truncated $[H_21]^{2-}$ framework allows for the formation of diiron complexes.

In a parallel study, the Borovik Lab developed homobimetallic complexes in various dinucleating ligands that contain a central pyrazolate "linchpin" group and various H-bond donating arms, inspired by the work of Meyer (see above).[203-206] The larger M···M separation (> 3.5 Å) allowed for installation of exogenous terminal ligands (e.g., hydroxido), as commonly observed and/or proposed for essential intermediates in bimetallic enzymes. The combined effects of metal-metal cooperation and the secondary coordination sphere are best illustrated in the hydration of acetonitrile by $[Co^{II}_2H_4P^Rbuam(\mu\text{-}OH)]^{2-}$ (R = *t*Bu, *i*Pr; $[H_4P^Rbuam]^{5-}$ = 3,5-bis{bis[(*N*'-R-ureaylato)-*N*-ethyl]-aminomethyl}-1*H*-pyrazolate; Scheme 1.2).[204] Upon addition of stoichiometric CH_3CN, a di-Co^{II} complex with a bridging $[(CH_3)C(O)N(H)]^-$ ligand can be isolated. It was proposed a CH_3CN

molecule disrupts the Co^{II}–(μ-OH)–Co^{II} core to form independent, terminal Co^{II}–($NCCH_3$) and Co^{II}–OH motifs. Binding to Co^{II} increases the electrophilicity at the central carbon in CH_3CN, and intramolecular H-bonding to the urea N–H and CH_3CN increases the nucleophilicity of the hydroxido ligand; these result in the coupling of the two exogenous ligands to form the $[(CH_3)C(O)N(H)]^-$ adduct. While these homobimetallic systems can serve as useful models for biological active sites, their oxidation chemistry was relatively unexplored.[207] The synthesis of these dinucleating frameworks is challenging (up to 13 steps),[206,208] as is the selective assembly of heterobimetallic cores.

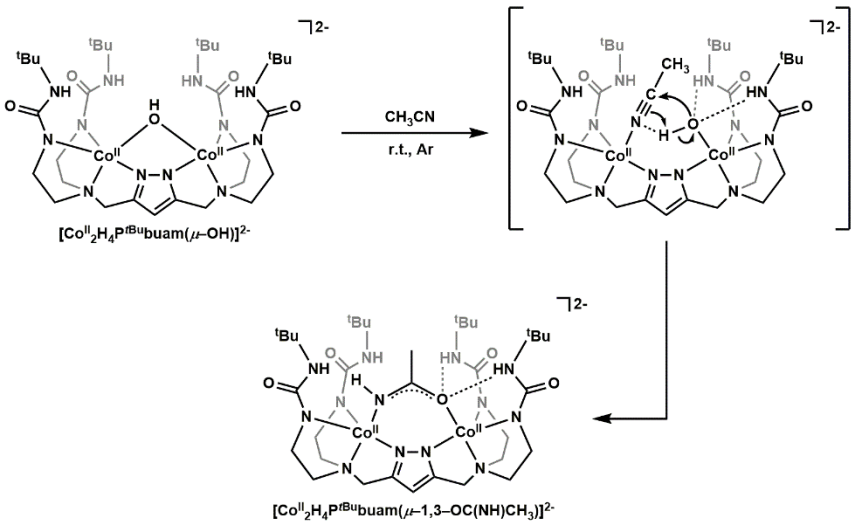

Scheme 1.2. A di-Co complex in the dinucleating ligand $[H_4P^{tBu}buam]^{5-}$ is proposed to use H-bond interactions to facilitate the hydration of acetonitrile.

In the study of the tripodal ligand $[MST]^{3-}$ (*N*,*N*',*N*''-[2,2',2''-nitrilotris(ethane-2,1-diyl)]tris(2,4,6-trimethylbenzenesulfonamido)), which contains sulfonamido groups intended to serve as H-bond acceptors, it was serendipitously discovered the S=O groups can also bind additional metal adducts (Figure 1.14). While the mononuclear $[Mn^{II}MST]^-$ displayed sluggish reactivity towards O_2, the oxidation is accelerated by nearly 100-fold in the presence of $Ca^{II}(OTf)_2$/15-crown-5 (15-c-5), and the final product can be isolated with the formulation of [(15-c-5)⊃Ca^{II}–(μ-OH)–$Mn^{III}MST]^+$;[209] subsequently, a large library of complexes was prepared *via* this stepwise assembly protocol, containing one M^{III} center (M = Mn, Fe, Co, Ga) bound to the N-donors of $[MST]^{3-}$, and a

Group II Lewis acidic metal site (LA^{II} = Ca^{II}, Sr^{II}, Ba^{II}) supported by the S=O groups and a crown-ether capping ligand (15-c-5 or 18-crown-6 (18-c-6)) in the auxiliary binding pocket.[210,211] These findings provided a new route to synthesize discrete heterobimetallic compounds in an unsymmetric scaffold.

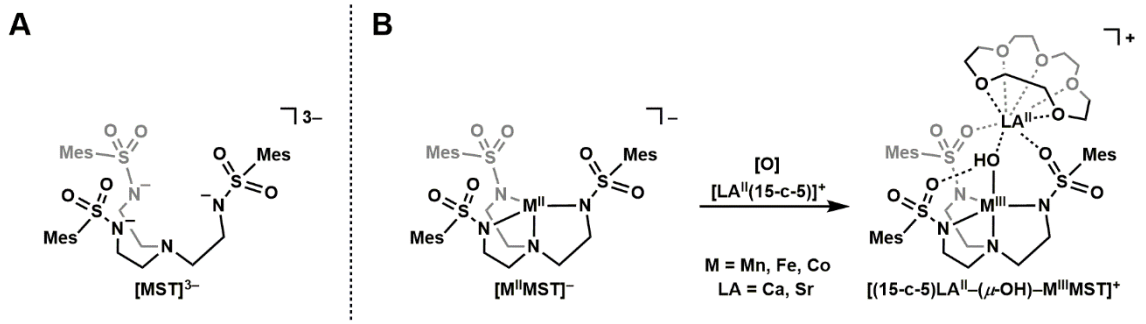

Figure 1.14. (A) Structure of $[MST]^{3-}$. (B) Stepwise assembly of $[(15\text{-c-5})LA^{II}–(\mu\text{-OH})–M^{III}poat]^{+}$ complexes *via* the hydroxido ligand and S=O groups.

The mixed-valent bimetallic $[MST]^{3-}$ library was further extended to incorporate two 3d metals ions, with a M^{III} center (M = Mn, Fe) bound to the N-donors, bridging through a hydroxido ligand to a divalent transition metal ion (M = Mn, Fe, Co, Ni, Cu, Zn) supported by the S=O groups and a [TMTACN] (1,4,7-trimethyl-1,4,7-triazacyclononane) capping ligand; the magnetic interactions between the valence localized metal centers were found to be similar across the series (Figure 1.15.A).[212,213] The tridentate [TMTACN] can be replaced by bidentate ligands such as [TMEDA] (*N*,*N*,*N*',*N*'-tetramethylethane-1,2-diamine), and the remaining coordinate site in the auxiliary metal center can be occupied by an exogenous ligand (Figure 1.15.B).[214] While the versatility of $[MST]^{3-}$ has allowed for construction of bimetallic complexes in an unusual unsymmetric scaffold, the sulfonamido ligand were found to be weak donors: the N-donors cannot support a metal center beyond +3,[215] and the S=O groups cannot support a metal adduct beyond +2. This has precluded synthetic modeling of high-valent bimetallic intermediates observed in nature using the $[MST]^{3-}$ scaffold.

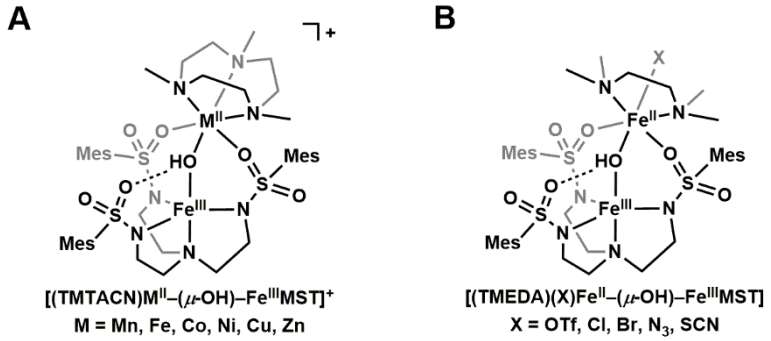

Figure 1.15. Structures of [(TMTACN)Fe^{II}–(μ-OH)–Fe^{III}MST]$^+$(A) and [(TMEDA)(X)Fe^{II}–(μ-OH)–Fe^{III}MST] complexes (B).

To address the limitations of [MST]$^{3-}$, a new tripodal ligand [poat]$^{3-}$ (*N*,*N*',*N*"-[nitrilotris(ethane-2,1-diyl)]tris(*P*,*P*-diphenylphosphinic amido)) was developed (Figure 1.16.A); it was reasoned [poat]$^{3-}$ exhibits similar donor strength as [H$_3$buea]$^{3-}$, and preserves the H-bond accepting and auxiliary metal binding capabilities in [MST]$^{3-}$.[216-218] Additionally, the tripodal ligand enforces trigonal geometry, which promotes high-spin electron configuration for the metal center. The stark difference in the N-atom donability between [poat]$^{3-}$ and [MST]$^{3-}$ is underscored in a recent comparative study between [Fe$^{III/II}$poat(NH$_3$)]$^{0/-}$ and [Fe$^{III/II}$MST(NH$_3$)]$^{0/-}$, in which the Fe$^{III/II}$ reduction potential was found to be 0.57 V more negative in the [poat]$^{3-}$ complex.[219] The strongly donating phosphinic amido groups has also allowed for the successful generation of the S = 2 [Fe^{IV}poat(O)]$^-$; the P=O groups in [poat]$^{3-}$ provide a metal binding site, and the electrostatic effects on the Fe^{IV}–oxido motif by Group II metal binding was studied (Figure 1.16.B).[220] This novel

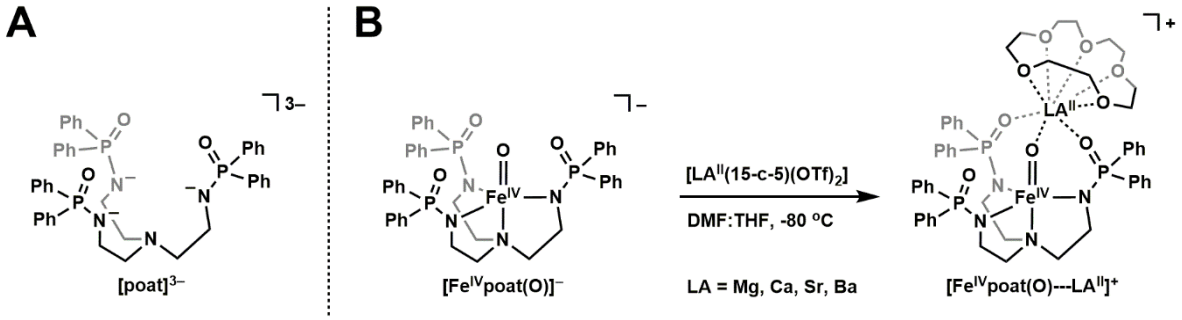

Figure 1.16. (A) Structure of [poat]$^{3-}$. (B) [Fe^{IV}poat(O)]$^-$ binds Group II metal adducts (LA^{II}) *via* the oxido ligand and P=O groups.

[poat]$^{3-}$ ligand offers many exciting opportunities to construct mono- and bimetallic complexes, and is employed heavily in the research discussed in this dissertation.

Overview of the Remaining Chapters

The research described in this dissertation first explores the oxidative chemistry of mononuclear non-heme Fe–hydroxido complexes in the [poat]$^{3-}$ ligand framework, and subsequently their usage as starting synthons to construct homo- and hetero-bimetallic complexes. These systems were interrogated by various structural, spectroscopic, and electrochemical techniques, and serve as useful synthetic models for biological active sites.

Chapter 2. The research described in this chapter re-examined previous work in the Borovik Lab to access a Fe^{IV}–OH species in the [poat]$^{3-}$ scaffold. The $Fe^{II/III}$–OH complexes were treated with $[FeCp_2]^+$ to produce an $S = 2$ species, but magnetic data demonstrates it is a spin-coupled system that contains antiferromagnetic interactions between $S = 5/2$ (Fe^{III}) and $S = 1/2$ centers. Different structures have been proposed for this new species (Scheme 1.3), but further evaluations concluded $[FeCp_2]^+$ does not act as an outer-sphere oxidant. Instead, the P=O groups in [poat]$^{3-}$, which are

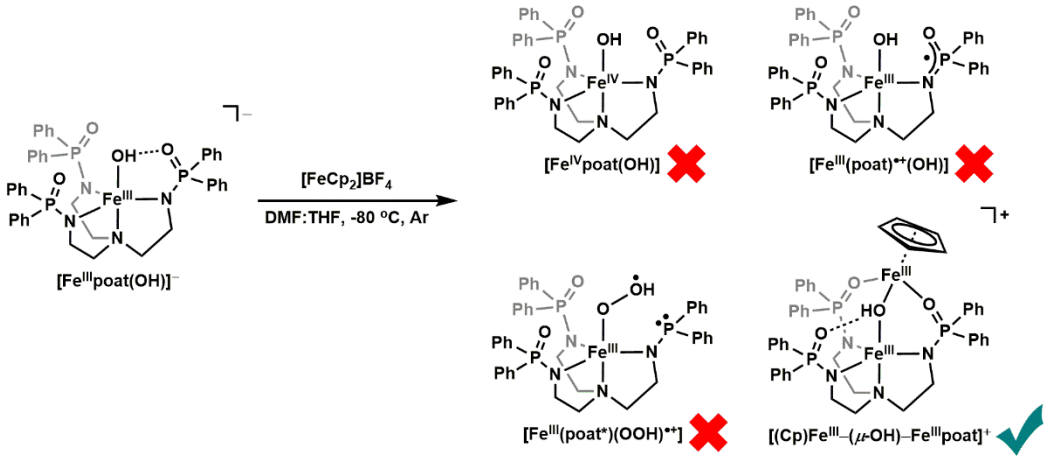

Scheme 1.3. Chapter 2 elucidates the structure of the mysterious species generated upon addition of $[FeCp_2]BF_4$ to $[Fe^{III}poat(OH)]^-$.

strong ligands, displace one cyclopentadienyl ring in $[FeCp_2]^+$ and form a μ-OH diferric species that contains two Fe^{III} centers with different spin states. This work highlights the utility of $[poat]^{3-}$ to construct bi- and multi-metallic complexes.

Chapter 3. A series of bimetallic $[poat]^{3-}$ complexes that contain a M^{II}–(μ-OH)–Fe^{III} core (M = Zn, Cu, Ni) are prepared and fully characterized, in which the divalent metals are capped with an N-based macrocycle ligand, [TMTACN]. Their properties were compared to their counterparts in an analogous framework that contains sulfonamido instead of phosphinic amido groups. A key discovery is the significant decrease in the $Fe^{III/II}$ reduction potentials (ΔE > 700 mV) in the $[poat]^{3-}$ complexes (Scheme 1.4), which supports the phosphinic amido groups being strong donors, and suggests higher valent compounds may be accessible.

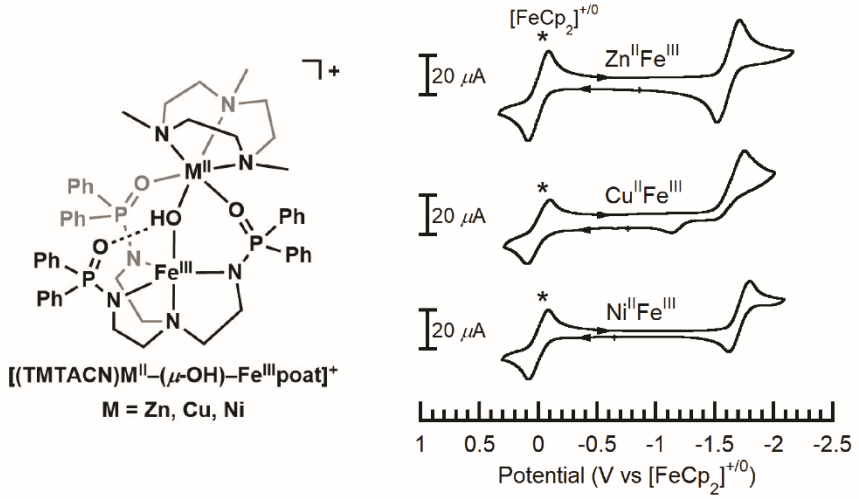

Scheme 1.4. Chapter 3 explores a series of heterobimetallic complexes with a [M^{II}–(μ-OH)–Fe^{III}] core.

Chapter 4. Inspired by the electrochemical findings discussed in the previous chapter, a series of bimetallic complexes were generated that contain a M^{II}–(μ-O)–Fe^{IV} core (M = Zn, Cu, Ni; Scheme 1.5). The spectroscopic properties of these species were compared to those for $[Fe^{IV}poat(O)\text{---}LA^{II}]^+$ (LA = Group II metal ion). An additional observation is the magnetic coupling between the Fe^{IV} and Cu^{II}/Ni^{II} centers facilitated by the oxido bridge; this indicates significant covalency between the

two metal centers, unlike in the Group II analogs where the interaction is electrostatic in nature. This series of high-valent bimetallic complexes represents a rare example of mixed valent (II,IV) systems.

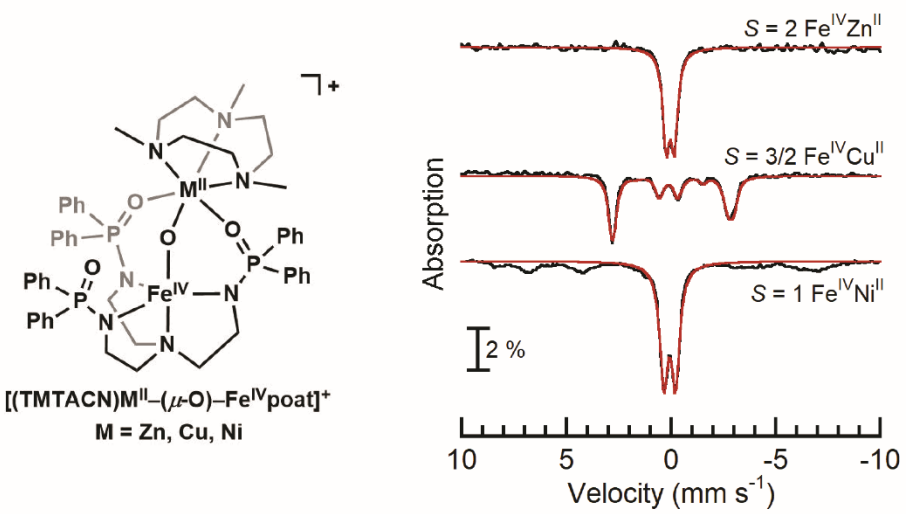

Scheme 1.5. Chapter 4 explores a series of heterobimetallic complexes with a [M^{II}–(μ-O)–Fe^{IV}] core.

Chapter 5. Using the synthetic strategies developed in the previous chapters, a series of diiron complexes were prepared in the [TMTACN/poat] framework (Scheme 1.6). These species span across four oxidation state levels, from (II,II) to (III,IV). One phosphinic amido arm in $[poat]^{3-}$ can stabilize the lower valent Fe–(μ-OH)–Fe core *via* intramolecular H-bond interactions, but the proton transfers from the hydroxido bridge to the N-atom of the phosphinic amido group and promotes ligand rearrangement at the diferric level, resulting in a Fe–(μ-O)–Fe core in a $[Hpoat]^{2-}$ framework; this illustrates another unique feature of $[poat]^{3-}$. A high-valent Fe^{III}–(μ-O)–Fe^{IV} species can be accessed and demonstrates reactivity towards phenolic substrates. This system serves as a suitable synthetic model for the R2 subunit of RNR Class Ia, and an alternative PCET pathway (contrary to the commonly proposed ET-PT mechanism) is proposed for the biological system.

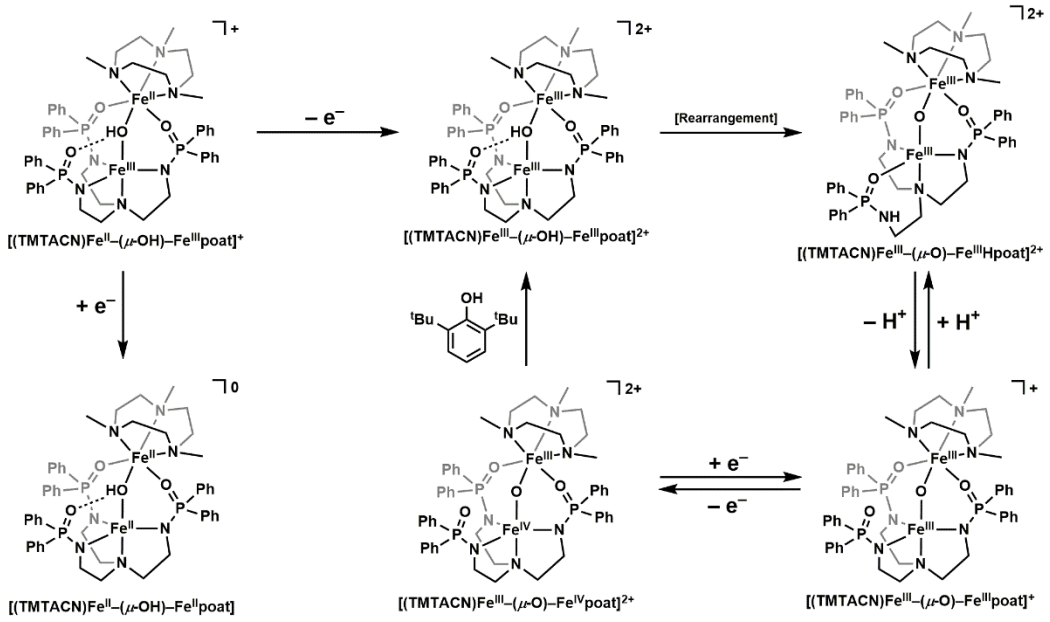

Scheme 1.6. Chapter 5 describes the preparation and characterization of a series of diiron complexes across four oxidation states.

Chapter 6. A subclass of O_2-binding/activating enzymes contains a FeMn core, and are proposed to undergo different reactivity pathways than their di-Fe counterparts. A new heterobimetallic FeMn system is developed, in which the Mn is bound to the [poat]$^{3-}$ N-donors, and the Fe is capped by the [TMTACN] ligand. Similar to the diiron system, a Fe^{III}–(μ-O)–Mn^{IV} species can be accessed (Scheme 1.7); this is only the second reported $Fe^{III}Mn^{IV}$ compound to date. Its reactivity towards phenol and carbon radical substrates was explored, and its relevance to biological FeMn active sites is discussed.

Chapter 7. The FeMn complexes described in Chapter 6 cannot be oxidized beyond the (III,IV) level. To attempt to access the $Fe^{IV}Mn^{IV}$ state observed in biological active sites, the system is redesigned by binding the Fe center to the [poat]$^{3-}$ N-donors, while the Mn site is capped with [TMTACN]. A series of MnFe complexes were prepared, and their electrochemical properties were interrogated by cyclic voltammetry (Scheme 1.8). Further oxidative processes were observed electrochemically, but their assignments cannot be corroborated without additional spectroscopic studies by chemical oxidation.

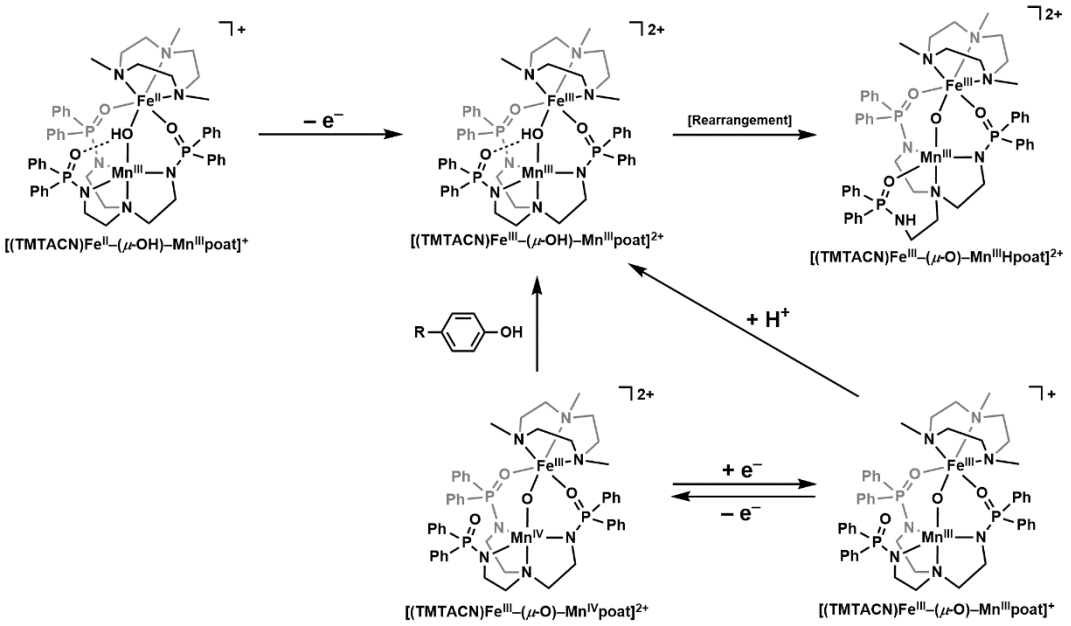

Scheme 1.7. Chapter 6 discusses the preparation and characterization of a series of FeMn complexes across three oxidation levels and various protonation states.

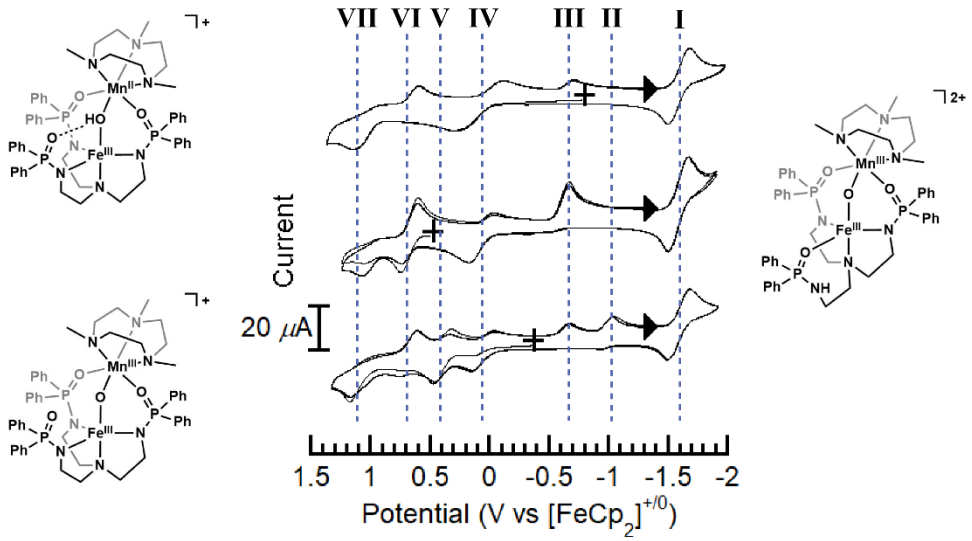

Scheme 1.8. Chapter 7 explores the electrochemical properties of a series of MnFe complexes to evaluate their ability to access the $Mn^{IV}Fe^{IV}$ level.

Chapter 8. In a serendipitous discovery, the P=O groups in $[poat]^{3-}$ were found to support an $S = 2$ Co^{III} center; almost all Co^{III} complexes in 6-coordinated geometry are diamagnetic due to dominant ligand field stabilization. To further the understanding of the P=O groups as ligands, a series of $Co^{III/II}Fe^{III}$ and $Co^{III/II}Ga^{III}$ bimetallic complexes were prepared. Through structural and magnetic

studies, it was discovered the Co^{III} center is diamagnetic in the μ-hydroxido bridged compounds, but adopts an $S = 2$ ground state in a Co^{III}–(μ-O)–Fe^{III} core (Scheme 1.9). This finding suggests both the P=O groups and the bridging ligand (which facilitates spin exchange interaction between the two metal sites) play a significant role in modulating the electronic structure of the Co center.

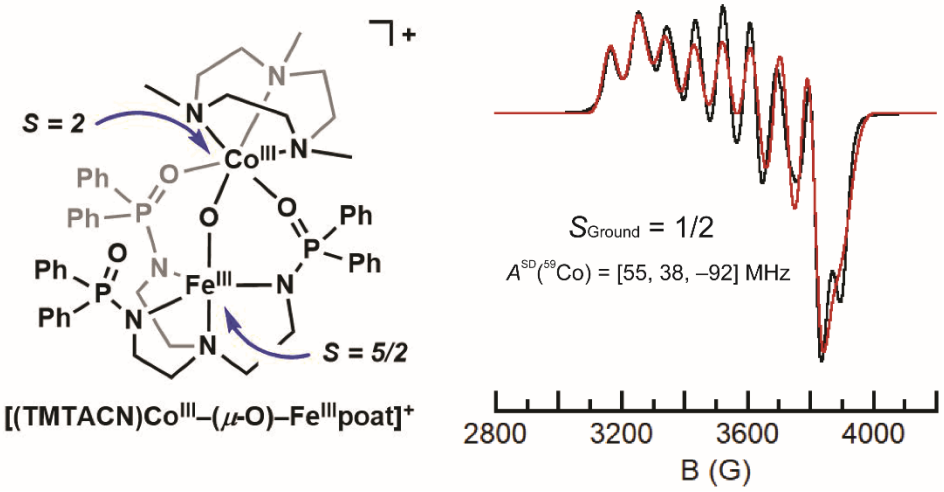

Scheme 1.9. Chapter 8 explores bimetallic complexes that contain a rare high-spin six-coordinated Co(III) center.

References

(1) Holm, R. H.; Kennepohl, P.; Solomon, E. I. Structural and Functional Aspects of Metal Sites in Biology. *Chem. Rev.* **1996**, *96*, 2239.

(2) Dawson, J. H. Probing Structure-Function Relations in Heme-Containing Oxygenases and Peroxidases. *Science* **1988**, *240*, 433-439.

(3) Liu, J.; Chakraborty, S.; Hosseinzadeh, P.; Yu, Y.; Tian, S.; Petrik, L.; Bhagi, A.; Lu, Y. Metalloproteins Containing Cytochrome, Iron–Sulfur, or Copper Redox Centers. *Chem. Rev.* **2014**, *114*, 4366-4469.

(4) Huang, X.; Groves, J. T. Oxygen Activation and Radical Transformations in Heme Proteins and Metalloporphyrins. *Chem. Rev.* **2018**, *118*, 2491-2553.

(5) Krest, C. M.; Onderko, E. L.; Yosca, T. H.; Calixto, J. C.; Karp, R. F.; Livada, J.; Rittle, J.; Green, M. T. Reactive Intermediates in Cytochrome P450 Catalysis. *J. Biol. Chem.* **2013**, *288*, 17074-17081.

(6) Costas, M.; Mehn, M. P.; Jensen, M. P.; Que, L. Dioxygen Activation at Mononuclear Nonheme Iron Active Sites: Enzymes, Models, and Intermediates. *Chem. Rev.* **2004**, *104*, 939-986.

(7) Shook, R. L.; Borovik, A. S. Role of the Secondary Coordination Sphere in Metal-Mediated Dioxygen Activation. *Inorg. Chem.* **2010**, *49*, 3646-3660.

(8) Guo, M.; Corona, T.; Ray, K.; Nam, W. Heme and Nonheme High-Valent Iron and Manganese Oxo Cores in Biological and Abiological Oxidation Reactions. *ACS Cent. Sci.* **2019**, *5*, 13-28.
(9) Kovaleva, E. G.; Lipscomb, J. D. Versatility of Biological Non-Heme Fe(II) Centers in Oxygen Activation Reactions. *Nat. Chem. Biol.* **2008**, *4*, 186-193.
(10) Lee, J. L.; Ross, D. L.; Barman, S. K.; Ziller, J. W.; Borovik, A. S. C–H Bond Cleavage by Bioinspired Nonheme Metal Complexes. *Inorg. Chem.* **2021**, *60*, 13759-13783.
(11) Cook, S. A.; Borovik, A. S. Molecular Designs for Controlling the Local Environments around Metal Ions. *Acc. Chem. Res.* **2015**, *48*, 2407-2414.
(12) Borovik, A. S. Bioinspired Hydrogen Bond Motifs in Ligand Design: The Role of Noncovalent Interactions in Metal Ion Mediated Activation of Dioxygen. *Acc. Chem. Res.* **2005**, *38*, 54-61.
(13) Span, E. A.; Suess, D. L. M.; Deller, M. C.; Britt, R. D.; Marletta, M. A. The Role of the Secondary Coordination Sphere in a Fungal Polysaccharide Monooxygenase. *ACS Chem. Biol.* **2017**, *12*, 1095-1103.
(14) Yang, J.; Kloek, A. P.; Goldberg, D. E.; Mathews, F. S. The structure of *Ascaris* hemoglobin domain I at 2.2 Å resolution: Molecular features of oxygen avidity. *Proc. Natl. Acad. Sci. U.S.A.* **1995**, *92*, 4224-4228.
(15) Vojtěchovský, J.; Chu, K.; Berendzen, J.; Sweet, R. M.; Schlichting, I. Crystal Structures of Myoglobin-Ligand Complexes at Near-Atomic Resolution. *Biophys. J.* **1999**, *77*, 2153-2174.
(16) Bren, K. L.; Eisenberg, R.; Gray, H. B. Discovery of the magnetic behavior of hemoglobin: A beginning of bioinorganic chemistry. *Proc. Natl. Acad. Sci.* **2015**, *112*, 13123-13127.
(17) Wilson, S. A.; Green, E.; Mathews, I. I.; Benfatto, M.; Hodgson, K. O.; Hedman, B.; Sarangi, R. X-ray absorption spectroscopic investigation of the electronic structure differences in solution and crystalline oxygemoglobin. *Proc. Natl. Acad. Sci. U.S.A.* **2013**, *110*, 16333-16338.
(18) Poulos, T. L. Heme Enzyme Structure and Function. *Chem. Rev.* **2014**, *114*, 3919-3962.
(19) Kurtz, D. M. Oxo- and Hydroxo-Bridged Diiron Complexes: A Chemical Perspective on a Biological Unit. *Chem. Rev.* **1990**, *90*, 585-606.
(20) Cohen, I. A.; Caughey, W. S.; Substituted Deuteroporphyrins. IV. Kinetics and Mechanism of Reactions of Iron(II) Porphyrins with Oxygen. *Biochemistry* **1968**, *7*, 636-641.
(21) Hoffman, A. B.; Collins, D. M.; Day, V. W.; Fleischer, E. B.; Srivastava, T. S.; Hoard, J. L. The Crystal Structure and Molecular Stereochemistry of *μ*-Oxo-bis[*a*,*β*,*γ*,*δ*-tetraphenylporphinatoiron(III)]. *J. Am. Chem. Soc.* **1972**, *94*, 3620-3626.
(22) Shikama, K. Stability Properties of Dioxygen-Iron(II) Porphyrins: An Overview from Simple Complexes to Myoglobin. *Coord. Chem. Rev.* **1988**, *83*, 73-91.
(23) 2-Oxoglutarate-Dependent Oxygenase; Schofield, C. J., Hausinger, R. P., Eds; Royal Society of Chemistry: Cambridge, U.K., 2015.
(24) Kal, S.; Que, L. Dioxygen Activation by Nonheme Iron Enzymes with the 2-His-1-Carbosylate Facial Triad That Generate High-Valent Oxoiron Oxidants. *JBIC, J. Biol. Inorg. Chem.* **2017**, *22*, 339-365
(25) Hausinger, R. P. Fe(II)/*a*-Ketoglutarate-Dependent Hydroxylases and Related Enzymes. *Crit. Rev. Biochem. Mol. Biol.* **2004**, *39*, 21-68.
(26) Koehntop, K. D.; Emerson, J. P.; Que, L. The 2-His-1-Carbosylate Facial Triad: A Versatile Platforms for Dioxygen Activation by Mononuclear Non-Heme Iron(II) Enzymes. *JBIC, J. Biol. Inorg. Chem.* **2005**, *10*, 87-93.
(27) Barry, S. M.; Challis, G. L. Mechanism and Catalytic Diversity of Rieske Non-Heme Iron-Dependent Oxygenases. *ACS Catal.* **2013**, *3*, 2362-2370.

(28) Chakrabarty, S.; Austin, R. N.; Deng, D.; Groves, J. T.; Lipscomb, J. D. Radical Intermediates in Monooxygenase Reactions of Rieske Dioxygenases. *J. Am. Chem. Soc.* **2007**, *129*, 3514-3515.
(29) Krebs, C.; Galonić Fujimori, D.; Walsh, C. T.; Bollinger, J. M. Non-Heme Fe(IV)–Oxo Intermediates. *Acc. Chem. Res.* **2007**, *40*, 484-492.
(30) Martinez, S.; Hausinger, R. P. Catalytic Mechanisms of Fe(II)- and 2-Oxoglutarate-Dependent Oxygenases. *J. Biol. Chem.* **2015**, *290*, 20702-20711.
(31) Chang, W.-C.; Liu, P.; Guo, Y. Mechanistic Elucidation of Two Catalytically Versatile Iron(II)- and *a*-Ketoglutarate-Dependent Enzymes: Cases Beyond Hydroxylation. *Comments Inorg. Chem.* **2018**, *38*, 127-165.
(32) Sutherlin, K. D.; Rivard, B. S.; Böttger, L. H.; Liu, L. V.; Rogers, M. S.; Srnec, M.; Park, K.; Yodan, Y.; Kitao, S.; Kobayashi, Y.; Saito, M.; Seto, M.; Hu, M.; Zhao, J.; Lipscomb, J. D.; Solomon, E. I. NRVS Studies of the Peroxide Shunt Intermediate in a Rieske Dioxygenase and its Relation to the Native Fe^{II} O_2 Reaction. *J. Am. Chem. Soc.* **2018**, *140*, 5544-5559.
(33) Wang, Y.; Li, J.; Liu, A. Oxygen Activation by Mononuclear Nonheme Iron Dioxygenases Involved in the Degradation of Aromatics. *JBIC, J. Biol. Inorg. Chem.* **2017**, *22*, 395-405.
(34) Jasniewski, A. J.; Que, L. Dioxygen Activation by Nonheme Diiron Enzymes: Diverse Dioxygen Adducts, High-Valent Intermediates, and Related Model Complexes. *Chem. Rev.* **2018**, *118*, 2554-2592.
(35) Kurtz, D. M. Oxo- and Hydroxo-Bridged Diiron Complexes: A Chemical Perspective on a Biological Unit. *Chem. Rev.* **1990**, *90*, 585-606.
(36) Klotz, I. M.; Kurtz, D. M. Binuclear Oxygen Carriers: Hemerythrin. *Acc. Chem. Res.* **1984**, *17*, 16-22.
(37) Stenkamp, R. E. Dioxygen and Hemerythrin. *Chem. Rev.* **1994**, *94*, 715-726.
(38) Holmes, M. A.; Le Trong, I.; Turley, S.; Sieker, L. C.; Stenkamp, R. E. Structures of Deoxy and Oxy Hemerythrin at 2.0 Å Resolution. *J. Mol. Biol.* **1991**, *218*, 583-593.
(39) Brunold, T. C.; Solomon, E. I. Reversible Dioxygen Binding to Hemerythrin. 2. Mechanism of the Proton-Coupled Two-Electron Transfer to O_2 at a Single Iron Center. *J. Am. Chem. Soc.* **1999**, *121*, 8288-8295.
(40) Tshuva, E. Y.; Lippard, S. J. Synthetic Models for Non-Heme Carboxylate-Bridged Diiron Metalloproteins: Strategies and Tactics. *Chem. Rev.* **2004**, *104*, 987-1012.
(41) Kurtz, D. M.; Boice, E.; Caranto, J. D.; Frederick, R. E.; Masitas, C. A.; Miner, K. D. Iron: Non-Heme Proteins with Diiron-Carboxylate Active Sites. In *Encyclopedia of Inorganic and Bioinorganic Chemistry*; John Wiley & Sons, Ltd.: Hoboken, New Jersey, 2005.
(42) Rardin, R. L.; Tolman, W. B.; Lippard, S. J. Monodentate Carboxylate Complexes and the Carbosylate Shift: Implications for Polymetalloprotein Structure and Function. *New J. Chem.* **1991**, *15*, 417-430.
(43) Rosenzweig, A. C.; Nordlund, P.; Takahara, P. M.; Frederick, C. A.; Lippard, S. J. Geometry of the soluble methane monooxygenase catalytic diiron center in two oxidation states. *Chemistry & Biology* **1995**, *2*, 409-418.
(44) Tinberg, C. E.; Lippard, S. J. Dioxygen Activation in Soluble Methane Monooxygenase. *Acc. Chem. Res.* **2011**, *44*, 280-288.
(45) Rosenzweig, A. C.; Brandstetter, H.; Whittington, D. A.; Nordlund, P.; Lippard, S. J.; Frederick, C. A. Crystal Structures of the Methane Monooxygenase Hydroxylase from *Methylococcus capsulatus* (Bath): Implications for Substrate Gating Component Interactions. *Proteins* **1997**, *29*, 141-152

(46) Whittington, D. A.; Lippard, S. J. Crystal Structures of the Soluble Methane Monooxygenase Hydroxylase from *Methylococcus capsulatus* (Bath) Demonstrating Geometrical Variability at the Dinuclear Iron Active Site. *J. Am. Chem. Soc.* **2001**, *123*, 827-838.
(47) Liu, K. E.; Wang, D.; Huynh, B. H.; Edmondson, D. E.; Salifoglou, A.; Lippard, S. J. Spectroscopic Detection of Intermediates in the Reaction Dioxygen with the Reduced Methane Monooxygenase Hydroxylase from *Methylococcus capsulatus* (Bath). *J. Am. Chem. Soc.* **1994**, *116*, 7465-7466.
(48) Lee, S. K.; Nesheim, J. C.; Lipscomb, J. D. Transient intermediates of the methane monooxygenase catalytic cycle. *J. Biol. Chem.* **1993**, *268*, 21569-21577.
(49) Tinberg, C. E.; Lippard, S. J. Revisiting the Mechanism of Dioxygen Activation in Soluble Methane Monooxygenase from *M. capsulatus* (Bath): Evidence for a Multi-Step, Proton-Dependent Reaction Pathway. *Biochemistry* **2009**, *48*, 12145-12158.
(50) Lipscomb, J. D.; Que, L. MMO: P450 in Wolf's Clothing? *JBIC, J. Biol. Inorg. Chem.* **1998**, *3*, 331-336.
(51) Merkx, M.; Kopp, D. A.; Sazinsky, M. H.; Blazyk, J. L.; Müller, J.; Lippard, S. J. Dioxygen Activation and Methane Hydroxylation by Soluble Methane Monooxygenase: A Tale of Two Irons and Three Proteins. *Angew. Chem., Int. Ed.* **2001**, *40*, 2782-2807.
(52) Ross, M. O.; Rosenzweig, A. C. A Tale of Two Methane Monooxygenases. *JBIC, J. Biol. Inorg. Chem.* **2017**, *22*, 307-319.
(53) Haynes, C. A.; Gonzalez, R. Rethinking biological activation of methane and conversion to liquid fuels. *Nat. Chem. Biol.* **2014**, *10*, 331-339.
(54) Tang, P.; Zhu, Q.; Wu, Z.; Ma, D. Methane activation: the past and future. *Energy Environ. Sci.* **2014**, *7*, 2580-2591.
(55) Groves, J. T.; McClusky, G. A. Aliphatic Hydroxylation via Oxygen Rebound. Oxygen Transfer Catalyzed by Iron. *J. Am. Chem. Soc.* **1976**, *98*, 859-861.
(56) Huang, X.; Groves, J. T. Beyond Ferryl-Mediated Hydroxylation: 40 Years of the Rebound Mechanism and C−H Activation. *JBIC, J. Biol. Inorg. Chem.* **2017**, *22*, 185-207.
(57) Yosca, T. H.; Rittle, J.; Krest, C. M.; Onderko, E. L.; Silakov, A.; Calixto, J. C.; Behan, R. K.; Green, M. T. Iron(IV)Hydroxide pKa and the Role of Thiolate Ligation in C−H Bond Activation by Cytochrome P450. *Science* **2013**, *342*, 825-829.
(58) Jacobs, A. B.; Banerjee, R.; Deweese, D. E.; Braun, A.; Babicz, J. T.; Gee, L. B.; Sutherlin, K. D.; Böttger, L. H.; Yoda, Y.; Saito, M.; Kitao, S.; Kobayashi, Y.; Seto, M.; Tamasaku, K.; Lipscomb, J. D.; Park, K.; Solomon, E. I. *J. Am. Chem. Soc.* **2021**, *143*, 16007-16029.
(59) Shu, L.; Nesheim, J. C.; Kauffmann, K.; Münck, E.; Lipscomb, J. D.; Que, L. An $Fe_2^{IV}O_2$ Diamond Core Structure for the Key Intermediate Q of Methane Monooxygenase. *Science* **1997**, *275*, 515-518.
(60) Rinaldo, D.; Philipp, D. M.; Lippard, S. J.; Friesner, R. A. Intermediates in Dioxygen Activation by Methane Monooxygenase: A QM/MM Study. *J. Am. Chem. Soc.* **2007**, *129*, 3135-3147.
(61) Han, W.-G.; Noodleman, L. Structural Model Studies for the Peroxo Intermediate P and the Reaction Pathway from P → Q of Methane Monooxygenase Using Broken-Symmetry Density Functional Calculations. *Inorg. Chem.* **2008**, *47*, 2975-2986.
(62) Huang, S.-P.; Shiota, Y.; Yoshizawa, K. DFT Study of the Mechanism for Methane Hydroxylation by Soluble Methane Monooxygenase (sMMO): Effects of Oxidation State, Spin State, and Coordination Number. *Dalton Trans.* **2013**, *42*, 1011-1023.
(63) Costas, M.; Rohde, J.-U.; Stubna, A.; Ho, R. Y. N.; Quaroni, L.; Münck, E.; Que, L. *J. Am. Chem. Soc.* **2001**, *123*, 12931-12932.

(64) Que, L.; Tolman, W. B. Bis(*μ*-oxo)dimetal "Diamond" Cores in Copper and Iron Complexes Relevant to Biocatalysis. *Angew. Chem., Int. Ed.* **2002**, *41*, 1114-1137.
(65) Puri, M.; Que, L. Toward the Synthesis of More Reactive *S* = 2 Non-Heme Oxoiron(IV) Complexes. *Acc. Chem. Res.* **2015**, *48*, 2443-2452.
(66) Castillo, R. G.; Banerjee, R.; Allpress, C. J.; Rohde, G. T.; Bill, E.; Que, L.; Lipscomb, J. D.; DeBeer, S. High-Energy-Resolution Fluorescence-Detected X-ray Absorption of the Q Intermediate of Soluble Methane Monooxygenase. *J. Am. Chem. Soc.* **2017**, *139*, 18024-18033.
(67) Cutsail, G. E.; Banerjee, R.; Zhou, A.; Que, L.; Lipscombe, J. D.; DeBeer, S. High-Resolution Extended X-ray Absorption Fine Structure Analysis Provides Evidence for a Longer Fe···Fe Distance in the Q Intermediate of Methane Monooxygenase. *J. Am. Chem. Soc.* **2018**, *140*, 16807-16820.
(68) Schulz, C. E.; Castillo, R. G.; Pantazis, D. A.; DeBeer, S.; Neese, F. Structure–Spectroscopy Correlations for Intermediate Q of Soluble Methane Monooxygenase: Insights from QM/MM Calculations. *J. Am. Chem. Soc.* **2021**, *143*, 6560-6577.
(69) Voegtli, W. C.; Sommerhalter, M.; Saleh, L.; Baldwin, J.; Bollinger, J. M.; Rosenzweig, A. C. Variable Coordination Geometries at the Diiron(II) Active Site of Ribonucleotide Reductase R2. *J. Am. Chem. Soc.* **2003**, *125*, 15822-15830.
(70) Högbom, M.; Galander, M.; Andersson, M.; Kolberg, M.; Hofbauer, W.; Lassmann, G.; Nordlund, P.; Lendzian, F. Displacement of the Tyrosyl Radical Cofactor in Ribonucleotide Reductase Obtained by Single-Crystal High-Field EPR and 1.4-Å X-ray Data. *Proc. Natl. Acad. Sci.* **2003**, *100*, 3209-3214.
(71) Nordlund, P.; Reichard, P. Ribonucleotide Reductases. *Annu. Rev. Biochem.* **2006**, *75*, 681-706.
(72) Minnihan, E. C.; Nocera, D. G.; Stubbe, J. Reversible, Long-Range Radical Transfer in *E. Coli* Class Ia Ribonucleotide Reductase. *Acc. Chem. Res.* **2013**, *46*, 2524-2535.
(73) Kang, G.; Taguchi, A. T.; Stubbe, J.; Drennan, C. L. Structure of a Trapped Radical Transfer Pathway within a Ribonucleotide Reductase Holocomplex. *Science* **2020**, *368*, 424-427.
(74) Greene, B. L.; Kang, G.; Cui, C.; Bennati, M.; Nocera, D. G.; Drennan, C. L.; Stubbe, J. Ribonucleotide Reductases: Structure, Chemistry, and Metabolism Suggest New Therapeutic Targets. *Annu. Rev. Biochem.* **2020**, *89*, 45-75.
(75) Ravi, N.; Bollinger, J. M.; Huynh, B. H.; Stubbe, J.; Edmondson, D. E. Mechanism of Assembly of the Tyrosyl Radical-Diiron(III) Cofactor of *E. Coli*. Ribonucleotide Reductase: 1. Mössbauer Characterization of the Diferric Radical Precursor. *J. Am. Chem. Soc.* **1994**, *116*, 8007-8014.
(76) Sturgeon, B. E.; Burdi D.; Chen, S.; Huynh, B.-H.; Edmondson, D. E.; Stubbe, J.; Hoffman, B. M. Reconsideration of X, the Diiron Intermediate Formed during Cofactor Assembly in *E. Coli* Ribonucleotide Reductase. *J. Am. Chem. Soc.* **1996**, *118*, 7551-7557.
(77) Bollinger, J. M.; Edmondson, D. E.; Huynh, B. H.; Filley, J.; Norton, J. R.; Stubbe, J. Mechanism of Assembly of the Tyrosyl Radical-Dinuclear Iron Cluster Cofactor of Ribonucleotide Reductase. *Science* **1991**, *253*, 292-298.
(78) Bollinger, J. M.; Stubbe, J.; Huynh, B. H.; Edmondson, D. E. Novel Diferric Radical Intermediate Responsible for Tyrosyl Radical Formation in Assembly of the Cofactor of Ribonucleotide Reductase. *J. Am. Chem. Soc.* **1991**, *113*, 6289-6291.
(79) Cox, N.; Ogata, H.; Stolle, P.; Reijerse, E.; Auling, G.; Lubitz, W. A Tyrosyl-Dimanganese Coupled Spin System is the Native Metalloradical Cofactor of the R2F Subunit of the Ribonucleotide Reductase of *Corynebacterium ammoniagenes*. *J. Am. Chem. Soc.* **2010**, *132*, 11197-11213.
(80) Cotruvo, J. A.; Stubbe, J. *Escherichia coli* Class Ib Ribonucleotide Reductase Contains a Dimanganese(III)-Tyrosyl Radical Cofactor *in vivo*. *Biochemistry* **2-11**, *50*, 1672-1681.

(81) Cotruvo, J. A.; Stubbe; J. Class I Ribonucleotide Reductases: Metallocofactor Assembly and Repair In Vitro and In Vivo. *Annu. Rev. Biochem.* **2011**, *80*, 733-767.
(82) Jiang, W.; Yun, D.; Saleh, L.; Barr, E. W.; Xing, G.; Hoffart, L. M.; Maslak, M.-A.; Krebs, C.; Bollinger, J. M. A manganese(IV)/iron(III) cofactor in Chamydia trachomatis ribonucleotide reductase. *Science* **2007**, *316*, 1188-1191.
(83) Andersson, C. S.; Högbom, M. A Mycobacterium tuberculosis ligand-binding Mn/Fe protein reveals a new cofactor in a remodeled R2-protein scaffold. *Proc. Natl. Acad, Sci. U.S.A.* **2009**, *106*, 5633-5638.
(84) Griese, J. J.; Roos, K.; Cox, N.; Shafaat, H. S.; Branca, R. M. M.; Lehtio, J.; Graslund, A.; Lubitz, W.; Siegbahn, P. E. M.; Högbom, M. Direct observation of structurally encoded metal discrimination and ether bond formation in a heterodinuclear metalloprotein. *Proc. Natl. Acad. Sci. U.S.A.* **2013**, *110*, 17189-17194.
(85) Schenk, G.; Mitić, N.; Gahan, L. R.; Ollis, D. L.; McGeary, R. P.; Guddat, L. W. Binuclear Metallohydrolases: Complex Mechanistic Strategies for a Simple Chemical Reaction. *Acc. Chem. Res.* **2012**, *45*, 1593-1603.
(86) Jiang, W.; Hoffart, L. M.; Krebs, C.; Bollinger, J. M. A Manganese(IV)/Iron(IV) Intermediate in Assembly of the Manganese(IV)/Iron(III) Cofactor of *Chlamydia trachomatis* Ribonucleotide Reductase. *Biochemistry* **2007**, *46*, 8709-8716.
(87) Younker, J. M.; Krest, C. M.; Jiang, W.; Krebs, C.; Bollinger, J. M.; Green, M. T. Structural Analysis of the Mn(IV)/Fe(III) Cofactor of *Chlamydia trachomatis* Ribonucleotide Reductase by Extended X-ray Absorption Fine Structure Spectroscopy and Density Functional Theory Calculations. *J. Am. Chem. Soc.* **2008**, *130*, 15022-15027.
(88) Bollinger, J. M.; Jiang, W.; Green, M. T.; Krebs, C. The manganese(IV)/iron(III) cofactor of *Chlamydia trachomatis* ribonucleotide reductase: structure, assembly, radical initiation, and evolution. *Curr. Opin. Struct. Biol.* **2008**, *18*, 650-657.
(89) Dassama, L. M. K.; Krebs, C.; Bollinger, J. M.; Rosenzweig, A. C.; Boal, A. K. Structural Basis for Assembly of the Mn^{IV}/Fe^{III} Cofactor in the Class Ic Ribonucleotide Reductase from *Chlamydia trachomatis*. *Biochemistry* **2013**, *52*, 6424-6436.
(90) Kwak, Y.; Jiang, W.; Dassama, L. M. K.; Park, K.; Bell, C. B.; Liu, L. V.; Wong, S. D.; Saito, M.; Kobayashi, Y.; Kitao, S.; Seto, M.; Yoda, Y.; Alp, E. E.; Zhao, J.; Bollinger, J. M.; Krebs, C.; Solomon, E. I. Geometric and Electronic Structure of the Mn(IV)Fe(III) Cofactor in Class Ic Ribonucleotide Reductase: Correlation to the Class Ia Binuclear Non-Heme Iron Enzyme. *J. Am. Chem. Soc.* **2013**, *135*, 17573-17584.
(91) Livada, J.; Martinie, R. J.; Dassama, L. M. K.; Krebs, C.; Bollinger, J. M.; Silakov, A. Direct Measurement of the Radical Translocation Distance in the Class I Ribonucleotide Reductase from *Chlamydia trachomatis*. *J. Phys. Chem. B.* **2015**, *119*, 13777-13784.
(92) Martinie, R. J.; Blaesi, E. J.; Krebs, C.; Bollinger, J. M.; Silakov, A.; Pollock, C. J. Evidence for a Di-μ-oxo Diamond Core in the Mn(IV)/Fe(IV) Activation Intermediate of Ribonucleotide Reductase from *Chlamydia trachomatis*. *J. Am. Chem. Soc.* **2017**, *139*, 1950-1957.
(93) Miller, E. K.; Trivelas, N. E.; Maugeri, P. T.; Blaesi, E. J.; Shafaat, H. S. Time-Resolved Investigations of Heterobimetallic Cofactor Assembly in R2lox Reveal Distinct Mn/Fe Intermediates. *Biochemistry* **2017**, *56*, 3369-3379.
(94) Kisgeropoulos, E. C.; Griese, J. J.; Smith, Z. R.; Branca, R. M. M.; Schneider, C. R.; Högbom, M.; Shafaat, H. S. Key Structural Motifs Balance Metal Binding and Oxidative Reactivity in a Heterobimetallic Mn/Fe Protein. *J. Am. Chem. Soc.* **2020**, *142*, 5338-5354.
(95) Fox, B. G.; Shanklin, J.; Somerville, C.; Münck, E. Stearoyl-Acyl Carrier Protein Δ^9 Desaturase from *Ricinus communis* Is a Diiron-Oxo Protein. *Proc. Natl. Acad. Sci. U.S.A.* **1993**, *90*, 2486-2490.

(96) Hayashi, T.; Caranto, J. D.; Wampler, D. A.; Kurtz, D. M.; Moënne-Loccoz, P. Insights into the Nitric Oxide Reductase Mechanism of Flavodiiron Proteins from a Flavin-Free Enzyme. *Biochemistry* **2010**, *49*, 7040-7049.

(97) Jasniewski, A. J.; Engstrom, L. M.; Vu, V. V.; Park, M. H.; Que, L. X-Ray Absorption Spectroscopic Characterization of the Diferric-Peroxo Intermediate of Human Deoxyhypusine Hydroxylase in the Presence of Its Substrate EIF5A. *JBIC, J. Biol. Inorg. Chem.* **2016**, *21*, 605-618.

(98) Kopp, D. A.; Lippard, S. J. Soluble Methane Monooxygenase: Activation of Dioxygen and Methane. *Curr. Opin. Chem. Biol.* **2002**, *6*, 568-576.

(99) Ambundo, E. A.; Friesner, R. A.; Lippard, S. J. Reactions of Methane Monooxygenase Intermediate Q with a Series of Derivatized Methanes Substrates. *J. Am. Chem. Soc.* **2002**, *124*, 8770-8771.

(100) Brazeau, B. J.; Wallar, B. J.; Lipscomb, J. D. Unmasking of Deuterium Kinetic Isotope Effects on the Methane Monooxygenase Compound Q Reaction by Site-Directed Mutagenesis of Component B. *J. Am. Chem. Soc.* **2001**, *123*, 10421-10422.

(101) Murray, K. S. Binuclear Oxo-Bridged Iron(III) Complexes. *Coord. Chem. Rev.* **1974**, *12*, 1-35.

(102) Wieghardt, K.; Pohl, K.; Gebert, W. $[\{(C_6H_{15}N_3)Fe\}_2(\mu\text{-}O)(\mu\text{-}CH_3CO_2)_2]^{2+}$, a Dinuclear Iron(III) Complex with a Metazidohemerythrin-Type Structure. *Angew. Chem., Int. Ed.* **1983**, *22*, 727.

(103) Armstrong, W. H.; Lippard, S. J. (*μ*-Oxo)bis(*μ*-acetato)bis(tri-1-pyrazolylborato)diiron(III), $[(HBpz_3)FeO(CH_3CO_2)_2Fe(HBpz_3)]$: Model for the Binuclear Iron Center of Hemerythrin. *J. Am. Chem. Soc.* **1983**, *105*, 4837-4838.

(104) Armstrong, W. H.; Spool, A.; Papaefthymioum G. C.; Frankel, R. B.; Lippard, S. J. Assembly and Characterization of an Acetate Model for the Diiron Center in Hemerythrin. *J. Am. Chem. Soc.* **1984**, *106*, 3653-3667.

(105) Hotzelmann, R.; Wieghardt, K.; Flörke, U.; Haupt, H.-J.; Weatherburn, D. C.; Bonvoisin, J.; Blondin, G.; Girerd, J.-J. Spin Exchange Coupling in Asymmetric Heterodinuclear Complexes Containing the *μ*-Oxo-bis(*μ*-acetato)dimetal Core. *J. Am. Chem. Soc.* **1992**, *114*, 1681-1696.

(106) Slep, L. D.; Mijovilovich, A.; Meyer-Klaucke, W.; Weyhermüller, T.; Bill, E.; Bothe, E.; Neese, K.; Wieghardt, K. Mixed-Valent $\{Fe^{IV}(\mu\text{-}O)(\mu\text{-carboxylato})_2Fe^{III}\}^{3+}$ Core. *J. Am. Chem. Soc.* **2003**, *125*, 15554-15570.

(107) Kitajima, N.; Tamura, N.; Amagai, H.; Fukui, H.; Moro-oka, Y.; Mizutani, Y.; Kitagawa, T.; Mathur, R.; Heerwegh, K.; Reed, C. A.; Randall, C. R.; Que, L.; Tatsumi, K. Monomeric Carboxylate Ferrous Complexes as Models for the Dioxygen Binding Sites in Non-Heme Iron Proteins. The Reversible Formation and Characterization of *μ*-Peroxo Differic Complexes. *J. Am. Chem. Soc.* **1994**, *116*, 9071-9085.

(108) Kim, K.; Lippard, S. J. Structure and Mössbauer Spectrum of a (*μ*-1,2-Peroxo)bis(*μ*-carboxylato)diiron(III) Model for the Peroxo Intermediate in the Methane Monooxygenase Hydroxylase Reaction Cycle. *J. Am. Chem. Soc.* **1996**, *118*, 4914-4915.

(109) Dong, Y.; Fujii, H.; Hendrich, M. P.; Leising, R. A.; Pan, G.; Randall, C. R.; Wilkinson, E. C.; Zang, Y.; Que, L.; Fox, B. G.; Kauffmann, K.; Münck, E. A High-Valent Nonheme Iron Intermediate. Structure and Properties $[Fe_2(\mu\text{-}O)_2(5\text{-Me-TPA})_2](ClO_4)_3$. *J. Am. Chem. Soc.* **1995**, *117*, 2778-2792.

(110) Hsu, H.-F.; Dong, Y.; Shu, L.; Young, V. G.; Que, L. Crystal Structure of a Synthetic High-Valent Complex with an $Fe_2(\mu\text{-}O)_2$ Diamond Core. Implications for the Core Structures of Methane Monooxygenase Intermediate Q and Ribonucleotide Reductase Intermediate X. *J. Am. Chem. Soc.* **1999**, *121*, 5230-5237.

(111) Xue, G.; Wang, D.; De Hont, R.; Fiedler, A. T.; Shan, X.; Münck, E.; Que, L. A synthetic precedent for the [$Fe^{IV}_2(\mu$-O)$_2$] diamond core proposed for methane monooxygenase intermediate Q. *Proc. Natl. Acad. Sci. U.S.A.* **2007**, *104*, 20713-20718.
(112) Xue, G.; Fiedler, A. T.; Martinho, M.; Münck, E.; Que, L. Insights into the P-to-Q conversion in the catalytic cycle of the methane monooxygenase from a synthetic model system. *Proc. Natl. Acad. Sci. U.S.A.* **2008**, *105*, 20615-20620.
(113) Xue, G.; De Hont, R.; Münck, E.; Que, L. Million-fold activation of the [$Fe_2(\mu$-O)$_2$] diamond core for C–H bond cleavage. *Nat. Chem.* **2010**, *2*, 400-405.
(114) De Hont, R. F.; Xue, G.; Hendrich, M. P.; Que, L.; Bominaar, E. L.; Münck, E. Mössbauer, Electron Paramagnetic Resonance, and Density Functional Theory Studies of Synthetic S = 1/2 Fe^{III}–O–Fe^{IV}=O Complexes. Superexchange-Mediated Spin Transition at the Fe^{IV}=O Site. *Inorg. Chem.* **2010**, *49*, 8310-8322.
(115) Stoian, S. A.; Xue, G.; Bominaar, E. L.; Que, L.; Münck, E. Spectroscopic and Theoretical Investigation of a Complex with an [O=Fe^{IV}–O–Fe^{IV}=O] Core Related to Methane Monooxygenase Intermediate Q. *J. Am. Chem. Soc.* **2014**, *136*, 1545-1558.
(116) Ghosh, A.; Tiago de Oliveira, F.; Yano, T.; Nishioka, T.; Beach, E. S.; Kinoshita, I.; Münck, E.; Ryabov, A. D.; Horwitz, C. P.; Collins, T. J. Catalytically Active μ-Oxodiiron(IV) Oxidants from Iron(III) and Dioxygen. *J. Am. Chem. Soc.* **2005**, *127*, 2505-2513.
(117) Collins, T. J.; Ryabov, A. D. Targeting of High-Valent Iron-TAML Activators at Hydrocarbons and Beyond. *Chem. Rev.* **2017**, *117*, 9140-9162.
(118) Wieghardt, K.; Bossek, U.; Number, B.; Weiss, J.; Bonvoisin, J.; Corbella, M.; Vitols, S. E.; Girerd, J. J. Synthesis, Crystal Structures, Reactivity, and Magnetochemistry of a Series of Binuclear Complexes of Manganese(II), -(III), and -(IV) of Biological Relevance. The Crystal Structure of [L'$Mn^{IV}(\mu$-O)$_3$$Mn^{IV}$L'](PF$_6$)$_2$·H$_2$O Containing an Unprecedented Short Mn···Mn Distance of 2.296 Å. *J. Am. Chem. Soc.* **1988**, *110*, 7398-7411.
(119) Schoenfeldt, N. J.; Ni Z.; Korinda, A. W.; Meyer R. J.; Notestein J. M. Manganese Triazacyclononane Oxidation Catalysts Grafted under Reaction Conditions on Solid Cocatalytic Supports. *J. Am. Chem. Soc.* **2011**, *133*, 18684–18695.
(120) Steen, J. D.; Stepanovic, S.; Parvizian, M.; De Boer, J. W.; Hage, R.; Chen, J.; Swart, M.; Gruden, M.; Browne, W. R. Lewis versus Brønsted Acid Activation of a Mn(IV) Catalyst for Alkene Oxidation. *Inorg. Chem.* **2019**, *58*, 14924-14930.
(121) Rice, D. B.; Munasinghe, A.; Grotemeyer, E. N.; Burr, A. D.; Day, V. W.; Jackson, T. A. Structure and Reactivity of (μ-Oxo)dimanganese(III,III) and Mononuclear Hydroxomanganese(III) Adducts Supported by Derivatives of an Amide-Containing Pentadentate Ligand. *Inorg. Chem.* **2019**, *58*, 622-636.
(122) Spencer, Douglas, J. E.; Aboelella, N. W.; Reynolds, A. M.; Holland, P. L.; Tolman, W. B. β-Diketiminate Ligand Backbone Structural Effects on Cu(I)/O_2 Reactivity: Unique Copper–Superoxo and Bis(μ-oxo) Complexes. *J. Am. Chem. Soc.* **2002**, *124*, 2108-2109.
(123) VanNatta, P. E.; Ramirez, D. A.; Velarde, A. R.; Ali, G.; Kieber-Emmons, M. T. Exceptionally High O–H Bond Dissociation Free Energy of a Dicopper(II) μ-Hydroxo Complex and Insights into the Geometric and Electronic Structure Origins Thereof. *J. Am. Chem. Soc.* **2020**, *142*, 16292-16312.
(124) Gersten, S. W.; Samuels, G. J.; Meyer, T. J. Catalytic Oxidation of Water by an Oxo-Bridged Ruthenium Dimer. *J. Am. Chem. Soc.* **1982**, *104*, 4029-4030.
(125) Liu, F.; Concepcion, J. J.; Jurss, J. W.; Cardolaccia, T.; Templeton, J. L.; Meyer, T. J. *Inorg. Chem.* **2008**, *47*, 1727-1752.

(126) Evans, W. J.; Ulibarri, T. A.; Ziller, J. W. Isolation and X-ray Crystal Structure of the First Dinitrogen Complex of an f-Element Metal, $[(C_5Me_5)_2Sm]_2N_2$. *J. Am. Chem. Soc.* **1988**, *110*, 6877-6879.

(127) Evans, W. J.; Lee, D. S.; Rego, D. B.; Perotti, J. M.; Kozimor, S. A.; Moore, E. K.; Ziller, J. W. Expanding Dinitrogen Reduction Chemistry to Trivalent Lanthanides via the LnZ_3/Alkali Metal Reduction System: Evaluation of the Generality of Forming $Ln_2(\mu\text{-}\eta^2\text{:}\eta^2\text{-}N_2)$ Complexes via LnZ_3/K. *J. Am. Chem. Soc.* **2004**, *126*, 14574-14582.

(128) Kodera, M.; Itoh, M.; Kano, K.; Funabiki, T.; Reglier, M. A Diiron Center Stabilized by a Bis-TPA Ligand as a Model of Soluble Methane Monooxygenase: Predominant Alkene Epoxidation with H_2O_2. *Angew. Chem., Int. Ed.* **2005**, *44*, 7104-7106.

(129) Borovik, A. S.; Papafthymiou, V.; Taylor, L. F.; Anderson, O. P.; Que, L. Models for Iron–Oxo Proteins. Structures and Properties of $Fe^{II}Fe^{III}$, $Zn^{II}Fe^{III}$, and $Fe^{II}Ga^{III}$ Complexes with (μ-Phenoxo)bis(μ-carboxylato)dimetal Cores. *J. Am. Chem. Soc.* **1989**, *111*, 6183-6195.

(130) Borovik, A. S.; Hendrich, M. P.; Holman, T. R.; Münck, E.; Papaefthymiou, V.; Que, L. Models for Diferrous Forms of Iron-Oxo Proteins. Structure and Properties of $[Fe_2BPMP(O_2CR)_2]BPh_4$ Complexes. *J. Am. Chem. Soc.* **1990**, *112*, 6031-6038.

(131) Cao, R.; Elrod, L. T.; Lehane, R. L.; Kim, E.; Karlin, K. D. A Peroxynitrite Dicopper Complex: Formation via Cu–NO and Cu–O_2 Intermediates and Reactivity via O–O Cleavage Chemistry. *J. Am. Chem. Soc.* **2016**, *138*, 16148-16158.

(132) Rrkubo, T.; Sugimoto, H.; Nagayama, T.; Masuda, H.; Sato, T.; Tanaka, K.; Maeda, Y.; Okawa, H.; Hayashi, Y.; Uehara, A.; Suzuki, M. *cis*-μ-1,2-Peroxo Diiron Complex: Structure and Reversible Oxygenation. *J. Am. Chem. Soc.* **1996**, *118*, 701-702.

(133) Dalle, K. E.; Meyer, F. Modelling Binuclear Metallobiosites: Insights from Pyrazole-Supported Biomimetic and Bioinspired Complexes. *Eur. J. Inorg. Chem.* **2015**, 3391-3405.

(134) Duan, P.-C.; Manz, D.-H.; Dechert, S.; Demeshko, S.; Meyer, F. Reductive O_2 Binding at a Dihydride Complex Leading to Redox Interconvertible μ-1,2-Peroxo and μ-1,2-Superoxo Dinickel(II) Intermediates. *J. Am. Chem. Soc.* **2018**, *140*, 4929-4939.

(135) Stevens, H.; Duan, P.-C.; Dechert, S.; Meyer, F. Competing H_2 versus Intramolecular C–H Activation at a Dinuclear Nickel Complex via Metal–Metal Cooperative Oxidative Addition. *J. Am. Chem. Soc.* **2020**, *142*, 6717-6728.

(136) Kindermann, N.; Günes, C.-J.; Dechert, S.; Meyer, F. Hydrogen Atom Abstraction Thermodynamics of a μ-1,2-Superoxo Dicopper(II) Complex. *J. Am. Chem. Soc.* **2017**, *139*, 9831-9834.

(137) Brinkmeier, A.; Scholz, R. A.; Buchhorn, M.; Spyra, C.-J.; Dechert, S.; Demeshko, S.; Krewald, V.; Meyer, F. Structurally Characterized μ-1,2-Peroxo/Superoxo Dicopper(II) Pair. *J. Am. Chem. Soc.* **2021**, *143*, 10361-10366.

(138) Neudeck, S.; Maji, S.; López, I.; Meyer, S.; Meyer, F.; Llobet, A. New Powerful and Oxidatively Rugged Dinuclear Ru Water Oxidation Catalyst: Control of Mechanistic Pathways by Tailored Ligand Design. *J. Am. Chem. Soc.* **2014**, *136*, 24-27.

(139) Neudeck, S.; Maji, S.; López, I.; Dechert, S.; Benet-Buchholz, J.; Llobet, A.; Meyer, F. Establishing the Family of Diruthenium Water Oxidation Catalysts Based on the Bis(bipyridyl)pyrazolate Ligand System. *Inorg. Chem.* **2016**, *55*, 2508-2521.

(140) Kindermann, N.; Schober, A.; Demeshko, S.; Lehnert, N.; Meyer, F. Reductive Transformations of a Pyrazolate-Based Bioinspired Diiron-Dinitrosyl Complex. *Inorg. Chem.* **2016**, *55*, 11538-11550.

(141) Ferretti, E.; Dechert, S.; Meyer, F. Reductive Binding and Ligand-Based Redox Transformations of Nitrosobenzene at a Dinickel(II) Core. *Inorg. Chem.* **2019**, *58*, 5154-5162.

(142) Peralta, R. A.; Bortoluzzi, A. J.; De Souza, B.; Jovito, R.; Xavier, F. R.; Couto, R. A. A.; Casellato, A.; Nome, F.; Dick, A.; Gahan, L. R.; Schenk, G.; Hanson, G. R.; De Paula, F. C. S.; Pereira-Maia, E. C.; de P. Machado, S.; Severino, P. C.; Pich, C.; Bortolotto, T.; Terenzi, H.; Castellano, E. E.; Neves, A.; Riley, M. J. Electronic Structure and Spectro-Structural Correlations of $Fe^{III}Zn^{II}$ Biomimetics for Purple Acid Phosphatases: Relevance to DNA Cleavage and Cytotoxic Activity. *Inorg. Chem.* **2010**, *49*, 11421–11438.

(143) Fukuzumi, S.; Morimoto, Y.; Kotani, H.; Naumov, P.; Lee, Y.-M.; Nam, W. Crystal structure of a metal ion-bound oxoiron(IV) complex and implications for biological electron transfer. *Nat. Chem.* **2010**, *2*, 756-759.

(144) Swart, M. A Change in the Oxidation State of Iron: Scandium Is Not Innocent. *Chem. Commun.* **2013**, *49*, 6650-6652.

(145) Prakash, J.; Rohde, G. T.; Meier, K. K.; Jasniewski, A. J.; Van Heuvelen, K. M.; Münck, E.; Que, L. Spectroscopic Identification of an Fe^{III} Center, not Fe^{IV}, in the Crystalline Sc–O–Fe Adduct Derived from $[Fe^{IV}(O)(TMC)]^{2+}$. *J. Am. Chem. Soc.* **2015**, *137*, 3478-3481.

(146) Zhou, A.; Crossland, P. M.; Draksharapu, A.; Jasniewski, A. J.; Kleespies, S. T.; Que, L. Oxoiron(IV) compelxes as synthons for the assembly of heterobimetallic centers such as the Fe/Mn active site of Class Ic ribonucleotide reductases. *JBIC, J. Biol. Inorg. Chem.* **2018**, *23*, 155-165.

(147) Crossland, P. M.; Guo, Y.; Que, L. Spontaneous Formation of an Fe/Mn Diamond Core: Models for the Fe/Mn Sites in Class 1c Ribonucleotide Reductases. *Inorg. Chem.* **2021**, *60*, 8710-8721.

(148) Eisenhart, R. J.; Clouston, L. J.; Lu, C. C. Configuring Bonds between First-Row Transition Metals. *Acc. Chem. Res.* **2015**, *48*, 2885-2894.

(149) Cammarota, R. C.; Clouston, L. J.; Lu, C. C. Leveraging Molecular Metal–Support Interactions for H_2 and N_2 Activation. *Coord. Chem. Rev.* **2017**, *334*, 100-111.

(150) Moore, J. T.; Chatterjee, S.; Tarrago, M.; Clouston, L. J.; Sproules, S.; Bill, E.; Bernales, V.; Gagliardi, L.; Ye, S.; Lancaster, K. M.; Lu, C. C. Enhanced Fe-Centered Redox Flexibility in Fe–Ti Heterobimetallic Complexes. *Inorg. Chem.* **2019**, *58*, 6199-6214.

(151) Krogman, J. P.; Thomas, C. M. Metal–Metal Multiple Bonding in C_3-Symmetric Bimetallic Complexes of the First Row Transition Metals. *Chem. Commun.* **2014**, *50*, 5115-5127.

(152) Greer, S. M.; McKay, J.; Gramigna, K. M.; Thomas, C. M.; Stoian, S. A.; Hill, S. Probing Fe–V Bonding in a C_3-Symmetric Heterobimetallic Complex. *Inorg. Chem.* **2018**, *57*, 5870-5878.

(153) Zhang, H.; Hatzis, G. P.; Moore, C. E.; Dickie, D. A.; Bezpalko, M. W.; Foxman, B. M.; Thomas, C. M. O_2 Activation by a Heterobimetallic Zr/Co Complex. *J. Am. Chem. Soc.* **2019**, *141*, 9516-9520.

(154) Rosenkoetter, K. E.; Ziller, J. W.; Heyduk, A. F. A Heterobimetallic W−Ni Complex Containing a Redox-Active $W[SNS]_2$ Metalloligand. *Inorg. Chem.* **2016**, *55*, 6794-6798.

(155) Wojnar, M. K.; Ziller, J. W.; Heyduk, A. F. Heterobimetallic and Heterotrimetallic Clusters Containing a Redox-Active Metalloligand. *Eur. J. Inorg. Chem.* **2017**, No. 47, 5571-5575.

(156) Shaik, S.; Hirao, H.; Kumar, D. Reactivity of High-Valent Iron−Oxo Species in Enzymes and Synthetic Reagents: A Tale of Many States. *Acc. Chem. Res.* **2007**, *40*, 532-542.

(157) Decker, A.; Rohde, J.-U.; Klinker, E. J.; Wong, S. D.; Que, L.; Solomon, E. I. Spectroscopic and Quantum Chemical Studies on Low-Spin Fe^{IV}=O Complexes: Fe-O Bonding and Its Contributions to Reactivity. *J. Am. Chem. Soc.* **2007**, *129*, 15983-15996.

(158) Geng, C.; Ye, S.; Neese, F. Analysis of Reaction Channels for Alkane Hydroxylation by Nonheme Iron(IV)−Oxo Complexes. *Angew. Chem., Int. Ed.* **2010**, *49*, 5717-5720.

(159) Collman, J. P.; Gagne, R. T.; Reed, C. A. Paramagnetic Dioxygen Complex of Iron(II) Derived from a Picket Fence Porphyrin. Further Models for Hemoproteins. *J. Am. Chem. Soc.* **1974**, *96*, 2629–2631.
(160) Collman, J. P.; Gagne, R. R.; Reed, C. A.; Robinson, W. T.; Rodley, G. A. Structure of an Iron(II) Dioxygen Complex; a Model for Oxygen Carrying Hemeproteins. *Proc. Natl. Acad. Science. U. S. A.* **1974**, *71*, 1326-1329.
(161) Wuenschell, G. E.; Tetreau, C.; Lavalette, D.; Reed, C. A. Hydrogen-Bonded Oxyhemoglobin Models with Substituted Picket-Fence Porphyrins: the Model Compound Equivalent of Site-Directed Mutagenesis. *J. Am. Chem. Soc.* **1992**, *114*, 3346-3355.
(162) Shook, R. L.; Gunderson, W. A.; Greaves, J.; Ziller, J. W.; Hendrich, M. P.; Borovik, A. S. A Monomeric Mn^{III}-Peroxo Complex Derived Directly from Dioxygen. *J. Am. Chem. Soc.* **2008**, *130*, 8888–8889.
(163) Bhadra, M.; Lee, J. Y. C.; Cowley, R. E.; Kim, S.; Siegler, M. A.; Solomon, E. I.; Karlin, K. D. Intramolecular Hydrogen Bonding Enhances Stability and Reactivity of Mononuclear Cupric Superoxide Complexes. *J. Am. Chem. Soc.* **2018**, *140*, 9042-9045.
(164) Diaz, D. E.; Quist, D. A.; Herzog, A. E.; Schaefer, A. W.; Kipouros, I.; Bhadra, M.; Solomon, E. I.; Karlin, K. D. Impact of Intramolecular Hydrogen Bonding on the Reactivity of Cupric Superoxide Complexes with O–H and C–H Substrates. *Angew. Chem., Int. Ed.* **2019**, *131*, 17736-17740.
(165) Wada, A.; Ogo, S.; Nagatomo, S.; Kitagawa, T.; Watanabe, Y.; Jitsukawa, K.; Masua, H. Reactivity of Hydroperoxide Bound to a Mononuclear Non-Heme Iron Site. *Inorg. Chem.* **2002**, *41*, 616-618.
(166) Kitajima, N.; Komatsuzaki, H.; Hikichi, S.; Osawa, M.; Moro-oka, Y. A Monomeric Side-On Peroxo Manganese(III) Complex: $Mn(O_2)(3,5\text{-}iPr_2pzH)(HB(3,5\text{-}iPr_2pz)_3)$. *J. Am. Chem. Soc.* **1994**, *116*, 11596-11597.
(167) Hammes, B. S.; Young, V. G.; Borovik, A. S. Hydrogen-Bonding Cavities about Metal Ions: A Redox Pair of Coordinatively Unsaturated Paramagnetic Co-OH Complexes. *Angew. Chem. Int. Ed.* **1999**, *38*, 666-669.
(168) Shirin, Z.; Hammes, B. S.; Young, V. G.; Borovik, A. S. Hydrogen Bonding in Metal–Oxo Complexes: Synthesis and Structure of a Monomeric Manganese(III)–Oxo Complex and Its Hydroxo Analogue. *J. Am. Chem. Soc.* **2000**, *122*, 1836-1837.
(169) Parsell, T. H.; Behan, R. K.; Green, M. T.; Hendrich, M. P.; Borovik, A. S. Preparation and Properties of a Monomeric Mn^{IV}–Oxo Complex. *J. Am. Chem. Soc.* **2006**, *128*, 8728-8729.
(170) Lucas, R.; Zart, M. K.; Mukherjee, J.; Sorrell, T. N.; Powell, D. R.; Borovik, A. S. A Modular Approach toward Regulating the Secondary Coordination Sphere of Metal Ions: Differential Dioxygen Activation Assisted by Intramolecular Hydrogen Bonds. *J. Am. Chem. Soc.* **2006**, *128*, 15476-15489.
(171) Mukherjee, J.; Lucas, R. L.; Zart, M. K.; Powell, D. R.; Day, V. W.; Borovik, A. S. Synthesis, Structure and Physical Properties for a Series of Monomeric Iron(III)–Hydroxo Complexes with Varying Hydrogen-Bond Networks. *Inorg. Chem.* **2008**, *47*, 5780-5786.
(172) Weitz, A. C.; Hill, E. A.; Oswald, V. F.; Bominaar, E. L.; Borovik, A. S.; Hendrich, M. P.; Guo, Y. Probing hydrogen bonding interactions to iron-oxido/hydroxido units via ^{57}Fe nuclear resonance vibrational spectroscopy. *Angew. Chem. Int. Ed.* **2018**, *57*, 16010-16014.
(173) Ford, C.; Park, Y. J.; Matson, E. M.; Gordon, Z.; Fout, A. R. A Bioinspired iron Catalyst for Nitrate and Perchlorate Reduction. *Science* **2016**, *354*, 741-743.
(174) Park, Y. J.; Matson, E. M.; Nilges, M. J.; Fout, A. R. Exploring Mn–O Bonding in the Context of an Electronically Flexible Secondary Coordination Sphere: Synthesis of a Mn(III)–Oxo. *Chem. Commun.* **2015**, *51*, 5310-5313.

(175) Yadav, V.; Gordon, J. B.; Siegler, M. A.; Goldberg, D. P. Dioxygen-Derived Nonheme Mononuclear Fe^{III}(OH) Complex and Its Reactivity with Carbon Radicals. *J. Am. Chem. Soc.* **2019**, *141*, 10148-10153.
(176) Reed, C. J.; Agapie, T. A Terminal Fe^{III}–Oxo in a Tetranuclear Cluster: Effects of Distal Metal Centers on Structure and Reactivity. *J. Am. Chem. Soc.* **2019**, *141*, 9479-9484.
(177) Helm, M. L.; Stewart, M. P.; Bullock, R. M.; DuBois, M. R.; DuBois, D. L. A Synthetic Nickel Electrocatalyst with a Turnover Frequency above 100,000 s^{-1} for H_2 Production. *Science.* **2011**, *333*, 863-866.
(178) Wilson, A. D.; Newell, R. H.; McNevin, M. J.; Muckerman, J. T.; DuBois, M. R.; DuBois, D. L. Hydrogen Oxidation and Production Using Nickel-Based Molecular Catalysts with Positioned Proton Relays. *J. Am. Chem. Soc.* **2006**, *128*, 358-366.
(179) Wallen, C. M.; Palatinus, L.; Basca, J.; Scarborough, C. C. Hydrogen Peroxide Coordination to Cobalt(II) Facilitated by Second-Sphere Hydrogen Bonding. *Angew. Chem.,Int.Ed.* **2016**, *128*, 12081-12085.
(180) Shanahan, J. P.; Szymczak, N. K. Hydrogen Bonding to a Dinitrogen Complex at Room Temperature: Impacts on N_2 Activation. *J. Am. Chem. Soc.* **2019**, *141*, 8550-8556.
(181) Barman, S. K.; Jones, J. R.; Sun. C.; Hill, E. A.; Ziller, J. W.; Borovik, A. S. Regulating the Basicity of Metal–Oxido Complexes with a Single Hydrogen Bond and Its Effect on C–H Bond Cleavage. *J. Am. Chem. Soc.* **2019**, *141*, 11142-11150.
(182) Drummond, M. J.; Ford, C. L.; Gray, D. L.; Popescu, C. V.; Fout, A. R. Radical Rebound Hydroxylation Versus H-Atom Transfer in Non-Heme Iron(III)-Hydroxo Complexes: Reactivity and Structural Differentiation. *J. Am. Chem. Soc.* **2019**, *141*, 6639-6650.
(183) Opalade, A. A.; Hessefort, L.; Day, V. W.; Jackson, T. A. Controlling the Reactivity of a Metal-Hydroxo Adduct with a Hydrogen Bond. *J. Am. Chem. Sci.* 2021, *143*, 15159-15175.
(184) Tutusaus-Santandreu, O.; Ni, C.; Szymczak, N. K. A Transition Metal Lewis Acid/Base Triad System for Cooperative Substrate Binding. *J. Am. Chem. Soc.* **2013**, *135*, 3403-3406.
(185) Kiernicki, J. J.; Zeller, M.; Szymczak, N. K. Hydrazine Capture and N–N Bond Cleavage at Iron Enabled by Flexible Appended Lewis Acids. *J. Am. Chem. Soc.* **2017**, *139*, 18194-18197.
(186) Kiernicki, J. J.; Zeller, M.; Szymczak, N. K. Requirements for Lewis Acid-Mediated Capture and N–N Bond Cleavage of Hydrazine at Iron. *Inorg. Chem.* **2019**, *58*, 1147-1154.
(187) Kiernicki, J. J.; Norwine, E. E.; Zeller, M.; Szymczak, N. K. Tetrahedral Iron Featuring an Appended Lewis Acid: Distinct Pathways for the Reduction of Hydroxylamine and Hydrazine. *Chem. Commun.* **2019**, *55*, 11896-11899.
(188) Kiernicki, J. J.; Zeller, M.; Szymczak, N. K. Examining the Generality of Metal–Ligand Cooperativity Across a Series of First-Row Transition Metals: Capture, Bond Activation, and Stabilization. *Inorg. Chem.* **2020**, *59*, 9279-9286.
(189) Chantarojsiri, T.; Reath, A. H.; Yang, J. J. Cationic Charges Leading to an Inverse Free-Energy Relationship for N–N Bond Formation by Mn^{VI} Nitrides. *Angew. Chem., Int. Ed.* **2018**, *57*, 14037-14042.
(190) Dahl, E. W.; Dong, H. T.; Szymczak, N. K. Phenylamino Derivatives of Tris(2-pyridylmethyl)amine: Hydrogen-Bonded Peroxodicopper Complexes. *Chem. Commun.* **2018**, *54*, 892-895.
(191) Dahl, E. W.; Kiernicki, J. J.; Zeller, M.; Szymczak, N. K. Hydrogen Bonds Dictate O_2 Capture and Release within a Zinc Tripod. *J. Am. Chem. Soc.* **2018**, *140*, 10075-10079.
(192) Ford, C. L.; Miller, T. J.; Park, Y. J.; Iranmanesh, N.; Gray, D. L.; Fout, A. R. Varying the Secondary Coordination Sphere: Synthesis of Cobalt and Iron Complexes of a Tripodal Ligand Featuring Two Hydrogen-bond Donors or Acceptors. *J Coord. Chem.* **2020**, *73*, 2195-2208.

(193) Arii, H.; Funahashi, Y.; Jitsukawa, K.; Masuda, H. Preparation and Structural Characterization of a Novel Dicopper(II) Complex with a Terminal Hydroxide: A Structural Model of an Active Site in Phosphohydrolases. *Dalton Trans.* **2003**, 2115-2116.
(194) Graef, T.; Galezowska, J.; Dechert, S.; Meyer, F. Decorating the Second Coordination Sphere in Pyrazolate-Based Dinickel(II) Complexes with H-Bond Donors. *Eur. J. Inorg. Chem.* **2011**, 4161-4167.
(195) MacBeth, C. E.; Hammes, B. S.; Young, V. G.; Borovik, A. S. Hydrogen-Bonding Cavities about Metal Ions: Synthesis, Structure, and Physical Properties for a Series of Monomeric M–OH Complexes Derived from Water. *Inorg. Chem.* **2001**, *40*, 4733-4741.
(196) MacBeth, C. E.; Gupta, R.; Mitchell-Koch, K. R.; Young, V. G.; Lushington, G. H.; Thompson, W. H.; Hendrich, M. P.; Borovik, A. S. Utilization of Hydrogen Bonds To Stabilize M–O(H) Units: Synthesis and Properties of Monomeric Iron and Manganese Complexes with Terminal Oxo and Hydroxo Ligands. *J. Am. Chem. Soc.* **2004**, *126*, 2556–2567.
(197) MacBeth, C. E.; Golombek, A. P.; Young, V. G.; Yang, C.; Kuczera, K.; Hendrich, M. P.; Borovik, A. S. O_2 Activation by Nonheme Iron Complexes: A Monomeric Fe(III)–Oxo Complex Derived from O_2. *Science,* **2000**, *289*, 938-941.
(198) Lacy, D. C.; Gupta, R.; Stone, K. L.; Greaves, J.; Ziller, J. W.; Hendrich, M. P.; Borovik, A. S. Formation, Structure, and EPR Detection of a High Spin Fe^{IV}–Oxo Species Derived from Either an Fe^{III}–Oxo or Fe^{III}–OH Complex. *J. Am. Chem. Soc.* **2010**, *132*, 12188-12190.
(199) Gupta, R.; Lacy, D. C.; Bominaar, E. L.; Borovik, A. S.; Hendrich, M. P. Electron Paramagnetic Resonance and Mössbauer Spectroscopy and Density Functional Theory Analysis of a High-Spin Fe^{IV}–Oxo Complex. *J. Am. Chem. Soc.* **2012**, *134*, 9775-9784.
(200) Lacy, D. C.; Mukherjee, J.; Lucas, R. L.; Powell, D. R.; Day, V. W.; Borovik, A. S. Complexes with Varying Intramolecular Hydrogen Bonding Networks. *Polyhedron* **2013**, *44*, 261-267.
(201) Zart, M. K.; Sorrell, T. N.; Powell, D.; Borovik, A. S. Development of bio-inspired chelates with hydrogen bond donors: synthesis and structure and monomeric metal acetate complexes with intramolecular hydrogen bonds. *Dalton Trans.* **2003**, 1986-1992.
(202) Zart, M. K.; Powell, D.; Borovik, A. S. Synthesis and structures of dimeric iron(III)-Oxo and -imido complexes containing intramolecular hydrogen bonds. *Inorg. Chim. Acta* **2007**, *360*, 2397-2402.
(203) Zinn, P. J.; Powell, D. R.; Day, V. W.; Hendrich. M. P.; Sorrell, T. N.; Borovik, A. S. Pyrazolate-Bridging Dinucleating Ligands Containing Hydrogen-Bond Doners: Synthesis and Structure of Their Cobalt Analogues. *Inorg. Chem.* **2006**, *45*, 3484-3486.
(204) Zinn, P. J.; Sorrell, T. N.; Powell, D. R.; Day, V. W.; Borovik, A. S. Acetonitrile Hydration and Ethyl Acetate Hydrolysis by Pyrazolate-Bridged Cobalt(II) Dimers Containing. *Inorg. Chem.* **2007**, *46*, 10120-10132.
(205) Ng, G. K.-Y.; Ziller, J. W.; Borovik, A. S. Structural Diversity in Metal Complexes with a Dinucleating Ligand Containing Carboxyamidopyridyl Groups. *Inorg. Chem.* **2011**, *50*, 7922-7924.
(206) Ng, G. K.-Y.; Ziller, J. W.; Borovik, A. S. Preparation and Structures of Dinuclear Complexes Containing M^{II}–OH centers. *Chem. Commun.* **2012**, *48*, 2546-2548.
(207) Zinn, P. J. Doctoral Dissertation, University of Kansas, Lawrence, KS, 2006.
(208) Ng, K. Doctoral Dissertation, University of California-Irvine, Irvine, CA, 2012.
(209) Park, Y. J.; Ziller, J. W.; Borovik, A. S. The Effects of Redox-Inactive metal Ions on the Activation of Dioxygen: Isolation and Characterization of a Heterobimetallic Complex Containing a Mn^{III}–(μ-OH)–Ca^{II} Core. *J. Am. Chem. Soc.* **2011**, *133*, 9258-9261.

(210) Lacy, D. C.; Park, Y. J.; Ziller, J. W.; Yano, J.; Borovik, A. S. Assembly and Properties of Heterobimetallic $Co^{II/III}/Ca^{II}$ Complexes with Aquo and Hydroxo Ligands. *J. Am. Chem. Soc.* **2012**, *134*, 17526-17535.
(211) Park, Y. J.; Cook, S.; Sickerman, N. S.; Sano, Y.; Ziller, J. W.; Borovik, A. S. Heterobimetallic Complexes with M^{III}–(μ-OH)–M^{II} Cores (M^{III} = Fe, Ga, Mn; M^{II} = Ca, Sr and Ba): Structural, Kinetic, and Redox Properties. *Chem. Sci.* **2013**, *4*, 717-726.
(212) Sano, Y.; Weitz, A. C.; Ziller, J. W.; Hendrich, M. P.; Borovik, A. S. Unsymmetrical Bimetallic Complexes with M^{II}–(μ-OH)–M^{III} Cores ($M^{II}M^{III}$ = $Fe^{II}Fe^{III}$, $Mn^{II}Fe^{III}$, $Mn^{II}Mn^{III}$): Structural, Magnetic, and Redox Properties. *Inorg. Chem.* **2013**, *52*, 10229-10231.
(213) Sano, Y.; Lau, N.; Weitz, A. C.; Ziller, J. W.; Hendrich, M. P.; Borovik, A. S. Models for Unsymmetrical Active Sites in Metalloproteins: Structural, Redox, and Magnetic Properties of Bimetallic Complexes with M^{II}-(μ-OH)-Fe^{III} Cores. *Inorg. Chem.* 2017, *56*, 14118-14128.
(214) Lau, N.; Sano, Y.; Ziller, J. W.; Borovik, A. S. Modular bimetallic complexes with a sulfonamido-based ligand. *Dalton Trans.* **2018**, *47*, 12362-12372.
(215) Cook, S. A.; Ziller, J. W.; Borovik, A. S. Iron(II) Complexes Supported by Sulfonamido Tripodal Ligands: Endogenous versus Exogenous Substrate Oxidation. *Inorg. Chem.* **2014**, *53*, 11029-11035.
(216) Sickerman, N. S. Doctoral Dissertation, University of California-Irvine, Irvine, CA, 2014.
(217) Oswald, V. F. Doctoral Dissertation, University of California-Irvine, Irvine, CA, 2018.
(218) Oswald, V. F.; Weitz, A. C.; Biswas, S.; Ziller, J .W.; Hendrich, M. P.; Borovik, A. S. Manganese–Hydroxido Complexes Supported by a Urea/Phosphinic Amide Tripodal Ligand. *Inorg. Chem.* **2018**, *57*, 13341-13350.
(219) Sun, C.; Oswald, V. F.; Hill, E. A.; Ziller, J. W.; Borovik, A. S. Investigation of iron-ammine and amido complexes within a C_3-symmetrical phosphinic amido tripodal ligand. *Dalton Trans*. **2021**, *50,* 11197-11205.
(220) Oswald, V. F.; Lee, J. L.; Biswas, S.; Weitz, A. C.; Mittra, K.; Fan, R.; Li, J.; Zhao, J.; Hu, M. Y.; Alp, E. E.; Bominaar, E. L.; Guo, Y.; Green, M. T.; Hendrich, M. P.; Borovik, A. S. Effects of Non-covalent Interactions on High-spin Fe(IV)-oxido Complexes. *J. Am. Chem. Soc.* **2020**, *142*, 11804-11817.

Chapter 2

Demystifying "*g* 10"

Introduction

This dissertation begins with my work in synthetic modelling of mononuclear Fe enzyme active sites that perform C–H bond activation. Unlike the traditional organometallic approach that utilizes late second- and third-row transition-metal complexes to cleave the C–H bond *via* oxidative addition,[1-6] nature employs Fe=O and Fe–OH motifs that are operative within proteins.[7-14] For heme systems (e.g. Cytochrome P450s), a formally Fe^{V}=O species (denoted as compound I) is formed upon O_2 activation, but spectroscopic studies conclusively show that the competent oxidant is an Fe^{IV}=O unit coupled to a porphyrin radical (Scheme 2.1).[15] After C–H bond cleavage, an Fe^{IV}–OH species is produced (denoted as compound II) that recombines with the substrate carbon radical to form an Fe^{III}–O(H)CH_3 species.[16-18] It is the interplay between these two high-valent Fe species that drives biological C–H bond cleavage in Cytochrome P450s. The properties of the Fe^{IV}–OH motif in compound II are unique, because high-valent metal–oxido species are generally weak electrophiles due to their multiple-bond character and are difficult to protonate.[19] To support this premise, Green experimentally determined a pK_a(OH) of 12 for compound II, and attributed the high value to the basic cysteine thiolate bound trans to the hydroxido ligand; comparable species in other heme proteins with histidine axial ligands have estimated pK_a(OH) values of less than 5.[18] Similar intermediates have been proposed for non-heme systems, but they lack experimental verifications;[20-22] likewise, synthetic verification of Fe^{IV}–OH species has also been difficult to achieve. Several reports have claimed to generate an Fe^{IV}–OH species, but they lack detailed oxidation state assignments,[23] or precise determination of the H^+ location.[24,25] These examples demonstrate that care

must be taken in the assignment of protonation state in high-valent metal–oxido complexes, which remains an ongoing challenge within the field.[7]

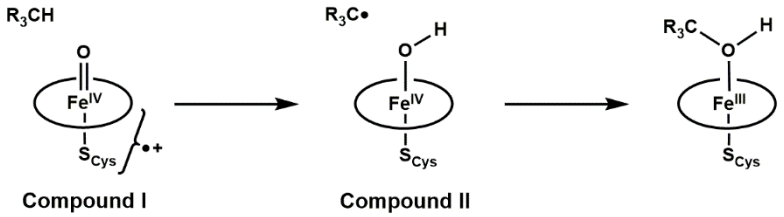

Scheme 2.1. Aliphatic hydroxylation by Cytochrome P450 Enzymes.

A former member of the Borovik Lab, Dr. Victoria Oswald, has performed extensive experiments in an attempt to trap an Fe^{IV}–OH species utilizing the $[poat]^{3-}$ ligand framework. As introduced in the previous chapter, $[poat]^{3-}$ provides a trianionic ligand field that supports high-valent metal centers,[26] and contains H-bond accepting functionalities in the phosphinic amido P=O groups to stabilize Brönsted acidic exogenous ligands (e.g. a high-valent M–OH motif).[27,28] Two reversible oxidation events were observed at < –1 V (vs $[FeCp_2]^{+/0}$) for the Fe^{II} starting synthon, $K_2[Fe^{II}poat(OH)]$, which suggests that two higher oxidation levels above the Fe^{II} state can be achieved for this complex.[29] Treatment of $K_2[Fe^{II}poat(OH)]$ with two equivalents of $[FeCp_2]BF_4$ in the presence of 18-crown-6 (18-c-6) yielded a new species observable by parallel-mode electron paramagnetic resonance (EPR) spectroscopy (Scheme 2.2). The feature has a derivative-shape with g = 9.7 which supports a spin state assignment of 2,[25,30] but is distinct from the signal for the previously reported $[Fe^{IV}poat(O)]^-$ species.[26] ^{57}Fe Mössbauer experiments revealed a doublet spectrum (~ 40% yield) that is consistent with a non-Kramer (i.e. integer-spin) system, but the isomer shift (δ) and quadrupole splitting (ΔE_Q) values of 0.33/0.98 mm s^{-1} are more consistent with an Fe^{III} center, not Fe^{IV}.[26,31,32] Further examination of the g = 9.7 EPR signal revealed its temperature-dependent nature, and an increase in measurement temperature resulted in a lowering of intensity of the signal with a concomitant growth of a new feature at g = 13.4. This lower field feature is consistent with a spin state of S = 3.[33] The combined magnetic studies suggest that the

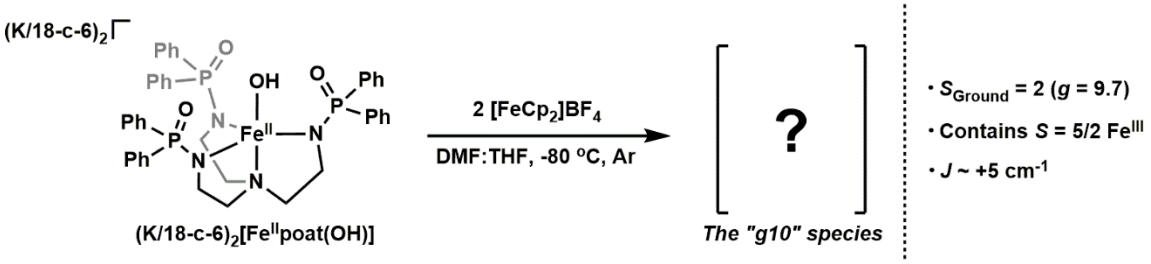

Scheme 2.2. Previously reported generation of the "g10" species from the addition of 2 equivalents $[FeCp_2]BF_4$ to $[Fe^{II}poat(OH)]^{2-}$. $K_2[^{57}Fe^{II}poat(OH)]$ was used for Mössbauer measurements. A summary of the properties for this species is listed in the right panel.

new complex does not have a single paramagnetic $S = 2$ center, but instead is a spin-exchange system, containing an $S = 5/2$ Fe^{III} center coupled to an $S = 1/2$ site. A spin exchange constant J was measured to be ~ +5 cm^{-1} ($\mathcal{H} = JS_1 \bullet S_2$), which indicates weak antiferromagnetic interactions. This new compound is hereby termed the "*g*10" species due to its unusual EPR feature; it is highly unstable, which precludes preparation of pure samples for other spectroscopic techniques.

In this chapter, I sought to elucidate the identity of the "*g*10" species. Efforts to improve its synthetic preparation, and the re-evaluation of the electrochemical properties of the Fe–hydroxido complexes and the redox-inactive Ga analog are discussed. A proposed structure for this species is supported by new electrochemical, magnetic, and structural evidence.

Results & Discussion

Proposed structures for the "g10" species. Several structures have been proposed for this mysterious "*g*10" species. The initial goal to synthesize $[Fe^{IV}poat(OH)]$ (Figure 2.1.A) proved unsuccessful, as the temperature-dependent EPR measurements showed this new species to be a spin-exchange system (with a ground spin state of $S = 2$ and an excited spin state of $S = 3$), and Mössbauer results demonstrated that the complex contains a high-spin Fe^{III} center. These findings, as well as other attempts using various tripodal frameworks developed by the Borovik Lab,[29,32,34] demonstrate the difficulty in generating a non-heme Fe^{IV}–OH species. A plausible proposal is the formation of an

[Fe^{III}(poat)$^{\bullet+}$(OH)] complex (Figure 2.1.B), in which the oxidation takes place on the [poat]$^{3-}$ ligand. Ligand oxidation is known to occur in biological and synthetic systems;[33,35-40] one example is the Fe^{IV}-oxido coupled to a ligand radical in P450 Compound I discussed above.[15] However, there is no evidence of ligand non-innocence observed in the >50 well-characterized complexes in the [poat]$^{3-}$ ligand or related frameworks developed by the Borovik Lab,[26-29,34,41-43] and the spin exchange constant J (~ 5 cm^{-1}) is not strong enough to be considered for a metal center antiferromagnetically coupled to a paramagnetic nitrogen-rich ligand framework.[36,44,45]

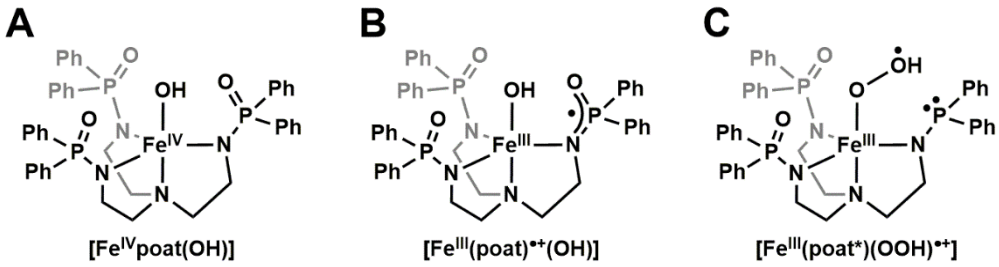

Figure 2.1. Different proposed structures for the "g10" species: (A) [Fe^{IV}poat(OH)] from metal oxidation; (B) [Fe^{III}(poat)$^{\bullet+}$(OH)] from ligand oxidation; (C) [Fe^{III}(poat*)(OOH)$^{\bullet+}$] from intramolecular O–O bond formation.

The small magnitude of J led us to consider the other structural possibilities for the "*g*10" species, such as Fe complexes with an exogenous ligand that contains a radical center. One intriguing suggestion was a (hydro)superoxido ligand, which is illustrated in Figure 2.1.C. A [Fe^{III}(poat*)(OOH)$^{\bullet+}$] species is proposed to be generated via intramolecular O–O bond formation, arising from the coupling of the Fe–OH motif and the P=O group in one of the phosphinic amido arms in [poat]$^{3-}$.[29] Non-heme Fe^{III}–superoxido species have been observed in both enzymatic and synthetic systems with the J value ranging between 6 – 15 cm^{-1}, which is within range of what is observed for the "*g*10" species.[33,46,47] The even integer overall spin state and high-spin Fe^{III} character of the "*g*10" species are also consistent with an Fe^{III}–superoxido formulation. However, much further characterization is necessary to support any assignment of the "g10" species.

Improved synthesis of K[Fe^{III}poat(OH)] and generation of the "g10" species. Past experiments to characterize the "*g*10" species employed K$_2$[Fe^{II}poat(OH)] as a starting synthon,[29] but since two equivalents of [FeCp$_2$]BF$_4$ were required to generate this species, it is conceivable that Fe^{III}–OH was generated by the first equivalent oxidant. I hypothesized using K[Fe^{III}poat(OH)] would reduce the overall reaction by one step and provide purer samples of the "*g*10" species for characterization.

The synthesis (Scheme 2.3) and characterization of K$_2$[Fe^{II}poat(OH)] are documented and the details are not further discussed here (the molecular structure is illustrated in Figure 2.2.A,C).[29] While the K[Fe^{III}poat(OH)] complex was prepared by previous Borovik lab members,[29,34] the crystalline yield was consistently low (< 20 %). The synthesis of K[Fe^{III}poat(OH)] was improved by treatment of one equivalent of O_2 to K[Fe^{II}poat] generated *in situ*, and recrystallization from a CH_2Cl_2/Et_2O mixture provided dark yellow crystals with yields of ~ 35 % (Scheme 2.3).[27] The molecular structure reveals a cluster that contains two molecules of [Fe^{III}poat(OH)]$^-$, which are linked by two K$^+$ counterions (Figure 2.2.B,D); it is also worth-noting that the Fe^{II} analog also recrystallizes as an aggregate, with an overall formulation of {K$_2$[Fe^{II}poat(OH)]}$_2$•4THF. The structure metrical parameters for both complexes have been reported.[29] The EPR and Mössbauer spectra were consistent with an S = 5/2 Fe^{III} center, with g-values of 9.44 and 4.30, and $\delta/\Delta E_Q$ values of 0.32 and 0.92 mm s^{-1} (Figure 2.3).[34]

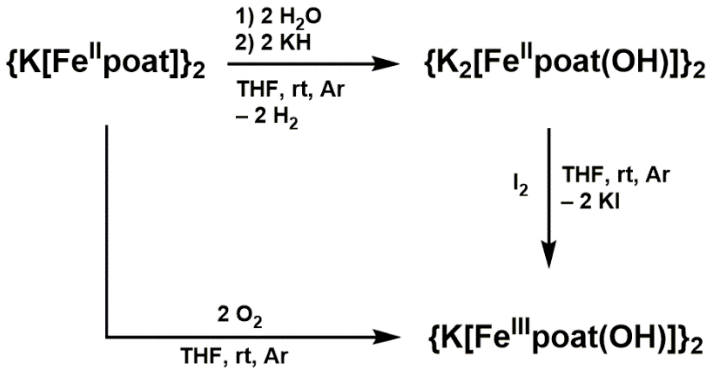

Scheme 2.3. Preparative routes to K[Fe^{III}poat(OH)].

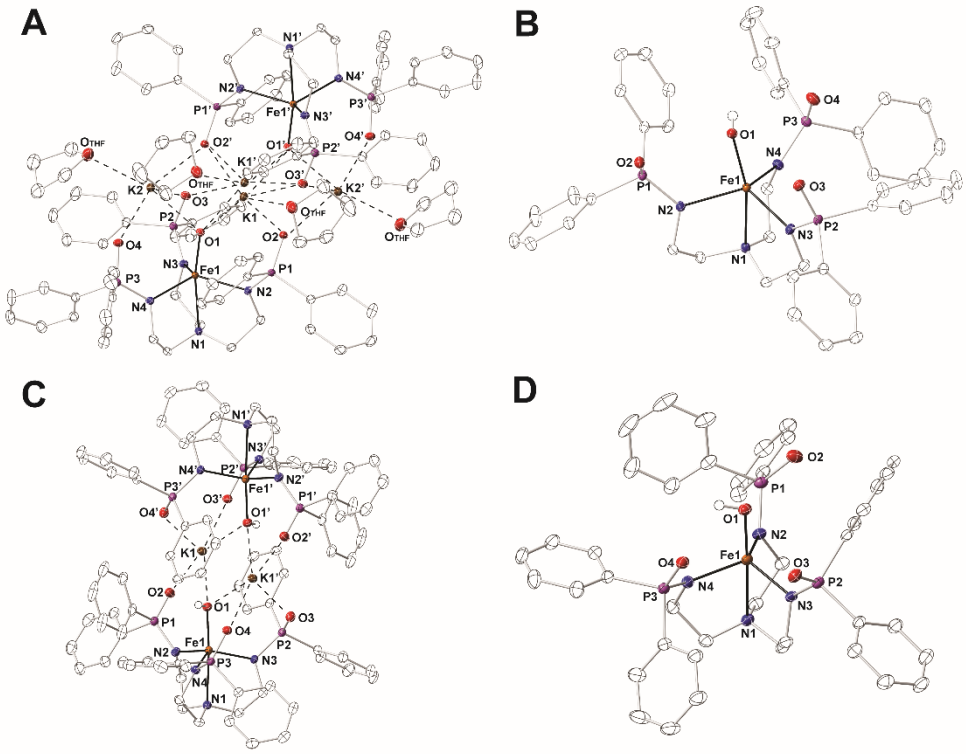

Figure 2.2. Thermal ellipsoid diagrams depicting the molecular structures of $\{K_2[Fe^{II}poat(OH)\}_2$•4THF (A) and $\{K[Fe^{III}poat(OH)]\}_2$ (C) by X-ray diffraction. The $[Fe^{II}poat(OH)]^{2-}$ and $[Fe^{III}poat(OH)]^{-}$ fragments are illustrated in (B) and (D), respectively. Ellipsoids are drawn at the 50% probability level, and only the hydroxido H atoms are shown for clarity.

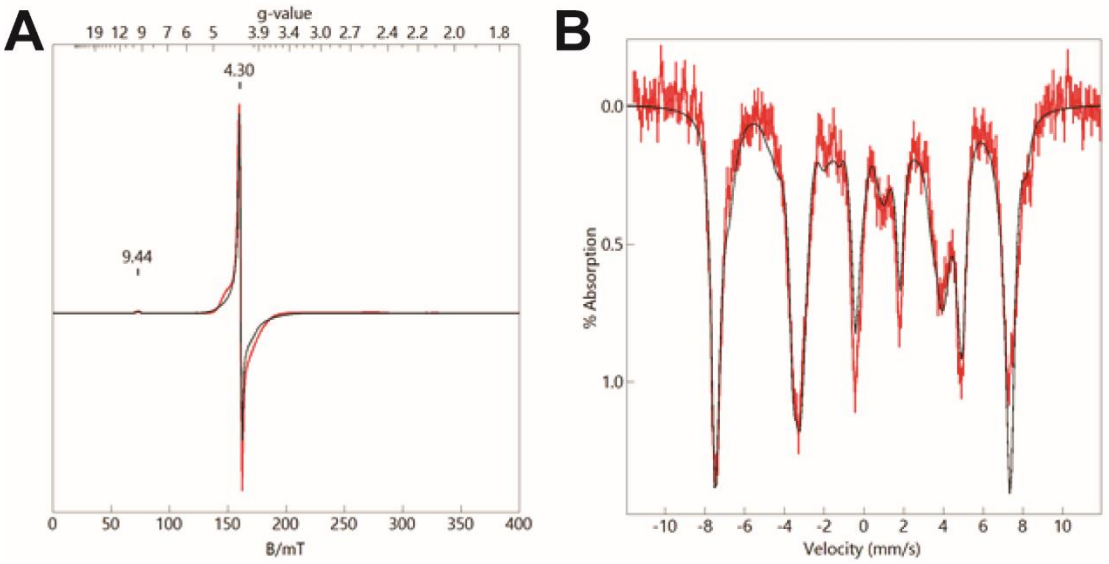

Figure 2.3. EPR (A) and Mössbauer (B) spectra of 1.6mM (K/18c6)[$^{57}Fe^{III}$poat(OH)] in 1:1 DMF:THF (red plots). Experimental parameters: (A) microwaves, 0.2 mW at 9.645 GHz; temperature, 12 K; (B) magnetic field 45 mT parallel to γ-ray direction, temperature, 4.2 K. The black lines are simulation for: S = 5/2, D = 1 cm^{-1}, E/D = 0.27, A_{57Fe} = (-20, -19, -19) T, δ = 0.32 mm s^{-1}, ΔE_Q = 0.92 mm s^{-1}, η = 0.9.

In the presence of 18-c-6 to improve the solubility of the complex, K[Fe^{III}poat(OH)] was treated with 1 equivalent [$FeCp_2$]BF_4 at -78 °C, and a feature at g = 9.7 in the parallel-mode EPR spectrum appeared, which matches the unidentified "g10" species (Figure 2.4). However, the reaction yield is still estimated to be ~ 50% by EPR simulation, which is not a significant improvement from the reaction of two equivalents of $[FeCp_2]^+$ and $[Fe^{II}poat(OH)]^{2-}$ (~ 40 %).

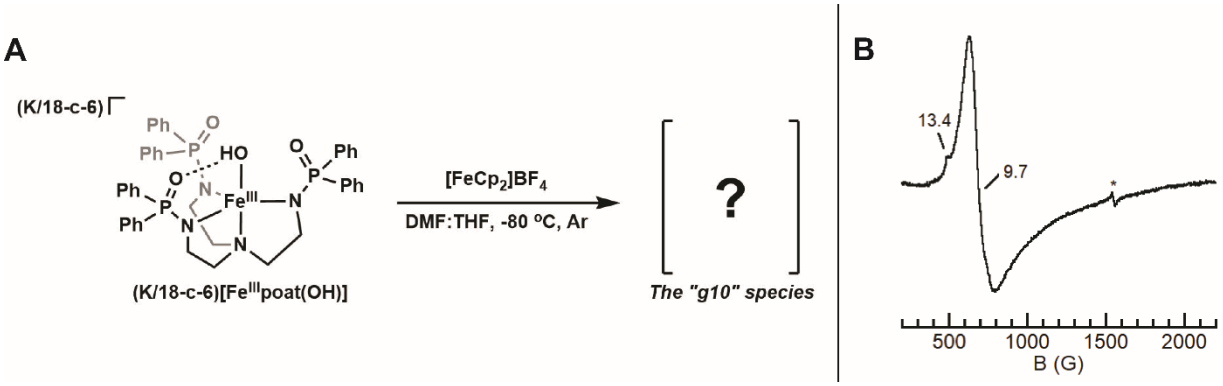

Figure 2.4. Generation of the "g10" species from $[Fe^{III}poat(OH)]^-$ (A). Parallel-mode EPR spectrum (B) of the "g10" species generated from addition of [$FeCp_2$]BF_4 to K[Fe^{III}poat(OH)]/18-c-6. Experimental parameters: (A) concentration, 21.1-mM; microwaves, 0.2 mW at 9.3 GHz; temperature, 15.4 K. The asterisk (*) indicates minor high-spin ferric impurities.

Re-evaluation of the electrochemical properties of $[Fe^{II}poat(OH)]^{2-}$ and $[Fe^{III}poat(OH)]^-$. The electrochemical properties of K_2[Fe^{II}poat(OH)] were previously investigated using cyclic voltammetry,[29] and have been re-evaluated and illustrated in Figure 2.5.A. The cyclic voltammogram exhibits two reversible processes at -1.79 and -1.07 V (vs $[FeCp_2]^{+/0}$), which was initially assigned as the $Fe^{III/II}$ and $Fe^{IV/III}$ (or $[Fe^{III}L^{\bullet+}]/[Fe^{III}L]$) events, respectively. However, these electrochemical experiments were performed in the absence of 18-crown-6, which was added during spectroscopic studies in hopes of 1) improving the solubility of the complex, 2) encapsulating the potassium counterions, and 3) breaking apart the cluster to form discrete mononuclear $[Fe^npoat(OH)]^{n-4}$ molecules (n = +2 or +3). In the presence of 4.0 equivalents 18-c-6 (two per potassium), the cyclic voltammogram for K_2[Fe^{II}poat(OH)] was different (Figure 2.5.B): the oxidative wave at -1.73 V disappeared, and the oxidative process at E_{pa} = -1.04 V approximately doubled in current intensity. This strongly indicates

the two processes observed for $K_2[Fe^{II}poat(OH)]$ in the absence of 18-c-6 do not correspond to two oxidations of the mononuclear $[Fe^{II}poat(OH)]^{2-}$ complex, but instead two oxidations of $\{K_2[Fe^{II}poat(OH)]\}_2$ cluster: the first oxidation produces a $(\{K_2[Fe^{II}poat(OH)]\}\{K_2[Fe^{III}poat(OH)]\})^{+}$ aggregate, and the second oxidation generates $(\{K_2[Fe^{III}poat(OH)]\}_2)^{2+}$. These results also suggested the diiron(II) cluster (Figure 2.2.A) does not readily dissociate into mononuclear Fe complexes in solution in the absence of encapsulating agents (e.g. 18-c-6). Synthetic efforts to replace the K^+ counterions with noncoordinating cations for $[Fe^{II}poat(OH)]^{2-}$ and $[Fe^{III}poat(OH)]^{-}$ have been largely unsuccessful.

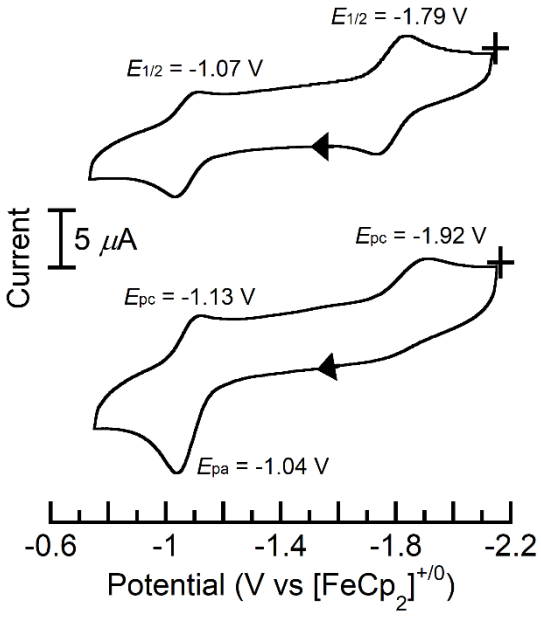

Figure 2.5. Cyclic voltammograms of (A) $K_2[Fe^{II}poat(OH)]$ in the absence of 18-c-6, and (B) $K_2[Fe^{II}poat(OH)]$ in the presence of 18-c-6. The cyclic voltammograms were collected at 100 mV s^{-1} in DMF.

I then turned my focus to the oxidation chemistry of $K[Fe^{III}poat(OH)]$ (Figure 2.6.A). In the presence of 2.0 equivalents 18-c-6, the cyclic voltammogram for $K[Fe^{III}poat(OH)]$ is comparable with that for $K_2[Fe^{II}poat(OH)]$/18-c-6 (Figure 2.6.B, 2.5.B). Although the reductive process at E_{pc} = -1.07 V and oxidative process at E_{pa} = -1.01 V are close in potentials (ΔE = 60 mV), they do not correspond to the same one-electron event, as no current was detected in the electrochemical window between -0.7 and -1.5 V (Figure 2.6.C). Instead, the oxidative process at E_{pa} = -1.01 V only

appears after accessing the reduction at E_{pc} = -1.96 V (Figure 2.6.B), and the reductive process at E_{pc} = -1.07 V appears after accessing the oxidations at E_{pa} > +0.1 V (Figure 2.6.D). While the electrochemical properties in the more positive region are complicated, the irreversible oxidation processes are at least 100 mV more positive than the $[FeCp_2]^{+/0}$ reference couple, so a mild oxidant such as $[FeCp_2]^+$ should not be able to achieve the oxidation of $[Fe^{III}poat(OH)]^-$. It is clear that while $[FeCp_2]BF_4$ reacts with $[Fe^{III}poat(OH)]^-$ to produce the transient "*g*10" species spectroscopically, but its role is still ambiguous.

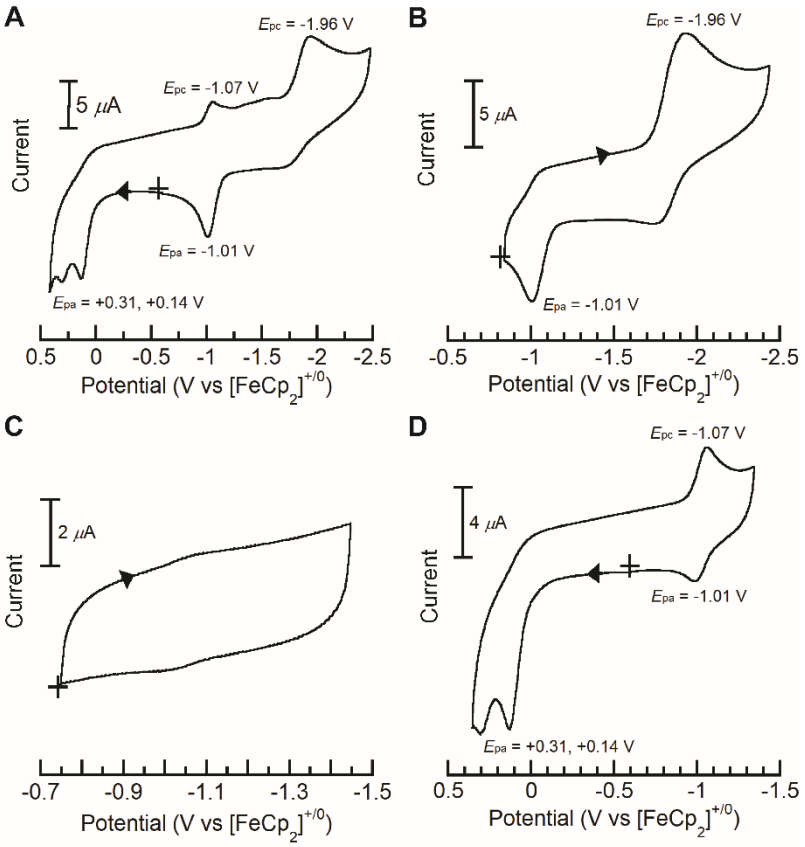

Figure 2.6. Cyclic voltammograms of $K[Fe^{III}poat(OH)]$ in the presence of 18-c-6. (A) Full window. (B) The more negative potential window. (C) The mid-potential window. (D) The more positive potential window. The cyclic voltammograms were collected at 100 mV s^{-1} in DMF.

Synthesis and properties of K[Ga^{III}poat(OH)]. To further probe the electrochemical and magnetic properties of $[Fe^{III}poat(OH)]^-$, the diamagnetic $[Ga^{III}poat(OH)]^-$ complex was developed. Ga^{III} is

often used as a redox-inactive analogue for Fe^{III}, due to their same charge, similar ionic radii, and comparable Lewis acidities.[48-51] In a typical reaction, metalation of $[poat]^{3-}$ with NMe_4GaCl_4, followed by treatment of water and base, yielded the desired $K[Ga^{III}poat(OH)]$ product (Scheme 2.4). Recrystallization of the crude compound provided colorless crystals suitable for various structural and spectroscopic characterization methods. X-ray diffraction revealed a molecular structure that is isomorphous to $\{K[Fe^{III}poat(OH)]\}_2$, with two molecules of $[Ga^{III}poat(OH)]^-$ crosslinked by two potassium counter ions to form a cluster (Figure 2.7, Table 2.1). The Ga^{III} center adopts a trigonal bipyramidal (tbp) geometry ($\tau_5 = 0.968$) with an axial exogenous hydroxido ligand. The Ga1–O1 (1.873(1) Å), Ga1–N1 (2.409(1) Å), and Ga1–N_{eq} (1.961(1) Å) bond distances are all comparable to those for $K[Fe^{III}poat(OH)]$ (1.896(1) Å, 2.373(1) Å, 2.011(1) Å, respectively). The enforced cluster aggregation prevents intramolecular H-bonding between the hydroxido ligands and the phosphinic amido P=O group ($d(O1\cdots O_{P=O}) > 3$ Å). $K[Ga^{III}poat(OH)]$ exhibited a diamagnetic ^1H NMR spectrum, in which all $[poat]^{3-}$ proton resonances can be assigned.

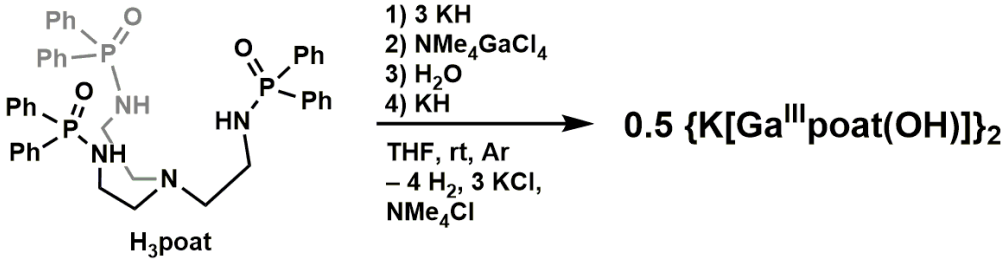

Scheme 2.4. Preparative route to $K[Ga^{III}poat(OH)]$.

Gallium(III) complexes have been previously used as a surrogate for their Fe^{III} counterparts to investigate redox (non-)innocence of ligand frameworks.[52-54] In the presence of 18-c-6, the cyclic voltammogram of $K[Ga^{III}poat(OH)]$ exhibits an irreversible oxidation at $E_{pa} = +0.37$ V (Figure 2.8.B), suggesting only oxidants with a higher potential may be able to oxidize the Ga^{III} complex by one-electron (e.g. $[Ga^{III}(poat)^{\bullet+}(OH)]$). $[FeCp_2]^+$ is not sufficiently potent to access that potential and oxidize the ligand, which further supports that reactivity of $K[Fe^{III}poat(OH)]$/18-c-6 towards

$[FeCp_2]BF_4$ is not a simple outer sphere redox process, and rules out the possibility of the $[Fe^{III}(poat)^{\bullet+}(OH)]$ formulation for the "*g*10" species.

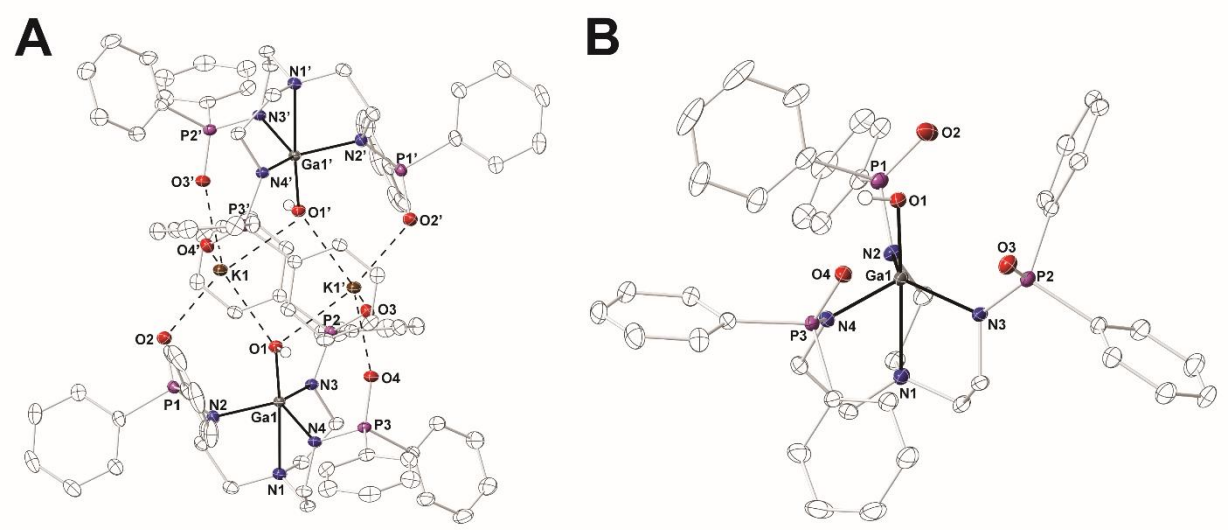

Figure 2.7. Thermal ellipsoid diagrams depicting the molecular structure of $\{K[Ga^{III}poat(OH)]\}_2$ by X-ray diffraction (A). The $[Ga^{III}poat(OH)]^-$ fragment is illustrated in (B). Ellipsoids are drawn at the 50% probability level, and only the hydroxido H atoms are shown for clarity.

Table 2.1. Selected metrical parameters for $\{K[Ga^{III}poat(OH)]\}_2$.

	Bond Lengths (Å)		Angles (°)
Ga1–N1	2.409(1)	O1–Ga1–N1	176.30(5)
Ga1–N2	1.970(2)	N2–Ga1–N3	114.16(6)
Ga1–N3	1.959(1)	N3–Ga1–N4	114.67(6)
Ga1–N4	1.953(1)	N2–Ga1–N4	118.22(6)
Ga1–O1	1.873(1)	Ga1–O1–K1	137.78(6)
K1–O1	2.728(1)	Ga1–O1–K1'	122.90(6)
K1–O2	2.666(1)		
K1'–O1	2.870(1)		
K1'–O3	2.656(1)		Calculated Values
K1'–O4	2.650(1)	τ_5[a] (Fe1)	0.968
av Ga1–N_{eq}	1.961(1)		
d[Ga1–N_{eq}]	0.413		

[a]Trigonality structural parameter, $\tau_5 = (\beta - a)/60^o$. β is the largest bond angle observed, and a is the second largest bond angle observed.

A new hypothesis. With the characterization thus far, it has been determined the "*g*10" species is an integer-spin system that contains a high-spin Fe^{III} center ($\delta/\Delta E_Q$ = 0.33/0.98 mm s^{-1}) antiferromagnetically coupled to an S = 1/2 site. It has a ground spin state of 2, but the excited state

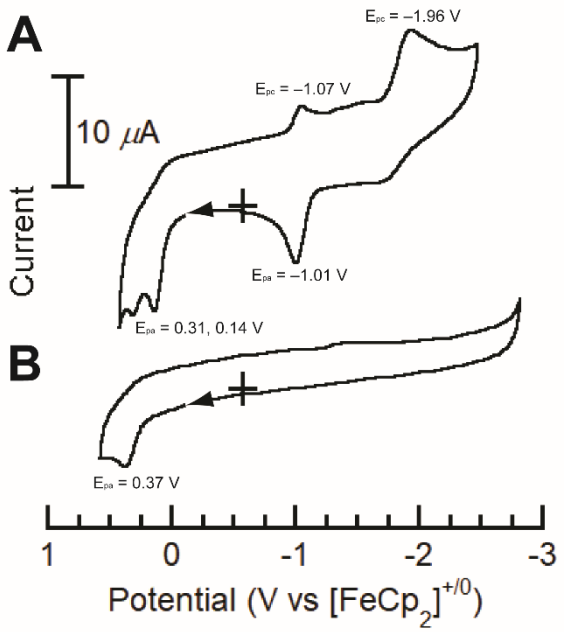

Figure 2.8. Cyclic voltammograms of K[Fe^{III}poat(OH)] (A) and K[Ga^{III}poat(OH)] (B) in the absence of 18-c-6. The cyclic voltammograms were collected at 100 mV s^{-1} in DMF.

S = 3 can be accessed due to a small J coupling constant of ~ +5 cm^{-1}. Magnetic measurements rule out an Fe^{IV} center ([Fe^{IV}poat(OH)]), and electrochemical evidence for the Fe and Ga complexes suggests [FeCp$_2$]BF$_4$ cannot oxidize the ligand framework ([Fe^{III}(poat)$^{\bullet+}$(OH)]). As previously stated, an Fe^{III}-superoxido species arising from O–O bond formation is an intriguing proposal due to its relevance to biological water oxidation (see *Outlook* section). The small J constant is consistent with weak coupling between paramagnetic centers, which arises from the unpaired spin not being localized on an atom that is directly bound to the Fe center. The experimentally determined J constant is comparable in magnitude with other enzymatic and synthetic Fe^{III}-superoxido species.[33,46,47] A recent report by Rittle on a crystallographically-characterized, high-spin Fe^{III}-superoxido complex exhibits similar magnetic properties (δ = 0.37 mm s^{-1}, g = 9.3 in parallel-mode EPR).[55] While the notion of intramolecular O–O bond formation from a M–O(H) center would be an important discovery, more evidence is necessary to make a conclusive assignment. Experiments were attempted to trap an O_2 adduct (e.g. peroxide tests, metal complexes known to bind O_2 units) but provided inconclusive results. It is worth noting that while the spin states of [Fe^{III}poat(OH)]$^-$ (S

= 5/2) and the "*g*10" species (S = 2) are different, their Mössbauer parameters are almost identical ($\delta/\Delta E_Q$ = 0.32/0.92 and 0.33/0.98 mm s^{-1}, respectively), suggesting that the properties of the Fe center in the $[poat]^{3-}$ are not significantly perturbed upon treatment with $[FeCp_2]BF_4$.

The study into the oxidation chemistry of the mononuclear $[Fe^{III}poat(OH)]^-$ complex was performed concurrently with the syntheses of bimetallic complexes described in the remaining chapters of this dissertation. As I gained a better understanding of those systems, it became clear that the phosphinic amido P=O groups are excellent at binding metal ions/adducts. Weakly-coordinating ligands, such as triflate, are easily substituted by the strongly-donating P=O groups as expected, but it has also been observed that other multidentate ligands, e.g. crown-ethers and tetramethylethylenediamine, can sometimes be displaced. These observations have prompted me to reconsider and carefully choose any inorganic/organometallic reagents for metal/$[poat]^{3-}$ complexes to avoid undesired aggregation of bi- or multimetallic clusters.

A new hypothesis for the identity of the "*g*10" species is proposed and illustrated in Scheme 2.5. While $FeCp_2$ is known to be substitution-inert (S = 0, d^6), $[FeCp_2]^+$ is open-shelled, and the Cp^- ligands may be susceptible to displacement by other strongly-donating ligands; this has been observed for various "piano stool"-type complexes.[57-59] With this in mind, as well as the tendency of the P=O ligands to displace other ligands, it is possible that $[Fe^{III}poat(OH)]^-$ reacts with $[FeCp_2]^+$

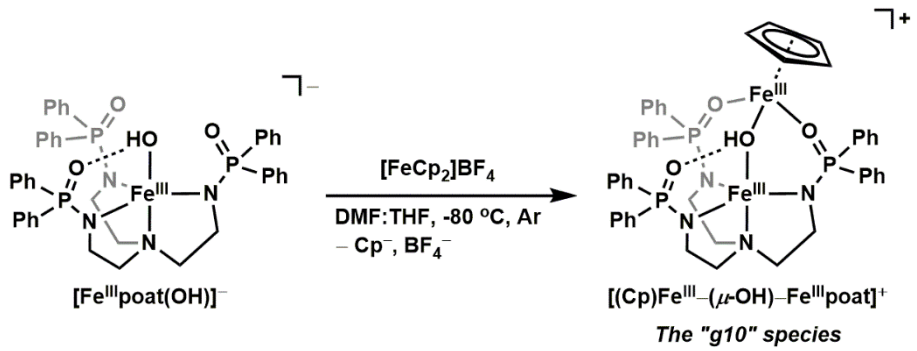

Scheme 2.5. A new hypothesis for the identity of the "g10" species: $[Fe^{III}poat(OH)]^-$ displaces the Cp^- ring in $[FeCp_2]^+$ to form $[(Cp)Fe^{III}–(\mu\text{-}OH)–Fe^{III}poat]^+$.

not *via* a redox process, but by replacing one of the Cp^- ligands with the two P=O groups and the axial hydroxido ligand, forming a putative $[(Cp)Fe^{III}–(\mu\text{-}OH)–Fe^{III}poat]^+$ species that gives rise to the $g = 9.7$ signal in parallel-mode EPR spectroscopy.

It has been established that the "*g*10" species is a spin-coupled system that involves two paramagnetic centers, one of which being high-spin Fe^{III}; while it was always presumed the second paramagnetic site to be an $S = 1/2$ organic-based radical, the possibility of the binding of another metal center ($S = 1/2$ Fe^{III}) was never considered, nor was the possibility of functionalization of $[FeCp_2]^+$. While all reported Fe^{III} complexes in the $[poat]^{3-}$ framework are high-spin,[7,27,28] they are in a trigonal symmetry with an N_4O or N_5 geometry, and it is reasonable that the strongly σ-donating $[Cp]^-$ ligand can promote a low-spin configuration. To further support the idea of an $S = 1/2$ metal complex binding, two bimetallic complexes had been reported by the Borovik Lab, $[(TMTACN)Cu^{II}–(\mu\text{-}OH)–Fe^{III}MST]^+$ and $[(TMTACN)Cu^{II}–(\mu\text{-}OH)–Fe^{III}poat]^+$ (see Chapter 3),[27,60] which are $S = 2$ systems that contain an $S = 5/2$ Fe^{III} center antiferromagnetically coupled to an $S = 1/2$ Cu^{II} center. These complexes exhibit nearly identical parallel-mode EPR features as that observed for the "*g*10" species.

One important consideration is that although the proposed structure is a diiron complex, only one iron species ($\delta/\Delta E_Q = 0.33/0.98$ mm s^{-1}) was observed by Mössbauer spectroscopy, which is useful at examining all iron species in a given sample as long as the ^{57}Fe content (~ 2% natural abundance) is high enough for detection (typically > 0.4 mM ^{57}Fe). Our lab has taken advantage of the sensitivity of this technique in the past to generate high-valent Fe complexes using ^{57}Fe-enriched complexes and natural abundance $[FeCp_2]BF_4$, which mitigates the features of the $[FeCp_2]$ byproduct.[31,32,61] Similarly, in the initial Mössbauer studies of the "*g*10" species, $K_2[^{57}Fe^{II}poat(OH)]$ and $[FeCp_2]BF_4$ were used, and the fate of the metallocene reagent was not monitored. If the "*g*10" species were a diiron complex, features for the $[Fe^{III}Cp]^{2+}$ adduct would not be detected due to the

low natural abundance of ^{57}Fe (~ 2 %). Therefore, Mössbauer experiments using natural abundance compounds for both K[Fe^{III}poat(OH)] and [FeCp$_2$]BF$_4$ (or ^{57}Fe-enriched complexes for both) are necessary to support this hypothesis.

Demystifying "g10". Several experiments were conducted to support the new formulation for the "*g*10" species. Cyclic voltammetry was performed on FeCp$_2$ in the presence of stoichiometric (1 equivalent) K[Fe^{III}poat(OH)]/18-c-6, and the [FeCp$_2$]$^{+/0}$ redox process becomes irreversible (Figure 2.9.B), with a current ratio i_{pc}/i_{pa} of nearly one-half (0.49). In the presence of 2 equivalents of K[Fe^{III}poat(OH)]/18-c-6, there is little reduction current detected for the [FeCp$_2$]$^{+/0}$ event (Figure 2.9.C). These experiments were repeated using different working electrodes, and the same observations were made. The half and full consumptions of [FeCp$_2$]$^+$ with one and two equivalents of K[Fe^{III}poat(OH)]/18-c-6, respectively, suggest that [FeCp$_2$]$^+$ generated at the electrode surface is reacting with [Fe^{III}poat(OH)]$^-$ at a ~1:2 ratio. The consumption of [FeCp$_2$]$^+$ resulted in little return reduction current for the [FeCp$_2$]$^{+/0}$ process, and supports the notion that the Cp$^-$ rings in [FeCp$_2$]$^+$ are sequentially replaced, possibly by the P=O groups. Future bulk electrolysis experiments may provide more accurate information on the electron uptake/current passed.

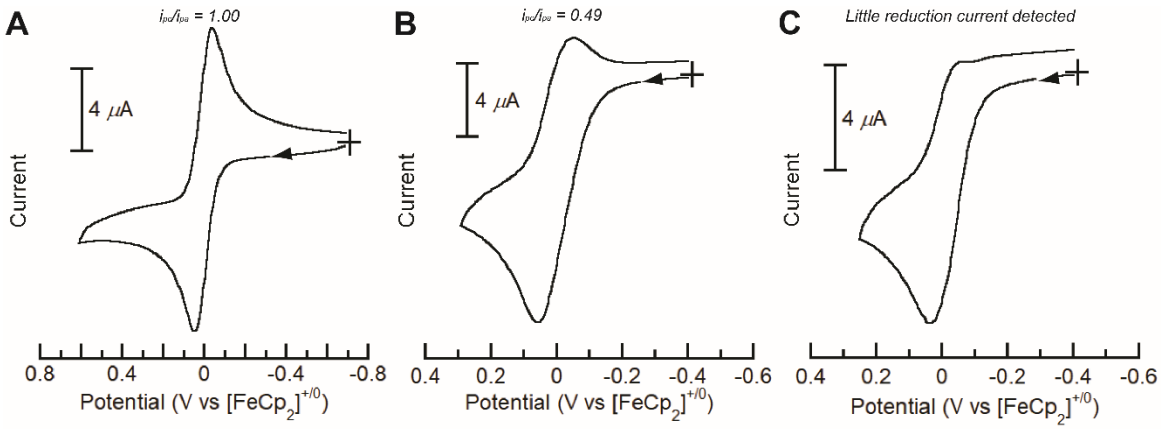

Figure 2.9. Cyclic voltammograms of FeCp$_2$ (A), and FeCp$_2$ in the presence of 1.0 equivalent (B) and 2.0 equivalents (C) of K[Fe^{III}poat(OH)]/18-c-6. The reversibility of the [FeCp$_2$]$^{+/0}$ decreases in the presence of K[Fe^{III}poat(OH)]/18-c-6. The cyclic voltammograms were collected at 10 mV s^{-1} in DMF.

The "*g*10" species was re-investigated by the combination of EPR and Mössbauer spectroscopies. K[Fe^{III}poat(OH)]/18-c-6 was treated with [$FeCp_2$]BF_4 at -80 °C (both natural abundance in Fe), and the g = 9.7 signal was observed in parallel-mode EPR at > 50% yield (Figure 2.10.A); exact quantification of this feature was challenging due to low reaction yield and small J coupling constant. The Mössbauer spectrum was more complicated (Figure 2.10.C). Minor impurities were observed (likely $FeCp_2$, < 20 %, $\delta/\Delta E_Q$ = 0.56/2.44 mm s^{-1}, black dashed trace; see Figure 2.10.B for the $FeCp_2$ reference spectrum), as well as a doublet feature that was previously observed for the "*g*10" species ($\delta/\Delta E_Q$ = 0.33/0.98 mm s^{-1}, green solid trace). Most significantly, we observed a new doublet with $\delta/\Delta E_Q$ values of 0.61/0.26 mm s^{-1} (purple solid trace). It is typical of Fe^{III}-cyclopentadienyl complexes to exhibit higher isomer shift values.[62,63] Both Fe^{III} features (δ = 0.33 and 0.61 mm s^{-1}) are quantified to the same concentration, indicating a 1:1 ratio. In addition,

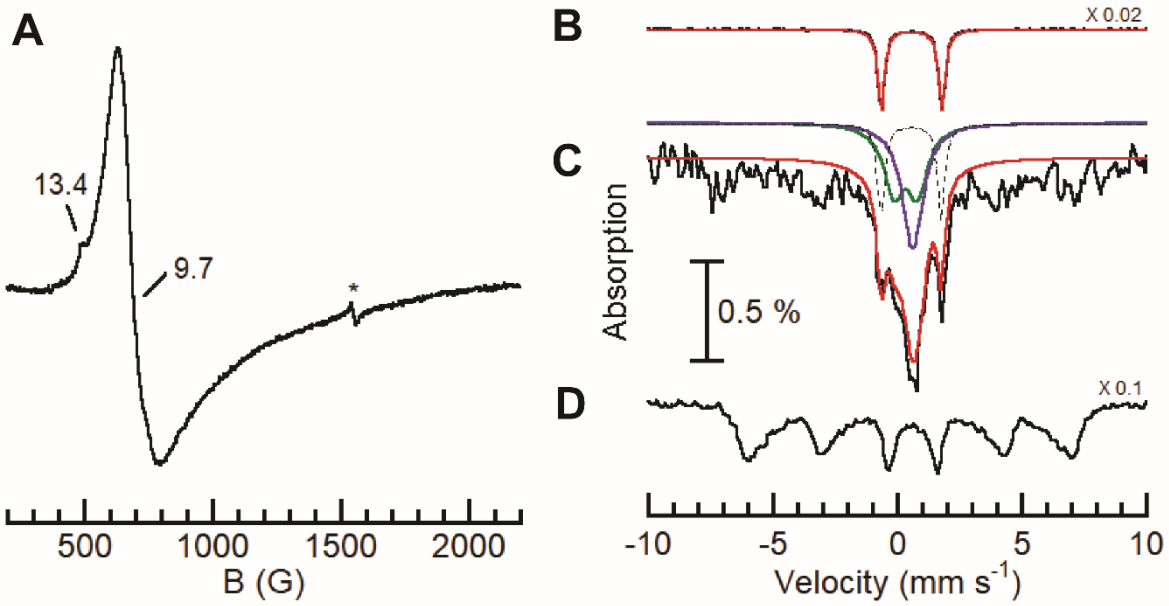

Figure 2.10. EPR (A) and Mössbauer (C) spectra of the "g10" species generated from addition of 1.0 equivalent [$FeCp_2$]BF_4 to (K/18c6)[Fe^{III}poat(OH)] in 1:1 DMF:THF (black plots). The final concentration was 21.1-mM. The Mössbauer spectra for $FeCp_2$ (B, 130-mM) and [$FeCp_2$]BF_4 (D, 125-mM) are illustrated for comparison. The red traces are simulations. The simulated Mössbauer spectrum in C (red trace) is composed of three species: a doublet with $\delta/\Delta E_Q$ = 0.33/0.98 mm s^{-1} (green solid trace); a doublet with $\delta/\Delta E_Q$ = 0.61/0.26 mm s^{-1} (purple solid trace); and a doublet with $\delta/\Delta E_Q$ = 0.56/2.44 mm s^{-1} (black dashed trace). The first two doublets are of equal concentration, and the last doublet is a minor species (< 20 %, likely $FeCp_2$). Experimental parameters: (A) microwaves, 0.2 mW at 9.3 GHz; temperature, 15.4 K; (B, C, D) magnetic field 45 mT parallel to γ-ray direction; temperature, 4.2 K.

they exhibit doublet spectra instead of six-line spectra, which are typically seen for mononuclear Fe^{III} species (see the spectrum for $[FeCp_2]BF_4$ as an example, Figure 2.10.D). These findings indicate the two Fe centers are part of the same integer spin system. Overall, the natural abundance Fe EPR and Mössbauer measurements suggests the "*g*10" species is a diferric complex ($S_{Ground} = 2$; $S_1 = 5/2$; $S_2 = 1/2$) and supports the formulation of $[(Cp)Fe^{III}–(\mu\text{-}OH)–Fe^{III}poat]^+$.

The experimentally measured spin-exchange constant of ~ 5 cm^{-1} is small for a $Fe^{III}–(\mu\text{-}OH)–Fe^{III}$ motif; these cores in both biological and synthetic systems generally have *J* values of 20 – 50 cm^{-1}.[64] However, the Fe^{III} centers in μ-hydroxido diiron complexes typically have (nearly) identical coordination spheres, and therefore have the same spin states (e.g. both are $S = 5/2$).[65,66] There has only been one reported example of an $S = 2$ diferric species that contains one $S = 5/2$ Fe^{III} center and one $S = 1/2$ Fe^{III} center; however, the *J* constant was not reported for this system.[67] Therefore, the effect on the spin exchange interaction between two Fe^{III} sites with different spin states is not well-studied.

Since the "*g*10" species is too unstable for structural characterizations, we sought to do a bulk reaction of $K[Fe^{III}poat(OH)]$/18-c-6 and $[FeCp_2]BF_4$, isolate and structurally identify the room-temperature stable product, and deduce the identity of "*g*10" by retrosynthesis. A DMF:THF solution containing $K[Fe^{III}poat(OH)]$/18c6 was treated with 1 equivalent $[FeCp_2]BF_{4s}$, and the dark yellow color turned brown immediately. The product was recrystallized in a DMF:Et_2O mixture to yield dark crystals suitable for XRD in low yield (Scheme 2.6). The molecular structure revealed a triiron complex, $[poatFe^{III}–(\mu\text{-}OH)–Fe^{III}–(\mu\text{-}OH)–Fe^{III}poat]^+$ (Figure 2.11, Table 2.2). Bulk synthesis using $K_2[Fe^{II}poat(OH)]$ and 2 equivalents $[FeCp_2]BF_4$ was also performed and yielded crystals of the same compound. The complex has a [Fe1–(μ-OH)–Fe3–(μ-OH)–Fe2] core, with Fe1–O1/Fe2–O5 bond lengths of 1.897(2) and 1.898(2) Å, and Fe3–O1/O5 bond lengths of 1.952(2) and 1.954(2) Å. The Fe1/2···Fe3 distances of 3.445(1)/3.469(1) Å and the Fe1/2–O1/5–Fe3 angles of

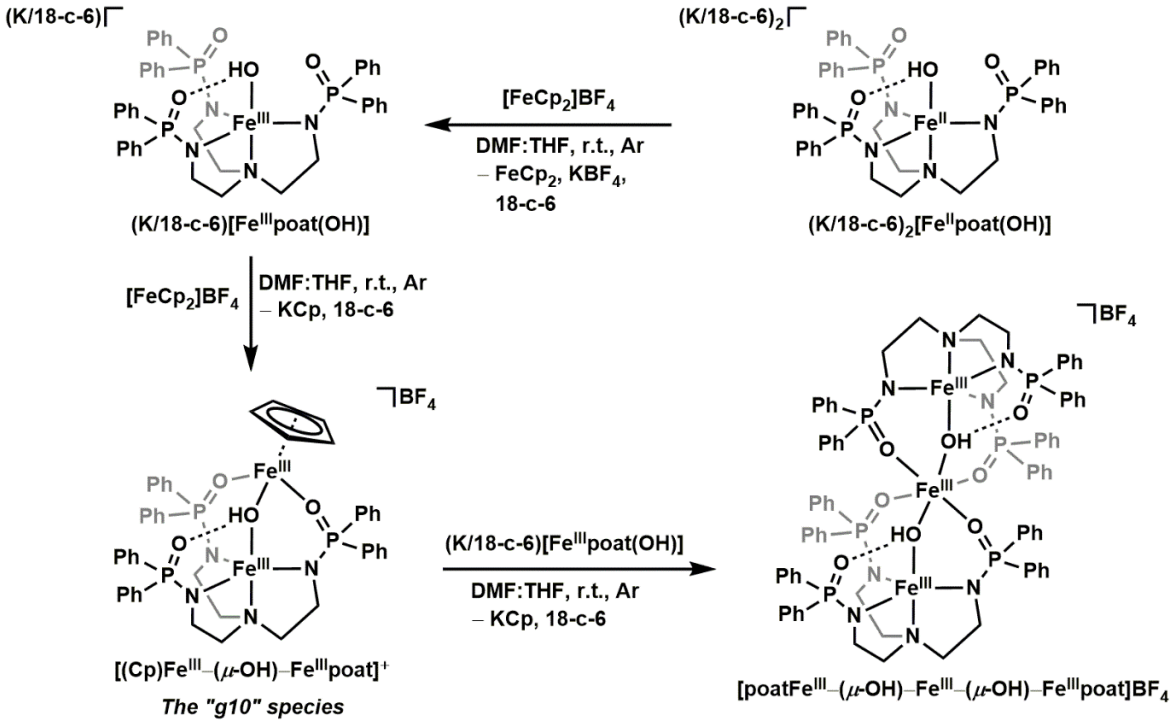

Scheme 2.6. Synthesis of the triiron cluster, [poatFe^{III}–(μ-OH)–Fe^{III}–(μ-OH)–Fe^{III}poat]$^{+}$.

126.91(11)/128.52(11) ° are consistent with Fe–(μ-OH)–Fe motifs. Fe1 and Fe2 retains a tbp N_4O geometry, while the central Fe3 site has an O_6 binding mode, with its coordination sphere filled by 2 bridging hydroxido ligands and 4 P=O groups from the two [Fe^{III}poat(OH)]$^{-}$ components. Finally, the phosphinic amido groups that do not bind to Fe3 participate in an intramolecular H-bonding interaction with the bridging hydroxido ligand (2.599(3), 2.596(3) Å). There have been >50 molecular structures of mono-, di- and tetra-nuclear complexes developed by the Borovik Lab in the [poat]$^{3-}$ ligand framework, but this new species is one of the only three tri-metallic complexes.[28,68] This unique compound may pave way for future development of new multimetallic clusters, which is discussed further in the *Outlook* section.

The electrochemical and magnetic findings support the formulation of [(Cp)Fe^{III}–(μ-OH)–Fe^{III}poat]$^{+}$ as the "*g*10" species. Additionally, bulk synthesis of this reaction yielded a final product of [poatFe^{III}–(μ-OH)–Fe^{III}–(μ-OH)–Fe^{III}poat]$^{+}$, which requires further characterization (e.g. to

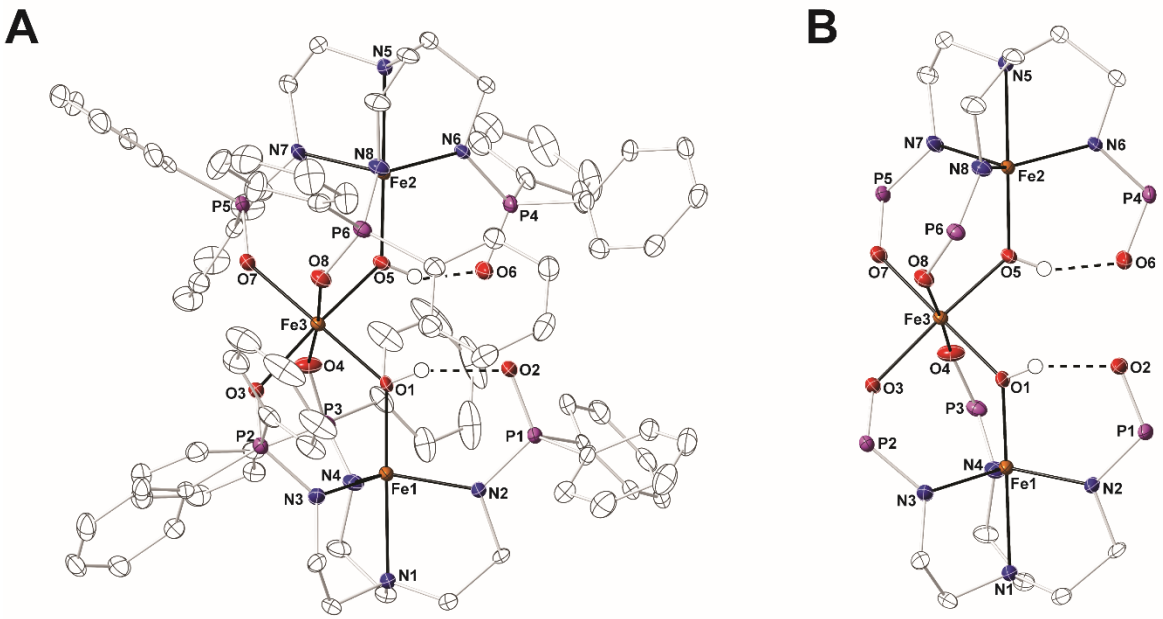

Figure 2.11. Thermal ellipsoid diagrams depicting the molecular structure of [poatFe^{III}–(μ-OH)–Fe^{III}–(μ-OH)–Fe^{III}poat]$^{+}$ by X-ray diffraction (A). The triiron core (with the phenyl rings removed) is illustrated in (B). Ellipsoids are drawn at the 50% probability level, and only the hydroxido H atoms are shown for clarity.

determine the bulk purity); the formation of this trinuclear core is consistent with the mechanism illustrated in Scheme 2.6. [Fe^{III}poat(OH)]$^{-}$ first displaces one Cp^{-} ring in [FeCp$_2$]$^{+}$, and the resultant [Fe^{III}Cp]$^{2+}$ adduct binds to form the transient [(Cp)Fe^{III}–(μ-OH)–Fe^{III}poat]$^{+}$ species; subsequently, the other Cp^{-} ring is displaced by a second molecule of [Fe^{III}poat(OH)]$^{-}$ to produce [poatFe^{III}–(μ-OH)–Fe^{III}–(μ-OH)–Fe^{III}poat]$^{+}$.

Conclusion & Outlook

In this chapter, the possible identity of the "*g*10" species has been postulated as [(Cp)Fe^{III}–(μ-OH)–Fe^{III}poat]$^{+}$. A variety of synthetic, spectroscopic, and electrochemical methods were utilized to support this assignment. [FeCp$_2$]BF$_4$, a common mild oxidant, provides an Fe^{III} ion to cross-link two molecules of [Fe^{III}poat(OH)]$^{-}$ to form the stable [poatFe^{III}–(μ-OH)–Fe^{III}–(μ-OH)–Fe^{III}poat]$^{+}$ product. This study serves as a cautionary tale that the fate of an oxidant, or any reagent, should

Table 2.2. Selected metrical parameters for [poatFe^{III}–(μ-OH)–Fe^{III}–(μ-OH)–Fe^{III}poat]BF_4.

	Bond Lengths/Distances (Å)		Bond Lengths/Distances (Å)
Fe1–N1	2.241(2)	Fe2–N5	2.220(2)
Fe1–N2	1.986(2)	Fe2–N6	1.984(2)
Fe1–N3	1.992(2)	Fe2–N7	1.992(3)
Fe1–N4	1.997(2)	Fe2–N8	1.995(2)
Fe1–O1	1.897(2)	Fe2–O5	1.898(2)
O1···O2	2.599(3)	O5···O6	2.596(3)
Fe3–O1	1.952(2)	Fe3–O5	1.954(2)
Fe3–O3	2.047(2)	Fe3–O7	2.027(2)
Fe3–O4	2.012(2)	Fe3–O8	2.004(2)
Fe1···Fe3	3.445(1)	Fe2···Fe3	3.469(1)
av Fe1–N_{eq}	1.992(2)	av Fe2–N_{eq}	1.990(2)
d[Fe1–N_{eq}]	0.338	*d*[Fe2–N_{eq}]	0.329
d[Fe3–O1/3/4]	1.189	*d*[Fe3–O5/7/8]	1.178
O1···O5	2.748		
	Angles (°)		Angles (°)
O1–Fe1–N1	174.58(10)	O5–Fe2–N5	179.40(10)
N2–Fe1–N3	124.92(11)	N6–Fe2–N7	118.95(11)
N3–Fe1–N4	108.54(11)	N7–Fe2–N8	110.98(11)
N2–Fe1–N4	117.97(11)	N6–Fe2–N8	122.01(10)
Fe1–O1–Fe3	126.91(11)	Fe2–O5–Fe3	128.52(11)
O3–Fe3–O4	88.82(9)	O7–Fe3–O8	88.05(9)
O1–Fe3–O7	175.83(9)	O3–Fe3–O5	175.87(9)
O4–Fe3–O8	175.26(9)		
	Calculated Values		Calculated Values
$\tau_5{}^a$ (Fe1)	0.828	$\tau_5{}^a$ (Fe2)	0.957

[a]Trigonality structural parameter, $\tau_5 = (\beta - \alpha)/60°$. β is the largest bond angle observed, and α is the second largest bond angle observed.

never be ignored, as it may perform undesirable chemistry: we must always be able to balance the reaction equation! In this instance, the fate of the $[FeCp_2]^+$ reagent was not monitored in our initial Mössbauer measurements, and that proved to be essential in the assignment of the "*g*10" species. Another important finding in this study is that the P=O groups in $[poat]^{3-}$ are strongly donating ligands that can out-compete other ligands, including the monoanionic Cp^-. This ability has allowed us to synthesize a large library of discrete bimetallic complexes using the $[poat]^{3-}$ framework, which is discussed in the remaining chapters of this dissertation.

The [poatFe^{III}–(μ-OH)–Fe^{III}–(μ-OH)–Fe^{III}poat]$^+$ complex offers a unique architecture that is worth further investigation as a synthetic model for biological water oxidation. The oxygen evolving

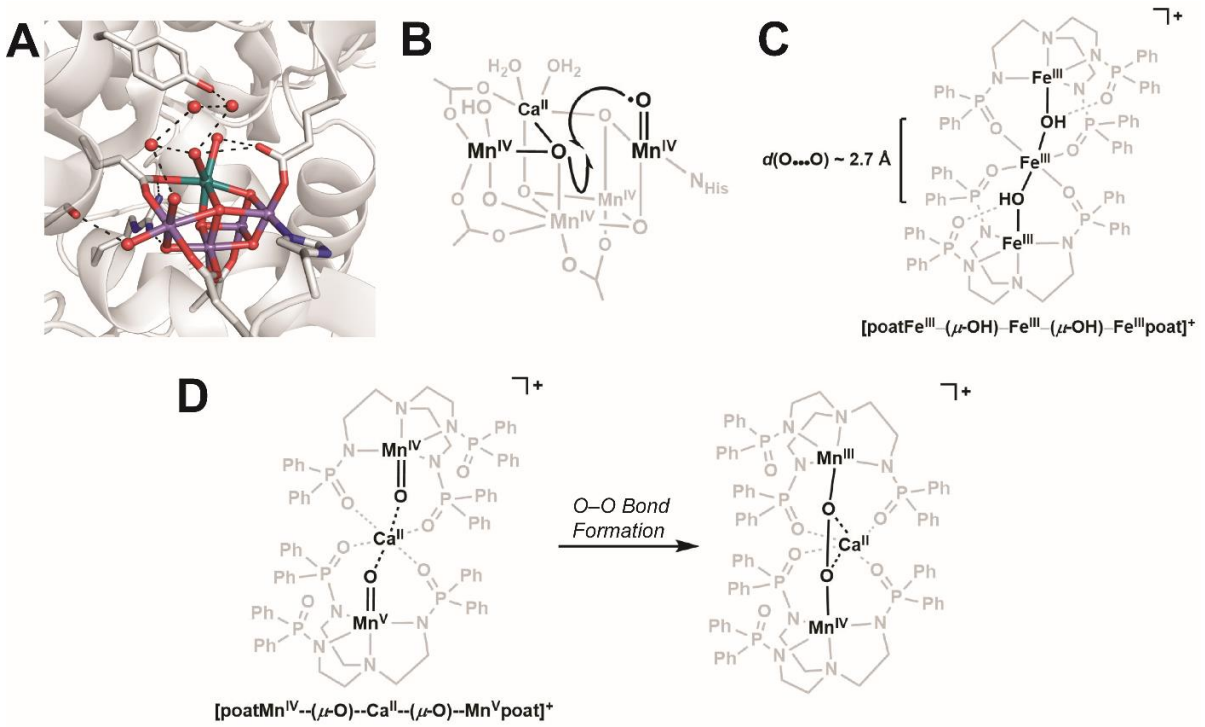

Figure 2.12. (A) The resting state of the oxygen evolving complex in Photosystem II (PDB: 3WU2). Mn is shown as a purple sphere, Ca is shown as a turquoise sphere, and O is shown as a red sphere. (B) One proposed structure for the S_4 intermediate in which the key O–O bond formation takes place. (C) The orientation and proximity of the two hydroxido ligands bound to a Lewis acidic Fe^{III} center in [poatFe^{III}–(μ-OH)–Fe^{III}–(μ-OH)–Fe^{III}poat]$^+$ provides an opportunity to synthetically model biological water oxidation. (D) Proposed high-valent trinuclear Mn_2Ca cluster to facilitate O–O bond formation.

complex (OEC) in Photosystem II (PSII) contains a Mn_4O_5Ca cluster that catalyzes the conversion of water to dioxygen in a 4 H^+/4 e^- process (Figure 2.12.A).[69-72] One proposed structure for the S_4 species in the key O–O bond formation step involves nucleophilic attack/radical coupling of a high valent Mn–O(H) with the O atom in a Mn–(μ-O)–Ca motif (Figure 2.12.B).[73-77] The redox-inactive Ca^{II} ion has been demonstrated to be essential at facilitating catalysis.[78-81] While modeling of the S_4 state using molecular systems is an important research focus within the field, it is synthetically challenging to assemble multimetallic complexes that contain multiple H_2O-derived ligands in close proximity and can perform multi-H^+/e^- processes, but [poatFe^{III}–(μ-OH)–Fe^{III}–(μ-OH)–Fe^{III}poat]$^+$ (or similar trinuclear complexes) provides us an exciting opportunity. The two bridging hydroxido ligands are coordinated to the Fe3 atom in a *cis* manner (Figure 2.12.C), and while the O1···O5

distance of 2.748 Å is too long to for the O-atoms to interact, the central Fe3 atom may serve as a "linchpin" within the cluster, and allow flexible "scissoring" motions for the two units of $[Fe^{III}poat(OH)]^-$, thus bringing the OH groups closer to each other. While the assembly of $[poatFe^{III}–(\mu\text{-}OH)–Fe^{III}–(\mu\text{-}OH)–Fe^{III}poat]^+$ using $[FeCp_2]BF_4$ is rather unconventional, it may provide us a synthetic route to prepare similar trimetallic complexes, such as $[poatMn^{III}\text{--}(\mu\text{-}OH)\text{--}Ca^{II}\text{--}(\mu\text{-}OH)\text{--}Mn^{III}poat]$. Upon multiple oxidations and deprotonations, the high-valent Mn–oxido motifs bound to the Ca^{II} ion are well-positioned to form an O_2 adduct (Figure 2.12.D), which is encapsulated within the bulky $[poat]^{3-}$ ligands to allow us to study O–O bond formation using various structural and spectroscopic techniques.

Experimental

General Procedures. All reagents were purchased from commercial sources and used as received unless otherwise noted. Solvents were sparged with argon and purified using a JC Meyer Co. solvent purification system with columns containing Q-5 and molecular sieves. Potassium hydride (KH) as a 30 % dispersion in mineral oil was filtered with a medium porosity glass frit and washed 5 times each with pentane and diethyl ether (Et_2O). Solid KH was dried under vacuum and stored under an inert atmosphere. All synthetic manipulations were conducted in a Vacuum Atmosphere, Co. drybox under an argon atmosphere. H_3poat,[26] $Fe(OAc)_2$,[82] $K[Fe^{II}poat]$,[26] $K_2[Fe^{II}poat(OH)]$,[29] $[FeCp_2]BF_4$,[83] and NMe_4GaCl_4[84] were synthesized according to previous reports. Tetrabutylammonium hexafluorophosphate (TBAP) was recrystallized using absolute EtOH.

Physical Methods. Electronic absorbance spectra were recorded with a Cary 50 spectrophotometer using a 1.00 cm quartz cuvette. Solid-state Fourier transform infrared (FTIR) spectra were collected on a Thermo Scientific Nicolet iS5 FT-IR spectrometer equipped with an iD5 ATR accessory. Cyclic

voltammetry experiments were conducted using a CHI600G electrochemical analyzer. A 2.0 mm glassy carbon or 1.0 mm platinum electrode was used as the working electrode at scan velocities between 0.01 and 0.5 $V \cdot s^{-1}$. A ferrocenium/ferrocene ($[FeCp_2]^{+/0}$) or decamethylferrocenium/decamethylferrocene ($[Fe(C_5Me_5)_2]^{+/0}$) standard was used as an internal reference to monitor the reference electrode (Ag^+/Ag). TVAP was used as the supporting electrolyte at a concentration of 0.1 M. Elemental analyses were performed on a Perkin-Elmer 2400 Series II CHNS elemental analyzer. X-band EPR spectra were recorded on a Bruker ELEXSYS spectrometer equipped with an Oxford ESR-910 liquid helium cryostat and a Bruker bimodal cavity for the generation of microwave fields parallel and transverse to the applied magnetic field. The microwave frequency was calibrated with a frequency counter, and the magnetic field was measured with an NMR gaussmeter. The sample temperature was calibrated against a calibrated cernox sensor (Lakeshore CX-1050) mounted inside an EPR tube. A modulation frequency of 100 kHz was used for all EPR spectra. Mössbauer spectra were recorded on either a variable field or a weak-field spectrometer operating in a constant acceleration mode in a transmission geometry using Janis Research Inc. cryostats that allow for a variation in temperature from 4 to 300 K. One of the dewars housed a superconducting magnet that allowed for the application of magnetic fields up to 8 T parallel to the γ-radiation. Isomer shifts are reported relative to Fe metal at 298 K. The simulation software SpinCount was written by Prof. Michael P. Hendrich (Carnegie Mellon University).[85]

Synthesis of [Fe^{III}poat(OH)]

Route A: oxygenation of K[Fe^{II}poat]. K[Fe^{II}poat] was synthesized *in situ* as described in the reported procedure.[26] To a solution of H_3poat (0.400 g, 0.536 mmol) in anhydrous THF (13 mL) was added KH (0.0680 g, 1.64 mmol), and the reaction was allowed to proceed until gas evolution ceased and all solids were dissolved. To the solution was added $Fe^{II}(OAc)_2$ (0.096 g, 0.56 mmol). The yellow

solution was stirred for 25 minutes and then filtered through a medium fritted glass funnel to remove insoluble material. The yellow filtrate was transferred to a 50 mL Schlenk flask, which was sealed with a rubber septum and brought out from the glove box. Anhydrous O_2 (12 mL, T = 298 K, P = 1 atm, 0.54 mmol) was injected into the headspace via syringe. The initial yellow solution turned dark brown and stirred for 1 hour. After the reaction was complete, all volatiles were removed under vacuum, and the reaction flask was brought into the glovebox. The residues were redissolved in CH_2Cl_2 (6 mL), and were layered with Et_2O to afford dark yellow crystals (35%).

Route B: chemical oxidation of K[Fe^{II}poat(OH)]. K_2[Fe^{II}poat(OH)] was first synthesized *in situ* as described in the reported procedure.[29] To a solution of H_3poat (0.200 g, 0.268 mmol) in anhydrous THF (6 mL) was added KH (0.033 g, 0.82 mmol), and the reaction was allowed to proceed until gas evolution ceased and all solids were dissolved. To the solution was added Fe^{II}(OAc)$_2$ (0.048 g, 0.28 mmol). The yellow solution was stirred for 25 minutes and H_2O (5 μL, 0.3 mmol) was added via syringe. After 5 minutes, the reaction mixture was filtered through a medium porosity glass frit to remove insoluble material. KH (0.011 g, 0.27 mmol) was added to the filtrate, which turned orange and was allowed to stir for 10 minutes. The reaction mixture was then filtered through a medium porosity glass frit to remove any insoluble material. 0.5 equivalent of I_2 (0.034 g, 0.13 mmol) was added to the orange solution, which turned yellow brown and stirred for 30 minutes. The reaction mixture was then reduced to dryness and triturated with Et_2O until the residue was a free-flowing powder. The powder was redissolved in MeCN and filtered to remove KI. Et_2O was allowed to diffuse into the MeCN solution resulting in dark yellow crystals (20%).

Elemental analysis calcd. (found) for K[Fe^{III}poat(OH)]·(CH$_3$CN)·(H$_2$O), $C_{42}H_{43}FeKN_4O_4P_3$·(CH$_3$CN)·(H$_2$O); C, 57.77 (57.74); H, 5.29 (5.09); N, 7.66 (7.32) %. UV-Vis (DMF:THF solution with 2 equivalents 18-crown-6, λ_{max}/nm (ε_{max}/M^{-1}cm^{-1})) 370 (3800). FTIR (ATR, cm^{-1}): 3562, 3068, 3051, 3006, 2972, 2945, 2931, 2897, 2848, 2839, 1591, 1572, 1481, 1458,

1446, 1435, 1400, 1373, 1346, 1336, 1302, 1281, 1255, 1190, 1176, 1161, 1107, 1092, 1068, 1041, 1028, 999, 958, 924, 852, 787, 750, 735, 715, 696, 619, 579, 559, 532. X-band, perpendicular-mode EPR (DMF:THF with 2 equivalents 18-crown-6, 12 K) g = 9.44, 4.30. Mössbauer (DMF:THF with 2 equivalents 18-crown-6, 4.2 K) δ = 0.32 mm s^{-1}; ΔE_Q = 0.92 mm s^{-1}.

Synthesis of K[Ga^{III}poat(OH)]. To a solution of H_3poat (0.200 g, 0.268 mmol) in anhydrous THF (6 mL) was added KH (0.033 g, 0.82 mmol), and the reaction was allowed to proceed until gas evolution ceased and all solids were dissolved. To the solution was added NMe_4GaCl_4 (0.080 g, 0.28 mmol), and DMF (1 mL) to improve solubility. Precipitates immediately formed, and the cloudy white mixture was stirred for 3 hours. The insoluble material was removed by filtering the reaction mixture though a fine-porosity fitted glass funnel, and H_2O (5 μL, 0.3 mmol) was added via syringe to the clear colorless solution. After 30 minutes, KH (0.011 g, 0.27 mmol) was added, which immediately produced a white precipitate. After 30 minutes of stirring, the insoluble material was separated via filtration, and the volatiles were removed *in vacuo*. The white residue was triturated several times with Et_2O, and was then redissolved in CH_2Cl_2 and layered under Et_2O for recrystallization. Colorless crystals suitable for XRD were obtained after 2 days (60-70 %). Elemental analysis calcd. (found) for K[Ga^{III}poat(OH)]·0.5CH_2Cl_2·0.5C_5H_{12}, $C_{42}H_{43}GaKN_4O_4P_3$·0.5CH_2Cl_2·0.5C_5H_{12}; C, 57.01 (57.06); H, 5.32 (5.20); N, 5.91 (5.78) %. FTIR (ATR, cm^{-1}): 3595, 3070, 3053, 3006, 2962, 2952, 2931, 2898, 2893, 2848, 2843, 1591, 1570, 1493, 1481, 1458, 1434, 1373, 1352, 1342, 1290, 1261, 1242, 1194, 1180, 1159, 1109, 1092, 1068, 1049, 1001, 966, 930, 854, 800, 750, 737, 715, 694, 619, 579, 565, 548, 534. ^{1}H NMR (400 MHz, CD_2Cl_2, ppm): 2.19 (6H, br s), 2.89 (6H, br d), 7.23 – 7.31 (20H, m, o-/p-Ar), 7.70 (12H, dd, m-Ar). ^{31}P NMR (162 MHz, CD_2Cl_2, ppm): 29.9.

Generation of [(Cp)Fe^{III}–(μ-OH)–Fe^{III}poat]$^{+}$ (the "g10" species) for EPR and Mössbauer studies. A 22.4-mM solution of K[Fe^{III}poat(OH)] (0.0479 g, 0.0560 mmol) with 18-c-6 (0.0592 g, 0.224 mmol) was prepared in DMF:THF (2.5 mL) at room temperature in a glovebox under argon atmosphere and added to a 1-cm quartz. The cuvette was then sealed with a rubber septum and precooled to -80 °C in a Unisoku Unispeks cryostat typically used for UV-vis experiments outside the glovebox. The solution of metal complex was allowed to equilibrate to the desired temperature for at least 20 min. A stock solution of [FeCp$_2$]BF$_4$ was prepared at 371 mM in DMF:THF, and an aliquot of the reagent (0.0557 mmol, 0.150 mL) was added via a gas-tight syringe. After stirring for 1.5 minutes, the septum was sliced open with a razor under a strong flow of argon. The rubber septum was removed and the content in the cuvette was quickly poured into liquid nitrogen. The frozen solid was ground into fine slush and then packed into pre-cooled Mössbauer cups and EPR tubes. This method ensures the same reaction mixture is examined by the two spectroscopic techniques. The final concentration is 21.1-mM.

Synthesis of [poatFe^{III}–(μ-OH)–Fe^{III}–(μ-OH)–Fe^{III}poat]BF$_4$. To a 1:1 DMF:THF (4 mL) solution containing K[Fe^{III}poat(OH)] (0.0502 g, 0.0587 mmol) and 18-c-6 (0.0356 g, 0.135 mmol) was added [FeCp$_2$]BF$_4$ (0.0165 g, 0.0604 mmol). The solution turned brown and was allowed to stir for 30 minutes. The reaction mixture was filtered through a fine-porosity fritted glass funnel, and the filtrate was layered under Et$_2$O to yield dark crystals. This complex has only been characterized by X-ray diffraction; further spectroscopic characterizations are required.

Crystallography.

{K[Ga^{III}poat(OH)]}$_2$. A colorless crystal of approximate dimensions 0.259 x 0.237 x 0.219 mm was mounted in a cryoloop and transferred to a Bruker SMART APEX II diffractometer. The APEX2[86]

program package was used to determine the unit-cell parameters and for data collection (30 sec/frame scan time for a sphere of diffraction data). The raw frame data was processed using SAINT[87] and SADABS[88] to yield the reflection data file. Subsequent calculations were carried out using the SHELXTL[89] program. The diffraction symmetry was 2/*m* and the systematic absences were consistent with the monoclinic space group $P2_1/c$ that was later determined to be correct.

The structure was solved by dual space methods and refined on F^2 by full-matrix least-squares techniques.The analytical scattering factors[90] for neutral atoms were used throughout the analysis. The hydroxide hydrogen atom (H1) was located from a difference-Fourier map and refined (x,y,z and U_{iso}). The remaining hydrogen atoms were included using a riding model. The structure was a dimmer located about an inversion center. There was one diethylether solvent molecule per dimeric formula-unit. The ether molecule was disordered about inversion center and included with site-occupancy-factors set to 0.50.

Least-squares analysis yielded wR2 = 0.0957 and Goof = 1.040 for 522 variables refined against 12270 data (0.71Å), R1 = 0.0372 for those 10365 data with $I > 2.0\sigma(I)$.

[poatFe^{III}*–(μ-OH)–*Fe^{III}*–(μ-OH)–*Fe^{III}*poat]*BF_4. A red crystal of approximate dimensions 0.176 x 0.304 x 0.351 mm was mounted in a cryoloop and transferred to a Bruker SMART APEX II diffractometer system. The APEX2[86] program package was used to determine the unit-cell parameters and for data collection (30 sec/frame scan time). The raw frame data was processed using SAINT[87] and SADABS[88] to yield the reflection data file. Subsequent calculations were carried out using the SHELXTL[89] program package. The diffraction symmetry was *mmm* and the systematic absences were consistent with the orthorhombic space group $P2_12_12_1$ that was later determined to be correct.

The structure was solved by direct methods and refined on F^2 by full-matrix least-squares techniques. The analytical scattering factors[90] for neutral atoms were used throughout the analysis.

Hydrogen atoms H(1) and H(5) were located from a difference-Fourier map and refined (x,y,z and U_{iso}) with initial d(O-H) = 0.80Å. The remaining hydrogen atoms were included using a riding model. There were two molecules of diethylether solvent and one molecule of dimethylformamide solvent present.

Least squares analysis yielded wR2 = 0.0724 and Goof = 1.050 for 1175 variables refined against 21396 data (0.78 Å), R1 = 0.0298 for those 20001 data with I > 2.0σ(I). The structure was refined as a two-component inversion twin and the Flack[91] parameter refined to 0.033(9).

Table 2.3. Crystallographic data for $\{K[Ga^{III}poat(OH)]\}_2$ and $[poatFe^{III}–(\mu\text{-}OH)–Fe^{III}–(\mu\text{-}OH)–Fe^{III}poat]BF_4$.

	$\{K[Ga^{III}poat(OH)]\}_2$	$[poatFe^{III}–(\mu\text{-}OH)–Fe^{III}–(\mu\text{-}OH)–Fe^{III}poat]BF_4$
Formula	$C_{88}H_{96}Ga_2K_2N_8O_9P_6$	$C_{84}H_{86}BF_4Fe_3N_8O_8P_6\cdot 2(C_4H_{10}O)\cdot C_3H_7NO$
fw	1813.18	1997.12
T (K)	88(2)	88(2)
Crystal system	Monoclinic	Orthorhombic
Space group	$P2_1/c$	$P2_12_12_1$
a (Å)	15.8158(8)	17.8338(15)
b (Å)	14.3774(7)	18.5841(16)
c (Å)	19.7829(10)	29.305(3)
α (°)	90	90
β (°)	110.9118(8)	90
γ (°)	90	90
Z	2	4
V (Å^3)	4202.1(4)	9712.5(14)
δ_{calc} (mg/m^3)	1.433	1.366
Independent reflections	12270	21396
R1	0.0372	0.0298
wR2	0.0957	0.0724
Goof	1.040	1.050

$wR2 = [\Sigma[w(F_o^2-F_c^2)^2] / \Sigma[w(F_o^2)^2]]^{1/2}$
$R1 = \Sigma||F_o|-|F_c|| / \Sigma|F_o|$
Goof = $S = [\Sigma[w(F_o^2-F_c^2)^2] / (n-p)]^{1/2}$ where n is the number of reflections and p is the total number of parameters refined.
The thermal ellipsoid plot is shown at the 50% probability level.

References

(1) Arndtsen, B. A.; Bergman, R. G.; Mobley, T. A.; Peterson, T. H. Selective Intermolecular Carbon−Hydrogen Bond Activation by Synthetic Metal Complexes in Homogeneous Solution. *Acc. Chem. Res.* **1995**, *28*, 154-162.

(2) Neufeldt, S. R.; Sanford, M. S. Controlling Site Selectivity in Palladium-Catalyzed C−H Bond Functionalization. *Acc. Chem. Res.* **2012**, *45*, 936-946.

(3) Thirunavukkarasu, V. S.; Kozhushkov, S. I.; Ackermann, L. C−H Nitrogenation and Oxygenation by Ruthenium Catalysis. *Chem. Commun.* **2014**, *50*, 29-39.

(4) Colby, D. A.; Bergman, R. G.; Ellman, J. A. Rhodium-Catalyzed C−C Bond Formation via Heteroatom-Directed C−H Bond Activation. *Chem. Rev.* **2010**, *110*, 624-655.

(5) Bergman, R. G. Activation of Alkanes with Organotransition Metal Complexes. *Science* **1984**, *223*, 902-908.

(6) Bergman, R. G. Activation of Carbon-Hydrogen Bonds in Alkanes and Other Organic Molecules Using Organotransition Metal Complexes. In *Homogeneous Transition Metal Catalyzed Reactions*; Moser, W. R., Slocum, D. W., Eds.; American Chemical Society: Washington, DC, 1992; Vol. 230, pp 211-220.

(7) Lee, J. L.; Ross, D. L.; Barman, S. K.; Ziller, J. W.; Borovik, A. S. C–H Bond Cleavage by Bioinspired Nonheme Metal Complexes. *Inorg. Chem.* **2021**, *60*, 13759-13783.

(8) Huang, X.; Groves, J. T. Oxygen Activation and Radical Transformations in Heme Proteins and Metalloporphyrins. *Chem. Rev.* **2018**, *118*, 2491-2553.

(9) Krest, C. M.; Onderko, E. L.; Yosca, T. H.; Calixto, J. C.; Karp, R. F.; Livada, J.; Rittle, J.; Green, M. T. Reactive Intermediates in Cytochrome P450 Catalysis. *J. Biol. Chem.* **2013**, *288*, 17074-17081.

(10) Costas, M.; Mehn, M. P.; Jensen, M. P.; Que, L. Dioxygen Activation at Mononuclear Nonheme Iron Active Sites: Enzymes, Models, and Intermediates. *Chem. Rev.* **2004**, *104*, 939-986.

(11) Shook, R. L.; Borovik, A. S. Role of the Secondary Coordination Sphere in Metal-Mediated Dioxygen Activation. *Inorg. Chem.* **2010**, *49*, 3646-3660.

(12) Cook, S. A.; Borovik, A. S. Molecular Designs for Controlling the Local Environments around Metal Ions. *Acc. Chem. Res.* **2015**, *48*, 2407-2414.

(13) Guo, M.; Corona, T.; Ray, K.; Nam, W. Heme and Nonheme High-Valent Iron and Manganese Oxo Cores in Biological and Abiological Oxidation Reactions. *ACS Cent. Sci.* **2019**, *5*, 13-28.

(14) Kovaleva, E. G.; Lipscomb, J. D. Versatility of Biological Non-Heme Fe(II) Centers in Oxygen Activation Reactions. *Nat. Chem. Biol.* **2008**, *4*, 186-193.

(15) Rittle, J.; Green, M. T. Cytochrome P450 Compound I: Capture, Characterization, and C–H Bond Activation Kinetics. *Science* **2010**, *330*, 933-937.

(16) Groves, J. T.; McClusky, G. A. Aliphatic Hydroxylation via Oxygen Rebound. Oxygen Transfer Catalyzed by Iron. *J. Am. Chem. Soc.* **1976**, *98*, 859-861.

(17) Huang, X.; Groves, J. T. Beyond Ferryl-Mediated Hydroxylation: 40 Years of the Rebound Mechanism and C−H Activation. *JBIC, J. Biol. Inorg. Chem.* **2017**, *22*, 185-207.

(18) Yosca, T. H.; Rittle, J.; Krest, C. M.; Onderko, E. L.; Silakov, A.; Calixto, J. C.; Behan, R. K.; Green, M. T. Iron(IV)Hydroxide pKa and the Role of Thiolate Ligation in C−H Bond Activation by Cytochrome P450. *Science* **2013**, *342*, 825-829.

(19) Gray, H. B.; Winkler, J. R. Living with Oxygen. *Acc. Chem. Res.* **2018**, *51*, 1850-1857.

(20) Barry, S. M.; Challis, G. L. Mechanism and Catalytic Diversity of Rieske Non-Heme Iron-Dependent Oxygenases. *ACS Catal.* **2013**, *3*, 2362-2370

(21) Wang, Y.; Li, J.; Liu, A. Oxygen Activation by Mononuclear Nonheme Iron Dioxygenases Involved in the Degradation of Aromatics. *JBIC, J. Biol. Inorg. Chem.* **2017**, *22*, 395-405.
(22) Schulz, C. E.; Castillo, R. G.; Pantazis, D. A.; DeBeer, S.; Neese, F. Structure−Spectroscopy Correlations for Intermediate Q of Soluble Methane Monooxygenase: Insights from QM/MM Calculations. *J. Am. Chem. Soc.* **2021**, *143*, 6560-6577.
(23) Zaragoza, J. P. T.; Yosca, T. H.; Siegler, M. A.; Moënne-Loccoz, P.; Green, M. T.; Goldberg, D. P. Direct Observation of Oxygen Rebound with an Iron-Hydroxide Complex. *J. Am. Chem. Soc.* **2017**, *139*, 13640-13643.
(24) Xue, G.; Fiedler, A. T.; Martinho, M.; Münck, E.; Que, L. Insights into the P-to-Q conversion in the catalytic cycle of methane monooxygenase from a synthetic model system. *Proc. Nat. Acad. Sci. U.S.A.* **2008**, *105*, 20615-20620.
(25) Weitz, A. C.; Mills, M. R.; Ryabov, A. D.; Collins, T. J.; Guo, Y.; Bominaar, E. L.; Hendrich, M. P. A Synthetically Generated $LFe^{IV}OH_n$ Complex. *Inorg. Chem.* **2019**, *58*, 2099-2108.
(26) Oswald, V. F.; Lee, J. L.; Biswas, S.; Weitz, A. C.; Mittra, K.; Fan, R.; Li, J.; Zhao, J.; Hu, M. Y.; Alp, E. E.; Bominaar, E. L.; Guo, Y.; Green, M. T.; Hendrich, M. P.; Borovik, A. S. Effects of Non-covalent Interactions on High-spin Fe(IV)-oxido Complexes. *J. Am. Chem. Soc.* **2020**, *142*, 11804-11817.
(27) Lee, J. L.; Oswald, V. F.; Biswas, S.; Hill, E. A.; Ziller, J. W.; Hendrich, M. P.; Borovik, A. S. Stepwise assembly of heterobimetallic complexes: synthesis, structure, and physical properties. *Dalton Trans*. **2021**, *50*, 8111-8119.
(28) Sun, C.; Oswald, V. F.; Hill, E. A.; Ziller, J. W.; Borovik, A. S. Investigation of iron-ammine and amido complexes within a C_3-symmetrical phosphinic amido tripodal ligand. *Dalton Trans*. **2021**, *50,* 11197-11205.
(29) Oswald, V. F. Doctoral Dissertation, University of California-Irvine, Irvine, CA, 2018.
(30) Kostka, K. L.; Fox, B. G.; Hendrich, M. P.; Collins, T. J.; Rickard, C. E.; Weight, L. J.; Münck, E. High-valent transition metal chemistry. Mössbauer and EPR studies of high-spin (S = 2) iron(IV) and intermediate-spin (S = 3/2) iron(III) complexes with a macrocyclic tetraamido-N ligand. *J. Am. Chem. Soc.* **1993**, *115*, 6746-6757.
(31) Gupta, R.; Lacy, D. C.; Bominaar, E. L.; Borovik, A. S.; Hendrich, M. P.; Electron Paramagnetic Resonance and Mössbauer Spectroscopy and Density Functional Theory Analysis of a High-Spin Fe^{IV}–Oxo Complex. *J. Am. Chem. Soc.* **2012**, *134*, 9775-9784.
(32) Hill, E. A.; Weitz, A. C.; Onderko, E.; Romero-Rivera, A.; Guo, Y.; Swart, M.; Bominaar, E. L.; Green, M. T.; Hendrich, M. P.; Lacy, D. C.; Borovik, A. S. Reactivity of an Fe^{IV}-Oxo Complex with Protons and Oxidants. *J. Am. Chem. Soc.* **2016**, *138*, 13143-13146.
(33) Mbughuni, M. M.; Chakrabarti, M.; Hayden, J. A.; Bominaar, E. L.; Hendrich, M. P.; Münck, E.; Lipscomb, J. D. Trapping and spectroscopic characterization of an Fe^{III}-superoxo intermediate from a nonheme mononuclear iron-containing enzyme. *Proc. Nat. Acad. Sci. U.S.A.* **2010**, *107*, 16788-16793.
(34) Hill, E. A. Doctoral Dissertation, University of California-Irvine, Irvine, CA, 2016.
(35) Stubbe, J.; Nocera, D. G.; Yee, C. S.; Chang, M. C. Y. Radical Initiation in the Class I Ribonucleotide Reductase: Long-Range Proton-Coupled Electron Transfer? *Chem. Rev.* **2003**, *103*, 2167-2202.
(36) Römelt, C.; Weyhermüller, T.; Wieghardt, K. Structural characteristics of redox-active pyridine-1,6-diimine complexes: Electronic structures and ligand oxidation levels. *Coord. Chem. Rev.* **2019**, *380*, 287-317.

(37) Patterson, R. E.; Gordon-Wylie, S. W.; Woomer, C. G.; Norman, R. E.; Weintraub, S. T.; Horwitz, C. P.; Collins, T. J. Electron-Transfer Oxidation by Phase-Separating Reagents. *Inorg. Chem.* **1998**, *37*, 4748-4750.
(38) Haneline, M. R.; Heyduk, A. F. C–C Bond-Forming Reductive Elimination from a Zirconium(IV) Redox-Active Ligand Complex. *J. Am. Chem. Soc.* **2006**, *128*, 8410-8411.
(39) Nguyen, A. I.; Blackmore, K. J.; Carter, S. M.; Zarkesh, R. A.; Heyduk, A. F. One- and Two-Electron Reactivity of a Tantalum(V) Complex with a Redox-Active Tris(amido) Ligand. *J. Am. Chem. Soc.* **2009**, *131*, 3307-3316.
(40) Charette, B. J.; Ziller, J. W.; Heyduk, A. F. Metal-Ion Influence on Ligand-Centered Hydrogen-Atom Transfer. *Inorg. Chem.* **2021**, *60*, 1579-1589.
(41) Sun, C. Doctoral Dissertation, University of California-Irvine, Irvine, CA, 2021.
(42) Oswald, V. F.; Weitz, A. C.; Biswas, S.; Ziller, J .W.; Hendrich, M. P.; Borovik, A. S. Manganese-Hydroxido Complexes Supported by a Urea/Phosphinic Amide Tripodal Ligand. *Inorg. Chem.* **2018**, *57*, 13341-13350.
(43) Weitz, A. C.; Hill, E. A.; Oswald, V. F.; Bominaar, E. L.; Borovik, A. S.; Hendrich, M. P.; Guo, Y. Probing hydrogen bonding interactions to iron–oxido/hydroxido units via ^{57}Fe nuclear resonance vibrational spectroscopy. *Angew. Chem. Int. Ed.* **2018**, *57*, 16010-16014.
(44) Leconte, N.; Moutet, J.; Herasymchuk, K.; Clarke, R. M.; Philouze, C.; Luneau, D.; Storr, T.; Thomas, Fabrice. Mn(IV) and Mn(V)-radical species supported by the redox non-innocent bis(2-amino-3,5-di-*tert*-butylphenyl)amine pincer ligand. *Chem. Commun.* **2017**, *53*, 2764-2767.
(45) Balaghi, S. E.; Safaei, E.; Chiang, L.; Wong, E. W. Y.; Savard, D.; Clarke, R. M.; Storr, T. Synthesis, characterization and catalytic activity of copper(II) complexes containing a redox-active benzoxazole iminosemiquinone ligand. *Dalton Trans.* **2013**, *42*, 6829-6839.
(46) Chiang, C.-W.; Kleespies, S. T.; Stout, H. D.; Meier, K. K.; Li, P.-Y.; Bominaar, E. L.; Que, L.; Münck, E.; Lee, W.-Z. Characterization of a Paramagnetic Mononuclear Nonheme Iron-Superoxo Complex. *J. Am. Chem. Soc.* **2014**, *136*, 10846-10849.
(47) Stout, H. D.; Kleespies, S. T.; Chiang, C.-W.; Lee, W.-Z.; Que, L.; Münck, E.; Bominaar, E. L. Spectroscopic and Theoretical Study of Spin-Dependent Electron Transfer in an Iron(III) Superoxo Complex. *Inorg. Chem.* **2016**, *55*, 5215-5226.
(48) Park, Y. J.; Cook, S.; Sickerman, N. S.; Sano, Y.; Ziller, J. W.; Borovik, A. S. Heterobimetallic Complexes with M^{III}–(μ-OH)–M^{II} Cores (M^{III} = Fe, Ga, Mn; M^{II} = Ca, Sr and Ba): Structural, Kinetic, and Redox Properties. *Chem. Sci.* **2013**, *4*, 717-726.
(49) Sickerman, N. S.; Peterson, S. M.; Ziller, J. W.; Borovik, A. S. Synthesis, structure, and reactivity of $Fe^{II}/^{III}$ –NH_3 complexes bearing a tripodal sulfonamido ligand. *Chem. Commun.* **2014**, *50*, 2515-2517.
(50) Shannon, R. D. Revised Effective Ionic Radii and Systematic Studies of Interatomic Distances in Halides and Chalcogenides. *Acta. Cryst.* **1976**, *A32*, 751-767.
(51) Perrin, D. D. *Dissociation Constant of Inorganic Acids and Bases in Aqueous Solution*; Pergamon: New York, 1982.
(52) Borovik, A. S.; Papaefthymiou, V.; Taylor, L. F., Anderson, O. P.; Que, L. Models for Iron-Oxo Proteins. Structures and Properties of $Fe^{II}Fe^{III}$, $Zn^{II}Fe^{III}$, and $Fe^{II}Ga^{III}$ Complexes with (*μ*-Phenoxo)bis(*μ*-carboxylato)dimetal Cores. *J. Am. Chem. Soc.* **1989**, *111*, 6183-6195.
(53) Cook, S. A.; Bogart, J. A.; Levi, N.; Weitz, A.; Moore, C. E.; Rheingold, A. L.; Ziller, J. W.; Hendrich, M. P.; Borovik, A. S. Mononuclear Complexes of a Tridentate Redox-Active Ligand with Sulfonamide Groups: Structure, Properties, and Reactivity. *Chem. Sci.* **2018,** 9, 6540-6547.

(54) Adam, B.; Bill, E.; Bothe, E.; Goerdt, B.; Haselhorst, G.; Hildenbrand, K.; Sololowski, A.; Steenken, S.; Weyhermüller, T.; Wieghardt, K. Phenoxyl Radical Complexes of Gallium, Scandium, Iron and Manganese. *Chem. Eur. J.* **1997**, *3*, 308-319.
(55) Winslow, C.; Lee, H. B.; Field, M. J.; Teat, S. J.; Rittle, J. Structure and Reactivity of a High-Spin, Nonheme Iron(III)-Superoxo Complex Supported by Phosphinimide Ligands. *J. Am. Chem. Soc.* **2021**, *143*, 13686-13693.
(57) Astruc, D. Organo-Iron Complexes of Aromatic Compounds. Applications in Synthesis. *Tetrahedron* **1983**, *39*, 4027-4095.
(58) Catheline, D.; Astruc, D. Piano-Stool (Pentamethylcyclopentadienyl)iron Complexes: Syntheses and Simple Coordination Chemistry. *Organometallics* **1984**, *3*, 1094-1100.
(59) Humphrey, B. D.; Castilo, R. E.; Vega, A. H.; Feliciano, A.; Squires, M. E. The synthesis and cyclic voltammetry of select ferrocene piano-stool isocyanide complexes. *Inorganica Chimica Acta* **2011**, *368*, 271-274.
(60) Sano, Y.; Lau, N.; Weitz, A. C.; Ziller, J. W.; Hendrich, M. P.; Borovik, A. S. Models for Unsymmetrical Active Sites in Metalloproteins: Structural, Redox, and Magnetic Properties of Bimetallic Complexes with M^{II}-(μ-OH)-Fe^{III} Cores. *Inorg. Chem.* **2017**, 56, 14118-14128**.**
(61) Lacy, D. C.; Gupta, R.; Stone, K. L.; Greaves, J.; Ziller, J. W.; Hendrich, M. P.; Borovik, A. S. Formation, Structure, and EPR Detection of a High Spin Fe^{IV}–Oxo Species Derived from Either an Fe^{III}–Oxo or Fe^{III}–OH Complex. *J. Am. Chem. Soc.* **2010**, *132*, 12188-12190.
(62) Birchall, T.; Drummond, I. Mössbauer Spectroscopy of Bis(carbollyl)iron Anions and Related Molecules. *Inorg, Chem.* **1971**, *10*, 399-401.
(63) Miller, J. S.; Zhang, J. H.; Reiff, W. M. Ferromagnetic Behavior of Linear Chain Charge Transfer Complexes. Structural and Magnetic Characterization of Decamethylferrocenium Hexacynaobutadiene (1:1): $[Fe(C_5Me_5)]^{\bullet+}[C_4(CN)_6]^{\bullet-}$. *J. Am. Chem. Soc.* **1987**, *109*, 4584-4592.
(64) Kurtz, D. M. Oxo- and Hydroxo-Bridged Diiron Complexes: A Chemical Perspective on a Biological Unit. *Chem. Rev.* **1990**, *90*, 585-606.
(65) Tshuva, E. Y.; Lippard, S. J. Synthetic Models for Non-Heme Carboxylate-Bridged Diiron Metalloproteins: Strategies and Tactics. *Chem. Rev.* **2004**, *104*, 987-1012.
(66) Jasniewski, A. J.; Que, L. Dioxygen Activation by Nonheme Diiron Enzymes: Diverse Dioxygen Adducts, High-Valent Intermediates, and Related Model Complexes. *Chem. Rev.* **2018**, *118*, 2554-2592.
(67) Hummel, H.; Mekmouche, Y.; Duboc-Toia, C.; Ho, R. Y. N.; Que, L.; Schünemann, V.; Thomas, F.; Trautwein, A. X.; Lebrun, C.; Fontecave, M.; Ménage, S. A Diferric Peroxo Complex with an Unprecedented Spin Configuration: An S=2 System Arising from an S=5/2, 1/2 Pair. *Angew. Chem., Int. Ed.* **2002**, *41*, 617-620
(68) Sickerman, N. S. Doctoral Dissertation, University of California-Irvine, Irvine, CA, 2014.
(69) Yano, J.; Kern, J.; Sauer, K.; Latimer, M. J.; Pushkar, Y.; Biesiadka, J.; Loll, B.; Saenger, W.; Messinger, J.; Zouni, A.; Yachandra, V. K. Where Water Is Oxidized to Dioxygen: Structure of the Photosynthetic Mn_4Ca Cluster. *Science* **2006**, *314*, 821-825.
(70) Britt, R. D.; Campbell, K. A.; Peloquin, J. M.; Gilchrist, M. L.; Aznar, C. P.; Dicus, M. M.; Robblee, J.; Messinger, J. Recent pulsed EPR studies of the Photosystem II oxygen-evolving complex: implications as to water oxidation mechanisms. *Biochim. Acta Bioenerg.* **2004**, *1655*, 158-171.
(71) Pantazis, D. A. The S_3 State of the Oxygen-Evolving Complex: Overview of Spectroscopy and XFEL Crystallography with a Critical Evaluation of Early-Onset Models for O–O Bond formation. *Inorganics* **2019**, *7*, 55.

(72) Cox, N.; Pantazis, D. A.; Lubitz, W. Current Understanding of the Mechanism of Water Oxidation in Photosystem II and Its Relation to XFEL Data. *Annu. Rev. Biochem.* **2020**, *89*, 795-820.
(73) Gupta, R.; Taguchi, T.; Lassalle-Kaiser, B.; Bominaar, E. L.; Yano, J.; Hendrich, M. P.; Borovik, A. S. High-spin Mn–oxo complexes and their relevance to the oxygen-evolving complex within photosystem II. *Proc. Nat. Acad. Sci. U.S.A.* **2015**, *112*, 5319-5324.
(74) Pecoraro, V. L.; Baldwin, M. J.; Caudle, M. T.; Hsieh, W.-Y.; Law, N. A. A proposal for water oxidation in photosystem II. *Pure Appl. Chem.* **1998**, *70*, 925-929.
(75) Cox, N.; Retegan, M.; Neese, F.; Pantazis, D. A.; Boussac, A.; Lubitz, W. Photosynthesis. Electronic Structure of the Oxygen-Evolving Complex in Photosystem II prior to O–O Bond Formation. *Science* **2014**, *345*, 804-808.
(76) Siegbahn, P. E. M. Structures and energetics for O_2 formation in photosystem II. *Acc. Chem. Res.* **2009**, *42*, 1871-1880.
(77) Cox, N.; Pantazis, D. A.; Neese, F.; Lubitz, W. Biological water oxidation. *Acc. Chem. Res.* **2013**, *46*, 1588-1596.
(78) Yocum, C. The Calcium and Chloride Requirements of the O_2 Evolving Complex. *Coord. Chem. Rev.* **2008**, *252*, 296-305.
(79) Boussac, A.; Zimmermann, J.-L.; Rutherford, A. W. Factors Influencing the Formation of Modified S2 EPR Signal and the S3 EPR Signal in Ca^{2+}-Depleted Photosystem II. *FEBS Lett.* **1990**, *277*, 69-74.
(80) Ghanotakis, D. F.; Babcock, G. T.; Yocum, C. F. Calcium Reconstitutes High Rates of Oxygen Evolution in Polypeptide Depleted Photosystem II Preparations. *FEBS Lett.* **1984**, *167*, 127-130.
(81) Ono, T.; Inoue, Y. Discrete Extraction of the Ca Atom Functional for O_2 Evolution in Higher Plant Photosystem II by a Simple Low pH Treatment. *FEBS Lett.* **1988**, *227*, 147-152.
(82) Weber, B. Betz, R.; Bauer, W.; Schlamp, S. Crystal Structure of Iron(II) Acetate. *Z. Anorg. Allg. Chem.* **2011**, *637*, 102-107.
(83) Connelly, N. G.; Geiger, W. E. Chemical Redox Agents for Organometallic Chemistry. *Chem. Rev.* **1996**, *96*, 877-910.
(84) Wilson, R. J.; Jones, J. R.; Bennett, M. V. Unprecedented Gallium-Nitrogen Anions: Synthesis and Characterization of $[(Cl_3Ga)_3N]^{3-}$ and $[(Cl_3Ga)_2NSnMe_3]^{2-}$. *Chem. Commun.* **2013**, *49*, 5049-5051.
(85) Petasis, D. T.; Hendrich, M. P. Quantitative Interpretation of Multifrequency Multimode EPR Spectra of Metal Containing Proteins, Enzymes, and Biomimetic Complexes. *Methods Enzymol.* **2015**, *563*, 171-208.
(86) APEX2 Version 2014.11-0, Bruker AXS, Inc.; Madison, WI 2014.
(87) SAINT Version 8.34a, Bruker AXS, Inc.; Madison, WI 2013.
(88) Sheldrick, G. M. SADABS, Version 2014/5, Bruker AXS, Inc.; Madison, WI 2014.
(89) Sheldrick, G. M. SHELXTL, Version 2014/7, Bruker AXS, Inc.; Madison, WI 2014
(90) International Tables for Crystallography 1992, Vol. C., Dordrecht: Kluwer Academic Publishers.
(91) Parson, S.; Flack, H. D.; Wagner, T. *Acta Cryst.* **2013**, *B69*, 249-259.

Chapter 3

Stepwise Assembly of Heterobimetallic Complexes with a [M^{II}–(μ-OH)–Fe^{III}] Core

Introduction

Complexes with discrete bimetallic cores are found in a number of biological and synthetic systems and have impact on both physical and functional properties.[1–4] Within a biological context, chemical transformations are often regulated by the cooperative effects of bimetallic cores in which each metal center usually has a different primary coordination sphere.[5–13] Replicating these structural features within synthetic systems has been difficult because many preparative methods lead to each metal center have identical sets of ligand donors.[14–23] These methodological restrictions also hinder the preparation of complexes in which the bimetallic cores contain different metal ions.[24–26] One approach to circumvent these problems is to design a metal complex with an auxiliary binding site that can bind an additional, and different, metal complex.[27–36] Notable examples that use this approach are the heterobimetallic complexes of Thomas and Lu who have designed ligands that promote formation of complexes with M–M' bonds.[37–42]

We are developing a different approach for the stepwise assembly of heterobimetallic complexes that produces systems with [M^{II}–(μ-OH)–Fe^{III}] cores. The general design uses a monomeric Fe^{III}–OH synthon that contains a tripodal ligand with three structural characteristics: 1) it contains a trianionic, tetradentate binding site for the Fe^{III}–OH unit, 2) it contains scaffolding to append hydrogen bond (H–bond) acceptors to form intramolecular H-bonds with the Fe^{III}–OH unit, and 3) it contains an auxiliary metal binding site that includes the hydroxido ligand.[43] These design principles were illustrated in our use of the tripodal ligand $[MST]^{3-}$ (*N,N′,N″*-[2,2',2"-nitrilotris(ethane-2,1-diyl)]tris(2,4,6-trimethylbenzenesulfonamido), Figure 3.1A) that contains three deprotonated sulfonamide groups[44] and was used to prepare a variety of different complexes with

[M^{II}–(μ-OH)–Fe^{III}] cores (Figure 3.1B).[45–47] We recently introduced a tripodal ligand [poat]$^{3-}$ (*N,N′,N″*-[nitrilotris(ethane-2,1-diyl)]tris(*P,P*-diphenylphosphinic amido)) that instead of sulfonamido groups contains phosphinic amido groups (Figure 3.1C).[48] We reasoned that the similarities in the structures of the two tripodal ligands would prepare the analogous [M^{II}–(μ-OH)–Fe^{III}] complexes to compare their properties. The starting synthon, [Fe^{III}poat(OH)]$^-$, is well-characterized and discussed in Chapter 2 of this Dissertation as well as in other reports.[49] In this Chapter, we now report our findings for a series of [(TMTACN)M^{II}–(μ-OH)–Fe^{III}poat]$^+$ (M^{II} = Zn, Cu, Ni; TMTACN = 1,4,7-trimethyl-1,4,7-triazacyclononane) complexes that show these types of complexes can be readily assembled to form discrete heterobimetallic complexes. Although they have similar structural and physical properties, the complexes with [poat]$^{3-}$ have significantly lower redox potentials than their sulfonamido counterparts.

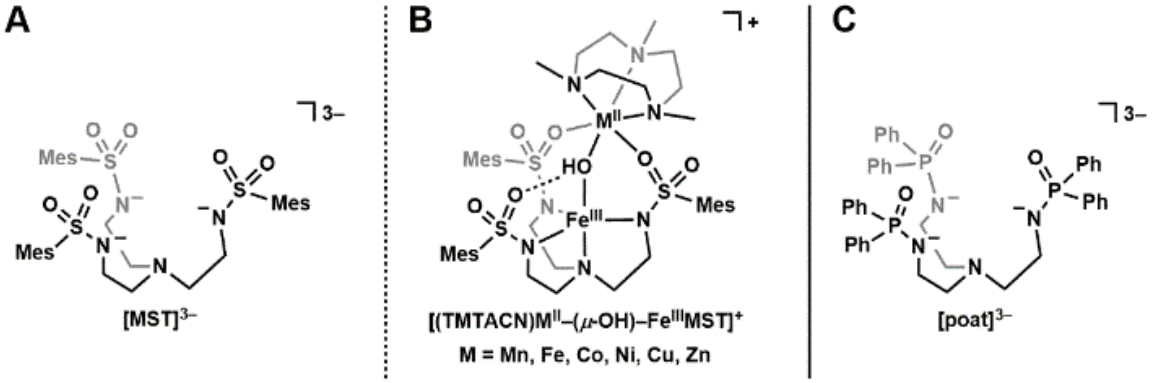

Figure 3.1. Structures of [MST]$^{3-}$ (A), [(TMTACN)M^{II}–(μ-OH)–Fe^{III}MST]$^+$ (B), and [poat]$^{3-}$ (C).

Results & Discussion

Preparation of [(TMTACN)TM^{II}–(μ-OH)–Fe^{III}poat]OTf. The preparation of the discrete heterobimetallic complexes [(TMTACN)M^{II}–(μ-OH)–Fe^{III}poat]OTf (M^{II} = Zn, Cu, Ni and denoted [M^{II}(OH)Fe^{III}]$^+$) was achieved via the preparative route outlined in Scheme 3.1. In a typical reaction, NMe_4OAc was added to a CH_2Cl_2 solution of K[Fe^{III}poat(OH)], and after removal of the insoluble KOAc, the resulting mixture was treated with the appropriate [M^{II}(TMTACN)]$^{2+}$ complex.

$[Zn^{II}(TMTACN)(OTf)_2]$ and $[Cu^{II}(TMTACN)(OTf)_2]\cdot CH_3CN$[50] salts were used to synthesize the $[Zn^{II}(OH)Fe^{III}]^+$ and $[Cu^{II}(OH)Fe^{III}]^+$ species; however, attempts to synthesize and isolate $[Ni^{II}(TMTACN)(OTf)_2]$ in high purity had been unsuccessful, which led to this salt being generated *in situ* by mixing equimolar of $Ni^{II}(OTf)_2\cdot 5CH_3CN$ and TMTACN in CH_2Cl_2. The $[M^{II}(OH)Fe^{III}]OTf$ salts were first purified as powders via precipitation from diethyl ether-CH_2Cl_2 mixtures, and were then further purified via recrystallization as yellow sheet-like crystals from pentane (or hexane)-CH_2Cl_2 mixtures. These crystals were suitable for single crystal X-ray diffraction measurements, elemental analysis, and additional characterization methods. The formulations of the $[M^{II}(OH)Fe^{III}]^+$ complexes were supported by ESI-MS, in which the m/z values and experimental isotope patterns matched those calculated for $[M^{II}(OH)Fe^{III}]^+$ (Figure 3.2). The three complexes have similar optical properties with absorbance features around λ_{max} = 315, 372, and 460 nm (Figure 3.3). In particular, the absorbance feature with a λ_{max} = 372 nm is similar to those previously reported in our related heterobimetallic complexes with the $[MST]^{3-}$ ligand.[46]

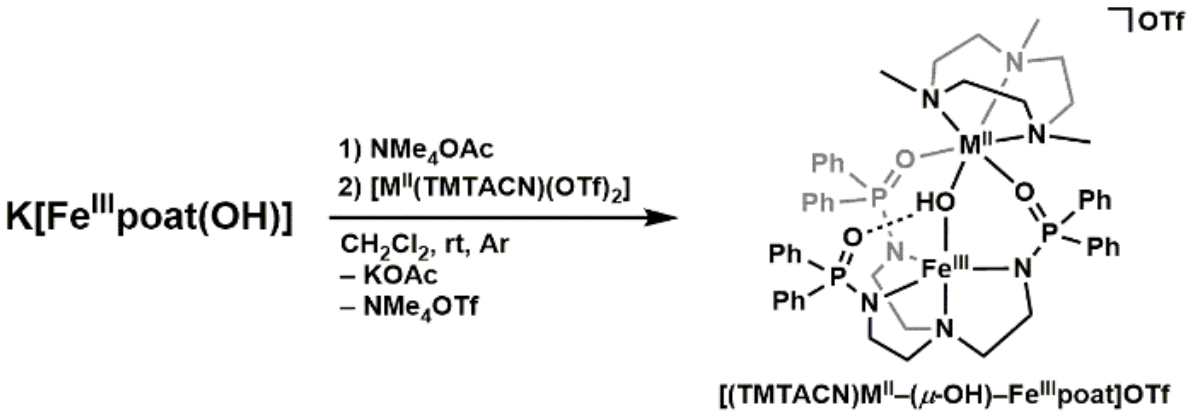

Scheme 3.1. Preparative route to the bimetallic $[M^{II}(OH)Fe^{III}]^+$ complexes (M = Zn, Cu, Ni).

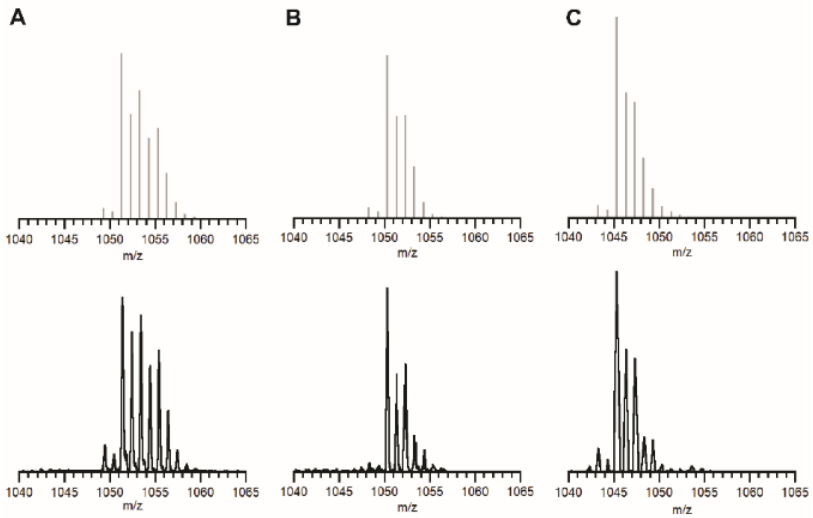

Figure 3.2. ESI-MS spectra of (A) $[Zn^{II}(O)Fe^{III}]^+$, (B) $[Cu^{II}(OH)Fe^{III}]^+$, and (C) $[Ni^{II}(OH)Fe^{III}]^+$, with the simulated spectra given in grey.

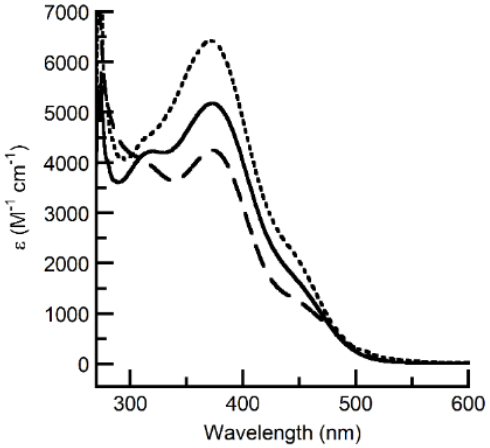

Figure 3.3. Electronic absorbance spectra for (A) $[Zn^{II}(O)Fe^{III}]^+$ (black solid line), (B) $[Cu^{II}(OH)Fe^{III}]^+$ (black dashed line), and (C) $[Ni^{II}(OH)Fe^{III}]^+$ (black dotted line) complexes. Absorbance measurements were performed on a 0.10 mM CH_2Cl_2 solution at room temperature.

Vibrational Properties of $[M^{II}(OH)Fe^{III}]^+$ Complexes. Solid-state vibrational properties of the $[M^{II}(OH)Fe^{III}]^+$ compounds were investigated by FTIR spectroscopy and exhibit similar features (Figures 3.4). For example, the vibrational spectrum of $[Zn^{II}(OH)Fe^{III}]OTf$ revealed a weak vibrational feature at 3141 cm^{-1} that is assigned to the ν(O–H) band. This energy is lower, and the peak is broader than the corresponding ν(O–H) feature observed in the analogous complex with the

$[MST]^{3-}$ ligand, which appears at an energy of 3238 cm^{-1}.[46] These observations are consistent with the phosphinic amido P=O group in $[poat]^{3-}$ being a stronger H-bond acceptor than the sulfonamido S=O group in $[MST]^{3-}$. For $[Ni^{II}(OH)Fe^{III}]^{+}$, the ν(O–H) band is at 3160 cm^{-1} and it is similarly broad to suggest that the hydroxido ligand is involved in H-bond formation. We were unable to detect the ν(O–H) feature in the $[Cu^{II}(OH)Fe^{III}]^{+}$ which could be attributed to the relatively lower Lewis acidity of Cu^{II} ion,[51] and that would strengthen the H-bond and broaden any ν(O–H) feature. The remaining portion of the vibrational spectra of the three complexes are nearly identical, implying that the overall solid-state structures for the three complexes could be similar.

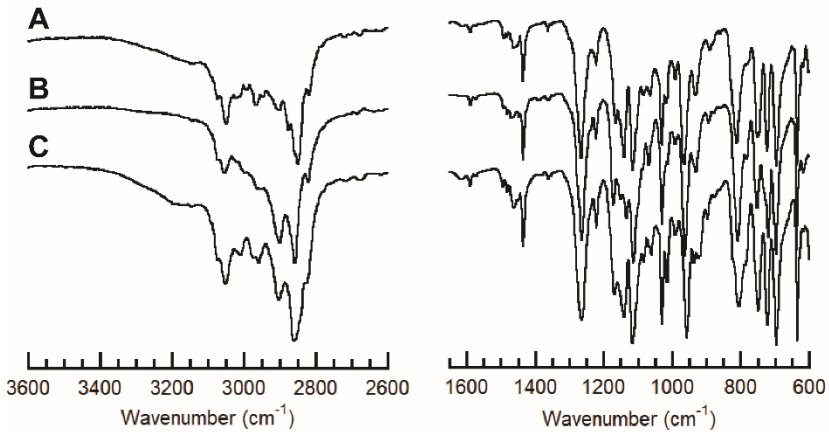

Figure 3.4. FTIR spectra for $[Zn^{II}(OH)Fe^{III}]^{+}$ (A), $[Cu^{II}(OH)Fe^{III}]^{+}$ (B), and $[Ni^{II}(OH)Fe^{III}]^{+}$ (C).

Solid-State Molecular Structures of $[M^{II}(OH)Fe^{III}]^{+}$ Complexes. The molecular structures of the $[M^{II}(OH)Fe^{III}]^{+}$ complexes were determined by X-ray diffraction methods and revealed discrete bimetallic core structures (Figure 3.5). There are two crystallographically different, but chemically equivalent, molecules in the asymmetric unit and we will discuss the averages of the metrical parameters and calculated values, which are shown in Table 3.1. The triflate counter anion is outer-sphere and not interacting with the complex. The Fe^{III} site adopts a similar tbp geometry as found in $[Fe^{III}poat(OH)]^{-}$ with an N_4O primary coordination sphere, comprising of the $[poat]^{3-}$ ligand and the hydroxido ligand. The complexes have τ_5 values ranging 0.877 to 0.885, which are less than that

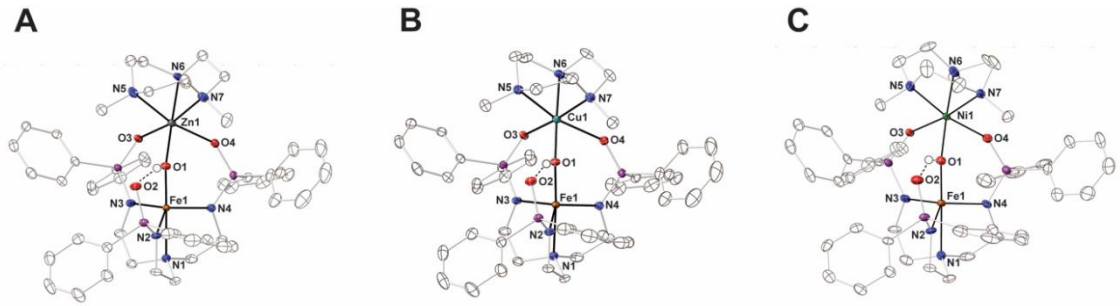

Figure 3.5. Thermal ellipsoid diagrams depicting the molecular structures of (A) $[Zn^{II}(O)Fe^{III}]^{+}$, (B) $[Cu^{II}(OH)Fe^{III}]^{+}$, and (C) $[Ni^{II}(OH)Fe^{III}]^{+}$ determined by X-ray diffraction. Ellipsoids are shown at the 50% probability level, and only the hydroxido H atoms are shown for clarity.

found in $[Fe^{III}poat(OH)]^{-}$ (see above). The Fe1–O1 bond distances are statistically identical within the series (1.887(4) – 1.900(2) Å), and are comparable with those previously reported in $[(TMTACN)M^{II}–(\mu\text{-}OH)–Fe^{III}MST]^{+}$ (1.884(2) to 1.892(5) Å).[46]

The M^{II} sites in the series are all 6-coordinated with N_3O_3 primary coordination spheres that are comprised of the TMTACN ligand, two O-atom donors from the phosphinic amido groups of $[poat]^{3-}$, and the bridging hydroxido ligand. A Jahn-Teller distortion is observed in the Cu^{II} site of $[Cu^{II}(OH)Fe^{III}]^{+}$, in which the axial Cu1–O3 and Cu1–N7 bond distances are significantly elongated, while the equatorial Cu1–O1/Cu1–O4/Cu1–N5/Cu1–N6 bond distances are contracted in comparison with those observed in the Zn^{II} and Ni^{II} analogues (Table 3.1). We note that a similar Jahn-Teller distortion was also observed in the $[(TMTACN)Cu^{II}–(\mu\text{-}OH)–Fe^{III}MST]^{+}$ complex.[46]

We further examined the M^{II}–O=P and $M^{II}–N_{TMTACN}$ bonds in the $[M^{II}(OH)Fe^{III}]^{+}$ complex series; the Cu^{II} analogue is excluded from this discussion because of the aforementioned Jahn-Teller distortion (see above). The M^{II}–O=P bond distances range between 2.089(4) – 2.115(2) Å; these values are significantly smaller than the corresponding M^{II}–O(S) bond distances observed in the sulfonamido complexes that range from 2.148(2) – 2.362(3) Å.[46] The difference in M^{II}–O bond lengths suggests the phosphinic amido P=O groups are stronger donating ligands than the sulfonamide S=O groups. Moreover, the $M^{II}–N_{TMTACN}$ bond distances trans to the O=P groups are lengthened in $[M^{II}(OH)Fe^{III}]^{+}$ (2.144(5) – 2.257(2) Å), in comparison with those reported for the

MST analogues (2.102(2) – 2.164 (3) Å).[46] These observations are consistent with stronger trans influence in the $[poat]^{3-}$ system, in which the O=P donors form stronger M^{II}–O=P bond that cause a weakening and lengthening the M^{II}–N_{TMTACN} bonds.

Table 3.1. Selected bond lengths/distances (Å) and angles (°) for $[M^{II}(OH)Fe^{III}]^{+}$ complexes.[a]

	M^{II}		
$[M^{II}(OH)Fe^{III}]^{+}$	Zn^{II}	Cu^{II}	Ni^{II}
	Bond Lengths/Distances (Å)		
Fe1–N1	2.207(2)	2.205(1)	2.224(5)
Fe1–N2	2.022(2)	2.024(1)	2.017(4)
Fe1–N3	2.005(2)	1.996(1)	2.000(5)
Fe1–N4	2.007(2)	2.006(1)	2.007(5)
Fe1–O1	1.900(2)	1.898(1)	1.887(4)
O1···O2	2.653(2)	2.641(2)	2.655(5)
M1–O1	1.983(2)	1.910(1)	1.981(4)
M1–O3	2.115(2)	2.354(1)	2.091(4)
M1–O4	2.097(2)	2.019(1)	2.089(4)
M1–N5	2.240(2)	2.132(1)	2.144(5)
M1–N6	2.154(2)	2.038(1)	2.106(5)
M1–N7	2.257(2)	2.357(2)	2.156(5)
Fe1···M1	3.416(1)	3.409(1)	3.423(1)
av Fe1–N_{eq}	2.011(2)	2.009(1)	2.008(5)
av M1–N_{TMTACN}	2.217(2)	2.176(1)	2.135(5)
d[Fe1–N_{eq}]	0.364	0.360	0.370
d[M1–N_{TMTACN}]	1.474	1.405	1.370
	Angles (°)		
O1–Fe1–N1	174.54(8)	173.69(5)	174.54(17)
N2–Fe1–N3	121.44(9)	120.87(6)	121.94(20)
N3–Fe1–N4	109.64(9)	110.75(6)	108.92(20)
N2–Fe1–N4	119.26(9)	118.91(6)	119.09(19)
Fe1–O1–M1	123.26(9)	127.04(7)	124.45(20)
O3–M1–O4	96.68(7)	94.24(4)	94.46(15)
N5–M1–N6	81.31(8)	84.55(6)	84.03(18)
N5–M1–N7	78.96(8)	79.74(5)	81.99(19)
N6–M1–N7	81.35(9)	82.01(6)	83.70(20)
		Calculated Values	
τ_5[b]	0.885	0.880	0.877

[a]Bond lengths, distances, and angles are reported as an average. [b]Trigonality structural parameter, $\tau_5 = (\beta - \alpha)/60^{o}$. β is the largest bond angle observed, and α is the second largest bond angle observed.

The remaining phosphinic amido tripodal arm that does not coordinate to the M^{II} ion participates in an intramolecular H-bond with the bridging hydroxido group; the O1⋯O2 distances range from 2.641(2) to 2.655(5) Å, which are indicative of H-bonds and consistent with the observation obtained from FTIR spectroscopy. The O⋯O distances found in $[M^{II}(OH)Fe^{III}]^{+}$ are comparable with those found in the $[(TMTACN)M^{II}–(\mu\text{-}OH)–Fe^{III}MST]^{+}$ complexes (2.619(4) – 2.644(3) Å).[46]

Table 3.2. Crystallographic data for $[(TMTACN)M^{II}–(\mu\text{-}OH)–Fe^{III}poat]OTf$ complexes (M^{II} = Zn, Cu, Ni)

	$[(TMTACN)Zn^{II}–(\mu\text{-}OH)–Fe^{III}poat]OTf$	$[(TMTACN)Cu^{II}–(\mu\text{-}OH)–Fe^{III}poat]OTf$	$[(TMTACN)Ni^{II}–(\mu\text{-}OH)–Fe^{III}poat]OTf$
Formula	$C_{52}H_{64}F_3FeN_7O_7P_3SZn$	$C_{52}H_{64}CuF_3FeN_7O_7P_3S$	$C_{52}H_{64}F_3FeN_7NiO_7P_3S$
fw	1202.29	1200.46	1195.63
T (K)	88(2)	133(2)	93(2)
Crystal system	Triclinic	Triclinic	Orthorhombic
Space group	$P\bar{1}$	$P\bar{1}$	$Pca2_1$
a (Å)	14.8745(7)	14.8537(13)	21.3910(9)
b (Å)	17.1815(8)	17.1335(15)	17.3399(8)
c (Å)	21.4499(10)	21.4044(19)	29.1742(13)
α (°)	89.3968(8)	90.9050(15)	90
β (°)	89.9334(8)	91.3032(14)	90
γ (°)	81.8418(8)	98.1532(14)	90
Z	4	4	8
V (Å^3)	5426.1(4)	5389.9(8)	10821.2(8)
δ_{calc} (mg/m^3)	1.472	1.479	1.468
Independent reflections	32345	31356	27950
R1	0.0504	0.0355	0.0532
wR2	0.1138	0.0899	0.0988
Goof	1.016	1.026	1.010
CCDC#	2072601	2072602	2072603

$wR2 = [\Sigma[w(F_o^2-F_c^2)^2] / \Sigma[w(F_o^2)^2]]^{1/2}$
$R1 = \Sigma||F_o|-|F_c|| / \Sigma|F_o|$
Goof = $S = [\Sigma[w(F_o^2-F_c^2)^2] / (n-p)]^{1/2}$ where n is the number of reflections and p is the total number of parameters refined.
The thermal ellipsoid plot is shown at the 50% probability level.

Electrochemical Properties of $[M^{II}(OH)Fe^{III}]^+$ Complexes. The electrochemical properties of the $[M^{II}(OH)Fe^{III}]^+$ series were investigated using cyclic voltammetry. The $[Zn^{II}(OH)Fe^{III}]^+$ complex exhibited a reversible one-electron redox event at -1.62 V vs. $[FeCp_2]^{+/0}$ (i_{pc}/i_{pa} = 1.01, ΔE = 0.20 V, $\Delta E([FeCp_2]^{+/0})$ = 0.18 V) that is assigned to the $Zn^{II}Fe^{III}/Zn^{II}Fe^{II}$ couple (Figure 3.6A).

The $[Cu^{II}(OH)Fe^{III}]^+$ complex exhibited complex redox behavior, with a single reduction and oxidation events at -1.76 V and -1.13 V, respectively (Figure 3.6B). One possible explanation for this electrochemical behavior is that the Cu^{II} center has a similar reduction potential, which likely results in a large structural change that could influence the reversibility of an electrochemical event.

The $[Ni^{II}(OH)Fe^{III}]^+$ complex exhibited a reversible one-electron redox event at -1.71 V vs. $[FeCp_2]^{+/0}$ (i_{pc}/i_{pa} = 1.07, ΔE = 0.18 V, $\Delta E([FeCp_2]^{+/0})$ = 0.17 V) that is assigned to the $Ni^{II}Fe^{III}/Ni^{II}Fe^{II}$ couple (Figure 3.6C). The reduction potentials of the $[M^{II}(OH)Fe^{III}]^+$ complexes are significantly more negative than their $[(TMTACN)M^{II}–(\mu\text{-}OH)–Fe^{III}MST]^+$ analogs. For instance, the potential for the $[Zn^{II}(OH)Fe^{III}]^+$ complex is more negative by 0.73 V than that found for the

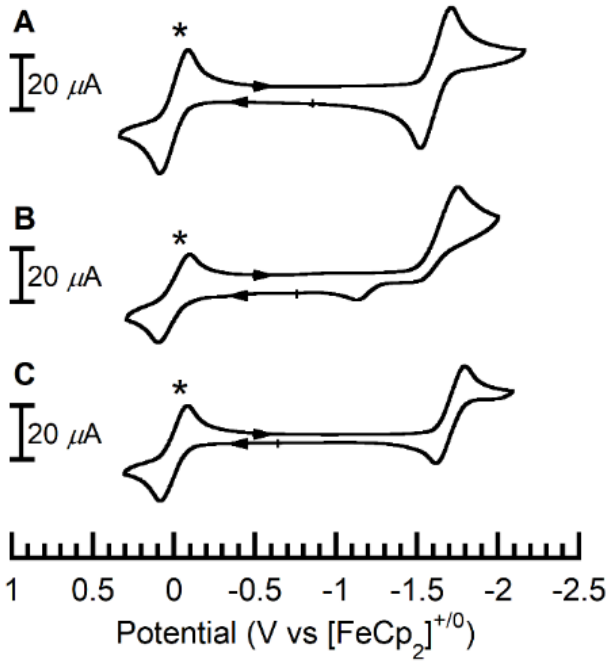

Figure 3.6. Cyclic voltammograms of (A) $[Zn^{II}(O)Fe^{III}]^+$, (B) $[Cu^{II}(OH)Fe^{III}]^+$, and (C) $[Ni^{II}(OH)Fe^{III}]^+$. The cyclic voltammograms were collected at 100 mV s^{-1} in the presence of $[FeCp_2]$ (*) in CH_2Cl_2.

same process in [(TMTACN)Zn^{II}–(μ-OH)–Fe^{III}MST]$^+$ (-0.89 V).[46] The observed difference between the two systems is again consistent with [poat]$^{3-}$ being a stronger donating ligand than [MST]$^{3-}$, and highlights the ability of phosphinic amido groups to stabilize higher valent metal centers.[48]

Electron Paramagnetic Resonance (EPR) Properties of [M^{II}(OH)Fe^{III}]$^+$ Complexes. The magnetic properties of the bimetallic complexes were examined and analyzed using EPR spectroscopy in collaboration with Prof. Michael Hendrich's group (Carnegie Mellon University). The [Zn^{II}(OH)Fe^{III}]$^+$ complex showed signals (Figure 3.7A) from an $S = 5/2$ species in perpendicular mode, with $g = 4.96$ and 3.82 arising from the $M_s = \pm 3/2$ doublet and weaker resonances at $g = 9.85$ and 9.15 from the $M_s = \pm 5/2$ and $\pm 1/2$ doublets, respectively. The simulation indicated $D = -1.7$ cm^{-1} and $E/D = 0.21$. The spin concentration (5 mM) determined from simulation was within error equal to that determined by the

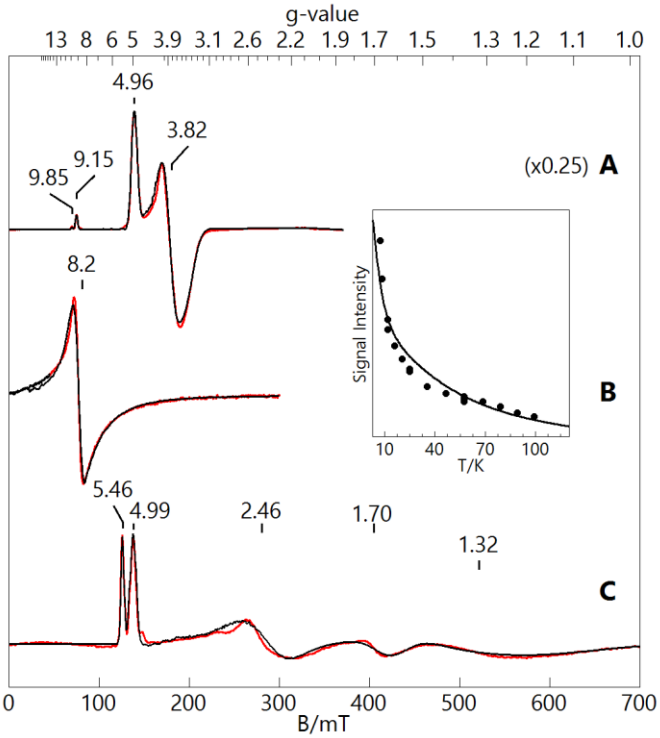

Figure 3.7. EPR spectra (red lines) and simulations (black lines) of (A) [Zn^{II}(OH)Fe^{III}]$^+$, (B) [Cu^{II}(OH)Fe^{III}]$^+$, and (C) [Ni^{II}(OH)Fe^{III}]$^+$. Sample concentrations: 5 mM in CH_2Cl_2:THF. Instrumental conditions: temperature, 16 K; microwave frequency, 9.645 GHz, $B_1 \perp B$ (A, C), 9.343 GHz, $B_1 \parallel B$ (B); microwave power, 0.2 mW. See text for simulation. parameters.

weight of the added complex. The electronic properties of this complex are comparable to that of $[(TMTACN)Zn^{II}–(\mu\text{-}OH)–Fe^{III}MST]^+$ (D = -2.5 cm^{-1}, E/D = 0.21).

The $[Cu^{II}(OH)Fe^{III}]^+$ complex showed a signal (Figure 3.7B) from the S = 2 system of the antiferromagnetically exchange-coupled S = 1/2 (Cu^{II}) and S = 5/2 (Fe^{III}) ions.[46,48] The inset shows the temperature dependence of the signal intensity and a theoretical curve for the exchange-coupled spin system with J = +25 cm^{-1} and D_{Fe} = -1.7 cm^{-1}. The simulation overlaid on the spectrum assumes an S = 2 spin Hamiltonian with D = -2.3 cm^{-1}, E/D = 0.15, g_z = 2. The conversions from the uncoupled site parameters to an S = 2 system parameters are: D = 4/3 D_{Fe} , g_z = 2 – $\Delta g_{z,Cu}/6$ and A_z = 1/6 $A_{z,Cu}$. For Cu^{II}, $g_{z,Cu} \approx 2.2$,[50] and $\Delta g_{z,Cu} = g_{z,Cu} - 2 \approx 0.2$, giving $g_z \approx 2$. The significant reduction of the system A_z value is cause by spin coupling that renders the Cu hyperfine unresolvable. The value of J is the same as that observed for the MST analog.

The $[Ni^{II}(OH)Fe^{III}]^+$ complex showed signals (Figure 3.7C) from the S = 3/2 system of the antiferromagnetically exchange-coupled S = 1 (Ni^{II}) and S = 5/2 (Fe^{III}) ions. The signals at g = 4.99, 2.46, 1.70 are from the $M_s = \pm 1/2$ doublet and g = 5.46, 1.32 are from the $M_s = \pm 3/2$ doublet. The simulation overlaid on the spectrum uses J = +35 cm^{-1}, D_{Fe} = -1.7 cm^{-1}, E/D_{Fe} = 0.21, D_{Ni} = +12 cm^{-1}, E/D_{Ni} = 0.11, g_{Ni} = (2.24, 2.17, 2.18). All these values are comparable to the MST analog. The spin concentration (5 mM) determined from simulation was within error equal to that determined by the weight of the added complex.

Conclusion & Outlook

We have demonstrated the stepwise assembly of heterobimetallic complexes from the Fe^{III}–OH synthon, $[Fe^{III}poat(OH)]^-$, and $[M^{II}(TMTACN)(OTf)_2]$. Spectroscopic and structural studies confirm that the metal centers have different primary coordination spheres with the Fe^{III} being five-coordinated and the M^{II} being six-coordinated. Moreover, our findings show that each complex

contains an [M^{II}–(μ-OH)–Fe^{III}] core structure that persists in both solution and solid states. Results from XRD and vibrational measurements indicate that each complex contains an intramolecular H-bond between the hydroxido ligand and a P=O moiety from one of the phosphinic amido groups.

The formation of bimetallic complexes with a bridging hydroxido ligand has relevance to active sites within metalloproteins.[9–12,52] The diverse examples that have these types of core structures include the di-Fe centers in the respiratory protein hemerythrin that also contain one five- and one six-coordinate site,[7] and the FeZn site in purple acid phosphatase that degrades organophosphates.[8] The isolation of the [(TMTACN)M^{II}–(μ-OH)–Fe^{III}poat]$^{+}$ complex further allowed comparisons to the related series of complexes, [(TMTACN)M^{II}–(μ-OH)–Fe^{III}MST]$^{+}$, that are made with a sulfonamido tripod. We found major differences in the one-electron reduction potentials between these two sets of bimetallic complexes with those prepared with [poat]$^{3-}$ having significantly lower potentials. This finding indicates that phosphinic amido donors create stronger ligand fields than comparable sulfonamido donors. In addition, the M^{II}–$O_{P=O}$ bonds are shorter than the analogous M^{II}–$O_{S=O}$ which suggests that the P=O units, with its larger dipole, can form stronger M–O bonds. These results suggest that ligands with phosphinic amido groups could stabilize higher valent bimetallic complexes. We pointed out that one limitation of complexes with sulfonamido tripods is the inability to access higher valent metal centers. Tripodal ligands with phosphinic amido donors should help correct this deficiency because our data indicates that [poat]$^{3-}$ is better at stabilizing higher oxidized metal center than the corresponding sulfonamido ligand. Our recent detection of the Fe^{IV}=O complex [Fe^{IV}poat(O)]$^{-}$ supports this premise and, taken together with the work presented here, illustrates the versatility and promise of this type of ligand.[48] This hypothesis proved well-founded: the preparation of bimetallic complexes up to a valence state of (III,IV) is described in the following chapters. First, a higher oxidation level than [M^{II}(OH)Fe^{III}]$^{+}$ is examined.

Experimental

General Procedures. All reagents were purchased from commercial sources and used as received unless otherwise noted. Solvents were sparged with argon and purified using a JC Meyer Co. solvent purification system with columns containing Q-5 and molecular sieves. Potassium hydride (KH) as a 30 % dispersion in mineral oil was filtered with a medium porosity glass frit and washed 5 times each with pentane and diethyl ether (Et_2O). Solid KH was dried under vacuum and stored under an inert atmosphere. All synthetic manipulations were conducted in a Vacuum Atmosphere, Co. drybox under an argon atmosphere. H_3poat,[48] TMTACN,[53,54] $Zn^{II}(OTf)_2 \cdot 2CH_3CN$,[55] $[Cu^{II}(TMTACN)(OTf)_2] \cdot CH_3CN$,[50] and $Ni^{II}(OTf)_2 \cdot 5CH_3CN$[55] were synthesized according to previous reports.

Physical Methods. Electronic absorbance spectra were recorded with a Cary 50 spectrophotometer using a 1.00 cm quartz cuvette. High resolution mass spectra were collected using Waters Micromass LCT Premier Mass Spectrometer. Solid-state Fourier transform infrared (FTIR) spectra were collected on a Thermo Scientific Nicolet iS5 FT-IR spectrometer equipped with an iD5 ATR accessory. Cyclic voltammetry experiments were conducted using a CHI600G electrochemical analyzer. A 2.0 mm glassy carbon electrode was used as the working electrode at scan velocities between 0.01 and 0.5 $V \cdot s^{-1}$. A ferrocenium/ferrocene ($[FeCp_2]^{+/0}$) standard was used as an internal reference to monitor the reference electrode (Ag^+/Ag). Tetrabutylammonium hexafluorophosphate (TBAP) was used as the supporting electrolyte at a concentration of 0.1 M. Elemental analyses were performed on a Perkin-Elmer 2400 Series II CHNS elemental analyzer. X-band EPR spectra were recorded on a Bruker ELEXSYS spectrometer equipped with an Oxford ESR-910 liquid helium cryostat and a Bruker bimodal cavity for the generation of microwave fields parallel and transverse to the applied magnetic field. The microwave frequency was calibrated with a frequency counter, and the magnetic field was measured with an NMR gaussmeter. The sample temperature was calibrated

against a calibrated cernox sensor (Lakeshore CX-1050) mounted inside an EPR tube. A modulation frequency of 100 kHz was used for all EPR spectra. The simulation software SpinCount was written by one of the authors.[56] The software diagonalizes the electronic terms of the spin Hamiltonian, and performs least-squares fitting of simulations to the spectra. The quantitative simulations are generated with consideration of all intensity factors, which allows the computation of simulated spectra for a specified sample concentration. The quantification of all signals was performed relative to a CuEDTA spin standard prepared from a copper atomic absorption standard (Sigma-Aldrich). Additional information for EPR data analysis and crystallographic details are summarized in Supporting Information.

Synthesis of [Zn^{II}(TMTACN)(OTf)$_2$]. Zn^{II}(OTf)$_2$·2CH$_3$CN (104.7 mg, 0.2350 mmol) was suspended in 20 mL CH_2Cl_2, and TMTACN (46.0 μL, 40.7 mg, 0.237 mmol) was added in one portion using a syringe. The reaction mixture turned clear and was allowed to react for 2 h. The solution was filtered with a fine porosity glass frit to remove any insoluble materials, and all volatiles were removed under vacuum. The white residue was redissolved in 2 mL CH_2Cl_2, and white solids were precipitated after the addition of 20 mL Et_2O. The white solids were collected on a fine porosity glass frit and dried under vacuum, affording the product (115 mg, 91.5 %). Elemental analysis calcd for [Zn^{II}(TMTACN)(OTf)$_2$], $C_{11}H_{21}F_6N_3O_6S_2Zn$: C, 24.70; H, 3.96; N, 7.86%, found: C, 24.86; H, 3.98; N, 7.66%.

Synthesis of [(TMTACN)Zn^{II}–(μ-OH)–Fe^{III}poat]OTf. K[Fe^{III}poat(OH)] (92.4 mg, 0.108 mmol) was dissolved in 4 mL anhydrous CH_2Cl_2. NMe_4OAc (15.6 mg, 0.117 mmol) was added in one portion, and the mixture was allowed to stir for 1 h. The reaction mixture was filtered with a fine porosity glass frit, and the filtrate was added dropwise to a 1 mL CH_2Cl_2 solution of [Zn^{II}(TMTACN)(OTf)$_2$] (58.2 mg, 0.109 mmol). The reaction was allowed to proceed for 1 h, and the mixture was filtered with a medium porosity glass frit to remove any insoluble materials. The filtrate was layered with

Et_2O to yield a light brown powder. After the light brown powder was collected and dried, it was redissolved in CH_2Cl_2, and was layered with pentane to yield yellow sheet-like crystals. The crystals were collected on a glass frit and dried under vacuum, affording the product in yields that ranged from 40-50 %. Elemental analysis calcd for [(TMTACN)Zn^{II}–(μ-OH)–Fe^{III}poat]OTf·1.5CH_2Cl_2, $C_{52}H_{64}F_3FeN_7O_7P_3SZn$·1.5$CH_2Cl_2$; C, 48.33; H, 5.08; N, 7.37%, found: C, 48.64; H, 4.85; N, 7.67%. FTIR (diamond ATR, cm^{-1}): 3141 (OH), 3074, 3049, 3020, 2993, 2964, 2947, 2902, 2877, 2848, 2817, 1591, 1493, 1483, 1464, 1435, 1363, 1267, 1223, 1165, 1140, 1115, 1084, 1065, 1030, 1016, 991, 964, 931, 891, 812, 750, 723, 696, 636. EPR (X-band, ⊥-mode, CH_2Cl_2:THF, 16 K): g = 9.85, 9.15, 4.96, 3.82. UV-vis λ_{max}(CH_2Cl_2)/nm ($\varepsilon/M^{-1}cm^{-1}$): 319 (4200), 372 (5200), 460 (sh). Electronspray ionization mass spectrometry (ESI-MS) (CH_3CN, ES^+, m/z): exact mass calcd for [Zn^{II}(OH)Fe^{III}]$^+$, $C_{51}H_{64}FeN_7O_4P_3Zn$, 1051.2875; found, 1051.2848. $E_{1/2}$ (CH_2Cl_2, V versus $[FeCp_2]^{+/0}$): -1.62.

Synthesis of [(TMTACN)Cu^{II}–(μ-OH)–Fe^{III}poat]OTf. This salt was prepared using the method described above for [(TMTACN)Zn^{II}–(μ-OH)–Fe^{III}poat]OTf with the following modifications: K[Fe^{III}poat(OH)] (125.7 mg, 0.1469 mmol), NMe_4OAc (21.2 mg, 0.159 mmol), [Cu^{II}(TMTACN)$(OTf)_2$]·CH_3CN (85.1 mg, 0.148 mmol). Yellow sheet-like crystals (40-50% yield) suitable for X-ray diffraction were grown from a concentrated CH_2Cl_2 solution layered with hexane. Elemental analysis calcd for [(TMTACN)Cu^{II}–(μ-OH)–Fe^{III}poat]OTf·2CH_2Cl_2, $C_{52}H_{64}CuF_3FeN_7O_7P_3S$·2$CH_2Cl_2$; C, 47.33; H, 5.00; N, 7.16%, found: C, 46.93; H, 4.88; N, 7.26%. FTIR (diamond ATR, cm^{-1}): 3053, 2987, 2962, 2900, 2858, 2821, 1589, 1491, 1483, 1469, 1441, 1435, 1360, 1263, 1223, 1173, 1149, 1134, 1115, 1068, 1030, 1014, 993, 962, 931, 893, 877, 808, 783, 752, 719, 696, 636. EPR (X-band, //-mode, CH_2Cl_2:THF, 16 K): g = 8.2. UV-vis λ_{max}(CH_2Cl_2)/nm ($\varepsilon/M^{-1}cm^{-1}$): 315 (sh), 372 (4200), 460 (sh). ESI-MS (CH_3CN, ES^+, m/z): exact mass calcd for

$[Cu^{II}(OH)Fe^{III}]^+$, $C_{51}H_{64}CuFeN_7O_4P_3$, 1050.2880; found, 1050.2909. E_{pa} (CH_2Cl_2, V versus $[FeCp_2]^{+/0}$): -1.13. E_{pc} (CH_2Cl_2, V versus $[FeCp_2]^{+/0}$): -1.76.

Synthesis of [(TMTACN)Ni^{II}–(μ-OH)–Fe^{III}poat]OTf. This salt was prepared using the method described above for [(TMTACN)Zn^{II}–(μ-OH)–Fe^{III}poat]OTf with the following modifications: K[Fe^{III}poat(OH)] (190.0 mg, 0.2231 mmol), NMe_4OAc (31.2 mg, 0.238 mmol), 6 mL CH_2Cl_2. $Ni^{II}(OTf)_2 \cdot 5CH_3CN$ (125.9 mg, 0.2240 mmol) and TMTACN (44.0 μL, 38.9 mg, 0.227 mmol) were pre-mixed for 1 h before using. Dark yellow crystals (50-60% yield) suitable for X-ray diffraction were grown from a concentrated CH_2Cl_2 solution layered with hexane. Elemental analysis calcd for [(TMTACN)Ni^{II}–(μ-OH)–Fe^{III}poat]OTf·0.5C_5H_{12}, $C_{52}H_{64}F_3FeN_7NiO_7P_3S \cdot 0.5C_5H_{12}$; C, 53.15; H, 5.73; N, 7.96%, found: C, 53.15; H, 5.53; N, 7.90%. FTIR (diamond ATR, cm^{-1}): 3160 (br, OH), 3064, 3050, 3008, 2970, 2960, 2904, 2860, 2827, 1614, 1591, 1572, 1484, 1471, 1462, 1450, 1435, 1379, 1361, 1263, 1222, 1169, 1140, 1117, 1082, 1061, 1030, 1014, 991, 957, 935, 924, 897, 876, 806, 785, 750, 721, 696, 636. EPR (X-band, ⊥-mode, CH_2Cl_2:THF, 16 K): g = 5.46, 4.99, 2.46, 1.70, 1.32. UV-vis λ_{max}(CH_2Cl_2)/nm (ε/$M^{-1}cm^{-1}$): 312 (sh), 372 (6400), 455 (sh), 513 (sh). ESI-MS (CH_3CN, ES^+, m/z): exact mass calcd for $[Ni^{II}(OH)Fe^{III}]^+$, $C_{51}H_{64}FeN_7NiO_4P_3$, 1045.2937; found, 1045.2939. $E_{1/2}$ (CH_2Cl_2, V versus $[FeCp_2]^{+/0}$): -1.71.

Crystallography

Structure of [(TMTACN)Zn^{II}–(μ-OH)–Fe^{III}poat]OTf. A yellow crystal of approximate dimensions 0.247 x 0.208 x 0.152 mm was mounted in a cryoloop and transferred to a Bruker SMART APEX II diffractometer. The APEX2[57] program package was used to determine the unit-cell parameters and for data collection (30 sec/frame scan time for a sphere of diffraction data). The raw frame data was processed using SAINT[58] and SADABS[59] to yield the reflection data file. Subsequent calculations were carried out using the SHELXTL[60] program. There were no systematic absences nor any diffraction symmetry other than the Friedel condition. The centrosymmetric triclinic space group *P*

$\bar{1}$ was assigned and later determined to be correct. The structure was solved by direct methods and refined on F^2 by full-matrix least-squares techniques. The analytical scattering factors[61] for neutral atoms were used throughout the analysis. The hydroxide hydrogen atoms (H1 and H8) were located from a difference-Fourier map and refined (x,y,z and U_{iso}). The remaining hydrogen atoms were included using a riding model. There were two molecules of the formula-unit present (Z = 4). Disordered atoms were included as isotropic atoms using multiple components with partial site-occupancy factors.

Least-squares analysis yielded wR2 = 0.1138 and Goof = 1.016 for 1341 variables refined against 32345 data (0.70 Å), R1 = 0.0504 for those 24496 data with $I > 2.0\sigma(I)$.

Structure of [(TMTACN)Cu^{II}–(μ-OH)–Fe^{III}poat]OTf. A yellow crystal of approximate dimensions 0.276 x 0.189 x 0.131 mm was mounted in a cryoloop and transferred to a Bruker SMART APEX II diffractometer. The APEX2[57] program package was used to determine the unit-cell parameters and for data collection (90 sec/frame scan time for a sphere of diffraction data). The raw frame data was processed using SAINT[58] and SADABS[59] to yield the reflection data file. Subsequent calculations were carried out using the SHELXTL[60] program. There were no systematic absences nor any diffraction symmetry other than the Friedel condition. The centrosymmetric triclinic space group *P* $\bar{1}$ was assigned and later determined to be correct. The structure was solved by direct methods and refined on F^2 by full-matrix least-squares techniques. The analytical scattering factors[61] for neutral atoms were used throughout the analysis. The hydroxide hydrogen atoms (H1 and H8) were located from a difference-Fourier map and refined (x,y,z and U_{iso}). The remaining hydrogen atoms were included using a riding model. There were two molecules of the formula-unit present (Z = 4). Disordered atoms were included as isotropic atoms using multiple components with partial site-occupancy factors.

Least-squares analysis yielded wR2 = 0.0899 and Goof = 1.026 for 1396 variables refined against 31356 data (0.70 Å), R1 = 0.0355 for those 25498 data with I > 2.0σ(I).

Structure of [(TMTACN)Ni^{II}–(μ-OH)–Fe^{III}poat]OTf. An orange crystal of approximate dimensions 0.258 x 0.099 x 0.086 mm was mounted in a cryoloop and transferred to a Bruker SMART APEX II diffractometer. The APEX2[57] program package was used to determine the unit-cell parameters and for data collection (180 sec/frame scan time for a sphere of diffraction data). The raw frame data was processed using SAINT[58] and SADABS[59] to yield the reflection data file. Subsequent calculations were carried out using the SHELXTL[60] program. The diffraction symmetry was *mmm* and the systematic absences were consistent with the orthorhombic space groups *Pbcm* and $Pca2_1$. It was later determined that space group $Pca2_1$ was correct. The structure was solved by direct methods and refined on F^2 by full-matrix least-squares techniques. The analytical scattering factors[61] for neutral atoms were used throughout the analysis. The hydroxide hydrogen atoms (H1 and H8) were located from a difference-Fourier map and refined (x,y,z and U_{iso}) with fixed length. The remaining hydrogen atoms were included using a riding model. There were two molecules of the formula-unit present (Z = 4). Disordered atoms were included as isotropic atoms using multiple components with partial site-occupancy factors.

Least-squares analysis yielded wR2 = 0.0988 and Goof = 1.010 for 1356 variables refined against 27950 data (0.74 Å), R1 = 0.0532 for those 21063 data with I > 2.0σ(I). The structure was refined as a two-component twin. The absolute structure was assigned by refinement of the Flack[62] parameter.

Data Analysis of EPR Measurements

The simulation software *SpinCount* diagonalizes the electronic terms of the spin Hamiltonian

$$H = J\mathbf{S_1}\cdot\mathbf{S_2} + H_1 + H_2 \qquad \text{Eq. 3.1}$$

with

$$H_i = \beta \mathbf{S}_i \cdot \mathbf{g}_i \cdot \mathbf{B} + \mathbf{S}_i \cdot \mathbf{D}_i \cdot \mathbf{S}_i \qquad i = 1, 2$$

and

$$\mathbf{S}_i \cdot \mathbf{D}_i \cdot \mathbf{S}_i = D_i[\mathbf{S}_{zi}^2 - \mathbf{S}_i(\mathbf{S}_i + 1)/3 + (E/D)_i(\mathbf{S}_{xi}^2 - \mathbf{S}_{yi}^2)] \qquad i = 1, 2$$

where the parameters have the usual definitions,[63] and performs least-squares fitting of simulations to the spectra. The spin $\mathbf{S}_i$ refers to individual Fe^{III} ($S = 5/2$) or M^{II} sites depending on the M^{II} ion incorporated into the ligand. $\mathbf{D}_i$ is assumed coaxial with $\mathbf{g}_i$ unless specified.[64]

References

(1) Kurtz, D. M. Oxo- and Hydroxo-Bridged Diiron Complexes: A Chemical Perspective on a Biological Unit. *Chem. Rev.* **1990**, *90*, 585–606.

(2) Wu, A. J.; Penner-Hahn, J. E.; Pecoraro, V. L. Structural, Spectroscopic, and Reactivity Models for the Manganese Catalases. *Chem. Rev.* **2004**, *104*, 903–938.

(3) Holm, R. H.; Kennepohl, P.; Solomon, E. I. Structural and Functional Aspects of Metal Sites in Biology. *Chem. Rev.* **1996**, *96*, 2239–2314.

(4) Jasniewski, A. J.; Que, L. Dioxygen Activation by Nonheme Diiron Enzymes: Diverse Dioxygen Adducts, High-Valent Intermediates, and Related Model Complexes. *Chem. Rev.* **2018**, *118*, 2554–2592.

(5) Greene, B. L.; Kang, G.; Cui, C.; Bennati, M.; Nocera, D. G.; Drennan, C. L.; Stubbe, J. Ribonucleotide Reductases: Structure, Chemistry, and Metabolism Suggest New Therapeutic Targets. *Annu. Rev. Biochem.* **2020**, *89*, 45–75.

(6) Martinie, R. J.; Blaesi, E. J.; Krebs, C.; Bollinger, J. M.; Silakov, A.; Pollock, C. J. Evidence for a Di-μ-Oxo Diamond Core in the Mn(IV)/Fe(IV) Activation Intermediate of Ribonucleotide Reductase from Chlamydia Trachomatis. *J. Am. Chem. Soc.* **2017**, *139*, 1950–1957.

(7) Stenkamp, R. E. Dioxygen and Hemerythrin. *Chem. Rev.* **1994**, *94*, 715–726.

(8) Schenk, G.; Mitić, N.; Gahan, L. R.; Ollis, D. L.; McGeary, R. P.; Guddat, L. W. Binuclear Metallohydrolases: Complex Mechanistic Strategies for a Simple Chemical Reaction. *Acc. Chem. Res.* **2012**, *45*, 1593–1603.

(9) Fabiane, S. M.; Sohi, M. K.; Wan, T.; Payne, D. J.; Bateson, J. H.; Mitchell, T.; Sutton, B. J. Crystal Structure of the Zinc-Dependent β-Lactamase from Bacillus Cereus at 1.9 Å Resolution: Binuclear Active Site with Features of a Mononuclear Enzyme. *Biochemistry* **1998**, *37*, 12404–12411.

(10) Benini, S.; Rypniewski, W. R.; Wilson, K. S.; Miletti, S.; Ciurli, S.; Mangani, S. A New Proposal for Urease Mechanism Based on the Crystal Structures of the Native and Inhibited Enzyme from Bacillus Pasteurii: Why Urea Hydrolysis Costs Two Nickels. *Structure* **1999**, *7*, 205–216.

(11) Rosenzweig, A. C.; Frederick, C. A.; Lippard, S. J.; Nordlund, P. Crystal Structure of a Bacterial Non-Haem Iron Hydroxylase That Catalyses the Biological Oxidation of Methane. *Nature* **1993**, *366*, 537–543.

(12) Klabunde, T.; Eicken, C.; Saccettini, J. C.; Krebs, B. Crystal Structure of a Plant Catechol

Oxidase: A Dicopper Center for Activation of Dioxygen. *Nat. Struct. Biol.* **1998**, *5*, 1084–1090.

(13) Kung, Y.; Drennan, C. L. A Role for Nickel-Iron Cofactors in Biological Carbon Monoxide and Carbon Dioxide Utilization. *Curr. Opin. Chem. Biol.* **2011**, *15*, 276–283.

(14) Hsu, H.-F.; Dong, Y.; Shu, L.; Young, V. G.; Que, L. Crystal Structure of a Synthetic High-Valent Complex with an $Fe_2(\mu\text{-}O)_2$ Diamond Core. Implications for the Core Structures of Methane Monooxygenase Intermediate Q and Ribonucleotide Reductase Intermediate X. *J. Am. Chem. Soc.* **1999**, *121*, 5230–5237.

(15) Xue, G.; Wang, D.; De Hont, R.; Fiedler, A. T.; Shan, X.; Münck, E.; Que, L. A Synthetic Precedent for the $[Fe^{IV}_2(\mu\text{-}O)_2]$ Diamond Core Proposed for Methane Monooxygenase Intermediate Q. *Proc. Natl. Acad. Sci. U. S. A.* **2007**, *104*, 20713–20718.

(16) Kim, K.; Lippard, S. J. Structure and Mössbauer Spectrum of a (μ-1,2-Peroxo)Bis(μ-Carboxylato)Diiron(III) Model for the Peroxo Intermediate in the Methane Monooxygenase Hydroxylase Reaction Cycle. *J. Am. Chem. Soc.* **1996**, *118*, 4914–4915.

(17) Ghosh, A.; Tiago de Oliveira, F.; Yano, T.; Nishioka, T.; Beach, E. S.; Kinoshita, I.; Münck, E.; Ryabov, A. D.; Horwitz, C. P.; Collins, T. J. Catalytically Active μ-Oxodiiron(IV) Oxidants from Iron(III) and Dioxygen. *J. Am. Chem. Soc.* **2005**, *127*, 2505–2513.

(18) Smith, J. M.; Sadique, A. R.; Cundari, T. R.; Rodgers, K. R.; Lukat-Rodgers, G.; Lachicotte, R. J.; Flaschenriem, C. J.; Vela, J.; Holland, P. L. Studies of Low-Coordinate Iron Dinitrogen Complexes. *J. Am. Chem. Soc.* **2006**, *128*, 756–769.

(19) Wieghardt, K.; Bossek, U.; Nuber, B.; Weiss, J.; Bonvoisin, J.; Corbella, M.; Vitols, S. E.; Girerd, J. J. Synthesis, Crystal Structures, Reactivity, and Magnetochemistry of a Series of Binuclear Complexes of Manganese(II), -(III), and -(IV) of Biological Relevance. The Crystal Structure of $[L'Mn^{IV}(\mu\text{-}O)_3Mn^{IV}L'](PF_6)_2.H_2O$ Containing an Unprecedented Short Mn···Mn. *J. Am. Chem. Soc.* **1988**, *110*, 7398–7411.

(20) Dalle, K. E.; Meyer, F. Modelling Binuclear Metallobiosites: Insights from Pyrazole-Supported Biomimetic and Bioinspired Complexes. *Eur. J. Inorg. Chem.* **2015**, No. 21, 3391–3405.

(21) Zhao, N.; Filatov, A. S.; Xie, J.; Hill, E. A.; Rogachev, A. Y.; Anderson, J. S. Generation and Reactivity of a $Ni^{III}_2(\mu$-1,2-Peroxo) Complex. *J. Am. Chem. Soc.* **2020**, *142*, 21634–21639.

(22) Zinn, P. J.; Sorrell, T. N.; Powell, D. R.; Day, V. W.; Borovik, A. S. Acetonitrile Hydration and Ethyl Acetate Hydrolysis by Pyrazolate-Bridged Cobalt(II) Dimers Containing Hydrogen-Bond Donors. *Inorg. Chem.* **2007**, *46*, 10120–10132.

(23) Ng, G. K.-Y.; Ziller, J. W.; Borovik, A. S. Preparation and Structures of Dinuclear Complexes Containing M^{II}–OH Centers. *Chem. Commun.* **2012**, *48*, 2546–2548.

(24) Borovik, A. S.; Papaefthymiou, V.; Taylor, L. F.; Anderson, O. P.; Que, L. Models for Iron–Oxo Proteins. Structures and Properties of $Fe^{II}Fe^{III}$, $Zn^{II}Fe^{III}$, and $Fe^{II}Ga^{III}$ Complexes with (μ-Phenoxo)Bis(μ-Carboxylato)Dimetal Cores. *J. Am. Chem. Soc.* **1989**, *111*, 6183–6195.

(25) Buchanan, R. M.; Mashuta, M. S.; Richardson, J. F.; Webb, R. J.; Oberhausen, K. J.; Nanny, M. A.; Hendrickson, D. N. Synthesis, Structure, and Properties of a Novel Heterobimetallic $Fe^{III}Mn^{II}$ Complex Containing a Septadentate Polyimidazole Ligand. *Inorg. Chem.* **1990**, *29*, 1299–1301.

(26) Blusch, L. K.; Mitevski, O.; Martin-Diaconescu, V.; Pröpper, K.; Debeer, S.; Dechert, S.; Meyer, F. Selective Synthesis and Redox Sequence of a Heterobimetallic Nickel/Copper Complex of the Noninnocent Siamese-Twin Porphyrin. *Inorg. Chem.* **2014**, *53*, 7876–7885.

(27) Peralta, R. A.; Bortoluzzi, A. J.; De Souza, B.; Jovito, R.; Xavier, F. R.; Couto, R. A. A.; Casellato, A.; Nome, F.; Dick, A.; Gahan, L. R.; Schenk, G.; Hanson, G. R.; De Paula, F. C. S.; Pereira-Maia, E. C.; de P. Machado, S.; Severino, P. C.; Pich, C.; Bortolotto, T.; Terenzi,

H.; Castellano, E. E.; Neves, A.; Riley, M. J. Electronic Structure and Spectro-Structural Correlations of $Fe^{III}Zn^{II}$ Biomimetics for Purple Acid Phosphatases: Relevance to DNA Cleavage and Cytotoxic Activity. *Inorg. Chem.* **2010**, *49*, 11421–11438.

(28) Rosenkoetter, K. E.; Ziller, J. W.; Heyduk, A. F. A Heterobimetallic W−Ni Complex Containing a Redox-Active $W[SNS]_2$ Metalloligand. *Inorg. Chem.* **2016**, *55*, 6794–6798.

(29) Wojnar, M. K.; Ziller, J. W.; Heyduk, A. F. Heterobimetallic and Heterotrimetallic Clusters Containing a Redox-Active Metalloligand. *Eur. J. Inorg. Chem.* **2017**, No. 47, 5571–5575.

(30) Chantarojsiri, T.; Reath, A. H.; Yang, J. Y. Cationic Charges Lead to Inverse Free-Energy Relationship for N–N Bond Formation by MnVI Nitrides. *Angew. Chemie Int. Ed.* **2018**, *57*, 14037–14042.

(31) Delgado, M.; Ziegler, J. M.; Seda, T.; Zakharov, L. N.; Gilbertson, J. D. Pyridinediimine Iron Complexes with Pendant Redox-Inactive Metals Located in the Secondary Coordination Sphere. *Inorg. Chem.* **2016**, *55*, 555–557.

(32) Brazzolotto, D.; Gennari, M.; Queyriaux, N.; Simmons, T. R.; Pécaut, J.; Demeshko, S.; Meyer, F.; Orio, M.; Artero, V.; Duboc, C. Nickel-Centred Proton Reduction Catalysis in a Model of [NiFe] Hydrogenase. *Nat. Chem.* **2016**, *8*, 1054–1060.

(33) Pearson, T. J.; Fataftah, M. S.; Freedman, D. E. Enhancement of Magnetic Anisotropy in a Mn–Bi Heterobimetallic Complex. *Chem. Commun.* **2016**, *52*, 11394–11397.

(34) Coste, S. C.; Vlaisavljevich, B.; Freedman, D. E. Magnetic Anisotropy from Main-Group Elements: Halides versus Group 14 Elements. *Inorg. Chem.* **2017**, *56*, 8195–8202.

(35) Gu, N. X.; Ung, G.; Peters, J. C. Catalytic Hydrazine Disproportionation Mediated by a Thiolate-Bridged VFe Complex. *Chem. Commun.* **2019**, *55*, 5363–5366.

(36) Fajardo, J.; Peters, J. C. Tripodal P_3XFe-N_2 Complexes (X = B, Al, Ga): Effect of the Apical Atom on Bonding, Electronic Structure, and Catalytic N_2-to-NH_3 Conversion. *Inorg. Chem.* **2021**, *60*, 1220–1227.

(37) Krogman, J. P.; Thomas, C. M. Metal–Metal Multiple Bonding in C_3-Symmetric Bimetallic Complexes of the First Row Transition Metals. *Chem. Commun.* **2014**, *50*, 5115–5127.

(38) Greer, S. M.; McKay, J.; Gramigna, K. M.; Thomas, C. M.; Stoian, S. A.; Hill, S. Probing Fe–V Bonding in a C_3-Symmetric Heterobimetallic Complex. *Inorg. Chem.* **2018**, *57*, 5870–5878.

(39) Zhang, H.; Hatzis, G. P.; Moore, C. E.; Dickie, D. A.; Bezpalko, M. W.; Foxman, B. M.; Thomas, C. M. O_2 Activation by a Heterobimetallic Zr/Co Complex. *J. Am. Chem. Soc.* **2019**, *141*, 9516–9520.

(40) Eisenhart, R. J.; Clouston, L. J.; Lu, C. C. Configuring Bonds between First-Row Transition Metals. *Acc. Chem. Res.* **2015**, *48*, 2885–2894.

(41) Cammarota, R. C.; Clouston, L. J.; Lu, C. C. Leveraging Molecular Metal–Support Interactions for H_2 and N_2 Activation. *Coord. Chem. Rev.* **2017**, *334*, 100–111.

(42) Moore, J. T.; Chatterjee, S.; Tarrago, M.; Clouston, L. J.; Sproules, S.; Bill, E.; Bernales, V.; Gagliardi, L.; Ye, S.; Lancaster, K. M.; Lu, C. C. Enhanced Fe-Centered Redox Flexibility in Fe–Ti Heterobimetallic Complexes. *Inorg. Chem.* **2019**, *58*, 6199–6214.

(43) Cook, S. A.; Borovik, A. S. Molecular Designs for Controlling the Local Environments around Metal Ions. *Acc. Chem. Res.* **2015**, *48*, 2407–2414.

(44) Schwarz, A. D.; Herbert, K. R.; Paniagua, C.; Mountford, P. Ligand Variations in New Sulfonamide-Supported Group 4 Ring-Opening Polymerization Catalysts. *Organometallics* **2010**, *29*, 4171–4188.

(45) Park, Y. J.; Cook, S. A.; Sickerman, N. S.; Sano, Y.; Ziller, J. W.; Borovik, A. S. Heterobimetallic Complexes with M^{III}-(μ-OH)-M^{II} Cores (M^{III} = Fe, Mn, Ga; M^{II} = Ca, Sr, and Ba): Structural, Kinetic, and Redox Properties. *Chem. Sci.* **2013**, *4*, 717–726.

(46) Sano, Y.; Lau, N.; Weitz, A. C.; Ziller, J. W.; Hendrich, M. P.; Borovik, A. S. Models for Unsymmetrical Active Sites in Metalloproteins: Structural, Redox, and Magnetic Properties of Bimetallic Complexes with M^{II}-(μ-OH)-Fe^{III} Cores. *Inorg. Chem.* **2017**, *56*, 14118–14128.
(47) Lau, N.; Sano, Y.; Ziller, J. W.; Borovik, A. S. Modular Bimetallic Complexes with a Sulfonamido-Based Ligand. *Dalt. Trans.* **2018**, *47*, 12362–12372.
(48) Oswald, V. F.; Lee, J. L.; Biswas, S.; Weitz, A. C.; Mittra, K.; Fan, R.; Li, J.; Zhao, J.; Hu, M. Y.; Alp, E. E.; Bominaar, E. L.; Guo, Y.; Green, M. T.; Hendrich, M. P.; Borovik, A. S. Effects of Noncovalent Interactions on High-Spin Fe(IV)–Oxido Complexes. *J. Am. Chem. Soc.* **2020**, *142*, 11804–11817.
(49) Lee, J. L.; Oswald, V. F.; Biswas, S.; Hill, E. A.; Ziller, J. W.; Hendrich, M. P.; Borovik, A. S. Stepwise Assembly of Heterobimetallic Complexes: Synthesis, Structure, and Physical Properties. *Dalt. Trans.* **2021**, *50*, 8111–8119.
(50) Yang, L.; Tolman, W. B. Type 1 Copper Site Synthetic Model Complexes with Increased Redox Potentials. *J. Biol. Inorg. Chem.* **2012**, *17*, 285–291.
(51) D. D. Perrin. *Dissociation Constant of Inorganic Acids and Bases in Aqueous Solution*; Pergamon: New York, NY, 1982.
(52) Kwak, Y.; Jiang, W.; Dassama, L. M. K.; Park, K.; Bell, C. B.; Liu, L. V.; Wong, S. D.; Saito, M.; Kobayashi, Y.; Kitao, S.; Seto, M.; Yoda, Y.; Alp, E. E.; Zhao, J.; Bollinger, J. M.; Krebs, C.; Solomon, E. I. Geometric and Electronic Structure of the Mn(IV)Fe(III) Cofactor in Class Ic Ribonucleotide Reductase: Correlation to the Class Ia Binuclear Non-Heme Iron Enzyme. *J. Am. Chem. Soc.* **2013**, *135*, 17573–17584.
(53) Schoenfeldt, N. J.; Ni, Z.; Korinda, A. W.; Meyer, R. J.; Notestein, J. M. Manganese Triazacyclononane Oxidation Catalysts Grafted under Reaction Conditions on Solid Cocatalytic Supports. *J. Am. Chem. Soc.* **2011**, *133*, 18684–18695.
(54) Cao, R.; Müller, P.; Lippard, S. J. Tripodal Tris-Tacn and Tris-Dpa Platforms for Assembling Phosphate-Templated Trimetallic Centers. *J. Am. Chem. Soc.* **2010**, *132*, 17366–17369.
(55) Heintz, R. A.; Smith, J. A.; Szalay, P. S.; Weisgerber, A.; Dunbar, K. R. Homoleptic Transition Metal Acetonitrile Cations with Tetrafluoroborate or Trifluoromethanesulfonate Anions. *Inorg. Synth.* **2002**, *33*, 75–83.
(56) Petasis, D. T.; Hendrich, M. P. Quantitative Interpretation of Multifrequency Multimode EPR Spectra of Metal Containing Proteins, Enzymes, and Biomimetic Complexes. *Methods Enzymol.* **2015**, *563*, 171–208.
(57) APEX2 Version 2014.11-0, Bruker AXS, Inc.; Madison, WI 2014.
(58) SAINT Version 8.34a, Bruker AXS, Inc.; Madison, WI 2013.
(59) Sheldrick, G. M. SADABS, Version 2014/5, Bruker AXS, Inc.; Madison, WI 2014.
(60) Sheldrick, G. M. SHELXTL, Version 2014/7, Bruker AXS, Inc.; Madison, WI 2014.
(61) International Tables for Crystallography 1992, Vol. C., Dordrecht: Kluwer Academic Publishers.
(62) Parsons, S., Flack, H. D., Wagner, T. Acta Cryst. B69, 249-259, 2013.
(63) Abragam, A.; Bleaney, B. *Electron Paramagnetic Resonance of Transition Metal Ions*; Clarendon Press: Oxford, U.K., 1970.
(64) Brink, D. M.; Satchler, G. R. *Angular momentum*, 3rd ed.; Clarendon Press: Oxford, U.K., 1994.

Chapter 4

Electronic and Magnetic Properties of Bimetallic Complexes with an [M^{II}–(μ-O)–Fe^{IV}] Core

Introduction

Multinuclear metalloenzymes are ubiquitous in nature and often play an important role in small molecule activation.[1] Prominent examples include the [FeMn] center in ribonucleotide reductases,[2] the [FeFe] center in soluble methane monooxygenase,[3,4] the [Mn_4O_5Ca] core in the oxygen evolving complex,[5-7] and the [FeZn] center in purple acid phosphatases.[8] Metal–metal cooperativity is one feature of multinuclear metalloenzymes that enhances reactivity, which aids in substrate activation, lowers redox potential, and influences electron transfer. A high-valent M–(μ-O)–M core is commonly proposed for the reactive intermediates in many of these enzymes,[9-14] so it is important to design synthetic systems to model these biologically-relevant intermediates to further the understanding of the structure/function relationship in multinuclear metalloenzymes.

Previous work in the Borovik lab has synthesized and spectroscopically characterized [Fe^{IV}poat(O)]$^-$, which was then used to bind Group II metal ions to study the electrostatic effects on the properties of the Fe–oxido motif (Scheme 4.1.A).[15] It was experimentally verified the Lewis acidic metal ions can modulate the Fe–O π-bonding, and the perturbations can be monitored using electronic absorption and Mössbauer spectroscopies. Binding of LA^{II} also prompted significant distortion to the C_3-symmetric [Fe^{IV}poat(O)]$^-$, which is reflected by the rhombicity parameter (E/D) determined by electron paramagnetic resonance (EPR) spectroscopy. Upon completion of that work, my goal was to expand the library of bimetallic complexes by binding 3d transition metal ions to [Fe^{IV}poat]$^-$; this was inspired by the development of [(TMTACN)M^{II}–(μ-OH)–Fe^{III}poat]$^+$ complexes (denoted [M^{II}(OH)Fe^{III}]$^+$; M = Zn, Cu, Ni), which are fully characterized and discussed in the previous chapter (Scheme 4.1.B).[16]

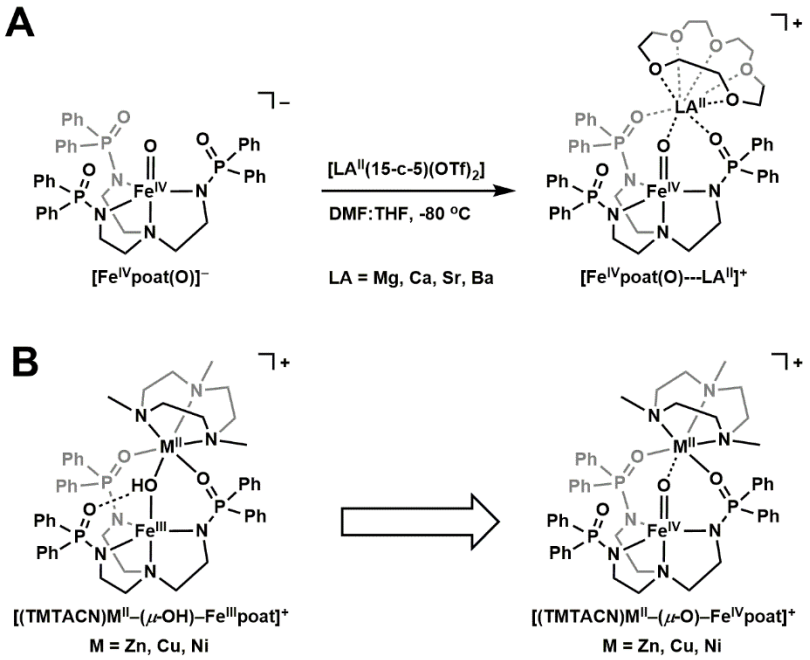

Scheme 4.1. (A) Binding of Group II metal ions to $[Fe^{IV}poat(O)]^-$, where LA^{II} = Mg^{II}, Ca^{II}, Sr^{II}, and Ba^{II}. (B) Proposed binding of 3d divalent transition metal adducts to $[Fe^{IV}poat(O)]^-$.

$[Fe^{IV}poat(O)]^-$ provides several features that are not present in other synthetic bimetallic systems. Due to a trianionic ligand scaffold and the strong ligand field around the Fe^{IV} center, this complex is not a potent oxidant. This could allow for the generation of $[M^{II}–(\mu\text{-}O)–Fe^{IV}]$ upon the second metal binding, without the Fe center being reduced; reduction of the Fe center has been observed for several cationic Fe^{IV}–oxido systems upon binding of a second metal ion.[17-20] The $[Fe^{IV}poat(O)]^-$ species can serve as a chelating scaffold for a second metal ion; while many synthetic bimetallic complexes with unsymmetrical coordination sites have been investigated, similar complexes that contain an $[M^{II}–(\mu–O)–Fe^{IV}]$ core have not been reported.[17-26] Finally, the binding of a paramagnetic metal ion to the Fe–oxido moiety can be examined by various magnetic and spectroscopic methods because strong magnetic exchange is likely, and thus the effect of metal binding on the electronic structure of the Fe–oxido unit can be studied. In this chapter, the preparation of discrete heterobimetallic $M^{II}Fe^{IV}$ species (M = Zn, Cu, Ni) is discussed. Their

electronic and magnetic properties were interrogated by electronic absorbance, EPR, and Mössbauer spectroscopies, which determined the oxidation and spin states for these complexes.

Results & Discussion

Preparation of the starting Fe^{IV}–oxido synthon and bimetallic complexes. The generation of $[Fe^{IV}poat(O)]^-$ is previously reported.[15] The procedural details and characterizations are provided in the experimental section. The preparation of the heterobimetallic complexes $[(TMTACN)M^{II}–(\mu\text{-}O)–Fe^{IV}poat]^+$ (denoted $[M^{II}(O)Fe^{IV}]^+$, M = Zn, Cu, Ni) was achieved by treating $[Fe^{IV}poat(O)]^-$ with $[M^{II}(TMTACN)]^{2+}$ reagents (Scheme 4.2). $Zn^{II}(TMTACN)(OTf)_2$ and $Cu^{II}(TMTACN)(OTf)_2{\cdot}CH_3CN$ were used as the Zn^{II}- and Cu^{II}-TMTACN adducts, respectively. Attempts to isolate $Ni^{II}(TMTACN)(OTf)_2$ had been unsuccessful, therefore stoichiometric $Ni^{II}(OTf)_2{\cdot}5CH_3CN$ and TMTACN were added sequentially to produce $[Ni^{II}(O)Fe^{IV}]^+$.

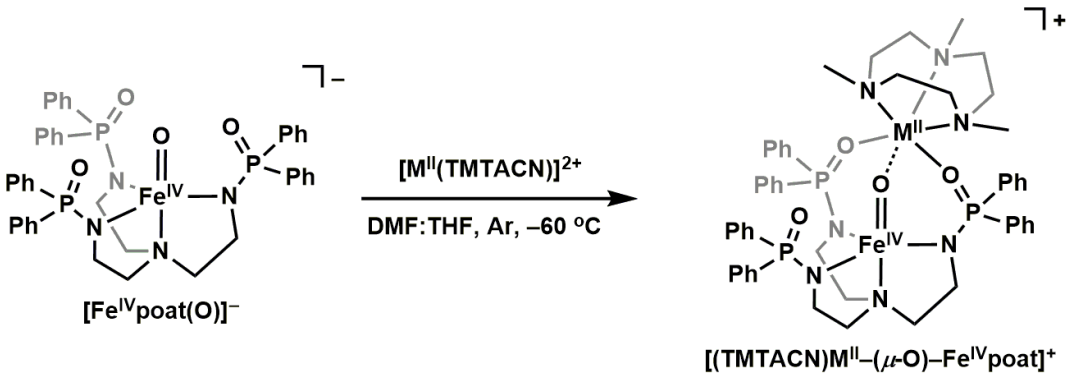

Scheme 4.2. Binding of $[M^{II}(TMTACN)]^{2+}$ adducts to $[Fe^{IV}poat(O)]^-$ produces $[M^{II}(O)Fe^{IV}]^+$ (M = Zn, Cu, Ni).

Electronic Absorption Properties of $[M^{II}(O)Fe^{IV}]^+$ Complexes. Formation of the bimetallic $[M^{II}(O)Fe^{IV}]^+$ complexes were monitored by electron absorption spectroscopy. The optical spectrum of $[Fe^{IV}poat(O)]^-$ has previously been reported (Figure 4.1, grey traces);[15] it contains a low energy

feature at λ_{max} (ε, M^{-1} cm^{-1}) = 925 nm (180) that is assigned as a d–d transition ($^5A \rightarrow {}^5E$) observed in most non-heme Fe^{IV}–oxido complexes.[27-29] The d–d band was used as a spectroscopic handle to interrogate the interaction of Group II Lewis acid metal ions with the Fe–oxido moiety.[15] Treatment of $[Fe^{IV}poat(O)]^-$ with Zn^{II}(TMTACN)$(OTf)_2$ produced a new species at -60°C in DMF:THF. Spectrophotometric monitoring of the reaction showed replacement of the characteristic bands of $[Fe^{IV}poat(O)]^-$ at λ_{max} (ε, M^{-1} cm^{-1}) = 320 (6500), 370 (7500), 520 (sh), and 925 nm (180) with new features at λ_{max} (ε, M^{-1} cm^{-1}) = 314 (8700), 480 (sh), 720 (sh), and 835 nm (350) (Figure 4.1.A; Table 4.1). The blue shift in energy of the d–d transition is consistent with the binding of a Lewis acidic metal ion to the Fe^{IV}–oxido, which results in the lowering in energy of the E{xz,yz} level.[15] Notably, the wavelength of this transition is comparable to that found for $[Fe^{IV}poat(O)\text{---}Mg^{II}]^+$ (λ_{max} = 840 nm), which suggests the Zn^{II}(TMTACN) and Mg^{II}(15-crown-5) adducts have similar effects on the Fe–O motif. The change in absorption properties supports the binding of a Zn^{II} ion and the formulation of $[Zn^{II}(O)Fe^{IV}]^+$.

The binding of $[Cu^{II}$(TMTACN)$]^{2+}$ and $[Ni^{II}$(TMTACN)$]^{2+}$ were also monitored spectrophotometrically and displayed similar optical spectra to each other. Addition of Cu^{II}(TMTACN)$(OTf)_2 \cdot CH_3CN$ showed growth of new absorbance features at λ_{max} (ε, M^{-1} cm^{-1}) = 332 (10500), 500 (sh), 700 (440), 780 (sh), 850 (sh), and 1000 nm (sh) (Figure 4.1.B); addition of $Ni^{II}(OTf)_2 \cdot 5CH_3CN$ then TMTACN showed growth of new absorbance features at λ_{max} (ε, M^{-1} cm^{-1}) = 315 (9400), 450 (4200), 670 (650), 735 (480), 830 (sh), and 935 nm (sh) (Figure 4.1.C). The origin of the multiple low energy d–d transitions in these new species is currently unknown; it is possible they arise from Cu^{II} and Ni^{II} ligand field transitions. These changes in the optical spectra support the formation of $[Cu^{II}(O)Fe^{IV}]^+$ and $[Ni^{II}(O)Fe^{IV}]^+$ complexes.

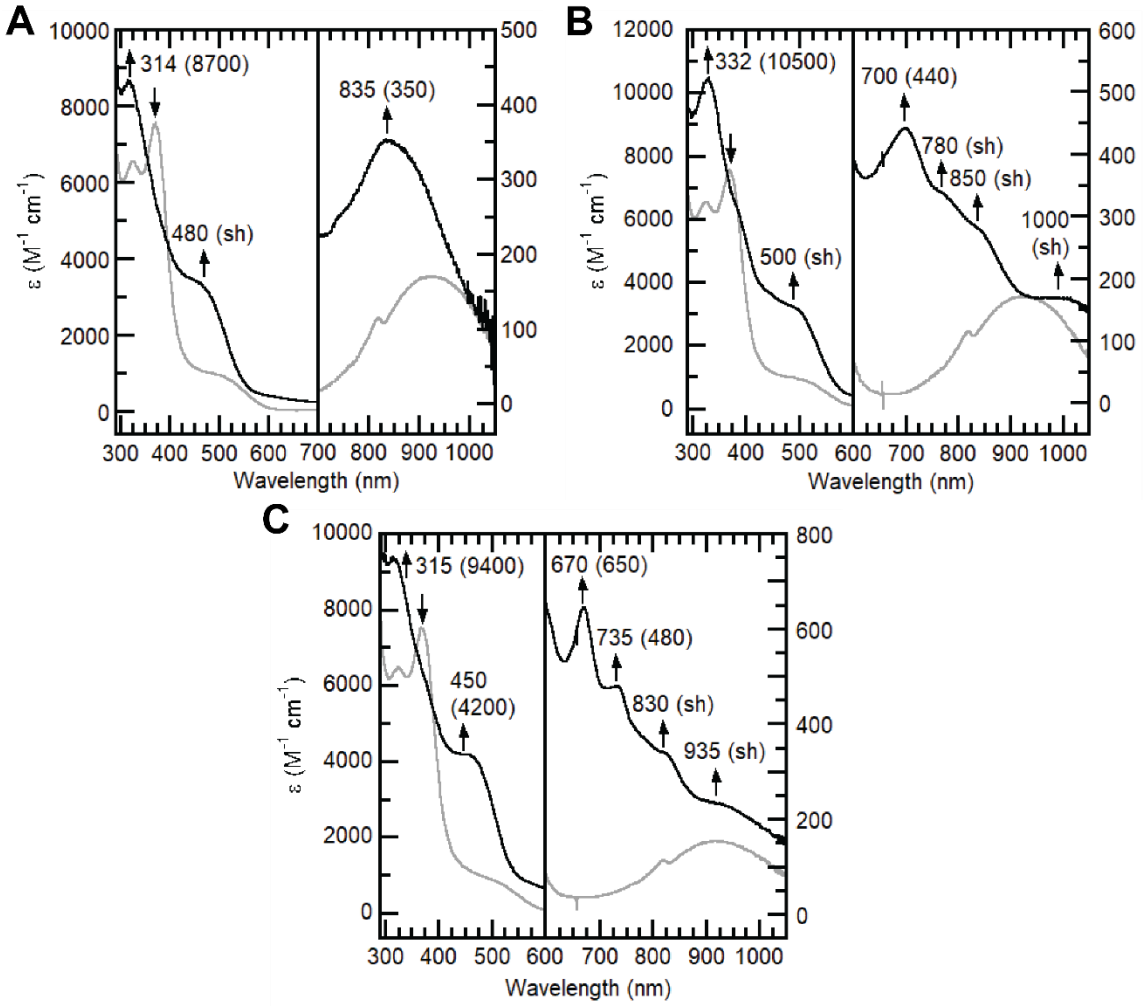

Figure 4.1. Electronic Absorbance spectra (black) for $[Zn^{II}(O)Fe^{IV}]^+$ (A), $[Cu^{II}(O)Fe^{IV}]^+$ (B), and $[Ni^{II}(O)Fe^{IV}]^+$ (C) complexes. The grey spectra correspond to the $[Fe^{IV}poat(O)]^-$ starting synthon. Absorbance measurements were performed on a 0.20 mM DMF:THF solution at -60°C.

Table 4.1. Spectroscopic properties of mono- and heterometallic Fe^{IV}poat complexes.

Complex	S	Individual metal	d-d transition[a]	g-values	$\delta/\Delta E_Q$[b]
$[Fe^{IV}poat(O)]^-$[c]	2	S = 2 Fe^{IV}	925 (180)	8.0	0.11(1)/0.27(1)
$[Fe^{IV}poat(O)\text{---}Mg^{II}]^+$[c]	2	S = 2 Fe^{IV} S = 0 Mg^{II}	840 (450)	8.0	0.02(1)/0.43(1)
$[Zn^{II}(O)Fe^{IV}]^+$	2	S = 2 Fe^{IV} S = 0 Zn^{II}	835 (350)	8.11	0.04/0.39
$[Cu^{II}(O)Fe^{IV}]^+$	3/2	S = 2 Fe^{IV} S = 1/2 Cu^{II}	700 (440), 780 (sh), 850 (sh), 1000 (sh)	3.77, 1.99	0.04/0.48
$[Ni^{II}(O)Fe^{IV}]^+$	1	S = 2 Fe^{IV} S = 1 Ni^{II}	670 (650), 735 (480), 830 (sh), 935 (sh)	–	0.07/0.56

[a]nm (ε, M^{-1} cm^{-1}). [b]mm s^{-1}. [c]Ref 15.

Due to the unsuccessful attempt to isolate a $[Ni^{II}(TMTACN)(OTf)_2]$ salt, $Ni^{II}(OTf)_2 \cdot 5CH_3CN$ and TMTACN were added sequentially to $[Fe^{IV}poat(O)]^-$ to produce the $[Ni^{II}(O)Fe^{IV}]^+$ species. The optical spectra before and after the addition of TMTACN were similar but distinguishable, with the low energy features shifting slightly (Figure 4.2). This is consistent with a minor change in the ligand field of the Ni^{II} ion upon treatment of the capping ligand. It also suggests the capping ligand can be installed after the heterobimetallic complex has been assembled, and the ligands of the auxiliary metal center can be substituted. This ligand substitution event has been previously observed in a similar diiron complex in the Borovik Lab.[30]

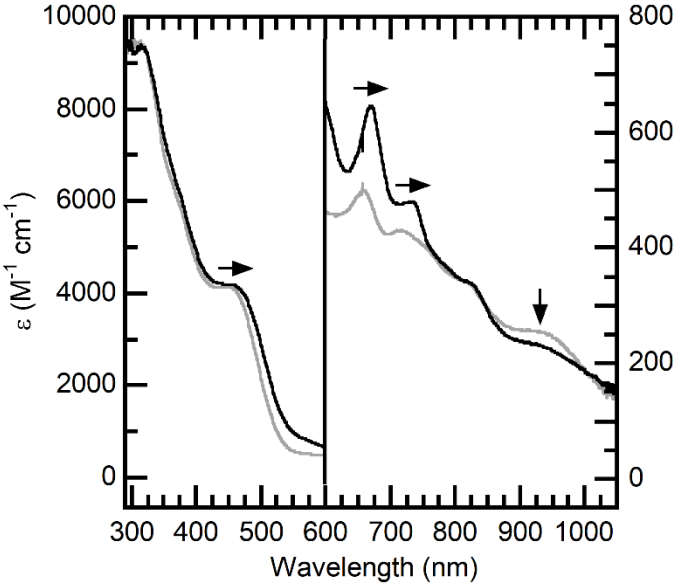

Figure 4.2. Electronic Absorbance spectra for the $Fe^{IV}Ni^{II}$ species before (grey) and after (black) the addition of the TMTACN capping ligand. Absorbance measurements were performed on a 0.20 mM DMF:THF solution at -60 °C.

EPR Properties of $[M^{II}(O)Fe^{IV}]^+$ Complexes. The $[Zn^{II}(O)Fe^{IV}]^+$ complex showed a signal (Figure 4.3.A) from an $S = 2$ species in parallel-mode, with $g = 8.11$ arising from the $M_s = \pm 2$ doublet. It is distinct from the $g = 8$ feature reported for the parent $[Fe^{IV}poat(O)]^-$ species, which is small in signal intensity that is due to the high symmetry of the C_3 complex and is reflected by the low E/D value (0.014(2)).[15] For an $S = 2$ system, the parallel-mode EPR signal intensity is proportional to $(E/D)^4$.[31]

Upon binding of Group 2 metal ions, the symmetry of complex is significantly perturbed (e.g., binding of Mg^{II} increases the E/D to 0.054(2)), which causes a large increase in the $g = 8$ signal intensity.[15] The signal associated with $[Zn^{II}(O)Fe^{IV}]^+$ is comparable with those reported for $[Fe^{IV}poat(O)\text{---}LA^{II}]^+$, suggesting the Zn^{II}(TMTACN) adduct has a similar effect on the Fe^{IV}–oxido moiety.

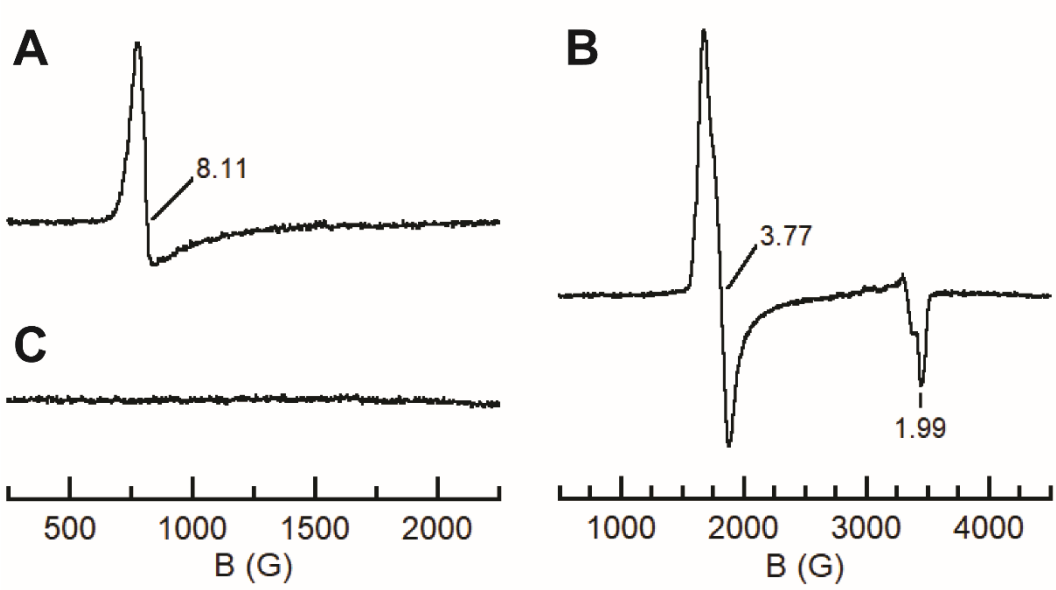

Figure 4.3. EPR spectra of $[Zn^{II}(O)Fe^{IV}]^+$ (A), $[Cu^{II}(O)Fe^{IV}]^+$ (B), and $[Ni^{II}(O)Fe^{IV}]^+$ in DMF:THF. (A) and (C) were collected in the parallel-mode (microwave frequency 9.3 GHz); (B) was collected in the perpendicular-mode (9.6 GHz). (A) was measured at 15.9 K; (B) and (C) were measured at 17.4 K.

While the bindings of closed-shell metals have provided useful insights into the electrostatic effect on the Fe^{IV}–oxido bonding, less is known about the M^{II}---oxido character (M = Mg, Ca, Sr, Ba, Zn). However, this interaction can be probed using paramagnetic metal ions. The $[Cu^{II}(O)Fe^{IV}]^+$ complex showed signals at $g = 3.77$ and 1.99 in the perpendicular-mode (Figure 4.3.B), which are consistent with a $S = 3/2$ system of the antiferromagnetically exchange-coupled $S = 1/2$ (Cu^{II}) and $S = 2$ (Fe^{IV}) ions. While the spin exchange constant J ($\mathcal{H} = JS_1 \bullet S_2$) is too large to be accurately determined using EPR spectroscopy ($J > 100$ cm^{-1}), the strongly coupled $S = 3/2$ system indicates significant covalency between the bridging-oxido ligand and the open-shell Cu^{II} ion.

$[Ni^{II}(O)Fe^{IV}]^+$ exhibited a silent spectrum in the parallel-mode (Figure 4.3.C), which suggests an $S = 0$ or 1 configuration. The latter is the likely assignment, which arises from antiferromagnetic coupling between $S = 1$ (Ni^{II}) and $S = 2$ (Fe^{IV}) ions. Similarly, the Ni^{II} center in $[Ni^{II}(OH)Fe^{III}]^+$ is determined to be $S = 1$ due to its 6-coordinated geometry (Chapter 3).[16] While it is rare to observe transitions for an $S = 1$ system by X-band EPR spectroscopy,[32,33] this formulation is indicative by Mössbauer spectroscopy (see below).

Mössbauer Properties of $[M^{II}(O)Fe^{IV}]^+$ Complexes. Mössbauer spectroscopy is useful for identifying the oxidation state(s) of Fe-containing compounds and examining spin-coupled magnetic interactions. $[Zn^{II}(O)Fe^{IV}]^+$ exhibited a pure doublet spectrum with isomer shift (δ)/quadrupole splitting (ΔE_Q) of 0.04/0.39 mm s^{-1}, respectively (Figure 4.4.A). These values are distinct from those for the $[Fe^{IV}poat(O)]^-$ synthon (0.11(1)/0.27(1) mm s^{-1}), and that can be attributed to the decrease in Fe–oxido π-bonding due to electrostatic field provided by the $[Zn^{II}$(TMTACN)] adduct. Similar perturbations were observed for the $[Fe^{IV}poat(O)\text{---}LA^{II}]^+$ complexes (e.g., the Mg^{II} analog has values of 0.02(1)/0.43(1) mm s^{-1}).[15]

$[Cu^{II}(O)Fe^{IV}]^+$ exhibited a complicated multi-line Mössbauer spectrum (Figure 4.4.B), but simulations revealed one $S = 3/2$ species in quantitative yield. The $\delta/\Delta E_Q$ values were determined to be 0.04/0.48 mm s^{-1}, which are consistent with an $S = 2$ Fe^{IV} center. This assignment is also corroborated with the $A(^{57}Fe)$ tensor, which is defined as:

$$A = A^{FC} + A^{SD} + A^{L} \qquad \text{Eq. 4.1}$$

where A^{FC} is the Fermi contact term, A^{SD} is the spin-dipolar term, and A^{L} is the orbital term. A^{FC} is the trace of the A tensor (i.e. the average of the A_x, A_y, and A_z values), and A^{L} is usually ignored for Fe^{IV} ions.[34,35] The $A(^{57}Fe)$ of [–14.5, –14.7, –27.5] T was experimentally determined by spectra simulation, and the spin-dipolar component was calculated to be [+4.4, +4.2, –8.6] T, which is

approximately at a (+1:+1: –2) ratio and consistent with an S = 2 Fe^{IV} assignment; for comparison, the $A^{SD}(^{57}Fe)$ for the starting $[Fe^{IV}poat(O)]^-$ synthon is [+4, +4, –8] T.[15,28,36-38] Other oxidation and spin states for Fe center can be ruled out: an S = 1 Fe^{IV} center exhibits an $A^{SD}(^{57}Fe)$ tensor in an (–1: –1:+2) ratio,[35,39,40] and the $A(^{57}Fe)$ tensor for an S = 5/2 Fe^{III} is expected to be isotropic (i.e., a (1:1:1) ratio).[18,28,41] Unlike the Group II ions and Zn^{II} complexes, the ΔE_Q of $[Cu^{II}(O)Fe^{IV}]^+$ increased upon binding of the divalent metal adduct; this observation may be explained by future theoretical studies. Overall, the Mössbauer results are consistent with the formulation of $[Cu^{II}(O)Fe^{IV}]^+$, which contains S = 1/2 (Cu^{II}) and S = 2 (Fe^{IV}) centers that are antiferromagnetically coupled.

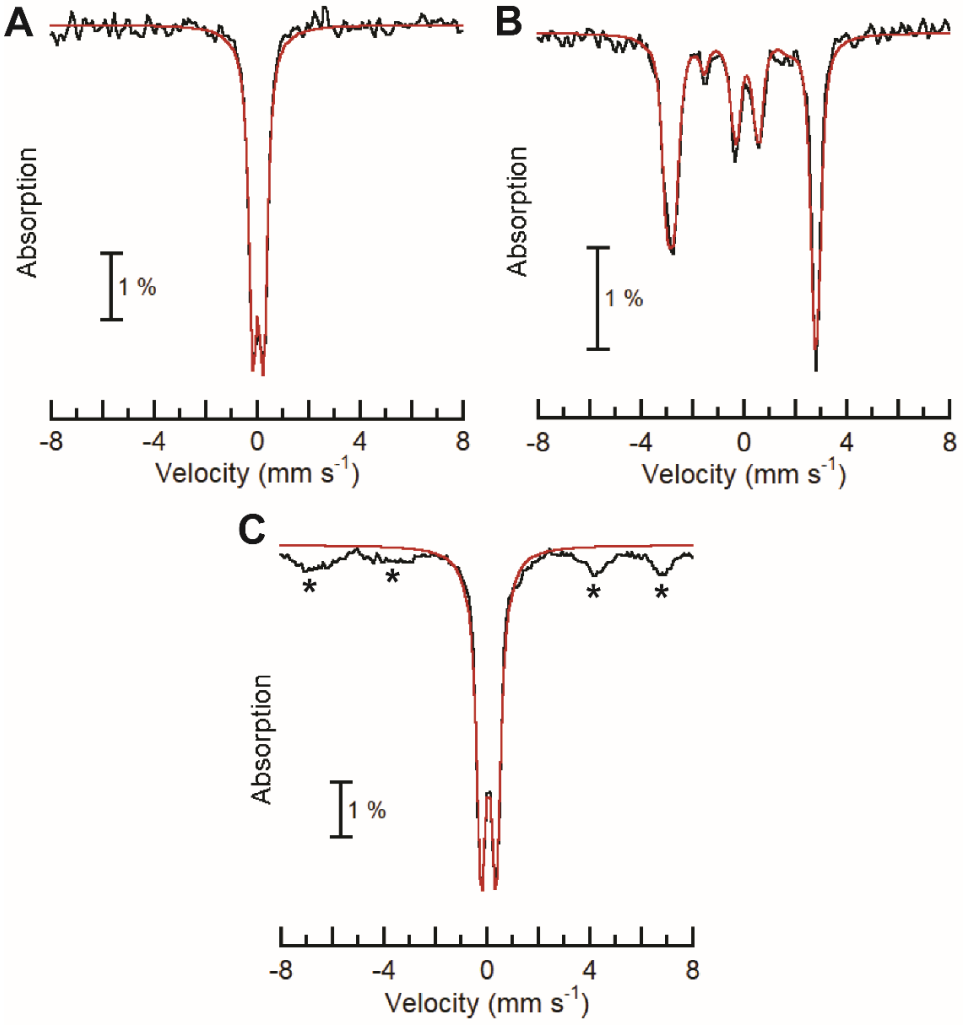

Figure 4.4. ^{57}Fe Mössbauer spectra (black, collected at 4.2 K) of $[Zn^{II}(O)Fe^{IV}]^+$ (A), $[Cu^{II}(O)Fe^{IV}]^+$ (B), and $[Ni^{II}(O)Fe^{IV}]^+$ (C). Simulations of the Mössbauer spectra are in red. Asterisks (*) indicate ferric impurities (40 %).

$[Ni^{II}(O)Fe^{IV}]^+$ exhibited a doublet spectrum, with $\delta/\Delta E_Q$ values of 0.07/0.56 mm s^{-1} (Figure 4.4.C). The doublet feature is indicative of an integer spin system, and variable-field measurements confirmed the $S = 1$ assignment for the bimetallic complex. Amongst the bimetallic complexes described in this chapter as well as the $[Fe^{IV}poat(O)\text{---}LA^{II}]^+$ series, $[Ni^{II}(O)Fe^{IV}]^+$ has the largest δ and ΔE_Q values. The factors behind these differences can be probed using a combination of structural (e.g., X-ray absorption spectroscopy), vibrational (e.g., resonance Raman spectroscopy), and theoretical studies.

Conclusion & Outlook

In this chapter, the preparation of discrete bimetallic $[M^{II}(O)Fe^{IV}]^+$ species (M = Zn, Cu, Ni) was discussed. Their electronic and magnetic properties were investigated by electronic absorbance, EPR, and Mössbauer spectroscopies, which unambiguously verify the oxidation and spin states for these complexes. This work represents a rare group of bimetallic compounds, in which the core adopts a mixed-valent (IV,II) configuration instead of one of (III,III). In conjunction with the work described in Chapter 3, the $[poat]^{3-}$ ligand has been demonstrated to support higher valent metal centers (e.g., Fe^{III}, Fe^{IV}) in its N_4 framework.

While the effect of M^{II} on the Fe^{IV}–oxido motif is now established, the M^{II}/oxido interaction is still not well-understood. In $[Fe^{IV}poat(O)\text{---}Mg^{II}]^+$, a dotted line is drawn between the oxido ligand and Mg^{II} to illustrate an electrostatic (i.e., non-covalent) interaction (Scheme 4.3.A).[15] Due to the closed-shell configuration of Zn^{II} and comparable spectroscopic properties with $[Fe^{IV}poat(O)\text{---}LA^{II}]^+$, it can be concluded the Zn^{II} adduct in $[Zn^{II}(O)Fe^{IV}]^+$ also exhibits an electrostatic interaction on the Fe–oxido motif (Scheme 4.3.B). However, strong antiferromagnetic coupling between the M^{II} and Fe^{IV} centers were observed for $[Cu^{II}(O)Fe^{IV}]^+$ and $[Ni^{II}(O)Fe^{IV}]^+$, which indicates substantial covalency in the M^{II}/oxido interaction. Therefore, it is more appropriate describe the M^{II}/oxido

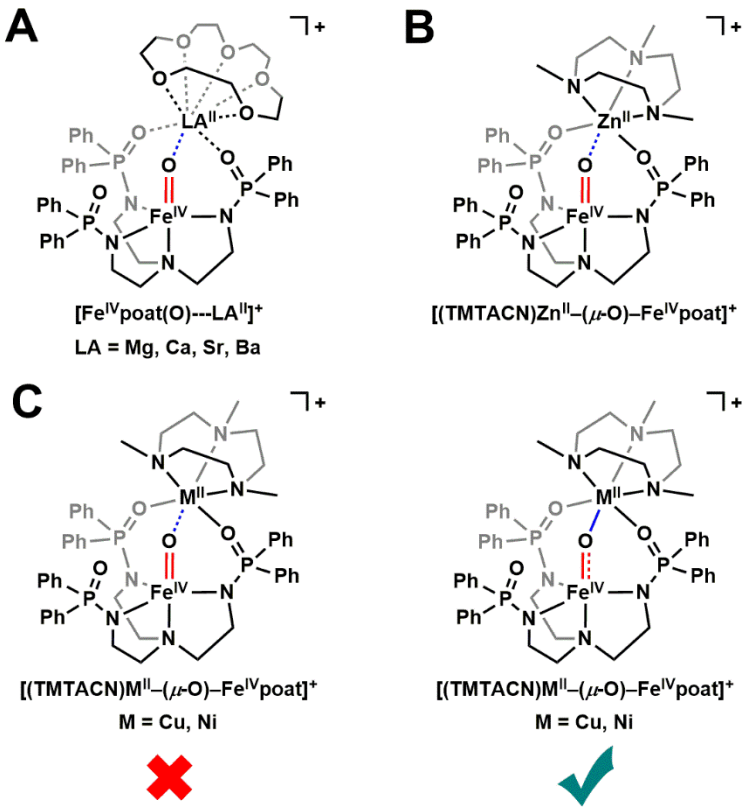

Scheme 4.3. The M^{II} adducts in $[Fe^{IV}poat(O)\text{---}LA^{II}]^+$ (A) and $[Zn^{II}(O)Fe^{IV}]^+$ (B) exhibit an electrostatic effect on the Fe^{IV}–oxido motif. The M^{II}/oxido interaction is better described as covalent in $[Cu^{II}(O)Fe^{IV}]^+$ and $[Ni^{II}(O)Fe^{IV}]^+$ (C).

character (M = Cu, Ni) as a covalent bond (Scheme 4.3.C). This would have a significant influence on the Fe–oxido bonding character, as its bond order is expected decrease significantly. An interesting observation is the increased ΔE_Q values in $[Cu^{II}(O)Fe^{IV}]^+$ and $[Ni^{II}(O)Fe^{IV}]^+$ in comparison to $[Zn^{II}(O)Fe^{IV}]^+$ and $[Fe^{IV}poat(O)\text{---}LA^{II}]^+$, which may be a reflection on the change in the Fe–oxido unit. Future structural, vibrational, and theoretical studies can help elucidate these uncertainties.

So far in this dissertation, (relatively) redox inert metal centers are installed in the auxiliary binding site of $[poat]^{3-}$ supported by the P=O groups; this has allowed for the controlled study of the oxidation chemistry and magnetic properties of Fe-containing bimetallic complexes. To better model biological dinuclear cores, which often employ two redox active metal ions, bimetallic complexes containing two redox active metal centers are described in the remaining chapters.

Experimental

General Procedures. All organic and inorganic syntheses and manipulations were performed under an argon atmosphere in a Vacuum Atmosphere Co. dry box. Solvents were sparged with argon and purified using a JC Meyer Co. solvent purification system with columns containing Q-5 and molecular sieves. All reagents, unless otherwise noted, were purchased from commercial sources and used as received. Potassium hydride (KH), as a 30% suspension in mineral oil, was filtered and washed with diethyl ether (5 X 10 mL) and pentane (5 X 10 mL) and dried under vacuum prior to use. Triethylamine was distilled prior to use. K[Fe^{II}poat],[15] isopropyl 2-iodoxybenzoate (IBX-*i*Pr),[42,43] [Cu^{II}(TMTACN)$(OTf)_2$]·CH_3CN,[44] $Ni^{II}(OTf)_2 \cdot 5CH_3CN$,[45] and TMTACN[46,47] were synthesized according to literature procedures. [Zn^{II}(TMTACN)$(OTf)_2$] was synthesized according to the procedure in Chapter 3.[16]

Physical Methods. UV-vis spectra were collected on an Agilent UV-vis spectrophotometer equipped with a Unisoku Unispeks cryostat in a 1 cm quartz cuvette. X-band (microwave frequencies 9.3 and 9.6 GHz) EPR spectra were collected on a Bruker ELEXSYS spectrometer equipped with an Oxford ESR-910 liquid helium cryostat and a Bruker bimodal cavity for the generation of microwave fields parallel and transverse to the applied magnetic field. Mössbauer spectra were recorded on either a variable field or a weak-field spectrometer operating in a constant acceleration mode n a transmission geometry using Janis Research Inc. cryostats that allow for a variation in temperature from 4 to 300 K. One of the dewars housed a superconducting magnet that allowed for the application of magnetic fields up to 8 T parallel to the γ-radiation. Isomer shifts are reported relative to Fe metal at 298 K. SpinCount was used to fit the experimental Mössbauer data.[48]

Spectroscopic characterizations of [Fe^{IV}poat(O)]$^-$. Procedural details of the generation of [Fe^{IV}poat(O)]$^-$ are previously described.[15] λ_{max}, nm (ε (M^{-1} cm^{-1})) = 330 (6600), 370 (7500), 525 (sh), and 925 (180). EPR (X-band Parallel, DMF:THF, 12 K) g = 8. Mössbauer (DMF:THF, 4.2 K, δ = 0.11(1) mm/s, ΔE_Q = 0.27(1) mm/s).

Low Temperature UV-vis Spectroscopic Studies. In a typical experiment, a stock solution of K[Fe^{II}poat] (20 mM) and 18-crown-6 (40 mM) was prepared in 1:1 DMF:THF in a dry box, and 30 μL of the stock solution was added *via* a gas-tight syringe to 3 mL DMF:THF in a 1 cm quartz cuvette with a stir bar inside. The cuvette was sealed with a rubber septum and brought out of the box. The cuvette was then placed in the Agilent UV-vis spectrophotometer equipped with a cryostat, and was allowed to cool at -60 °C for at least 15 minutes. Additional reagents were prepared at a concentration of 20 mM and were added *via* a gas-tight syringe.

Low Temperature EPR Spectroscopic Studies. In a typical experiment to generate [Zn^{II}(O)Fe^{IV}]$^+$, a stock solution of IBX-*i*Pr (30 mM) was prepared in 1:1 DMF:THF mixture in a dry box. 150 μL of the stock solution (0.0045 mmol) was added to a quartz EPR tube via a syringe, which was sealed with a rubber septum. The tube was brought out of the box, and was allowed to cool in a dry ice/acetone bath at -78 °C for at least 15 minutes. 80 μL of a solution of K[Fe^{II}poat] (45 mM, 0.0036 mmol) and 18-crown-6 (90 mM, 0.0072 mmol) was added via a gas-tight syringe to generate [Fe^{IV}poat(O)]$^-$. [Zn^{II}(TMTACN)(OTf)$_2$] (90 mM, 40 μL, 0.0036 mmol) were added via a gas-tight syringe. When the reaction was complete, the tube was taken out of the cold bath, wiped clean, and quickly frozen in liquid nitrogen. The final Fe concentration was 13 mM. The preparation for [Ni^{II}(O)Fe^{IV}]$^+$ follows the same protocol but uses Ni^{II}(OTf)$_2$·5CH$_3$CN and TMTACN. In a typical experiment to generate [Cu^{II}(O)Fe^{IV}]$^+$, a 6.0 mM solution (1.44 mL) of K[Fe^{II}poat] (0.0072 g, 0.0086 mmol) and 18-crown-6

(0.0046 g, 0.017 mmol) was prepared in 1:1 DMF:THF at room temperature in a glovebox under argon atmosphere, and kept in a -35 °C freezer for the duration of the experiment. A 1.0 mL aliquot of stock metal complex (0.0064 mmol) was added via syringe to a 1-cm quartz. The cuvette was then sealed with a rubber septum and precooled to -80 °C in a Unisoku Unispeks cryostat typically used for UV-vis experiments outside the glovebox. The solution of metal complex was allowed to equilibrate to the desired temperature for at least 20 min. A stock solution of IBX-iPr and $[Cu^{II}(TMTACN)(OTf)_2]\cdot CH_3CN$ were prepared at 30 and 26.4 mM in DMF:THF, respectively. An aliquot of IBX-iPr (0.0075 mmol, 0.25 mL) was added via a gas-tight syringe, followed up an aliquot of $[Cu^{II}(TMTACN)(OTf)_2]\cdot CH_3CN$ (0.0066 mmol, 0.25 mL). Upon completion of the reaction, the septum was sliced open with a razor under a strong flow of argon. The rubber septum was removed and the content in the cuvette was quickly poured into liquid nitrogen. The frozen solid was ground into fine powder and then packed into a pre-cooled EPR tube. The final Fe concentration was 4 mM.

Low Temperature Mössbauer Solution Studies. In a typical experiment to generate $[Zn^{II}(O)^{57}Fe^{IV}]^+$, a 6.0 mM solution (1.44 mL) of the 96% ^{57}Fe-enriched $K[^{57}Fe^{II}poat]$ (0.0072 g, 0.0086 mmol) and 18-crown-6 (0.0046 g, 0.017 mmol) was prepared in 1:1 DMF:THF at room temperature in a glovebox under argon atmosphere, and kept in a -35 °C freezer for the duration of the experiment. A 1.0 mL aliquot of stock metal complex (0.0064 mmol) was added via syringe to a 1-cm quartz. The cuvette was then sealed with a rubber septum and precooled to -80 °C in a Unisoku Unispeks cryostat typically used for UV-vis experiments outside the glovebox. The solution of metal complex was allowed to equilibrate to the desired temperature for at least 20 min. A stock solution of IBX-iPr and $[Zn^{II}(TMTACN)(OTf)_2]$ were prepared at 30 and 26.4 mM in DMF:THF, respectively. An aliquot of IBX-iPr (0.0075 mmol, 0.25 mL) was added via a gas-tight syringe, followed up an aliquot of

$[Zn^{II}(TMTACN)(OTf)_2]$ (0.0066 mmol, 0.25 mL). Upon completion of the reaction, the septum was sliced open with a razor under a strong flow of argon. The rubber septum was removed and the content in the cuvette was quickly poured into liquid nitrogen. The frozen solid was ground into fine powder and then packed into a pre-cooled Mössbauer cup. The final ^{57}Fe concentration was 4 mM. Preparation for $[Cu^{II}(O)^{57}Fe^{IV}]^+$ follows the same protocol but uses $[Cu^{II}(TMTACN)(OTf)_2]\cdot CH_3CN$ instead. Preparation for $[Ni^{II}(O)^{57}Fe^{IV}]^+$ follows the same protocol but uses $Ni^{II}(OTf)_2\cdot 5CH_3CN$ and TMTACN.

References

(1) Holm, R. H.; Kennepohl, P.; Solomon, E. I. Structural and Functional Aspects of Metal Sites in Biology. *Chem. Rev.* **1996**, *96*, 2239.

(2) Jiang, W.; Yun, D.; Saleh, L.; Barr, E. W.; Xing, G.; Hoffart, L. M.; Maslak, M.-A.; Krebs, C.; Bollinger, J. M. A manganese(IV)/iron(III) cofactor in Chamydia trachomatis ribonucleotide reductase. *Science* **2007**, *316*, 1188-1191.

(3) Lipscomb, J. D.; Que, L. MMO: P450 in wolf's clothing? *JBIC, J Biol. Inorg. Chem.* **1998**, *3*, 331-336.

(4) Ross, M. O.; Rosenzweig, A. C. A tale of two methane monooxygenases. *JBIC, J. Biol. Inorg. Chem.* **2017**, *22*, 307-319.

(5) Yano, J.; Kern, J.; Sauer, K.; Latimer, M. J.; Pushkar, Y.; Biesiadka, J.; Loll, B.; Saenger, W.; Messinger, J.; Zouni, A.; Yachandra, V. K. Where Water Is Oxidized to Dioxygen: Structure of the Photosynthetic Mn_4Ca Cluster. *Science* **2006**, *314*, 821-825.

(6) Britt, R. D.; Campbell, K. A.; Peloquin, J. M.; Gilchrist, M. L.; Aznar, C. P.; Dicus, M. M.; Robblee, J.; Messinger, J. Recent pulsed EPR studies of the Photosystem II oxygen-evolving complex: implications as to water oxidation mechanisms. *Biochim. Acta Bioenerg.* **2004**, *1655*, 158-171.

(7) Cox, N.; Pantazis, D. A.; Lubitz, W. Current Understanding of the Mechanism of Water Oxidation in Photosystem II and Its Relation to XFEL Data. *Annu. Rev. Biochem.* **2020**, *89*, 795-820.

(8) Schenk, G.; Mitić, N.; Gahan, L. R.; Ollis, D. L.; McGeary, R. P.; Guddat, L. W. Binuclear Metallohydrolases: Complex Mechanistic Strategies for a Simple Chemical Reaction. *Acc. Chem. Res.* **2012**, *45*, 1593-1603.

(9) Shu, L.; Nesheim, J. C.; Kauffman, K.; Münck, E.; Lipscomb, J. D.; Que, L. An $Fe_2^{IV}O_2$ Diamond Core Structure for the Key Intermediate Q of Methane Monooxygenase. *Science* **1997**, *275*, 515-518.

(10) Castillo, R. G.; Banerjee, R.; Allpress, C. J.; Rohde, G. T.; Bill, E.; Que, L.; Lipscomb, J. D.; DeBeer, S. High-Energy-Resolution Fluorescence-Detected X-ray Absorption of the Q Intermediate of Soluble Methane Monooxygenase. *J. Am. Chem. Soc.* **2017**, *139*, 18024-18033.

(11) Cutsail, G. E.; Banerjee, R.; Zhou, A.; Que, L.; Lipscombe, J. D.; DeBeer, S. High-Resolution Extended X-ray Absorption Fine Structure Analysis Provides Evidence for a

Longer Fe···Fe Distance in the Q Intermediate of Methane Monooxygenase. *J. Am. Chem. Soc.* **2018**, *140*, 16807-16820.
(12) Gupta, R.; Taguchi, T.; Lassalle-Kaiser, B.; Bominaar, E. L.; Yano, J.; Hendrich, M. P.; Borovik, A. S. High-spin Mn–oxo complexes and their relevance to the oxygen-evolving complex within photosystem II. *Proc. Natl. Acad. Sci. U.S.A.* **2015**, *112*, 5319-5324.
(13) Cox, N.; Retegan, M.; Neese, F.; Pantazis, D. A.; Boussac, A.; Lubitz, W. Photosynthesis. Electronic Structure of the Oxygen-Evolving Complex in Photosystem II prior to O–O Bond Formation. *Science* **2014**, *345*, 804-808.
(14) Siegbahn, P. E. M. Structures and energetics for O_2 formation in photosystem II. *Acc. Chem. Res.* **2009**, *42*, 1871-1880.
(15) Oswald, V. F.; Lee, J. L.; Biswas, S.; Weitz, A. C.; Mittra, K.; Fan, R.; Li, J.; Zhao, J.; Hu, M. Y.; Alp, E. E.; Bominaar, E. L.; Guo, Y.; Green, M. T.; Hendrich, M. P.; Borovik, A. S. Effects of Non-covalent Interactions on High-spin Fe(IV)-oxido Complexes. *J. Am. Chem. Soc.* **2020**, *142*, 11804-11817.
(16) Lee, J. L.; Oswald, V. F.; Biswas, S.; Hill, E. A.; Ziller, J. W.; Hendrich, M. P.; Borovik, A. S. Stepwise assembly of heterobimetallic complexes: synthesis, structure, and physical properties. *Dalton Trans.* **2021**, *50*, 8111-8119.
(17) Fukuzumi, S.; Morimoto, Y.; Kotani, H.; Naumov, P.; Lee, Y.-M.; Nam, W. Crystal structure of a metal ion-bound oxoiron(IV) complex and implications for biological electron transfer. *Nat. Chem.* **2010**, *2*, 756-759.
(18) Prakash, J.; Rohde, G. T.; Meier, K. K.; Jasniewski, A. J.; Van Heuvelen, K. M.; Münck, E.; Que, L. Spectroscopic Identification of an Fe^{III} Center, not Fe^{IV}, in the Crystalline Sc–O–Fe Adduct Derived from $[Fe^{IV}(O)(TMC)]^{2+}$. *J. Am. Chem. Soc.* **2015**, *137*, 3478-3481.
(19) Zhou, A.; Crossland, P. M.; Draksharapu, A.; Jasniewski, A. J.; Kleespies, S. T.; Que, L. Oxoiron(IV) compelxes as synthons for the assembly of heterobimetallic centers such as the Fe/Mn active site of Class Ic ribonucleotide reductases. *JBIC, J. Biol. Inorg. Chem.* **2018**, *23*, 155-165.
(20) Draksharapu, A.; Rasheed, W.; Klein, J. E. M. N.; Que, L. Facile and Reversible Formation of Iron(III)–Oxo–Cerium(IV) Adducts from Nonheme Oxoiron(IV) Complexes and Cerium(III). *Angew. Chem., Int. Ed.* **2017**, *56*, 9091-9095.
(21) Rosenkoetter, K. E.; Ziller, J. W.; Heyduk, A. F. A Heterobimetallic W–Ni Complex Containing a Redox-Active $W[SNS]_2$ Metalloligand. *Inorg. Chem.* **2016**, *55*, 6794-6798.
(22) Wojnar, M. K.; Ziller, J. W.; Heyduk, A. F. Heterobimetallic and Heterotrimetallic Clusters Containing a Redox-Active Metalloligand. *Eur. J. Inorg. Chem.* **2017**, 5571-5575.
(23) Greer, S. M.; McKay, J.; Gramigna, K. M.; Thomas, C. M.; Stoian, S. A.; Hill, S. Probing Fe–V Bonding in a C_3-Symmetric Heterobimetallic Complex. *Inorg. Chem.* **2018**, *57*, 5870-5878.
(24) Zhang, H.; Hatzis, G. P.; Moore, C. E.; Dickie, D. A.; Bezpalko, M. W.; Foxman, B. M.; Thomas, C. M. O_2 Activation by a Heterobimetallic Zr/Co Complex. *J. Am. Chem. Soc.* **2019**, *141*, 9516-9520.
(25) Barton, B. E.; Rauchfuss, T. B. Hydride-Containing Models for the Active Site of the Nickel-Iron Hydrogenases. *J. Am. Chem. Soc.* **2010**, *132*, 14877-14885.
(26) Eisenhart, R. J.; Clouston, L. J.; Lu, C. C. Configuring Bonds between First-Row Transition Metals. *Acc. Chem. Res.* **2015**, *48*, 2885-2894.
(27) Que. L. The Road to Non-Heme Oxoferryls and Beyond. *Acc. Chem. Res.* **2007**, *40*, 3493-500.
(28) Gupta, R.; Lacy, D. C.; Bominaar, E. L.; Borovik, A. S.; Hendrich, M. P.; Electron Paramagnetic Resonance and Mössbauer Spectroscopy and Density Functional Theory Analysis of a High-Spin Fe^{IV}–Oxo Complex. *J. Am. Chem. Soc.* **2012**, *134*, 9775-9784.

(29) Srnec, M.; Wong, S. D.; England, J.; Que, L.; Solomon, E. I. π-Frontier Molecular Orbitals in S = 2 Ferryl Species and Elucidation of Their Contributions to Reactivity. *Proc. Natl. Acad. Sci. U.S.A.* **2012**, *109*, 14326-14331.

(30) Lau, N.; Sano, Y.; Ziller, J. W.; Borovik, A. S. Modular bimetallic complexes with a sulfonamido-based ligand. *Dalton Trans.* **2018**, *47*, 12362-12372.

(31) Hendrich, M. P.; Debrunner, P. G. Integer-Spin Electron Paramagnetic Resonance of Iron Proteins. *Biophys. J.* **1989**, *56*, 489-506.

(32) Taguchi, T.; Gupta, R.; Lasselle-Kaiser, B.; Boyce, D. W.; Yachandra, V. K.; Tolman, W. B.; Yano, J.; Hendrich, M. P.; Borovik, A. S. Preparation and Properties of a Monomeric High-Spin Mn^{V}–Oxo Complex. *J. Am. Chem. Soc.* **2012**, *134*, 1996-1999.

(33) Gupta, R.; Taguchi, T.; Lassalle-Kaiser, B.; Bominaar, E. L.; Yano, J.; Hendrich, M. P.; Borovik, A. S. High-spin Mn–oxo complexes and their relevance to the oxygen-evolving complex within photosystem II. *Proc. Nat. Acad. Sci. U.S.A.* **2015**, *112*, 5319-5324.

(34) Sinnecker, S.; Slep, L. D.; Bill, E.; Neese, F. Performance of Nonrelativistic and Quasi-Relativistic Hybrid DFT for the Prediction of Electric and Magnetic Hyperfine Parameters in ^{57}Fe Mössbauer Spectra. *Inorg. Chem.* **2005**, *44*, 2245-2254.

(35) Weitz, A. C.; Biswas, S.; Rizzolo, K.; Elliott, S.; Bominaar, E. L.; Hendrich, M. P. Electronic State of the His/Tyr-Ligated Heme of BthA by Mössbauer and DFT Analysis. *Inorg. Chem.* **2020**, *59*, 10223-10233.

(36) England, J.; Martinho, M. M.; Farquhar, E. R.; Frisch, J. R.; Bominaar, E. L.; Münck, E.; Que, L. A Synthetic High-Spin Oxoiron(IV) Complex: Generation, Spectroscopic Characterization, and Reactivity. *Angew. Chem., Int. Ed.* **2009**, *48*, 3622-3626.

(37) Biswas, A. N.; Puri, M.; Meier, K. K.; Oloo, W. N.; Rohde, G. T.; Bominaar, E. L.; Münck, E.; Que, L. Modeling TauD-J: A High-Spin Nonheme Oxoiron(IV) Complex with High Reactivity toward C–H Bonds. *J. Am. Chem. Soc.* **2015**, *137*, 2428-2431.

(38) Sinnecker, S.; Svensen, N.; Barr, E. W.; Ye, S.; Bollinger, J. M.; Neese, F.; Krebs, C. Spectroscopic and Computational Evaluation of the Structure of the High-Spin Fe(IV)-Oxo Intermediates in Taurine: α-Ketoglutarate Dioxygenase from *Escherichia Coli* and Its His99Ala Ligand Variant. *J. Am. Chem. Soc.* **2007**, *129*, 6168-6179.

(39) Van Heuvelen, K. M.; Fiedler, A. T.; Shan, X.; De Hont, R. F.; Meier, K. K.; Bominaar, E. L.; Münck, E.; Que, L. One-electron oxidation of an oxoiron(IV) complex to form an $[O=Fe^{V}=NR]^{+}$ center. *Proc. Natl. Acad. Sci. U.S.A.* **2012**, *109*, 11933-11938.

(40) Schulz, C. E.; Rutter, R.; Sage, J. T.; Debrunner, P. G.; Hager, L. P. Mössbauer and electron paramagnetic resonance studies of horseradish peroxidase and its catalytic intermediates. *Biochemistry* **1984**, *23*, 4743-4754.

(41) Gütlich, P.; Eckard, B.; Trautein, A. X. *Mössbauer Spectroscopy and Transition Metal Chemistry*, 1st ed.; Springer-Verlag: Berlin, 2011.

(42) Zhdankin, V. V.; Litvinov, D. N.; Koposov, A. Y.; Luu, T.; Ferguson, M. J.; McDonald, R.; Tykwinski, R. R. Preparation and Structure of 2-Iodoxybenzoate Esters: Soluble and Stable Periodinane Oxidizing Reagents. *Chem. Commun.* **2004**, *263*, 106-107.

(43) Zhdankin, V. V.; Koposov, A. Y.; Litvinov, D. N.; Ferguson, M. J.; McDonald, R.; Luu, T.; Tykwinski, R. R. Esters of 2-Iodoxybenzoic Acid: Hypervalent Iodine Oxidizing Reagents with a Pseudobenziodoxole Structure. *J. Org. Chem.* **2005**, *70*, 6484-6491.

(44) Yang, L.; Tolman W. B.; Type 1 Copper Site Synthetic Model Complexes with Increased Redox Potentials. *JBIC, J. Biol. Inorg. Chem.* **2012**, *17*, 285-291.

(45) Heintz, R. A.; Smith, J. A.; Szalay, P. S.; Weisgerber, A.; Dunbar, K. R. Homoleptic Transition Metal Acetonitrile Cations with Tetrafluoroborate or Trifluoromethanesulfonate Anions. *Inorg. Synth.* **2002**, *33*, 75-83.

(46) Schoenfeldt, N. J.; Ni Z.; Korinda, A. W.; Meyer R. J.; Notestein J. M. Manganese Triazacyclononane Oxidation Catalysts Grafted under Reaction Conditions on Solid Cocatalytic Supports. *J. Am. Chem. Soc.* **2011**, *133*, 18684–18695.
(47) Cao R.; Müller, P.; Lippard, S. J. Tripodal Tris-tacn and Tris-dpa Platforms for Assembling Phosphate-Templated Trimetallic Centers. *J. Am. Chem. Soc.* **2010**, *132*, 17366–17369.
(48) Petasis, D. T.; Hendrich, M. P. Quantitative Interpretation of Multifrequency Multimode EPR Spectra of Metal Containing Proteins, Enzymes, and Biomimetic Complexes. *Methods Enzymol.* **2015**, *563*, 171-208.

Chapter 5

Bioinspired Di-Fe Complexes: Controlling Proton and Electron Transfer over Four Oxidation States

Introduction

Controlled proton and electron transfer processes within the active sites of metalloproteins are often necessary for function and to thwart undesirable reactivity.[1-4] The productive balance of these transfer processes is often managed by metallocofactors whose properties are regulated through a combination of effects at their primary and secondary coordination spheres.[5-7] Determining the interplay between these two coordination spheres is a necessary prerequisite before a complete mechanistic understanding of function can be achieved. To investigate these questions within systems containing di-Fe centers, we have developed a synthetic di-Fe^{II} species that can be oxidized in discrete one-electron steps to an $Fe^{III}Fe^{IV}$ species. This system is also able to control proton transfer via intramolecular processes, which increases the stability of the higher valent species and provides probes for studying biological oxidative chemistry.

Metalloproteins with di-Fe centers have a range of functions that include hemerythrin for O_2 binding,[8] soluble methane monooxygenase hydroxylase (sMMOH)[9] and the R2 subunit of class I ribonucleotide reductases (RNR R2)[10-13] for O_2 activation, flavin diiron proteins (FDP) for NO and O_2 reduction,[14,15] and Δ^9-desaturatase for oxidation of fatty acid chains.[16,17] Oxidation of the di-Fe centers are often accompanied by structural changes that include the transfer of protons from coordinated ligands (e.g., OH^- and H_2O).[18,19] These proton/electron transfer steps, and how they are linked, are often proposed in mechanisms but rarely supported by experimental evidence. For instance, the mechanism for RNR R2 includes the conversion of the resting di-Fe^{II} state to an $Fe^{III}Fe^{IV}$ intermediate (X) that is able to homolytically cleave the O–H bond at nearby tyrosine

residue to form a tyrosine radical (Figure 5.1.A), triggers a long-range electron transfer process (> 30 Å) that extends to the R1 subunit, where ribonucleotides are reduced to deoxyribonucleotides.[11,20,21] Synthetic complexes have been developed to probe the properties of these intermediates. In particular, di-Fe^{IV} and $Fe^{III}Fe^{IV}$ complexes have been prepared and studied.[22-31] However, thermodynamic parameters that govern the formation of these complexes from their lower valent precursors are lacking. In addition, the associated structural changes that occur upon oxidation are also rarely known.

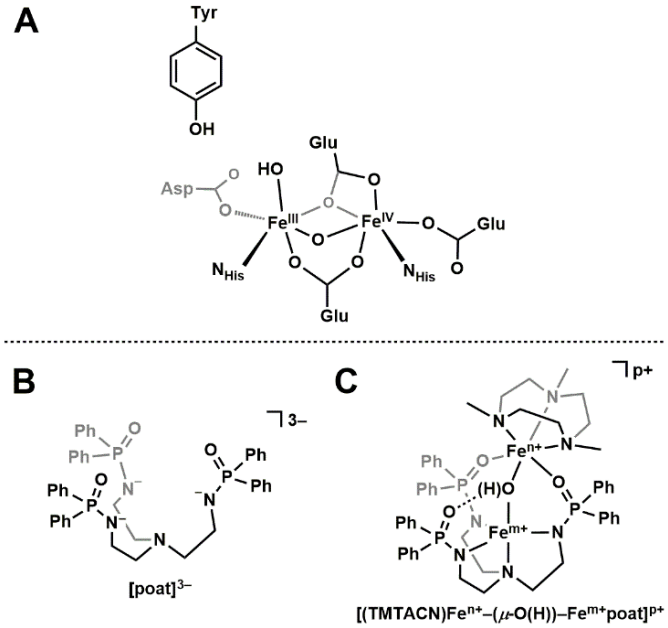

Figure 5.1. (A) The proposed chemical structure of Intermediate X in RNR R2. (B) Structure of $[poat]^{3-}$. (C) Structure of a generic $[(TMTACN)Fe^{n+}–(\mu\text{-}O)–Fe^{m+}poat]^{p+}$ complex.

We have approached this problem by developing an assembly process to preparing complexes with discrete di-Fe cores. One advantage of our approach is that we can use well-defined monomeric complexes which allow us to prepare di-Fe cores with different primary coordination sphere around each Fe center. This approach is made possible by the use of the multi-functional tripodal ligand $[poat]^{3-}$ (*N,N′,N″*-[nitrilotris(ethane-2,1-diyl)]tris(*P,P*-diphenylphosphinic amido), Figure 5.1.B) that we initially designed to stabilize high valent Fe^{IV}=O complexes.[33] We discovered that $[Fe^{III}poat(OH)]^-$ and $[Fe^{IV}poat(O)]^-$ complexes are able to bind a second Fe complex via

coordination to the O/OH ligand and two P=O units, producing triply bridge species that resemble di-Fe core found in biology (Figure 5.1.C).[33,34] In this report we describe the preparation and properties of a series of complexes with either [Fe–(μ-OH)–Fe] or [Fe–(μ-O)–Fe] cores that traverse four different oxidation levels. Our work demonstrates that $[poat]^{3-}$ can be used to control PT processes that occur during oxidation and provides access to a high valent [Fe^{III}–(μ-O)–Fe^{IV}] complex, which we used to examine the cleavage of X–H bonds, including reactions that are similar to those found within the active site of RNR R2. Our findings suggest an alternate mechanism for reactivity of X towards tyrosine, in which initial proton transfer first occurs at the oxido ligand that bridges between the two Fe centers, then proceeds to the terminal OH ligand on the Fe^{III} center.

Results

[(TMTACN)Fe^{II}–(μ-OH)–Fe^{III}poat]OTf and [(TMTACN)Fe^{II}–(μ-OH)–Fe^{II}poat]. We have previously prepared a mixed-valent $Fe^{II}Fe^{III}$ complex, [(TMTACN)Fe^{II}–(μ-O)–Fe^{III}MST]$^{+}$ ([Fe^{II}(OH)Fe^{III}MST]$^{+}$), in which an Fe^{III} center is bound to the sulfonamido-based tripodal ligand $[MST]^{3-}$ (*N*,*N*',*N*''-[2,2',2''-nitrilotris(ethane-2,1-diyl)]tris(2,4,6-trimethylbenzenesulfonamido)), and the Fe^{II} site is capped by an N-based macrocycle [TMTACN] (1,4,7-trimethyl-1,4,7-triazacyclononane).[34,35] However, we were not able to explore further oxidation of this complex, and our studies suggested that the sulfonamido groups were not suitable for stabilizing higher oxidation states. To circumvent this problem, we redesigned the ligand framework to include phosphinic amido group and recently reported that $[poat]^{3-}$ can facilitate the formation of the high valent species $[Fe^{IV}poat(O)]^{-}$ complex which can further bind group 2 metal ions.[32] In addition, we discovered that heterobimetallic complexes with the general formula of [(TMTACN)M^{II}–(μ-OH)–Fe^{III}poat]$^{+}$ (M = Ni, Cu, Zn) can be prepared.[33] We found that the same synthetic route provided access to di-Fe complexes and we initially synthesized [(TMTACN)Fe^{II}–(μ-OH)–Fe^{III}poat]OTf

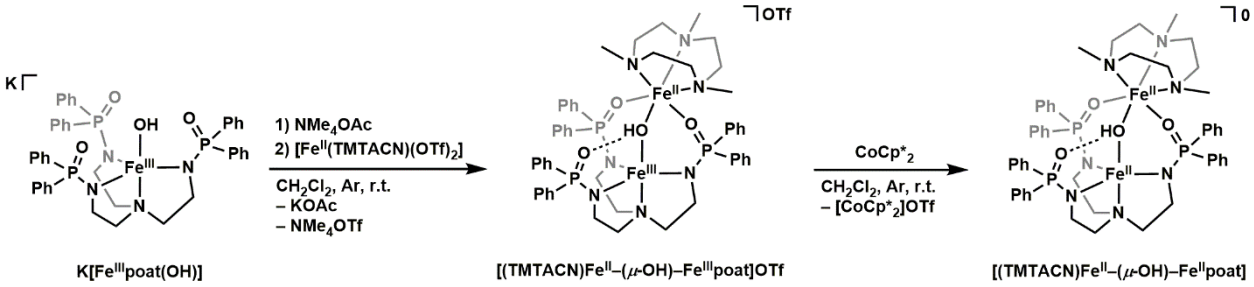

Scheme 5.1. Preparative routes for $[Fe^{II}(OH)Fe^{III}poat]^{+}$ and $[Fe^{II}(OH)Fe^{II}poat]$.

($[Fe^{II}(OH)Fe^{III}poat]OTf$) (Scheme 5.1). In a typical reaction, NMe_4Oac was added to a CH_2Cl_2 solution of $K[Fe^{III}poat(OH)]$ in a salt metathesis reaction. Upon removal of the insoluble KOAc, $[Fe^{II}(TMTACN)(OTf)_2]$ was added to the mixture to produce the bimetallic compound. The $[Fe^{II}(OH)Fe^{III}poat]OTf$ salt was initially purified as a powder from a diethyl ether-CH_2Cl_2 mixture, and then further purified as yellow sheet-like crystals from a hexane-CH_2Cl_2 mixture. The complex exhibits absorbance features at λ_{max} (ε, M^{-1} cm^{-1}) = 315 (sh), 372 (6400), 460 (sh), and 520 nm (sh) (Figure 5.2). The LMCT absorbance feature at λ_{max} = 372 nm is similar to those previously reported in our related bimetallic complexes with $[MST]^{3-}$ and $[poat]^{3-}$ ligands.[33,35] The FTIR spectrum of the $[Fe^{II}(OH)Fe^{III}poat]OTf$ salt revealed a weak vibrational feature at 3141 cm^{-1}, which we assigned to the *ν*(O–H) band that forms a strong intramolecular H-bond to the P=O group in $[poat]^{3-}$ (Figure 5.3).

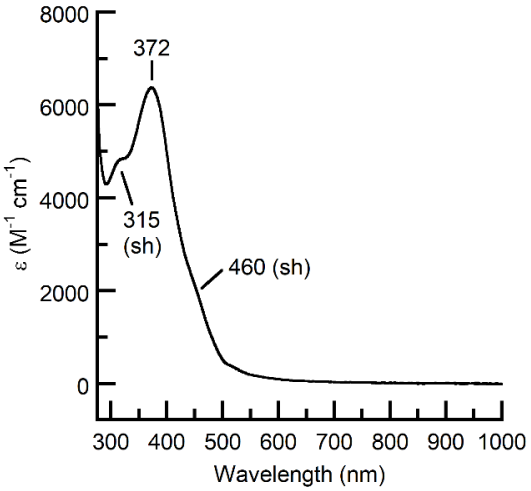

Figure 5.2. Electronic absorbance spectrum of $[Fe^{II}(OH)Fe^{III}poat]^{+}$. The spectrum was collected in CH_2Cl_2 at room temperature at a concentration of 0.10 mM.

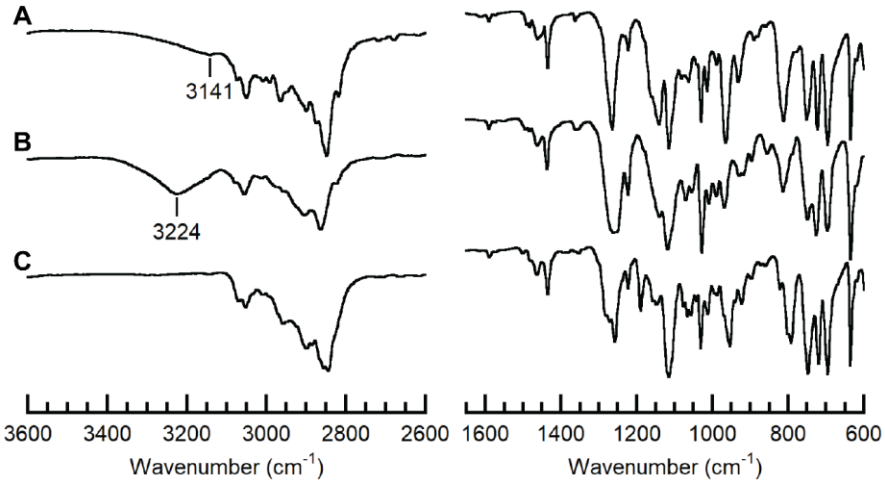

Figure 5.3. FTIR spectra of $[Fe^{II}(OH)Fe^{III}poat]^+$ (A), $[Fe^{III}(O)Fe^{III}Hpoat]^{2+}$ (B), and $[Fe^{III}(O)Fe^{III}poat]^+$ (C). The left panel shows the high energy region, and the right panel shows the low energy region.

Perpendicular (⊥)-mode electron paramagnetic resonance (EPR) spectroscopy reveals a rhombic $S = 1/2$ signal with features at $g = 1.94$, 1.49, and 1.20 (Figure 5.4). These parameters agree with the assignment of an $S = 5/2$ Fe^{III} center antiferromagnetically coupled to an $S = 2$ Fe^{II} center. The bimetallic complex was further analyzed by ^{57}Fe Mössbauer spectroscopy. The experimental spectrum of $[^{57}Fe^{II}(OH)^{57}Fe^{III}poat]^+$ was fitted with two distinct doublets for two Fe centers. One site has isomer shift (δ) and quadrupole splitting (ΔE_Q) values of 0.34 and -0.72 mm s^{-1}, and the other site has δ and ΔE_Q values of 1.20 and -2.84 mm s^{-1} (Figure 5.5.A). These parameters are

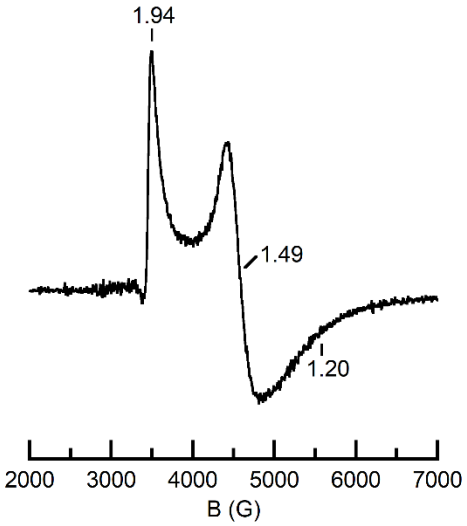

Figure 5.4. ⊥-mode EPR spectra of $[Fe^{II}(OH)Fe^{III}poat]^+$. Spectra were collected at 5.9 K in 5.0 mM CH_2Cl_2:THF.

consistent with high spin Fe^{III} and Fe^{II}, respectively.[36] Temperature and field-dependent measurements of this species revealed an exchanged-coupled $S = 1/2$ system with $J = 30$ cm^{-1} ($J(S_1 \cdot S_2)$); the magnitude of J is consistent with a hydroxido bridging ligand.[37]

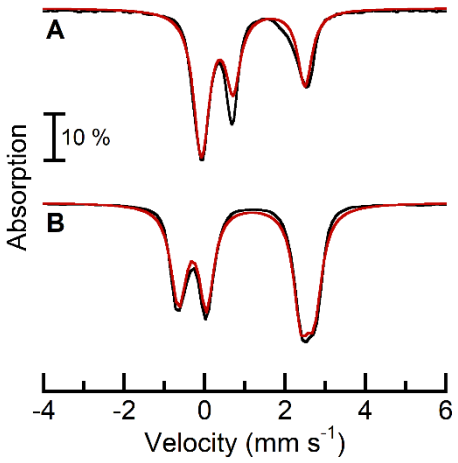

Figure 5.5. ^{57}Fe Mössbauer spectra (black) of $[^{57}Fe^{II}(OH)^{57}Fe^{III}poat]^+$ (A) and $[^{57}Fe^{II}(OH)^{57}Fe^{II}poat]$ (B) in PrCN at zero field. Spectrum A was collected at 100 K, and spectrum B was collected at 4.2 K. Simulations of the Mössbauer spectra are in red.

The molecular structure of $[Fe^{II}(OH)Fe^{III}poat]^+$ was determined by X-ray diffraction methods and revealed a discrete bimetallic structure (Figure 5.6). There are two crystallographically different, but chemically equivalent, molecules in the asymmetric unit and we will discuss the averages of the metrical parameters and calculated values, which are shown in Table 5.1. The Fe^{III} site in the $[poat]^{3-}$ framework adopts a trigonal bipyramidal geometry with an N_4O primary coordination sphere, comprising of the $[poat]^{3-}$ ligand and a bridging hydroxido ligand ($\tau_5 = 0.884$, where the ideal trigonal bipyramidal geometry has a $\tau_5 = 1$, and the ideal square pyramidal geometry has a $\tau_5 = 0$). The Fe^{II} site in the Fe-TMTACN adduct is 6-coordinated with an N_3O_3 primary coordination sphere, comprising of the TMTACN ligand, two phosphinic amido groups from the $[poat]^{3-}$ ligand, and a bridging hydroxido ligand. The significantly different Fe1–O1 and Fe2–O1 bond lengths of 1.894(1) and 2.015(2) Å agree with the results from our magnetic studies and reflect the distinct oxidation states of the two Fe centers. The di-Fe center in $[Fe^{II}(OH)Fe^{III}poat]^+$ is best

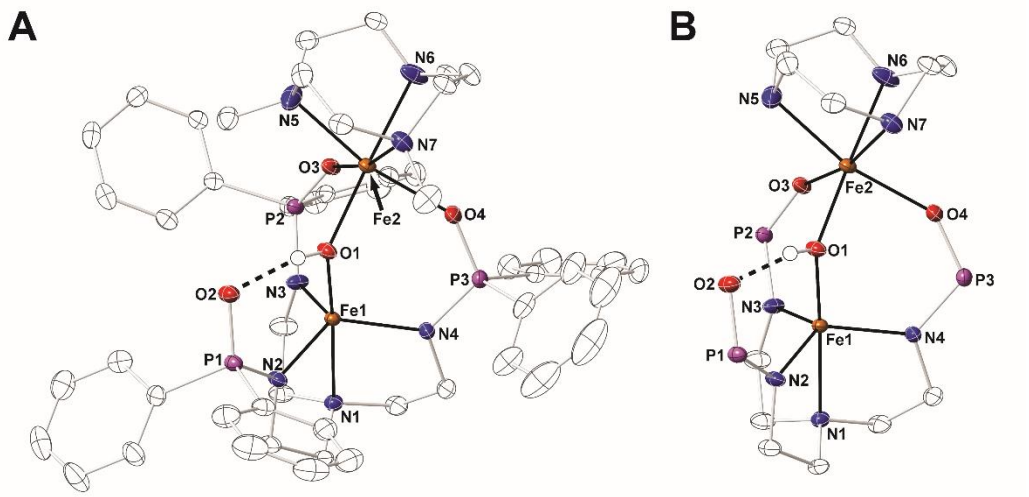

Figure 5.6. (A) Thermal ellipsoid diagram depicting the molecular structure of $[Fe^{II}(OH)Fe^{III}poat]^+$. Ellipsoids are drawn at the 50 % probability level, and only the hydroxido H atom is show for clarity. The triflate counter anion is outer-sphere and is not interacting with the cation. (B) The methyl and phenyl groups are removed, and only the diiron core is shown for clarity.

described as a triply bridge core with an Fe^{II}–(μ-OH)–Fe^{III} unit and two phosphinic amido bridges between the two Fe centers. The remaining phosphinic amido tripodal arm that does not bind to the Fe^{II} site forms an intramolecular H-bond with the hydroxido ligand with an O1···O2 distance of 2.649(2) Å. The metrical parameters around the Fe centers are comparable with those previously reported for the Zn/Cu/Ni analogues.[33] In addition, the Fe^{II}–O=P bond lengths (Fe2–O3, 2.094(1) and Fe2–O4, 2.124(1) Å) are significantly shorter than those for Fe^{II}–O=S in $[Fe^{II}(OH)Fe^{III}MST]^+$ (2.201(2) and 2.202(2) Å),[35] which supports the premise that phosphinic amido P=O groups serve as stronger donors and may support the Fe center at a higher oxidation state.

The electrochemical properties of $[Fe^{II}(OH)Fe^{III}poat]^+$ were investigated using cyclic voltammetry. The $[Fe^{II}(OH)Fe^{III}poat]^+$ complex exhibited two reversible one-electron redox events at -1.62 V and -0.42 V vs. $[Fe^{III/II}Cp_2]^{+/0}$, which are assigned to the $Fe^{II}Fe^{III}/Fe^{II}Fe^{II}$ and $Fe^{III}Fe^{III}/Fe^{II}Fe^{III}$ couples, respectively (Figure 5.7). These potentials are -0.7 V more negative than the same processes in the MST analogue (-0.86 and +0.35 V).[34] While it has been previously shown that the trianionic equatorial N-plane can support a higher-valent metal center (e.g., Fe^{IV}),[32] these

electrochemical results suggest experimentally that the P=O moieties can also readily support a metal ion beyond the +2 state in the auxiliary binding site.

Table 5.1. Selected bond lengths/distances (Å) and angles (°) for $[Fe^{II}(OH)Fe^{III}poat]^{+}$,[a] $[Fe^{III}(O)Fe^{III}Hpoat]^{2+}$, and $[Fe^{III}(O)Fe^{III}poat]^{+}$.

	$[Fe^{II}(OH)Fe^{III}poat]^{+}$	$[Fe^{III}(O)Fe^{III}Hpoat]^{2+}$	$[Fe^{III}(O)Fe^{III}poat]^{+}$
		Bond Distances (Å)	
Fe1–N1	2.210(2)	2.367(2)	2.292(2)
Fe1–N2	2.023(2)	–	2.008(2)
Fe1–O2	–	2.016(1)	–
Fe1–N3	2.011(2)	1.984(2)	2.024(2)
Fe1–N4	2.009(2)	1.999(2)	2.029(2)
Fe1–O1	1.894(1)	1.800(1)	1.799(2)
O1···O2	2.649(2)	–	3.212(3)
Fe2–O1	2.015(2)	1.792(1)	1.784(2)
Fe2–O3	2.094(1)	2.047(1)	2.018(2)
Fe2–O4	2.124(1)	2.002(1)	2.035(2)
Fe2–N5	2.275(2)	2.216(2)	2.231(2)
Fe2–N6	2.213(2)	2.245(2)	2.272(2)
Fe2–N7	2.252(2)	2.223(2)	2.219(2)
Fe1···Fe2	3.436(1)	3.182(1)	3.161(1)
av Fe1–N/O_{eq}	2.014(2)	2.000(2)	2.020(2)
av Fe2–N_{TMTACN}	2.247(2)	2.228(2)	2.241(2)
d[Fe1–N/O_{eq}]	0.363	0.295	0.367
d[Fe2–N_{TMTACN}]	1.522	1.512	1.525
		Bond Angles (deg)	
O1–Fe1–N1	174.52(6)	176.63(6)	179.22(8)
N2–Fe1–N3	119.21(7)	–	122.24(9)
O2–Fe1–N3	–	114.24(6)	–
N3–Fe1–N4	109.71(7)	106.48(7)	107.09(9)
N2–Fe1–N4	121.50(7)	–	120.87(9)
O2–Fe1–N4	–	132.60(6)	–
Fe1–O1–Fe2	123.06(8)	124.73(8)	123.82(10)
O3–Fe2–O4	98.31(5)	98.33(6)	95.72(8)
N5–Fe2–N6	79.50(8)	78.66(6)	77.88(8)
N5–Fe2–N7	78.27(7)	78.90(6)	79.45(8)
N6–Fe2–N7	79.54(6)	79.35(7)	78.94(8)
		Calculated Values	
τ_5[b]	0.884	0.734	0.950

[a]Bond lengths, distances, and angles are reported as an average. [b]Trigonality structural parameter, $\tau_5 = (\beta - a)/60^{o}$. β is the largest bond angle observed, and a is the second largest bond angle observed.

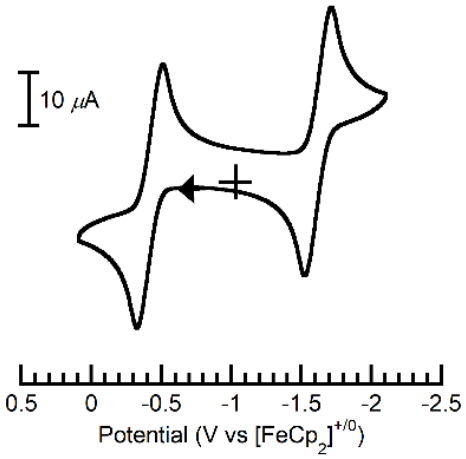

Figure 5.7. Cyclic voltammogram of $[Fe^{II}(OH)Fe^{III}poat]^+$ collected at scan rate of 100 mV s^{-1} in in CH_2Cl_2.

We explored the chemical reduction of $[Fe^{II}(OH)Fe^{III}poat]^+$using $CoCp^*_2$ ($E_{1/2}$ = -1.94 V vs. $[FeCp_2]^{+/0}$)[38] as the reductant (Scheme 5.1) and found a nearly featureless electronic absorption spectrum in the visible region (Figure 5.8). The ^{57}Fe Mossbauer spectrum contained two distinct quadrupole doublets with δ = 1.03 mm s^{-1}/$|\Delta E_Q|$ = 3.38 mm s^{-1} and δ = 1.22 mm s^{-1}/$|\Delta E_Q|$ = 2.37 mm s^{-1} that suggest two distinct Fe^{II} sites (Figure 5.5.B). Additional variable-temperature studies at 7 T determined an exchange coupling J value of 20 cm^{-1} that indicates moderate antiferromagnetic coupling between the Fe centers which is promoted by a bridging hydroxido ligand.[37] A silent EPR spectrum was observed that is consistent with an S = 0 ground state caused

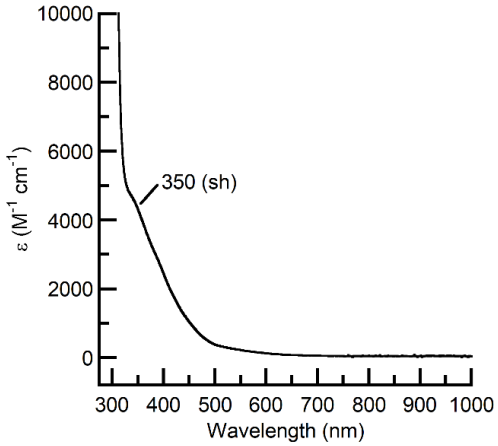

Figure 5.8. Electronic absorbance spectrum of $[Fe^{II}(OH)Fe^{II}poat]$. The spectrum was collected in CH_2Cl_2 at room temperature at a concentration of 0.10 mM.

by the antiferromagnetic interaction. These values are consistent with the formulation [(TMTACN)Fe^{II}–(μ-OH)–Fe^{II}poat]; however, several attempts to isolate a pure solid of this complex were unsuccessful with only [Fe^{II}(OH)Fe^{III}poat]$^{+}$ being obtained. We therefore focused our investigations on the oxidative chemistry associated with [Fe^{II}(OH)Fe^{III}poat]$^{+}$.

[(TMTACN)Fe^{III}–(μ-O)–Fe^{III}Hpoat](OTf)$_2$. Synthesis and Structure. The chemical oxidation of [Fe^{II}(OH)Fe^{III}poat]OTf was achieved using [$FeCp_2$]OTf (Scheme 5.2) to afford orange crystals after purification. The electron spray ionization mass spectrum of these crystals dissolved in CH_3CN contains the molecular weight and experimental isotope pattern that matched those calculated for {[Fe^{III}(OH)Fe^{III}poat](OTf)}$^{+}$ (Figure 5.9.A,C). However, the ESI-MS data alone cannot determine the molecular structure of this di-Fe^{III} complex, particularly whether the proton is still on the bridging ligand. To address this question, we determined its molecular structure via XRD methods to again find a triply bridged di-Fe complex but one with an Fe^{III}–(μ-O)–Fe^{III} core, [(TMTACN)Fe^{III}–(μ-O)–Fe^{III}Hpoat](OTf)$_2$ ([Fe^{III}(O)Fe^{III}Hpoat](OTf)$_2$); Figure 5.10.A,C; Table 5.1). Unlike in [Fe^{II}(OH)Fe^{III}poat]$^{+}$, the Fe1–O1 and Fe2–O1 bond distances of 1.800(1) and 1.792(1) Å

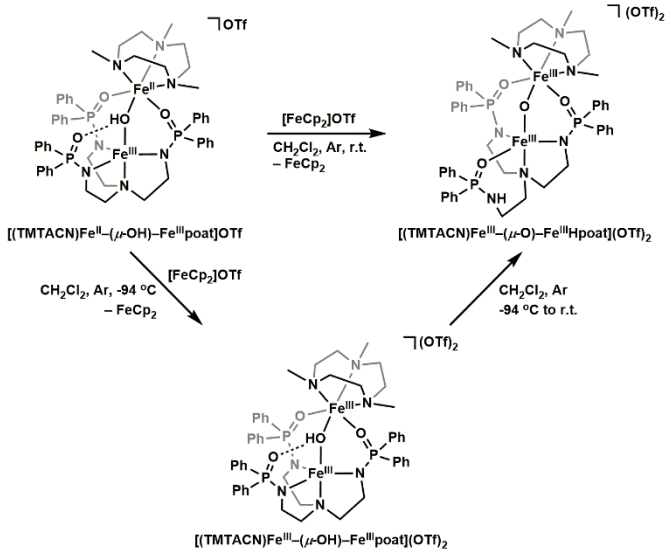

Scheme 5.2. Oxidation of [Fe^{II}(OH)Fe^{III}poat]$^{+}$ yields [Fe^{III}(OH)Fe^{III}poat]$^{2+}$, which further converts to [Fe^{III}(O)Fe^{III}Hpoat]$^{2+}$.

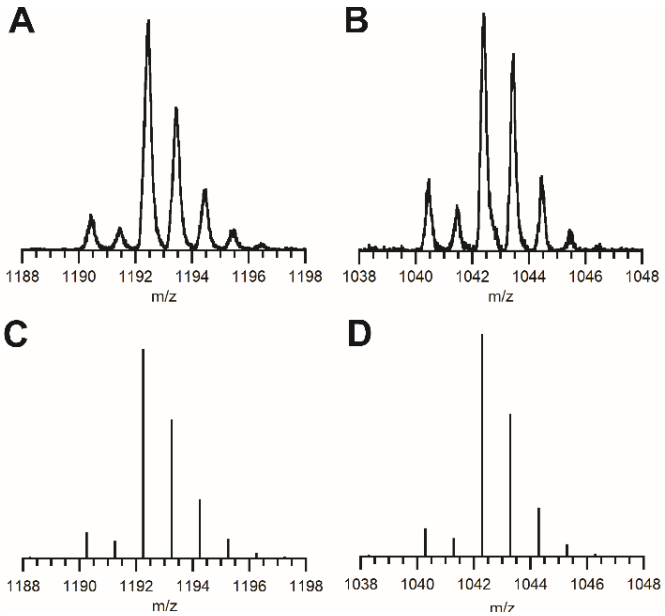

Figure 5.9. ESI-MS spectra of $[Fe^{III}(O)Fe^{III}Hpoat]^{2+}$ (A) and $[Fe^{III}(O)Fe^{III}poat]^{+}$ (B), with the simulated spectra shown in (C) and (D), respectively.

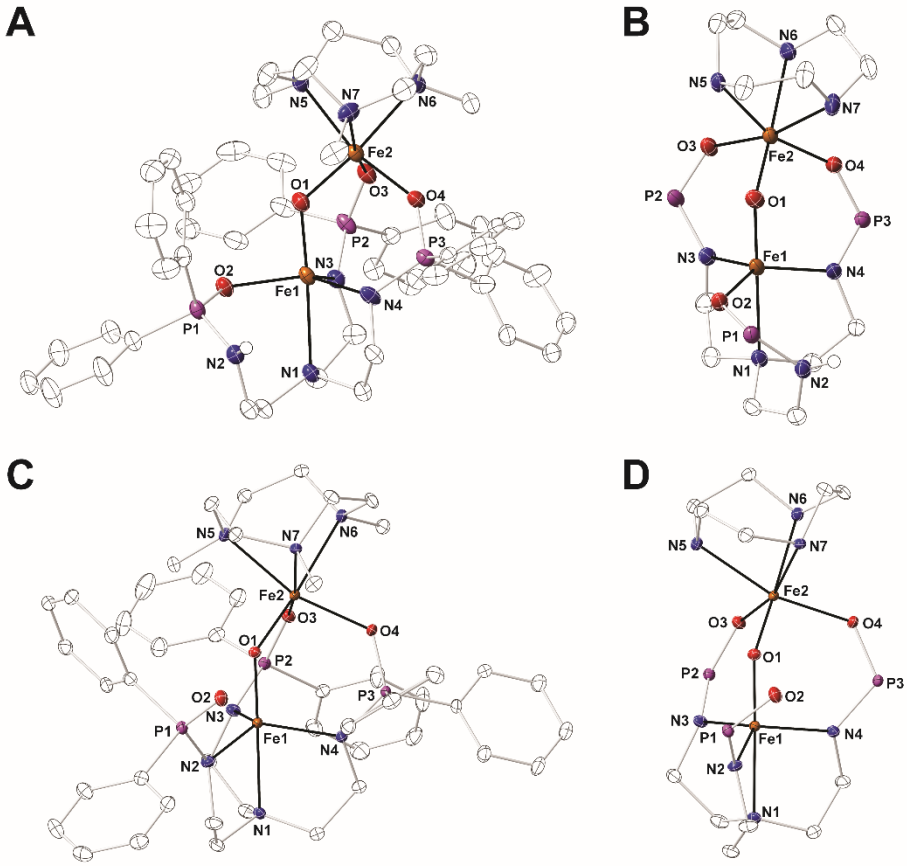

Figure 5.10. Thermal ellipsoid diagram depicting the molecular structure of $[Fe^{III}(O)Fe^{III}Hpoat]^{2+}$ (A) and $[Fe^{III}(O)Fe^{III}poat]^{+}$ (C). Ellipsoids are drawn at the 50 % probability level, and only the hydroxido and phosphinic amide H atoms are show for clarity. The triflate counter anions are outer-sphere and are not interacting with the cation. (B, D) The methyl and phenyl groups are removed, and only the diiron cores are shown for clarity.

in $[Fe^{III}(O)Fe^{III}Hpoat]^{2+}$ are within statistical error, which is often observed in μ-oxido diiron(III) systems. Two phosphinic amido groups of $[Hpoat]^{2-}$ serving as 3-atom bridging ligands and the Fe–O–Fe unit is bent at an angle of 124.73(8)°, which is similar to that observed in $[Fe^{II}(OH)Fe^{III}poat]^{+}$; however, contraction of the Fe–O bonds led to a decrease in the Fe···Fe distance from 3.436(1) to 3.182(1) Å. These metrical parameters are consistent with other triply-bridged μ-oxido diiron(III) complexes that have been reported in the literature.[37,39-42]

The conversion of species with Fe^{II}–(μ-OH)–Fe^{n} cores (n = II, III) to those with Fe^{III}–(μ-O)–Fe^{III} cores is known, presumably because the increased acidity of hydroxido proton unit upon oxidation results in the deprotonation. However, either an external base is needed to scavenge the proton or its whereabouts are unknown.[8,43-47] Within this context, the structure of $[Fe^{III}(O)Fe^{III}Hpoat]^{2+}$ is distinct in that one of phosphinic amido tripodal arms is protonated at its N-atom to form $[Hpoat]^{2-}$, causing a change to an N_3O_2 primary coordination sphere in which the P=O moiety is now bounded to the Fe^{III} center with an Fe1–O2 bond length of 2.016(1) Å. This binding mode results in a strained 7-member chelate ring, and a large distortion in the trigonal plane, as evidenced by a τ_5 value of 0.734. The Fe^{III} site in Fe-TMTACN maintains the same N_3O_3 primary coordination sphere, comprising of the TMTACN ligand, two phosphinic amido groups from the $[Hpoat]^{2-}$ ligand, and a bridging oxido ligand.

Spectroscopic Studies on $[Fe^{III}(O)Fe^{III}Hpoat]^{2+}$. The ⊥-mode X-band EPR spectrum for $[Fe^{III}(O)Fe^{III}Hpoat]^{2+}$ was featureless which indicated a magnetically coupled di-Fe^{III} core. To explore the magnetic properties further we used Mössbauer spectroscopy on ^{57}Fe-enriched samples in both solution and the solid-state. Two distinct doublets were identified in the solid-state sample that have Mössbauer parameters consistent with $S = 5/2$ Fe^{III} centers (Figure 5.11). The one with $\delta/\Delta E_Q$ parameters 0.49/1.83 mm s^{-1} corresponds to a six-coordinate Fe^{III} center and is therefore assigned to

the iron in the auxiliary binding site. The other doublet with parameters of $\delta/\Delta E_Q$ parameters of 0.44/1.26 mm s^{-1} is from the 5-coordinate Fe^{III} center which is coordinated to the $[Hpoat]^{2-}$ ligand. The solution sample displayed an identical spectrum as the solid-state sample, suggesting that the $[Fe^{III}(O)Fe^{III}Hpoat]^{2+}$ complex retains its molecular structure in solution (Figure 5.12.A). Moreover, simulations of Mössbauer spectra collected at high field (7 T) and various temperatures gave a J value of greater than >100 cm^{-1} that is within the range for complexes with antiferromagnetically coupled Fe–(μ-O)–Fe cores.[37] $[Fe^{III}(O)Fe^{III}Hpoat]^{2+}$ has electronic absorption features at λ_{max} (ε, M^{-1} cm^{-1}) = 380 (7000), 517 (970), and 705 nm (130) that are comparable with previously reported tri-bridged μ-oxido di-Fe^{III} species with Fe–O–Fe angles of ~ 120° (Figure 5.13.A,B, black).[39,42,48] Finally, the Fourier transform infrared (FTIR) spectrum of $[Fe^{III}(O)Fe^{III}Hpoat]^{2+}$ contained a broad feature at 3224 cm^{-1} that is assigned to a N–H vibration that is in agreement with protonation of one phosphinic amido group (see above, Figure 5.3.B).

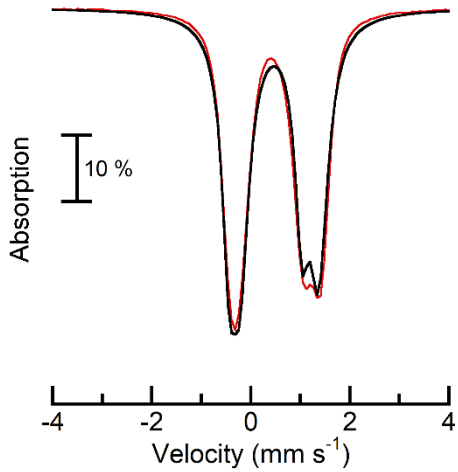

Figure 5.11. ^{57}Fe Mössbauer spectrum (black) of $[^{57}Fe^{III}(O)^{57}Fe^{III}Hpoat]^{2+}$ as a solid sample at zero field. Spectrum was collected at 4.2 K. Simulation of the Mössbauer spectrum is in red.

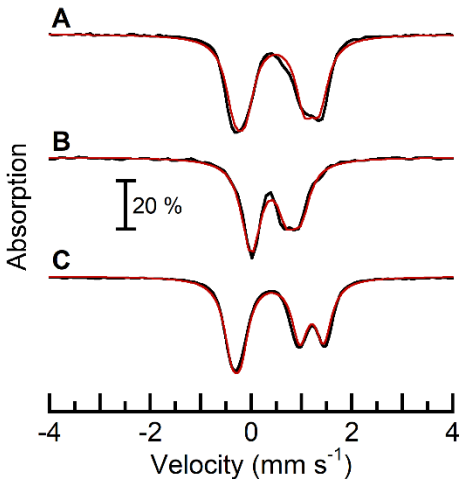

Figure 5.12. ^{57}Fe Mössbauer spectra (black) of $[^{57}Fe^{III}(O)^{57}Fe^{III}Hpoat]^{2+}$ (A), $[^{57}Fe^{III}(OH)^{57}Fe^{III}poat]^{2+}$ (B), and $[^{57}Fe^{III}(O)^{57}Fe^{III}poat]^{+}$ (C) in PrCN. Spectrum was collected at 4.2 K. Simulations of the Mössbauer spectra are in red.

Trapping of [(TMTACN)Fe^{III}–(μ-OH)–Fe^{III}poat]$^{2+}$. The isolation of $[Fe^{III}(O)Fe^{III}Hpoat]^{2+}$ was unexpected because the large structural change from $[Fe^{II}(OH)Fe^{III}Hpoat]^{+}$ did not agree with the reversible $Fe^{III}Fe^{III}/Fe^{II}Fe^{III}$ couple found by cyclic voltammetry (Figure 5.7). Based on the CV, we considered the possibility of whether the initial product of this oxidation was in fact $[(TMTACN)Fe^{III}–(\mu\text{-}OH)–Fe^{III}poat]^{2+}$ ($[Fe^{III}(OH)Fe^{III}poat]^{2+}$) which rearranged during isolation to $[Fe^{III}(O)Fe^{III}Hpoat]^{2+}$. To evaluate this premise, we attempted to trap $[Fe^{III}(OH)Fe^{III}poat]^{2+}$ by treating $[Fe^{II}(OH)Fe^{III}poat]^{+}$ with $[FeCp_2]OTf$ at -80 °C (Scheme 5.2), which produced a new species having absorption features at λ_{max} (ε, M^{-1} cm^{-1}) = 330 (8400), 370 (8100), 483 (sh), 513 (1900), 760 nm (300) (Figure 5.14.A,B). Upon warming, these features were replaced by those associated with $[Fe^{III}(O)Fe^{III}Hpoat]^{2+}$ (Figure 5.14.C,D). The Mössbauer spectrum of this new species has two doublets, which are distinct from those of $[^{57}Fe^{III}(O)^{57}Fe^{III}Hpoat]^{2+}$ with $\delta/|\Delta E_Q|$ values of 0.34/0.56 and 0.44/0.94 mm s^{-1} (Figure 5.12.B). Furthermore, variable-field and temperature measurements gave a J value of 44 cm^{-1}, which is consistent with species having an $[Fe^{III}–(\mu\text{-}OH)–Fe^{III}]$ core.[37] Taken together, these data indicate that $[Fe^{III}(OH)Fe^{III}poat]^{2+}$ can indeed be trapped at lower temperatures, but is unstable at room temperature which leads to the proton transferring to a phosphinic amido group to form $[Fe^{III}(O)Fe^{III}Hpoat]^{2+}$.

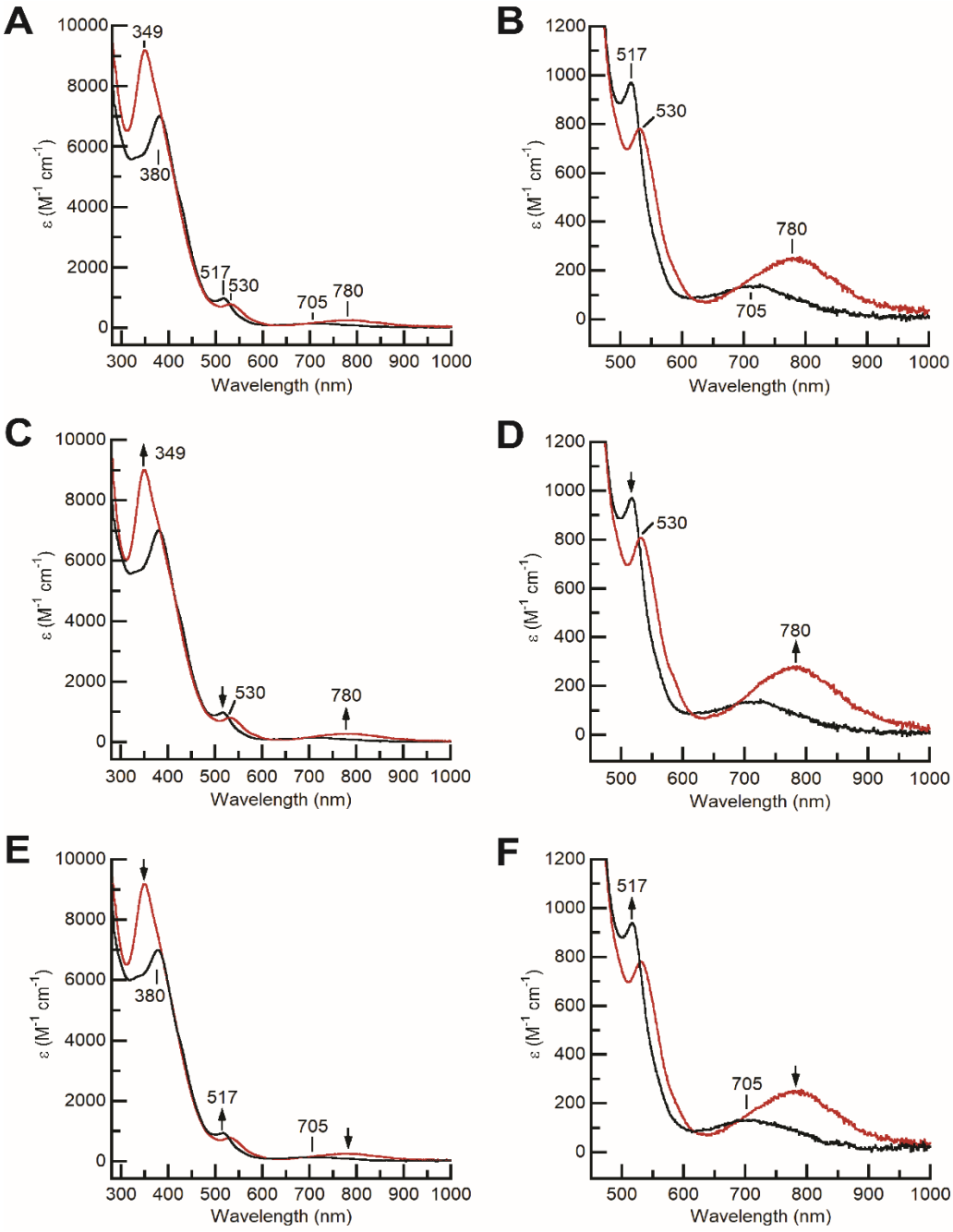

Figure 5.13. (A) Electronic absorbance spectra of $[Fe^{III}(O)Fe^{III}Hpoat]^{2+}$ (black) and $[Fe^{III}(O)Fe^{III}poat]^{+}$ (red), with (B) showing the low energy features. (C) Electronic absorbance spectra of the deprotonation of $[Fe^{III}(O)Fe^{III}Hpoat]^{2+}$ before (black) and after (red) the addition of NEt_3, with (D) showing the changes in the low energy features. (E) Electronic absorbance spectra of the protonation of $[Fe^{III}(O)Fe^{III}poat]^{+}$ before (red) and after (black) the addition of [2,6-HLut]OTf, with (F) showing the changes in the low energy features. Spectra were collected in CH_2Cl_2 at room temperature at a concentration of 0.10 mM.

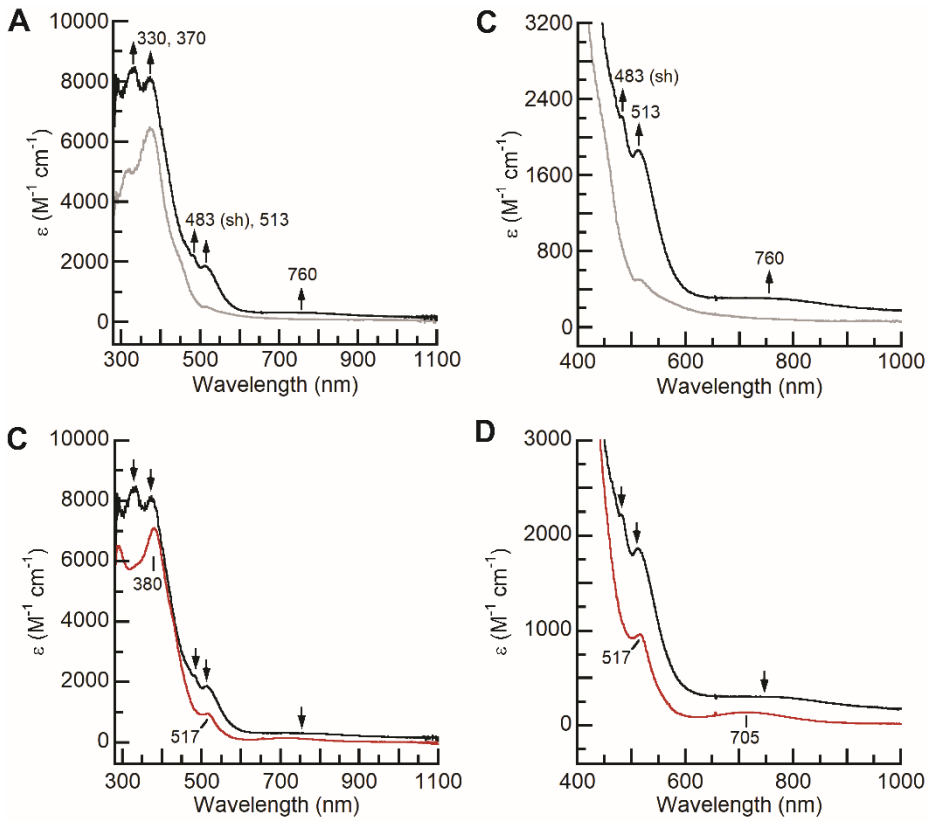

Figure 5.14. (A) Electronic absorbance spectra of the chemical oxidation of $[Fe^{II}(OH)Fe^{III}poat]^{+}$ before (grey) and after (black) the addition of $[FeCp_2]OTf$ at -80 °C, with (B) showing the changes to the low energy features. (C) Electronic absorbance spectra of the conversion of $[Fe^{III}(OH)Fe^{III}poat]^{2+}$ (black) to $[Fe^{III}(O)Fe^{III}Hpoat]^{2+}$ (red) upon warming from -80 °C to room temperature, with (D) showing the changes to the low energy features. The spectra were collected in CH_2Cl_2 at a concentration of 0.10 mM.

Preparation of [(TMTACN)Fe^{III}–(μ-O)–Fe^{III}poat]OTf. The discovery of $[Fe^{III}(O)Fe^{III}Hpoat]^{2+}$ provided the opportunity to examine whether the phosphinic amide group could be deprotonated to form another di-Fe species. We found that treatment of $[Fe^{III}(O)Fe^{III}Hpoat]^{2+}$ with one equivalent of triethylamine caused a change in the absorption spectrum to one with bands at λ_{max} (ε, M^{-1} cm^{-1}) = 349 (9200), 531 (780), and 780 nm (250) (Figure 5.13.C,D). This process is reversible: the spectrum associated with $[Fe^{III}(O)Fe^{III}Hpoat]^{2+}$ was regenerated when treated with one equivalent of 2,6-lutidinium triflate (Figure 5.13.E,F). These results are consistent with formation of $[(TMTACN)Fe^{III}–(\mu\text{-}O)–Fe^{III}poat]^{+}$ ($[Fe^{III}(O)Fe^{III}poat]^{+}$) in which all the phosphinic amide groups are deprotonated (Scheme 5.3). Attempts to isolate this new species via this deprotonation route in

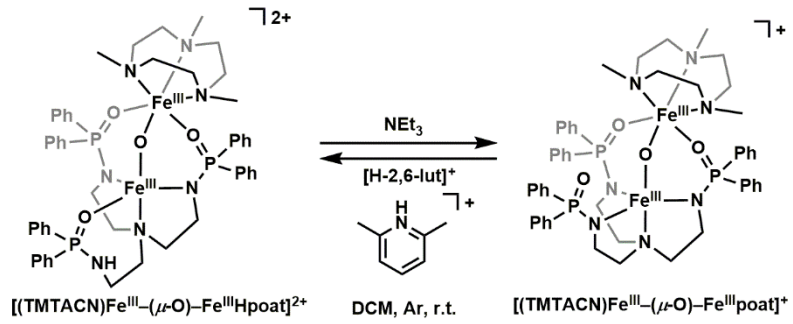

Scheme 5.3. Reversible (de)protonation between $[Fe^{III}(O)Fe^{III}Hpoat]^{2+}$ and $[Fe^{III}(O)Fe^{III}poat]^{+}$.

pure form were unsuccessful because of co-crystallization with the triethylammonium triflate byproduct. We therefore developed an independent synthetic route to this proposed di-Fe species via mixing $[Fe^{IV}poat(O)]^{-}$ with $[Fe^{II}(TMTACN)(OTf)_2]$ to produce a pure salt as red crystals (Scheme 5.4) – the product from the preparation had the identical absorption spectrum as found for the species produced from the deprotonation of $[Fe^{III}(O)Fe^{III}Hpoat]^{2+}$ (Figure 5.13.A,B). The formulation of this species as $[Fe^{III}(O)Fe^{III}poat]^{+}$ was further supported by results obtained by ESI-MS measurements (Figure 5.9.B,D) and FTIR studies (Figure 5.3.C) that showed a lack of features associated with either an O–H or N–H vibration. We again used XRD methods to confirm the molecular structure for $[Fe^{III}(O)Fe^{III}poat]^{+}$ (Figure 5.10.C,D, Table 5.1). The structure revealed that the N_4O primary coordination sphere from $[poat]^{3-}$ was restored with all the phosphinic amide arms being deprotonated and their N-atoms coordinated to the Fe^{III} center. This coordination provides a nearly ideal trigonal bipyramidal geometry (τ_5 = 0.950), in contrast to what was observed in $[Fe^{III}(O)Fe^{III}Hpoat]^{2+}$(see above). The Fe^{III} site coordinated to Fe-TMTACN is 6-coordinated with

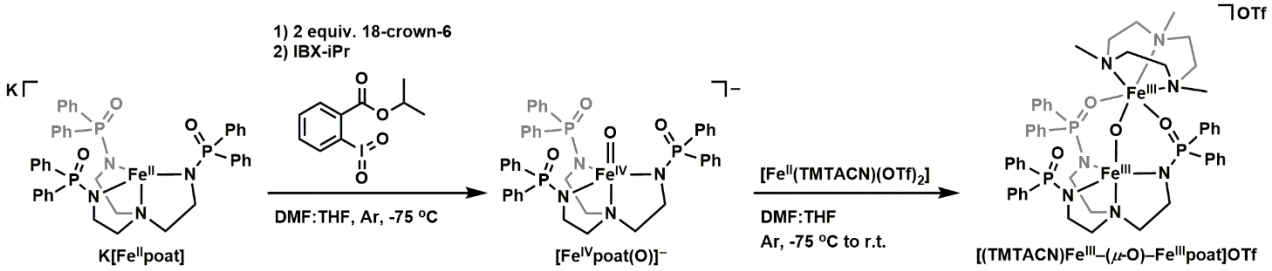

Scheme 5.4. Preparative route for $[Fe^{III}(O)Fe^{III}poat]^{+}$.

an N_3O_3 primary coordination sphere, consisting of the TMTACN ligand, two O-atoms from the phosphinic amido groups from the $[poat]^{3-}$ ligand, and a bridging oxido ligand. Comparing the structures of $[Fe^{III}(O)Fe^{III}Hpoat]^{2+}$ and $[Fe^{III}(O)Fe^{III}poat]^{+}$ showed that deprotonation had no structural effect on the Fe–(μ-O)–Fe core (Table 5.1). For instance, the Fe1–O1 and Fe2–O1 bond lengths in the two complexes are statistically equivalent, as are the Fe1···Fe2 separations (3.182(1) and 3.161(1) Å) and Fe1–O1–Fe2 bond angles (124.73(8) and 123.82(10)º). The phosphinic amido group that once participated in forming an intramolecular H-bond (Figure 5.6 for $[Fe^{II}(OH)Fe^{III}poat]^{+}$) is tilted away from the oxido ligand in $[Fe^{III}(O)Fe^{III}poat]^{+}$ presumably because of electrostatic repulsion (note that the O1···O2 distance is 3.212(3) Å).

The Mössbauer spectrum of $[^{57}Fe^{III}(O)^{57}Fe^{III}poat]^{+}$ was fit with two distinct doublets for two Fe centers, with $\delta/|\Delta E_Q|$ values of 0.38/1.16 and 0.53/1.86 mm s^{-1} (Figure 5.12.C). These parameters are consistent with high spin Fe^{III} centers, and the silent EPR spectrum supports an S = 0 ground state. Further variable field and temperature measurements allowed J to be estimated as > 100 cm^{-1}, which is consistent with a Fe–(μ-O)–Fe core.[37]

Higher Valent Species: [(TMTACN)Fe^{III}–(μ-O)–Fe^{IV}poat]$^{2+}$. The isolation of $[Fe^{III}(O)Fe^{III}poat]^{+}$ provided the opportunity to investigate more oxidized di-Fe species. Evidence was provided from cyclic voltammetry studies on $[Fe^{III}(O)Fe^{III}poat]^{+}$ which exhibited a reversible one-electron redox event at +0.55 V, which is assigned to the $Fe^{III}Fe^{IV}/Fe^{III}Fe^{III}$ couple (Figure 5.15.A). The reversibility of the electrochemical event and the relatively moderate potential suggested the one-electron oxidized species can be accessed by a chemical oxidant. Therefore, the treatment of $[Fe^{III}(O)Fe^{III}poat]^{+}$ with one equivalent of $[N(p\text{-}C_6H_4Br)_3]PF_6$ ($E_{1/2}$ = + 0.70 V vs. $[FeCp_2]^{+/0}$ in CH_2Cl_2)[38] at -90ºC in CH_2Cl_2 was monitored spectrophotometrically, and produced a new species

with absorbance features at λ_{max} = 440 (sh), 515 (sh), 620 (2700), 810 (sh), ~1100 nm (Scheme 5.5, Figure 5.15.B).

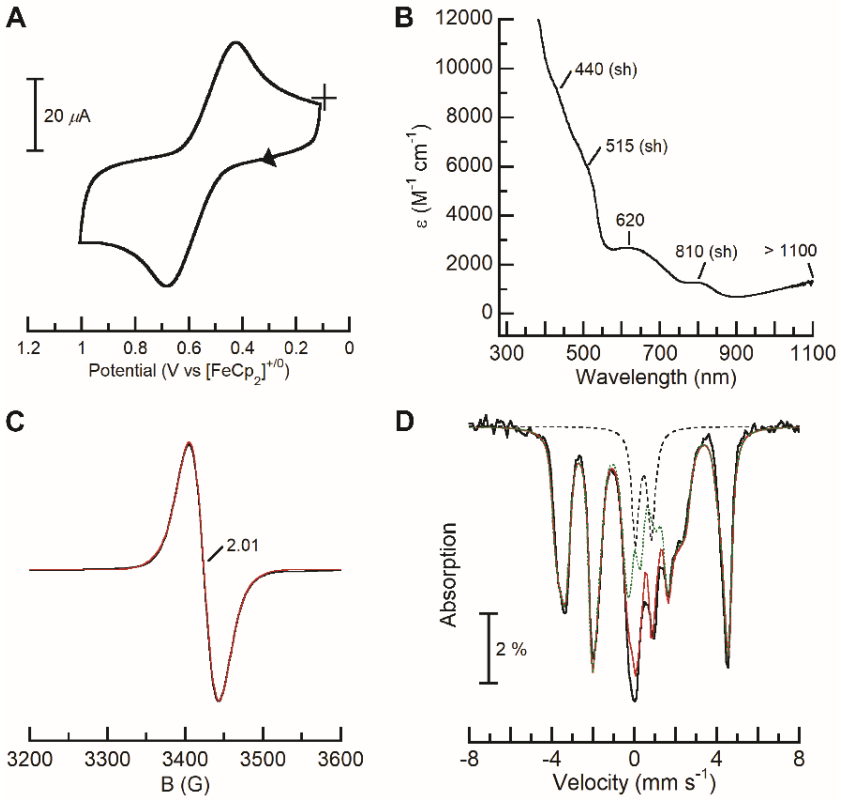

Figure 5.15. (A) Cyclic voltammogram of $[Fe^{III}(O)Fe^{III}poat]^+$ collected at scan rate of 1 V s^{-1} in in CH_2Cl_2. (B) Electronic spectrum of $[Fe^{III}(O)Fe^{IV}poat]^{2+}$ at -90 °C. Spectrum collected at 0.20 mM in CH_2Cl_2. (C) EPR spectrum (black) of the oxidation of $[Fe^{III}(O)Fe^{III}poat]^+$ collected at 10 K in CH_2Cl_2. Simulation for EPR spectrum is in red. (D) ^{57}Fe Mössbauer spectrum (black) of the oxidation of $[^{57}Fe^{III}(O)^{57}Fe^{III}poat]^+$ collected at 4.2 K and 0.45 kG in PrCN. The spectrum contains two species: $[^{57}Fe^{III}(O)^{57}Fe^{IV}poat]^{2+}$ (green dotted trace, 85%) and an unknown differic species (black dashed line, 15%). The summation of these two species gives the overall simulated plot (red).

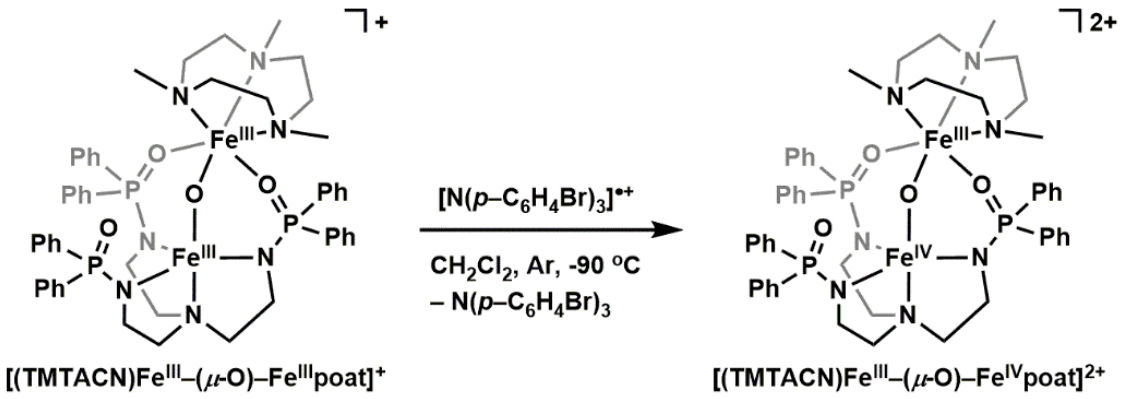

Scheme 5.5. Oxidation to $[Fe^{III}(O)Fe^{IV}poat]^{2+}$.

Support for this assignment came from EPR and Mössbauer results. The EPR spectrum of $[Fe^{III}(O)Fe^{IV}poat]^{2+}$ revealed an isotropic $S = 1/2$ signal centered at $g \sim 2.01$ that quantified to 92% of the expected concentration (5 mM, Figure 5.15.C). In addition, the Mössbauer spectrum of $[Fe^{III}(O)Fe^{IV}poat]^{2+}$ was simulated to consist of an $S = 1/2$ antiferromagnetically coupled system (88% yield) containing a high spin Fe^{III} and Fe^{IV} centers, with $\delta/\Delta E_Q$ values of 0.00/+0.53 and 0.46/-1.11 mm s^{-1}, respectively (Figure 5.15.D). These parameters agree with the formulation of $[Fe^{III}(O)Fe^{IV}poat]^{2+}$. This oxidation is reversible upon treatment of a reductant by both UV-vis (Figure 5.16) and EPR spectroscopy (Figure 5.17).

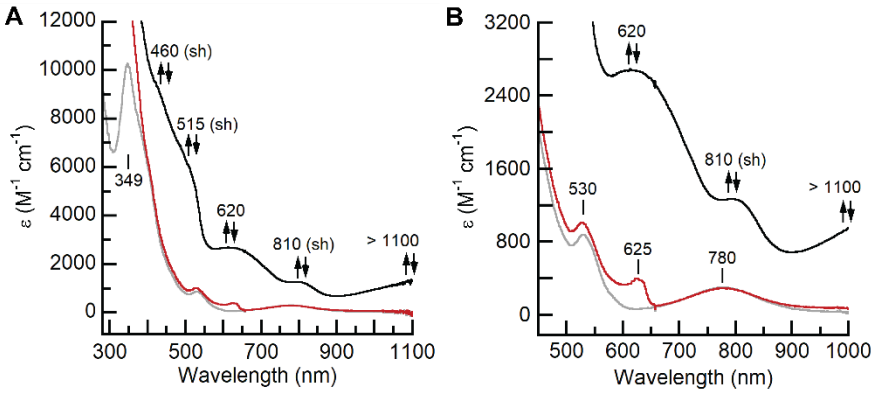

Figure 5.16. (A) Electronic absorbance spectra of the reversible oxidation of $[Fe^{III}(O)Fe^{III}poat]^{+}$ before (grey) and after (black) the addition of $[N(p\text{-}C_6H_4Br)_3]PF_6$, and after the addition of $FeCp_2$ (red), with (B) showing the changes to the low energy features. The spectra were collected in CH_2Cl_2 at -90 °C at a concentration of 0.10 mM.

Reactivity. We sought to investigate the reactivity of $[Fe^{III}(O)Fe^{IV}poat]^{2+}$ towards organic substrates that have cleavable X–H bonds (X = N, O, Scheme 5.6). Initial studies used 1,2-diphenylhydrazine (DPH, $BDFE_{N-H}(DMSO)$ = 67.1 kcal mol^{-1})[49] which when allowed to react with $[Fe^{III}(O)Fe^{IV}poat]^{2+}$ at -90°C showed optical changes that are consistent with formation of $[Fe^{III}(OH)Fe^{III}poat]^{2+}$ (λ_{max} = 483, 513, 760 nm, Figure 5.18.A,B). Upon warming, the hydroxido-bridged species further converted to $[Fe^{III}(O)Fe^{III}Hpoat]^{2+}$ with diagonstic features at λ_{max} = 517 and 705 nm (Figure 5.18.C,D). The organic product azobenzene was identified using gas chromatography-mass spectrometry (GC-MS) and NMR spectroscopy, and the absence of DPH in both methods supports

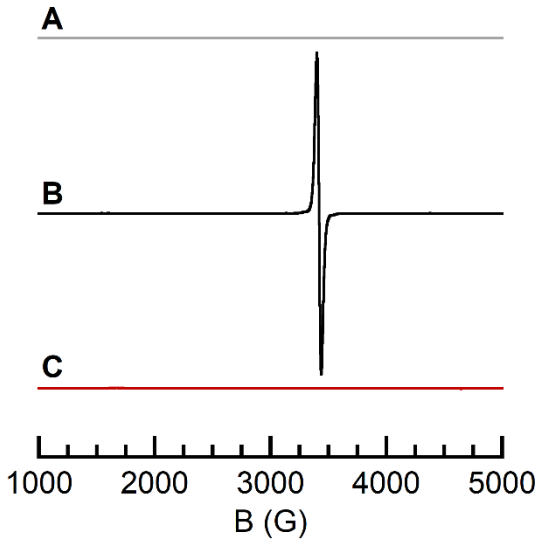

Figure 5.17. EPR spectra of the reversible oxidation of $[Fe^{III}(O)Fe^{III}poat]^{+}$ before (A, grey) and after (B, black) the addition of $[N(p\text{-}C_6H_4Br)_3]PF_6$, and after the addition of $FeCp_2$ (C, red). Spectra were collected in CH_2Cl_2 at 10 K.

the full conversion of DPH to azobenzene (Figures 5.19,5.20). These findings indicate that DPH undergoes initial proton-coupled electron transfer (PCET) in which proton transfer first occurs at the oxido ligand to form a bridging hydroxido ligand, and electron transfer occurs to reduce the Fe^{IV} center to Fe^{III}. Warming the reaction mixture to room temperature promotes an intramolecular

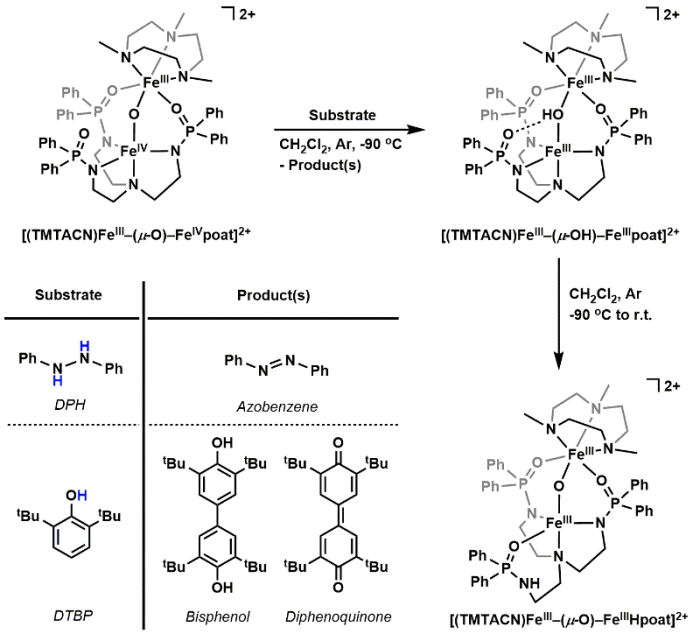

Scheme 5.6. Substrate reactivity of $[Fe^{III}(O)Fe^{IV}poat]^{2+}$.

proton transfer from the hydroxido ligand to one of the phosphinic amido groups to form $[Hpoat]^{2-}$ as we have observed previously.

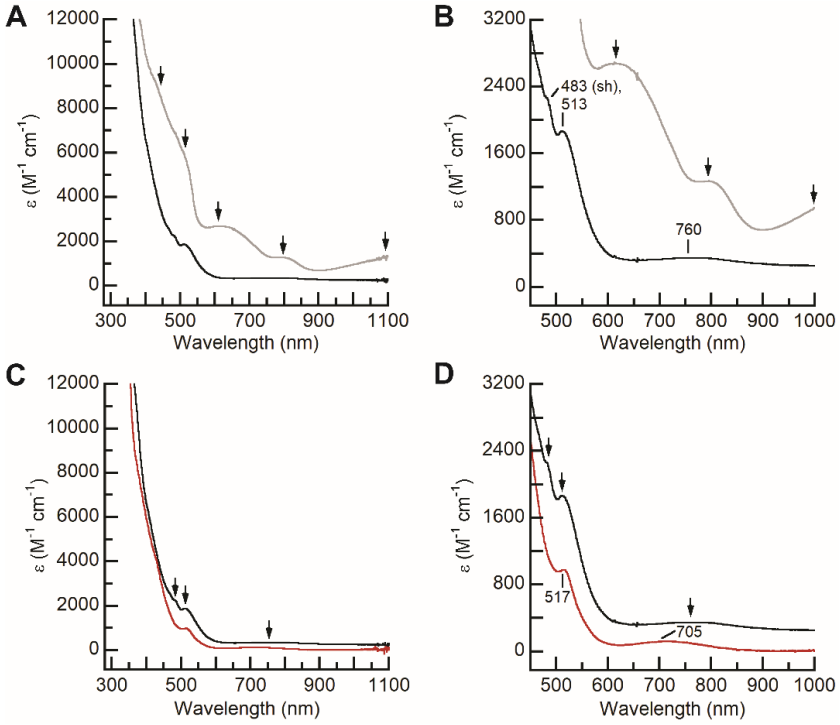

Figure 5.18. (A) Electronic absorbance spectra of the conversion of $[Fe^{III}(O)Fe^{IV}poat]^{2+}$ before (grey) and after (black) the addition of DPH at -90 °C, with (B) showing the changes to the low energy features. (C) Electronic absorbance spectra of the conversion of $[Fe^{III}(OH)Fe^{III}poat]^{2+}$ (black) to $[Fe^{III}(O)Fe^{III}Hpoat]^{2+}$ (red) upon warming from -90 °C to room temperature, with (D) showing the changes to the low energy features. The spectra were collected in CH_2Cl_2 at a concentration of 0.10 mM.

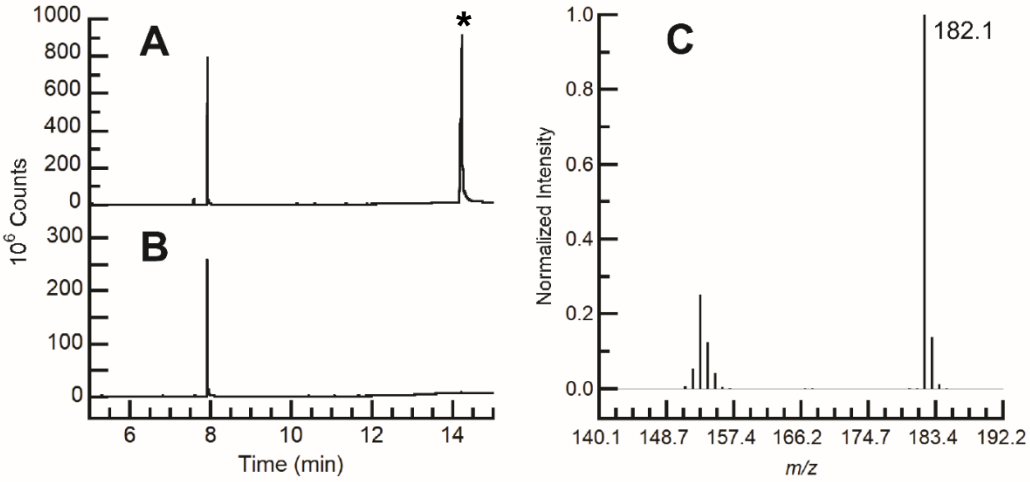

Figure 5.19. Gas chromatograms of (A) reaction between $[Fe^{III}(O)Fe^{IV}poat]^{2+}$ and DPH, and (B) azobenzene standard. * indicates the oxidant byproduct ($N(p\text{-}C_6H_4Br)_3$). (C) Mass spectrum of the species detected t = 7.9 min in gas chromatography corresponds to azobenzene (182.1 m/z).

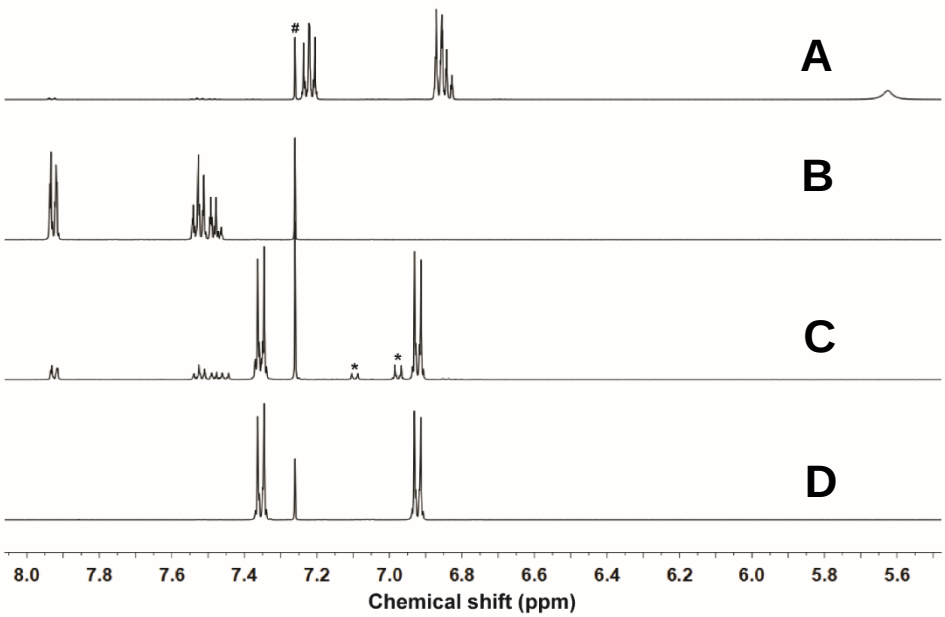

Figure 5.20. NMR spectra of DPH standard (A), azobenzene standard (B), bulk reaction of $[Fe^{III}(O)Fe^{IV}poat]^{2+}$ and DPH (C), and N(*p*-$C_6H_4Br)_3$ standard (D). Spectra were collected in $CDCl_3$ at room temperature. # indicates $CHCl_3$ solvent peak. * indicates unknown impurities.

We also explored the reactivity of $[Fe^{III}(O)Fe^{IV}poat]^{2+}$ with phenols to model the mechanistic steps proposed to occur in RNR R2 Class Ia whereby intermediate with an Fe^{III}–(μ-O)–Fe^{IV} core (denoted X) is kinetically competent to cleave the O–H bond of a nearby tyrosine residue.[11,20] Addition of excess 2,6-di-*tert*-butyl-phenol (DTBP, $BDFE_{O-H}$(DMSO) = 80.5 kcal mol^{-1})[49] at -90 °C in CH_2Cl_2 caused the features associated with $[Fe^{III}(O)Fe^{IV}poat]^{2+}$ to slowly disappear at a rate of k_{obs} = 0.0013(2) s^{-1} (Figure 5.21.A,C). Monitoring this process spectrophotometrically produced an absorption spectrum with bands that resembles those of $[Fe^{III}(OH)Fe^{III}poat]^{2+}$ but the spectrum was complicated by additional, unidentified features at λ_{max} = 650 (sh) and > 1100 nm. Support for the consumption of $[Fe^{III}(O)Fe^{IV}poat]^{2+}$ during the reaction comes from the disappearance of its characteristic isotropic EPR feature g = 2.01 (Figure 5.22). Moreover, warming the reaction mixture to room temperature produced the diagnostic absorption spectrum of $[Fe^{III}(O)Fe^{III}Hpoat]^{2+}$ (Figure 5.21.B). The organic products, 3,3',5,5'-tetra-*tert*-butyl[1,1'-biphenyl]-4,4'-diol (bisphenol) and 3,3',5,5'-tetra-*tert*-butyldiphenoquinone (diphenoquinone), were detected by GC-MS with a combined conversion of greater than 90 % (Figure 5.23). These results suggest DTBP undergoes

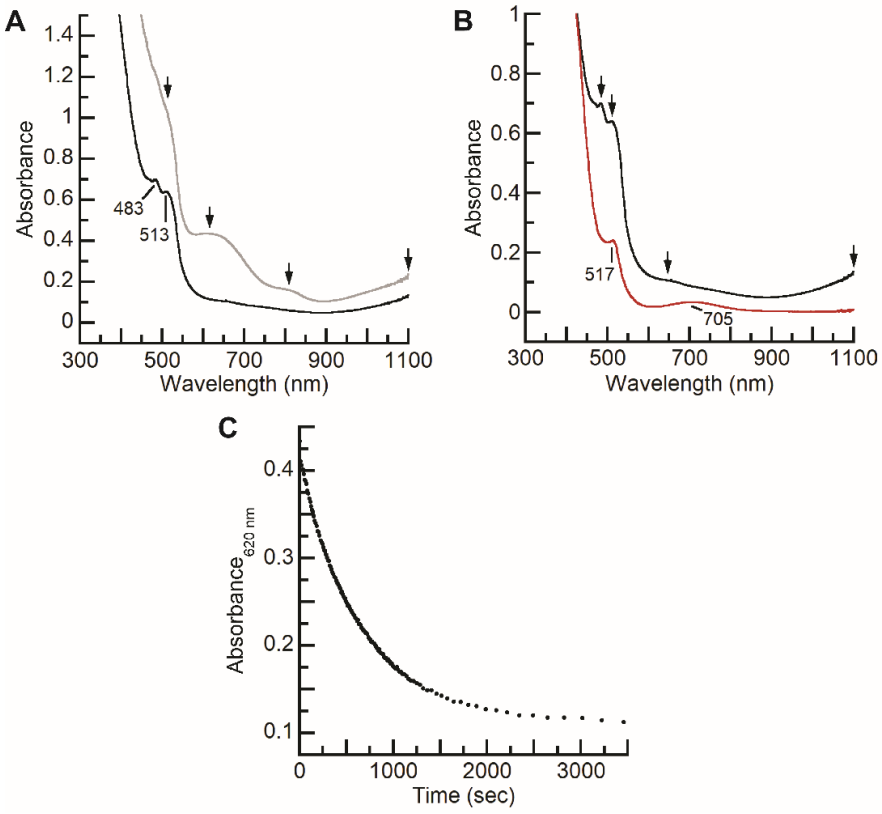

Figure 5.21. (A) Electronic absorbance spectra of the conversion of $[Fe^{III}(O)Fe^{IV}poat]^{2+}$ before (grey) and after (black) the addition of DTBP at -90 °C. (B) Electronic absorbance spectra of the subsequent conversion of $[Fe^{III}(OH)Fe^{III}poat]^{2+}$ (black) to $[Fe^{III}(O)Fe^{III}Hpoat]^{2+}$ (red) upon warming from -90 °C to room temperature. (C) Time trace of the decrease of the λ_{max} = 620 nm feature upon addition of DTBP. Spectra were collected in CH_2Cl_2 at a concentration of 0.23 mM.

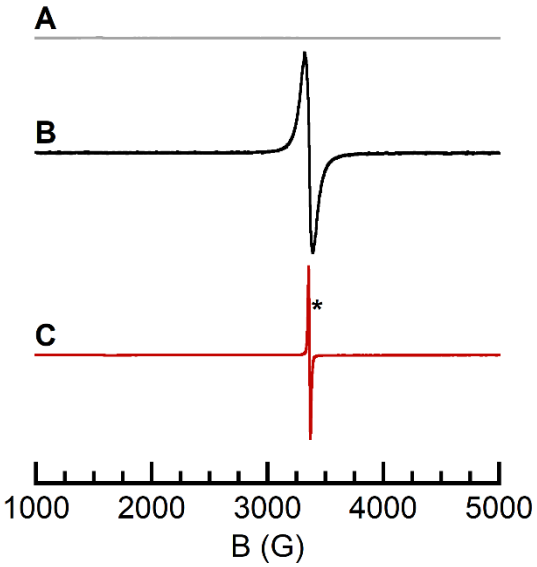

Figure 5.22. EPR spectra of $[Fe^{III}(O)Fe^{III}poat]^{+}$ (A, grey), after the addition of $[N(p\text{-}C_6H_4Br)_3]PF_6$ (B, black), then after the addition of 10 equiv of 2,6-*t*Bu-PhOH (C, red). Asterisk (*) indicates unreacted $[Fe^{III}(O)Fe^{IV}poat]^{2+}$ (< 5 %). Spectra were collected in CH_2Cl_2 at 77 K.

PCET with $[Fe^{III}(O)Fe^{IV}poat]^{2+}$ to initially produce $[Fe^{III}(OH)Fe^{III}poat]^{2+}$ and the corresponding phenoxyl radical. 2,6-*tert*-butyl-phenoxyl radical is known to react through bimolecular homo-coupling at the para-position to produce bisphenol,[50-52] which further reacts with remaining $[Fe^{III}(O)Fe^{IV}poat]^{2+}$ to produce diphenoquinone.[53,54]

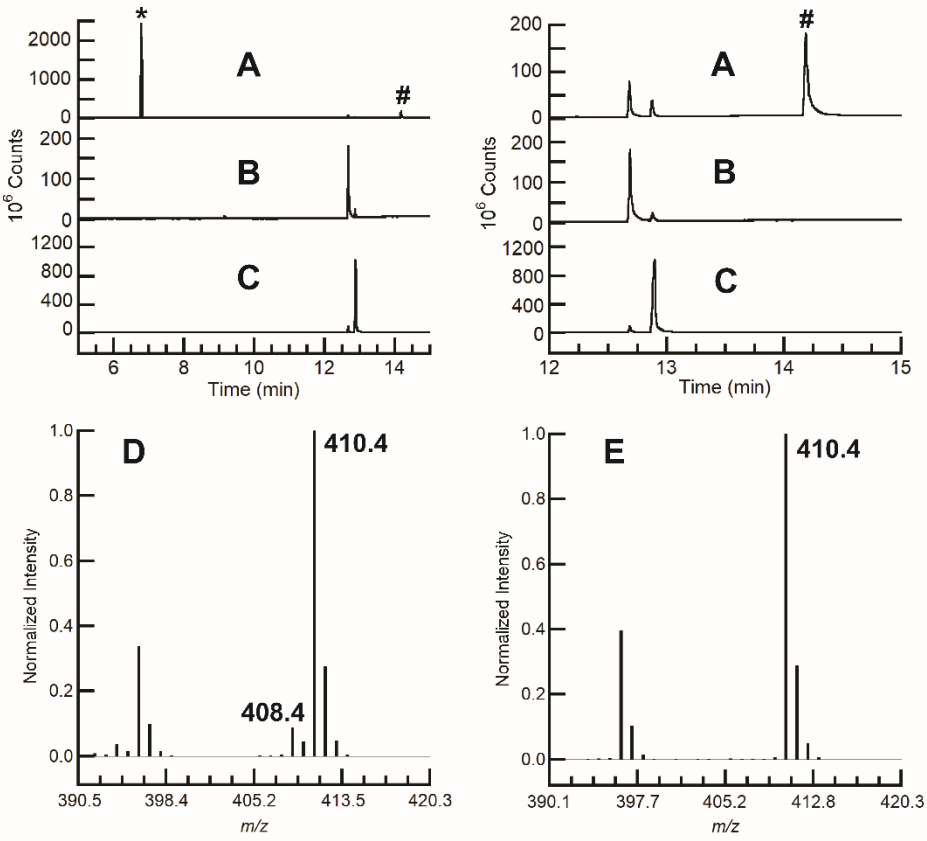

Figure 5.23. Gas chromatograms of (A) the reaction between $[Fe^{III}(O)Fe^{IV}poat]^{2+}$ and DTBP, (B) diphenoquinone standard, and (C) bisphenol standard. The left panel contains the full chromatograms, and the right panel contains the chromatograms at t = 12 to 15 min. * indicates unreacted DTBP, and # indicates the oxidant byproduct ($N(p\text{-}C_6H_4Br)_3$). (D) Mass spectrum of the species detected t =12.7 min in gas chromatography corresponds to diphenoquinone (408.4 m/z). (E) Mass spectrum of the species detected t = 12.9 min in gas chromatography corresponds to bisphenol (410.4 m/z).

Discussion

Spanning 4 Oxidation States. Di-Fe cores within the active sites of metalloproteins are known to access a variety of oxidation levels during turnover that are often accompanied by structural changes.[18] The active site within RNR R2 is an example and is known to proceed through a series of oxidation steps

from an di-Fe^{II} core to one that contains an $Fe^{III}Fe^{IV}$ center (intermediate X).[10-13,20,21] We are only aware of one synthetic system that is able to duplicate these types of oxidation steps[22,45,46] – in order to bridge this gap, we have developed a di-Fe complex that span four oxidation states: $Fe^{II}Fe^{II}$, $Fe^{II}Fe^{III}$, $Fe^{III}Fe^{III}$, and $Fe^{III}Fe^{IV}$ (Scheme 5.7; Table 5.2). Their preparation was initiated using an assembly approach that coupled the Fe^{III}–OH complex $[Fe^{III}poat(OH)]^-$ with $[Fe^{II}(TMTACN)(OTf)_2]$ to form the bimetallic complex $[Fe^{II}(OH)Fe^{III}poat]^+$. This mixed valent complex exhibited two reversible redox events (Figure 5.7) at relatively moderate potentials that allow access to both the one-electron reduced and oxidized analogs. The most reduced state, $[Fe^{II}(OH)Fe^{II}poat]$ was accessed by chemical reduction and we were able to trap the oxidized $[Fe^{III}(OH)Fe^{III}poat]^{2+}$ at low temperatures. However, we found that this di-Fe^{III} complex was

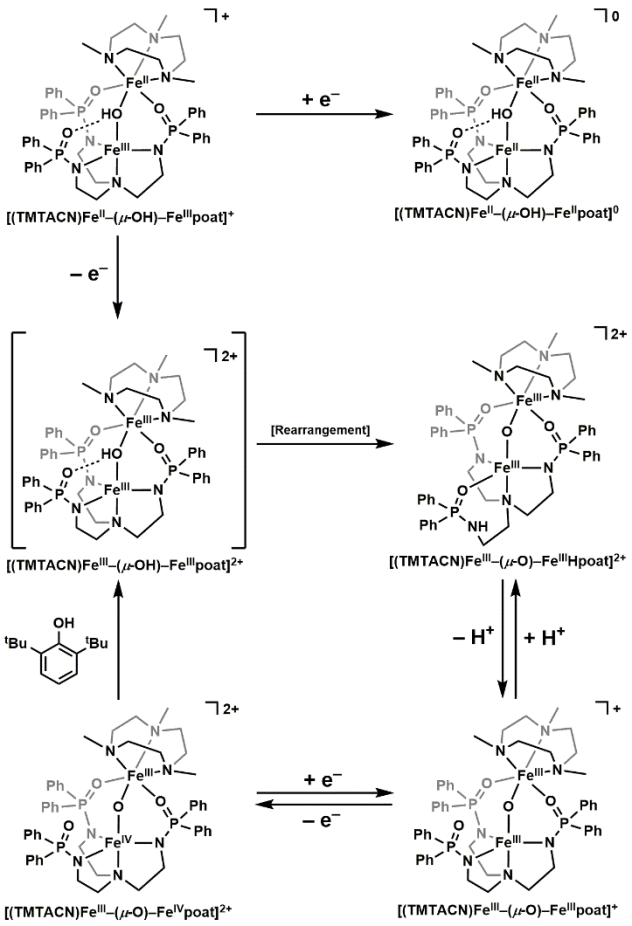

Scheme 5.7. Six diiron complexes spanning four oxidation levels and various protonation states.

unstable at room temperature and rearranged to $[Fe^{III}(O)Fe^{III}Hpoat]^{2+}$, which can be treated with external bases to produce $[Fe^{III}(O)Fe^{III}poat]^{+}$ and then chemically oxidize to $[Fe^{III}(O)Fe^{IV}poat]^{2+}$ at -90°C.

Table 5.2. Summary of the Spectroscopic Features for the di-Fe Complexes.

Complex	Optical features[a]	S	Fe_{TMTACN} S ($\delta/\Delta E_Q$)[b]	Fe_{poat} S ($\delta/\Delta E_Q$)[b]	J[c]
$[Fe^{II}(OH)Fe^{III}poat]^{+}$	315 (sh), 372 (6400), 460 (sh), 520 (sh)	1/2	2 (1.20/-2.84)	5/2 (0.34/-0.72)	30
$[Fe^{II}(OH)Fe^{II}poat]$	350 (sh)	0	2 (1.22/2.37)	2 (1.03/3.38)	20
$[Fe^{III}(O)Fe^{III}Hpoat]^{2+}$	380 (7000), 517 (970), 705 (130)	0	5/2 (0.49/1.83)	5/2 (0.44/1.26)	> 100
$[Fe^{III}(OH)Fe^{III}poat]^{2+}$	330 (8400), 370 (8100), 483 (sh), 513 (1900), 760 (300)	0	5/2 (0.44/0.94)	5/2 (0.34/0.56)	44
$[Fe^{III}(O)Fe^{III}poat]^{+}$	349 (9200), 531 (780), 780 (250)	0	5/2 (0.53/-1.86)	5/2 (0.38/1.16)	> 100
$[Fe^{III}(O)Fe^{IV}poat]^{2+}$	440 (sh), 515 (sh), 620 (2700), 810 (sh), ~ 1100	1/2	5/2 (0.46/-1.11)	2 (0.00/+0.53)	n.d.

[a] λ_{max}, nm (ε, M^{-1} cm^{-1}). [b] mm s^{-1}. [c] cm^{-1} ($\mathcal{H} = JS_1 \cdot S_2$); obtained by Mössbauer. N.d. = not determined.

Multi-Functional Properties of [poat]$^{3-}$ and Intramolecular Proton Transfer. The assembly of the di-Fe complexes involved two of the phosphinic amido groups from $[Fe^{III}poat(OH)]^{-}$ that coordinate the another Fe center through their P=O units. Together with the hydroxido/oxido ligand, triply bridged di-Fe cores are produced. Our electrochemical studies found that the P=O groups can stabilize Fe^{III} centers at relative low potentials, which could not be achieved with related tripodal ligands such as those with sulfonamido groups.[34,35] The third phosphinic amido arm is distinct from the other two and served multiple functions within this series of complexes. In $[Fe^{II}(OH)Fe^{III}poat]^{+}$ it is an H-bond acceptor to promote the formation of an intramolecular bond with the bridging hydroxido ligand. Room temperature oxidation produced the isolatable $[Fe^{III}(O)Fe^{III}Hpoat]^{2+}$ with

the distinct arm now serving as a site of protonated at its N-atom. This intramolecular proton transfer (PT) causes formation of an Fe^{III}–(μ-O)–Fe^{III} core and a structural rearrangement with the protonated phosphinic amide coordinating to the Fe center through its P=O unit. We are not aware of an example where an intramolecular proton transfer occurs within a synthetic construct; however, this type of process has been observed with the active sties of metalloproteins. For instance, in the binding of dioxygen in hemerythrin, the resting state Fe^{II}–(μ–OH)–Fe^{II} core converts to Fe^{III}–(μ–O)–Fe^{III}(OOH), as the proton on the hydroxido bridge transfers to the O_2 adduct during the oxygenation process.[8,55] The dual binding modes of the phosphinic amido/amide thus provides a dynamic coordination sphere to store a proton and stabilize higher valent species.

Although $[Fe^{III}(O)Fe^{III}Hpoat]^{2+}$ is the product isolated from the room temperature oxidation, our results suggest that the initial species formed is $[Fe^{III}(OH)Fe^{III}poat]^{2+}$ because of the reversibility of this process in the cyclic voltammogram. Moreover, when the oxidation is done at -80°C, we detect a species whose properties are consistent with $[Fe^{III}(OH)Fe^{III}poat]^{2+}$. We correlated the absorption spectra and the experimentally determined *J* spin exchange constants from Mössbauer measurements to gauge the protonation state of the O-atom bridge in each complex. It should be noted that most di-Fe complexes with bridging hydroxido ligand have *J*-values of less than 50 cm^{-1}, whereas the values for oxido bridged species are substantially large ($J > 60$ cm^{-1}).[37] The most reduced form, $[Fe^{II}(OH)Fe^{II}poat]$, has a $J = 20$ cm^{-1}, which supports the assignment of a bridging hydroxido ligand. For $[Fe^{II}(OH)Fe^{III}poat]^{+}$, the *J*-value increases to 30 cm^{-1}, and upon further oxidation, a *J*-value of 44 cm^{-1} was determined for $[Fe^{III}(OH)Fe^{III}poat]^{2+}$. The incremental rise in the *J* values is consistent with the increased Lewis acidity of the Fe centers and Brönsted acidity of the Fe–(μ–OH)–Fe core, which results in strengthened intramolecular H-bonding interactions between the OH and the P=O groups, and increased oxido character in the bridging

ligand. Finally, $[Fe^{III}(O)Fe^{III}Hpoat]^{2+}$ and $[Fe^{III}(O)Fe^{III}poat]^{+}$ had *J*-values of greater than 100 cm^{-1} that are consistent with oxido-bridged di-Fe cores.

Comparison of $[Fe^{III}(O)Fe^{IV}poat]^{2+}$ with Other Complexes. The oxidation of $[Fe^{III}(O)Fe^{III}poat]^{+}$ to $[Fe^{III}(O)Fe^{IV}poat]^{2+}$ was achieved in good yield (> 80 %), allowing us to perform magnetic studies on this high valent species. Our X-band EPR and Mössbauer data support the assignment of a mixed valent species with an $S = 1/2$ spin ground state. The EPR spectrum contained an isotropic feature centered at $g = 2.01$ (Figure 5.15.C) is consistent with Fe^{III}–(μ–O)–Fe^{IV} cores found in biological and other synthetic systems, including the intermediate X in RNR R2.[20,23,29,30,56] Our simulations of the Mössbauer spectra yielded two distinct Fe centers with $\delta/\Delta E_Q$ values of 0.00/0.53 mm s^{-1} and 0.46/-1.11 mm s^{-1} that are consistent with the valence localized assignment of $S = 2$ Fe^{IV} and $S = 5/2$ Fe^{III} (Figure 5.15.D), and are similar to those previously reported in the literature.[20,23,30,56] The trianionic $[poat]^{3-}$ framework that enforces local C_3 symmetry likely stabilizes high-spin Fe^{IV} center within the tripodal site. There have been reports of the detection and/or isolation of Fe^{III}–(μ–O)–Fe^{IV} species in various ligands;[22,23,25,26,29,30,50,51,57] however, $[Fe^{III}(O)Fe^{IV}poat]^{2+}$ is different in that the bimetallic core is housed within a unsymmetric ligand framework, and both Fe centers are high spin, making the complex a suitable synthetic model for high valent non-heme di-Fe active sites in proteins.

Reactivity Comparison with RNR. We explored the reactivity of $[Fe^{III}(O)Fe^{IV}poat]^{2+}$ towards external substrates to gain insights into the species that are formed after X–H bond cleavage. DPH and DTBP were used as substrates and in both instances the reaction mixtures show optical changes that are consistent with the generation of $[Fe^{III}(OH)Fe^{III}poat]^{2+}$ at -90°C (Figures 5.18,5.21). The results are consistent with a PCET process, whereby the proton is transferred to the bridging oxido ligand, and the electron is transferred to the Fe^{IV} center. The organic products in both reactions are

consistent with the homolytic cleavage of the X–H bonds to initially form radical species that reacts further to give more stable products. The $[Fe^{III}(OH)Fe^{III}poat]^{2+}$ species also converts to the more thermal stable $[Fe^{III}(O)Fe^{III}Hpoat]^{2+}$ species upon warming to room temperature. The ability of the distinct phosphinic arm in $[poat]^{3-}$ to be protonated while remaining coordinate to an Fe^{III} center highlights one method for controlling intramolecular PT within species having Fe–(μ–O)–Fe cores. This type of process may have relevance to the chemistry observed within the R2 subunit of RNR Class Ia.[10-13] The catalytically competent species, intermediate X, also contains Fe^{III}–(μ–O)–Fe^{IV} core and homolytically cleaves the O–H bond in a nearby tyrosine residue to produce a Fe^{III}–(μ–O)–Fe^{III} core with concomitant generation of a tyrosyl radical.[20] One common mechanism suggests the proton from this process is transferred to a terminally coordinated hydroxido ligand to form an aqua ligand.[2,11] We suggest a modified version of this mechanism in that the initial site of protonation is the oxido bridge to give an Fe^{III}–(μ–OH)–Fe^{III} core (Scheme 5.8). Similar to what we observed for $[Fe^{III}(OH)Fe^{III}poat]^{2+}$, intramolecular PT then occurs to form the aqua ligand. This additional PT step help stabilize the products by retaining the more stable Fe–(μ–O)–Fe core and controlling the proton movement to avoid additional unproductive reactions. Within this context, the active site in RNR and the di-Fe complexes of $[poat]^{3-}$ share similar structural aspects including dynamic coordination spheres that allows for the proton rearrangement for enhanced stability.

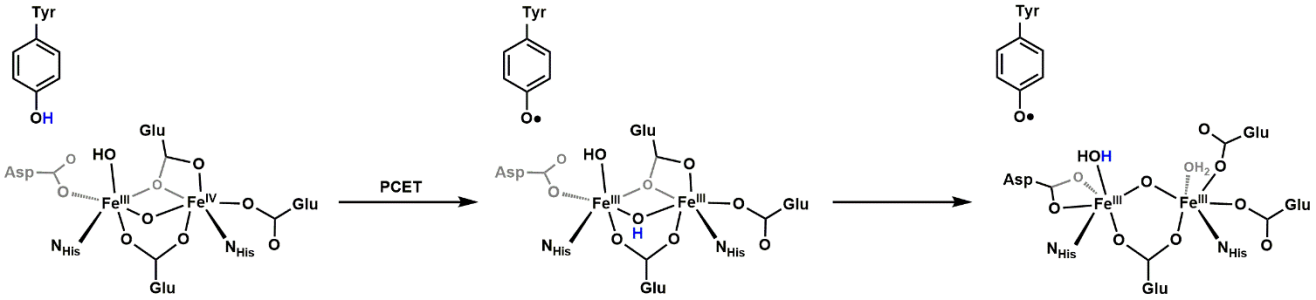

Scheme 5.8. Proposed modification to the mechanism in RNR R2 Ia: upon homolytic cleavage of the tyrosine O–H bond, the electron goes to the Fe^{IV} center, and the oxido bridge is first protonated, before the proton transfers to the terminal hydroxido ligand.

Conclusion & Outlook

In this chapter, the preparation of a series of di-Fe synthetic complexes in an unsymmetric scaffold is described and summarized in Scheme 5.7. These species contain Fe–(μ-O(H))–Fe cores that resemble those found in the active site of di-Fe-based enzymes, such as RNR R2 Class Ia and sMMOH.[8-17] One Fe site remains coordinatively saturated at all oxidation states with the TMTACN capping ligand, while the other Fe center is housed within the $[poat]^{3-}$ trigonal framework. This library of complexes spans across four different oxidation states and demonstrates the multiple features of the $[poat]^{3-}$ ligand. In Chapter 4 and other previous work,[32] it has been demonstrated $[poat]^{3-}$ can support an Fe^{IV} center; here, we show the P=O groups can support a metal at a +3 oxidation state, unlike the analogous sulfonamido-based tripodal ligands. The P=O groups can serve as H-bond acceptors as well as ligands to a second metal center, but we discovered they can also facilitate proton transfer from a Fe^{III}–(μ-OH)–Fe^{III} core to the N-atom of one phosphinic amido arm for better stabilization. A Fe^{III}–(μ-O)–Fe^{IV} species can be accessed and was studied spectroscopically, and its reactivity towards phenolic substrates was explored, which is relevant to the catalytic turnover of RNR R2.

After the thorough investigation into this di-Fe system, I next turned my attention towards preparing bioinspired high-valent heterobimetallic complexes. The stepwise assembly protocol developed in Chapters 3, 4, and 5 provide synthetic routes to systematically introduce metal ions/adducts of choice. These works are described in the following three chapters.

Experimental

General Methods. All reagents were purchased from commercial sources and used as received unless otherwise noted. Solvents were sparged with argon and purified using a JC Meyer Co. solvent purification system with columns containing Q-5 and molecular sieves. Butyronitrile (PrCN) was

purified according to a literature procedure.[58] Potassium hydride (KH) as a 30 % dispersion in mineral oil was filtered with a medium porosity glass frit and washed 5 times each with pentane and diethyl ether (Et_2O). Solid KH was dried under vacuum and stored under an inert atmosphere. All synthetic manipulations were conducted in a Vacuum Atmosphere, Co. drybox under an argon atmosphere. K[Fe^{III}poat(OH)],[33] K[Fe^{II}poat],[32] [Fe^{II}(TMTACN)$(OTf)_2$],[59] [$FeCp_2$]OTf,[38] IBX-iPr,[60,61] 2,6-lutidinium triflate,[62] and [N(*p*-$C_6H_4Br)_3$]PF_6[63,64] were synthesized according to previous reports. Triethylamine (NEt_3) was purified by vacuum distillation. 2,6-di-*tert*-butyl-phenol (DTBP) was purified by recrystallization in absolute ethanol twice. The ^{57}Fe-enriched complexes were prepared using $^{57}Fe^{II}(OAc)_2$[65] and $^{57}Fe^{II}(OTf)_2 \cdot 2CH_3CN$,[66] which were synthesized according to procedures for the natural abundance Fe precursors.

Physical Methods. Room temperature electronic absorbance spectra were recorded with a Cary 50 using a 1.00 cm quartz cuvette. Low temperature electronic absorbance spectra were recorded on an Agilent UV-vis spectrophotometer equipped with a Unisoku Unispeks cryostat in a 1.00 cm quarts cuvette. High resolution mass spectra were collected using Waters Micromass LCT Premier Mass Spectrometer. Solid-state Fourier transform infrared (FTIR) spectra were collected on a Thermo Scientific Nicolet iS5 FT-IR spectrometer equipped with an iD5 ATR accessory. Cyclic voltammetric experiments were conducted using a CHI600G electrochemical analyzer. A 2.0 mm glassy carbon electrode was used as the working electrode at scan velocities between 2 and 2000 mV s^{-1}. A ferrocenium/ferrocene ($[FeCp_2]^{+/0}$) or an acetylferrocenium/acetylferrocene ($[AcFc]^{+/0}$, + 0.27 V versus $[FeCp_2]^{+/0}$)[38] was used as an internal reference to monitor the reference electrode (Ag^+/Ag). Tetrabutylammonium hexafluorophosphate (TBAP) was used as the supporting electrolyte at a concentration of 0.1 M in CH_2Cl_2 or PrCN. Elemental analyses were performed on a Perkin-Elmer 2400 Series II CHNS elemental analyzer. ^{1}H–NMR spectra was collected on a Bruker CRYO500 spectrometer (500 MHz). X-band (microwave frequencies 9.6 GHz) EPR spectra were collected on a Bruker ELEXSYS spectrometer equipped with an Oxford ESR-910 liquid helium cryostat and a

Bruker bimodal cavity for the generation of microwave fields parallel and transverse to the applied magnetic field. Mössbauer spectra were recorded on either a variable field or a weak-field spectrometer operating in a constant acceleration mode in a transmission geometry using Janis Research Inc. cryostats that allow for a variation in temperature from 4 to 300 K. One of the dewars housed a superconducting magnet that allowed for the application of magnetic fields up to 8 T parallel to the γ-radiation. Isomer shifts are reported relative to Fe metal at 298 K. SpinCount was used to fit the experimental EPR and Mössbauer data.[66] Organic products were detected by gas-chromatography mass spectrometry (GC-MS) in the Mass Spectrometry Facility at the University of California, Irvine. The GC-MS was a Trace 1300 Gas Chromatograph from Thermo Scientific using a 15 m long x 0.25 mm i.d. TG-SQC column. The oven was held at 40 °C for 1 minute then heated at a rate of 20 °C min^{-1} to 290 °C and held for an additional 2 minutes. The mass spectrometry used electron ionization (70 eV) scanning (0.2/sec) from m/z 30 – 650.

Crystallography.

[(TMTACN)Fe^{II}–(μ-OH)–Fe^{III}poat]OTf. A yellow crystal of approximate dimensions 0.142 x 0.213 x 0.306 mm was mounted in a cryoloop and transferred to a Bruker SMART APEX II diffractometer system. The APEX2[68] program package was used to determine the unit-cell parameters and for data collection (45 sec/frame scan time). The raw frame data was processed using SAINT[69] and SADABS[70] to yield the reflection data file. Subsequent calculations were carried out using the SHELXTL[71] program package. There were no systematic absences nor any diffraction symmetry other than the Friedel condition. The centrosymmetric triclinic space group $P\bar{1}$ was assigned and later determined to be correct.

The structure was solved by direct methods and refined on F^2 by full-matrix least-squares techniques. The analytical scattering factors[72] for neutral atoms were used throughout the analysis. There were two molecules of the formula-unit present (Z = 4). Hydrogen atoms H(1) and H(5) were located from a difference-Fourier map and refined (x,y,z and U_{iso}). The remaining hydrogen atoms

were included using a riding model. Several atoms were disordered and included using multiple components with partial site-occupancy-factors.

Least-squares analysis yielded wR2 = 0.1027 and Goof = 1.020 for 1581 variables refined against 31868 data (0.69 Å), R1 = 0.0434 for those 22037 data with I > 2.0σ(I).

[(TMTACN)Fe^{III}–(μ-O)–Fe^{III}Hpoat](OTf)$_2$. A brown crystal of approximate dimensions 0.216 x 0.242 x 0.313 mm was mounted on a glass fiber and transferred to a Bruker SMART APEX II diffractometer system. The APEX2[68] program package was used to determine the unit-cell parameters and for data collection (20 sec/frame scan time). The raw frame data was processed using SAINT[69] and SADABS[70] to yield the reflection data file. Subsequent calculations were carried out using the SHELXTL[71] program package. The diffraction symmetry was 2/*m* and the systematic absences were consistent with the monoclinic space group $P2_1/c$ that was later determined to be correct.

The structure was solved by dual space methods and refined on F^2 by full-matrix least-squares techniques. The analytical scattering factors[72] for neutral atoms were used throughout the analysis. Hydrogen atom H(2) was located from a difference-Fourier map and refined (x,y,z and U_{iso}). The remaining hydrogen atoms were included using a riding model. Several atoms were disordered and included using multiple components with partial site-occupancy-factors. There was one molecule of chloroform solvent present.

Least-squares analysis yielded wR2 = 0.0979 and Goof = 1.022 for 872 variables refined against 18665 data (0.72 Å), R1 = 0.0401 for those 14338 data with I > 2.0σ(I).

There were several high residuals present in the final difference-Fourier map. It was not possible to determine the nature of the residuals although it was probable that *n*-hexane solvent was

present. The SQUEEZE[73] routine in the PLATON[74] program package was used to account for the electrons in the solvent accessible voids.

[(TMTACN)Fe^{III}–(μ-O)–Fe^{III}poat]OTf. A red crystal of approximate dimensions 0.236 x 0.265 x 0.266 mm was mounted in a cryoloop and transferred to a Bruker SMART APEX II diffractometer system. The APEX2[68] program package was used to determine the unit-cell parameters and for data collection (60 sec/frame scan time). The raw frame data was processed using SAINT[69] and SADABS[70] to yield the reflection data file. Subsequent calculations were carried out using the SHELXTL[71] program package. There were no systematic absences nor any diffraction symmetry other than the Friedel condition. The centrosymmetric triclinic space group $P\bar{1}$ was assigned and later determined to be correct.

The structure was solved by direct methods and refined on F^2 by full-matrix least-squares techniques. The analytical scattering factors[72] for neutral atoms were used throughout the analysis. Hydrogen atoms were included using a riding model. There were two molecules of dichloromethane solvent present. One of the chlorine atoms was disordered and included using two components with partial site-occupancy-factors.

Least-squares analysis yielded wR2 = 0.1473 and Goof = 1.073 for 737 variables refined against 17414 data (0.70 Å), R1 = 0.0539 for those 13231 data with $I > 2.0\sigma(I)$.

*Preparation of [(TMTACN)**Fe**^{II}–(μ-OH)–Fe^{III}poat]OTf.* K[Fe^{III}poat(OH)] (114.9 mg, 0.1343 mmol) was dissolved in 4 mL anhydrous CH_2Cl_2. NMe_4OAc (19.8 mg, 0.149 mmol) was added in one portion, and the mixture was allowed to stir for one hour. The reaction mixture was filtered with a fine porosity glass frit, and the filtrate was added dropwise to a 1 mL CH_2Cl_2 solution of [Fe^{II}(TMTACN)$(OTf)_2$] (70.7 mg, 0.135 mmol). The reaction was allowed to proceed for one hour, and the mixture was filtered with a medium porosity glass frit to remove any insoluble materials. The

filtrate was layered with Et_2O to yield a light brown powder. After the light brown powder was collected and dried, it was redissolved in CH_2Cl_2, and was layered with pentane to yield yellow sheet-like crystals. The crystals were collected on a glass frit and dried under vacuum, affording the product in yields that ranged from 45-60 %. Elemental analysis calcd. (found) for [(TMTACN)Fe^{II}–(μ-OH)–Fe^{III}poat]OTf·0.5C_5H_{12}, $C_{52}H_{64}F_3Fe_2N_7O_7P_3S$·0.5$C_5H_{12}$; C, 53.27 (53.33); H, 5.74 (5.52); N, 7.98 (7.98) %. UV-Vis (CH_2Cl_2 solution λ_{max}/nm (ε_{max}/$M^{-1}cm^{-1}$)) 315 (sh), 372 (6400), 460 (sh), 520 (sh). FTIR (ATR, cm^{-1}): 3141(OH), 3062, 3049, 3008, 2991, 2964, 2900, 2866, 2848, 2817, 1591, 1485, 1483, 1464, 1435, 1363, 1265, 1223, 1140, 1115, 1082, 1063, 1030, 1014, 989, 964, 931, 891, 812, 750, 723, 696, 634. $E_{1/2}$ (CH_2Cl_2, V versus $[FeCp_2]^{+/0}$): -1.62 , (i_{pc}/i_{pa} = 1.03, ΔE = 0.23 V, ΔE([FeCp(η-C_5H_4COMe)]$^{+/0}$) = 0.17 V), -0.42 (i_{pc}/i_{pa} = 0.99, ΔE = 0.23 V, ΔE([FeCp(η-C_5H_4COMe)]$^{+/0}$) = 0.17 V).

Preparation of [(TMTACN)Fe^{II}–(μ-OH)–Fe^{II}poat]. [(TMTACN)Fe^{II}–(μ-OH)–Fe^{III}poat]OTf (6.1 mg, 0.0051 mmol) was dissolved in 1.0 mL anhydrous CH_2Cl_2, and solid $CoCp^*_2$ (2.5 mg, 0.0076 mmol) was added in one portion to the brown solution. The solution turned dark orange and was allowed to stir for 1 hour. An aliquot of 250 μL solution was added to an EPR tube via a syringe, and the sample (5.0 mM) was frozen in liquid nitrogen. An aliquot of 60 μL metal solution was diluted by 3.0 mL CH_2Cl_2, and the mixture was transferred into a 1-cm quartz cuvette, which was sealed with a rubber septum and measured by a UV-Vis spectrometer. The synthesis of [$^{57}Fe^{II}$(OH)$^{57}Fe^{II}$poat] was achieved using the same method with the following modifications: 96% ^{57}Fe-enriched [$^{57}Fe^{II}$(OH)$^{57}Fe^{III}$poat]OTf (15.1 mg, 0.0126 mmol) and $CoCp^*_2$ (5.0 mg, 0.015 mmol) were reacted in 2.53 mL PrCN.

Preparation of [(TMTACN)Fe^{III}–(μ-O)–Fe^{III}Hpoat](OTf)$_2$. [(TMTACN)Fe^{II}–(μ-OH)–Fe^{III}poat]OTf (95.0 mg, 0.0796 mmol) was dissolved in 3 mL anhydrous CH_2Cl_2, and solid $[FeCp_2]$OTf (27.8 mg, 0.0830 mmol) was added in one portion to the brown solution. The solution immediately turned dark red,

and was allowed to stir for 1.5 hours. All volatiles were then removed under vacuum. The residues were triturated with 20 mL pentane, which was then removed by decanting; the washing process was repeated four times. The residues were redissolved in 6 mL CH_2Cl_2, which was layered with pentane to yield orange needle-like crystals. The crystals were collected on a glass frit and washed with pentane and Et_2O. The crystals were then dried under vacuum, affording the product in yields that ranged from 90-95 %. Elemental analysis calcd. (found) for [(TMTACN)Fe^{III}–(μ-O)–Fe^{III}Hpoat](OTf)$_2$·1.5CH_2Cl_2, $C_{53}H_{64}F_6Fe_2N_7O_{10}P_3S_2$·1.5$CH_2Cl_2$; C, 44.55 (44.54); H, 4.60 (4.38); N, 6.67 (6.92) %. UV-Vis (CH_2Cl_2 solution λ_{max}/nm (ε_{max}/$M^{-1}cm^{-1}$)) 380 (7000), 517 (970), 705 (130). FTIR (ATR, cm^{-1}): 3224 (NH), 3078, 3055, 3012, 2902, 2864, 2823, 1591, 1495, 1473, 1464, 1437, 1360, 1255, 1223, 1140, 1119, 1070, 1055, 1028, 1009, 989, 968, 930, 918, 897, 854, 814, 748, 725, 696, 634. ESI-MS (CH_3CN, ES^+, m/z): exact mass calcd for [Fe^{III}(O)Fe^{III}Hpoat(OTf)]$^+$, $C_{52}H_{64}F_3Fe_2N_7O_7P_3S$, 1192.2455; found, 1192.2485.

Preparation of [(TMTACN)Fe^{III}–(μ-O)–Fe^{III}poat]OTf. K[Fe^{II}poat] (121.4 mg, 0.1447 mmol) and 18-crown-6 (76.8 mg, 0.291 mmol) were dissolved in 7 mL anhydrous THF and 1 mL anhydrous DMF. The yellow solution was transferred to a 50 mL Schlenk flask, which was sealed with a septum and cooled in a -75 °C cold bath outside the glovebox for at least 15 minutes. A 2 mL DMF solution of IBX-iPr (57.8 mg, 0.179 mmol), prepared in the glovebox, was added dropwise into the Schlenk flask via syringe. The reaction mixture immediately turned red, indicative of the formation of [Fe^{IV}poat(O)]$^-$, and was allowed to stir for 20 minutes. A 0.6 mL DMF solution of [Fe^{II}(TMTACN)(OTf)$_2$] (80.1 mg, 0.152 mmol), prepared in the glovebox, was then added dropwise into the Schlenk flask via syringe. The reaction mixture turned brownish red gradually, and was allowed to stir for 1.5 hours. The Schlenk flask was then warmed up to room temperature, and all volatiles were removed under vacuum. The flask was transferred back in a glovebox, where the residue was redissolved in CH_2Cl_2 and was layered with diethyl ether to yield a brown powder over three days. After the brown powder was collected and dried, it was redissolved in CH_2Cl_2, and was

layered with pentane to yield dark red crystalline needles. The crystals were collected on a glass frit and dried under vacuum, affording the product in yields that ranged from 45-55 %. Elemental analysis calcd. (found) for [(TMTACN)Fe^{III}–(μ-O)–Fe^{III}poat]OTf·CH_2Cl_2·C_5H_{12}, $C_{52}H_{63}F_3Fe_2N_7O_7P_3S$·$CH_2Cl_2$·$C_5H_{12}$; C, 51.65 (51.56); H, 5.75 (5.40); N, 7.27 (7.49) %. UV-Vis (CH_2Cl_2 solution λ_{max}/nm (ε_{max}/$M^{-1}cm^{-1}$)) 349 (9200), 531 (780), 780 (250). FTIR (ATR, cm^{-1}): 3070, 3053, 3033, 3008, 2956, 2933, 2898, 2885, 2856, 2844, 1589, 1572, 1500, 1464, 1435, 1390, 1381, 1354, 1276, 1271, 1257, 1227, 1190, 1151, 1147, 1115, 1076, 1066, 1057, 1041, 1032, 1012, 987, 955, 938, 922, 897, 872, 858, 822, 793, 748, 719, 696, 636. ESI-MS (CH_3CN, ES^+, m/z): exact mass calcd for [Fe^{III}(O)Fe^{III}poat]$^+$, $C_{51}H_{63}Fe_2N_7O_4P_3$, 1042.2856; found, 1042.2855. $E_{1/2}$ (CH_2Cl_2, V versus $[FeCp_2]^{+/0}$): +0.55.

Low-temperature UV-vis solution studies. In a typical experiment, a 10 mM solution of the diiron compound was prepared in CH_2Cl_2 at room temperature and kept in a -35 °C freezer for the duration of the experiment. A 30 - 60 μL aliquot of stock metal complex was added via air-tight syringe to the solvent mixture (3 mL) in a 1-cm quartz cuvette to give the desired concentration for oxidation experiments (0.10 – 0.20 mM). The cuvette was then sealed with a rubber septum and precooled to the desired temperature in an 8453 Agilent UV-vis spectrophotometer equipped with an Unisoku Unispeks cryostat. The solution of metal complex was allowed to equilibrate to the desired temperature for at least 15 min. Stock solutions of other reagents were prepared at concentrations between 10 and 100 mM in the same solvent and added via gas-tight syringe. Reactions were monitored spectrophotometrically by UV-vis spectroscopy.

Low-temperature EPR solution studies. In a typical experiment to generate [Fe^{III}(OH)Fe^{III}poat]$^{2+}$, a 5.8 mM solution (1.97 mL) of [Fe^{II}(OH)Fe^{III}poat]OTf (0.0135 g, 0.0113 mmol) was prepared in the desired solvent at room temperature in a glovebox under argon atmosphere, and kept in a -35 °C freezer for the duration of the experiment. A 200 μL aliquot of stock metal complex (0.00115 mmol,

1.00 equiv) was added via syringe to a quartz EPR tube. The tube was then sealed with a rubber septum and precooled to the desired temperature in -78 °C cold bath outside the glovebox, allowing the solution to equilibrate to the desired temperature for at least 15 min. A 1 mL stock solution of $[FeCp_2]OTf$ was prepared at 46 mM (0.0154 g, 0.0460 mmol) in CH_2Cl_2, and a 30 μL aliquot (0.00138 mmol, 1.25 equiv) added via a gas-tight syringe. The reaction was allowed to incubate for 5 minutes before freezing in liquid nitrogen. The synthesis of $[Fe^{III}(O)Fe^{IV}poat]^{2+}$ was achieved using the same method with the following modifications: 200 μL of 6.5 mM $[Fe^{III}(O)Fe^{III}poat]OTf$ solution (0.0013 mmol, 1.0 equiv) and an additional 30 μL CH_2Cl_2 were reacted with 30 μL of 43.3 mM $[N(p\text{-}C_6H_4Br)_3]PF_6$ solution (0.0013 mmol, 1.0 equiv) at -94 °C.

Room-temperature Mössbauer studies. The Mössbauer samples for $[^{57}Fe^{II}(OH)^{57}Fe^{III}poat]^+$, $[^{57}Fe^{III}(O)^{57}Fe^{III}Hpoat]^{2+}$, and $[^{57}Fe^{III}(O)^{57}Fe^{III}poat]^+$ were prepared at room temperature. In a typical experiment, a 5 mM solution of the 96% ^{57}Fe-enriched diiron compound was prepared, and was transferred into a Mössbauer cup before freezing in liquid nitrogen. For the solid sample of $[^{57}Fe^{III}(O)^{57}Fe^{III}Hpoat](OTf)_2$, ~ 20 mg of the complex was added to the bottom of a Mössbauer cup in an even layer. Anhydrous Nujol mull was added until it reached the top of the sample holder, which was then frozen in liquid nitrogen. The preparation for $[^{57}Fe^{II}(OH)^{57}Fe^{II}poat]$ is discussed above.

Low-temperature Mössbauer solution studies. In a typical experiment to generate $[^{57}Fe^{III}(OH)^{57}Fe^{III}poat]^{2+}$, a 5.5-mM solution of the 96% ^{57}Fe-enriched $[^{57}Fe^{II}(OH)^{57}Fe^{III}poat]OTf$ (0.0074 g, 0.0062 mmol, 1.12 mL) was prepared in PrCN at room temperature in a glovebox under argon atmosphere, and kept in a -35 °C freezer for the duration of the experiment. A 1.0 mL aliquot of stock metal complex (0.0055 mmol) was added via syringe to a 1-cm quartz. The cuvette was then sealed with a rubber septum and precooled to -80 °C in a Unisoku Unispeks cryostat typically used for UV-vis

experiments outside the glovebox. The solution of metal complex was allowed to equilibrate to the desired temperature for at least 20 min. A stock solution of $[FeCp_2]OTf$ was prepared at 66 mM in PrCN, and an aliquot of the oxidant (0.0066 mmol, 0.10 mL) was added via a gas-tight syringe. Upon completion of the reaction, the septum was sliced open with a razor under a strong flow of argon. The rubber septum was removed and the content in the cuvette was quickly poured into liquid nitrogen. The frozen solid was ground into fine powder and then packed into pre-cooled Mössbauer cups. The synthesis of $[^{57}Fe^{III}(O)^{57}Fe^{IV}poat]^{2+}$ was achieved using the same method with the following modifications: 1.5 mL of 5.5 mM $[^{57}Fe^{III}(O)^{57}Fe^{III}poat]OTf$ solution (9.9 mg, 0.0083 mmol) was reacted with 0.15 mL of 83 mM $[N(C_6H_4Br)_3]PF_6$ solution (7.8 mg, 0.012 mmol) at -94 ^oC.

Kinetic measurements. These experiments were performed in collaboration with Dr. Chen Sun. All kinetic experiments were measured in CH_2Cl_2 at -90 ^oC in a cuvette (containing a magnetic stirbar) with 1 cm pathlength. 11.7 mM of $[Fe^{III}(O)Fe^{III}poat]^+$ stock solution, 9.8 mM of $[N(p\text{-}C_6H_4Br)_3]PF_6$ stock solution, and 87 mM of 2,6-di-*tert*-butyl-phenol (DTBP) stock solution were prepared at room temperature. All stock solutions were stored at -35 ^oC for the duration of the experiment and warmed back to room temperature for 10 min prior to use. A cuvette filled with 2 mL CH_2Cl_2 solvent was sealed with a rubber septum and transferred into the cryostat of the spectrophotometer to equilibrate with the temperature for > 20 min. First, 40 μL of the $[Fe^{III}(O)Fe^{III}poat]^+$ stock solution was injected into the cuvette via airtight syringe and mixed for 150-200 sec to give the desired concentration (0.23 mM). Then, the reaction was initiated with injecting 40 μL (0.85 equiv.) of the $[N(p\text{-}C_6H_4Br)_3]PF_6$ stock solution into the cuvette via airtight syringe while closely monitoring the appearance of absorbance features at λ_{max} = 440, 515, 620, 810, ~1100 nm that is indicative of formation of $[Fe^{III}(O)Fe^{IV}poat]^{2+}$. Sub-stoichiometric amount of oxidant was added since $[N(p\text{-}C_6H_4Br)_3]PF_6$ also reacts with DTBP. After the spectrum of $[Fe^{III}(O)Fe^{IV}poat]^{2+}$ reached equilibrium

(t = 150 sec), 75 μL of the DTBP stock solution (10 equiv.) was injected into the cuvette via airtight syringe. The progress of the reaction was monitored by following the decrease in absorbance at 620 nm. After reaction was completed, the mixture in the cuvette ended as clear orange solution.

Under these conditions, the substrate concentration was in excess compared to the complex concentration to provide pseudo first-order reaction conditions. The expression, $\ln[(A_t - A_f)/(A_i - A_f)]$, was plotted against the reaction time for the first three half-lives of any reaction to provide linear plots. Here, A_i is the initial absorbance, A_t is the absorbance at time t, and A_f is the absorbance at the endpoint of the reaction at 900 nm. The observed pseudo first-order rate constants (k_{obs}, s^{-1}) for the reaction was determined from the slope of the above-mentioned linear plots.

GC-MS experiments. Typically, the solution from a UV-vis kinetics experiment with DPH and DTBP is directly subjected to a GC-MS measurement without further workup. The percent conversion from DTBP to diphenoquinone and bisphenol is calculated by comparing the relative area of diphenoquinone and bisphenol with unreacted DTBP. Additionally, the following factors are taken into account: 1) DTBP was added in 10-fold excess; 2) two equivalents of $[Fe^{III}(O)Fe^{IV}poat]^{2+}$ reacts with one equivalent of diphenylhydrazine; and 3) sub-stoichiometric $[N(C_6H_4Br)_3]PF_6$ (0.8 equiv.) was added to avoid reaction between the unreacted oxidant and DTBP. The percent conversions are calculated to be > 90%.

NMR identification of organic products. $[Fe^{III}(O)Fe^{III}poat]OTf$ (0.0299 g, 0.0251 mmol, 1.0 equiv) was dissolved in 3 mL CH_2Cl_2 and transferred to a 50 mL Schlenk flask in a glove box. The flask was sealed with a septum, brought out of the box, and chilled in a -94 °C bath for 20 minutes. An aliquot of $[N(p\text{-}C_6H_4Br)_3]PF_6$ (0.0150 g, 0.0239 mmol, 0.95 equiv) in 0.25 mL CH_2Cl_2 was added *via* a gas-tight syringe, and the red solution turned dark brownish green immediately and was allowed to stir for 5 minutes. An aliquot of DPH (0.0023 mg, 0.013, 0.52 equiv) in 0.070 mL CH_2Cl_2 was injected

via a gas-tight syringe, and the brownish green solution turned to dark red. The mixture was allowed to stir for 10 minutes, before warming to room temperature for 1 hour. All volatiles were removed *in vacuo* using a Schlenk line, and the Schlenk flask was brought back into the glove box. The red residue was triturated with three portions of 20 mL Et_2O, which were combined as a pale yellow solution with minor particulates. The Et_2O solution was filtered to remove the insoluble material, and the solvent was removed *in vacuo* to afford an orange-yellow residue as the organic product. The isolated product was redissolved in 0.65 mL $CDCl_3$ (1% TMS), and the NMR spectrum was collected.

Table 5.3. Crystallographic data for $[Fe^{II}(OH)Fe^{III}poat]^+$, $[Fe^{III}(O)Fe^{III}Hpoat]^{2+}$, and $[Fe^{III}(O)Fe^{III}poat]^+$.

	[(TMTACN)Fe^{II}–(μ-OH)–Fe^{III}poat]OTf	[(TMTACN)Fe^{III}–(μ-O)–Fe^{III}Hpoat](OTf)$_2$	[(TMTACN)Fe^{III}–(μ-O)–Fe^{III}poat]OTf
Formula	C_{54} H_{64} F_3 Fe_2 N_7 O_7 P_3 S	C_{54} H_{65} Cl_3 F_6 Fe_2 N_7 O_{10} P_3 S_2	C_{54} H_{67} Cl_4 F_3 Fe_2 N_7 O_7 P_3 S
fw	1192.77	1461.21	1361.61
T (K)	133(2)	93(2)	93(2)
Crystal system	Triclinic	Monoclinic	Triclinic
Space group	$P\bar{1}$	$P2_1/c$	$P\bar{1}$
a (Å)	14.918(2)	16.6081(6)	10.5370(5)
b (Å)	17.229(3)	14.8447(5)	13.6903(7)
c (Å)	21.457(3)	27.0177(9)	21.8456(11)
α (°)	89.463(3)	90	93.1573(8)
β (°)	89.920(3)	91.9316(6)	101.4197(8)
γ (°)	81.928(3)	90	104.7658(8)
Z	4	4	2
V (Å^3)	5460.0(14)	6657.2(4)	2968.4(3)
δ_{calc} (mg/m^3)	1.451	1.458	1.523
Independent reflections	31868	18665	17414
R1	0.0434	0.0401	0.0539
wR2	0.1027	0.0979	0.1473
Goof	1.020	1.022	1.073

wR2 = $[\Sigma[w(F_o^2-F_c^2)^2] / \Sigma[w(F_o^2)^2]]^{1/2}$
R1 = $\Sigma||F_o|-|F_c|| / \Sigma|F_o|$
Goof = S = $[\Sigma[w(F_o^2-F_c^2)^2] / (n-p)]^{1/2}$ where n is the number of reflections and p is the total number of parameters refined.
The thermal ellipsoid plots are shown at the 50% probability level.

References

(1) Reece, S. Y.; Nocera, D. G. Proton-Coupled Electron Transfer in Biology: Results from Synergistic Studies in Natural and Model Systems. *Annu. Rev. Biochem.* **2009**, *78*, 673-699.

(2) Migliore, A.; Polizzi, N. F.; Therien, M. J.; Beratan, D. N. Biochemistry and Theory of Proton-Coupled Electron Transfer. *Chem. Rev.* **2014**, *114*, 3381-3465.

(3) Gray, H. B.; Winkler, J. R. Hole hopping through tyrosine/tryptophan chains protects proteins from oxidative damage. *Proc. Natl. Acad. Sci. U.S.A.* **2015**, *112*, 10920-10925.

(4) Warren, J. J.; Mayer, J. M. Moving Protons and Electrons in Biomimetic Systems. *Biochemistry* **2015**, *54*, 1863-1878.

(5) Shook, R. L.; Borovik, A. S. Role of the Secondary Coordination Sphere in Metal-Mediated Dioxygen Activation. *Inorg. Chem.* **2010**, *49*, 3646-3660.

(6) Cook, S. A.; Hill, E. A.; Borovik, A. S. Lessons from Nature: A Bio-Inspired Approach to Molecular Design. *Biochemistry* **2015**, *54*, 4167-4180.

(7) Span, E. A.; Suess, D. L. M.; Deller, M. C.; Britt, R. D.; Marletta, M. A. The Role of the Secondary Coordination Sphere in a Fungal Polysaccharide Monooxygenase. *ACS Chem. Biol.* **2017**, *12*, 1095-1103.

(8) Klotz, I. M.; Kurtz, D. M. Binuclear Oxygen Carriers: Hemerythrin. *Acc. Chem. Res.* **1984**, *17*, 16-22.

(9) Tinberg, C. E.; Lippard, S. J. Dioxygen Activation in Soluble Methane Monooxygenase. *Acc. Chem. Res.* **2011**, *44*, 280-288.

(10) Nordlund, P.; Reichard, P. Ribonucleotide Reductases. *Annu. Rev. Biochem.* **2006**, *75*, 681-706.

(11) Minnihan, E. C.; Nocera, D. G.; Stubbe, J. Reversible, Long-Range Radical Transfer in *E. Coli* Class Ia Ribonucleotide Reductase. *Acc. Chem. Res.* **2013**, *46*, 2524-2535.

(12) Kang, G.; Taguchi, A. T.; Stubbe, J.; Drennan, C. L. Structure of a Trapped Radical Transfer Pathway within a Ribonucleotide Reductase Holocomplex. *Science* **2020**, *368*, 424-427.

(13) Greene, B. L.; Kang, G.; Cui, C.; Bennati, M.; Nocera, D. G.; Drennan, C. L.; Stubbe, J. Ribonucleotide Reductases: Structure, Chemistry, and Metabolism Suggest New Therapeutic Targets. *Annu. Rev. Biochem.* **2020**, *89*, 45-75.

(14) Caranto, J. D.; Weitz, A.; Giri, N.; Hendrich, M. P.; Kurtz, D. M. A Diferrous-Dinitrosyl Intermediate in the N_2O-Generating Pathway of a Deflavinated Flavo-Diiron protein. *Biochemistry* **2014**, *53*, 5631-5637.

(15) Hayashi, T.; Caranto, J. D.; Wampler, D. A.; Kurtz, D. M.; Moënne-Loccoz, P. Insights into the Nitric Oxide Reductase Mechanism of Flavodiiron Proteins from a Flavin-Free Enzyme. *Biochemistry* **2010**, *49*, 7040-7049.

(16) Fox, B. G.; Shanklin, J.; Somerville, C.; Münck, E. Stearoyl-Acyl Carrier Protein Δ^9 Desaturase from *Ricinus communis* Is a Diiron-Oxo Protein. *Proc. Natl. Acad. Sci. U.S.A.* **1993**, *90*, 2486-2490.

(17) Yang, Y.-S.; Broadwater, J. A.; Pulver, S. C.; Fox, B. G.; Solomon, E. I. Circular Dichroism and Magnetic Circular Dichroism Studies of the Reduced Binuclear Non-Heme Iron Site of Stearoyl-ACP Δ^9-Desaturase: Substrate Binding and Comparison to Ribonucleotide Reductase. *J. Am. Chem. Soc.* **1999**, *121*, 2770-2783.

(18) Jasniewski, A. J.; Que, L. Dioxygen Activation by Nonheme Diiron Enzymes: Diverse Dioxygen Adducts, High-Valent Intermediates, and Related Model Complexes. *Chem. Rev.* **2018**, *118*, 2554-2592.

(19) Kurtz, D. M. Structural similarity and functional diversity in diiron-oxo proteins. *JBIC, J. Biol. Inorg. Chem.* **1997**, *2*, 159-167.

(20) Sturgeon, B. E.; Burdi D.; Chen, S.; Huynh, B.-H.; Edmondson, D. E.; Stubbe, J.; Hoffman, B. M. Reconsideration of X, the Diiron Intermediate Formed during Cofactor Assembly in *E. Coli* Ribonucleotide Reductase. *J. Am. Chem. Soc.* **1996**, *118*, 7551-7557.
(21) Doan, P. E.; Shanmugam, M.; Stubbe, J.; Hoffman, B. M. Composition and Structure of the Inorganic Core of Relaxed Intermediate X(Y122F) of *Escherichia coli* Ribonucleotide Reductase. *J. Am. Chem. Soc.* **2015**, *137*, 15558-15566.
(22) Slep, L. D.; Mijovilovich, A.; Meyer-Klaucke, W.; Weyhermüller, T.; Bill, E.; Bothe, E.; Neese, K.; Wieghardt, K. Mixed-Valent $\{Fe^{IV}(\mu\text{-}O)(\mu\text{-carboxylato})_2Fe^{III}\}^{3+}$ Core. *J. Am. Chem. Soc.* **2003**, *125*, 15554-15570.
(23) Lee, D.; Pierce, B.; Krebs, C.; Hendrich, M. P.; Huynh, B. H.; Lippard, S. J. Functional Mimic of Dioxygen-Activating Centers in Non-Heme Diiron Enzymes: Mechanistic Implications of Paramagnetic Intermediates in the Reactions between Diiron(II) Complexes and Dioxygen. *J. Am. Chem. Soc.* **2002**, *124*, 3993-4007.
(24) Ghosh, A.; Tiago de Oliveira, F.; Yano, T.; Nishioka, T.; Beach, E. S.; Kinoshita, I.; Münck, E.; Ryabov, A. D.; Horwitz, C. P.; Collins, T. J. Catalytically Active μ-Oxodiiron(IV) Oxidants from Iron(III) and Dioxygen. *J. Am. Chem. Soc.* **2005**, *127*, 2505-2513.
(25) Wang, D.; Farquhar, E. R.; Stubna, A.; Münck, E.; Que, L. A diiron(IV) complex that cleaves strong C-H and O-H bonds. *Nat. Chem.* **2009**, *1*, 145-150.
(26) Hsu, H.-F.; Dong, Y.; Shu, L.; Young, V. G.; Que, L. Crystal Structure of a Synthetic High-Valent Complex with an $Fe_2(\mu\text{-}O)_2$ Diamond Core. Implications for the Core Structures of Methane Monooxygenase Intermediate Q and Ribonucleotide Reductase Intermediate X. *J. Am. Chem. Soc.* **1999**, *121*, 5230-5237.
(27) Xue, G.; Wang, D.; De Hont, R.; Fiedler, A. T.; Shan, X.; Münck, E.; Que, L. A synthetic precedent for the $[Fe^{IV}_2(\mu\text{-}O)_2]$ diamond core proposed for methane monooxygenase intermediate Q. *Proc. Natl. Acad. Sci. U.S.A.* **2007**, *104*, 20713-20718.
(28) Xue, G.; Fiedler, A. T.; Martinho, M.; Münck, E.; Que, L. Insights into the P-to-Q conversion in the catalytic cycle of the methane monooxygenase from a synthetic model system. *Proc. Natl. Acad. Sci. U.S.A.* **2008**, *105*, 20615-20620.
(29) Xue, G.; De Hont, R.; Münck, E.; Que, L. Million-fold activation of the $[Fe_2(\mu\text{-}O)_2]$ diamond core for C–H bond cleavage. *Nat. Chem.* **2010**, *2*, 400-405.
(30) De Hont, R. F.; Xue, G.; Hendrich, M. P.; Que, L.; Bominaar, E. L.; Münck, E. Mössbauer, Electron Paramagnetic Resonance, and Density Functional Theory Studies of Synthetic $S = 1/2$ Fe^{III}–O–Fe^{IV}=O Complexes. Superexchange-Mediated Spin Transition at the Fe^{IV}=O Site. *Inorg. Chem.* **2010**, *49*, 8310-8322.
(31) Stoian, S. A.; Xue, G.; Bominaar, E. L.; Que, L.; Münck, E. Spectroscopic and Theoretical Investigation of a Complex with an [O=Fe^{IV}–O–Fe^{IV}=O] Core Related to Methane Monooxygenase Intermediate Q. *J. Am. Chem. Soc.* **2014**, *136*, 1545-1558.
(32) Oswald, V. F.; Lee, J. L.; Biswas, S.; Weitz, A. C.; Mittra, K.; Fan, R.; Li, J.; Zhao, J.; Hu, M. Y.; Alp, E. E.; Bominaar, E. L.; Guo, Y.; Green, M. T.; Hendrich, M. P.; Borovik, A. S. Effects of Non-covalent Interactions on High-spin Fe(IV)-oxido Complexes. *J. Am. Chem. Soc.* **2020**, *142*, 11804-11817.
(33) Lee, J. L.; Oswald, V. F.; Biswas, S.; Hill, E. A.; Ziller, J. W.; Hendrich, M. P.; Borovik, A. S. Stepwise assembly of heterobimetallic complexes: synthesis, structure, and physical properties. *Dalton Trans.* **2021**, *50*, 8111-8119.
(34) Sano, Y.; Weitz, A. C.; Ziller, J. W.; Hendrich, M. P.; Borovik, A. S. Unsymmetrical Bimetallic Complexes with M^{II}–(μ-OH)–M^{III} Cores ($M^{II}M^{III}$ = $Fe^{II}Fe^{III}$, $Mn^{II}Fe^{III}$, $Mn^{II}Mn^{III}$): Structural, Magnetic, and Redox Properties. *Inorg. Chem.* **2013**, *52*, 10229-10231.

(35) Sano, Y.; Lau, N.; Weitz, A. C.; Ziller, J. W.; Hendrich, M. P.; Borovik, A. S. Models for Unsymmetrical Active Sites in Metalloproteins: Structural, Redox, and Magnetic Properties of Bimetallic Complexes with M^{II}-(μ-OH)-Fe^{III} Cores. *Inorg. Chem.* **2017**, *56*, 14118-14128**.**

(36) Tshuva, E. Y.; Lippard, S. J. Synthetic Models for Non-Heme Carboxylate-Bridged Diiron Metalloproteins: Strategies and Tactics. *Chem. Rev.* **2004**, *104*, 987-1012.

(37) Kurtz, D. M. Oxo- and Hydroxo-Bridged Diiron Complexes: A Chemical Perspective on a Biological Unit. *Chem. Rev.* **1990**, *90*, 585-606.

(38) Connelly, N. G.; Geiger, W. E. Chemical Redox Agents for Organometallic Chemistry. *Chem. Rev.* **1996**, *96*, 877-910.

(39) Wieghardt, K.; Pohl, K.; Gebert, W. $[\{(C_6H_{15}N_3)Fe\}_2(\mu\text{-}O)(\mu\text{-}CH_3CO_2)_2]^{2+}$, a Dinuclear Iron(III) Complex with a Metazidohemerythrin-Type Structure. *Angew. Chem., Int. Ed.* **1983**, *22*, 727.

(40) Hotzelmann, R.; Wieghardt, K.; Flörke, U.; Haupt, H.-J.; Weatherburn, D. C.; Bonvoisin, J.; Blondin, G.; Girerd, J.-J. Spin Exchange Coupling in Asymmetric Heterodinuclear Complexes Containing the *μ*-Oxo-bis(*μ*-acetato)dimetal Core. *J. Am. Chem. Soc.* **1992**, *114*, 1681-1696.

(41) Armstrong, W. H.; Lippard, S. J. (*μ*-Oxo)bis(*μ*-acetato)bis(tri-1-pyrazolylborato)diiron(III), $[(HBpz_3)FeO(CH_3CO_2)_2Fe(HBpz_3)]$: Model for the Binuclear Iron Center of Hemerythrin. *J. Am. Chem. Soc.* **1983**, *105*, 4837-4838.

(42) Armstrong, W. H.; Spool, A.; Papaefthymioum G. C.; Frankel, R. B.; Lippard, S. J. Assembly and Characterization of an Acetate Model for the Diiron Center in Hemerythrin. *J. Am. Chem. Soc.* **1984**, *106*, 3653-3667.

(43) Stubna, A.; Jo, D.-H.; Costas, M.; Brenessel, W. W.; Andres, H.; Bominaar, E. L.; Münck, E.; Que, L. A Structural and Mössbauer Study of Complexes with $Fe_2(\mu\text{-}O(H))_2$ Cores: Stepwise Oxidation from $Fe^{II}(\mu\text{-}OH)_2Fe^{II}$ through $Fe^{II}(\mu\text{-}OH)_2Fe^{III}$ to $Fe^{III}(\mu\text{-}O)(\mu\text{-}OH)Fe^{III}$. *Inorg. Chem.* **2004**, *43*, 3067-3079.

(44) Kryatov, S. V.; Taktak, S.; Korendovych, I. V.; Rybak-Akimova, E. V.; Kaizer, J.; Torelli, S.; Shan, X.; Mandal, S.; MacMurdo, V. L.; Mairata i Payeras, A.; Que, L. Dioxygen Binding to Complexes with $Fe^{II}_2(\mu\text{-}OH)_2$ Cores: Steric Control of Activation Barriers and O_2-Adduct Formation. *Inorg. Chem.* **2005**, *44*, 85-99.

(45) Chaudhury, P.; Wieghardt, K.; Nuber, B.; Weiss, J. $[L_2Fe^{II}_2(\mu\text{-}OH)(\mu\text{-}CH_3CO_2)](ClO_4)\cdot H_2O$, a Model Compound for the Diiron Centers in Deoxyhemerythrin. *Angew. Chem., Int. Ed.* **1985**, *24*, 778-779.

(46) Bossek, U.; Hummel, H.; Weyhermüller, T.; Bill, E.; Wieghardt, K. The First *μ*(OH)-Bridged Model Complex for the Mixed-Valent $Fe^{II}Fe^{III}$ Form of Hemerythrin. *Angew. Chem., Int. Ed.* **1996**, *34*, 2642-2645.

(47) Bradić, Z.; Harrington, P. C.; Wilkins, R. G. Yoneda, G. Role of mixed oxidation states in the oxidation of hemerythrin species by ferricyanide ion. *Biochemistry* **1980**, *19*, 4149-4155.

(48) Sanders-Loehr, J.; Wheeler, W. D.; Shiemke, A. K.; Averill, B. A.; Loehr, T. M. Electronic and Raman Spectroscopic Properties of Oxo-Bridged Dinuclear Iron Centers in Proteins and Model Compounds. *J. Am. Chem. Soc.* **1989**, *111*, 8084-8093.

(49) Warren, J. J.; Tronic, T. A.; Mayer, J. M. Thermochemistry of Proton-Coupled Electron Transfer Reagents and its Implications. *Chem. Rev.* **2010**, *110*, 6961-7001.

(50) Lee, D.; Du Bois, J.; Petasis, D.; Hendrich, M. P.; Krebs, C.; Huynh, B. H.; Lippard, S. J. Formation of Fe(III)Fe(IV) Species from the Reaction between a Diiron(II) Complex and Dioxygen: Relevance to Ribonucleotide Reductase Intermediate X. *J. Am. Chem. Soc.* **1999**, *121*, 9893-9894.

(51) Kim, C.; Dong, Y.; Que, L. Modeling Nonheme Diiron Enzymes: Hydrocarbon Hydroxylation and Desaturation by a High-Valent Fe_2O_2 Core. *J. Am. Chem. Soc.* **1997**, *119*, 3635-3636.
(52) Mondal, P.; Pirovano, P.; Das, A.; Farqujar, E. R.; McDonald, A. R. Hydrogen Atom Transfer by a High-Valent Nickel-Chloride Complex. *J. Am. Chem. Soc.* **2018**, *140*, 1834-1841.
(53) Wu, T.; MacMillan, S. N.; Rajabimoghadam, K.; Siegler, M. A.; Lancaster, K. M.; Garcia-Bosch, I. Structure, Spectroscopy, and Reactivity of a Mononuclear Copper Hydroxide Complex in Three Molecular Oxidation States. *J. Am. Chem. Soc.* **2020**, *142*, 12265-12276.
(54) Türk, H.; Çimen, Y. Oxidation of 2,6-di-tert-butylphenol with tert-butylhydroperoxide catalyzed by cobalt(II) phthalocyanine tetrasulfonate in a methanol–water mixture and formation of an unusual product 4,4'-dihydroxy-3,3'-5,5'-tetra-tert-butylbiphenyl. *J. Mol. Catal. A: Chem.* **2005**, *234*, 19-24.
(55) Holmes, M. A.; Le Trong, I.; Turley, S.; Sieker, L. C.; Stenkamp, R. E. Structures of Deoxy and Oxy Hemerythrin at 2.0 Å Resolution. *J. Mol. Biol.* **1991**, *218*, 583-593.
(56) Zheng, H.; Yoo, S. J.; Münck, E.; Que, J. The Flexible $Fe_2(\mu\text{-O})_2$ Diamond Core: A Terminal Iron(IV)–Oxo Species Generated from the Oxidation of a Bis(μ-oxo)diiron(III) Complex. *J. Am. Chem. Soc.* **2000**, *122*, 3789-3790.
(57) Dong, Y.; Fujii, H.; Hendrich, M. P.; Leising, R. A.; Pan, G.; Randall, C. R.; Wilkinson, E. C.; Zang, Y.; Que, L.; Fox, B. G.; Kauffmann, K.; Münck, E. A High-Valent Nonheme Iron Intermediate. Structure and Properties $[Fe_2(\mu\text{-O})_2(5\text{-Me-TPA})_2](ClO_4)_3$. *J. Am. Chem. Soc.* **1995**, *117*, 2778-2792.
(58) Armarego, L. F.; Chai, C. L. L. *Purification of Laboratory Chemicals,* 5th ed.; Elsevier: Oxford, UK, 2003.
(59) Blakesley, D. W.; Payne, S. C.; Hagen, K. S. Spin-State Variation in Solid State and Solution of Mononuclear Iron(II) 1,4,7-Trimethyl-1,4,7-triazacyclononane Complexes. *Inorg. Chem.* **2000**, *39*, 1979–1989.
(60) Zhdankin, V. V.; Litvinov, D. N.; Koposov, A. Y.; Luu, T.; Ferguson, M. J.; McDonald, R.; Tykwinski, R. R. Preparation and structure of 2-iodoxybenzoate esters: soluble and stable periodinane oxidizing reagents. *Chem. Commun.* **2004**, 106–107.
(61) Zhdankin, V. V.; Koposov, A. Y.; Litvinov, D. N.; Ferguson, M. J.; McDonald, R.; Luu, T.; Tykwinski, R. R. Esters of 2-Iodoxybenzoic Acid: Hypervalent Iodine Oxidizing Reagents with a Pseudobenziodoxole Structure. *J. Org. Chem.* **2005**, *70*, 6484–6491.
(62) Curley, J. J.; Bergman, R. G.; Tilley, T. D. Preparation and physical properties of early-late heterobimetallic compounds featuring Ir–M bonds (M = Ti, Zr, Hf). *Dalton Trans.* **2012**, *41*, 192–200.
(63) Bell, F. A.; Ledwith, A.; Sherrington, D. C. Cations-radicals: tris-(*p*-bromophenyl)amminium perchlorate and hexachloroantimonate. *J. Chem. Soc. C* **1969**, 2719–2720.
(64) Eberson, L.; Larsson, B. Electron Transfer Reactions in Organic Chemistry. XII. Reactions of 4-Substituted Triarylaminium Radical Cations with Nucleophiles; Polar vs. Electron Transfer Pathways. *Acta. Chemica Scandinavica* **1987**, *B 41*, 367–378.
(65) Weber, B.; Betz, R.; Bauer, W.; Schlamp, S. Crystal Structure of Iron(II) Acetate. *Z. Anorg. Allg. Chem.* **2011**, *637*, 102–107.
(66) Hagadorn, J. R.; Que, L.; Tolman, W. B. N-Donor Effects on Carboxylate Binding in Mononuclear Fe(II) Complexes of a Sterically Hindered Benzoate Ligand. *Inorg. Chem.* **2000**, *39*, 6086–6090.
(67) Petasis, D. T.; Hendrich, M. P. Quantitative Interpretation of Multifrequency Multimode EPR Spectra of Metal Containing Proteins, Enzymes, and Biomimetic Complexes. *Methods Enzymol.* **2015**, *563*, 171-208.

(68) APEX2 Version 2014.11-0, Bruker AXS, Inc.; Madison, WI 2014.
(69) SAINT Version 8.34a, Bruker AXS, Inc.; Madison, WI 2013.
(70) Sheldrick, G. M. SADABS, Version 2014/5, Bruker AXS, Inc.; Madison, WI 2014.
(71) Sheldrick, G. M. SHELXTL, Version 2014/7, Bruker AXS, Inc.; Madison, WI 2014.
(72) International Tables for Crystallography 1992, Vol. C., Dordrecht: Kluwer Academic Publishers.
(73) Spek, A. L. SQUEEZE, *Acta Cryst.* **2015**, *C71*, 9–19.
(74) Spek, A. L. PLATON, *Acta. Cryst.* **2009**, *D65*, 148–155.

Chapter 6

Accessing a Fe^{III}–(μ-O)–Mn^{IV} Core and its Biological Relevance

Introduction

Many O_2-binding/activating metalloproteins contain a dinuclear active site, with most of them utilizing a diiron core, including the hydroxylase component of soluble methane monooxygenase (sMMO), and the R2 subunit of Class Ia ribonucleotide reductase (RNR).[1-5] In the past 10 – 15 years, however, an increasing number of dinuclear enzymes have been reported to employ a heterobimetallic MnFe active site to bind and activate dioxygen.[6-8] The reproducible coordination of one Mn and one Fe ion in designated sites is unusual: the Irving-Williams series supports stronger binding of Fe^{II} over Mn^{II}, so a $Fe^{II}Fe^{II}$ active site is more likely to form than a $Mn^{II}Fe^{II}$ one.[9] It has been proposed the tertiary structures of proteins enforces the site-specific binding of these metal ions.[10] Examples of enzymes with MnFe sites include the R2 subunit of Class Ic RNR (RNR R2 Class Ic, Figure 6.1.A) and the R2-like ligand-binding oxidase (R2lox, Figure 6.1.B). Like the other members of the RNR family, the MnFe active site of RNR R2 Class Ic facilitates the long-range (43 ± 1 Å) electron transfer process that initiates the conversion of

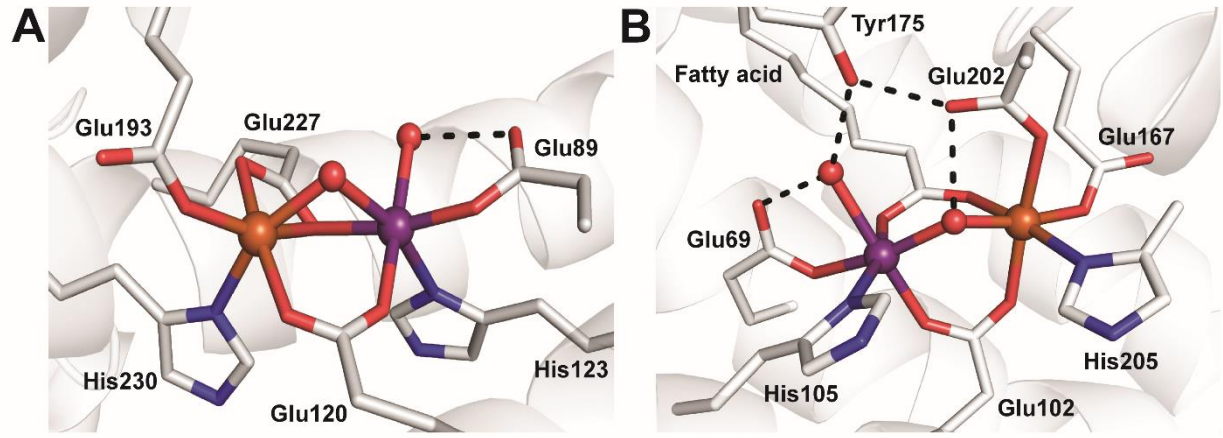

Figure 6.1. Structures of the RNR R2 Class Ic (A, PDB: 4M1I) and R2lox (B, PDB: 4HR0) active sites. Fe is shown as an orange sphere, Mn is shown as a purple sphere, and O is shown as a red sphere. Dotted lines indicate H-bonds.

ribonucleotides to deoxyribonucleotides.[8,11-17] The active site of R2lox is very similar to that of RNR R2 Class Ic (4 Glu, 2 His),[10] but it lacks RNR function. Instead, R2lox is found to oxidatively cross-link a valine and tyrosine residue in close proximity to the metallocofactor (see below for more mechanistic details).[6,7,18] The performance of these heterobimetallic enzymes raise several intriguing questions: 1) What structural factors govern the selective binding of Mn^{II} over Fe^{II}, contrary to the Irving-Williams series? 2) Why does the active site adopt a heterobimetallic (MnFe) core instead of a homobimetallic one (FeFe or MnMn) for specific functions? 3) Does the incorporation of a Mn site allow the enzyme to access reaction pathways that are not possible with Fe, or does it help avoid unreproductive pathways?

Synthetic model compounds are useful in addressing many of these considerations. However, preparation of heterobimetallic complexes is synthetically difficult, and few examples of MnFe systems have been reported relative to the FeFe and MnMn analogues.[19-23] Most of these complexes are at the (III,II) level, and their oxidation chemistry has rarely been explored. Two important contributions are highlighted here: Wieghardt and Girerd synthesized $[(TMTACN)Fe^{III}–(\mu\text{-}O)(\mu\text{-}1,3\text{-}OAc)_2–Mn^{III}(TACN)]^{2+}$ and $[(TMTACN)Mn^{III}–(\mu\text{-}O)(\mu\text{-}1,3\text{-}OAc)_2–Fe^{III}(TACN)]^{2+}$ (TACN = 1,4,7-triazacyclononane, TMTACN = 1,4,7-trimethyl-1,4,7-triazacyclononane) by combining $[Fe^{III}/Mn^{III}(TMTACN)]^{3+}$ and $[Mn^{III}/Fe^{III}(TACN)]^{3+}$ precursors in the presence of acetates (Scheme 6.1.A); the increased steric of the [TMTACN] ligand is essential in this self-recognition assembly, and appears to hinder homo-dimerization di-Fe or di-Mn products.[24] The singly oxidized $Mn^{IV}Fe^{III}$ species was also isolated, but little spectroscopic and magnetic data is available. Recently, Que utilized Fe^{IV}–oxido compounds in the [TPA] framework (or [TPA]-derivatives, [TPA] = tris(2-methylpyridine)) to bind an $[Mn^{II}(TPA)]^{2+}$ adduct.[25,26] A series of heterobimetallic $Fe^{III}Mn^{III}$ complexes were produced (Scheme 6.1.B), and the interconversion between $Fe^{III}–(\mu\text{-}O)–Mn^{III}$ and $Fe^{III}–(\mu\text{-}O)(\mu\text{-}OH)–Mn^{III}$ cores was studied under acidic and basic

conditions. However, the thermal instability of these complexes prevented their complete characterizations.

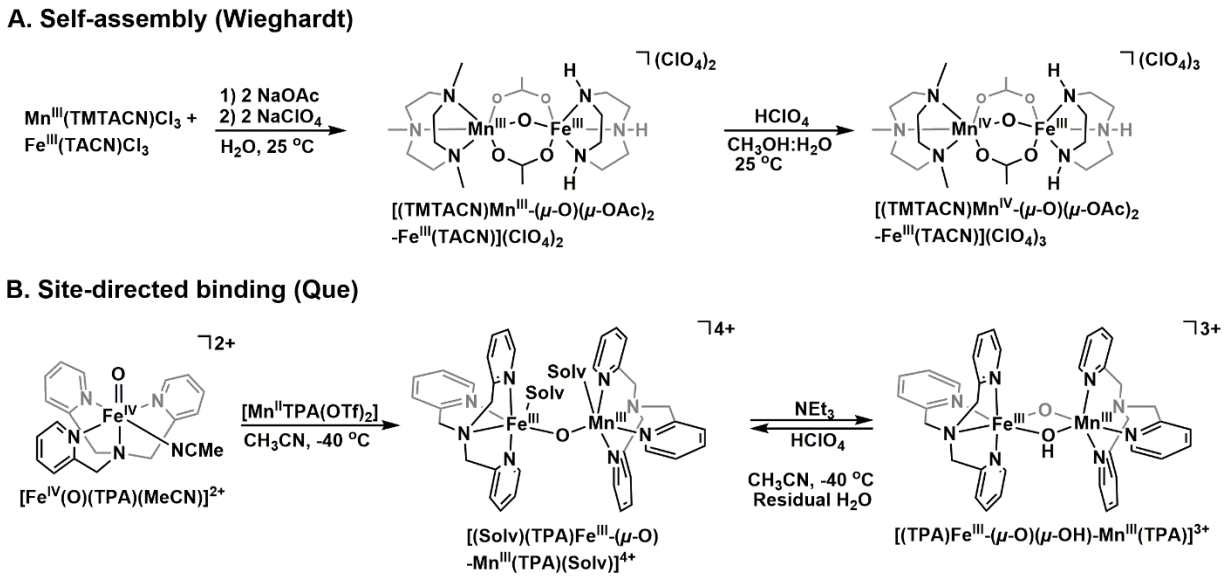

Scheme 6.1. Different synthetic strategies employed by Wieghardt (A) and Que (B) in the synthesis of $Mn^{III}Fe^{III}$ complexes.

So far in this dissertation, the successes in the synthesis of discrete bimetallic complexes in the poat/TMTACN unsymmetric framework have been discussed. Inspired by the trapping of the high-valent $[(TMTACN)Fe^{III}–(\mu\text{-}O)–Fe^{IV}poat]^{2+}$ (Chapter 5), a FeMn system was developed in a parallel study. The Fe site is capped by a TMTACN ligand, and the Mn center binds to the $[poat]^{3-}$ N-donors; it is reasoned the trianionic ligand field can better support a Mn^{IV} oxidation state. The preparation, structural, spectroscopic, and electrochemical properties of a series of MnFe complexes are described in this chapter. Their relevance to biological MnFe active sites is also discussed.

Results & Discussion

Starting Synthons. The preparations of the FeMn complexes are adapted from those for the analogous FeFe complexes described in Chapter 5. The syntheses for the starting synthons, $K[Mn^{III}poat(OH)]$ and $K[Mn^{II}poat]$, were developed within the Borovik Lab and will not be discussed here (see the experimental section for synthetic and characterization details). It should be noted that

K[Mn^{III}poat(OH)] is unstable in solution, which affects the yield and purity of subsequent FeMn complex syntheses. Recently, the analogous Na[Mn^{III}poat(OH)] was isolated in bulk quantities and crystallographically characterized. Future experiments to assemble bimetallic complexes using [Mn^{III}poat(OH)]$^-$ as a starting synthon should utilize the purer and more stable Na salt.

Preparation and Properties of [(TMTACN)Fe^{II}–(μ-OH)–Mn^{III}poat]$^+$. The preparation of [(TMTACN)Fe^{II}–(μ-OH)–Mn^{III}poat]OTf (denoted [Fe^{II}(OH)Mn^{III}poat]OTf) was adapted from syntheses of similar bimetallic complexes described in Chapters 3 and 5, and is outlined in Figure 6.2.A.[27] After multiple rounds of recrystallizations in mixtures of CH_2Cl_2/Et_2O and CH_2Cl_2/hexane, green crystals suitable for single crystal X-ray diffraction (XRD) were obtained, which confirmed the molecular structure of [Fe^{II}(OH)Mn^{III}poat]$^+$ (Figure 6.2.B). There are two crystallographically different, but chemically equivalent, molecules in the asymmetric unit, the averages of the metrical parameters and calculated values are discussed, which are shown in Table 6.1. The bimetallic complex contains a 5-coordinated Mn^{III} center and a 6-coordinated Fe^{II} center, bridged by a hydroxido ligand that forms an intramolecular H-bond (2.660(3) Å) to a phosphinic amido tripodal arm. The Mn1–O1 and Mn1–N1 distances (1.845(2) and 2.053(2) Å, respectively) are shorter than those observed for the [TM^{II}(OH)Fe^{III}poat]$^+$ (TM = Zn, Cu, Ni, Fe) complexes (1.887(4) – 1.900(2) and 2.205(1) – 2.224(5) Å, respectively) described in Chapters 3 and 5,[27] which is consistent with the absence of an electron

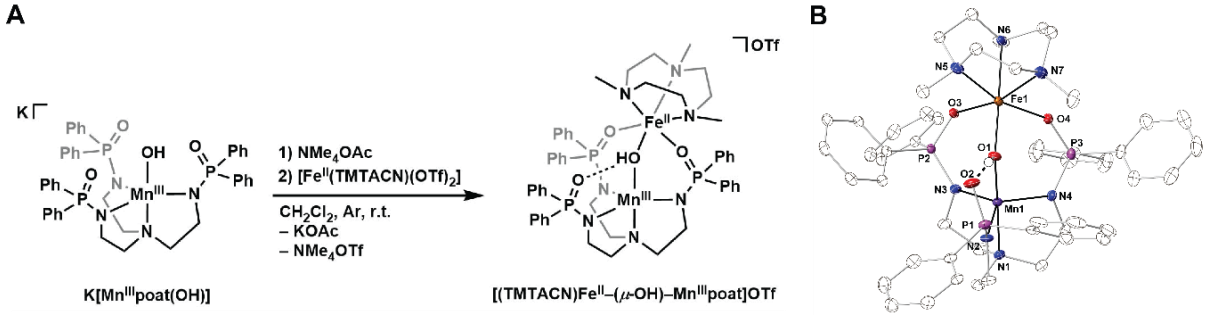

Figure 6.2. (A) Preparation of [Fe^{II}(OH)Mn^{III}poat]OTf. (B) Thermal ellipsoid diagrams depicting the molecular structures of [Fe^{II}(OH)Mn^{III}poat]$^+$ determined by X-ray diffraction. Ellipsoids are shown at the 50% probability level, and only the hydroxido H atom is shown for clarity.

in the dz^2/σ^* orbital for a d^4 Mn^{III} ion in trigonal bipyramidal (tbp) geometry. The metrical parameters around the Fe^{II} center are comparable between $[Fe^{II}(OH)Mn^{III}poat]^+$ and the di-Fe analog (Chapter 5), suggesting the electrochemical properties of the auxiliary Fe site to be similar as well.

Table 6.1. Selected bond lengths/distances (Å) and angles (°) for $[Fe^{II}(OH)Mn^{III}poat]^+$,[a] $[Fe^{III}(O)Mn^{III}Hpoat]^{2+}$, and $[Fe^{III}(O)Mn^{III}poat]^+$.

Complex	$[Fe^{II}(OH)Mn^{III}poat]^+$	$[Fe^{III}(O)Mn^{III}Hpoat]^{2+}$	$[Fe^{III}(O)Mn^{III}poat]^+$
		Bond Lengths/Distances (Å)	
Mn1–N1	2.053(2)	2.288(2)	2.074
Mn1–N2	2.024(2)	-	2.018
Mn1–O2	-	2.033(2)	-
Mn1–N3	2.061(2)	2.007(2)	2.058
Mn1–N4	2.065(2)	2.009(2)	2.062
Mn1–O1	1.845(2)	1.793(2)	1.762
O1···O2	2.660(3)	-	-
Fe1–O1	2.022(2)	1.795(2)	1.800
Fe1–O3	2.091(2)	2.000(1)	2.042
Fe1–O4	2.066(2)	2.060(2)	2.030
Fe1–N5	2.264(2)	2.234(2)	2.219
Fe1–N6	2.214(2)	2.211(2)	2.273
Fe1–N7	2.291(2)	2.212(2)	2.211
Mn1···Fe1	3.433(1)	3.206(1)	3.203
av Mn1–N/O_{eq}	2.050(2)	2.016(2)	2.046
av Fe1–N_{TMTACN}	2.256(2)	2.219(2)	2.234
d[Mn1–N_{eq}]	0.295	0.244	0.299
d[Fe1–N_{TMTACN}]	1.533	1.499	1.525
		Angles (°)	
O1–Mn1–N1	177.05(9)	178.25(7)	178.35
N2–Mn1–N3	124.08(9)	-	129.84
O2–Mn1–N3	-	133.29(7)	-
N3–Mn1–N4	108.05(9)	107.64(7)	104.19
N2–Mn1–N4	121.67(9)	-	119.48
O2–Mn1–N4	-	114.56(7)	-
Mn1–O1–Fe1	125.10(10)	126.62(8)	128.10
O3–Fe1–O4	101.37(7)	98.29(6)	96.00
N5–Fe1–N6	79.53(8)	79.89(7)	77.93
N5–Fe1–N7	77.67(9)	78.84(7)	78.99
N6–Fe1–N7	79.34(9)	79.29(7)	78.53
		Calculated Values	
τ_5[b]	0.883	0.749	0.809

[a]Bond lengths, distances, and angles are reported as an average.
[b]Trigonality structural parameter, $\tau_5 = (\beta - a)/60^o$. β is the largest bond angle observed, and a is the second largest bond angle observed.

The complex exhibits optical features at λ_{max} (ε, M^{-1} cm^{-1}) = 470 (sh) and 705 nm (460) (Figure 6.3.A). The broad d-d transition at ~700 nm has been observed for other bimetallic complexes containing a M^{II}–(μ-OH)–Mn^{III} core.[19,28-30] The electrochemical properties of [Fe^{II}(OH)Mn^{III}poat]$^+$ were investigated using cyclic voltammetry (Figure 6.3.B). The complex exhibited a reversible one-electron redox event at -1.20 V (i_{pc}/i_{pa} = 1.05), which is assigned to the $Fe^{II}Mn^{III}/Fe^{II}Mn^{II}$ couple. An additional nearly reversible process at -0.38 V (i_{pc}/i_{pa} = 0.86) was observed, which is assigned to the $Fe^{III}Mn^{III}/Fe^{II}Mn^{III}$ event. This potential is nearly identical to that found for the $Fe^{III}Fe^{III}/Fe^{II}Fe^{III}$ process in [Fe^{II}(OH)Fe^{III}poat]$^+$ (-0.42 V; Chapter 5), supporting that this redox event takes place at the Fe center. Further characterizations (e.g., EPR, elemental analysis) are required upon improved purification of this compound: the solution instability of the starting synthon K[Mn^{III}poat(OH)] is problematic, and switching to Na[Mn^{III}poat(OH)] for future syntheses should yield a purer bimetallic product.

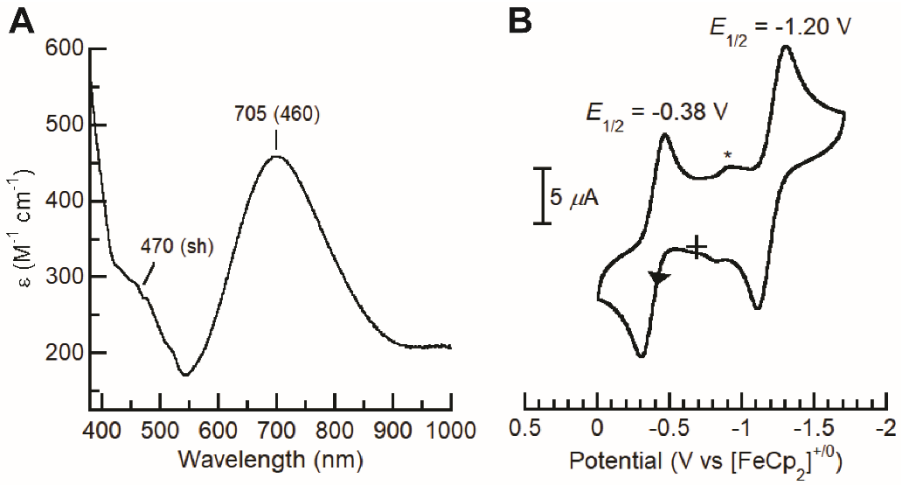

Figure 6.3. (A) Electronic absorbance spectrum for [Fe^{II}(OH)Mn^{III}poat]$^+$ (1.0 mM CH_2Cl_2 solution at room temperature). (B) Cyclic voltammogram of [Fe^{II}(OH)Mn^{III}poat]$^+$ collected at 100 mV s^{-1} in CH_2Cl_2. Asterisk (*) indicates minor unknown impurities.

Preparation and properties of [(TMTACN)Fe^{III}–(μ-O)–Mn^{III}Hpoat]$^{2+}$. With a redox potential at -0.38 V for the $Fe^{III}Mn^{III}/Fe^{II}Mn^{III}$ couple, [Fe^{II}(OH)Mn^{III}poat]$^+$ can be readily oxidized using [$FeCp_2$]OTf (Scheme 6.2). Upon recrystallization, brownish-green crystals were obtained, and XRD reveals the

molecular structure of [(TMTACN)Fe^{III}–(μ-O)–Mn^{III}Hpoat]$^{2+}$ (denoted [Fe^{III}(O)Mn^{III}Hpoat]$^{2+}$, Figure 6.4A, C). Similar to what was observed for the diferric analog described in Chapter 5, the proton in the bridging-hydroxido ligand transfers to the basic phosphinic amido N-atom in [poat]$^{3-}$ upon oxidation, resulting in a Fe^{III}–(μ-O)–Mn^{III} core, and a protonated [Hpoat]$^{2-}$ framework bound to the Mn^{III} center through the P=O group in a strained 7-member chelate ring. The Mn1–O1 and Fe1–O1 bond lengths are comparable despite being different metals (1.793(2) and 1.795(2) Å, respectively; Table 6.1), which is consistent with other heterobimetallic complexes with M^{III}–(μ-O)–M^{III} cores reported in the literature.[24-26] The Mn1···Fe1 distance contracts from 3.444(1) to 3.206(1) Å upon oxidation, but the Mn1–O1–Fe1 angle remains unaffected (125.10(10) to 126.62(8) °).

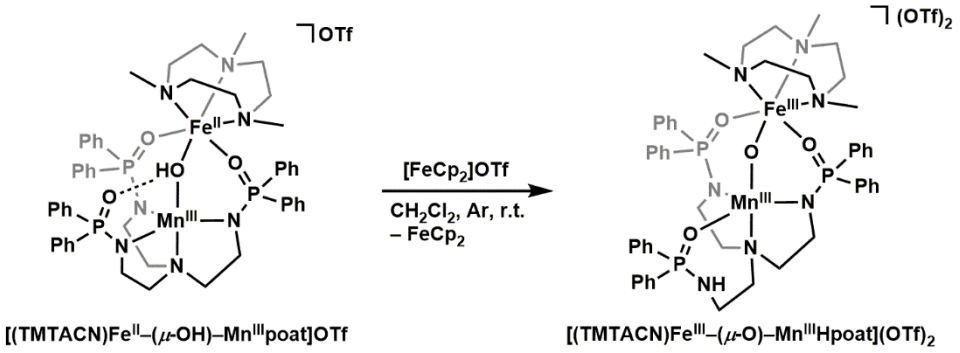

Scheme 6.2. Preparative route of [Fe^{III}(O)Mn^{III}Hpoat](OTf)$_2$.

The [Fe^{III}(O)Mn^{III}Hpoat]$^{2+}$ complex exhibits optical features at λ_{max} (ε, M^{-1} cm^{-1}) = 394 (sh), 426 (sh), 525 (sh), 570 (520), and 648 nm (510) (Figure 6.5.A, black). Similar 500 – 700 nm features are also observed in Wieghardt's and Que's $Mn^{III}Fe^{III}$ complexes.[24-26] The solid-state vibrational spectrum exhibits a strong and broad ν(N–H) feature at 3260 cm^{-1} (Figure 6.5.B, black); a similar band is also observed for [Fe^{III}(O)Fe^{III}Hpoat]$^{2+}$ (3224 cm^{-1}; Chapter 5), and is consistent with the protonation of a phosphinic amido arm. The ability to store an equivalent of proton in the [Hpoat]$^{2-}$ ligand while protecting the μ-oxido bimetallic core may facilitate proton-coupled electron transfer (PCET) reactions with high-valent complexes without unproductive damages to the complex (e.g., demetallation, cleavage of phosphinic amide P–N bonds).

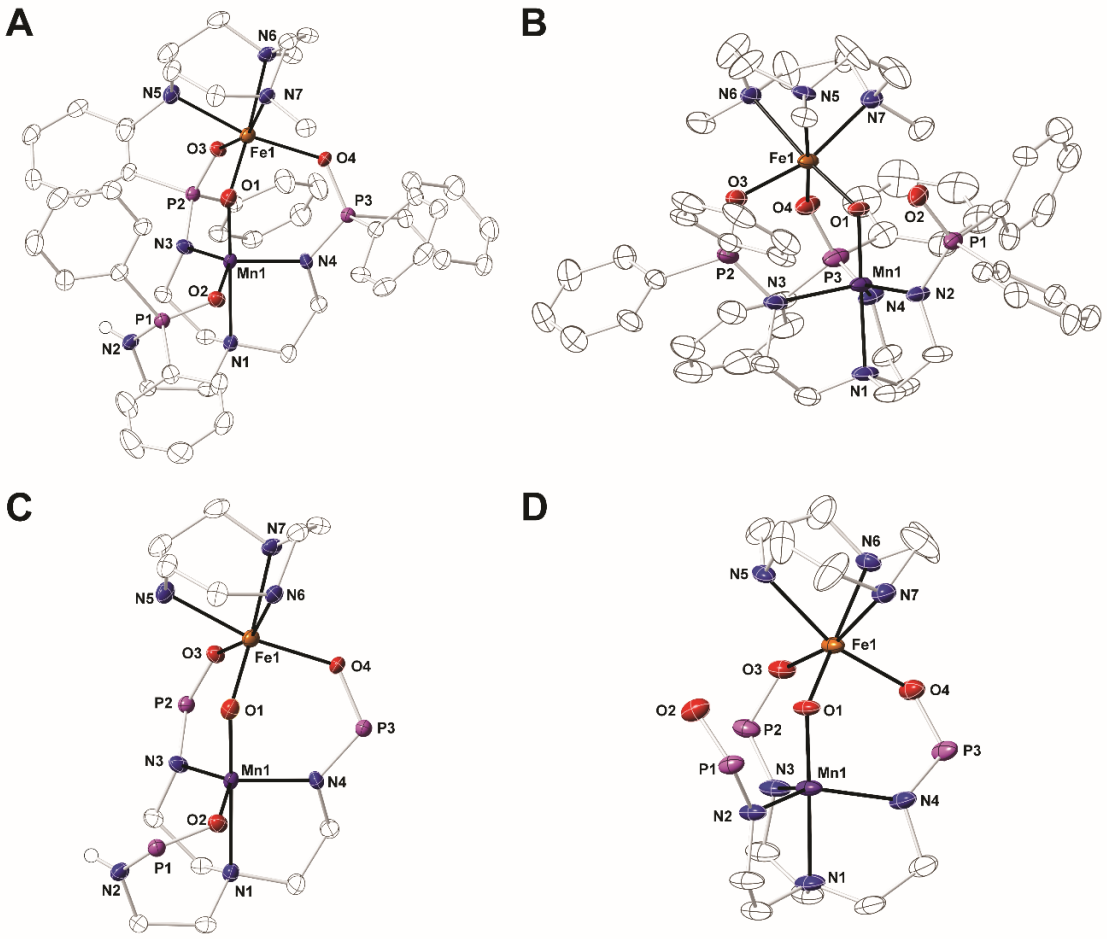

Figure 6.4. Thermal ellipsoid diagrams depicting the molecular structures of $[Fe^{III}(O)Mn^{III}Hpoat]^{2+}$ (A) and $[Fe^{III}(O)Mn^{III}poat]^{+}$ (B) determined by X-ray diffraction. Ellipsoids are shown at the 50% probability level, and only the phosphinic amide H atom is shown for clarity. The methyl and phenyl groups are removed in (C) and (D), respectively, for clarity.

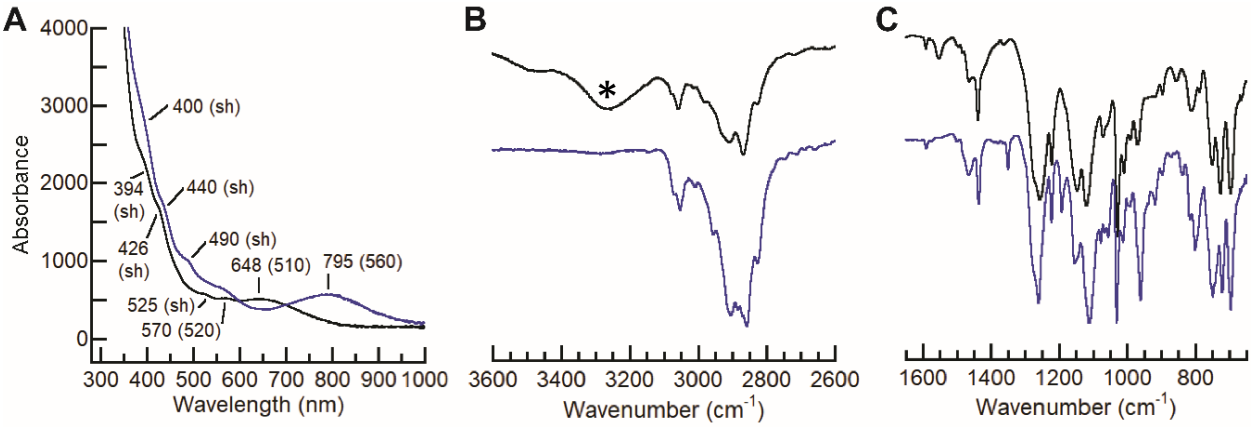

Figure 6.5. (A) Electronic absorbance spectra and (B, C) FT-IR spectra for $[Fe^{III}(O)Mn^{III}Hpoat]^{2+}$ (black) and $[Fe^{III}(O)Mn^{III}poat]^{+}$ (blue). Electronic spectra were collected at room temperature in a 0.10 mM CH_2Cl_2 solution at room temperature. FT-IR spectra are separated into the high (B) and low (C) energy regions for clarity. Asterick (*) indicates ν(N–H).

Preparation of [(TMTACN)Fe^{III}–(μ-O)–Mn^{III}poat]$^{+}$. [(TMTACN)Fe^{III}–(μ-O)–Mn^{III}poat]OTf (denoted [Fe^{III}(O)Mn^{III}poat]OTf) was prepared by treating K[Mn^{II}poat] with the O-atom transfer reagent, isopropyl 2-iodoxybenzoate (IBX-iPr), in the presence of two equivalents of 18-crown-6 (18-c-6) and [Fe^{II}(TMTACN)(OTf)$_2$] (Scheme 6.3). Current work in our lab has developed a library of C_3-symmetric bimetallic complexes, in which a [(M')^{II}(TMTACN)]$^{2+}$ adduct binds to all three phosphinic amido P=O groups in a [(M)^{II}poat]$^{-}$ complex without additional single-atom bridged ligands (Scheme 6.3, intermediate). A similar process is likely happening here as a color change is observed upon mixing of [Mn^{II}poat]$^{-}$ and [Fe^{II}(TMTACN)(OTf)$_2$] in solution, before the addition of the O-atom donor. Therefore, it is conceivable a Fe^{II}Mn^{II} species is first assembled, before an O-atom is inserted into the cluster. This is unlike the preparative route for [(TMTACN)Fe^{III}–(μ-O)–Fe^{III}poat]$^{+}$, in which [Fe^{IV}poat]$^{-}$ is first generated, before [Fe^{II}(TMTACN)(OTf)$_2$] was added (Chapter 5). Brown crystalline needles suitable for single crystal XRD were obtained after multiple rounds of recrystallization in the mixtures of CH_2Cl_2:Et_2O and CH_2Cl_2:pentane, and XRD supports the assignment of [Fe^{III}(O)Mn^{III}poat]$^{+}$ (Figure 6.4.B,D).

The molecular structure of [Fe^{III}(O)Mn^{III}poat]$^{+}$ reveals a bimetallic Fe–(μ-O)–Mn core that is similar to [Fe^{III}(O)Mn^{III}Hpoat]$^{2+}$. The major difference in the ligand coordination is that the 5-coordinated Mn^{III} has an N_4O geometry, as all three phosphinic amido N atoms in [poat]$^{3-}$ bind to the Mn center. The primary coordination sphere of the Fe center remains largely unaffected, with the N_3O_3 coordination mode retained and the bond metrics relatively unperturbed. The P=O group that does not bind to the Fe center tilts away from the bridging oxido ligand, presumably due to electrostatic repulsion. The structural parameters of the Mn–(μ-O)–Fe core, including the Mn1–O1–Fe1 angle (128.10 °), the Mn1···Fe1 distance (3.203 Å), the Mn1–O1 (1.762 Å) and Fe1–O1 (1.800 Å) bond lengths, are all comparable to those for [Fe^{III}(O)Mn^{III}Hpoat]$^{2+}$.

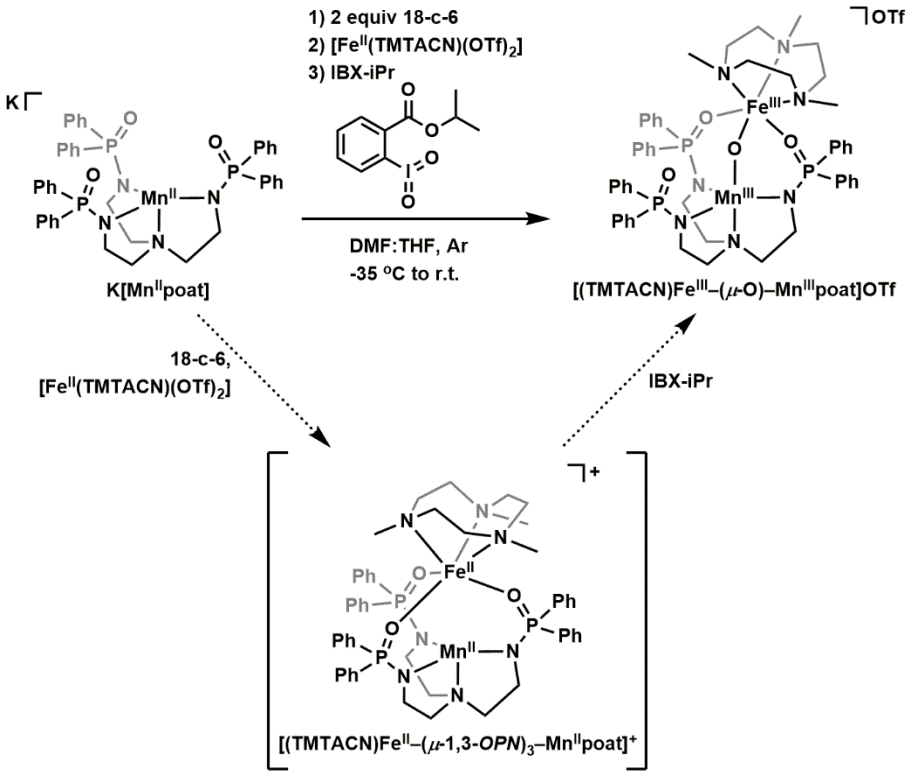

Scheme 6.3. Preparative route of $[Fe^{III}(O)Mn^{III}poat]OTf$.

The $[Fe^{III}(O)Mn^{III}poat]^{+}$ complex exhibits optical features at λ_{max} (ε, M^{-1} cm^{-1}) = 348 (sh), 400 (sh), 440 (sh), 490 (sh), 570 (sh), and 795 nm (560) (Figure 6.5.A, blue). The ligand field transition is red-shifted from 648 nm in $[Fe^{III}(O)Mn^{III}Hpoat]^{2+}$ to 795 nm in $[Fe^{III}(O)Mn^{III}poat]^{+}$, similar to the energy shift of the 705 nm feature to 780 nm observed for the deprotonation of $[Fe^{III}(O)Fe^{III}Hpoat]^{2+}$ to $[Fe^{III}(O)Fe^{III}poat]^{+}$ (Chapter 5). No vibrational feature was observed greater than 3100 cm^{-1}, supporting the lack of O–H or N–H groups in $[Fe^{III}(O)Mn^{III}poat]^{+}$ (Figure 6.5.B, blue).

Trapping of [(TMTACN)Fe^{III}–(μ-OH)–Mn^{III}poat]$^{2+}$. The successful isolation of $[Fe^{III}(O)Mn^{III}poat]^{+}$ and $[Fe^{III}(O)Mn^{III}Hpoat]^{2+}$ allowed for the investigation into the (de)protonation of these complexes in more great details. Upon treatment with 1.0 equiv 2,6-lutidinium triflate ([2,6-HLut]OTf) to $[Fe^{III}(O)Mn^{III}poat]^{+}$ at -60 °C (Scheme 6.4), a new species appeared with optical feature at λ_{max} (ε, M^{-1}

s^{-1}) = 750 nm (~340) appeared (Figure 6.6.A), which are replaced by features associated with $[Fe^{III}(O)Mn^{III}Hpoat]^{2+}$ at λ_{max} = 570 and 648 nm after 1 hour or upon warming (Figure 6.6.B). The new, thermally unstable species is tentatively assigned as $[(TMTACN)Fe^{III}–(\mu\text{-}OH)–Mn^{III}poat]^{2+}$ (denoted $[Fe^{III}(OH)Mn^{III}poat]^{2+}$). Coincidentally, the di-Fe analogue, $[Fe^{III}(OH)Fe^{III}poat]^{2+}$, exhibits a similar optical band at λ_{max} (ε, M^{-1} s^{-1}) = 760 nm (300; Chapter 5). Further magnetic and vibrational data are required to confirm this assignment of a μ–hydroxido bimetallic species.

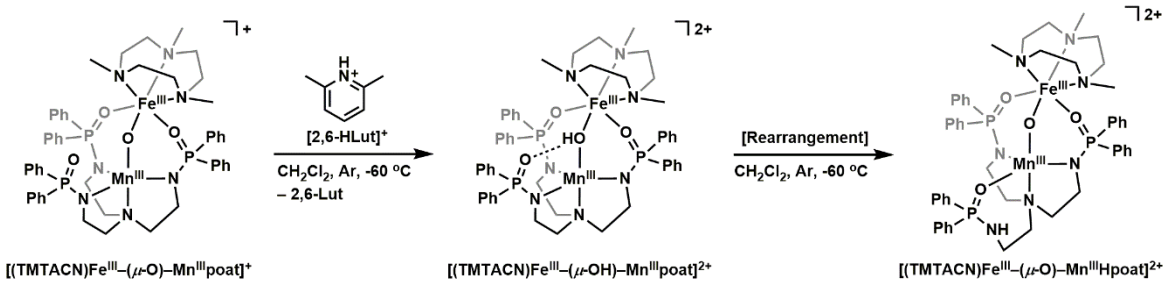

Scheme 6.4. Protonation of $[Fe^{III}(O)Mn^{III}poat]^{+}$ produces $[Fe^{III}(OH)Mn^{III}poat]^{2+}$, which undergoes intramolecular proton transfer to generate $[Fe^{III}(O)Mn^{III}Hpoat]^{2+}$.

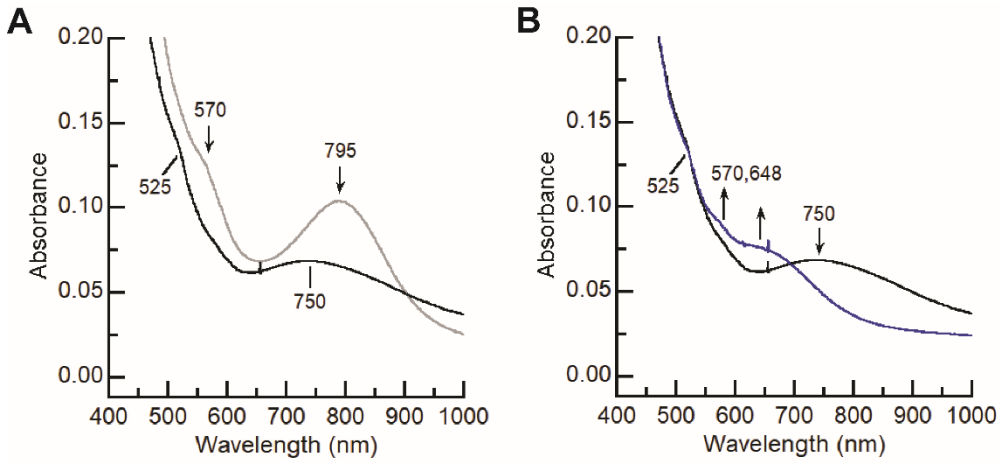

Figure 6.6. (A) UV-vis spectral changes before (grey) and after (black) the addition of [2,6-HLut]OTf to $[Fe^{III}(O)Mn^{III}poat]^{+}$ (0.20 mM CH_2Cl_2 solution at -60 °C). (B) $[Fe^{III}(OH)Mn^{III}poat]^{2+}$ (black) undergoes intramolecular proton transfer to generate $[Fe^{III}(O)Mn^{III}Hpoat]^{2+}$ (blue, 0.20 mM CH_2Cl_2 solution at -60 °C).

Magnetic properties of the Fe^{III}–(μ-O(H))–Mn^{III} complexes. The magnetic properties of the three $Fe^{III}Mn^{III}$ complexes were investigated using EPR and Mössbauer spectroscopies in collaboration with Prof. Michael Hendrich's lab (Carnegie Mellon University). The perpendicular (⊥)-mode X-band (9.6 GHz) EPR spectra for all three species (Figure 6.7.A,B,C) reveal distinct six-line, anisotropic feature

centered at around $g \sim 2$, which is consistent with an $S = 1/2$ spin-exchange system containing an $S = 5/2$ Fe^{III} site antiferromagnetically coupled to an $S = 2$ Mn^{III} center. These spectra appear to be similar, which is unsurprising due to their comparable molecular structures and Fe^{III}–(μ-O(H))–Mn^{III} cores. Their differences were resolved using S-band (3.5 GHz) EPR spectroscopy (Figure 6.7.D,E,F), and tandem simulations for spectra in both frequencies provided accurate g- and $A(^{55}Mn)$-tensors (summarized in Table 6.2). The six-line pattern is consistent with hyperfine features associated with a ^{55}Mn nucleus, and a hyperfine value of 200 – 340 MHz is comparable with those for high-spin mono- and dinuclear Mn^{III} complexes.[26,30-33] It should be noted that upon warming, the EPR features associated with $[Fe^{III}(OH)Mn^{III}poat]^{2+}$ are replaced by those for $[Fe^{III}(O)Mn^{III}Hpoat]^{2+}$, supporting the premise of intramolecular rearrangement to the thermodynamically stable product (Scheme 6.4).

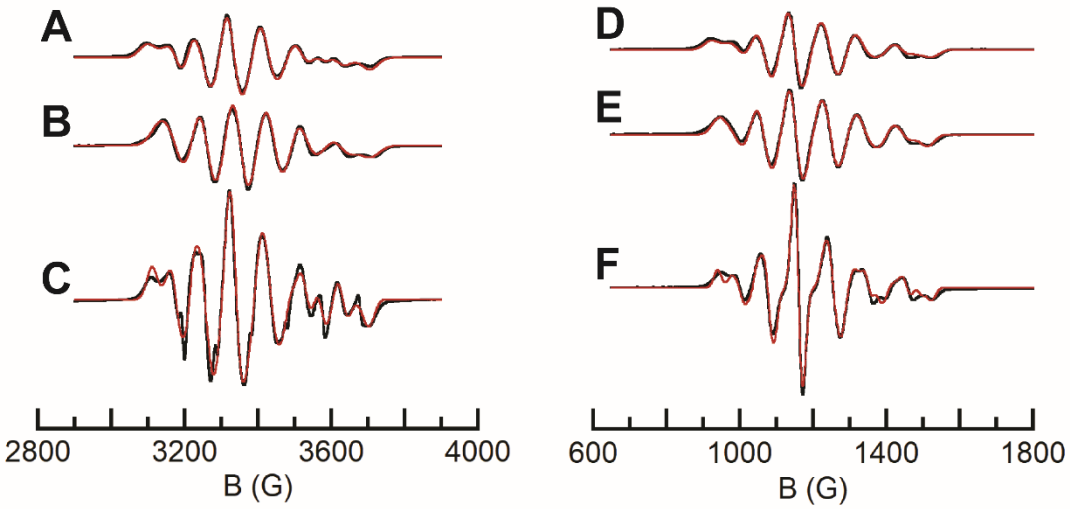

Figure 6.7. ⊥-mode X-band (A, B, C) and S-band (D, E, F) EPR spectra of $[Fe^{III}(O)Mn^{III}poat]^{+}$ (A, D, 5.0 mM CH_2Cl_2), $[Fe^{III}(OH)Mn^{III}poat]^{2+}$ (B, E, 5.0 mM CH_2Cl_2), and $[Fe^{III}(O)Mn^{III}Hpoat]^{2+}$ (C, F, 5.0 mM CH_2Cl_2:THF). X-band (9.6 GHz) spectra were collected at 17.4 K, and S-band (3.5 GHz) spectra were collected at 20.0 K. Experimental spectra are in red, and simulated spectra are in black.

$[Fe^{III}(O)Mn^{III}poat]^{+}$ was also interrogated by ^{57}Fe Mössbauer spectroscopy. Variable-field spectra (Figure 6.8) are complicated, but their simulations yielded isomer shift (δ) of 0.53 mm s^{-1} and quadrupole splitting (ΔE_Q) of -1.84 mm s^{-1}, which are consistent with a high spin Fe^{III} center that is

Table 6.2. Magnetic properties of various $Fe^{III}Mn^{III}$ and $Fe^{III}Mn^{IV}$ complexes.

Complex	S	Individual metal sites	$g_{x,y,z}$	$A_{x,y,z}(^{55}Mn)^a$	^{57}Fe $\delta/\Delta E_Q{}^b$	$A_{x,y,z}(^{57}Fe)^c$	J^d
$[Fe^{III}(O)Mn^{III}poat]^+$	1/2	S = 2 Mn^{III} S = 5/2 Fe^{III}	2.034 2.041 2.005	212.8 340.5 245.9	0.53/-1.84	-19.5 -20.0 -19.6	> 100
$[Fe^{III}(OH)Mn^{III}poat]^{2+}$	1/2	S = 2 Mn^{III} S = 5/2 Fe^{III}	2.027 2.026 2.004	209.4 322.4 257.1	n.d.	n.d.	n.d.
$[Fe^{III}(O)Mn^{III}Hpoat]^{2+}$	1/2	S = 2 Mn^{III} S = 5/2 Fe^{III}	2.028 2.008 2.004	206.3 329.2 255.3	n.d.	n.d.	n.d.
$[Fe^{III}(O)Mn^{IV}poat]^{2+}$	1	S = 3/2 Mn^{IV} S = 5/2 Fe^{III}	–	–	0.46/1.21	-20.3 -21.9 -20.0	> 100

n.d. = not determined. [a]MHz. [b]mm s^{-1}. [c]T. [d]cm^{-1} ($\mathcal{H} = JS_1 \bullet S_2$); obtained by Mössbauer.

part of an S = 1/2 coupled system. The disagreement between the experimental and simulated spectra at 0.45 kG is attributed to intermolecular interactions between MnFe molecules in these sample conditions (Figure 6.8.A). The variable-field measurements also determined the ^{57}Fe A-tensor to be nearly isotropic ([-19.5, -20.0, -19.6] T), which supports an S = 5/2 Fe^{III} site. Finally, a lower limit of 100 cm^{-1} was determined for the spin-exchange constant J ($\mathcal{H} = JS_1 \bullet S_2$), which is consistent with a bridging-oxido ligand.[24,34] Similar spectroscopic studies for $[Mn^{III}(OH)Fe^{III}poat]^{2+}$

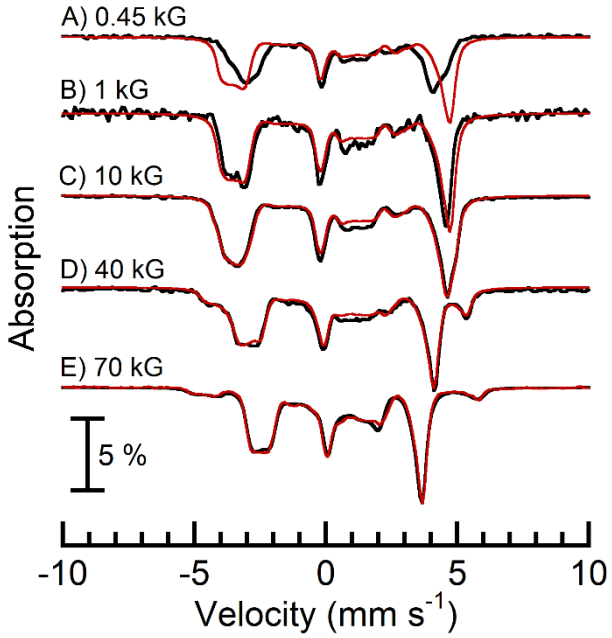

Figure 6.8. ^{57}Fe Mössbauer spectra (black, collected at 4.2 K) of $[Fe^{III}(O)Mn^{III}poat]^+$ at 0.45 kG (A), 1 kG (B), 10 kG (C), 40 kG (D), and 70 kG (E). Simulations of the Mössbauer spectra are in red.

and $[Mn^{III}(O)Fe^{III}Hpoat]^{2+}$ are needed to further the understanding of these heterobimetallic spin-coupled systems.

Accessing [(TMTACN)Fe^{III}–(μ-O)–Mn^{IV}poat]$^{2+}$. To evaluate the oxidation chemistry of $[Fe^{III}(O)Mn^{III}poat]^{+}$, cyclic voltammetry was performed to reveal a nearly reversible one-electron oxidation event at +0.20 V (vs $[FeCp_2]^{+/0}$, i_{pc}/i_{pa} = 0.75) that is assigned to the $Fe^{III}Mn^{IV}/Fe^{III}Mn^{III}$ process (Figure 6.9). This is greater than 0.3 V more negative than seen in the di-Fe analogue (Chapter 5) and consistent with what has been previously observed when accessing Mn^{IV} against Fe^{IV} in a trianionic tbp ligand field,[35,36] and the difference in the electrochemical potentials also suggests the oxidation takes place at the tripodal metal center.

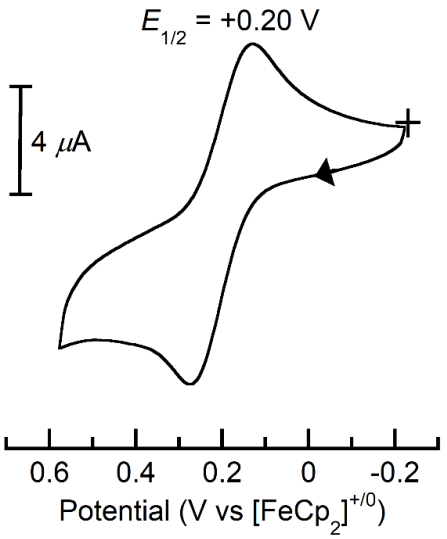

Figure 6.9. Cyclic voltammogram of $[Fe^{III}(O)Mn^{III}poat]^{+}$ collected at 100 mV s^{-1} in CH_2Cl_2.

The chemical oxidation of this complex was then monitored spectroscopically (Scheme 6.5). Upon treatment with acetylferrocenium triflate ($[FeCp(C_5H_4COMe)]OTf$ or [AcFc]OTf, +0.27 V vs $[FeCp_2]^{+/0}$)[37] or tolylamminium radical ($[N(tol)_3]OTf$, +0.40 V vs $[FeCp_2]^{+/0}$)[37] at -60 °C, a new optical spectrum was observed, but the features were not well-resolved (λ_{max} = 420 (sh), 490 (sh), 610 nm (sh), Figure 6.10.A). Notably, the electronic absorption spectrum is similar to that reported

for the $Fe^{III}Mn^{IV}$ catalytic intermediate in RNR R2 Class Ic reported by Solomon, Krebs, and Bollinger, who used a combination of optical and (magnetic) circular dichroism ((M)CD) spectroscopies to interrogate poorly-resolved transitions.[15] The new species exhibited a silent ⊥-mode EPR spectrum (Figure 6.10.B), and the low-field ^{57}Fe Mössbauer spectrum revealed a doublet spectrum with $\delta/\Delta E_Q$ values of 0.46/1.21 mm s^{-1} (Figure 6.10.C); the $Fe^{III}Mn^{IV}$ species in RNR R2 has values of 0.43/0.81 mm s^{-1}.[8] The doublet feature suggests an even-integer spin system, and spectral simulations supports an $S = 1$ ground state. Variable-field measurements revealed a nearly isotropic ^{57}Fe A-tensor of [-20.3, -21.9, -20.0] T, which, in conjunction with the large isomer shift, suggests a high-spin Fe^{III} center (Figure 6.10.D, Table 6.2). There has not been any documented observation of ligand oxidation for $[poat]^{3-}$ or [TMTACN], so the oxidation most likely occurs at the Mn^{III} center. Finally, the variable-field data supports the J coupling constant to be greater than 100 cm^{-1}, consistent with a bridging-oxido ligand. This new species is therefore formulated as $[(TMTACN)Fe^{III}–(\mu\text{-}O)–Mn^{IV}poat]^{2+}$ ($[Fe^{III}(O)Mn^{IV}poat]^{2+}$), a bimetallic system that contains an $S = 3/2$ Mn^{IV} center antiferromagnetically coupled to an $S = 5/2$ Fe^{III} site. To our knowledge, this is the second example of a synthetic $Fe^{III}Mn^{IV}$ species,[24] which demonstrates the utility of our stepwise assembly of heterobimetallic complexes to access high valent species.

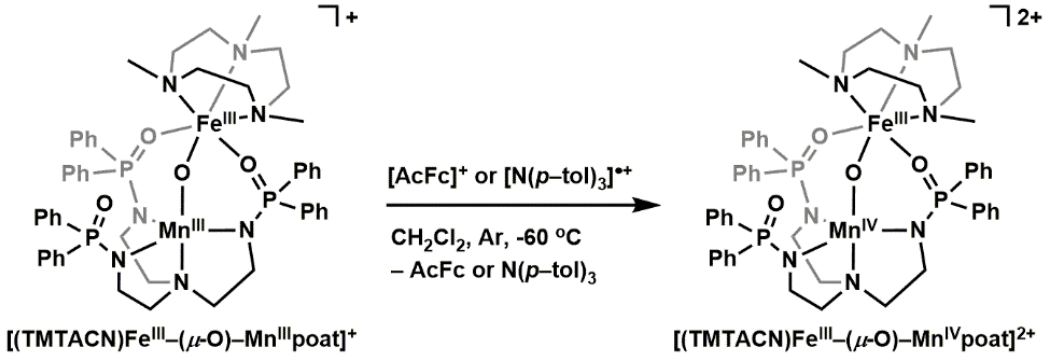

Scheme 6.5. Generation of $[Fe^{III}(O)Mn^{IV}poat]^{2+}$.

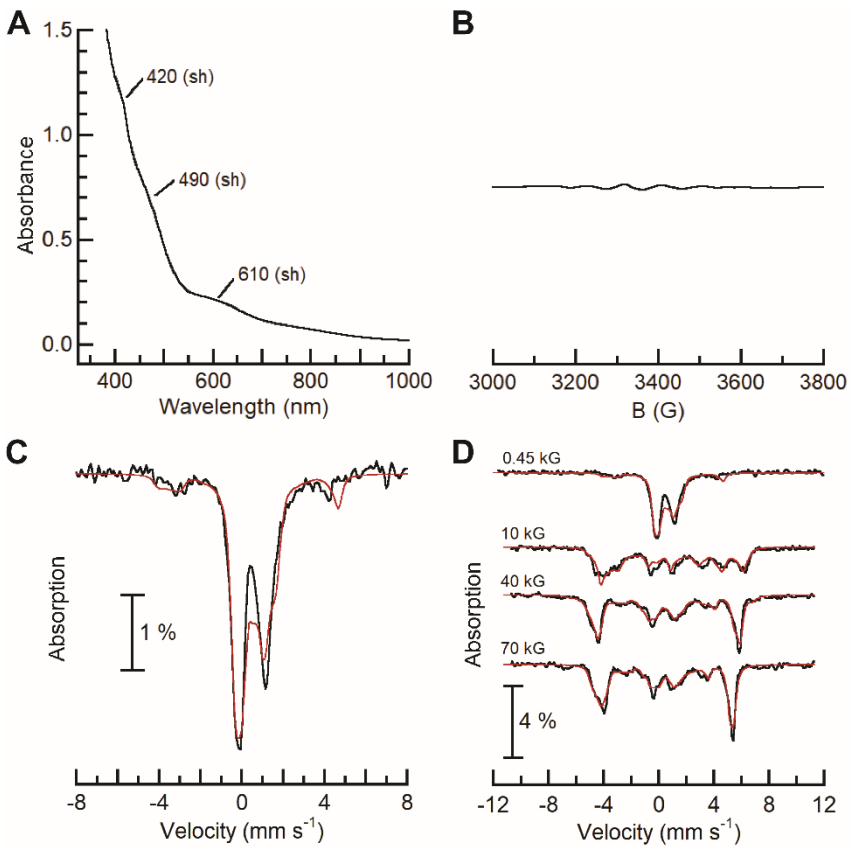

Figure 6.10. (A) Electronic absorbance spectrum for $[Fe^{III}(O)Mn^{IV}poat]^{2+}$ (0.2 mM CH_2Cl_2 solution at -60 °C). (B) Silent ⊥-mode X-band EPR spectrum of $[Fe^{III}(O)Mn^{IV}poat]^{2+}$ (collected at 16 K, CH_2Cl_2). The spectrum contains ~ 10 % unreacted $[Fe^{III}(O)Mn^{III}poat]^{+}$. (C) ^{57}Fe Mössbauer spectrum (black, collected at 4.2 K) of $[Fe^{III}(O)Mn^{IV}poat]^{2+}$ at 0.45 kG. The spectrum contains ~ 15 % unreacted $[Fe^{III}(O)Mn^{III}poat]^{+}$. (D) ^{57}Fe Mössbauer spectra (black, collected at 4.2 K) of $[Fe^{III}(O)Mn^{IV}poat]^{2+}$ at variable magnetic fields (0.45, 10, 40, 70 kG). Simulation of the Mössbauer spectrum is in red.

Reactivity towards phenolic substrates. $[Fe^{III}(O)Mn^{IV}poat]^{2+}$ was treated with the same 2,6-di-*tert*-butyl-4-R-phenol (R = MeO (BDE(O–H) = 77.4 kcal mol^{-1}), *t*Bu (80.6), H (80.5))[38] as $[Fe^{III}(O)Fe^{IV}poat]^{2+}$ (Chapter 5) and the reaction was monitored using UV-vis spectroscopy, but no reactivity was observed. However, $[Fe^{III}(O)Mn^{IV}poat]^{2+}$ does react with 4-R-phenol (R = MeO (82.6), *t*Bu (86.1), F (87.4);[38,39] Scheme 6.6): preliminary kinetics results suggest the reaction rates are dependent on the bond dissociation free energy of the phenol O–H bond. While the trisubstituted phenols have weaker O–H bonds, their steric bulk likely prevents any reaction with the $Fe^{III}Mn^{IV}$ species; the less bulky *para*-substituted phenols are much better suited to approach the Fe–(*μ*-O)–Mn core. Upon

treatment with 5 equiv 4-MeO-phenol, the optical features associated with $[Fe^{III}(O)Mn^{IV}poat]^{2+}$ were replaced by a band at λ_{max} = 750 nm (Figure 6.11.A, black), consistent with the formation of $[Fe^{III}(OH)Mn^{III}poat]^{2+}$ (Figure 6.6.A). The substrate reactivity was also monitored by ⊥-mode EPR spectrum, and the $S = 1/2$ signal associated with $[Fe^{III}(OH)Mn^{III}poat]^{2+}$ appeared after the addition of 4-MeO-PhOH in near quantitative amount (> 90 % by EPR quantification; Figure 6.11.B, black). The organic product of the reaction was analyzed by gas chromatography-mass spectrometry (GC-MS), and 5,5'-dimethoxy-[1,1'-biphenyl]-2,2'-diol (bisphenol, 246.2 m/z) was detected in near-quantitative amount (> 95 % by GC-MS quantification; Figure 6.11.C,D). Both the inorganic and organic products suggest the phenol undergoes a PCET reaction with $[Fe^{III}(O)Mn^{IV}poat]^{2+}$ to form a phenoxyl radical. Unsubstituted phenoxyl radicals are known to react through bimolecular homo-coupling at the ortho- and/or para-positions to produce bisphenol compound.[40-42] The detailed characterizations of $[Fe^{III}(O)Mn^{III}poat]^{+}$, $[Fe^{III}(O)Mn^{IV}poat]^{2+}$, and $[Fe^{III}(OH)Mn^{III}poat]^{2+}$ have allowed for monitoring the electron-transfer (ET) and PCET interconversions between these species. Thus far, no reactivity towards C–H substrates has been observed for $[Fe^{III}(O)Mn^{IV}poat]^{2+}$, including tetrahydrofuran, 9,10-dihydroanthracene, xanthene, toluene, cumene, and ethylbenzene.

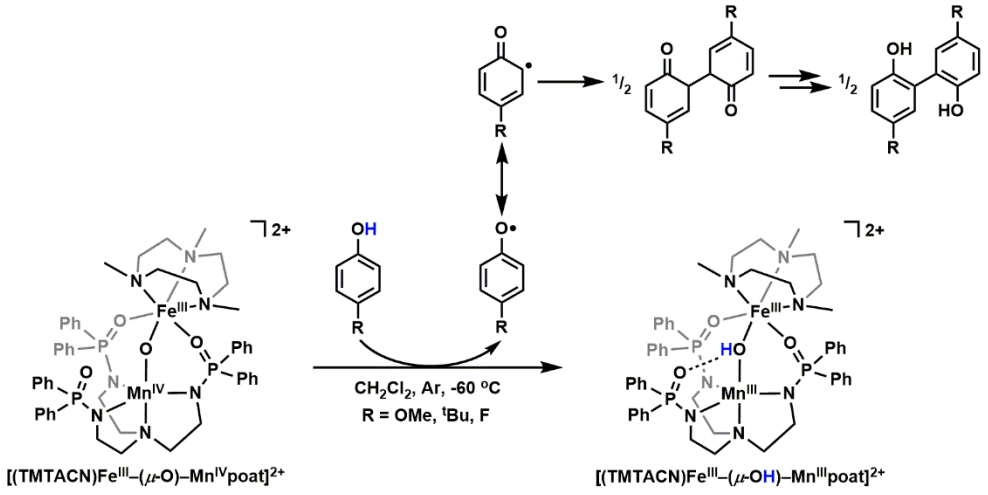

Scheme 6.6. $[Fe^{III}(O)Mn^{IV}poat]^{2+}$ reacts with 4-R-substituted phenol to produce $[Fe^{III}(OH)Mn^{III}poat]^{2+}$ and bisphenol.

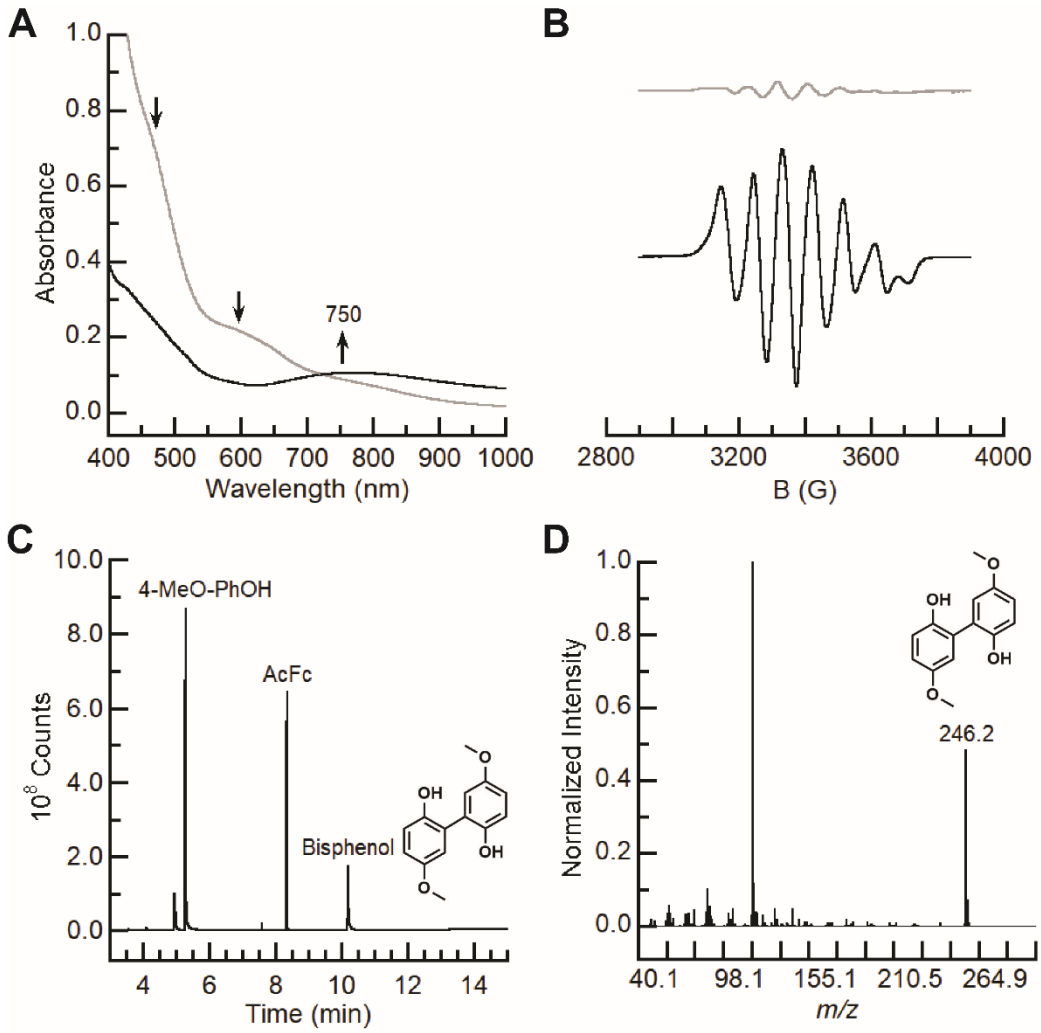

Figure 6.11. (A) Electronic absorbance spectra before (grey) and after (black) the addition of 5 equiv 4-MeO-PhOH to $[Fe^{III}(O)Mn^{IV}poat]^{2+}$ (0.2 mM CH_2Cl_2 solution at -60 °C). (B) ⊥-mode X-band EPR spectra before (grey) and after (black) the addition of 5 equiv 4-MeO-PhOH to $[Fe^{III}(O)Mn^{IV}poat]^{2+}$ (5.0 mM CH_2Cl_2 solution at -60 °C). EPR spectra were collected at 16 K. (C) Gas chromatograph of the GC-MS analysis on the reaction between $[Fe^{III}(O)Mn^{IV}poat]^{2+}$ and 4-MeO-PhOH. The t = 10.2 min detection corresponds to the bisphenol product. (D) Mass spectrum of the GC-MS analysis for the compound detected at t = 10.2 min.

Biological relevance. Tyrosine – a biological phenol – is essential in the catalytic mechanism in di-Fe RNR Class Ia, but it is replaced by a phenylalanine residue in the active site for RNR Class Ic, which contains a MnFe core.[13] While a PCET reaction with the $Mn^{IV}Fe^{III}$ cofactor is still proposed to facilitate the electron transfer from the R1 to R2 subunits, the proton and electron do not originate from the same aromatic amino acid side chain, as is the case for RNR Class Ia.[4] Therefore, the reactivity of $[Fe^{III}(O)Mn^{IV}poat]^{2+}$ towards phenols has limited relevance to RNR functions.

Another class of MnFe enzymes is R2lox, which contains a MnFe core that promotes the cross-linking of a valine and tyrosine residues in the secondary coordination sphere by forming an ether bond.[6,7,10] Shafaat monitored the O_2 binding and activation of the $Mn^{II}Fe^{II}$ resting state by electronic absorbance and EPR spectroscopy, and proposed a mechanism illustrated in Scheme 6.7.[18] The transient intermediate I_2, which is tentatively formulated as a [Mn^{III}–(μ-η^2:η^2-O_2)–Fe^{III}] or [Mn^{IV}–(μ-O)$_2$–Fe^{IV}] species, homolytically cleaves the C–H bond in the valine isopropyl group instead of the O–H bond in the tyrosine, despite OH groups in general being more kinetically susceptible to activation.[38,43,44] In addition, the resultant [Mn^{IV}–(μ-O)(μ-OH)–Fe^{III}] species does not recombine the hydroxido ligand with the carbon radical to form a tertiary alcohol in a "rebound" mechanism that is typically seen in heme and non-heme oxygenases,[46-49] nor does it further react with the tyrosine residue in a PCET reaction as observed in RNR R2 Class Ia.[4] Instead, the $Mn^{IV}Fe^{III}$ core is proposed to undergo ET with the valine radical to produce a [Mn^{III}–(μ-O)(μ-OH)–Fe^{III}] species and a carbocation, which is susceptible to nucleophilic attack by a tyrosine residue to form an ether linkage. We want to investigate the factors behind the $Mn^{IV}Fe^{III}$ core preferring an ET mechanism with the carbon radical over PCET with a phenolic amino acid residue to assess Shafaat's proposals, so we turned our attention to study the selectivities for these reactions using our model complexes.

Preliminary reactivity towards carbon radicals. The reactivity of [Fe^{III}(O)Mn^{IV}poat]$^{2+}$ towards carbon radical substrates was investigated. Triphenylmethyl radical (trityl radical, $(C_6H_5)_3C$•), more commonly known as Gomberg's dimer, exists as a radical monomer at only ~ 2% at room temperature;[50,51] however, substitution at the para-position of the phenyl rings prevents the radical dimerization even at low temperature.[52] Goldberg has reported the synthesis of a library of (p-R-$C_6H_4)_3C$• reagents and their respective $[Ar_3C]^{\bullet/+}$ reduction potentials.[52] For instance, (p-MeO-$C_6H_4)_3C$• has a reduction

potential of -0.58 V (vs $[FeCp_2]^{+/0}$ in toluene), so it should readily reduce $[Fe^{III}(O)Mn^{IV}poat]^{2+}$ ($E_{1/2}(Mn^{IV}Fe^{III}/Mn^{III}Fe^{III})$ = +0.20 V).

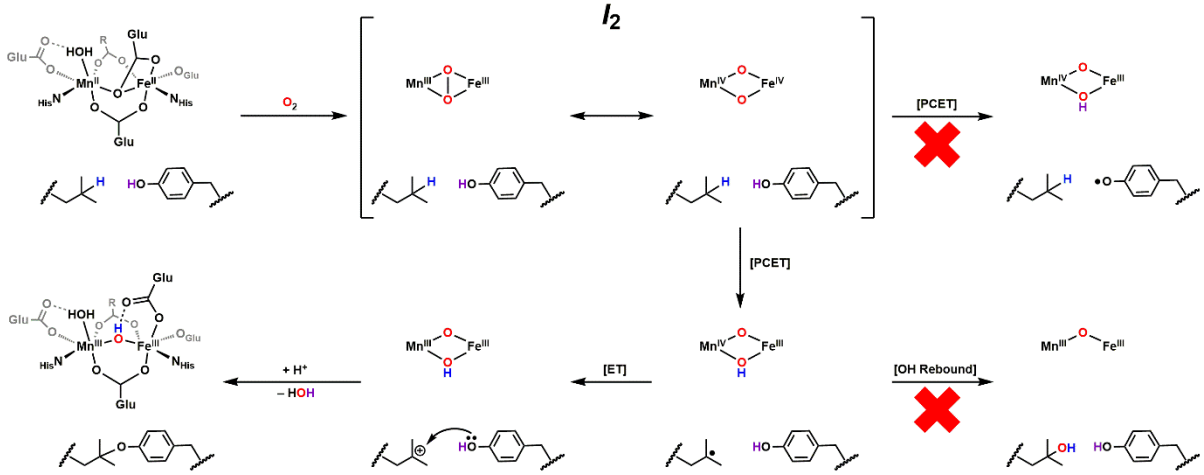

Scheme 6.7. Proposed mechanism for R2lox enzyme, which facilitates the cross-linking of the valine and tyrosine residues in the active site. The $Mn^{IV}Fe^{III}$ core preferentially undergoes ET with the valine radical over PCET with the tyrosine residue.

The literature preparation for $(p\text{-MeO-C}_6H_4)_3C\bullet$ is low-yielding (50 %),[52] so a new synthetic protocol was developed (Scheme 6.8). $(p\text{-MeO-C}_6H_4)_3CCl$ was first treated with $AgBF_4$, and pure $[(p\text{-MeO-C}_6H_4)_3C]BF_4$ was obtained. $[(p\text{-MeO-C}_6H_4)_3C]^+$ was then reduced to $(p\text{-MeO-C}_6H_4)_3C\bullet$ with $CoCp_2$, and the carbon radical mixture can be used as a stock solution for spectroscopic experiments. The disappearance of the λ_{max} = 496 nm feature confirms the absence of the MeO-trityl cation, and the feature at λ_{max} (ε, M^{-1} cm^{-1}) = 536 nm (560) is consistent with that for $(p\text{-MeO-C}_6H_4)_3C\bullet$ reported in the literature (Figure 6.12.A).[52] Quantification by EPR spectroscopy found the

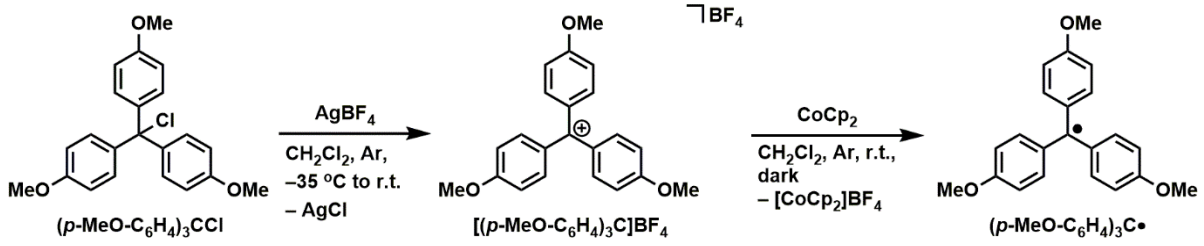

Scheme 6.8. New synthetic preparation for $(p\text{-MeO-C}_6H_4)_3C\bullet$.

reduction yield was quantitative for the trityl radical (Figure 6.12.B), suggesting this preparative route provides pure carbon radical species suitable for spectroscopic studies. The electrochemical properties of $[(p\text{-MeO-C}_6\text{H}_4)_3\text{C}]^+$ was re-evaluated in CH_2Cl_2, and cyclic voltammetry revealed a reversible one-electron $[Ar_3C]^{\bullet/+}$ process at -0.66 V (Figure 6.12.C).

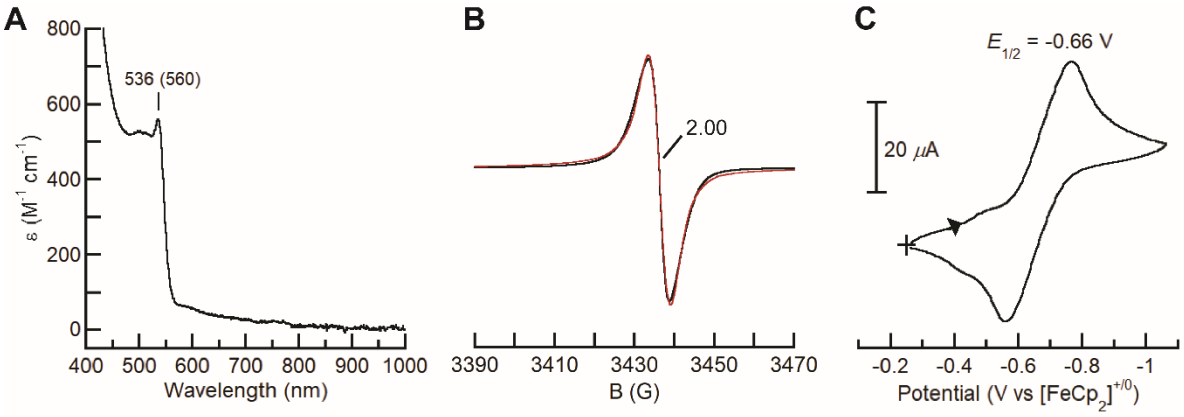

Figure 6.12. (A) Electronic absorbance spectrum of $(p\text{-MeO-C}_6\text{H}_4)_3\text{C}\bullet$, *via* reduction of the trityl cation using $CpCp_2$ (0.10 mM CH_2Cl_2 solution at room temperature). (B) ⊥-mode X-band EPR spectrum (collected at 103.6 K, black) of $(p\text{-MeO-C}_6\text{H}_4)_3\text{C}\bullet$, *via* reduction of the trityl cation using $CpCp_2$ (10 mM CH_2Cl_2 solution at room temperature). Simulated spectrum is in red. (C) Cyclic voltammogram of $[(p\text{-MeO-C}_6\text{H}_4)_3\text{C}]^+$ collected at 100 mV s^{-1}.

Treatment of $[Fe^{III}(O)Mn^{IV}poat]^{2+}$ with $(p\text{-MeO-C}_6\text{H}_4)_3\text{C}\bullet$ resulted in slow growth of an optical feature at λ_{max} = 496 nm that indicates the generation of the MeO-trityl cation, and that an ET reaction had occurred (Scheme 6.9; Figure 6.13). However, the diagnostic feature for $[Fe^{III}(O)Mn^{III}poat]^+$ at λ_{max} = 795 nm was not observed. EPR spectroscopy will be useful in monitoring the generation of any S = 1/2 $Mn^{III}Fe^{III}$ species and/or disappearance of the carbon radical in future experiments. It is noteworthy that the ET reaction of the high valent species towards MeO-trityl radical was slow in spite of an 800 mV difference in reduction potentials between $[Fe^{III}(O)Mn^{IV}poat]^{2+}$ and $(p\text{-MeO-C}_6\text{H}_4)_3\text{C}\bullet$: one plausible explanation could be the bulkiness of both species hinders a normally-facile ET process, similar to the lack of reactivity with trisubstituted phenol substrates.

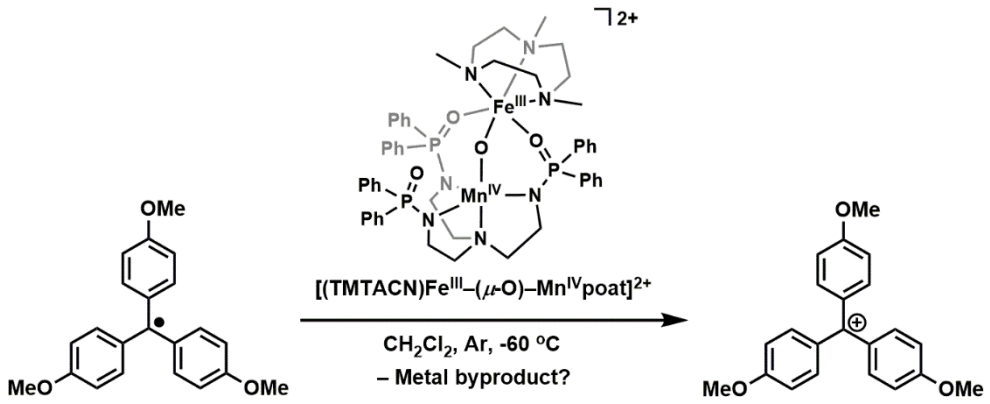

Scheme 6.9. Treatment of (p-MeO-C_6H_4)$_3$C• to [Fe^{III}(O)Mn^{IV}poat]$^{2+}$ produces [(p-MeO-C_6H_4)$_3$C]$^+$, but the metal product species is yet unidentified.

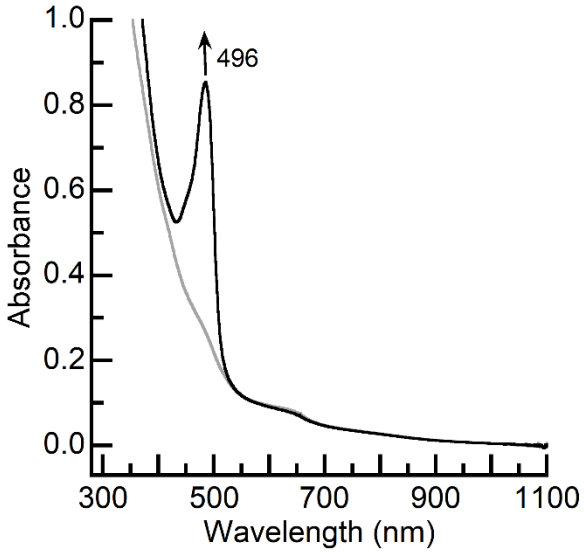

Figure 6.13. Electronic absorbance spectra before (grey) and after (black) the addition of (p-MeO-C_6H_4)$_3$C• to [Fe^{III}(O)Mn^{III}poat]$^+$ (0.10 mM CH_2Cl_2 solution at -60 °C).

Conclusion & Outlook

In this chapter, the preparation of a series of heterobimetallic FeMn synthetic complexes in an unsymmetric scaffold is described and summarized in Scheme 6.10. These species contain Fe–(μ-O(H))–Mn cores that resemble those found in the active site of MnFe-based enzymes, such as RNR R2 Class Ic and R2lox.[6-8] The Fe site remains coordinatively saturated at all oxidation states with the TMTACN capping ligand, while the Mn center is housed within the [poat]$^{3-}$ trigonal framework. This library of complexes spans across three different oxidation states and share many characteristics

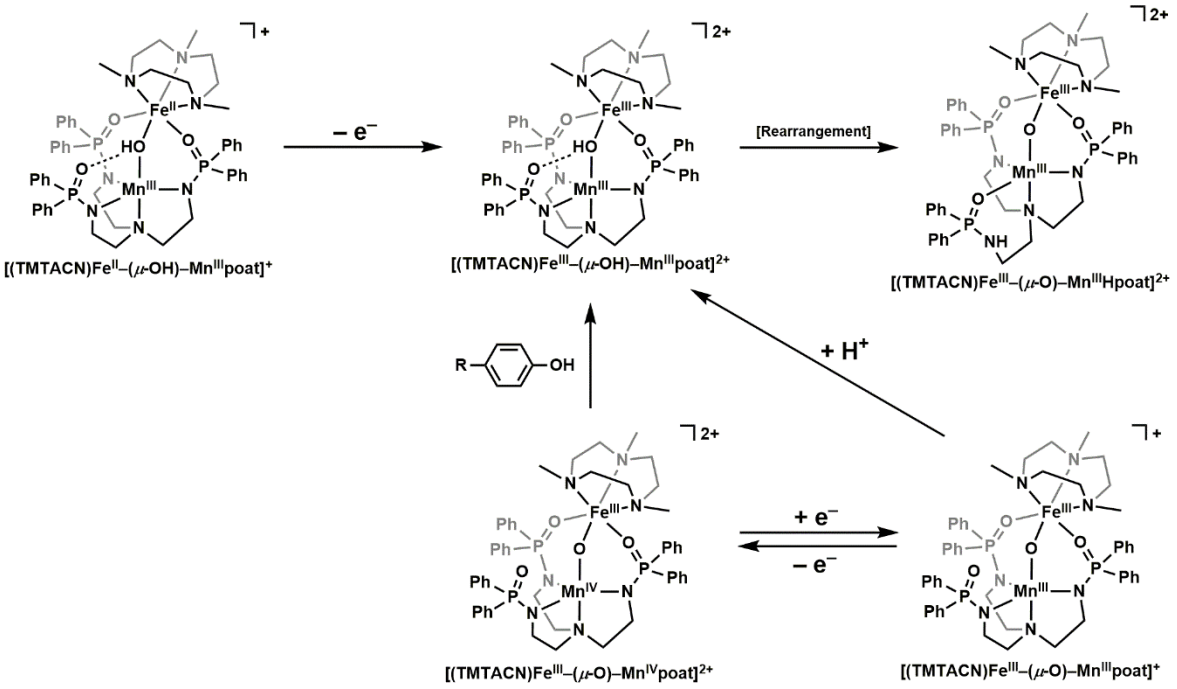

Scheme 6.10. A summary of the MnFe complexes discussed in this chapter.

with the di-Fe analogues described in Chapter 5, including the proton transfer from the Fe^{III}–(μ-OH)–Mn^{III} core to one phosphinic amido arm for better stabilization. However, there are key distinctions: most notably, the $S = 1/2$ ground state of the three $Fe^{III}Mn^{III}$ complexes and the spin-active ^{55}Mn nucleus provided us an opportunity to probe the magnetic properties of these compounds *via* EPR spectroscopy that is not feasible with the di-Fe system. A Fe^{III}–(μ-O)–Mn^{IV} species is trapped and studied spectroscopically; this is only the second example of a synthetic $Fe^{III}Mn^{IV}$ species and can serve as an invaluable model complex for FeMn active sites in nature. $[Fe^{III}(O)Mn^{IV}poat]^{2+}$ exhibits PCET reactivities towards *para*-substituted phenols, and its reactivity towards carbon radicals is currently being studied to help elucidate the mechanism of the ether linkage formation observed in R2lox.

While the generation of $[Fe^{III}(O)Mn^{IV}poat]^{2+}$ is an important finding, the high valent species has thus far demonstrated little reactivity towards substrates outside of organic phenols; in particular, C–H bond functionalization is of interest due to its biological relevance. For instance, a

putative $Mn^{IV}Fe^{IV}$ core in R2lox is proposed to activate the valine methine C–H bond to initiate the crosslink between amino acid side chains (Scheme 6.7).[18] Efforts to access the one-electron oxidized "$[Fe^{IV}(O)Mn^{IV}poat]^{3+}$" have been unsuccessful, likely due to insufficient σ-donation by the TMTACN tertiary amine groups. To address this limitation, minor adjustments were made on the heterobimetallic system, which is discussed in the following chapter.

Experimental

General Procedures. Organic syntheses, unless otherwise noted, did not require the use of an inert atmosphere. All inorganic syntheses and manipulations were performed under an argon atmosphere in a Vacuum Atmosphere Co. dry box. Solvents were sparged with argon and purified using a JC Meyer Co. solvent purification system with columns containing Q-5 and molecular sieves. All reagents, unless otherwise noted, were purchased from commercial sources and used as received. Butyronitrile (PrCN) was purified according to a literature procedure.[53] Potassium hydride (KH) as a 30 % dispersion in mineral oil was filtered with a medium porosity glass frit and washed 5 times each with pentane and diethyl ether (Et_2O). Solid KH was dried under vacuum and stored under an inert atmosphere. Tetrabutylammonium hexafluorophosphate (TBAP) was recrystallized from hot EtOH. H_3poat,[54] $[Fe^{II}$(TMTACN)$(OTf)_2]$,[55] $[FeCp_2]OTf$,[37] IBX-iPr,[56,57] 2,6-lutidinium triflate,[58] and $[N(p\text{-tol})_3]OTf$[37] were synthesized according to previous reports. $[^{57}Fe^{II}$(TMTACN)$(OTf)_2]$ was synthesized using the $^{57}Fe^{II}(OTf)_2{\cdot}2CH_3CN$ precursor, which was metathesized from $^{57}Fe^{II}Cl_2$. 4-MeO-phenol was purified by sublimation.

Physical Methods. Room temperature UV-vis spectra were collected on a Cary 50 or 60 UV-vis spectrophotometer in a 1 cm quartz cuvette; low temperature spectra were collected on an Agilent UV-vis spectrophotometer equipped with a Unisoku Unispeks cryostat. Solid-state Fourier transform infrared (FTIR) spectra were collected on a Thermo Scientific Nicolet iS5 FT-IR

spectrometer equipped with an iD5 ATR accessory. Cyclic voltammetry experiments were conducted using a CHI600G electrochemical analyzer. A 2.0 mm glassy carbon electrode was used as the working electrode at scan velocities between 0.01 and 0.5 $V \cdot s^{-1}$. A ferrocenium/ferrocene ($[FeCp_2]^{+/0}$) standard was used as an internal reference to monitor the reference electrode (Ag^+/Ag). TBAP was used as the supporting electrolyte at a concentration of 0.1 M. Elemental analyses were performed on a Perkin-Elmer 2400 Series II CHNS elemental analyzer. ^1H NMR spectra was collected on a Bruker CRYO500 spectrometer (500 MHz). X-band (microwave frequencies 9.6 GHz) and S-band (3.5 MHz) EPR spectra were collected on a Bruker ELEXSYS spectrometer equipped with an Oxford ESR-910 liquid helium cryostat and a Bruker bimodal cavity for the generation of microwave fields parallel and transverse to the applied magnetic field. Mössbauer spectra were recorded on either a variable field or a weak-field spectrometer operating in a constant acceleration mode in a transmission geometry using Janis Research Inc. cryostats that allow for a variation in temperature from 4 to 300 K. One of the dewars housed a superconducting magnet that allowed for the application of magnetic fields up to 8 T parallel to the γ-radiation. Isomer shifts are reported relative to Fe metal at 298 K. SpinCount was used to fit the experimental EPR and Mössbauer data.[59] Organic products were detected by gas-chromatography mass spectrometry (GC-MS) in the Mass Spectrometry Facility at the University of California, Irvine. The GC-MS was a Trace 1300 Gas Chromatograph from Thermo Scientific using a 15 m long x 0.25 mm i.d. TG-SQC column. The oven was held at 40 °C for 1 minute then heated at a rate of 20 °C min^{-1} to 290 °C and held for an additional 2 minutes. The mass spectrometry used electron ionization (70 eV) scanning (0.2/sec) from m/z 30 – 650.

Synthesis of K[Mn^{II}poat]. This preparation is adapted from the procedure developed in the Borovik Lab. To a solution of H_3poat (0.200 g, 0.268 mmol) in anhydrous THF (5 mL) was added KH (0.0340 g, 0.848 mmol), and the reaction was allowed to proceed until gas evolution ceased and all solids were dissolved. To the solution was added $Mn^{II}(OAc)_2$ (0.0520 g, 0.301 mmol). The mixture

was stirred for 3 hours and then filtered through a fine fritted glass funnel to remove insoluble material. All volatiles in the pale-yellow filtrate were removed under vacuum to afford an off-white paste. The residues were re-dissolved in 3 mL THF, and 20 mL Et_2O was added to precipitate the product. The mixture was allowed to triturate for 20 min, and the white solids were then collected and dried on a fine fritted glass funnel (70 – 80 % yield). Single crystals were obtained by layering a concentrated K[Mn^{II}poat] solution in CH_2Cl_2 under pentane in low yield (< 10 %). Elemental analysis calc. (found) for K[Mn^{II}poat]·$0.5C_5H_{12}$, $C_{42}H_{42}KMnN_4O_3P_3$·$0.5C_5H_{12}$; C, 61.16 (61.39); H, 5.54 (5,43); N, 6.41 (6.72) %. X-band, ⊥-mode EPR (CH_2Cl_2:THF) g = 7.81, 4.54, 2.85, 1.67, 1.32.

Synthesis of K[Mn^{III}poat(OH)]. This preparation is adapted from the procedure developed in the Borovik Lab. To a solution of H_3poat (0.400 g, 0.536 mmol) in anhydrous THF (14 mL) was added KH (0.0665 g, 1.66 mmol), and the reaction was allowed to proceed until gas evolution ceased and all solids were dissolved. To the solution was added $Mn^{II}(OAc)_2$ (0.0980 g, 0.566 mmol). The pale-yellow solution was stirred for 3 hours, then H_2O (10 μL, 0.55 mmol) was added via syringe. After 15 minutes, the reaction mixture was filtered through a medium porosity glass frit to remove insoluble material. KH (0.0225 g, 0.561 mmol) was added to the filtrate, which was allowed to stir for 1 hour. The reaction mixture was then filtered through a medium porosity glass frit to remove any insoluble material. 0.5 equivalent of I_2 (0.0681 g, 0.268 mmol) was added to the pale-yellow solution, which turned dark green and stirred for 30 minutes. The reaction mixture was filtered using a fine porosity glass frit and then concentrated until ~ 3 mL THF remained. Excess pentane (30 mL) was added to crash out the product, which was triturated with pentane until the residue was a free-flowing powder. The green powder was collected on a fine porosity glass funnel, washed with 2 portions of 20 mL pentane, and dried (80 – 90 %). Elemental analysis calc. (found) for K[Mn^{III}poat(OH)]·$0.5KI$·$0.5H_2O$, $C_{42}H_{43}KMnN_4O_4P_3$·$0.5KI$·$0.5H_2O$; C, 53.28 (53.17); H, 4.68

(4.53); N, 5.92 (5.98) %. FTIR (diamond ATR, cm^{-1}): 3197 (br, OH), 3071, 3045, 3018, 3007, 2076, 2953, 2900, 2855, 2837, 1589, 1572, 1481, 1434, 1307, 1266, 1234, 1165, 1112, 1067, 1025, 996, 963, 927, 860, 794, 746, 717, 694.

Synthesis of [(TMTACN)Fe^{II}–(μ-OH)–Mn^{III}poat]OTf. This salt was prepared using the method described for [(TMTACN)Zn^{II}–(μ-OH)–Fe^{III}poat]OTf (Chapter 3)[27] with the following modifications: K[Mn^{III}poat(OH)] (0.0879 g, 0.103 mmol), NMe_4OAc (0.0212 g, 0.111 mmol), [Fe^{II}(TMTACN)$(OTf)_2$]·CH_3CN (0.0540 g, 0.103 mmol). Green crystals (20 – 30 % yield) suitable for X-ray diffraction were grown from a concentrated CH_2Cl_2 solution layered with hexane. UV-vis $\lambda_{max}(CH_2Cl_2)$/nm (ε/$M^{-1}cm^{-1}$): 470 (sh), 705 (~460). $E_{1/2}$ (CH_2Cl_2, V versus $[FeCp_2]^{+/0}$): -1.20, -0.38. Multiple attempts at elemental analysis were unsuccessful.

Synthesis of [(TMTACN)Fe^{III}–(μ-O)–Mn^{III}Hpoat](OTf)$_2$. [(TMTACN)Fe^{II}–(μ-OH)–Mn^{III}poat]OTf (0.0401 g, 0.0336 mmol) was dissolved in 2 mL anhydrous CH_2Cl_2, and solid $[FeCp_2]$OTf (0.0119 g, 0.0355 mmol) was added in one portion to the green solution. The solution immediately turned dark brown and was allowed to stir for 1.5 hours. All volatiles were then removed under vacuum. The residues were triturated with 20 mL pentane, which was then removed by decanting; the washing process was repeated three times. The residues were redissolved in 3 mL CH_2Cl_2, which was layered with pentane to yield green crystalline needles (70 – 80 %). Single crystals suitable for X-ray diffraction were obtained from layering a concentrated MnFe solution in CH_2Cl_2 under hexane. FTIR (diamond ATR, cm^{-1}): 3466, 3260 (NH), 3070, 3057, 2977, 2905, 2869, 2824, 1591, 1550, 1464, 1438, 1363, 1254, 1223, 1146, 1119, 1070, 1028, 1009, 990, 969, 919, 896, 854, 812, 788, 749, 725, 696. EPR (X-band, ⊥-mode, CH_2Cl_2:THF, 17.4 K): $g_{x,y,z}$ = 2.028, 2.008, 2.004; $A_{x,y,z}(^{55}Mn)$ =

206.3, 329.2, 255.3 MHz. UV-vis $\lambda_{max}(CH_2Cl_2)$/nm ($\varepsilon/M^{-1}cm^{-1}$): 394 (sh), 426 (sh), 525 (sh), 570 (520), 648 (510). Multiple attempts at elemental analysis were unsuccessful.

Synthesis of [(TMTACN)Fe^{III}–(μ-O)–Mn^{III}poat]OTf. K[Mn^{II}poat] (0.0590 g, 0.0700 mmol) and 18-crown-6 (0.0400 g, 0.151 mmol) were dissolved in 2 mL anhydrous DMF, and mixed for 10 min. [Fe^{II}(TMTACN)(OTf)$_2$] (0.0372 g, 0.0708 mmol) was added in one portion, and the pale solution turned yellow immediately, and was allowed to stir for an additional 15 min. The reaction vial was placed in a pre-cooled aluminum block and chilled in a -35 °C freezer for 20 minutes. IBX-iPr (0.0314 g, 0.0972 mmol) was then added in one portion to the mixture, which turned dark brown. The reaction was allowed to stir for 5 min inside the Al block, before returning to chill inside the freezer for 5 min; this is repeated for eight times (a total of 40 min of stirring time). The solution was then warmed up to room temperature, and all volatiles were removed under vacuum. The residue was redissolved in CH_2Cl_2 and was layered with diethyl ether to yield a brown powder over three days. After the brown powder was collected and dried, it was redissolved in CH_2Cl_2, and was layered with pentane to yield dark brown crystalline needles. The crystals were collected on a glass frit and dried under vacuum, affording the product in yields that ranged from 30 – 40 %. Elemental analysis calcd. (found) for [(TMTACN)Fe^{III}–(μ-O)–Mn^{III}poat]OTf·1.5CH_2Cl_2, $C_{52}H_{63}F_3FeMnN_7O_7P_3S$·1.5$CH_2Cl_2$; C, 48.74 (48.90); H, 5.05 (5.20); N, 7.44 (7.64) %. UV-Vis (CH_2Cl_2 solution λ_{max}/nm ($\varepsilon_{max}/M^{-1}cm^{-1}$)) 348 (sh), 400 (sh), 440 (sh), 490 (sh), 570 (sh), 795 (560). FTIR (ATR, cm^{-1}): 3061, 3052, 3008, 2954, 2903, 2884, 2857, 2825, 1588, 1499, 1464, 1436, 1350, 1259, 1223, 1192, 1153, 1111, 1078, 1066, 1056, 1031, 1011, 991, 961, 919, 896, 836, 801, 748, 720, 695, 636. EPR (X-band, ⊥-mode, CH_2Cl_2:THF, 17.4 K): $g_{x,y,z}$ = 2.034, 2.041, 2.005; $A_{x,y,z}(^{55}Mn)$ = 212.8, 340.5, 245.9 MHz. Mössbauer (5 mM ^{57}Fe-enriched sample, PrCN, 4.2 K) δ = 0.53 mm s^{-1}; ΔE_Q = -1.84 mm s^{-1}. $E_{1/2}$ (CH_2Cl_2, V versus $[FeCp_2]^{+/0}$): +0.20.

Low-temperature UV-vis solution studies. In a typical experiment, a 10 – 20 mM solution of the MnFe compound was prepared in CH_2Cl_2 at room temperature and kept in a -35 °C freezer for the duration of the experiment. A 30 - 60 μL aliquot of stock metal complex was added via air-tight syringe to the solvent mixture (3 mL) in a 1-cm quartz cuvette to give the desired concentration for oxidation experiments (0.10 - 0.20 mM). The cuvette was then sealed with a rubber septum and precooled to the desired temperature in an 8453 Agilent UV-vis spectrophotometer equipped with an Unisoku Unispeks cryostat. The solution of metal complex was allowed to equilibrate to the desired temperature for at least 15 min. Stock solutions of other reagents were prepared at concentrations between 10 and 100 mM in the same solvent and added via gas-tight syringe. Reactions were monitored spectrophotometrically by UV-vis spectroscopy.

Low-temperature EPR solution studies. In a typical experiment, a 5 – 6 mM solution of the MnFe compound was prepared in CH_2Cl_2 at room temperature and kept in a -35 °C freezer of the glovebox for the duration of the experiment. A 200 μL aliquot of stock metal complex was added via air-tight syringe to an EPR tube, which was then sealed with a rubber septum and precooled to the desired temperature in a cold bath outside the glovebox. The solution of metal complex was allowed to equilibrate to the desired temperature for at least 15 min. Stock solutions of other reagents were prepared at concentrations between 40 and 250 mM in the same solvent and added via gas-tight syringe. The target final concentration is ~ 5 mM.

Room-temperature Mössbauer solution studies. The Mössbauer sample for $[^{57}Fe^{III}(O)Mn^{III}poat]^+$ was prepared at room temperature. A 2.75 mM solution of the 96% ^{57}Fe-enriched

[$^{57}Fe^{III}$(O)Mn^{III}poat]OTf (0.0055 g, 0.0046 mmol) was prepared in PrCN, and an aliquot of 0.6 mL was transferred into a Mössbauer cup before freezing in liquid nitrogen.

Low-temperature Mössbauer solution studies. In a typical experiment to generate [$^{57}Fe^{III}$(O)Mn^{III}poat]$^{2+}$, a 2.75 mM solution of the 96% ^{57}Fe-enriched [$^{57}Fe^{III}$(O)Mn^{III}poat]OTf (0.0055 g, 0.0046 mmol, 1.12 mL) was prepared in PrCN at room temperature in a glovebox under argon atmosphere, and kept in a -35 °C freezer for the duration of the experiment. A 1.0 mL aliquot of stock metal complex (0.0027 mmol) was added via syringe to a 1-cm quartz. The cuvette was then sealed with a rubber septum and precooled to -80 °C in a Unisoku Unispeks cryostat typically used for UV-vis experiments outside the glovebox. The solution of metal complex was allowed to equilibrate to the desired temperature for at least 20 min. A stock solution of [N(p-tol)$_3$]OTf was prepared at 41.25 mM in PrCN, and an aliquot of the oxidant (0.0041 mmol, 0.10 mL) was added via a gas-tight syringe. Upon completion of the reaction, the septum was sliced open with a razor under a strong flow of argon. The rubber septum was removed and the content in the cuvette was quickly poured into liquid nitrogen. The frozen solid was ground into fine powder and then packed into a pre-cooled Mössbauer cup.

Synthesis of [(p-MeO-C$_6$H$_4$)$_3$C]BF$_4$. This preparation is modified from a literature procedure.[60] In one flask, (*p*-MeO-C$_6$H$_4$)$_3$CCl (0.3800 g, 1.030 mmol) was dissolved in 2 mL CH_2Cl_2; in a different flask, $AgBF_4$ (0.2370 g, 1.217 mmol) was suspended in 4 mL CH_2Cl_2. Both flasks were cooled in a -35 °C freezer of the glovebox for 20 minutes. The trityl chloride solution was then added dropwise to the $AgBF_4$ suspension; the mixture was allowed to stir for 2 hours at -35 °C. The unreacted $AgBF_4$ and AgCl byproduct was removed by a fine porosity glass fritted funnel with a pad of celite, and the

volatiles were removed *in vacuo* to afford a red solid (80 – 90 %). ^{1}H NMR (500 MHz, CD_2Cl_2) δ 7.57 (6H, dt), 7.29 (6H, dt), 4.10 (9H, s). $E_{1/2}$ (CH_2Cl_2, V versus $[FeCp_2]^{+/0}$): -0.66.

Generation of (p-MeO-C$_6$H$_4$)$_3$C•. In a typical experiment, [(*p*-MeO-C_6H_4)$_3$C]BF_4 (0.0094 g, 0.022 mmol) and $CoCp_2$ (0.0043 g, 0.023 mmol) were mixed in 2.24 mL CH_2Cl_2 at room temperature in the dark. The resultant solution is suitable for spectroscopic experiments. EPR (X-band, ⊥-mode, CH_2Cl_2, 77 K): g = 2.00. UV-vis $\lambda_{max}(CH_2Cl_2)$/nm (ε/$M^{-1}cm^{-1}$): 505 (520), 536 (560).

Crystallography

[(TMTACN)Fe^{II}–(μ-OH)–Mn^{III}poat]OTf. A green crystal of approximate dimensions 0.098 x 0.157 x 0.160 mm was mounted in a cryoloop and transferred to a Bruker SMART APEX II diffractometer system. The APEX2[61] program package was used to determine the unit-cell parameters and for data collection (120 sec/frame scan time). The raw frame data was processed using SAINT[62] and SADABS[63] to yield the reflection data file. Subsequent calculations were carried out using the SHELXTL[64] program package. There were no systematic absences nor any diffraction symmetry other than the Friedel condition. The centrosymmetric triclinic space group $P\bar{1}$ was assigned and later determined to be correct.

The structure was solved by direct methods and refined on F^2 by full-matrix least-squares techniques. The analytical scattering factors[65] for neutral atoms were used throughout the analysis. Hydrogen atoms H(1) and H(8) were located from a difference-Fourier map and refined (x,y,z and U_{iso}). The remaining hydrogen atoms were included using a riding model. There were two molecules of the formula-unit present (Z = 4). Several atoms were disordered and included using multiple components with partial site-occupancy-factors.

Least-squares analysis yielded wR2 = 0.0978 and Goof = 1.001 for 1369 variables refined against 24005 data (0.78 Å), R1 = 0.0474 for those 16338 data with I > 2.0σ(I).

[(TMTACN)Fe^{III}–(μ-O)–Mn^{III}Hpoat](OTf)$_2$. A green crystal of approximate dimensions 0.206 x 0.279 x 0.280 mm was mounted on a glass fiber and transferred to a Bruker SMART APEX II diffractometer system. The APEX2[61] program package was used to determine the unit-cell parameters and for data collection (30 sec/frame scan time). The raw frame data was processed using SAINT[62] and SADABS[63] to yield the reflection data file. Subsequent calculations were carried out using the SHELXTL[64] program package. The diffraction symmetry was 2/*m* and the systematic absences were consistent with the monoclinic space group $P2_1/c$ that was later determined to be correct.

The structure was solved by direct methods and refined on F^2 by full-matrix least-squares techniques. The analytical scattering factors[65] for neutral atoms were used throughout the analysis. Hydrogen atom H(2) was located from a difference-Fourier map and refined (x,y,z and U_{iso}). The remaining hydrogen atoms were included using a riding model. There was one molecule of chloroform solvent present.

Least-squares analysis yielded wR2 = 0.0914 and Goof = 1.034 for 791 variables refined against 13112 data (0.81 Å), R1 = 0.0344 for those 10852 data with I > 2.0σ(I).

There were several high residuals present in the final difference-Fourier map. It was not possible to determine the nature of the residuals although it was probable that *n*-hexane solvent was present. The SQUEEZE[66] routine in the PLATON[67] program package was used to account for the electrons in the solvent accessible voids.

Table 6.3. Crystallographic data for $[Fe^{II}(OH)Mn^{III}poat]^{+}$ and $[Fe^{III}(O)Mn^{III}Hpoat]^{2+}$.

	[(TMTACN)Fe^{II}–(μ-OH)–Mn^{III}poat]OTf	[(TMTACN)Fe^{III}–(μ-O)–Mn^{III}Hpoat](OTf)$_2$
Formula	C_{52} H_{64} F_3 Fe Mn N_7 O_7 P_3 S	C_{53} H_{64} F_6 Fe Mn N_7 O_{10} P_3 S_2·$CHCl_3$
fw	1191.86	1460.30
T (K)	93(2)	93(2)
Crystal system	Triclinic	Monoclinic
Space group	$P\bar{1}$	$P2_1/c$
a (Å)	14.8784(8)	16.7414(9)
b (Å)	17.2401(9)	14.8414(8)
c (Å)	21.4396(11)	26.8159(15)
α (°)	90.8210(10)	90
β (°)	90.3550(9)	92.1641(10)
γ (°)	98.1446(9)	90
Z	4	4
V (Å^3)	5443.2(5)	6658.1(6)
δ_{calc} (mg/m^3)	1.454	1.457
Independent reflections	24005	13112
R1	0.0474	0.0344
wR2	0.0978	0.0914
Goof	1.001	1.034

$wR2 = [\Sigma[w(F_o^2-F_c^2)^2] / \Sigma[w(F_o^2)^2]]^{1/2}$
$R1 = \Sigma||F_o|-|F_c|| / \Sigma|F_o|$
Goof = $S = [\Sigma[w(F_o^2-F_c^2)^2] / (n-p)]^{1/2}$ where n is the number of reflections and p is the total number of parameters refined.
The thermal ellipsoid plots are shown at the 50% probability level.

References

(1) Tinberg, C. E.; Lippard, S. J. Dioxygen Activation in Soluble Methane Monooxygenase. *Acc. Chem. Res.* **2011**, *44*, 280-288.

(2) Lipscomb, J. D.; Que, L. MMO: P450 in wolf's clothing? *JBIC, J Biol. Inorg. Chem.* **1998**, *3*, 331-336.

(3) Ross, M. O.; Rosenzweig, A. C. A tale of two methane monooxygenases. *JBIC, J. Biol. Inorg. Chem.* **2017**, *22*, 307-319.

(4) Stubbe, J.; Nocera, D. G.; Yee, C. S.; Chang, M. C. Y. Radical Initiation in the Class I Ribonucleotide Reductase: Long-Range Proton-Coupled Electron Transfer? *Chem. Rev.* **2003**, *103*, 2167-2202.

(5) Jasniewski, A. J.; Que, L. Dioxygen Activation by Nonheme Diiron Enzymes: Diverse Dioxygen Adducts, High-Valent Intermediates, and Related Model Complexes. *Chem. Rev.* **2018**, *118*, 2554-2592.

(6) Andersson, C. S.; Högbom, M. A Mycobacterium tuberculosis ligand-binding Mn/Fe protein reveals a new cofactor in a remodeled R2-protein scaffold. *Proc. Natl. Acad, Sci. U.S.A.* **2009**, *106*, 5633-5638.

(7) Griese, J. J.; Roos, K.; Cox, N.; Shafaat, H. S.; Branca, R. M. M.; Lehtio, J.; Graslund, A.; Lubitz, W.; Siegbahn, P. E. M.; Högbom, M. Direct observation of structurally encoded metal discrimination and ether bond formation in a heterodinuclear metalloprotein. *Proc. Natl. Acad. Sci. U.S.A.* **2013**, *110*, 17189-17194.

(8) Jiang, W.; Yun, D.; Saleh, L.; Barr, E. W.; Xing, G.; Hoffart, L. M.; Maslak, M.-A.; Krebs, C.; Bollinger, J. M. A manganese(IV)/iron(III) cofactor in Chamydia trachomatis ribonucleotide reductase. *Science* **2007**, *316*, 1188-1191.

(9) Irving, H.; Williams, R. J. P. The Stability of Transition-Metal Complexes. *J. Chem. Soc.* **1953**, 3192-3210.

(10) Kisgeropoulos, E. C.; Griese, J. J.; Smith, Z. R.; Branca, R. M. M.; Schneider, C. R.; Högbom, M.; Shafaat, H. S. Key Structural Motifs Balance Metal Binding and Oxidative Reactivity in a Heterobimetallic Mn/Fe Protein. *J. Am. Chem. Soc.* **2020**, *142*, 5338-5354.

(11) Jiang, W.; Hoffart, L. M.; Krebs, C.; Bollinger, J. M. A Manganese(IV)/Iron(IV) Intermediate in Assembly of the Manganese(IV)/Iron(III) Cofactor of *Chlamydia trachomatis* Ribonucleotide Reductase. *Biochemistry* **2007**, *46*, 8709-8716.

(12) Younker, J. M.; Krest, C. M.; Jiang, W.; Krebs, C.; Bollinger, J. M.; Green, M. T. Structural Analysis of the Mn(IV)/Fe(III) Cofactor of *Chlamydia trachomatis* Ribonucleotide Reductase by Extended X-ray Absorption Fine Structure Spectroscopy and Density Functional Theory Calculations. *J. Am. Chem. Soc.* **2008**, *130*, 15022-15027.

(13) Bollinger, J. M.; Jiang, W.; Green, M. T.; Krebs, C. The manganese(IV)/iron(III) cofactor of *Chlamydia trachomatis* ribonucleotide reductase: structure, assembly, radical initiation, and evolution. *Curr. Opin. Struct. Biol.* **2008**, *18*, 650-657.

(14) Dassama, L. M. K.; Krebs, C.; Bollinger, J. M.; Rosenzweig, A. C.; Boal, A. K. Structural Basis for Assembly of the Mn^{IV}/Fe^{III} Cofactor in the Class Ic Ribonucleotide Reductase from *Chlamydia trachomatis*. *Biochemistry* **2013**, *52*, 6424-6436.

(15) Kwak, Y.; Jiang, W.; Dassama, L. M. K.; Park, K.; Bell, C. B.; Liu, L. V.; Wong, S. D.; Saito, M.; Kobayashi, Y.; Kitao, S.; Seto, M.; Yoda, Y.; Alp, E. E.; Zhao, J.; Bollinger, J. M.; Krebs, C.; Solomon, E. I. Geometric and Electronic Structure of the Mn(IV)Fe(III) Cofactor in Class Ic Ribonucleotide Reductase: Correlation to the Class Ia Binuclear Non-Heme Iron Enzyme. *J. Am. Chem. Soc.* **2013**, *135*, 17573-17584.

(16) Livada, J.; Martinie, R. J.; Dassama, L. M. K.; Krebs, C.; Bollinger, J. M.; Silakov, A. Direct Measurement of the Radical Translocation Distance in the Class I Ribonucleotide Reductase from *Chlamydia trachomatis*. *J. Phys. Chem. B.* **2015**, *119*, 13777-13784.
(17) Martinie, R. J.; Blaesi, E. J.; Krebs, C.; Bollinger, J. M.; Silakov, A.; Pollock, C. J. Evidence for a Di-μ-oxo Diamond Core in the Mn(IV)/Fe(IV) Activation Intermediate of Ribonucleotide Reductase from *Chlamydia trachomatis*. *J. Am. Chem. Soc.* **2017**, *139*, 1950-1957.
(18) Miller, E. K.; Trivelas, N. E.; Maugeri, P. T.; Blaesi, E. J.; Shafaat, H. S. Time-Resolved Investigations of Heterobimetallic Cofactor Assembly in R2lox Reveal Distinct Mn/Fe Intermediates. *Biochemistry* **2017**, *56*, 3369-3379.
(19) Sano, Y.; Weitz, A. C.; Ziller, J. W.; Hendrich, M. P.; Borovik, A. S. Unsymmetrical Bimetallic Complexes with M^{II}–(μ-OH)–M^{III} Cores ($M^{II}M^{III}$ = $Fe^{II}Fe^{III}$, $Mn^{II}Fe^{III}$, $Mn^{II}Mn^{III}$): Structural, Magnetic, and Redox Properties. *Inorg. Chem.* **2013**, *52*, 10229-10231.
(20) Sano, Y.; Lau, N.; Weitz, A. C.; Ziller, J. W.; Hendrich, M. P.; Borovik, A. S. Models for Unsymmetrical Active Sites in Metalloproteins: Structural, Redox, and Magnetic Properties of Bimetallic Complexes with M^{II}-(μ-OH)-Fe^{III} Cores. *Inorg. Chem.* **2017**, *56*, 14118-14128**.**
(21) Holman, T. R.; Wang, Z.; Hendrich, M. P.; Que, L. Structural and Spectroscopic Properties of Antiferromagnetically Coupled $Fe^{III}Mn^{II}$ and $Fe^{II}Mn^{II}$ Complexes. *Inorg. Chem.* **1995**, *34*, 134-139.
(22) Carboni, M.; Clémancey, M.; Molton, F.; Pécaut, J.; Lebrun, C.; Dubois, L.; Blondin, G.; Latour, J. M. Biologically Relevant Heterodinuclear Iron-Manganese Complexes. *Inorg. Chem.* **2012**, *51*, 10447-10460.
(23) Das, B.; Daver, H.; Singh, A.; Singh, R.; Haukka, M.; Demeshko, S.; Meyer, F.; Lisensky, G.; Jarenmark, M.; Himo, F.; Nordlander, E. A Heterobimetallic $Fe^{III}Mn^{II}$ Complex of an Unsymmetrical Dinucleating Ligand: A Structural and Functional Model Complex for the Active Site of Purple Acid Phosphatase of Sweet Potato. *Eur. J. Inorg. Chem.* **2014**, 2204-2212.
(24) Hotzelmann, R.; Wieghardt, K.; Flörke, U.; Haupt, H.-J.; Weatherburn, D. C.; Bonvoisin, J.; Blondin, G.; Girerd, J.-J. Spin Exchange Coupling in Asymmetric Heterodinuclear Complexes Containing the μ-Oxo-bis(μ-acetato)dimetal Core. *J. Am. Chem. Soc.* **1992**, *114*, 1681-1696.
(25) Zhou, A.; Crossland, P. M.; Draksharapu, A.; Jasniewski, A. J.; Kleespies, S. T.; Que, L. Oxoiron(IV) compelxes as synthons for the assembly of heterobimetallic centers such as the Fe/Mn active site of Class Ic ribonucleotide reductases. *JBIC, J. Biol. Inorg. Chem.* **2018**, *23*, 155-165.
(26) Crossland, P. M.; Guo, Y.; Que, L. Spontaneous Formation of an Fe/Mn Diamond Core: Models for the Fe/Mn Sites in Class 1c Ribonucleotide Reductases. *Inorg. Chem.* **2021**, *60*, 8710-8721.
(27) Lee, J. L.; Oswald, V. F.; Biswas, S.; Hill, E. A.; Ziller, J. W.; Hendrich, M. P.; Borovik, A. S. Stepwise assembly of heterobimetallic complexes: synthesis, structure, and physical properties. *Dalton Trans***. 2021**, *50*, 8111-8119.
(28) Park, Y. J.; Ziller, J. W.; Borovik, A. S. The Effects of Redox-Inactive Metal Ions on the Activation of Dioxygen: Isolation and Characterization of a Heterobimetallic Complex Containing a Mn^{III}–(μ-OH)–Ca^{II} Core. *J. Am. Chem. Soc.* **2011**, *133*, 9258-9261.
(29) Park, Y. J.; Cook, S.; Sickerman, N. S.; Sano, Y.; Ziller, J. W.; Borovik, A. S. Heterobimetallic Complexes with M^{III}–(μ-OH)–M^{II} Cores (M^{III} = Fe, Ga, Mn; M^{II} = Ca, Sr and Ba): Structural, Kinetic, and Redox Properties. *Chem. Sci.* **2013**, *4*, 717-726.
(30) Oswald, V. F. Doctoral Dissertation, University of California-Irvine, Irvine, CA, 2018.

(31) Gupta, R.; Taguchi, T.; Borovik, A. S.; Hendrich, M. P. Characterization of Monomeric $Mn^{II/III/IV}$ Complexes from X- and Q-band Dual Mode EPR spectroscopy. *Inorg. Chem.* **2013**, *52*, 12568-12575.
(32) Gupta, R.; Taguchi, T.; Lassalle-Kaiser, B.; Bominaar, E. L.; Yano, J.; Hendrich, M. P.; Borovik, A. S. High-spin Mn–oxo complexes and their relevance to the oxygen-evolving complex within photosystem II. *Proc. Nat. Acad. Sci. U.S.A.* **2015**, *112*, 5319-5324.
(33) Oswald, V. F.; Weitz, A. C.; Biswas, S.; Ziller, J .W.; Hendrich, M. P.; Borovik, A. S. Manganese-Hydroxido Complexes Supported by a Urea/Phosphinic Amide Tripodal Ligand. *Inorg. Chem.* **2018**, *57*, 13341-13350.
(34) Kurtz, D. M. Oxo- and Hydroxo-Bridged Diiron Complexes: A Chemical Perspective on a Biological Unit. *Chem. Rev.* **1990**, *90*, 585-606.
(35) Parsell, T. H.; Behan, R. K.; Green, M. T.; Hendrich, M. P.; Borovik, A. S. Preparation and Properties of a Monomeric Mn^{IV}–Oxo Complex. *J. Am. Chem. Soc.* **2006**, *128*, 8728-8729.
(36) Lacy, D. C.; Gupta, R.; Stone, K. L.; Greaves, J.; Ziller, J. W.; Hendrich, M. P.; Borovik, A. S. Formation, Structure, and EPR Detection of a High Spin Fe^{IV}–Oxo Species Derived from Either an Fe^{III}–Oxo or Fe^{III}–OH Complex. *J. Am. Chem. Soc.* **2010**, *132*, 12188-12190.
(37) Connelly, N. G.; Geiger, W. E. Chemical Redox Agents for Organometallic Chemistry. *Chem. Rev.* **1996**, *96*, 877-910.
(38) Warren, J. J.; Tronic, T. A.; Mayer, J. M. Thermochemistry of Proton-Coupled Electron Transfer Reagents and its Implications. *Chem. Rev.* **2010**, *110*, 6961-7001.
(39) Luo, Y.-R. *Comprehensive Handbook of Chemical Bond Energies*; CRC Press, Taylor & Francis Group: Boca Raton, FL, 2007.
(40) Lee, D.; Du Bois, J.; Petasis, D.; Hendrich, M. P.; Krebs, C.; Huynh, B. H.; Lippard, S. J. Formation of Fe(III)Fe(IV) Species from the Reaction between a Diiron(II) Complex and Dioxygen: Relevance to Ribonucleotide Reductase Intermediate X. *J. Am. Chem. Soc.* **1999**, *121*, 9893-9894.
(41) Mondal, P.; Pirovano, P.; Das, A.; Farqujar, E. R.; McDonald, A. R. Hydrogen Atom Transfer by a High-Valent Nickel-Chloride Complex. *J. Am. Chem. Soc.* **2018**, *140*, 1834-1841.
(42) Wu, T.; MacMillan, S. N.; Rajabimoghadam, K.; Siegler, M. A.; Lancaster, K. M.; Garcia-Bosch, I. Structure, Spectroscopy, and Reactivity of a Mononuclear Copper Hydroxide Complex in Three Molecular Oxidation States. *J. Am. Chem. Soc.* **2020**, *142*, 12265-12276.
(43) Mayer, J. M. Proton-Coupled Electron Transfer: A Reaction Chemist's View. *Annu. Rev. Phys. Chem.* **2004**, *55*, 363-390.
(44) Darcy, J. W.; Koronkiewicz, B.; Parada, G. A.; Mayer, J. M. A Continuum of Proton-Coupled Electron Transfer Reactivity. *Acc. Chem. Res.* **2018**, *51*, 2391-2399.
(45) Huang, X.; Groves, J. T. Oxygen Activation and Radical Transformations in Heme Proteins and Metalloporphyrins. *Chem. Rev.* **2018**, *118*, 2491-2553.
(46) Groves, J. T.; McClusky, G. A. Aliphatic Hydroxylation via Oxygen Rebound. Oxygen Transfer Catalyzed by Iron. *J. Am. Chem. Soc.* **1976**, *98*, 859-861.
(47) Huang, X.; Groves, J. T. Beyond Ferryl-Mediated Hydroxylation: 40 Years of the Rebound Mechanism and C−H Activation. *JBIC, J. Biol. Inorg. Chem.* **2017**, *22*, 185-207.
(48) Price, J. C.; Barr, E. W.; Tirupati, B.; Bollinger, J. M.; Krebs, C. The First Direct Characterization of a High-Valent Iron Intermediate in the Reaction of an *a*-Ketoglutarate-Dependent Dioxygenase: A High-Spin Fe(IV) Complex in Taurine/*a*-Ketoglutarate Dioxygenase (TauD) from *Escherichia Coli*. *Biochemistry* **2003**, *42*, 7497-7508.
(49) Matthews, M. L.; Krest, C. M.; Barr, E. W.; Vaillancourt, F. H.; Walsh, C. T.; Green, M. T.; Krebs, C.; Bollinger, J. M. Substrate-Triggered Formation and Remarkable Stability of the

C–H Bond-Cleaving Chloroferryl Intermediate in the Aliphatic Halogenase, SyrB2. *Biochemistry* **2009**, *48*, 4331-4343.
(50) Gomberg, M. An Instance of Trivalent Carbon: Triphenylmethyl. *J. Am. Chem. Soc.* **1900**, *22*, 757-771.
(51) March, J. Free Radicals. In *March's Advanced Organic Chemistry: reactions, mechanisms, and structure*, 5th e.d.; Smith, M. B.; March, J., ed.; John Wiley & Sons, Inc: New York, 2001; pp. 241.
(52) Zaragoza, J. P. T.; Yosca, T. H.; Siegler, M. A.; Moënne-Loccoz, P.; Green, M. T.; Goldberg, D. P. Direct Observation of Oxygen Rebound with an Iron-Hydroxide Complex. *J. Am. Chem. Soc.* **2017**, *139*, 13640-13643.
(53) Armarego, W. L. F.; Chai, C. L. L In *Purification of Laboratory Chemicals*, 5th e.d.; Elsevier: Oxford, UK, 2003.
(54) Oswald, V. F.; Lee, J. L.; Biswas, S.; Weitz, A. C.; Mittra, K.; Fan, R.; Li, J.; Zhao, J.; Hu, M. Y.; Alp, E. E.; Bominaar, E. L.; Guo, Y.; Green, M. T.; Hendrich, M. P.; Borovik, A. S. Effects of Non-covalent Interactions on High-spin Fe(IV)-oxido Complexes. *J. Am. Chem. Soc.* **2020**, *142*, 11804-11817.
(55) Blakesley, D. W.; Payne, S. C.; Hagen, K. S. Spin-State Variation in Solid State and Solution of Mononuclear Iron(II) 1,4,7-Trimethyl-1,4,7-triazacyclononane Complexes. *Inorg. Chem.* **2000**, *39*, 1979-1989.
(56) Zhdankin, V. V.; Litvinov, D. N.; Koposov, A. Y.; Luu, T.; Ferguson, M. J.; McDonald, R.; Tykwinski, R. R. Preparation and Structure of 2-Iodoxybenzoate Esters: Soluble and Stable Periodinane Oxidizing Reagents. *Chem. Commun.* **2004**, *263*, 106-107.
(57) Zhdankin, V. V.; Koposov, A. Y.; Litvinov, D. N.; Ferguson, M. J.; McDonald, R.; Luu, T.; Tykwinski, R. R. Esters of 2-Iodoxybenzoic Acid: Hypervalent Iodine Oxidizing Reagents with a Pseudobenziodoxole Structure. *J. Org. Chem.* **2005**, *70*, 6484-6491.
(58) Curley, J. J.; Bergman, R. G.; Tilley, T. D. Preparation and physical properties of early-late heterobimetallic compounds featuring Ir–M bonds (M = Ti, Zr, Hf). *Dalton Trans.* **2012**, *41*, 192-200.
(59) Petasis, D. T.; Hendrich, M. P. Quantitative Interpretation of Multifrequency Multimode EPR Spectra of Metal Containing Proteins, Enzymes, and Biomimetic Complexes. *Methods Enzymol.* **2015**, *563*, 171-208.
(60) Karim, A.; Schulz, N.; Andersson, H.; Nekoueishahraki, B.; Carlsson, A.-C. C.; Sarabi, D.; Valkonen, A.; Rissanen, K.; Gräfenstein, J.; Keller, S.; Erdélyi, M. Carbon's Three-Center, Four-Electron Tetrel Bond, Treated Experimentally. *J. Am. Chem. Soc.* **2018**, *140*, 17571-17579.
(61) APEX2 Version 2014.11-0, Bruker AXS, Inc.; Madison, WI 2014.
(62) SAINT Version 8.34a, Bruker AXS, Inc.; Madison, WI 2013.
(63) Sheldrick, G. M. SADABS, Version 2014/5, Bruker AXS, Inc.; Madison, WI 2014.
(64) Sheldrick, G. M. SHELXTL, Version 2014/7, Bruker AXS, Inc.; Madison, WI 2014
(65) International Tables for Crystallography 1992, Vol. C., Dordrecht: Kluwer Academic Publishers.
(66) Spek, A. L. SQUEEZE, Acta Cryst. 2015, C71, 9-19.
(67) Spek, A. L. PLATON, Acta. Cryst. 2009, D65, 148-155.

Chapter 7

The Road towards $Mn^{IV}Fe^{IV}$

Introduction

The previous chapter describes the trapping, characterization, and substrate reactivity of the high-valent [(TMTACN)Fe^{III}–(μ-O)–Mn^{IV}poat]$^+$ species (denoted [Fe^{III}(O)Mn^{IV}poat]$^+$), which contains a rare Fe^{III}–(μ-O)–Mn^{IV} core;[1] this compound serves as a useful synthetic model for the catalytically competent intermediates in the R2 subunit of ribonucleotide reductase Class Ic (RNR R2 Ic) and R2-like ligand-binding oxidase (R2lox).[2-5] However, higher-valent intermediates have been proposed and/or experimentally verified in these enzymatic systems.[6-8] For instance, a $Mn^{IV}Fe^{IV}$ species was observed by various spectroscopic techniques in RNR R2 Ic upon O_2 activation, before undergoing proton-coupled electron transfer (PCET) to convert to the key $Mn^{IV}Fe^{III}$ intermediate responsible for the electron transfer between two protein subunits (Scheme 7.1).[7,8] Unfortunately, the aforementioned [Fe^{III}(O)Mn^{IV}poat]$^+$ cannot be further oxidized, and modifications to the complex are required to synthetically model the $Mn^{IV}Fe^{IV}$ species observed in biological systems.

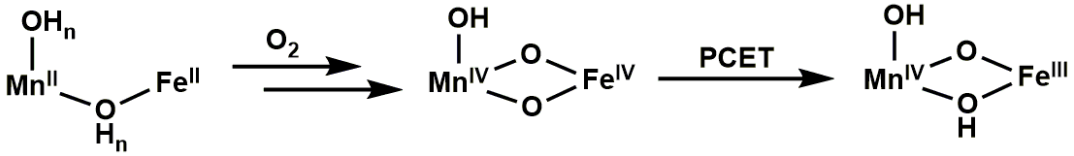

Scheme 7.1. The catalytic mechanism of RNR R2 Ic. A $Mn^{IV}Fe^{IV}$ is generated upon O_2 activation, and further converts to a $Mn^{IV}Fe^{III}$ species *via* PCET.

While the neutral TMTACN framework (and related ligands) struggles to support high-valent Fe centers (i.e. Fe^{IV} and beyond),[9] many Mn^{IV} complexes in the [(TM)TACN] scaffold have been reported. For example, [Mn^{IV}(TMTACN)$(OMe)_3$]$^+$ has been structurally characterized, and its low $Mn^{IV/III}$ reduction potential (E_{pc} = -0.94 V vs $[FeCp_2]^{+/0}$) highlights its stability at this oxidation

level (Figure 7.1.A).[10] Additionally, several other homo- and heterobimetallic complexes with a [Mn^{IV}((TM)TACN)] site demonstrate extraordinary stability, which illustrates the ability of the N-based macrocycle to support a high-valent Mn center (Figures 7.1.B,C).[1,11-13]

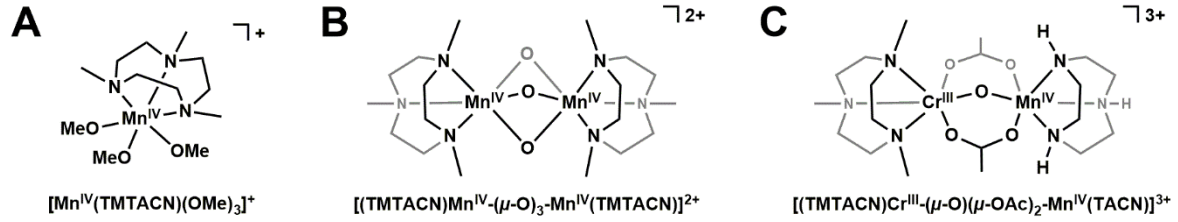

Figure 7.1. Literature examples of mono- and dinuclear complexes containing [Mn^{IV}TMTACN]: (A) [Mn^{IV}(TMTACN)(OMe)$_3$]$^+$; (B) [(TMTACN)Mn^{IV}–(μ-O)$_3$–Mn^{IV}(TMTACN)]$^{2+}$; (C) (B) [(TMTACN)Cr^{III}–(μ-O)(μ-OAc)$_2$–Mn^{IV}(TACN)]$^{3+}$.

The Borovik group previously prepared [(TMTACN)Mn^{II}–(μ-OH)–Fe^{III}MST]$^+$ (denoted [Mn^{II}(OH)Fe^{III}MST]$^+$), which struggled to access higher oxidation states (Figure 7.2.A).[14,15] However, this is likely due to the weak donability by the sulfonamido S=O groups, not [TMTACN]. We reason the anionic N- and P=O groups in [poat]$^{3-}$ are much stronger donors and more suitable to support a Fe^{IV} and Mn^{IV} centers, respectively, so a new [(TMTACN)Mn–(μ-O(H))–Fe(H)poat] system was developed, with the Fe site located in the [poat]$^{3-}$ framework and the Mn capped by the TMTACN ligand (Figure 7.2.B). In this chapter, a series of [MnFepoat] complexes was prepared, and characterized by various structural and spectroscopic methods. A strong emphasis is placed on the study of their electrochemical properties, which revealed at least four redox levels can be electrochemically accessed, including high valent MnFe species at the formally (IV,III) level.

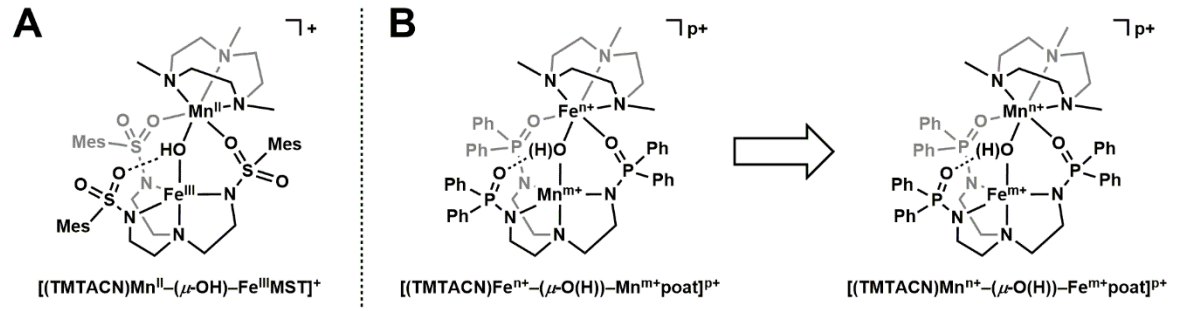

Figure 7.2. (A) Molecular structure of [(TMTACN)Mn^{II}–(μ-OH)–Fe^{III}MST]$^+$; (B) Re-design of [(TMTACN)Mn^{n+}–(μ-O(H))–Fe^{m+}poat]$^{p+}$ to access higher oxidation states.

However, the instability of these species in the [TMTACN/poat] system may preclude further spectroscopic characterizations, so additional modifications to the bimetallic framework are suggested.

Results & Discussion

Preparations of MnFe complexes. The preparation of [(TMTACN)Mn^{II}–(μ-OH)–Fe^{III}poat]OTf (denoted [Mn^{II}(OH)Fe^{III}poat]OTf) was adapted from syntheses of similar bimetallic complexes described in the previous chapters, and is outlined in Scheme 7.2.[16] After multiple rounds of recrystallizations, brown crystals suitable for X-ray diffraction (XRD) were obtained, which confirmed the molecular structure of [Mn^{II}(OH)Fe^{III}poat]$^+$ in the crystalline phase. [Mn^{II}(OH)Fe^{III}poat]$^+$ can be readily oxidized using AgOTf or [N(p-tol)$_3$]OTf (Scheme 7.2). Upon recrystallization, brownish-green crystals were obtained, and XRD reveals the molecular structure of [(TMTACN)Mn^{III}–(μ-O)–Fe^{III}Hpoat]$^{2+}$ (denoted [Mn^{III}(O)Fe^{III}Hpoat]$^{2+}$). The fully deprotonated complex, [(TMTACN)Mn^{III}–(μ-O)–Fe^{III}poat]OTf (denoted [Mn^{III}(O)Fe^{III}poat]OTf), can be prepared in an analogous procedure for [(TMTACN)Fe^{III}–(μ-O)–Fe^{III}poat]OTf (Chapter 5): [Fe^{II}poat]$^-$ was first treated with the O-atom transfer reagent, isopropyl 2-iodoxybenzoate (IBX-iPr), to produce [Fe^{IV}poat(O)]$^-$,[17] and [Mn^{II}(TMTACN)(OTf)$_2$] was subsequently added to generate a new green species (Scheme 7.3). Green crystalline needles suitable for single crystal XRD were obtained after multiple rounds of recrystallization, and XRD supports the assignment of [Mn^{III}(O)Fe^{III}poat]$^+$.

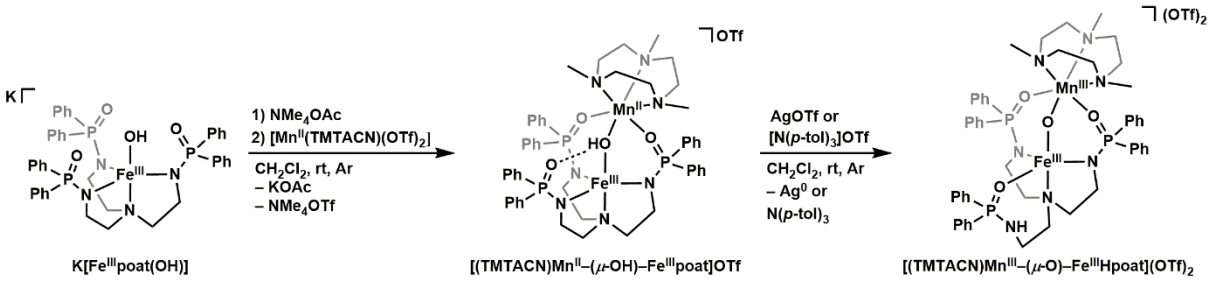

Scheme 7.2. Preparative routes for [(TMTACN)Mn^{II}–(μ-OH)–Fe^{III}poat]$^+$ and [(TMTACN)Mn^{III}–(μ-O)–Fe^{III}Hpoat]$^{2+}$.

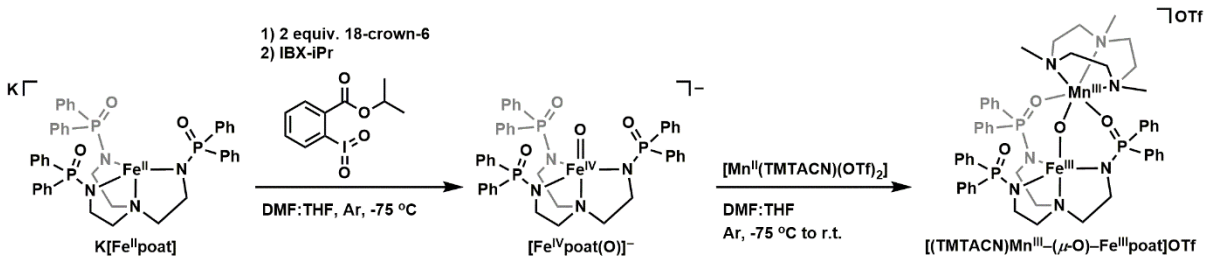

Scheme 7.3. Preparative routes for [(TMTACN)Mn^{III}–(μ-O)–Fe^{III}poat]$^+$.

Structural Properties. The thermal stability of these MnFe complexes allows for their isolation and structural characterizations by XRD methods. In the molecular structure for [Mn^{II}(OH)Fe^{III}poat]$^+$ (Figure 7.3.A,B), there are two crystallographically different, but chemically equivalent, molecules in the asymmetric unit. The averages of the metrical parameters and calculated values, which are shown in Table 7.1, will be discussed. The bimetallic complex contains a 5-coordinated Fe^{III} center and a 6-coordinated Mn^{II} center, bridged by a hydroxido ligand that forms an intramolecular H-bond (2.632(3) Å) to a phosphinic amido tripodal arm. The Fe1–O1 and Fe1–N1 distances (1.889(2) and 2.104(2) Å, respectively) are comparable with those observed for the [TM^{II}(OH)Fe^{III}poat]$^+$ (TM = Zn, Cu, Ni, Fe) complexes (Chapters 3 and 5),[16] but are longer than the Mn1–O1 and Mn1–N1 distances observed for [Fe^{II}(OH)Mn^{III}poat]$^+$ (1.845(2) and 2.053(2) Å, respectively; Chapter 6). This suggests the additional electron in the dz^2/σ^* orbital for a d^5 Fe^{III} ion in trigonal bipyramidal (tbp) geometry results in significant bond lengthening to the axially-coordinated ligands. The Mn1–O3/4 distances (2.125(2), 2.135(2) Å) are statistically shorter than those found in the analogous [Mn^{II}(OH)Fe^{III}MST]$^+$ (2.196(1) and 2.187(1) Å; Figure 7.2.A),[14,15] which suggests the phosphinic amido P=O groups are stronger donors and can stabilize higher valent Mn centers; this is reflected in the lengthened Mn1–N5/7 bonds trans to the P=O groups.

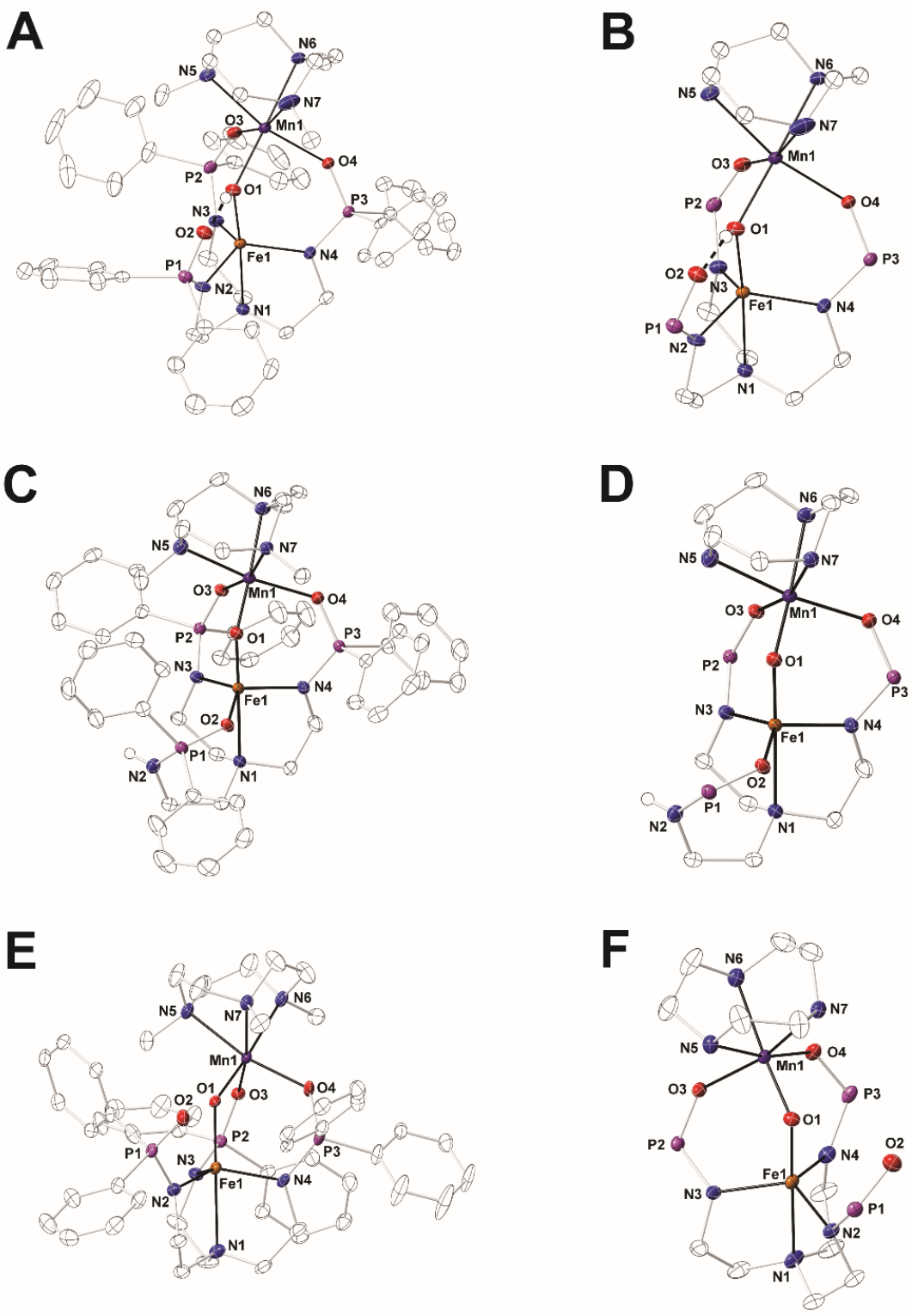

Figure 7.3. Thermal ellipsoid diagrams depicting the molecular structures of $[Mn^{II}(OH)Fe^{III}poat]^{+}$ (A, B), $[Mn^{III}(O)Fe^{III}Hpoat]^{2+}$ (C, D), and $[Mn^{III}(O)Fe^{III}poat]^{+}$ (E, F) determined by X-ray diffraction. Ellipsoids are shown at the 50% probability level, and only the phosphinic amide H atom is shown for clarity. The methyl and phenyl groups are removed in (B), (D), and (F) for clarity.

The molecular structure of $[Mn^{III}(O)Fe^{III}Hpoat]^{2+}$ (Figure 7.3.C,D) is similar to those for the FeFe and FeMn analogs described in Chapter 5 & 6. Upon oxidation, the proton in the bridging-hydroxido ligand transfers to the basic phosphinic amido N-atom in $[poat]^{3-}$, resulting in a Mn^{III}–(μ-O)–Fe^{III} core, and a protonated $[Hpoat]^{2-}$ framework bound to the Fe^{III} center through the P=O group in a strained 7-member chelate ring. The Fe1–O1 and Mn1–O1 bond lengths (1.837(2) and 1.756(2) Å; Table 7.1) are significantly different, while those found in $[Fe^{III}(O)Fe^{III}Hpoat]^{2+}$ (1.800(1) and 1.792(1) Å; Chapter 5) and $[Fe^{III}(O)Mn^{III}Hpoat]^{2+}$ (1.795(2) and 1.793(2) Å; Chapter 6) are comparable. The distinction of M–O1 bond lengths can again be attributed to the additional electron in the anti-bonding d_z^2 orbital for a d^5 ion in tbp geometry; these observations demonstrate the ability to modulate unsymmetric M'–(μ-O)–M cores using our stepwise-assembly approach. The Fe1···Mn1 distance contracts from 3.429(1) to 3.198(1) Å upon oxidation, and the Fe1–O1–Mn1 angle increases from 121.45(9) to 125.71(8) °.

The molecular structure of $[Mn^{III}(O)Fe^{III}poat]^{+}$ (Figure 7.3.E,F) reveals a bimetallic Mn–(μ-O)–Fe core that is similar to $[Mn^{III}(O)Fe^{III}Hpoat]^{2+}$. The major difference is that the 5-coordinated Fe^{III} has an N_4O geometry, as all three phosphinic amido N atoms in $[poat]^{3-}$ are deprotonated and bind to the Fe center. The primary coordination sphere of the Mn center remains largely unaffected, with the N_3O_3 coordination mode retained and the bond metrics relatively unperturbed. The P=O group that does not bind to the Fe center tilts away from the bridging oxido ligand, presumably due to electrostatic repulsion (> 3.2 Å). The structural parameters of the Mn–(μ-O)–Fe core, including the Mn1–O1–Fe1 angle (125.80(9) °), the Fe1···Mn1 distance (3.233(1) Å), the Fe1–O1 (1.847(2) Å) and Mn1–O1 (1.785(2) Å) bond lengths, are all comparable to those for $[Mn^{III}(O)Fe^{III}Hpoat]^{2+}$.

Table 7.1. Selected bond lengths/distances (Å) and angles (°) for $[Mn^{II}(OH)Fe^{III}poat]^{+}$,[a] $[Mn^{III}(O)Fe^{III}Hpoat]^{2+}$, and $[Mn^{III}(O)Fe^{III}poat]^{+}$.

Complex	$[Mn^{II}(OH)Fe^{III}poat]^{+}$	$[Mn^{III}(O)Fe^{III}Hpoat]^{2+}$	$[Mn^{III}(O)Fe^{III}poat]^{+}$
		Bond Lengths/Distances (Å)	
Fe1–N1	2.204(2)	2.377(2)	2.302(2)
Fe1–N2	2.026(2)	-	2.010(2)
Fe1–O2	-	2.007(2)	-
Fe1–N3	2.013(2)	1.992(2)	2.021(2)
Fe1–N4	2.017(2)	1.983(2)	2.023(2)
Fe1–O1	1.889(2)	1.837(2)	1.847(2)
O1···O2	2.632(3)	-	3.237
Mn1–O1	2.042(2)	1.756(2)	1.785(2)
Mn1–O3	2.125(2)	2.023(2)	2.083(2)
Mn1–O4	2.135(2)	2.099(2)	2.072(2)
Mn1–N5	2.327(2)	2.245(2)	2.235(2)
Mn1–N6	2.267(2)	2.119(2)	2.149(2)
Mn1–N7	2.355(3)	2.215(2)	2.253(2)
Fe1···Mn1	3.429(1)	3.198(1)	3.233(1)
av Fe1–N/O_{eq}	2.019(2)	1.994(2)	2.018(2)
av Mn1–N_{TMTACN}	2.316(2)	2.193(2)	2.212(2)
d[Fe1–N_{eq}]	0.365	0.293	0.377
d[Mn1–N_{TMTACN}]	1.609	1.461	1.485
		Angles (°)	
O1–Fe1–N1	173.80(8)	177.03(7)	179.05(8)
N2–Fe1–N3	121.48(9)	-	120.73(8)
O2–Fe1–N3	-	130.39(7)	-
N3–Fe1–N4	109.26(9)	107.82(8)	107.82(8)
N2–Fe1–N4	119.63(9)	-	121.11(8)
O2–Fe1–N4	-	115.23(7)	-
Fe1–O1–Mn1	121.45(9)	125.71(8)	125.80(9)
O3–Mn1–O4	98.43(7)	97.14(6)	95.82(7)
N5–Mn1–N6	77.64(8)	81.33(7)	79.99(8)
N5–Mn1–N7	75.61(8)	79.30(7)	79.03(7)
N6–Mn1–N7	77.68(9)	80.42(7)	80.44(8)
		Calculated Values	
τ_5[b]	0.872	0.777	0.966

[a]Bond lengths, distances, and angles are reported as an average.
[b]Trigonality structural parameter, $\tau_5 = (\beta - \alpha)/60^{o}$. β is the largest bond angle observed, and α is the second largest bond angle observed.

Electronic absorbance properties. $[Mn^{II}(OH)Fe^{III}poat]^{+}$ exhibits optical features at λ_{max} (ε, M^{-1} cm^{-1}) = 315 (sh), 375 (5700), and 540 nm (sh) in CH_2Cl_2 (Figure 7.4.A), which are present across the series of $[TM^{II}(OH)Fe^{III}poat]^{+}$ complexes (TM = Zn, Cu, Ni, Fe; Chapters 3 and 5).[16] The UV-vis spectra of $[Mn^{III}(O)Fe^{III}Hpoat]^{2+}$ and $[Mn^{III}(O)Fe^{III}poat]^{+}$ are compared in Figure 7.4.B and C. Both exhibit an

oxido–metal charge transfer (CT) band at 350 nm, albeit at different intensities (ε = 8500 and 10000 M^{-1} cm^{-1}, respectively); $[Mn^{III}(O)Fe^{III}Hpoat]^{2+}$ has an additional CT feature at λ = 405 nm (sh). Like the FeFe and FeMn analogs, low energy ligand field transitions can be observed for the two complexes: the feature for $[Mn^{III}(O)Fe^{III}Hpoat]^{2+}$ is at λ_{max} (ε, M^{-1} cm^{-1}) = 585 nm (380), which red-shifts to 600 nm (290) in $[Mn^{III}(O)Fe^{III}poat]^{+}$. The decrease in energy of the d-d transition upon deprotonation of the $[(M')^{III}(O)(M)^{III}Hpoat]^{2+}$ species is also observed for the FeFe and FeMn analogs discussed in Chapters 5 & 6, which is indicative the similar modulation of the ligand field from $[Hpoat]^{2-}$ to $[poat]^{3-}$.

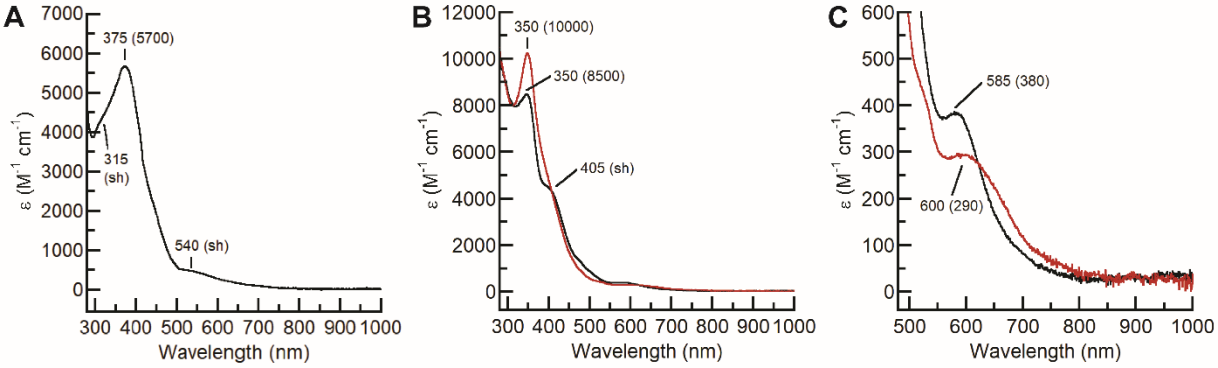

Figure 7.4. Electronic absorbance spectra: (A) $[Mn^{II}(OH)Fe^{III}poat]^{+}$; (B) overlay of $[Mn^{III}(O)Fe^{III}Hpoat]^{2+}$ (black) and $[Mn^{III}(O)Fe^{III}poat]^{+}$ (red); (C) zoomed in spectra for $[Mn^{III}(O)Fe^{III}Hpoat]^{2+}$ (black) and $[Mn^{III}(O)Fe^{III}poat]^{+}$ (red). Spectra were collected at 0.10 mM concentration in CH_2Cl_2 at room temperature.

Electron paramagnetic resonance (EPR) properties. The $[Mn^{II}(OH)Fe^{III}poat]^{+}$ complex did not show any signals in the parallel(//)-mode EPR spectrum at < 20 K (Figure 7.5). However, a new feature emerged as the measurement temperature increased, and resolved as a derivative-shaped signal at g = 11.3 at 79 K. This suggests $[Mn^{II}(OH)Fe^{III}poat]^{2+}$ has a S = 0 ground state due to antiferromagnetic coupling between the S = 5/2 Mn^{II} and Fe^{III} centers. The hydroxido bridging ligand provides moderate coupling, and the spin excited states (e.g. S = 1, 2, etc.) can be accessed at higher temperatures. A derivative-shaped feature at g = 11.0 was also observed for $[Mn^{II}(OH)Fe^{III}MST]^{+}$ (Figure 7.2.A) that originated from the S = 2 state: temperature-dependent measurements on that complex allowed the quantification of the population at this excited state, and a spin exchange

constant J ($\mathcal{H} = JS_1 \bullet S_2$) of 35(3) cm^{-1} was determined.[14,15] Similar variable temperature measurements of $[Mn^{II}(OH)Fe^{III}poat]^+$ are underway.

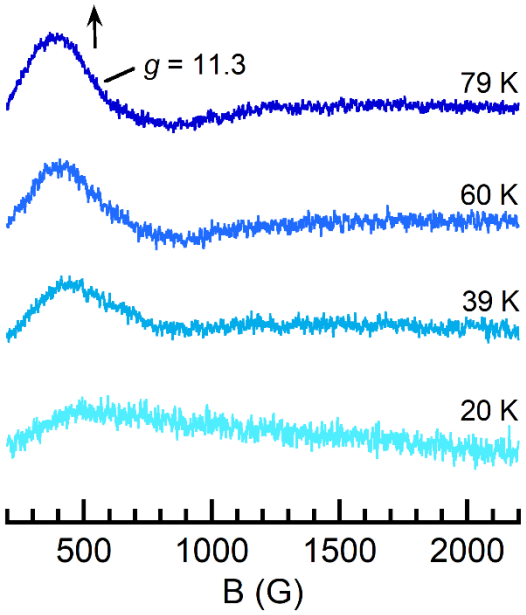

Figure 7.5. Variable-temperature //-mode EPR spectra of $[(TMTACN)Mn^{II}–(\mu\text{-}OH)–Fe^{III}poat]^+$ at 20, 39, 60, and 79 K. A new signal at g = 11.3 appears as measurement temperature increases.

The perpendicular (⊥)-mode EPR spectra for $[Mn^{III}(O)Fe^{III}Hpoat]^{2+}$ and $[Mn^{III}(O)Fe^{III}poat]^+$ (Figure 7.6) revealed distinct six-line, anisotropic signals centered at g = 2.04, which are consistent with S = 1/2 spin-exchange systems that contain an S = 2 Mn^{III} site antiferromagnetically coupled to an S = 5/2 Fe^{III} center.[2,5,18,19] The ^{55}Mn (I = 5/2) hyperfine features can be resolved at 77 K, and $A(^{55}Mn)$ values of 310 and 295 MHz are determined for the two complexes, respectively. The values are statistically larger than those found for $[Fe^{III}(O)Mn^{III}Hpoat]^{2+}$ and $[Fe^{III}(O)Mn^{III}poat]^+$ (260 and 243 MHz at 77 K; Chapter 6). The significance of these differences is currently being investigated; nevertheless, the ability to modulate the structural and magnetic properties of the Mn/Fe centers demonstrates a unique feature of our bimetallic assembly protocol.

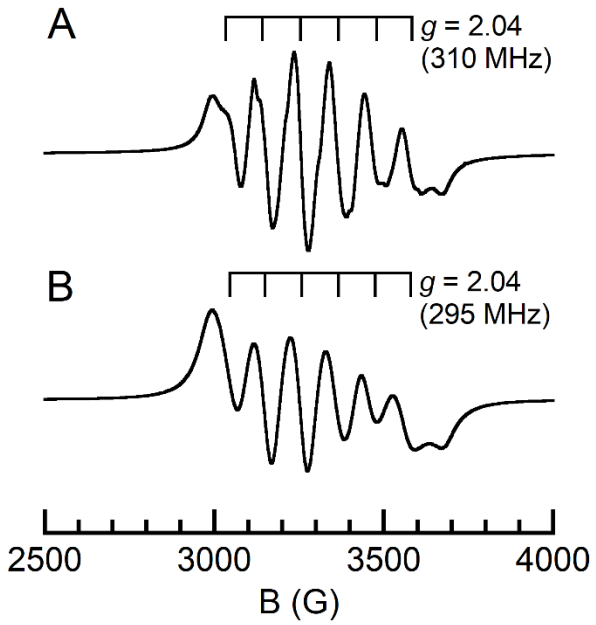

Figure 7.6. ⊥-mode EPR spectra of [(TMTACN)Mn^{III}–(μ-O)–Fe^{III}Hpoat]$^{2+}$ (A) and [(TMTACN)Mn^{III}–(μ-O)–Fe^{III}poat]$^{+}$ (B). Samples measured at 77 K in PrCN.

Electrochemical properties. The three MnFe complexes were interrogated in great depth by cyclic voltammetry (CV) to assess their ability to achieve high valent states. The full voltammogram for [Mn^{II}(OH)Fe^{III}poat]$^{+}$ in CH_2Cl_2 is illustrated in Figure 7.7.A and exhibits five distinct redox processes (**I**, **III**, **IV**, **VI**, **VII**). Process **I** is a reversible event at -1.59 V (vs $[FeCp_2]^{+/0}$, i_{pc}/i_{pa} = 1.05; Figure 7.7.B); this is assigned as the [Mn^{II}(OH)$Fe^{III/II}$poat]$^{+/0}$ process, and is comparable to those found for other $TM^{II}Fe^{III}$ complexes discussed in previous chapters (TM = Zn, Cu, Ni, Fe).[16] Process **IV** is quasi-reversible, with a potential at +0.06 V (i_{pc}/i_{pa} = 0.69); this is assigned to the [$Mn^{III/II}$(OH)Fe^{III}poat]$^{2+/+}$, and the irreversibility is attributed to the fast intramolecular proton transfer (PT) in the electrochemical time scale; this is consistent with the chemical isolation of [Mn^{III}(O)Fe^{III}Hpoat]$^{2+}$, in which a phosphinic amido arm is protonated (Figure 7.3.C,D). It is worth noting the analogous processes in [Mn^{II}(OH)Fe^{III}MST]$^{+}$ were observed at -0.87 and +0.71 V, which are more than 600 mV positive than those for [Mn^{II}(OH)Fe^{III}poat]$^{+}$; this is indicative the phosphinic amido N- and P=O ligands are stronger donors than their sulfonamido counterparts.[14] Process **III** is a reductive process at -0.67 V, but it was not independently observed within an electrochemical

window of +0.75 to -2.1 V (Figure 7.7.B). Process **VII** is an irreversible oxidative process at +1.14 V that is likely oxidation to a higher valent species (e.g., $[Mn(OH)Fepoat]^{3+}$); the oxidation state assignments or formulation will not be further speculated here without additional spectroscopic evidence (Figure 7.7.C). Process **VI** is not present unless the oxidative process **VII** is first accessed, and becomes increasingly reversible at +0.67 V (i_{pc}/i_{pa} = 1.52). The assignments of these three processes can be corroborated by further CV experiments on the other two complexes.

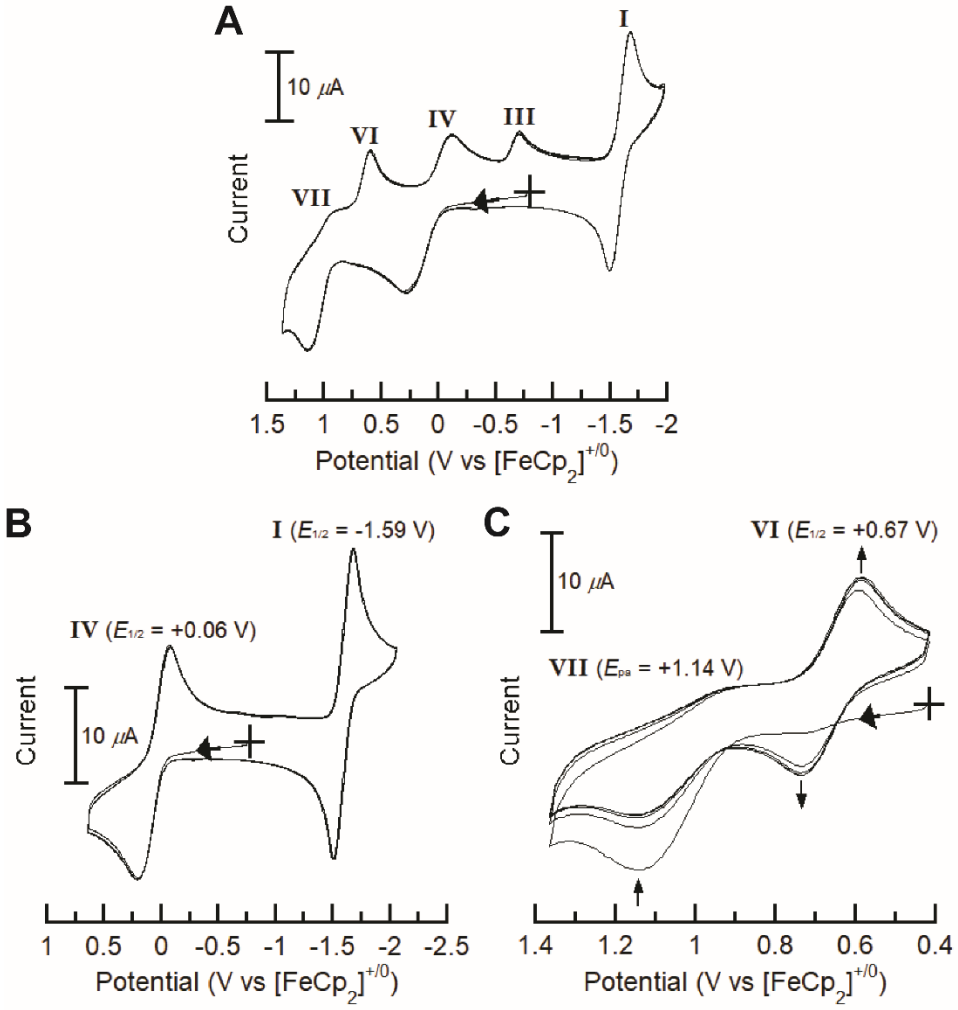

Figure 7.7. Cyclic voltammograms of $[Mn^{II}(OH)Fe^{III}poat]^{+}$: (A) full voltammogram; (B) the redox processes **IV** and **I** for $[Mn^{III/II}(OH)Fe^{III}poat]^{2+/+}$ and $[Mn^{II}(OH)Fe^{III/II}poat]^{+/0}$; (C) high potential region (**VII** and **VI**). All voltammograms collected in CH_2Cl_2 at 100 mV s^{-1}. The open circuit potential is indicated by +.

The full voltammogram for $[Mn^{III}(O)Fe^{III}Hpoat]^{2+}$ is illustrated in Figure 7.8.A and exhibits similar redox processes (**I**, **III**, **IV**, **VI**, **VII**) as $[Mn^{II}(OH)Fe^{III}poat]^{+}$ (Figure 7.7.A). However, process **VI** at +0.67 V exhibited strong current response and reversibility (i_{pc}/i_{pa} = 0.89; Figure 7.8.B) without accessing more positive oxidative events (e.g., process **VII**), unlike that observed for $[Mn^{II}(OH)Fe^{III}poat]^{+}$ (Figure 7.7.C). These findings suggest process **VI** to be the $[Mn(O)FeHpoat]^{3+}/[Mn^{III}(O)Fe^{III}Hpoat]^{2+}$ couple. A $[(M')(O)(M1)poat]^{3+}$ species at the (IV,III) level would be a welcome addition to the bimetallic library of [TMTACN/poat] complexes, as the analogous $[Fe^{III}(O)Fe^{III}Hpoat]^{2+}$ and $[Fe^{III}(O)Mn^{III}Hpoat]^{2+}$ cannot access one higher oxidation state (Chapters 5 & 6). A similarly strong current response for process **III** at -0.67 V is consistent with the reduction of $[Mn^{III}(O)Fe^{III}Hpoat]^{2+}$ to $[Mn^{II}(O)Fe^{III}Hpoat]^{+}$, but the basic oxido-bridging ligand likely promotes facile intramolecular PT to generate $[Mn^{II}(OH)Fe^{III}poat]^{+}$, and as a result there is no return oxidative wave for $[Mn^{II}(O)Fe^{III}Hpoat]^{+}$ (Figure 7.8.C). The current intensity of process **VII** increases upon multiple scans as well as the generation of $[Mn^{II}(OH)Fe^{III}poat]^{+}$ and then $[Mn^{III}(OH)Fe^{III}poat]^{2+}$ at the electrode surface, which supports **VII** to be a further oxidation to a higher valent species (Figure 7.8.C). The unstable species then further reacts to form $[Mn(O)FeHpoat]^{3+}$, which can be detected in process **VI**.

The cyclic voltammogram for $[Mn^{III}(O)Fe^{III}poat]^{+}$ is complicated (Figure 7.9.A): it contains processes observed for the other two complexes (**I**, **III**, **IV**, **VI**) as well as two additional ones (**II**, **V**). Process **V** becomes increasingly reversible at +0.39 V (i_{pc}/i_{pa} = 1.00) at faster scan rates, and is assigned as the $[Mn(O)Fepoat]^{2+}/[Mn^{III}(O)Fe^{III}poat]^{+}$ couple (Figure 7.9.B); irreversibility at slower scan rates is likely due to instability of $[Mn(O)Fepoat]^{2+}$. This potential is between +0.55 V for $[Fe^{III}(O)Fe^{IV/III}poat]^{2+/+}$ (Chapter 5) and +0.20 V for $[Fe^{III}(O)Mn^{IV/III}poat]^{2+/+}$ couples (Chapter 6), which complicates the assignment of oxidation states for the new species without further spectroscopic experiments. Process **II** is absent in the previous electrochemical measurements, but

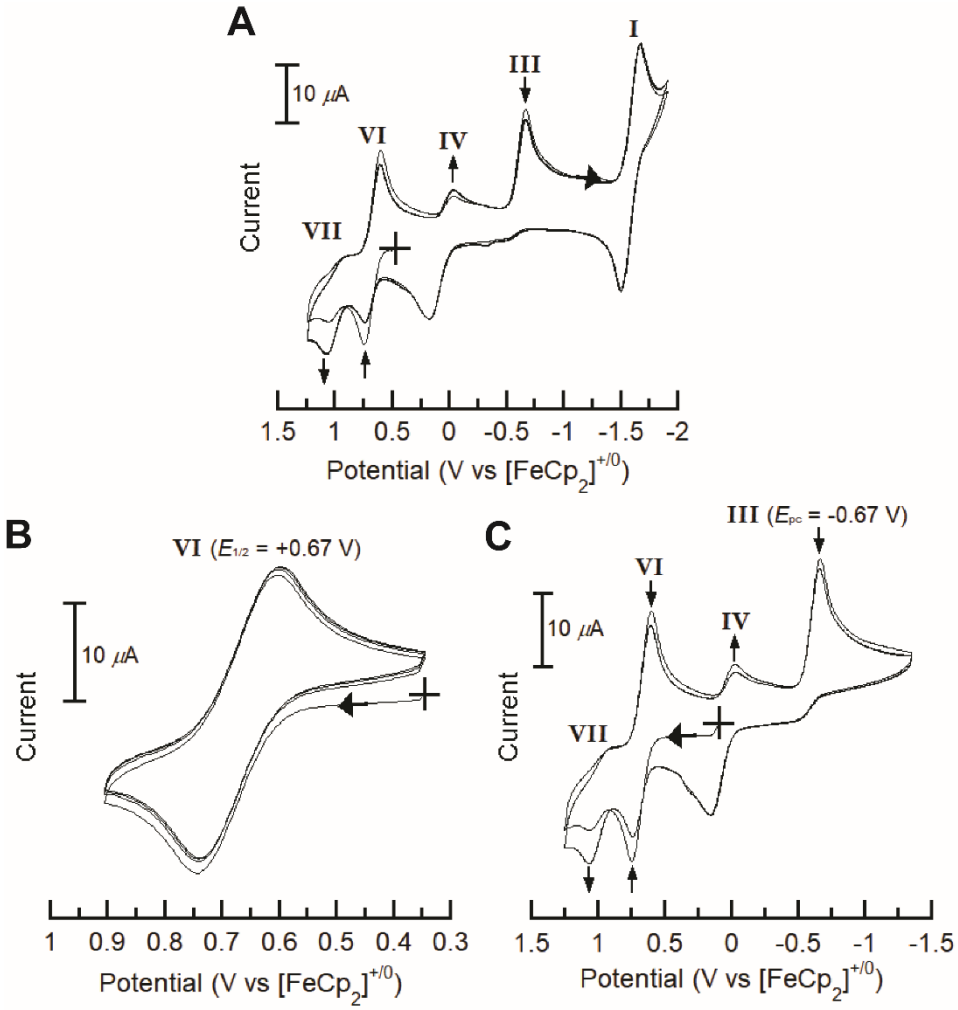

Figure 7.8. Cyclic voltammograms of $[Mn^{III}(O)Fe^{III}Hpoat]^{2+}$: (A) full voltammogram; (B) the redox process **VI** for $[Mn(O)FeHpoat]^{3+}/[Mn^{III}(O)Fe^{III}Hpoat]^{2+}$; (C) redox processes **VII**, **VI**, **IV** and **III**. All voltammograms collected at 100 mV s^{-1} in CH_2Cl_2. The open circuit potential is indicated by +.

exhibited strong reductive current response at -1.08 V for this complex (Figure 7.9.C): this suggests $[Mn^{III}(O)Fe^{III}poat]^{+}$ is reduced to $[Mn^{II}(O)Fe^{III}poat]$, where the basic oxido ligand causes the intermediate to further react (likely to form a stable $[Mn^{II}(OH)Fe^{III/II}poat]^{+/0}$ species, *via* a PT or PCET mechanism). Finally, an oxidative process is observed at +1.18 V, and the appearance of the **VI** couple ($[Mn(O)FeHpoat]^{3+}/[Mn^{III}(O)Fe^{III}Hpoat]^{2+}$) is dependent on this oxidation (Figure 7.9.D). The oxidation suggests the generation of a higher valent, unstable complex, and its high instability causes further reaction to produce $[Mn(O)FeHpoat]^{3+}$. It should be noted this oxidative process (+1.18 V) and process **VII** (+1.14 V) share similar redox potentials and could represent the

same event, so their assignments are ambiguous at this point. The irreversibility of these processes and instabilities of these species may prevent any chances of their trapping by chemical oxidation and further spectroscopic studies.

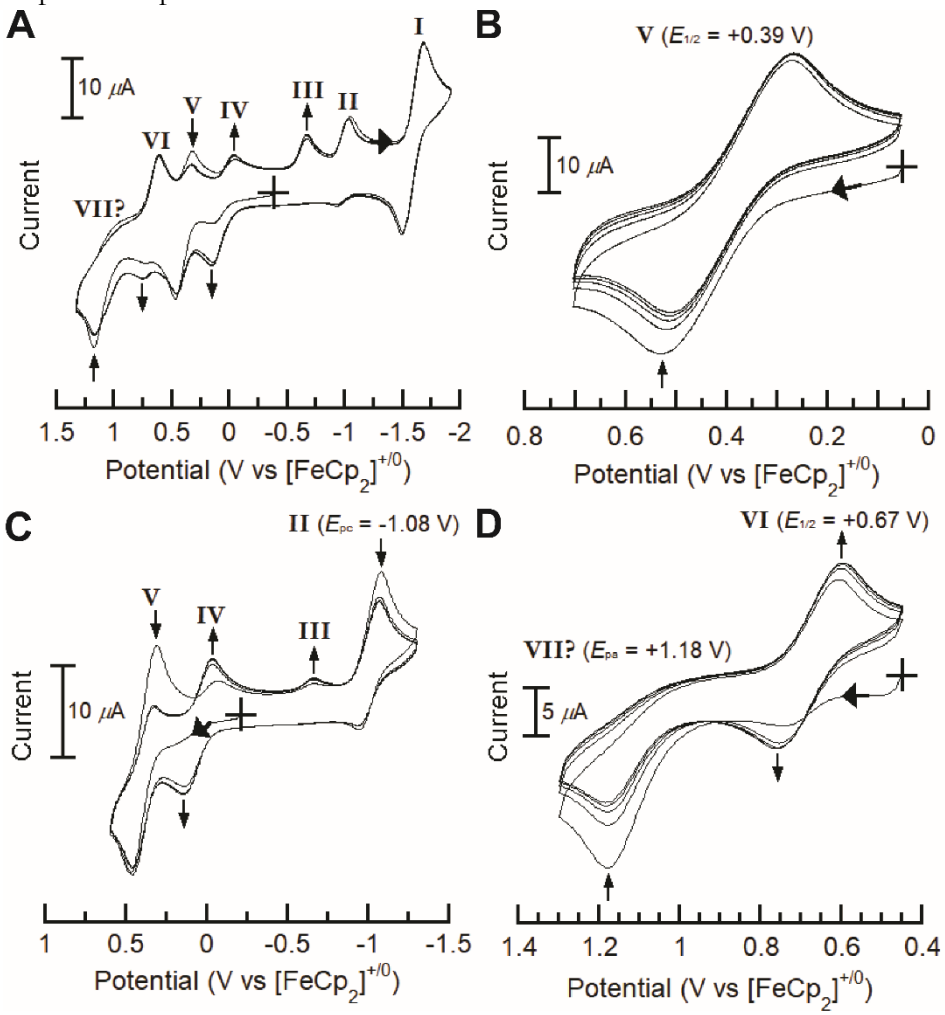

Figure 7.9. Cyclic voltammograms of $[Mn^{III}(O)Fe^{III}poat]^+$ in CH_2Cl_2: (A) full voltammogram; (B) the redox process **V** for $[Mn(O)Fepoat]^{2+}/[Mn^{III}(O)Fe^{III}poat]^+$; (C) redox processes **V**, **IV**, **III** and **II**; (D) high potential region. (A), (C), and (D) were collected at 100 mV s^{-1}; (B) was collected at 500 mV s^{-1}. The open circuit potential is indicated by +.

The cyclic voltammogram results are summarized in Figure 7.10 and Table 7.2; the ability to isolate and study the three complexes has provided a full electrochemical profile for this [MnFepoat] system. The electrochemically accessible species are illustrated in Figure 7.11, which span across at least four oxidation levels and various protonation states. These findings can provide a useful guide

in the spectroscopic and structural studies of the high valent complexes generated *via* chemical oxidation.

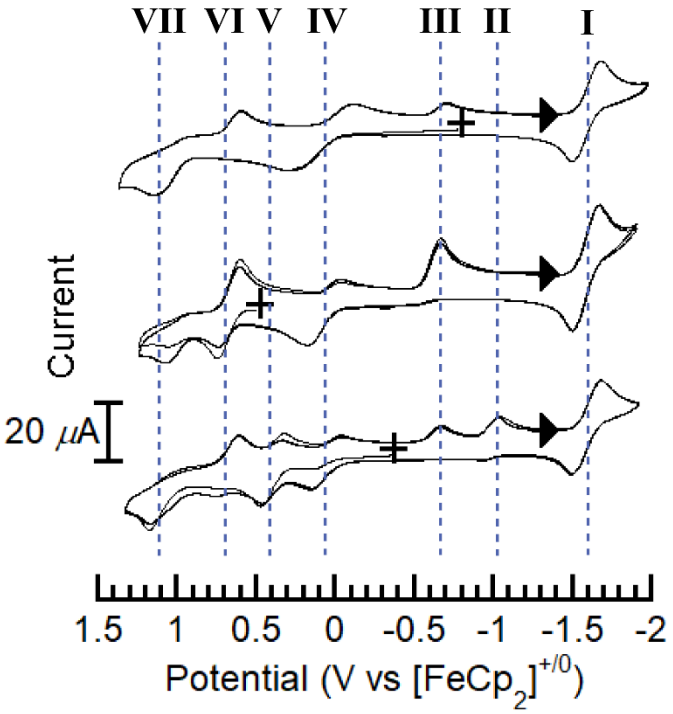

Figure 7.10. Full cyclic voltammograms of $[Mn^{II}(OH)Fe^{III}poat]^+$ (A), $[Mn^{III}(O)Fe^{III}Hpoat]^{2+}$ (B), and $[Mn^{III}(O)Fe^{III}poat]^+$ (C). All voltammograms collected at 100 mV s^{-1} in CH_2Cl_2. The open circuit potential is indicated by +.

Table 7.2. Compilation of electrochemical processes observed for $[Mn^{II}(OH)Fe^{III}poat]^+$, $[Mn^{III}(O)Fe^{III}Hpoat]^{2+}$, and $[Mn^{III}(O)Fe^{III}poat]^+$.

Redox event	Potential (V[a]) (i_{pc}/i_{pa})	Reversibility	Process[b]
I	-1.59[c] (1.05)	Reversible	$[Mn^{II}(OH)Fe^{III}poat]^+ \longleftrightarrow [Mn^{II}(OH)Fe^{II}poat]^0$
II	-1.08[d]	Irreversible	$[Mn^{III}(O)Fe^{III}poat]^+ \rightarrow [[Mn^{II}(O)Fe^{III}poat]^0] \rightarrow\rightarrow$
III	-0.67[d]	Reversible	$[Mn^{III}(O)Fe^{III}Hpoat]^{2+} \rightarrow [[Mn^{II}(O)Fe^{III}Hpoat]^+] \rightarrow\rightarrow [Mn^{II}(OH)Fe^{III}poat]^+$
IV	+0.06[c] (0.69)	Quasi-reversible	$[Mn^{III}(OH)Fe^{III}poat]^{2+} \longleftrightarrow [Mn^{II}(OH)Fe^{III}poat]^+$
V	+0.39[c] (1.00)	Reversible	$[Mn(O)Fepoat]^{2+} \longleftrightarrow [Mn^{III}(O)Fe^{III}poat]^+$
VI	+0.67[c] (0.89)	Reversible	$[Mn(O)FeHpoat]^{3+} \longleftrightarrow [Mn^{III}(O)Fe^{III}Hpoat]^{2+}$
VII	+1.14 to 1.18[e]	Irreversible	$[Mn^{III}(OH)Fe^{III}poat]^{2+} \rightarrow$ "High valent species" $\rightarrow\rightarrow [Mn(O)FeHpoat]^{3+}$ **OR** $[Mn(O)Fepoat]^{2+} \rightarrow$ "High valent species" $\rightarrow\rightarrow [Mn(O)FeHpoat]^{3+}$

[a] vs $[FeCp_2]^{+/0}$. [b] "$\longleftrightarrow$" indicates 1-e^- reversible process. "$\rightarrow$" indicates 1-e^- irreversible process. "$\rightarrow\rightarrow$" indicates further reaction. [c] $E_{1/2}$. [d] E_{pc}. [e] E_{pa}.

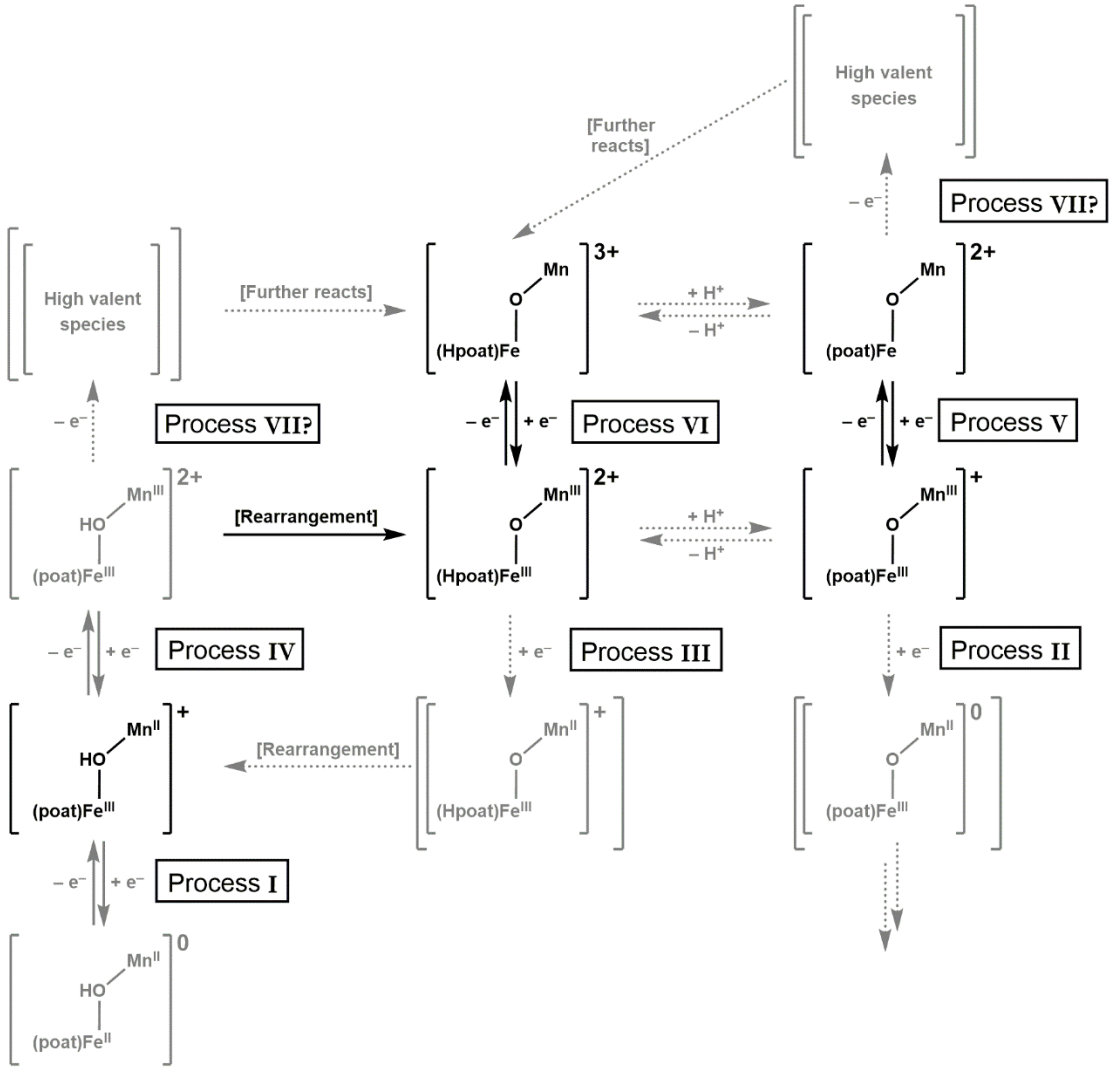

Figure 7.11. A compilation of electrochemically accessible [MnFepoat] species. The complexes and arrows in black indicate chemically isolated/generated compounds and reactions. The compounds and solid arrows in grey indicate electrochemically accessible species and reactions. The dashed grey arrows indicate proposed reaction pathways.

Accessing high-valent species. To test the hypotheses gained from the electrochemical studies, the chemical oxidations of $[Mn^{III}(O)Fe^{III}Hpoat]^{2+}$ and $[Mn^{III}(O)Fe^{III}poat]^{+}$ were monitored using EPR spectroscopy. As discussed, $[Mn^{III}(O)Fe^{III}Hpoat]^{2+}$ exhibits a reversible oxidation at +0.67 V (Figure 7.8.B), so the complex was treated with $[N(p\text{-}Br\text{-}C_6H_4)_3]PF_6$ ($E_{1/2}$ = -0.70 V in CH_2Cl_2) at -94 °C.[20] Indeed, the six-line, $S = 1/2$ feature associated with the complex disappeared (Figure 7.12.B), but was regenerated nearly quantitatively upon treatment with $FeCp(C_5H_4COMe)$ as a reductant (Figure 7.12.C). The lack of a ⊥-mode signal suggests an integer spin system, which is consistent with either

a $Mn^{III}Fe^{IV}$ (d^4/d^4) or $Mn^{IV}Fe^{III}$ (d^3/d^5) formulation; the oxidation states for both metal ions are not yet elucidated. These results support the oxidation to [(TMTACN)Mn–(μ-O)–FeHpoat]$^{3+}$ ([Mn(O)FeHpoat]$^{3+}$). This new species is an important finding, as the analogous [Fe^{III}(O)Fe^{III}Hpoat]$^{2+}$ and [Fe^{III}(O)Mn^{III}Hpoat]$^{2+}$ cannot be further oxidized. This offers an intriguing proposal that the oxidation may occur not at the Fe^{III}Hpoat center, but at the Mn^{III}(TMTACN) site.

An oxidation process at +0.39 V was observed for [Mn^{III}(O)Fe^{III}poat]$^+$ (Figure 7.9.B), which was treated with the same oxidant at -94 °C. Again, the S = 1/2 $Mn^{III}Fe^{III}$ signal completely disappeared (Figure 7.12.E), but returned in quantitative amount upon addition of $FeCp_2$ (Figure 7.12.F). The lack of a ⊥-mode signal indicates an integer spin system, and the oxidation state of the Fe site can best be determined by Mössbauer spectroscopy in future experiments. Regardless, these results support the generation of one-electron oxidized [(TMTACN)Mn–(μ-O)–Fepoat]$^{2+}$ ([Mn(O)Fepoat]$^{2+}$) species, similar to [Fe^{III}(O)Fe^{IV}poat]$^{2+}$ and [Fe^{III}(O)Mn^{IV}poat]$^{2+}$ discussed in the previous chapters.

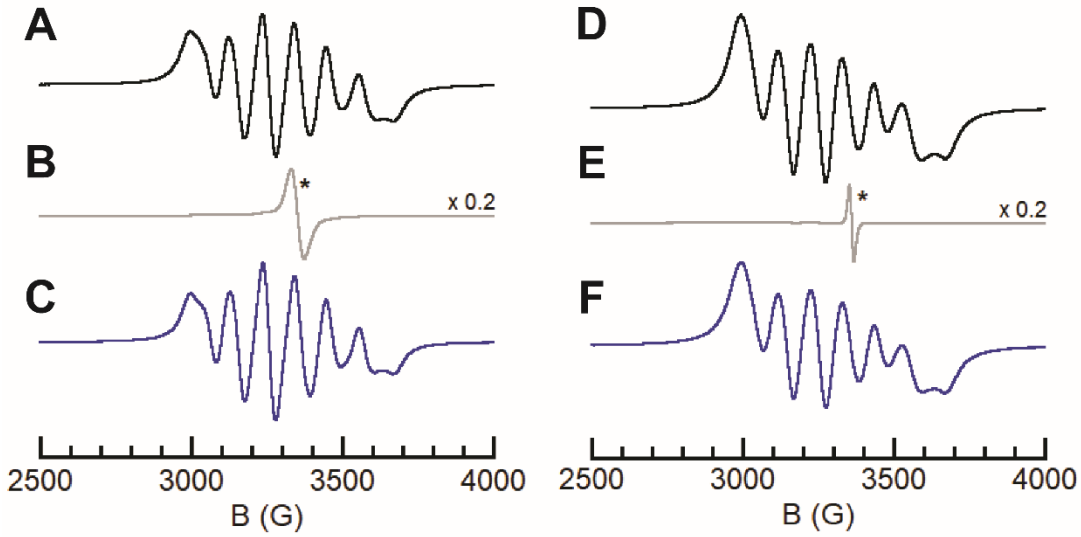

Figure 7.12. ⊥-mode EPR spectra of the reversible oxidation reactions of [Mn^{III}(O)Fe^{III}Hpoat]$^{2+}$ and [Mn^{III}(O)Fe^{III}poat]$^+$ before (A, D) and after (B, E) the addition of [N(*p*-$C_6H_4Br)_3$]PF_6, and after (C, F) the subsequent addition of $FeCp(C_5H_4COMe)$ and $FeCp_2$, respectively. Asterisks (*) indicate residual organic oxidants. Spectra were collected at 77 K. Spectra (A-C) were prepared in CH_2Cl_2 at 5 mM concentration; spectra (D-F) were prepared in PrCN at 5 mM concentration.

Conclusion & Outlook

In the pursuit of a $Mn^{IV}Fe^{IV}$ species, the development of a series of [MnFepoat] complexes was described in this chapter: this is inspired by prior reports of related $[Fe^{IV}poat]^{-}$[17] and $[Mn^{IV}TMTACN]$ systems.[1,10-13] $[Mn^{II}(OH)Fe^{III}poat]^{+}$, $[Mn^{III}(O)Fe^{III}Hpoat]^{2+}$, and $[Mn^{III}(O)Fe^{III}poat]^{+}$ were structurally characterized, and their redox properties were probed in detail. At least four oxidations states can be accessed electrochemically in this framework. EPR experiments support the reversible oxidations to $[Mn(O)FeHpoat]^{3+}$ and $[Mn(O)Fepoat]^{2+}$ species at the (IV,III) level, although Mössbauer experiments are necessary to confirm the Fe (and therefore Mn) oxidation states. In particular, the $[Mn(O)FeHpoat]^{3+}$ species is of great interest: it would be intriguing to explore whether the $[Hpoat]^{2-}$ or [TMTACN] is more suited to support the Mn^{IV} or Fe^{IV} center in $[Mn(O)FeHpoat]^{3+}$, and whether their roles change upon deprotonation to $[poat]^{3-}$ (Scheme 7.4).

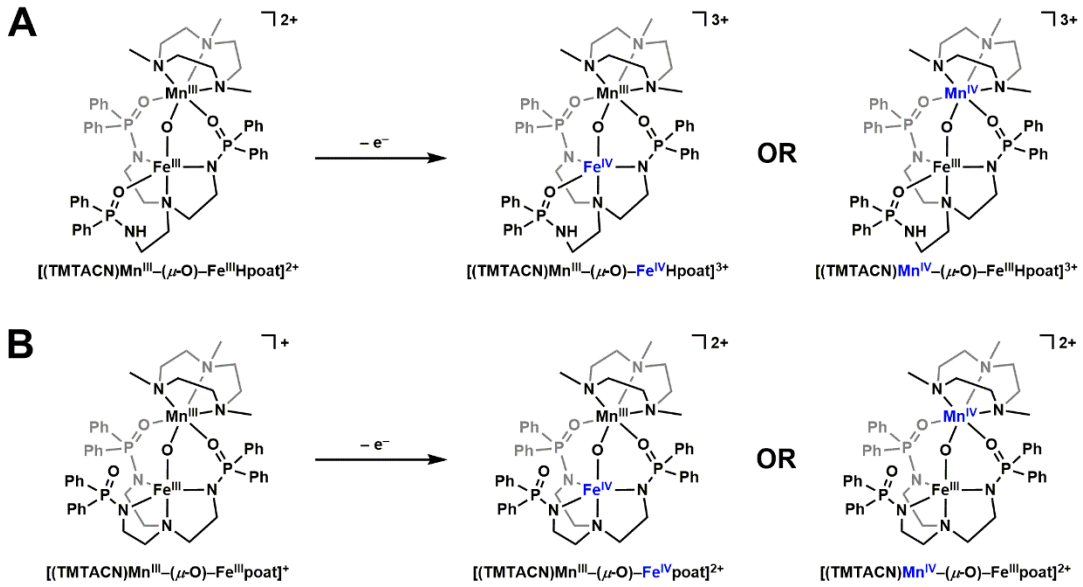

Scheme 7.4. Oxidation of $[Mn^{III}(O)Fe^{III}Hpoat]^{2+}$ (A) and $[Mn^{III}(O)Fe^{III}poat]^{+}$ (B) may result in different valence tautomers: the oxidized metal is highlighted in blue. Further magnetic measurements can determine the Fe (and therefore Mn) oxidation states.

In spite of my greatest effort, the elusive $Mn^{IV}Fe^{IV}$ species has not been spectroscopically detected. Further irreversible oxidations to higher valent species at E_{pa} = +1.14 to 1.18 V suggest it may be challenging, if not impossible, to trap and spectroscopically study these highly reactive

species in the [TMTACN/poat] system, so further modifications are likely needed to stabilize a Mn^{IV}–(μ-O)–Fe^{IV} core. While the trianionic $[poat]^{3-}$ ligand provides a strong ligand field to stabilize high-valent metal centers, the neutral amino donors in TMTACN are weaker donors; substitution of this capping group with more strongly donating ligands can increase the stabilization of a higher valent core. Two examples of tridentate ligands are shown in Figure 7.13. $[H_21]^{2-}$ was previously employed by the Borovik group, and provides a dianionic ligand field as well as H-bond donating ureate groups (Figure 7.13.A); a μ-oxido diferric complex was synthesized, in which the bridging ligand is stabilized by H-bond interactions.[21,22] Alternatively, the ligand $BnDPA^*$ was recently developed and contains electron-rich pyridine donors (Figure 7.13.B; see experimental for synthetic details); analogous ligands have been utilized to stabilize high valent diiron ($Fe^{III}Fe^{IV}$ and $Fe^{IV}Fe^{IV}$) complexes.[23-27] The stepwise bimetallic assembly approach developed in this dissertation allows for incorporation of any desired multidentate capping ligand, and highlights the multi-functional character of the $[poat]^{3-}$ system; a Mn^{IV}–(μ-O)–Fe^{IV} species is highly achievable within this framework in the future.

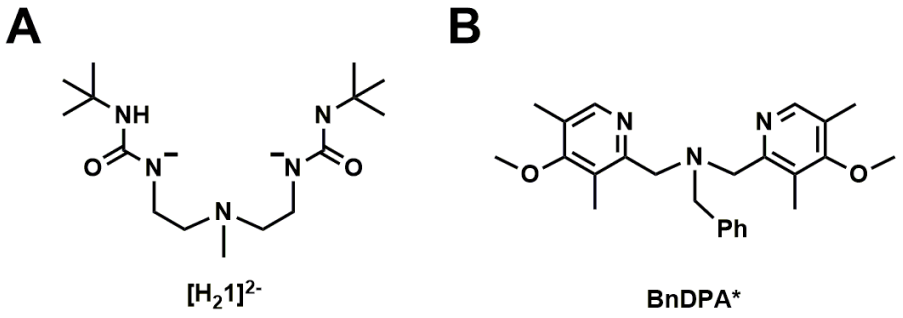

Figure 7.13. Proposed new capping ligands $[H_21]^{2-}$ (A) and $BnDPA^*$ (B).

Experimental

General Procedures. Organic syntheses, unless otherwise noted, did not require the use of an inert atmosphere. All inorganic syntheses and manipulations were performed under an argon atmosphere

in a Vacuum Atmosphere Co. dry box. Solvents were sparged with argon and purified using a JC Meyer Co. solvent purification system with columns containing Q-5 and molecular sieves. All reagents, unless otherwise noted, were purchased from commercial sources and used as received. Butyronitrile (PrCN) was purified according to a literature procedure.[28] Potassium hydride (KH) as a 30 % dispersion in mineral oil was filtered with a medium porosity glass frit and washed 5 times each with pentane and diethyl ether (Et_2O). Solid KH was dried under vacuum and stored under an inert atmosphere. Tetrabutylammonium hexafluorophosphate (TBAP) was recrystallized from hot EtOH. H_3poat,[17] K[Fe^{II}poat],[17] K[Fe^{III}poat(OH)],[16] TMTACN,[12,29] [$FeCp_2$]OTf,[20] IBX-iPr,[30,31] [N(*p*-$C_6H_4Br)_3$]PF_6,[32,33] and [N(*p*-tol)$_3$]OTf[20] were synthesized according to previous reports.

Physical Methods. Room temperature UV-vis spectra were collected on a Cary 50 UV-vis spectrophotometer in a 1 cm quartz cuvette. Solid-state Fourier transform infrared (FTIR) spectra were collected on a Thermo Scientific Nicolet iS5 FT-IR spectrometer equipped with an iD5 ATR accessory. Cyclic voltammetry experiments were conducted using a CHI600G electrochemical analyzer. A 2.0 mm glassy carbon electrode was used as the working electrode at scan velocities between 0.01 and 0.5 $V \cdot s^{-1}$. A ferrocenium/ferrocene ($[FeCp_2]^{+/0}$) standard was used as an internal reference to monitor the reference electrode (Ag^+/Ag). TBAP was used as the supporting electrolyte at a concentration of 0.1 M. Elemental analyses were performed on a Perkin-Elmer 2400 Series II CHNS elemental analyzer. ^{1}H NMR spectra was collected on a Bruker CRYO500 spectrometer (500 MHz). X-band (microwave frequency 9.6 GHz) EPR spectra were collected on a Bruker EMZ spectrometer equipped with an Oxford ESR-900 liquid helium cryostat and a Bruker bimodal (ER4116DM) or ⊥-mode (ER4119HS-W1) cavity for the generation of microwave fields parallel and transverse to the applied magnetic field.

Synthesis of [Mn^{II}(TMTACN)(OTf)$_2$]. $Mn^{II}Cl_2$ (0.147 g, 1.17 mmol) was suspended in 20 mL CH_3CN, and TMTACN (227 μL, 0.201 g, 1.17 mmol) was added in one portion via syringe. The reaction mixture initially turned to a white cloudy mixture upon stirring, then gradually became a colorless, homogenous solution. The reaction was allowed to stir overnight, before AgOTf (0.609 g, 2.37 mmol) was added, and AgCl precipitates immediately appeared. After 3 hours of stirring, the insoluble was removed using a fine porosity glass fritted funnel with a pad of Celite, and all volatiles were removed *in vacuo*. The white residue was triturated with two portions of 20 mL CH_2Cl_2 and 20 mL Et_2O before drying under vacuum for 2 hours (80 – 90 % yield). Elemental analysis calcd. (found) for $[Mn^{II}(TMTACN)(OTf)_2]\cdot CH_2Cl_2$, $C_{11}H_{21}F_6MnN_3O_6S_2\cdot CH_2Cl_2$; C, 23.66 (23.25); H, 3.80 (3.65); N, 6.90 (7.25) %.

Synthesis of [(TMTACN)Mn^{II}–(μ-OH)–Fe^{III}poat]OTf. This salt was prepared using the method described for [(TMTACN)Zn^{II}–(μ-OH)–Fe^{III}poat]OTf (Chapter 3)[16] with the following modifications: K[Fe^{III}poat(OH)] (0.0449 g, 0.0525 mmol), NMe_4OAc (0.0100 g, 0.0751 mmol), [Mn^{II}(TMTACN)(OTf)$_2$] (0.0274 g, 0.0522 mmol). Brown crystals (40 – 50 % yield) suitable for X-ray diffraction were grown from a concentrated CH_2Cl_2 solution layered with hexane. Elemental analysis calcd. (found) for [(TMTACN)Mn^{II}–(μ-OH)–Fe^{III}poat]OTf$\cdot 0.5CH_2Cl_2$, $C_{52}H_{64}F_3FeMnN_7O_7P_3S\cdot 0.5CH_2Cl_2$; C, 51.09 (50.74); H, 5.31 (5.34); N, 7.94 (8.24) %. FTIR (diamond ATR, cm^{-1}): 3140 (OH), 3071, 3051, 3006, 2987, 2956, 2899, 2858, 2818, 1590, 1493, 1483, 1464, 1441, 1435, 1364, 1264, 1224, 1147, 1136, 1116, 1087, 1065, 1031, 1016, 987, 961, 934, 890, 860, 809, 752, 721, 697, 636. UV-vis $\lambda_{max}(CH_2Cl_2)$/nm ($\varepsilon/M^{-1}cm^{-1}$): 325 (sh), 375 (5700), 540 (sh). $E_{1/2}$ (CH_2Cl_2, V versus $[FeCp_2]^{+/0}$): -1.59, +0.06. EPR (X-band, //-mode, CH_2Cl_2:THF, 40 – 79 K): g = 11.3.

Synthesis of [(TMTACN)Mn^{III}–(μ-O)–Fe^{III}Hpoat](OTf)$_2$. [(TMTACN)Mn^{II}–(μ-OH)–Fe^{III}poat]OTf (0.0323 g, 0.0271 mmol) was dissolved in 2 mL anhydrous CH_2Cl_2, and solid [N(*p*-tol)$_3$]OTf (0.0128 g, 0.0293 mmol) was added in one portion to the brown solution. The solution immediately turned dark red, then gradually dark brown over a period of 1.5 hours under stirring. All volatiles were then removed under vacuum. The residues were triturated with 20 mL Et_2O, which was then removed by decanting; the washing process was repeated four times. The residues were redissolved in 10 mL $CHCl_3$, which was layered under 10 mL hexane to yield dark brownish green crystalline needles (50 – 60 %). The bulk oxidation can also achieved using AgOTf, with the following modifications: [(TMTACN)Mn^{II}–(μ-OH)–Fe^{III}poat]OTf (0.0949 g, 0.0796 mmol), AgOTf (0.0227 g, 0.0883 mmol), 3 mL CH_2Cl_2. Elemental analysis calcd. (found) for [(TMTACN)Mn^{III}–(μ-O)–Fe^{III}Hpoat](OTf)$_2$·0.5CH_2Cl_2, $C_{53}H_{64}F_6FeMnN_7O_{10}P_3S_2$·0.5$CH_2Cl_2$; C, 46.45 (46.33); H, 4.75 (4.68); N, 7.09 (7.36) %. FTIR (diamond ATR, cm^{-1}):. 3224 (NH), 3057, 2900, 2861, 1591, 1484, 1461, 1438, 1363, 1253, 1223, 1119, 1071, 1055, 1028, 1006, 991, 969, 929, 917, 894, 857, 814, 750, 726, 696, 635. EPR (X-band, ⊥-mode, PrCN, 77 K): g = 2.04; A(^{55}Mn) = 310 MHz. UV-vis λ_{max}(CH_2Cl_2)/nm (ε/M^{-1}cm^{-1}): 350 (8500), 405 (sh), 480 (sh), 585 (380). $E_{1/2}$ (CH_2Cl_2, V versus [$FeCp_2$]$^{+/0}$): +0.67.

Synthesis of [(TMTACN)Mn^{III}–(μ-O)–Fe^{III}poat]OTf. K[Fe^{II}poat] (0.102 g, 0.122 mmol) and 18-crown-6 (0.065 g, 0.246 mmol) were dissolved in 5 mL anhydrous THF and 1 mL anhydrous DMF. The yellow solution was transferred to a 50 mL Schlenk flask, which was sealed with a septum and cooled in a -75 °C cold bath outside the glovebox for at least 15 minutes. A 2 mL DMF solution of IBX-iPr (0.0475 g, 0.147 mmol), prepared in the glovebox, was added dropwise into the Schlenk flask via syringe. The reaction mixture immediately turned red, indicative of the formation of [Fe^{IV}poat(O)]$^-$, and was allowed to stir for 20 minutes. A 1 mL 1:1 DMF:THF solution of

$[Mn^{II}(TMTACN)(OTf)_2]$ (0.0638 g, 0.122 mmol), prepared in the glovebox, was then added dropwise into the Schlenk flask via syringe. The reaction mixture turned dark green gradually, and was allowed to stir for 2 hours. The Schlenk flask was then warmed up to room temperature, and all volatiles were removed under vacuum. The flask was transferred back in a glovebox, where the residue was triturated with Et_2O, redissolved in CH_2Cl_2, and layered with diethyl ether to yield a brownish green powder over four days. After the powder was collected and dried, it was redissolved in CH_2Cl_2, and was layered with pentane to yield dark green crystals (30 – 40 %). UV-vis (CH_2Cl_2 solution λ_{max}/nm (ε_{max}/$M^{-1}cm^{-1}$)) 350 (10000), 600 (290). EPR (X-band, ⊥-mode, CH_2Cl_2:THF, 17.4 K): g = 2.04; $A(^{55}Mn)$ = 290 MHz. $E_{1/2}$ (CH_2Cl_2, V versus $[FeCp_2]^{+/0}$): +0.39.

Low-temperature EPR solution studies. In a typical experiment, a 5 – 6 mM solution of the MnFe compound was prepared in CH_2Cl_2 at room temperature and kept in a -35 °C freezer of the glovebox for the duration of the experiment. A 200 μL aliquot of stock metal complex was added via air-tight syringe to an EPR tube, which was then sealed with a rubber septum and precooled to the desired temperature in a cold bath outside the glovebox. The solution of metal complex was allowed to equilibrate to the desired temperature for at least 15 min. Stock solutions of other reagents were prepared at concentrations between 40 and 250 mM in the same solvent and added via gas-tight syringe. The target final concentration is ~ 5 mM.

Synthesis of BnDPA.* Benzylamine (0.7239 g, 6.756 mmol), 2-chloromethyl-4-methoxy-3,5-dimethylpyridine hydrochloride (2.997 g, 13.40 mmol), Na_2CO_3 (3.629 g, 34.24 mmol), tetrabutylammonium bromide (0.0050 g, 16 mmol), and 100 mL CH_3CN were added to a 250 mL round bottom flask, which was fitted with a condenser and heated under reflux at 80 °C for two days. The resultant peach-color solution was cooled to room temperature, and treated with 75 mL 1

M NaOH (aq) solution. The mixture was concentrated to remove the CH_3CN, and was extracted with four portions of 100 mL CH_2Cl_2. The organic layer was dried over Na_2SO_4 for one hour, which was subsequently removed *via* filtration. The CH_2Cl_2 solvent was removed in vacuo, producing an orange oil. After extensive drying, an orange solid was obtained (70 % yield). ^{1}H NMR (500 MHz, $CDCl_3$) δ 8.15 (2H, s, PyH), 7.14-7.26 (5H, m, PhH), 3.71 (4H, s, PyCH_2), 3.68 (6H, s, OCH_3), 3.56 (2H, s, PhCH_2), 2.21 (6H, s, CH_3), 1.92 (6H, s, CH_3).

Crystallography.

[(TMTACN)Mn^{II}–(μ-OH)–Fe^{III}poat]OTf. An orange crystal of approximate dimensions 0.060 x 0.149 x 0.183 mm was mounted in a cryoloop and transferred to a Bruker SMART APEX II diffractometer system. The APEX2[34] program package was used to determine the unit-cell parameters and for data collection (120 sec/frame scan time). The raw frame data was processed using SAINT[35] and SADABS[36] to yield the reflection data file. Subsequent calculations were carried out using the SHELXTL[37] program package. There were no systematic absences nor any diffraction symmetry other than the Friedel condition. The centrosymmetric triclinic space group $P\bar{1}$ was assigned and later determined to be correct.

The structure was solved by direct methods and refined on F^2 by full-matrix least-squares techniques. The analytical scattering factors[38] for neutral atoms were used throughout the analysis. Hydrogen atoms H(1) and H(8) were located from a difference-Fourier map and refined (x,y,z and U_{iso}) with d(O-H) = 0.82Å. The remaining hydrogen atoms were included using a riding model. There were two molecules of the formula-unit present (Z = 4). Several atoms were disordered and included using multiple components with partial site-occupancy-factors.

Least-squares analysis yielded wR2 = 0.0963 and Goof = 1.007 for 1461 variables refined against 22477 data (0.80 Å), R1 = 0.0448 for those 15845 data with I > 2.0σ(I).

[(TMTACN)Mn^{III}–(μ-O)–Fe^{III}Hpoat](OTf)$_2$. A green crystal of approximate dimensions 0.216 x 0.226 x 0.327 mm was mounted in a cryoloop and transferred to a Bruker SMART APEX II diffractometer system. The APEX2[34] program package was used to determine the unit-cell parameters and for data collection (15 sec/frame scan time). The raw frame data was processed using SAINT[35] and SADABS[36] to yield the reflection data file. Subsequent calculations were carried out using the SHELXTL[37] program package. The diffraction symmetry was 2/*m* and the systematic absences were consistent with the monoclinic space group $P2_1/c$ that was later determined to be correct.

The structure was solved by direct methods and refined on F^2 by full-matrix least-squares techniques. The analytical scattering factors[38] for neutral atoms were used throughout the analysis. Hydrogen atom H(2) was located from a difference-Fourier map and refined (x,y,z and U_{iso}). The remaining hydrogen atoms were included using a riding model. There was a molecule of chloroform solvent present

Least-squares analysis yielded wR2 = 0.1275 and Goof = 1.033 for 791 variables refined against 16643 data (0.75 Å), R1 = 0.0453 for those 13419 data with $I > 2.0\sigma(I)$.

There were several high residuals present in the final difference-Fourier map. It was probable that additional partially occupied chloroform solvent was present. The SQUEEZE[39] routine in the PLATON[40] program package was used to account for the electrons in the solvent accessible voids.

[(TMTACN)Mn^{III}–(μ-O)–Fe^{III}poat]OTf. A green crystal of approximate dimensions 0.187 x 0.238 x 0.277 mm was mounted on a glass fiber and transferred to a Bruker SMART APEX II diffractometer system. The APEX2[34] program package was used to determine the unit-cell

parameters and for data collection (10 sec/frame scan time). The raw frame data was processed using SAINT[35] and SADABS[36] to yield the reflection data file. Subsequent calculations were carried out using the SHELXTL[37] program package. There were no systematic absences nor any diffraction symmetry other than the Friedel condition. The centrosymmetric triclinic space group $P\bar{1}$ was assigned and later determined to be correct.

The structure was solved by direct methods and refined on F^2 by full-matrix least-squares techniques. The analytical scattering factors[38] for neutral atoms were used throughout the analysis. Hydrogen atoms were included using a riding model. The triflate ion was disordered and included using multiple components with partial site-occupancy-factors.

Least-squares analysis yielded wR2 = 0.1228 and Goof = 1.041 for 751 variables refined against 16612 data (0.70 Å), R1 = 0.0544 for those 12169 data with $I > 2.0\sigma(I)$.

There were several high residuals present in the final difference-Fourier map. It was probable that diethylether solvent was present. The SQUEEZE[39] routine in the PLATON[40] program package was used to account for the electrons in the solvent accessible voids.

Table 7.3. Crystallographic data for $[Mn^{II}(OH)Fe^{III}poat]^{+}$, $[Mn^{III}(O)Fe^{III}Hpoat]^{2+}$, and $[Mn^{III}(O)Fe^{III}poat]^{+}$.

	[(TMTACN)Mn^{II}–(μ-OH)–Fe^{III}poat]OTf	[(TMTACN)Mn^{III}–(μ-O)–Fe^{III}Hpoat](OTf)$_2$	[(TMTACN)Mn^{III}–(μ-O)–Fe^{III}poat]OTf
Formula	C_{52} H_{64} F_3 Fe Mn N_7 O_7 P_3 S	C_{54} H_{65} Cl_3 F_6 Fe Mn N_7 O_{10} P_3 S_2	C_{52} H_{63} F_3 Fe Mn N_7 O_7 P_3 S
fw	1191.86	1460.30	1190.85
T (K)	93(2)	133(2)	93(2)
Crystal system	Triclinic	Monoclinic	Triclinic
Space group	$P\bar{1}$	$P2_1/c$	$P\bar{1}$
a (Å)	14.9449(7)	16.712(4)	10.6980(8)
b (Å)	17.2187(7)	14.873(3)	13.7886(11)
c (Å)	21.4822(9)	26.838(6)	20.6110(16)
α (°)	89.3190(7)	90	108.7760(13)
β (°)	89.9234(8)	91.730(4)	91.1561(14)
γ (°)	82.0562(7)	90	104.1526(14)
Z	4	4	2
V (Å^3)	5474.6(4)	6668(3)	2774.9(4)
δ_{calc} (mg/m^3)	1.446	1.455	1.425
Independent reflections	22477	16643	16612
R1	0.0448	0.0453	0.0544
wR2	0.0963	0.1275	0.1228
Goof	1.007	1.033	1.041

wR2 = $[\Sigma[w(F_o^2-F_c^2)^2] / \Sigma[w(F_o^2)^2]]^{1/2}$
R1 = $\Sigma||F_o|-|F_c|| / \Sigma|F_o|$
Goof = S = $[\Sigma[w(F_o^2-F_c^2)^2] / (n-p)]^{1/2}$ where n is the number of reflections and p is the total number of parameters refined.
The thermal ellipsoid plots are shown at the 50% probability level.

References

(1) Hotzelmann, R.; Wieghardt, K.; Flörke, U.; Haupt, H.-J.; Weatherburn, D. C.; Bonvoisin, J.; Blondin, G.; Girerd, J.-J. Spin Exchange Coupling in Asymmetric Heterodinuclear Complexes Containing the μ-Oxo-bis(μ-acetato)dimetal Core. *J. Am. Chem. Soc.* **1992**, *114*, 1681-1696.

(2) Jiang, W.; Yun, D.; Saleh, L.; Barr, E. W.; Xing, G.; Hoffart, L. M.; Maslak, M.-A.; Krebs, C.; Bollinger, J. M. A manganese(IV)/iron(III) cofactor in Chamydia trachomatis ribonucleotide reductase. *Science* **2007**, *316*, 1188-1191.

(3) Younker, J. M.; Krest, C. M.; Jiang, W.; Krebs, C.; Bollinger, J. M.; Green, M. T. Structural Analysis of the Mn(IV)/Fe(III) Cofactor of *Chlamydia trachomatis* Ribonucleotide Reductase by Extended X-ray Absorption Fine Structure Spectroscopy and Density Functional Theory Calculations. *J. Am. Chem. Soc.* **2008**, *130*, 15022-15027.

(4) Kwak, Y.; Jiang, W.; Dassama, L. M. K.; Park, K.; Bell, C. B.; Liu, L. V.; Wong, S. D.; Saito, M.; Kobayashi, Y.; Kitao, S.; Seto, M.; Yoda, Y.; Alp, E. E.; Zhao, J.; Bollinger, J. M.; Krebs, C.; Solomon, E. I. Geometric and Electronic Structure of the Mn(IV)Fe(III) Cofactor in

Class Ic Ribonucleotide Reductase: Correlation to the Class Ia Binuclear Non-Heme Iron Enzyme. *J. Am. Chem. Soc.* **2013**, *135*, 17573-17584.

(5) Miller, E. K.; Trivelas, N. E.; Maugeri, P. T.; Blaesi, E. J.; Shafaat, H. S. Time-Resolved Investigations of Heterobimetallic Cofactor Assembly in R2lox Reveal Distinct Mn/Fe Intermediates. *Biochemistry* **2017**, *56*, 3369-3379.

(6) Bollinger, J. M.; Jiang, W.; Green, M. T.; Krebs, C. The manganese(IV)/iron(III) cofactor of *Chlamydia trachomatis* ribonucleotide reductase: structure, assembly, radical initiation, and evolution. *Curr. Opin. Struct. Biol.* **2008**, *18*, 650-657.

(7) Jiang, W.; Hoffart, L. M.; Krebs, C.; Bollinger, J. M. A Manganese(IV)/Iron(IV) Intermediate in Assembly of the Manganese(IV)/Iron(III) Cofactor of *Chlamydia trachomatis* Ribonucleotide Reductase. *Biochemistry* **2007**, *46*, 8709-8716.

(8) Martinie, R. J.; Blaesi, E. J.; Krebs, C.; Bollinger, J. M.; Silakov, A.; Pollock, C. J. Evidence for a Di-*μ*-oxo Diamond Core in the Mn(IV)/Fe(IV) Activation Intermediate of Ribonucleotide Reductase from *Chlamydia trachomatis*. *J. Am. Chem. Soc.* **2017**, *139*, 1950-1957.

(9) Slep, L. D.; Mijovilovich, A.; Meyer-Klaucke, W.; Weyhermüller, T.; Bill, E.; Bothe, E.; Neese, K.; Wieghardt, K. Mixed-Valent $\{Fe^{IV}(\mu\text{-}O)(\mu\text{-carboxylato})_2Fe^{III}\}^{3+}$ Core. *J. Am. Chem. Soc.* **2003**, *125*, 15554-15570.

(10) Quee-Smith, V. C.; DelPizzo, L.; Jureller, S. H.; Kerschner, J. L.; Hager, R. Synthesis, Structure, and Characterization of a Novel Manganese(IV) Monomer, $[Mn^{IV}(Me_3TACN)(OMe)_3](PF_6)$ (Me_3TACN = *N*,*N*',*N*''-Trimethyl-1,4,7-triazacyclononane), and Its Activity toward Olefin Oxidation with Hydrogen Peroxide. *Inorg. Chem.* **1996**, *35*, 6461-6465.

(11) Wieghardt, K.; Bossek, U.; Number, B.; Weiss, J.; Bonvoisin, J.; Corbella, M.; Vitols, S. E.; Girerd, J. J. Synthesis, Crystal Structures, Reactivity, and Magnetochemistry of a Series of Binuclear Complexes of Manganese(II), -(III), and -(IV) of Biological Relevance. The Crystal Structure of $[L'Mn^{IV}(\mu\text{-}O)_3Mn^{IV}L'](PF_6)_2\cdot H_2O$ Containing an Unprecedented Short Mn···Mn Distance of 2.296 Å. *J. Am. Chem. Soc.* **1988**, *110*, 7398-7411.

(12) Schoenfeldt, N. J.; Ni Z.; Korinda, A. W.; Meyer R. J.; Notestein J. M. Manganese Triazacyclononane Oxidation Catalysts Grafted under Reaction Conditions on Solid Cocatalytic Supports. *J. Am. Chem. Soc.* **2011**, *133*, 18684–18695.

(13) Steen, J. D.; Stepanovic, S.; Parvizian, M.; De Boer, J. W.; Hage, R.; Chen, J.; Swart, M.; Gruden, M.; Browne, W. R. Lewis versus Brønsted Acid Activation of a Mn(IV) Catalyst for Alkene Oxidation. *Inorg. Chem.* **2019**, *58*, 14924-14930.

(14) Sano, Y.; Weitz, A. C.; Ziller, J. W.; Hendrich, M. P.; Borovik, A. S. Unsymmetrical Bimetallic Complexes with M^{II}–(μ-OH)–M^{III} Cores ($M^{II}M^{III}$ = $Fe^{II}Fe^{III}$, $Mn^{II}Fe^{III}$, $Mn^{II}Mn^{III}$): Structural, Magnetic, and Redox Properties. *Inorg. Chem.* **2013**, *52*, 10229-10231.

(15) Sano, Y.; Lau, N.; Weitz, A. C.; Ziller, J. W.; Hendrich, M. P.; Borovik, A. S. Models for Unsymmetrical Active Sites in Metalloproteins: Structural, Redox, and Magnetic Properties of Bimetallic Complexes with M^{II}-(μ-OH)-Fe^{III} Cores. *Inorg. Chem.* **2017**, *56*, 14118-14128**.**

(16) Lee, J. L.; Oswald, V. F.; Biswas, S.; Hill, E. A.; Ziller, J. W.; Hendrich, M. P.; Borovik, A. S. Stepwise assembly of heterobimetallic complexes: synthesis, structure, and physical properties. *Dalton Trans***. 2021**, *50*, 8111-8119.

(17) Oswald, V. F.; Lee, J. L.; Biswas, S.; Weitz, A. C.; Mittra, K.; Fan, R.; Li, J.; Zhao, J.; Hu, M. Y.; Alp, E. E.; Bominaar, E. L.; Guo, Y.; Green, M. T.; Hendrich, M. P.; Borovik, A. S. Effects of Non-covalent Interactions on High-spin Fe(IV)-oxido Complexes. *J. Am. Chem. Soc.* **2020**, *142*, 11804-11817.

(18) Zhou, A.; Crossland, P. M.; Draksharapu, A.; Jasniewski, A. J.; Kleespies, S. T.; Que, L. Oxoiron(IV) compelxes as synthons for the assembly of heterobimetallic centers such as the

Fe/Mn active site of Class Ic ribonucleotide reductases. *JBIC, J. Biol. Inorg. Chem.* **2018**, *23*, 155-165.
(19) Crossland, P. M.; Guo, Y.; Que, L. Spontaneous Formation of an Fe/Mn Diamond Core: Models for the Fe/Mn Sites in Class 1c Ribonucleotide Reductases. *Inorg. Chem.* **2021**, *60*, 8710-8721.
(20) Connelly, N. G.; Geiger, W. E. Chemical Redox Agents for Organometallic Chemistry. *Chem. Rev.* **1996**, *96*, 877-910.
(21) Zart, M. K.; Sorrell, T. N.; Powell, D.; Borovik, A. S. Development of bio-inspired chelates with hydrogen bond donors: synthesis and structure and monomeric metal acetate complexes with intramolecular hydrogen bonds. *Dalton Trans.* **2003**, 1986-1992.
(22) Zart, M. K.; Powell, D.; Borovik, A. S. Synthesis and structures of dimeric iron(III)-Oxo and -imido complexes containing intramolecular hydrogen bonds. *Inorg. Chim. Acta* **2007**, *360*, 2397-2402.
(23) Xue, G.; Wang, D.; De Hont, R.; Fiedler, A. T.; Shan, X.; Münck, E.; Que, L. A synthetic precedent for the $[Fe^{IV}_2(\mu\text{-}O)_2]$ diamond core proposed for methane monooxygenase intermediate Q. *Proc. Natl. Acad. Sci. U.S.A.* **2007**, *104*, 20713-20718.
(24) Wang, D.; Farquhar, E. R.; Stubna, A.; Münck, E.; Que, L. A diiron(IV) complex that cleaves strong C-H and O-H bonds. *Nat. Chem.* **2009**, *1*, 145-150.
(25) Stoian, S. A.; Xue, G.; Bominaar, E. L.; Que, L.; Münck, E. Spectroscopic and Theoretical Investigation of a Complex with an $[O=Fe^{IV}–O–Fe^{IV}=O]$ Core Related to Methane Monooxygenase Intermediate Q. *J. Am. Chem. Soc.* **2014**, *136*, 1545-1558.
(26) Kryatov, S. V.; Taktak, S.; Korendovych, I. V.; Rybak-Akimova, E. V.; Kaizer, J.; Torelli, S.; Shan, X.; Mandal, S.; MacMurdo, V. L.; Mairata i Payeras, A.; Que, L. Dioxygen Binding to Complexes with $Fe^{II}_2(\mu\text{-}OH)_2$ Cores: Steric Control of Activation Barriers and O_2-Adduct Formation. *Inorg. Chem.* **2005**, *44*, 85-99.
(27) Cranswick, M. A.; Meier, K. K.; Shan, X.; Stubna, A.; Kaizer, J.; Mehn, M. P.; Münck, E.; Que, L. Protonation of a Peroxodiiron(III) Complex and Conversion to a Diiron(III/IV) Intermediate: Implications for Proton-Assisted O–O Bond Cleavage in Nonheme Diiron Enzymes. *Inorg. Chem.* **2012**, *51*, 10417-10426.
(28) Armarego, W. L. F.; Chai, C. L. L In *Purification of Laboratory Chemicals*, 5th e.d.; Elsevier: Oxford, UK, 2003.
(29) Cao R.; Müller, P.; Lippard, S. J. Tripodal Tris-tacn and Tris-dpa Platforms for Assembling Phosphate-Templated Trimetallic Centers. *J. Am. Chem. Soc.* **2010**, *132*, 17366–17369.
(30) Zhdankin, V. V.; Litvinov, D. N.; Koposov, A. Y.; Luu, T.; Ferguson, M. J.; McDonald, R.; Tykwinski, R. R. Preparation and Structure of 2-Iodoxybenzoate Esters: Soluble and Stable Periodinane Oxidizing Reagents. *Chem. Commun.* **2004**, *263*, 106-107.
(31) Zhdankin, V. V.; Koposov, A. Y.; Litvinov, D. N.; Ferguson, M. J.; McDonald, R.; Luu, T.; Tykwinski, R. R. Esters of 2-Iodoxybenzoic Acid: Hypervalent Iodine Oxidizing Reagents with a Pseudobenziodoxole Structure. *J. Org. Chem.* **2005**, *70*, 6484-6491.
(32) Bell, F. A.; Ledwith, A.; Sherrington, D. C. Cation-radicals:tris-(*p*-tribromophenyl)amminium perchlorate and hexachloroantimonate. *J. Chem. Soc. C* **1969**, 2719-2720.
(33) Eberson L.; Larsson, B. Electron Transfer Reactions in Organic Chemistry. XII. Reactions of 4-Substituted Triarylaminium Radical Cations with Nucleophiles; Polar vs. Electron Transfer Pathways. *Acta. Chemica. Scandinavica* **1987**, *B41*, 367-378.
(34) APEX2 Version 2014.11-0, Bruker AXS, Inc.; Madison, WI 2014.
(35) SAINT Version 8.34a, Bruker AXS, Inc.; Madison, WI 2013.
(36) Sheldrick, G. M. SADABS, Version 2014/5, Bruker AXS, Inc.; Madison, WI 2014.
(37) Sheldrick, G. M. SHELXTL, Version 2014/7, Bruker AXS, Inc.; Madison, WI 2014

(38) International Tables for Crystallography 1992, Vol. C., Dordrecht: Kluwer Academic Publishers.
(39) Spek, A. L. SQUEEZE, Acta Cryst. 2015, C71, 9-19.
(40) Spek, A. L. PLATON, Acta. Cryst. 2009, D65, 148-155.

Chapter 8

In Pursuit of a Rare $S = 2$ Co^{III} Supported by P=O Ligands

Introduction

Since its initial design, much is now known about the tripodal $[poat]^{3-}$ ligand.[1-7] We have learned that its phosphinic amido N–donors provide a comparably strong ligand field as the ureate framework ($[H_3buea]^{3-}$),[6,8] and one that is much stronger than the analogous sulfonamido-based ligands ($[RST]^{3-}$).[9-11] As a result, metal ions up to an oxidation state of +4 have so far been accessed within the trianionic framework.[3,5] The enforced C_3 symmetry promotes a high-spin electron configuration,[12] which is an important parameter to model for bioinspired synthetic complexes, as many Fe and Mn sites in proteins are high spin, and electronic structure is often correlated with reactivity.[13-15] The phosphinic amido arms can perform three functions: 1) they can serve as H–bond acceptors to stabilize exogenous $X–H_n$ (X = O, N) ligands;[6-8,16] 2) they can bind a second metal ion/adduct;[5,6] 3) the N-position can provide a site for intramolecular proton transfer. During the studies described in Chapters 5 – 7, it was found that the P=O groups can stabilize M^{III} centers (M = Fe, Mn); efforts to access M^{IV} in the auxiliary binding site to the P=O groups are ongoing (Chapter 7). What is less known but equally important is the ligand field strength of the metal center supported by the P=O groups. The bimetallic complexes discussed thus far in this dissertation are not prone to demetallation under ambient conditions, which suggests the P=O ligands are not easily displaced. Additional insights into the electronic structure, electrochemical properties, and steric factors of these phosphinic amido P=O groups will be valuable in the development and electronic/structural manipulations of bi- and multi-metallic complexes.

While phosphinic amido groups are a relatively new class of ligands,[17,18] other phosphine oxide and related ligands are studied in the literature, which give us a preliminary impression of these

P=O donating groups.[19-21] Two examples are highlighted here. Kläui developed a unique organometallic ligand $[CpCo^{III}\{P(O)RR'\}_3]^-$ ligand (commonly known as the Kläui ligand and abbreviated as $(L_{R,R'})^-$; R, R' = alkyl, aryl, alkoxyl) that can support both sandwich- and piano-stool type complexes, and has been used extensively in various fields, from catalysis to bioimaging (Figure 8.1.A).[22-25] One unique feature of this ligand is its ability to bind through the P=O groups to metal ions of different sizes, including Group 1/2/13 metals, 3/4/5*d* transition metals, and 4/5*f* rare earth metals. In addition, a recent report also demonstrated that the Kläui ligand can support technetium complexes in seven oxidation states.[23] These results highlight the adaptability of the P=O groups to support both hard and soft metal centers. A series of $[Co^{III}(L_{R,R'})_2]^+$ complexes were investigated for their spin-crossover properties, demonstrating the ability of a six-coordinated Co^{III} center to access a spin state of 2.[26,27] Nearly all six-coordinated Co^{III} complexes/clusters are diamagnetic, due to significant ligand field stabilization for a d^6 ion;[28,29] notable exceptions include $[Co^{III}F_6]^{3-}$ and $[Co^{III}F_3(OH_2)_3]$.[29,30] Kläui therefore labels the P=O-based scaffolds as weak field ligands within the spectrochemical series, in spite of their strongly donating nature. This is attributed to the strong π–donation from the P=O groups, which display similar characteristics as F^- ions.[22] Cummins also utilized a tridentate trimetaphosphate ($[P_3O_9]^{3-}$) ligand to study non-aqueous redox-flow batteries,

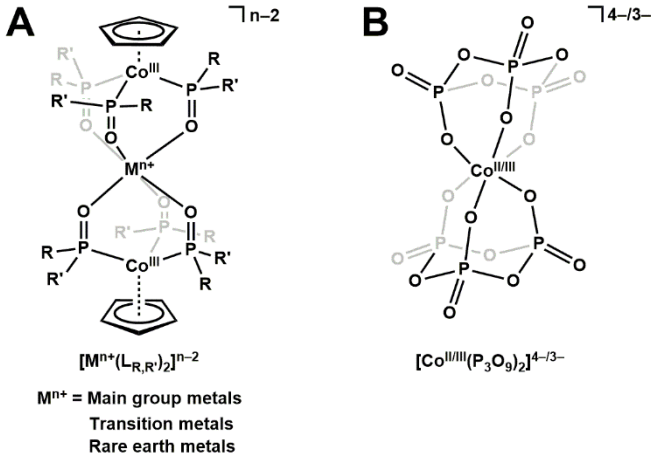

Figure 8.1. (A) A generic Kläui metal complex, in which M^{n+} is supported by the two equivalents of the ligand $[L_{R,R'}]^- = [CpCo^{III}\{P(O)R'R''\}_3]^-$ (R, R' = alkyl, aryl, alkoxyl). (B) $[Co^{II/III}(P_3O_9)_2]^{4-/3-}$ complexes developed by Cummins.

and discovered the $[Co^{III}(P_3O_9)_2]^{3-}$ species (Figure 8.1.B) exhibits similar spin-crossover behavior as the Co complexes with the Kläui ligand,[31] supporting the notion that these strongly π–donating P=O ligands are "weak and hard".[22]

In this chapter, I sought to test this premise by binding a Co ion/adduct to the P=O groups in $[M^{III}poat(O(H))]$ complexes. An unexpected $S = 2$ Co^{III} center was detected, and the electronic and structural factors behind the preference of the unusual spin state is systematically probed using electronic absorption, magnetic, and vibrational spectroscopies, and structural characterization methods.

Results & Discussion

Initial discovery of an S = 2 Co^{III}. In a similar preparative route for $[(TMTACN)TM^{II}–(\mu\text{-}O)–Fe^{IV}poat]^+$ (TM = Zn, Cu, Ni) as described in Chapter 4, treatment of $[Fe^{IV}poat(O)]^-$ with equimolar $Co^{II}(OAc)_2{\cdot}4H_2O$ (Scheme 8.1) showed growth of new absorbance features at λ_{max} = 325, 365 (sh), 445 (sh), 625, and ~ 1100 nm (Figure 8.2.A, black). The near–IR feature at λ_{max} ~1100 nm was new and is uncommonly low in energy for a non-heme Fe^{IV}–oxido system.[32] Perpendicular(⊥)–mode X-band EPR spectroscopy revealed a new anisotropic g ~ 2 signal at 3.6 K (Figure 8.2.B), with a partially-resolved 8-line hyperfine pattern due to the ^{59}Co nucleus (I = 7/2); minor high-spin ferric impurities were also observed. S-band EPR spectroscopy was performed in collaboration with Prof. Michael Hendrich's group (Carnegie Mellon University) on the putative [FeCo] species at 30 K,

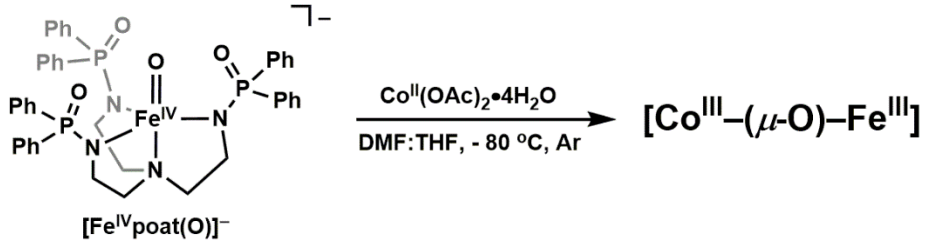

Scheme 8.1. Binding of Co^{II} ion to $[Fe^{IV}poat(O)]^-$ produces $[Co^{III}–(\mu\text{-}O)–Fe^{III}]$.

where a higher resolution spectrum was obtained that showed an 8-line hyperfine pattern centered around g = 1.98 (A = 240 MHz, Figure 8.2.C). Both X- and S-band EPR results suggest this species has an S = 1/2 spin ground state, and that only one Co nucleus is involved.

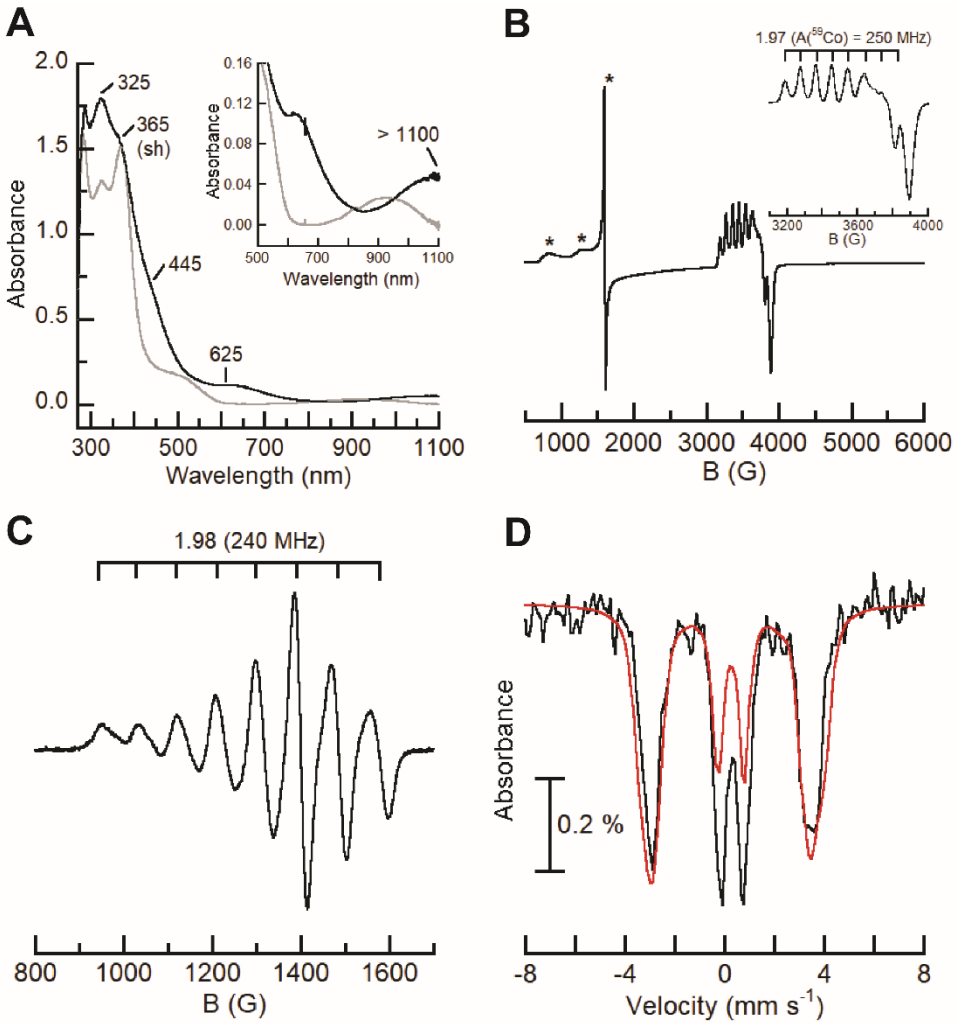

Figure 8.2. (A) UV-vis spectral changes before (grey) and after (black) the addition of $Co^{II}(OAc)_2 \cdot 4H_2O$ to $[Fe^{IV}poat(O)]^-$. Inset: low energy region. (B) ⊥–mode X-band EPR spectrum (collected at 3.6 K) of [Co^{III}–(μ-O)–Fe^{III}]. Inset: high field region. Asterisk (*) indicates minor ferric impurity. (C) ⊥–mode S-band EPR spectrum (collected at 30 K) of [Co^{III}–(μ-O)–Fe^{III}]. (D) Mössbauer spectrum (collected at 4.2 K) of [Co^{III}–(μ-O)–Fe^{III}] (black). Simulation of the Mössbauer spectrum is in red.

A four-line Mössbauer spectrum was observed at 4.2 K (Figure 8.2.D, black); simulation of the spectrum yielded isomer shift (δ) of 0.26 mm s^{-1} and quadrupole splitting (ΔE_Q) of 0.10 mm s^{-1} (red). It should be noted the spectrum contains at least one other unidentified minority species (< 35 %). Variable temperature and field Mössbauer measurements determined the ^{57}Fe A tensor to be

[–17.6, –17.6, –17.6] T: the isotropic A tensor is indicative of an Fe center with a highly symmetric electronic structure, i.e. all five d–orbitals are half-filled, which is consistent with a high-spin Fe^{III} center (S = 5/2). The large δ is also consistent with the iron being reduced to Fe^{III}, and therefore the cobalt center would be oxidized to the 3+ level. Since the [FeCo] species generated was an S = 1/2 system, it is reasoned the S = 5/2 Fe^{III} center is antiferromagnetically coupled to a high-spin Co^{III} center (S = 2), a rare spin configuration; some examples include the aforementioned $[Co^{III}F_6]^{3-}$ and Kläui Co complexes.[26,27,29,30] In addition, Rittle has recently reported a high-spin mononuclear Co^{III} complex supported by a P=N based ligand, albeit in a different geometry.[33] Therefore, it is conceivable the Co ion can adopt a high-spin configuration upon binding to this system at the +3 oxidation level. One–electron reduction of a high valent metal–oxido moiety upon binding of a Lewis acidic metal ion has been reported, so the reduction of the Fe^{IV} center and the oxidation to Co^{III} were not surprising.[34-37] These experimental results suggest the species formed to be an [Co^{III}–(μ-O)–Fe^{III}] system.

Preparation and Properties of [(TMTACN)Co^{II}–(μ–OH)–Fe^{III}poat]OTf. While the generation of [Co^{III}–(μ–O)–Fe^{III}] species provided intriguing results, efforts turned towards installing Co^{II} adducts containing a capping ligand to ensure the assembly of discrete heterobimetallic complexes. [(TMTACN)Co^{II}–(μ-OH)–Fe^{III}poat]OTf (denoted [Co^{II}(OH)Fe^{III}poat]OTf) was prepared (Scheme 8.2) using the method described for [(TMTACN)Ni^{II}–(μ-OH)–Fe^{III}poat]OTf (Chapter 3).[6] As in the case with Ni^{II}, attempts to synthesize and isolate [Co^{II}(TMTACN)$(OTf)_2$] in high purity have been unsuccessful, which led to this salt being generated *in situ* by mixing equimolar of $Co^{II}(OTf)_2$•$2CH_3CN$ and TMTACN in CH_2Cl_2. After multiple rounds of recrystallization in mixtures of CH_2Cl_2/Et_2O and CH_2Cl_2/hexane, the [Co^{II}(OH)Fe^{III}poat]OTf salt can be obtained as orange crystals suitable for single crystal X–ray diffraction and other analytical methods. The complex

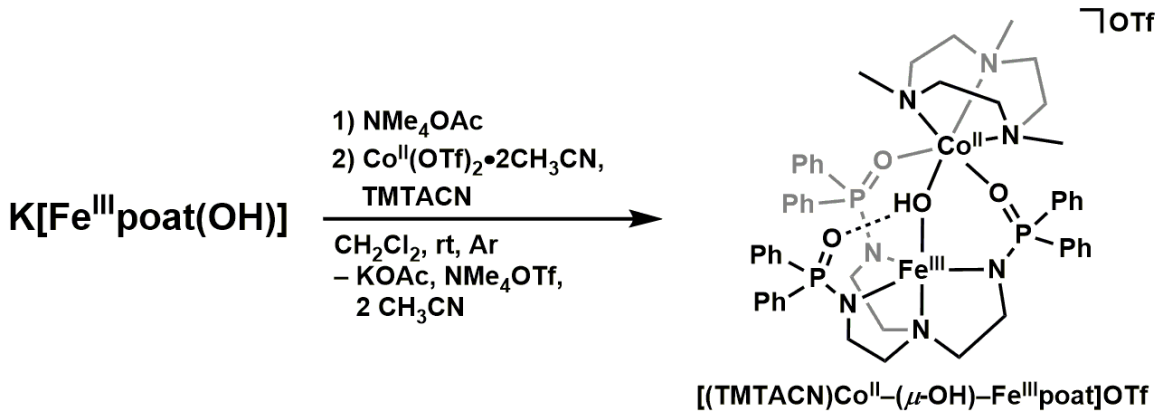

Scheme 8.2. Preparative route to $[Co^{II}(OH)Fe^{III}poat]^+$.

exhibits optical features at λ_{max} (ε, M^{-1} cm^{-1}) = 315 (sh), 372 (5300), and 460 nm (sh), which are similar to other $[M^{II}(OH)Fe^{III}poat]^+$ complexes described in Chapters 3, 5, and 7 (Figure 8.3.A).[6] The ⊥–mode EPR spectrum for this complex is silent, which suggests an integer-spin system (Figure 8.3.B). Indeed, a two-line ^{57}Fe Mössbauer spectrum was observed with isomer shift (δ)/quadrupole splitting (ΔE_Q) values of 0.34/0.73 mm s^{-1}, which are consistent with an S = 5/2 Fe^{III} that is part of an integer-spin system (Figure 8.3.C). This complex most likely has a ground state of S = 1, which contains an S = 5/2 Fe^{III} center antiferromagnetically coupled to S = 3/2 Co^{II}; further variable field/temperature magnetic measurements are required to confirm this assignment. Finally, the

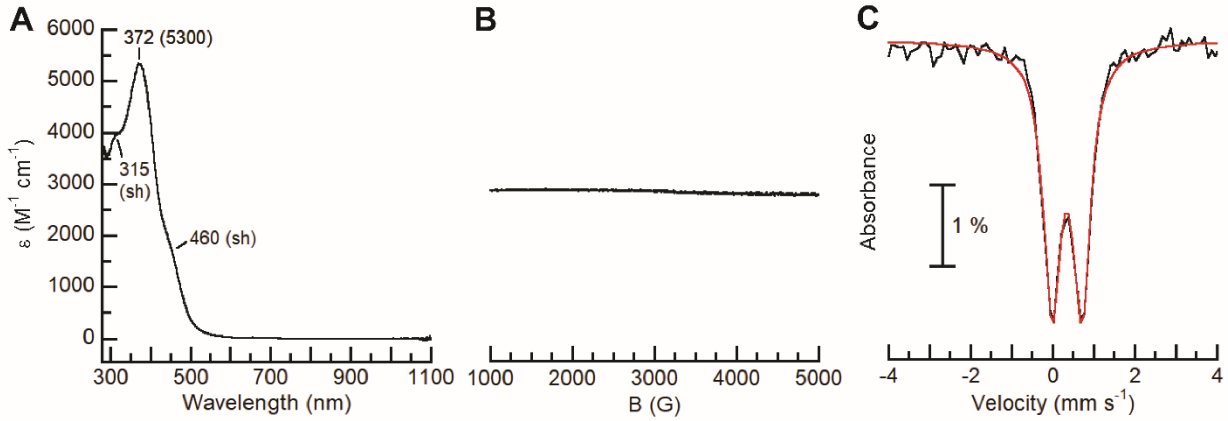

Figure 8.3. (A) Electronic absorbance spectrum for $[Co^{II}(OH)Fe^{III}poat]^+$ (0.10 mM CH_2Cl_2 solution at room temperature). (B) ⊥–mode X-band EPR spectrum (collected at 77 K) of $[Co^{II}(OH)Fe^{III}poat]^+$. (C) Mössbauer spectrum (black, collected at 4.2 K) of $[Co^{II}(OH)Fe^{III}poat]^+$. Simulation of the Mössbauer spectrum is in red.

vibrational spectrum of this complex revealed a weak feature at 3138 cm^{-1} that is assigned to the ν(O–H) band (Figure 8.4, black).

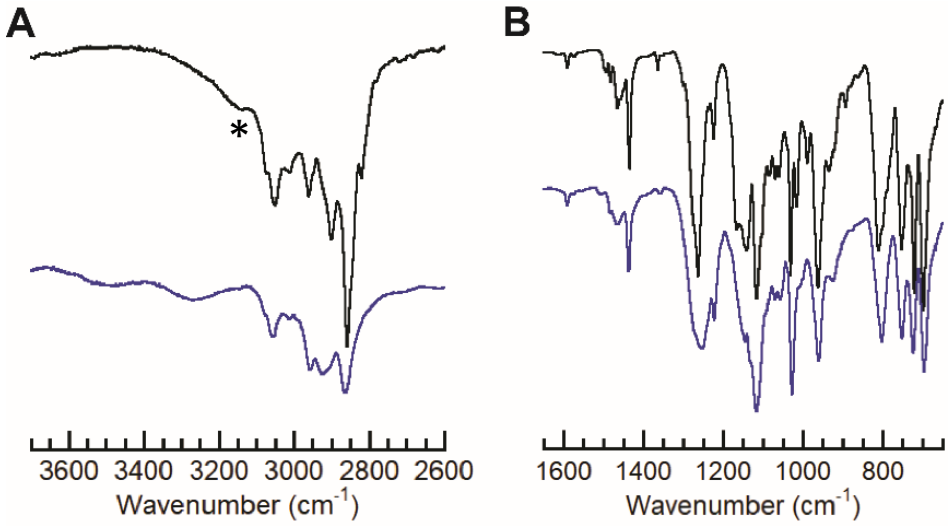

Figure 8.4. FTIR spectra for $[Co^{II}(OH)Fe^{III}poat]^{+}$ (black) and $[Co^{III}(OH)Fe^{III}poat]^{2+}$ (blue). The high (A) and low (B) energy regions are shown separately for clarity. Asterisk (*) indicates ν(O–H).

The molecular structure of $[Co^{II}(OH)Fe^{III}poat]^{+}$ was determined by X-ray diffraction (XRD), which reveals a bimetallic core containing a 5-coordinated Fe^{III} and a 6-coordinated Co^{III} centers, bridged by a hydroxido ligand forming an intramolecular H–bond to a phosphinic amido arm (Figure 8.5.A, Table 8.1). The overall structure is comparable with those for the other first-row TM analogs (Chapters 3, 5, 7).[6] The metrical parameters of the Co center are highlighted in the following sections since the emphasis of this chapter is on its redox properties and ligand field modulation. The Co1–O1 bond distance is 1.993(2) Å, while the other Co1–O/N bond lengths range between 2.100(2) – 2.200(3) Å. Co1 is displaced by 1.437 Å from the plane that contains the three TMTACN nitrogen atoms, and is 3.414(1) Å away from Fe1. These parameters are consistent with a M^{II}–(μ-OH)–M^{III} core.

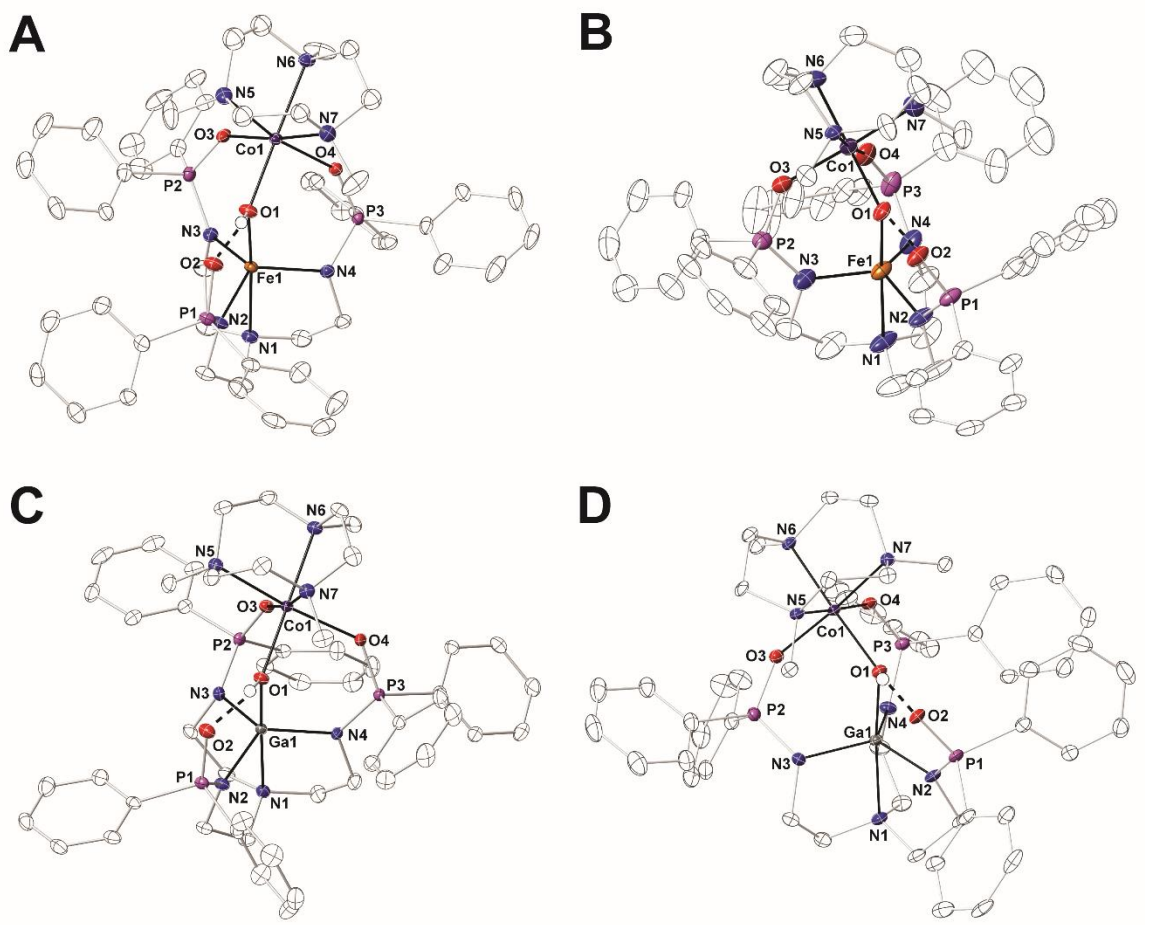

Figure 8.5. Thermal ellipsoid diagrams depicting the molecular structures of (A) $[Co^{II}(OH)Fe^{III}poat]^{+}$, (B) $[Co^{III}(OH)Fe^{III}poat]^{2+}$ (preliminary), (C) $[Co^{II}(OH)Ga^{III}poat]^{+}$, and (D) $[Co^{III}(OH)Ga^{III}poat]^{2+}$ determined by X-ray diffraction. Ellipsoids are shown at the 50% probability level, and only the hydroxido H atoms are shown for clarity.

The electrochemical properties of $[Co^{II}(OH)Fe^{III}poat]^{+}$ were investigated using cyclic voltammetry (Figure 8.6.A). The complex exhibited a reversible one-electron redox event at –1.65 V, which is assigned to the $Co^{II}Fe^{III}/Co^{II}Fe^{II}$ process. An additional anodic process at +0.68 V and cathodic process at –0.36 V were also observed; further measurements revealed the reduction at –0.36 V is not present without accessing the oxidation at +0.68 V, and they are thus assigned to the $Co^{III}Fe^{III}/Co^{II}Fe^{III}$ couple. The difference in current intensity and the large peak-to-peak separation (ΔE = 1.04 V) suggest the redox event is irreversible, and that a large structural change might take place upon oxidation of $[Co^{II}(OH)Fe^{III}poat]^{+}$. This is unsurprising, as the oxidation of $[Fe^{II}(OH)Fe^{III}poat]^{+}$ (Chapter 5), $[Fe^{II}(OH)Mn^{III}poat]^{+}$ (Chapter 6), and $[Mn^{II}(OH)Fe^{III}poat]^{+}$

Table 8.1. Selected bond lengths/distances (Å) and angles (°) for $[Co^{III/II}(OH)M^{III}poat]^{2+/+}$ complexes (M = Fe, Ga).

Complex	$[Co^{II}(OH)Fe^{III}poat]^{+}$	$[Co^{III}(OH)Fe^{III}poat]^{2+}$	$[Co^{II}(OH)Ga^{III}poat]^{+}$	$[Co^{III}(OH)Ga^{III}poat]^{2+}$
		Bond Lengths/Distances (Å)		
M1–N1	2.236(2)	2.196	2.266(3)	2.208(2)
M1–N2	2.014(2)	1.995	1.965(3)	1.950(2)
M1–N3	2.011(2)	1.988	1.953(3)	1.944(2)
M1–N4	2.011(2)	1.985	1.962(3)	1.937(2)
M1–O1	1.890(2)	1.927	1.881(2)	1.920(2)
O1···O2	2.657(3)	2.566	2.638(3)	2.631(3)
Co1–O1	1.993(2)	1.883	1.974(2)	1.889(2)
Co1–O3	2.100(2)	1.975	2.138(2)	1.954(2)
Co1–O4	2.121(2)	1.949	2.127(2)	1.979(2)
Co1–N5	2.200(3)	1.974	2.211(3)	1.981(2)
Co1–N6	2.169(2)	1.985	2.145(3)	1.982(2)
Co1–N7	2.190(3)	1.983	2.209(3)	1.984(2)
M1···Co1	3.414(1)	3.388	3.406(1)	3.387(1)
av M1–N_{eq}	2.012(2)	1.989	1.960(3)	1.944(2)
av Co1–N_{TMTACN}	2.186(3)	1.981	2.188(3)	1.982(2)
d[M1–N_{eq}]	0.345	0.322	0.310	0.248
d[Co1–N_{TMTACN}]	1.437	1.206	1.439	1.210
		Angles (°)		
O1–M1–N1	175.26(9)	174.99	178.31(11)	175.32(9)
N2–M1–N3	119.24(10)	120.27	112.07(11)	120.85(10)
N3–M1–N4	110.95(10)	108.50	118.59(11)	109.84(11)
N2–M1–N4	121.11(10)	123.42	121.96(11)	124.46(11)
M1–O1–Co1	123.06(11)	125.55	124.09(13)	125.61(11)
O3–Co1–O4	91.82(8)	90.85	89.32(9)	89.75(8)
N5–Co1–N6	81.20(9)	87.21	81.81(10)	87.24(10)
N5–Co1–N7	81.06(10)	86.14	80.33(11)	86.15(10)
N6–Co1–N7	82.20(10)	86.94	82.01(10)	86.54(10)
		Calculated Values		
τ_5[a]	0.903	0.860	0.939	0.848

[a]Trigonality structural parameter, $\tau_5 = (\beta - \alpha)/60^{o}$. β is the largest bond angle observed, and α is the second largest bond angle observed.

(Chapter 7) at room temperature all undergo significant structural changes and produce the corresponding $[(M')^{III}(O)(M)^{III}Hpoat]^{2+}$ species.

Isolation and characterization of [(TMTACN)Co^{III}–(μ-OH)–Fe^{III}poat](OTf)$_2$. Oxidation of $[Co^{II}(OH)Fe^{III}poat]^{+}$ can be achieved using silver triflate (AgOTf, $E_{1/2}$ = +0.65 V vs $[FeCp_2]^{+/0}$) or *para*-bromo amminium radical ($[N(p\text{-}C_6H_4Br)_3]PF_6$, $E_{1/2}$ = +0.70 V vs $[FeCp_2]^{+/0}$) in CH_2Cl_2 (Scheme

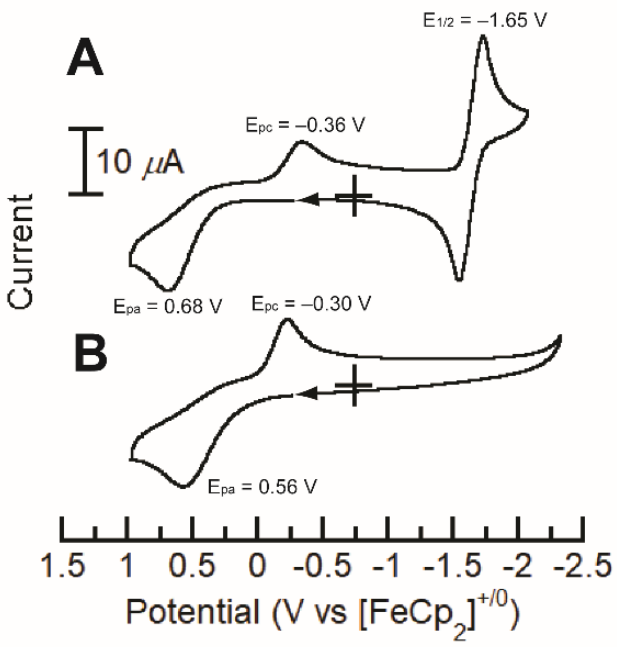

Figure 8.6. Cyclic voltammograms of (A) $[Co^{II}(OH)Fe^{III}poat]^+$, and (B) $[Co^{II}(OH)Ga^{III}poat]^+$ collected at 100 mV s^{-1} in CH_2Cl_2.

8.3).[38] The optical spectrum (Figure 8.7.A) for this new species exhibited features at λ_{max} (ε, M^{-1} cm^{-1}) = 370 (6600), 490 (sh), and 595 nm (sh). The product using either oxidant yielded identical ⊥–mode EPR spectra in CH_2Cl_2 that contains a rhombic S = 5/2 signal with features at g = 9.33, 4.84, and 4.01 (Figure 8.7.B). In addition, EPR measurements performed in a glassy solvent (PrCN) exhibited a very similar S = 5/2 spectrum as the well-characterized $[(TMTACN)Zn^{II}–(\mu\text{-}OH)–Fe^{III}poat]^+$ (Chapter 3) and $[(TMTACN)Mg^{II}–(\mu\text{-}OH)–Fe^{III}poat]^+$ (Figure 8.7.C), suggesting their molecular structures are comparable.[6,39] Additionally, the ^{57}Fe Mössbauer spectrum exhibited a six-line pattern, which is commonly observed for mononuclear S = 5/2 Fe^{III} centers ($\delta/\Delta E_Q$ = 0.32/–0.20 mm s^{-1},

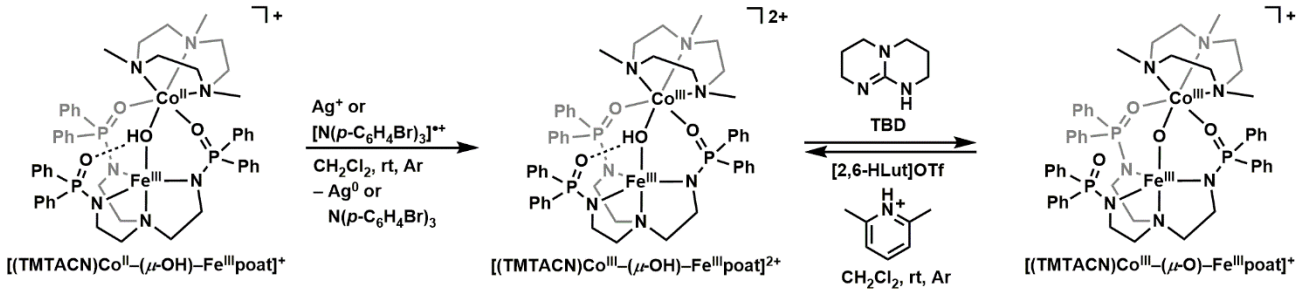

Scheme 8.3. A series of FeCo bimetallic complexes in different oxidation and protonation states.

Figure 8.7.D). These EPR and Mössbauer results raise concerns that the Co center may dissociate upon oxidation. While an ν(O–H) band at 3138 cm^{-1} was observed for $[Co^{II}(OH)Fe^{III}poat]^{+}$, two unidentified vibrational features at 3486 and 3266 cm^{-1} were observed in the FTIR spectrum of the new compound (Figure 8.4, blue): these features may represent O–H or N–H stretches, but this is inconsistent with our past observations of $M^{n+}X–H$ (X = O, N) vibrations shifting towards lower energy upon oxidation.[7,8]

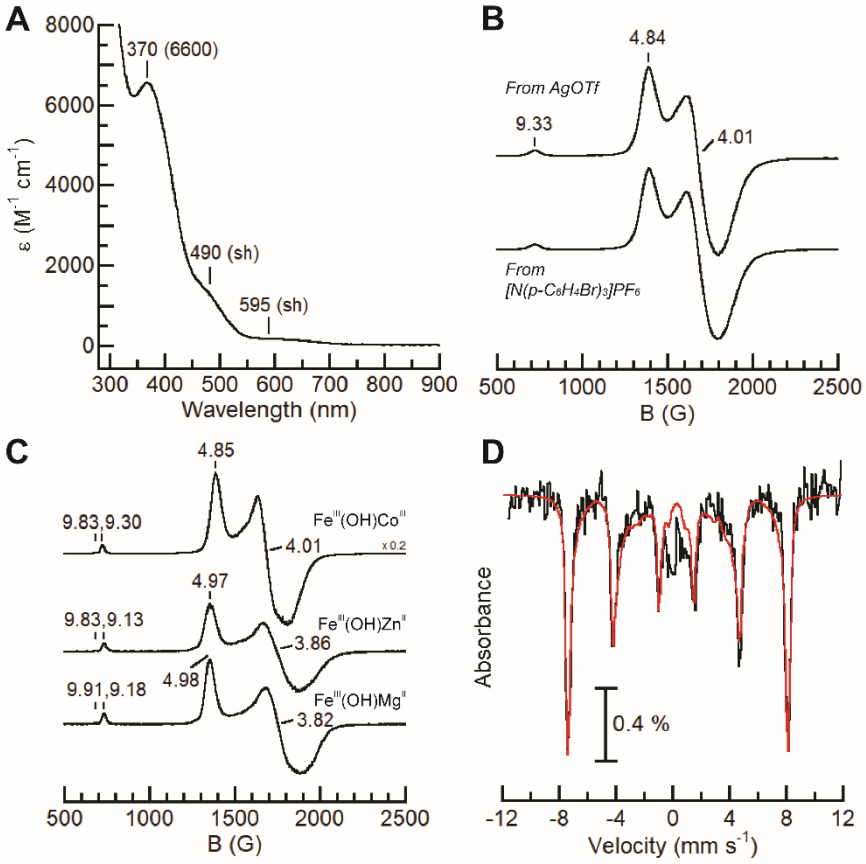

Figure 8.7. (A) Electronic absorbance spectra of $[Co^{III}(OH)Fe^{III}poat]^{2+}$ (0.10 mM CH_2Cl_2 solution at room temperature). (B) ⊥–mode X-band EPR spectra (collected at 77 K, CH_2Cl_2) of $[Co^{III}(OH)Fe^{III}poat]^{2+}$, generated as an isolated product using AgOTf (top), and *in situ* by chemical oxidation using $[N(p\text{-}C_6H_4Br)_3]PF_6$ (bottom). (C) ⊥–mode X-band EPR spectra (collected at 77 K) of $[Co^{III}(OH)Fe^{III}poat]^{2+}$ (top, PrCN, 29 mM), $[Zn^{II}(OH)Fe^{III}poat]^{+}$ (middle, 1:1 CH_2Cl_2:THF, 5 mM), and $[Mg^{II}(OH)Fe^{III}poat]^{+}$ (bottom, 1:1 CH_2Cl_2:THF, 5 mM). (D) Mössbauer spectrum (black, collected at 4.2 K) of $[Co^{III}(OH)Fe^{III}poat]^{2+}$. Simulation of the Mössbauer spectrum is in red.

XRD measurement revealed the molecular structure of $[(TMTACN)Co^{III}–(\mu\text{-}OH)–Fe^{III}poat]^{2+}$ (denoted $[Co^{III}(OH)Fe^{III}poat]^{2+}$; Figure 8.5.B; Table 8.1), which contained a $Co^{III}–(\mu$-

OH)–Fe^{III} core!!! The Fe and Co centers retain their 5- and 6-coordinate environments, respectively, and the bridging hydroxido ligand remains H–bonded to the phosphinic amido group. The O1•••O2 distance contracts by nearly 0.1 Å upon oxidation of $[Co^{II}(OH)Fe^{III}poat]^{+}$ to $[Co^{III}(OH)Fe^{III}poat]^{2+}$, which is indicative of a stronger intramolecular H–bond. Upon oxidation, all the bonds around the Co center contract: the Co1–O1 bond distance decreases to 1.883 Å, while the other Co1–O/N bond lengths range between 1.949 – 1.985 Å. In addition, the bond angles around Co1 are all approximately 90° (ranging 86.14 to 95.01 °). The geometry of the Co center is thus best described as octahedral. Co1 is displaced by only 1.206 Å from the plane that contains the three TMTACN nitrogen atoms (1.437 Å in $[Co^{II}(OH)Fe^{III}poat]^{+}$), due to the shortened Co1–N_{TMTACN} distances. The Fe1•••Co1 distance slightly contracts from 3.414 to 3.388 Å upon oxidation, which is consistent with a $(M')^{III}$–(μ-OH)–$(M)^{III}$ core.[ref] The molecular structure of $[Co^{III}(OH)Fe^{III}poat]^{2+}$ provides the first crystallographic example of a μ–OH bridged bimetallic complex with both metal ions in the +3 oxidation state, supported by the unsymmetric poat/TMTACN framework.

Together, the structural and spectroscopic studies of $[Co^{III}(OH)Fe^{III}poat]^{2+}$ provide greater insight into the properties of this bimetallic system. Upon oxidation, the previously high-spin Co center (S = 3/2 Co^{II}) now adopts a low-spin configuration (S = 0 Co^{III}). This is not unexpected, as most report six-coordinated Co^{III} centers are diamagnetic due to significant ligand–field stabilization for a d^6 ion.[28-30] As a result, the Mössbauer spectrum resembles that of a mononuclear S = 5/2 Fe^{III} species in the absence of spin–exchange coupling between multiple paramagnetic centers. The EPR spectra for $[Co^{III}(OH)Fe^{III}poat]^{2+}$, $[Zn^{II}(OH)Fe^{III}poat]^{+}$, and $[Mg^{II}(OH)Fe^{III}poat]^{+}$ are nearly identical, as Co^{III}, Zn^{II}, and Mg^{II} all serve as closed-shell Lewis acidic metal adducts.[6,39]

Several issues remain in question with this oxidative process. First, the oxidation to $[Co^{III}(OH)Fe^{III}poat]^{2+}$ was irreversible by cyclic voltammetry; however, there was little geometric changes within the bimetallic core between the two redox levels. Similar cyclic voltammograms have

been observed for Co bimetallic and multimetallic complexes which, like $[Co^{III/II}(OH)Fe^{III}poat]^{2+/+}$, did not exhibit significant geometric changes in the oxidation process.[40,41] Second, unlike the FeFe, MnFe, and FeMn analogs, in which the $[(M')^{III}(OH)(M)^{III}poat]^{2+}$ species rapidly rearrange to $[(M')^{III}(O)(M)^{III}Hpoat]^{2+}$ (Chapters 5, 6, 7), $[Co^{III}(OH)Fe^{III}poat]^{2+}$ is stable indefinitely at room temperature, and similar proton movement to the phosphinic amido arm has not been observed. Low-spin Co^{III} is more Lewis acidic than high-spin Fe^{III}/Mn^{III} due to a smaller ionic radius (0.545 vs 0.645 Å),[42] so the Co^{III}–(*μ*-OH)–Fe^{III} core should be the most Brönsted acidic out of the series of complexes, and facile intramolecular proton transfer to the ligand is expected. Finally, the $S = 0$ Co^{III} spin state in $[Co^{III}(OH)Fe^{III}poat]^{2+}$ is inconsistent with the $S = 2$ Co^{III} spin state observed in [Co^{III}–(*μ*-O)–Fe^{III}] generated by binding of $Co^{II}(OAc)_2$•$4H_2O$ to $[Fe^{IV}poat(O)]^-$ (Scheme 8.1). While it is recognized the two species have different bridging moieties (hydroxido versus oxido) which may cause the divergence in electronic structures, it also suggests the bridging ligand may be an important factor in modulating the spin state of the Co center.

Deprotonation of [(TMTACN)Co^{III}–(μ-OH)–Fe^{III}poat]$^{2+}$. To better model the magnetic properties of [Co^{III}–(*μ*-O)–Fe^{III}], $[Co^{III}(OH)Fe^{III}poat]^{2+}$ was treated with the organic base 1,5,7-triazabicyclo[4.4.0]dec-5-ene (TBD, Scheme 8.3), and new optical features at λ_{max} (ε, M^{-1} cm^{-1}) = 330 (9000), 370 (sh), 475 (sh), 795 (1000), and > 1100 nm were observed (Figure 8.8.A); these features are similar to those found for [Co^{III}–(*μ*-O)–Fe^{III}] (Figure 8.2.A). Addition of 2,6-lutidinium triflate ([2,6-HLut]OTf) regenerated most of the features that are attributed to $[Co^{III}(OH)Fe^{III}poat]^{2+}$ (> 80 %), suggesting this (de)protonation process is mostly reversible (Scheme 8.3, Figure 8.8.B). The addition of base was also followed by ⊥–mode X-band EPR spectroscopy, which revealed an anisotropic $g \sim 2$ signal with a partially-resolved 8-line hyperfine pattern ($I(^{59}Co) = 7/2$, Figure 8.8.C) in quantitative yield, similar to that for [Co^{III}–(*μ*-O)–Fe^{III}] (Figure 8.2.B). The $S = 1/2$ spin state can

arise from antiferromagnetic coupling between an $S = 5/2$ Fe^{III} and $S = 2$ Co^{III} centers. S-band EPR measurements were also performed on this species, and accurate g- and $A(^{59}Co)$ tensor values were experimentally verified by simulation of spectra obtained at different microwave frequencies (Figure 8.8.D). Notably, the spin-dipolar component (A^{SD}) of the $A(^{59}Co)$ tensor was determined to be [55, 38, –92] MHz, which is at an approximately (+1:+1:–2) ratio. While hyperfine constants have not been reported for Co^{III} complexes (due to their tendency to be diamagnetic), A^{SD} is a common spectroscopic handle to determine the spin states of Fe complexes;[43-45] in particular, an $A^{SD}(^{57}Fe)$

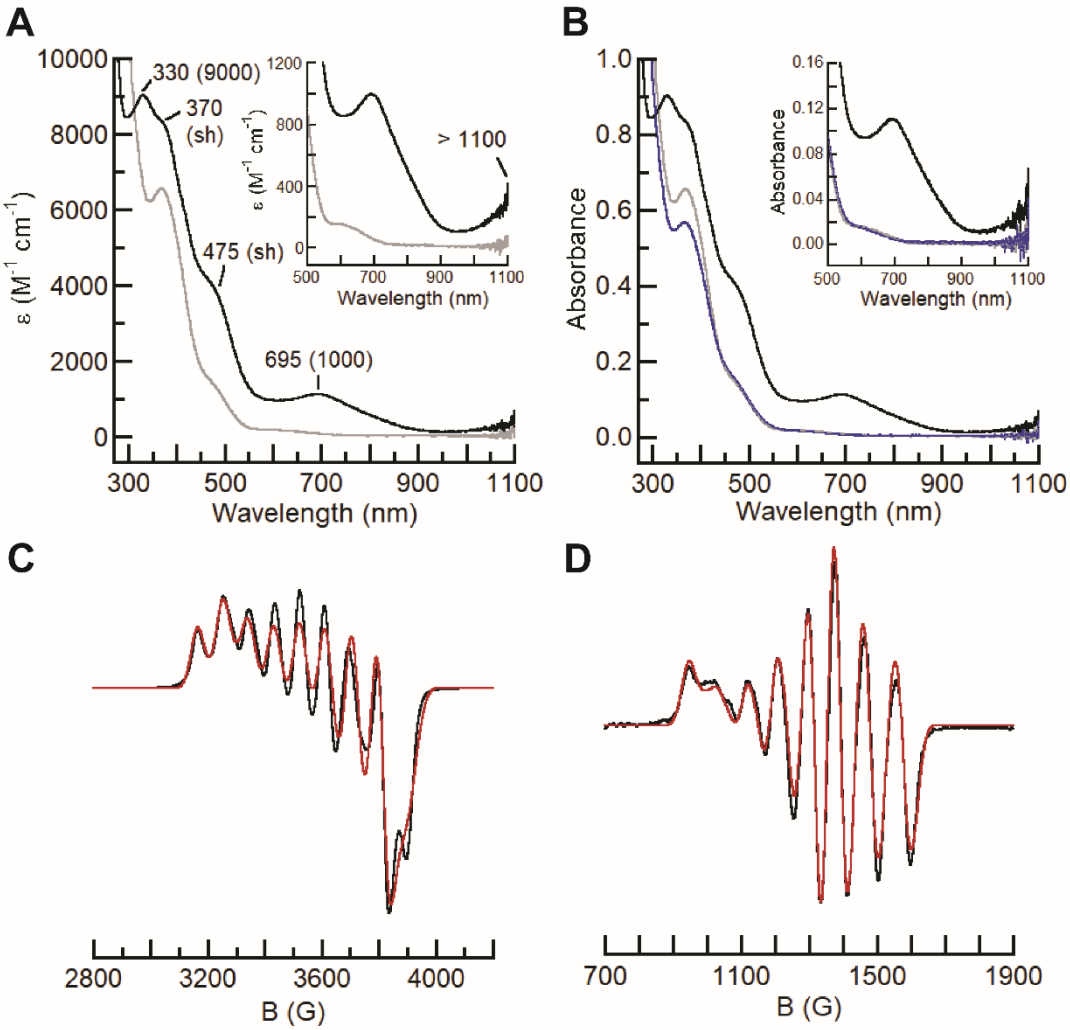

Figure 8.8. (A) Electronic absorbance spectra for the deprotonation to $[Co^{III}(O)Fe^{III}poat]^+$, before (grey) and after (black) the addition of TBD (0.10 mM CH_2Cl_2 solution at room temperature). (B) Electronic absorbance spectra for the reversible deprotonation of $[Co^{III}(OH)Fe^{III}poat]^{2+}$, before (grey), and after the addition of TBD (black), then the addition of [2,6-HLut]OTf (blue, 0.10 mM CH_2Cl_2 solution at room temperature). (C) ⊥–mode X-band and (D) S-band EPR spectra (black, collected at 17.4 and 20 K, respectively; CH_2Cl_2) of $[Co^{III}(O)Fe^{III}poat]^+$ after the addition of TBD. Simulated spectra are in red.

with a ratio of (+1:+1:–2) is indicative of an $S = 2$ spin state. For instance, the $S = 2$ $[Fe^{IV}poat(O)]^-$ species exhibits an $A^{SD}(^{57}Fe)$ of [+4, +4, –8] T.[5] It is therefore reasoned this new species contains an $S = 2$ Co^{III} center, and is formulated as $[(TMTACN)Co^{III}–(\mu\text{-}O)–Fe^{III}poat]^+$ (denoted $[Co^{III}(O)Fe^{III}poat]^+$). Efforts to characterize this complex by XRD and Mössbauer spectroscopy are ongoing.

The mechanism behind the spin state change at the Co center between $[Co^{III}(OH)Fe^{III}poat]^{2+}$ ($S_{Co} = 0$) and $[Co^{III}(O)Fe^{III}poat]^+$ ($S_{Co} = 2$) is still under investigation. The bridging ligand clearly has a dominant effect on the electronic properties of the Co center: an oxido ligand provides a stronger field than a hydroxido ligand in the spectrochemical series,[46-47] yet the Co^{III} center supported by a bridging oxido ligand adopts a high-spin configuration. It is worth noting the P=O ligands in $[poat]^{3-}$ can support a high-spin Co^{III}, similar to Kläui's, Cummins', and Rittle's complexes discussed above.[26,27,31,33] However, additional structural and vibrational characterizations of the three $Fe^{III}Co^{III}$ complexes are necessary to elucidate the factors behind the spin state change. If the bridging ligand and the spin exchange are crucial in modulating the Co ligand field, this premise can be tested by systematically replacing the paramagnetic Fe^{III} center with a diamagnetic metal ion of similar charge, Lewis acidity, and ionic radius, thus removing the spin coupling interaction.[48] The most suitable candidate is Ga^{III}, which was coordinated by the $[poat]^{3-}$ framework in Chapter 2 to understand the electrochemical properties of $[Fe^{III}poat(OH)]^-$.

Preparation and Properties of [(TMTACN)Co^{II}–(μ-OH)–Ga^{III}poat]OTf. The $Ga^{III}Co^{II}$ analog, $[(TMTACN)Co^{II}–(\mu\text{-}OH)–Ga^{III}poat]OTf$ (denoted $[Co^{II}(OH)Ga^{III}poat]OTf$), was prepared using a similar method described for $[Co^{II}(OH)Fe^{III}poat]OTf$ (Scheme 8.4). After multiple rounds of recrystallization in mixtures of CH_2Cl_2/Et_2O and CH_2Cl_2/hexane, the $[Co^{II}(OH)Ga^{III}poat]OTf$ salt can be obtained as pale pink crystals suitable for single crystal X–ray diffraction and other analytical

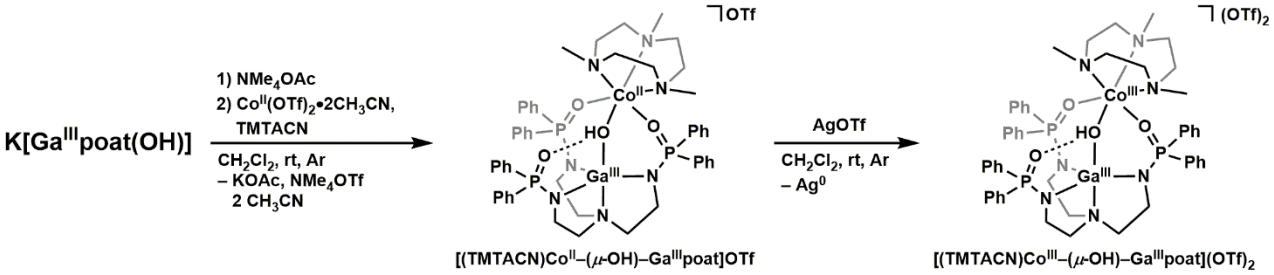

Scheme 8.4. Preparative routes of $[Co^{II}(OH)Ga^{III}poat]^{+}$ and $[Co^{III}(OH)Ga^{III}poat]^{2+}$.

methods. The complex exhibits optical features at λ_{max} (ε, M^{-1} cm^{-1}) = 478 (15), 485 (15), 555 (sh), ~1050 nm (Figure 8.9.A); the low extinction coefficients are consistent with spin- and Laporte-forbidden d–d transitions for a Co^{II} ion.[31,49-51] ⊥–mode X-band EPR spectrum of this complex exhibited features indicative of an S = 3/2 system, with g–values of 7.28 ($A(^{59}Co)$ = 883 MHz), 2.67, and 1.91 (Figure 8.9.B). The eight-line hyperfine pattern of the low field feature supports a single Co^{II} nucleus (Figure 8.9.C); it is worth noting the hyperfine value is unusually large for a high-spin Co^{II} complexes.[50,52] The vibrational spectrum of this complex revealed a feature at 3207 cm^{-1} that is assigned to the ν(O–H) band (Figure 8.10, black). The feature is sharper and at a higher energy than that for $[Co^{II}(OH)Fe^{III}poat]^{+}$ (Figure 8.4.A), indicating a weaker intramolecular H–bond. Finally, the molecular structure of $[Co^{II}(OH)Ga^{III}poat]^{+}$ was determined by XRD (Figure 8.5.C, Table 8.1), and the metrical parameters around the Co center are nearly identical to those of $[Co^{II}(OH)Fe^{III}poat]^{+}$.

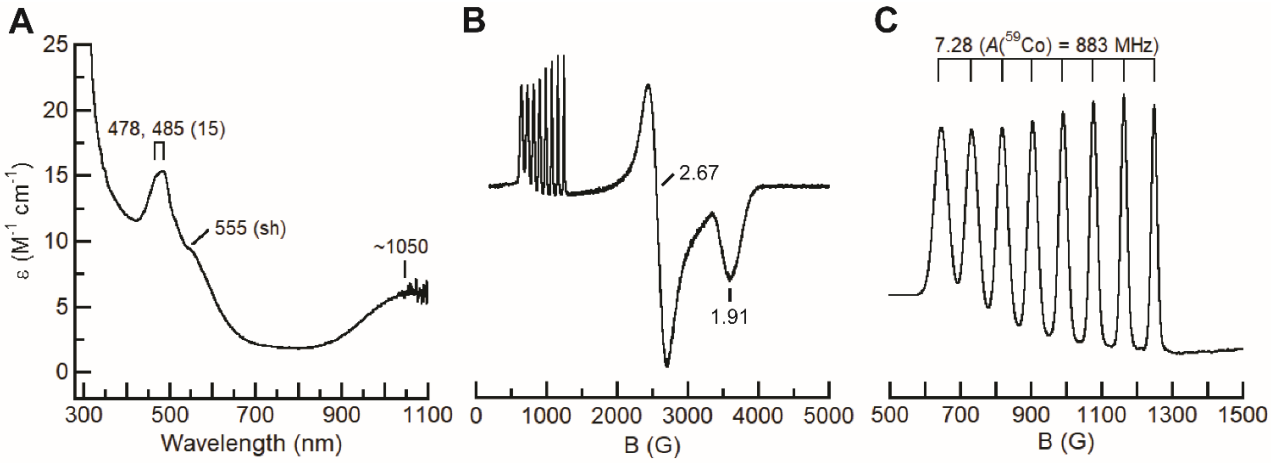

Figure 8.9. (A) Electronic absorbance spectrum for $[Co^{II}(OH)Ga^{III}poat]^{+}$ (12.3 mM CH_2Cl_2 solution at room temperature). (B) ⊥–mode X-band EPR spectrum (collected at 5 K, 5 mM, CH_2Cl_2) of $[Co^{II}(OH)Ga^{III}poat]^{+}$. (C) The low field region zoomed in from panel (B).

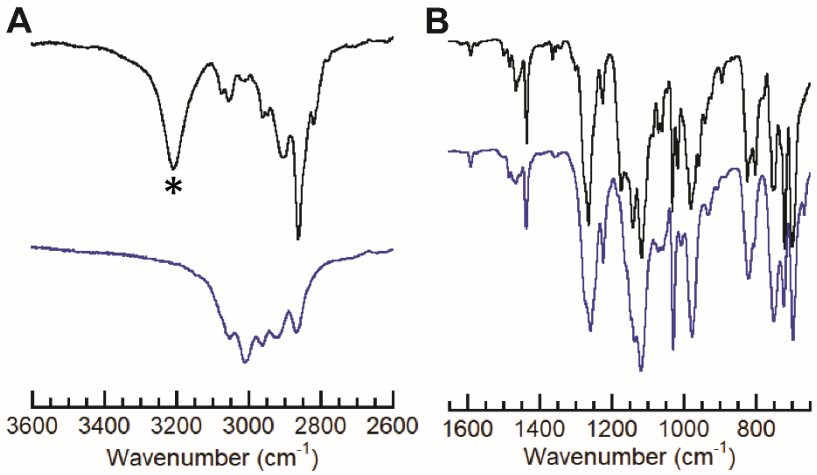

Figure 8.10. FTIR spectra for $[Co^{II}(OH)Ga^{III}poat]^{+}$ (black) and $[Co^{III}(OH)Ga^{III}poat]^{2+}$ (blue). The high (A) and low (B) energy regions are illustrated separately for clarity. Asterisk (*) indicates ν(O–H).

The electrochemical properties of $[Co^{II}(OH)Ga^{III}poat]^{+}$ were investigated using cyclic voltammetry (Figure 8.6B). The complex exhibited an anodic process at +0.56 V and cathodic process at –0.30 V; Similar to those found for $[Co^{II}(OH)Fe^{III}poat]^{+}$, the reduction at –0.30 V is not present without accessing the oxidation at +0.56 V, which support the assignment of the $Co^{III}Ga^{III}/Co^{II}Ga^{III}$ process. Despite the electrochemical irreversibility of this process, the structure of the oxidized analog is expected to be remained largely unaffected and retains a Co–(μ-OH)–Ga core based on studies of the Co–(μ-OH)–Fe analogue.

Isolation and preparation of [(TMTACN)Co^{III}–(μ-OH)–Ga^{III}poat](OTf)$_2$. Oxidation of $[Co^{II}(OH)Ga^{III}poat]^{+}$ can be achieved using AgOTf (Scheme 8.4). The optical spectrum (Figure 8.11.A) for this new species, $[(TMTACN)Co^{III}–(\mu\text{-}OH)–Ga^{III}poat]^{2+}$ (denoted $[Co^{III}(OH)Ga^{III}poat]^{2+}$), exhibited features at λ_{max} = 415 (sh) and 605 (110). The isolated product exhibited a silent ⊥–mode EPR spectrum (Figure 8.11.B). Since the Co^{III} center is expected to adopt a low spin configuration upon oxidation (as is the case in $[Co^{III}(OH)Fe^{III}poat]^{2+}$), the new species should be diamagnetic. Indeed, the oxidized complex exhibited a diamagnetic ^{1}H–NMR spectrum,

and nearly all 64 protons in $[Co^{III}(OH)Ga^{III}poat]^{2+}$ are accounted for (~ 62 H). Finally, the absence of a *ν*(O–H) band in the solid-state vibrational spectrum suggests a strong intramolecular H–bond between the bridging hydroxido ligand and the phosphinic amido P=O group (Figure 8.10, blue); this is different from what was observed for $[Co^{III}(OH)Fe^{III}poat]^{2+}$, which exhibits two unidentified vibrations between 3200 – 3500 cm^{-1} (Figure 8.4.A).

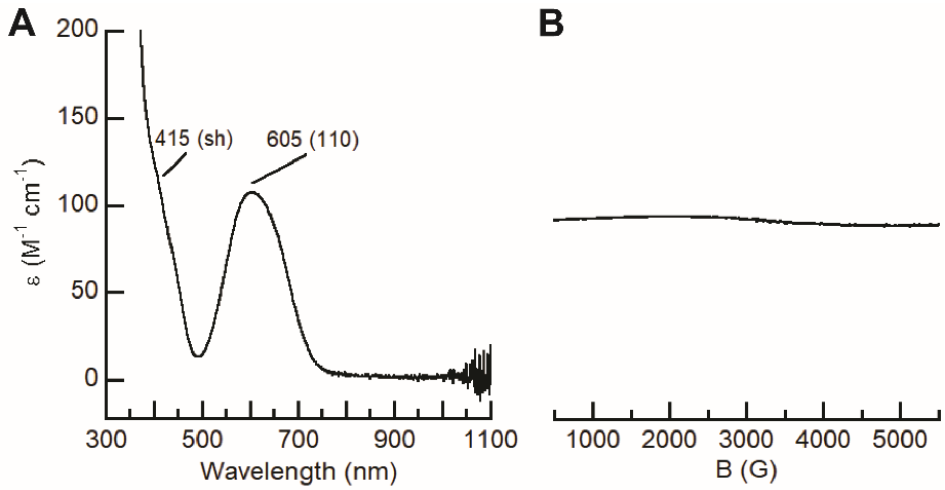

Figure 8.11. (A) Electronic absorbance spectrum for $[Co^{III}(OH)Ga^{III}poat]^{2+}$ (1.0 mM DMF solution at room temperature). (B) ⊥–mode X-band EPR spectrum (collected at 77 K) of $[Co^{III}(OH)Ga^{III}poat]^{2+}$.

The molecular structure of $[Co^{III}(OH)Ga^{III}poat]^{2+}$ reveals a Co–(*μ*-OH)–Ga core similar to that of $[Co^{III}(OH)Fe^{III}poat]^{2+}$ (Figure 8.5.D, Table 8.1). Upon oxidation, the Co1–O_{poat}/N_{TMTACN} bonds contracted by greater than 0.1 Å, suggesting a low-spin configuration for the Co center. Other structural parameters are also nearly identical to those for $[Co^{III}(OH)Fe^{III}poat]^{2+}$. Overall, $[Co^{III}(OH)Ga^{III}poat]^{2+}$ serves as an excellent structural analog for $[Co^{III}(OH)Fe^{III}poat]^{2+}$. Its diamagnetic nature may allow us to distinguish the effect of spin exchange interactions between paramagnetic metal centers from the ligand field supported by P=O ligands.

$[Co^{III}(OH)Fe^{III}poat]^{2+}$ reacts with organic bases such as TBD and $NaN(SiMe_3)_2$, but the identity of the inorganic product is not yet known. Successful generation of $[Co^{III}(O)Ga^{III}poat]^{+}$ may reveal the effects of the bridging oxido versus hydroxido ligand on the ligand field of the Co^{III} ion in

the absence of spin-exchange coupling, which in turn can provide insight into the electronic structures of the $Co^{III}(O(H))Fe^{III}$ complexes.

Conclusion & Outlook

In this chapter, the unexpected finding of a $S = 2$ Co^{III} center in the bimetallic species, [Co^{III}–(μ-O)–Fe^{III}], was discussed. This is an intriguing discovery, since most mono- and multinuclear Co^{III} complexes adopt a closed shell configuration. However, the ligand environment for the Co center in [Co^{III}–(μ-O)–Fe^{III}] is not well-defined, so the scaffold is redesigned to introduce a TMTACN capping ligand to complete the coordination sphere for the Co site and produce discrete bimetallic [(TMTACN)Co^{n+}–(μ–O(H))–Fe^{III}poat]$^{m+}$ complexes. While the Co center is diamagnetic in [Co^{III}(OH)Fe^{III}poat]$^{2+}$, it becomes $S = 2$ upon deprotonation to [Co^{III}(O)Fe^{III}poat]$^{+}$. Two hypotheses have been proposed for the spin state change: 1) the P=O ligands, which have been described as "strongly donating but weak field" in similar synthetic systems, can support high-spin metal centers; 2) the bridging ligand between the Fe and Co sites may modulate or determine the spin configuration of the Co center. Additional structural, spectroscopic, and theoretical studies are necessary to identify the factor(s) that control the spin state of the metal centers. In an attempt to delineate the effect of spin exchange interactions, the Fe site was replaced by the diamagnetic Ga^{III} ion, and the complexes [Co^{II}(OH)Ga^{III}poat]$^{+}$ and [Co^{III}(OH)Ga^{III}poat]$^{2+}$ were developed. Experiments to deprotonate the latter are ongoing, with a focus on interrogating the electron properties of the Co site in the absence of spin-coupled bimetallic system. New information regarding the electronic structure, electrochemical properties, and steric factors provided by these phosphinic amido P=O groups will be invaluable in the future development of bi- and multi-metallic complexes.

Experimental

General Procedures. Organic syntheses, unless otherwise noted, did not require the use of an inert atmosphere. All inorganic syntheses and manipulations were performed under an argon atmosphere in a Vacuum Atmosphere Co. dry box. Solvents were sparged with argon and purified using a JC Meyer Co. solvent purification system with columns containing Q-5 and molecular sieves. All reagents, unless otherwise noted, were purchased from commercial sources and used as received. Tetrabutylammonium hexafluorophosphate (TBAP) was recrystallized from hot EtOH. The syntheses of K[Fe^{III}poat(OH)] and K[Ga^{III}poat(OH)] were described in Chapter 2.[3,6] H_3poat,[5] K[Fe^{II}poat],[5,7] IBX-iPr,[52,53] TMTACN,[54,55] [N(*p*-$C_6H_4Br)_3$]PF_6,[56,57] and [2,6-HLut]OTf[58] were synthesized according to literature procedures.

Physical Methods. Room temperature UV-vis spectra were collected on a Cary 50 or 60 UV-vis spectrophotometer in a 1 cm quartz cuvette; low temperature spectra were collected on an Agilent UV-vis spectrophotometer equipped with a Unisoku Unispeks cryostat. Solid-state Fourier transform infrared (FTIR) spectra were collected on a Thermo Scientific Nicolet iS5 FT-IR spectrometer equipped with an iD5 ATR accessory. Cyclic voltammetry experiments were conducted using a CHI600G electrochemical analyzer. A 2.0 mm glassy carbon electrode was used as the working electrode at scan velocities between 0.01 and 0.5 $V \cdot s^{-1}$. A ferrocenium/ferrocene ($[FeCp_2]^{+/0}$) standard was used as an internal reference to monitor the reference electrode (Ag^+/Ag). TBAP was used as the supporting electrolyte at a concentration of 0.1 M. Elemental analyses were performed on a Perkin-Elmer 2400 Series II CHNS elemental analyzer. ^{1}H–NMR spectra was collected on a Bruker CRYO500 spectrometer (500 MHz). X-band (microwave frequencies 9.28, 9.43 and 9.62 GHz) and S-band (3.50 MHz) EPR spectra were collected on a Bruker EMX spectrometer equipped with an ER041XG microwave bridge, an Oxford Instrument liquid He

quartz cryostat, and a dual-mode (ER4116DM) or perpendicular-mode (ER4119HS-W1) cavity. Mössbauer spectra were recorded using a Janis Research Super-Varitemp cryostat. Isomer shifts are reported relative to Fe metal at 298 K. SpinCount was used to fit the experimental EPR and Mössbauer data.[59]

Generation of [Co^{III}–(μ-O)–Fe^{III}]. In a typical UV-vis experiment, a 20 mM stock solution of K[Fe^{II}poat] (0.0168 g, 0.0200 mmol, 1.0 eq) and 18-crown-6 (0.0106 g, 0.0401 mmol, 2.0 eq) was prepared in 1 mL of DMF:THF (1:1) in a dry box, and 30 μL of the stock solution was added to 3 mL DMF:THF (1:1) in a 1 cm quartz cuvette with a stir bar inside. The cuvette was sealed with a rubber septum and brought out of the box. The cuvette was then placed in the Agilent UV-vis spectrophotometer equipped with a cryostat, and was allowed to cool at –60 °C for at least 15 minutes. IBX-iPr (0.20 mg, 0.61 μmol) and $Co^{II}(OAc)_2 \cdot 4H_2O$ (0.15 mg, 0.60 μmol) were added via a gas-tight syringe sequentially, resulting in a final FeCo complex concentration of 0.20 mM. In a typical EPR experiment, a 30 mM stock solution of IBX-iPr was prepared in 1:1 DMF:THF mixture in a dry box. 150 μL of the stock solution (1.5 mg, 4.5 μmol) was added to a quartz EPR tube via a syringe, which was sealed with a rubber septum. The tube was brought out of the box, and was allowed to cool in a dry ice/acetone bath at –78 °C for at least 15 minutes. 80 μL of a solution of K[Fe^{II}poat] (3.0 mg, 3.6 μmol) and 18-crown-6 (1.9 mg, 7.2 μmol) was added via a gas-tight syringe to generate [Fe^{IV}poat(O)]$^-$. $Co^{II}(OAc)_2 \cdot 4H_2O$ (0.90 mg, 3.6 μmol) were added via a gas-tight syringe (40 μL). When the reaction was complete, the tube was taken out of the cold bath, wiped clean, and quickly frozen in liquid nitrogen. The final Fe concentration was 13 mM. In a typical Mössbauer experiment, a 72 mM stock solution of IBX-iPr was prepared in 3:1 DMF:THF mixture in a dry box. 167 μL of the stock solution (3.9 mg, 0.012 mmol) was added to a Mössbauer solution sample cup, which was allowed to cool in a cold well at –70 °C for at least 15 minutes. 167 μL of a pre-chilled mixture of

K[Fe^{II}poat] (8.4 mg, 0.010 mmol) and 18-crown-6 (5.3 mg, 0.020 mmol) was added via a syringe to generate [Fe^{IV}poat(O)]$^-$. $Co^{II}(OAc)_2 \cdot 4H_2O$ (2.7 mg, 0.011 mmol) was then added via a syringe (167 μL). After 5 minutes, the Mössbauer solution sample cup was slowly frozen in liquid nitrogen. The final natural abundance Fe concentration was 20 mM (~ 0.40 mM ^{57}Fe). EPR (X-band, ⊥–mode, DMF:THF, 3.6 K): g = 1.97 (A(^{59}Co) = 250 MHz). UV-vis λ_{max}(DMF:THF)/nm: 325, 365, 445, 625, > 1100. Mössbauer (DMF:THF, 4.2 K): δ = 0.26 mm s^{-1}, ΔE_Q = 0.10 mm s^{-1}.

Synthesis of [(TMTACN)Co^{II}–(μ-OH)–Fe^{III}poat]OTf. This salt was prepared using the method described for [(TMTACN)Ni^{II}–(μ-OH)–Fe^{III}poat]OTf (Chapter 3) with the following modifications:[6] K[Fe^{III}poat(OH)] (161.0 mg, 0.1882 mmol), NMe_4OAc (28.0 mg, 0.210 mmol), 3 mL CH_2Cl_2. $Co^{II}(OTf)_2 \cdot 2CH_3CN$ (82.8 mg, 0.189 mmol) and TMTACN (37.0 μL, 32.7 mg, 0.191 mmol) were pre-mixed for 1 h before using. Orange crystals (50 **– 60** % yield) suitable for X–ray diffraction were grown from a concentrated CH_2Cl_2 solution layered with pentane or hexane. Elemental analysis calcd for [(TMTACN)Co^{II}–(μ-OH)–Fe^{III}poat]OTf·0.5C_5H_{12}, $C_{52}H_{64}CoF_3FeN_7O_7P_3S \cdot 0.5C_5H_{12}$; C, 53.13; H, 5.73; N, 7.96%, found: C, 53.06; H, 5.46; N, 8.05%. FTIR (diamond ATR, cm^{-1}): 3138 (br, OH), 3072, 3050, 3009, 2960, 2899, 2859, 2819, 1590, 1495, 1483, 1465, 1436, 1363, 1264, 1225, 1165, 1140, 1116, 1085, 1069, 1061, 1032, 1016, 988, 961, 933, 894, 810, 752, 720, 697, 636. UV-vis λ_{max}(CH_2Cl_2)/nm (ε/M^{-1}cm^{-1}): 315 (sh), 372 (5300), 460 (sh). $E_{1/2}$ (CH_2Cl_2, V versus $[FeCp_2]^{+/0}$): –1.65; E_{pa} 0.68 ; E_{pc} = –0.36. Mössbauer (PrCN, 4.2 K): δ = 0.34 mm s^{-1}, ΔE_Q = 0.73 mm s^{-1}.

Synthesis of [(TMTACN)Co^{III}–(μ-OH)–Fe^{III}poat](OTf)$_2$. [Co^{II}(OH)Fe^{III}poat]OTf (0.0429 g, 0.0359 mmol) and AgOTf (0.0135 g, 0.0525 mmol) were stirred in 2 mL CH_2Cl_2 at room temperature, and the dark orange solution turned to dark brown over an 1 hour period. The mixture was then filtered through a fine porosity glass fritted funnel packed with a pad of celite to remove Ag^0 and excess

AgOTf. The CH_2Cl_2 solution was layered under pentane to yield dark brown residue (70 – 80 %). Yellow crystals suitable for X-ray diffraction were grown from Et_2O diffusing into a concentrated CH_3CN solution at room temperature. $[Co^{III}(OH)Fe^{III}poat]^{2+}$ can also be synthesized using $[N(p\text{-}C_6H_4Br)_3]PF_6$ as an oxidant. FTIR (diamond ATR, cm^{-1}): 3486, 3266, 3055, 3010, 2957, 2921, 2862, 1590, 1503, 1464, 1437, 1363, 1253, 1223, 1136, 1116, 1069, 1058, 1028, 959, 924, 802, 750, 723, 696. EPR (X-band, ⊥–mode, PrCN, 77 K): g = 9.83, 9.30, 4.85, 4.01. UV-vis $\lambda_{max}(CH_2Cl_2)$/nm ($\varepsilon/M^{-1}cm^{-1}$): 370 (6600), 490 (sh), 595 (sh). Mössbauer (PrCN, 4.2 K): δ = 0.32 mm s^{-1}, ΔE_Q = –0.20 mm s^{-1}.

Generation of [(TMTACN)Co^{III}–(μ-O)–Fe^{III}poat]$^+$. $[Co^{III}(O)Fe^{III}poat]^+$ can be generated by either deprotonation of $[Co^{III}(OH)Fe^{III}poat]^{2+}$, or sequential oxidation/deprotonation of $[Co^{II}(OH)Fe^{III}poat]^+$. In a typical UV-vis experiment, a 10 mM stock solution of $[Co^{III}(OH)Fe^{III}poat](OTf)_2$ was prepared in 1 mL of CH_2Cl_2 in a dry box, and 30 μL of the stock solution (0.40 mg, 0.30 μmol) was added to 3 mL CH_2Cl_2 in a 1 cm quartz cuvette with a stir bar inside. The cuvette was sealed with a rubber septum and brought out of the box. After the measurement of the initial spectrum, TBD (0.10 mg, 0.75 μmol) was added via a gas-tight syringe sequentially, resulting in a final FeCo complex concentration of 0.10 mM. In a typical EPR experiment, a 100 μL solution of $[N(p\text{-}C_6H_4Br)_3]PF_6$ (1.3 mg, 2.0 μmol) was added to $[Co^{II}(OH)Fe^{III}poat]OTf$ (2.4 mg, 2.0 μmol, 200 μL). A 100 μL solution of TBD (0.28 mg, 2.0 μmol) was then added to the mixture. 200 μL of the reaction mixture was transferred to a quartz EPR tube via a syringe. The tube was brought out of the box, and quickly frozen in liquid nitrogen. The final concentration was 5 mM. EPR (X-band, ⊥–mode, CH_2Cl_2, 17.4 K): $g_{x,y,z}$ = [1.978, 1.905, 1.862]; A_{iso} = –130 MHz; $A^{SD}(^{59}Co)$ = [+55, +38, –92] MHz). UV-vis $\lambda_{max}(CH_2Cl_2)$/nm ($\varepsilon/M^{-1}cm^{-1}$): 330 (9000), 370 (sh), 475 (sh), 695 (1000), > 1100.

Synthesis of [(TMTACN)Co^{II}–(μ-OH)–Ga^{III}poat]OTf. This salt was prepared using the method described for [Co^{II}(OH)Fe^{III}poat]OTf with the following modifications: K[Ga^{III}poat(OH)] (98.5 mg, 0.106 mmol), NMe_4OAc (24.1 mg, 0.181 mmol), 3 mL CH_2Cl_2. Co^{II}(OTf)$_2$·2CH_3CN (46.5 mg, 0.106 mmol) and TMTACN (21.0 μL, 18.6 mg, 0.108 mmol) were pre-mixed for 1 h before using. Pale pink crystals (40 – 50% yield) suitable for X–ray diffraction were grown from a concentrated CH_2Cl_2 solution layered with hexane. Elemental analysis calcd for [(TMTACN)Co^{II}–(μ-OH)–Ga^{III}poat]OTf·CH_2Cl_2, $C_{52}H_{64}CoF_3GaN_7O_7P_3S·CH_2Cl_2$; C, 49.17; H, 5.14; N, 7.57%, found: C, 48.85; H, 5.14; N, 7.57%. FTIR (diamond ATR, cm^{-1}): 3207 (OH), 3073, 3056, 3010, 2962, 2947, 2900, 2862, 2819, 1590, 1572, 1499, 1483, 1465, 1435, 1364, 1292, 1264, 1225, 1173, 1142, 1117, 1086, 1069, 1061, 1038, 1032, 1017, 980, 957, 940, 925, 895, 823, 801, 780, 753, 747, 720, 699. EPR (X-band, ⊥–mode, CH_2Cl_2:THF, 5 K): g = 7.28 (A(^{59}Co) = 883 MHz), 2.67, 1.91. UV-vis $\lambda_{max}(CH_2Cl_2)$/nm (ε/M^{-1}cm^{-1}): 478 (15), 485 (15), 555 (sh), ~1050. E_{pa} (CH_2Cl_2, V versus [$FeCp_2$]$^{+/0}$): 0.56; E_{pc} = –0.30.

Synthesis of [(TMTACN)Co^{III}–(μ-OH)–Ga^{III}poat](OTf)$_2$. [Co^{II}(OH)Ga^{III}poat]OTf (49.0 mg, 0.0405 mmol) and AgOTf (0.0135 g, 0.0525 mmol) were stirred in 3 mL CH_2Cl_2 at room temperature, and the solution turned to turquoise over an 1 hour period. The mixture was then filtered through a fine porosity glass fritted funnel packed with a pad of celite to remove Ag^0 and excess AgOTf. The CH_2Cl_2 solution was layered under pentane to yield a blue residue (75 – 85 %). Sky blue needle-like crystals suitable for X–ray diffraction were grown from Et_2O diffusing into a concentrated CH_3CN solution. Elemental analysis calcd for [(TMTACN)Co^{III}–(μ-OH)–Ga^{III}poat](OTf)$_2$, $C_{53}H_{64}CoF_6GaN_7O_{10}P_3S_2$; C, 46.85; H, 4.75; N, 7.22%, found: C, 46.68; H, 4.80; N, 6.88%. FTIR (diamond ATR, cm^{-1}): 3056, 3008, 2962, 2919, 2868, 1590, 1572, 1491, 1483, 1465, 1435, 1355,

1257, 1224, 1126, 1117, 1063, 1061, 1032, 1007, 980, 930, 906, 885, 819, 805, 750, 725, 699, 666. UV-vis λ_{max}(DMF)/nm ($\varepsilon/M^{-1}cm^{-1}$): 415 (sh), 605 (110). ^{1}H–NMR (500 MHz, CD_2Cl_2) δ 8.20 (1H, q, 7.3 Hz), 7.72 (4H, m), 7.53-7.64 (17H, m), 7.44 (4H, dt), 7.30 (4H, dt), 7.23 (1H, s), 3.28-3.35 (2H, m), 3.07-3.20 (7H, m), 3.02 (3H, s), 2.78 (2H, t, 5.6 Hz), 2.49-2.68 (11H, m), 2.36 (3H, m), 2.01 (3H, m).

Crystallography.

[(TMTACN)Co^{II}–(μ-OH)–Fe^{III}poat]OTf. An orange crystal of approximate dimensions 0.224 x 0.319 x 0.355 mm was mounted on a glass fiber and transferred to a Bruker SMART APEX II diffractometer system. The APEX2[60] program package was used to determine the unit-cell parameters and for data collection (10 sec/frame scan time). The raw frame data was processed using SAINT[61] and SADABS[62] to yield the reflection data file. Subsequent calculations were carried out using the SHELXTL[63] program package. The diffraction symmetry was 2/*m* and the systematic absences were consistent with the monoclinic space group *Pn* that was later determined to be correct.

The structure was solved by direct methods and refined on F^2 by full-matrix least-squares techniques. The analytical scattering factors[64] for neutral atoms were used throughout the analysis. Hydrogen atoms were either located from a difference-Fourier map and refined (x,y,z and U_{iso}) or were included using a riding model. Disordered atoms were included using multiple components with partial site-occupancy-factors. There was one molecule of dichloromethane solvent present.

Least-squares analysis yielded wR2 = 0.0812 and Goof = 1.039 for 773 variables refined against 18258 data (0.68 Å), R1 = 0.0348 for those 16395 data with $I > 2.0\sigma(I)$. The structure was refined as an inversion twin and the Flack[65] parameter was 0.012(9).

[(TMTACN)Co^{II}–(μ-OH)–Ga^{III}poat]OTf. A colorless crystal of approximate dimensions 0.196 x 0.253 x 0.308 mm was mounted in a cryoloop and transferred to a Bruker SMART APEX II diffractometer system. The APEX2[60] program package was used to determine the unit-cell parameters and for data collection (30 sec/frame scan time). The raw frame data was processed using SAINT[61] and SADABS[62] to yield the reflection data file. Subsequent calculations were carried out using the SHELXTL[63] program package. The diffraction symmetry was 2/*m* and the systematic absences were consistent with the monoclinic space group *Pn* that was later determined to be correct.

The structure was solved by direct methods and refined on F^2 by full-matrix least-squares techniques. The analytical scattering factors[64] for neutral atoms were used throughout the analysis. Hydrogen atoms were either located from a difference-Fourier map and refined (x,y,z and U_{iso}) or were included using a riding model. There was one molecule of dichloromethane solvent present.

Least-squares analysis yielded wR2 = 0.0787 and Goof = 1.042 for 711 variables refined against 17436 data (0.70 Å), R1 = 0.0365 for those 15533 data with $I > 2.0\sigma(I)$. The structure was refined as an inversion twin and the Flack[65] parameter was 0.013(7).

[(TMTACN)Co^{III}–(μ-OH)–Ga^{III}poat](OTf)$_2$. A blue crystal of approximate dimensions 0.111 x 0.255 x 0.340 mm was mounted in a cryoloop and transferred to a Bruker SMART APEX II diffractometer system. The APEX2[60] program package was used to determine the unit-cell parameters and for data collection (30 sec/frame scan time). The raw frame data was processed using SAINT[61] and SADABS[62] to yield the reflection data file. Subsequent calculations were carried out using the SHELXTL[63] program package. The diffraction symmetry was 2/*m* and the systematic absences were consistent with the monoclinic space group $P2_1/c$ that was later determined to be correct.

The structure was solved by direct methods and refined on F^2 by full-matrix least-squares techniques. The analytical scattering factors[64] for neutral atoms were used throughout the analysis. Hydrogen atom H(1) was located from a difference-Fourier map and refined (x,y,z and U_{iso}) with d(O-H) = 0.85Å. The remaining hydrogen atoms were included using a riding model. There was one molecule of acetonitrile solvent present. Several atoms were disordered and included using multiple components with partial site-occupancy-factors. Displacement constraints were employed for several disordered atoms.

Least-squares analysis yielded wR2 = 0.1199 and Goof = 1.031 for 845 variables refined against 13445 data (0.78 Å), R1 = 0.0472 for those 11002 data with I > 2.0σ(I).

Table 8.2. Crystallographic data for [(TMTACN)Co^{II}–(μ-OH)–M^{III}poat]OTf and [(TMTACN)Co^{III}–(μ-OH)–M^{III}poat](OTf)$_2$ complexes (M = Fe, Ga).

	[(TMTACN)Co^{II}–(μ-OH)–Fe^{III}poat]OTf	[(TMTACN)Co^{II}–(μ-OH)–Ga^{III}poat]OTf	[(TMTACN)Co^{III}–(μ-OH)–Ga^{III}poat](OTf)$_2$
Formula	C_{53} H_{66} Cl_2 Co F_3 Fe N_7 O_7 P_3 S	C_{53} H_{66} Cl_2 Co F_3 Ga N_7 O_7 P_3 S	C_{55} H_{67} Co F_6 Ga N_8 O_{10} P_3 S_2
fw	1280.77	1294.64	1399.84
T (K)	93(2)	93(2)	93(2)
Crystal system	Monoclinic	Monoclinic	Monoclinic
Space group	*Pn*	*Pn*	$P2_1/c$
a (Å)	14.7789(6)	13.8892(13)	14.4009(9)
b (Å)	13.9994(6)	14.0495(13)	15.6474(10)
c (Å)	15.2992(6)	15.5346(14)	27.5964(17)
α (°)	90	90	90
β (°)	109.6160(6)	107.8962(15)	101.4479(11)
γ (°)	90	90	90
Z	2	2	4
V (Å^3)	2981.6(2)	2884.7(5)	6094.8(7)
δ_{calc} (mg/m^3)	1.427	1.490	1.526
Independent reflections	18258	17436	13445
R1	0.0348	0.0365	0.0472
wR2	0.0812	0.0787	0.1199
Goof	1.039	1.042	1.031

$wR2 = [\Sigma[w(F_o^2-F_c^2)^2] / \Sigma[w(F_o^2)^2]]^{1/2}$
$R1 = \Sigma||F_o|-|F_c|| / \Sigma|F_o|$
Goof = $S = [\Sigma[w(F_o^2-F_c^2)^2] / (n-p)]^{1/2}$ where n is the number of reflections and p is the total number of parameters refined.
The thermal ellipsoid plot is shown at the 50% probability level.

References

(1) Sickerman, N. S. Doctoral Dissertation, University of California-Irvine, Irvine, CA, 2014.
(2) Hill, E. A. Doctoral Dissertation, University of California-Irvine, Irvine, CA, 2016.
(3) Oswald, V. F. Doctoral Dissertation, University of California-Irvine, Irvine, CA, 2018.
(4) Sun, C. Doctoral Dissertation, University of California-Irvine, Irvine, CA, 2021.
(5) Oswald, V. F.; Lee, J. L.; Biswas, S.; Weitz, A. C.; Mittra, K.; Fan, R.; Li, J.; Zhao, J.; Hu, M. Y.; Alp, E. E.; Bominaar, E. L.; Guo, Y.; Green, M. T.; Hendrich, M. P.; Borovik, A. S. Effects of Non-covalent Interactions on High-spin Fe(IV)-oxido Complexes. *J. Am. Chem. Soc.* **2020**, *142*, 11804-11817.
(6) Lee, J. L.; Oswald, V. F.; Biswas, S.; Hill, E. A.; Ziller, J. W.; Hendrich, M. P.; Borovik, A. S. Stepwise assembly of heterobimetallic complexes: synthesis, structure, and physical properties. *Dalton Trans*. **2021**, *50*, 8111-8119.
(7) Sun, C.; Oswald, V. F.; Hill, E. A.; Ziller, J. W.; Borovik, A. S. Investigation of iron-ammine and amido complexes within a C_3-symmetrical phosphinic amido tripodal ligand. *Dalton Trans*. **2021**, *50,* 11197-11205.
(8) Oswald, V. F.; Weitz, A. C.; Biswas, S.; Ziller, J .W.; Hendrich, M. P.; Borovik, A. S. Manganese-Hydroxido Complexes Supported by a Urea/Phosphinic Amide Tripodal Ligand. *Inorg. Chem.* **2018**, *57*, 13341-13350.
(9) Sano, Y.; Weitz, A. C.; Ziller, J. W.; Hendrich, M. P.; Borovik, A. S. Unsymmetrical Bimetallic Complexes with M^{II}–(μ-OH)–M^{III} Cores ($M^{II}M^{III}$ = $Fe^{II}Fe^{III}$, $Mn^{II}Fe^{III}$, $Mn^{II}Mn^{III}$): Structural, Magnetic, and Redox Properties. *Inorg. Chem.* **2013**, *52*, 10229-10231.
(10) Cook, S. A.; Ziller, J. W.; Borovik, A. S. Iron(II) Complexes Supported by Sulfonamido Tripodal Ligands: Endogenous versus Exogenous Substrate Oxidation. *Inorg. Chem.* **2014**, *53*, 11029-11035.
(11) Sano, Y.; Lau, N.; Weitz, A. C.; Ziller, J. W.; Hendrich, M. P.; Borovik, A. S. Models for Unsymmetrical Active Sites in Metalloproteins: Structural, Redox, and Magnetic Properties of Bimetallic Complexes with M^{II}-(μ-OH)-Fe^{III} Cores. *Inorg. Chem.* **2017**, *56*, 14118-14128**.**
(12) Mayer, J. M.; Thorn, D. L.; Tulip, T. H. Synthesis, Reactions, and Electronic Structure of Low-Valent Rhenium-oxo Compounds. Crystal and Molecular Structure of $Re(O)I(MeCCMe)_2$. *J. Am. Chem. Soc.* **1985**, *107*, 7454-7462.
(13) Shaik, S.; Hirao, H.; Kumar, D. Reactivity of High-Valent Iron−Oxo Species in Enzymes and Synthetic Reagents: A Tale of Many States. *Acc. Chem. Res.* **2007**, *40*, 532-542.
(14) Decker, A.; Rohde, J.-U.; Klinker, E. J.; Wong, S. D.; Que, L.; Solomon, E. I. Spectroscopic and Quantum Chemical Studies on Low-Spin Fe^{IV}=O Complexes: Fe–O Bonding and Its Contributions to Reactivity. *J. Am. Chem. Soc.* **2007**, *129*, 15983-15996.
(15) Geng, C.; Ye, S.; Neese, F. Analysis of Reaction Channels for Alkane Hydroxylation by Nonheme Iron(IV)−Oxo Complexes. *Angew. Chem., Int. Ed.* **2010**, *49*, 5717-5720.
(16) Weitz, A. C.; Hill, E. A.; Oswald, V. F.; Bominaar, E. L.; Borovik, A. S.; Hendrich, M. P.; Guo, Y. Probing hydrogen bonding interactions to iron–oxido/hydroxido units via ^{57}Fe nuclear resonance vibrational spectroscopy. *Angew. Chem. Int. Ed.* **2018**, *57*, 16010-16014.
(17) Sgro, M. J.; Stephan, D. W. Frustrated Lewis Pair Inspired Carbon Dioxide Reduction by a Ruthenium Tris(aminophosphine) Complex. *Angew. Chem., Int. Ed.* **2012**, *51*, 11343.
(18) Aydemir, M.; Baysal, A.; Gümgüm, B. Synthesis and characterization of tris{2-(*N*,*N*-bis(diphenylphosphino)aminoethyl} amine derivatives: Application of a palladium(II) complex as a pre-catalyst in the Heck and Suzuki cross-coupling reactions. *J. Organometallic Chem.* **2008**, *693*, 3810-3814.

(19) Platt, A. W. G. Lanthanide phosphine oxide complexes. *Coord. Chem. Rev.* **2017**, *340*, 62-78.
(20) Grushin, V. V. Mixed Phosphine-Phosphine Oxide Ligands. *Chem. Rev.* **2004**, *104*, 1629-1662.
(21) Shankar, B.; Elumalai, P.; Shanmugam, R.; Singh, V.; Masram, D. T.; Sathiyendiran, M. New Class of Phosphine Oxide Donor-Based Supramolecular Coordination Complexes from an in Situ Phosphine Oxidation Reaction or Phosphine Oxide Ligands. *Inorg. Chem.* **2013**, *52*, 10217-10219.
(22) Kläui, W. The Coordination Chemistry and Organometallic Chemistry of Tridentate Oxygen Ligands with π-Donor Properties. *Angew. Chem., Int. Ed.* **1990**, *29*, 627-637.
(23) Grunwald, A. C.; Scholtysik, C.; Hagenbach, A.; Abram, U. One Ligand, One Metal, Seven Oxidation States: Stable Technetium Complexes with the "Kläui Ligand". *Inorg. Chem.* **2020**, *59*, 9396-9405.
(24) So, Y.-M.; Wong, K.-L.; Sung, H. H. Y.; Williams, I. D.; Leung, W.-H. Ruthenium Aqua Complexes Supported by the Kläui Tripodal Ligand: Synthesis, Structure, and Application in Catalytic C–H Oxidation in Water. *Eur. J. Inorg. Chem.* **2019**, *2368-2374*.
(25) Lumetta, G. J.; McNamara, B. K.; Hubler, T. L.; Wester, D. W.; Li, J.; Latesky, S. L. Potential Application of Kläui Ligands in Actinide Separations. In *Separations for the Nuclear Fuel Cycle in the 21st Century*; Lumetta, G. J.; Nash, K. L.; Clark, S. B.; Friese, J. I., Eds.; American Chemical Society: Washington, DC, 2006; Vol. *933*, pp 201-218.
(26) Navon, G.; Kläui, W. ^{59}Co NMR of a Cobalt(III) Spin-Crossover Compound. *Inorg. Chem.* **1984**, *23*, 2722-2725.
(27) Kläui, W.; Eberspach, W.; Gütlich, P. Spin-Crossover Cobalt(III) Complexes: Steric and Electronic Control of Spin State. *Inorg. Chem.* **1987**, *26*, 3977-3982.
(28) Gispert, J. R. Crystal Field Theory and Spin-Orbit Coupling: Energy Terms and Multiplets. In *Coordination Chemistry*; Wiley-VCH: Weinheim, 2008; pp 237-272.
(29) Cotton, F. A.; Wilkinson, G. In *Advanced Inorganic Chemistry*, 5th ed; Wiley, New York, 1988; pp 724-741.
(30) Cotton, F. A.; Meyers, M. D. Magnetic and Spectra Properties of the Spin-Free $3d^6$ Systems Iron(II) and Cobalt(III) in Cobalt(III) Hexafluoride Ion: Probable Observation of Dynamic Jahn-Teller Effects. *J. Am. Chem. Soc.* **1960**, *82*, 5023-5026.
(31) Stauber, J. M.; Zhang, S.; Gvozdik, N.; Jiang, Y.; Avena, L.; Stevenson, K. J.; Cummins, C. C. Cobalt and Vanadium Trimetaphosphate Polyanions: Synthesis, Characterization, and Electrochemical Evaluation for Non-aqueous Redox-Flow Battery Applications. *J. Am. Chem. Soc.* **2018**, *140*, 538-541.
(32) Que. L. The Road to Non-Heme Oxoferryls and Beyond. *Acc. Chem. Res.* **2007**, *40*, 3493-500.
(33) Lee, H. B.; Ciolkowski, N.; Winslow, C.; Rittle, J. High Spin Cobalt Complexes Supported by a Tripodal Tris(phosphinimide) Ligand. *Inorg. Chem.* **2021**, *60*, 11830-11837.
(34) Fukuzumi, S.; Morimoto, Y.; Kotani, H.; Naumov, P.; Lee, Y.-M.; Nam, W. Crystal structure of a metal ion-bound oxoiron(IV) complex and implications for biological electron transfer. *Nat. Chem.* **2010**, *2*, 756-759.
(35) Prakash, J.; Rohde, G. T.; Meier, K. K.; Jasniewski, A. J.; Van Heuvelen, K. M.; Münck, E.; Que, L. Spectroscopic Identification of an Fe^{III} Center, not Fe^{IV}, in the Crystalline Sc–O–Fe Adduct Derived from $[Fe^{IV}(O)(TMC)]^{2+}$. *J. Am. Chem. Soc.* **2015**, *137*, 3478-3481.
(36) Zhou, A.; Crossland, P. M.; Draksharapu, A.; Jasniewski, A. J.; Kleespies, S. T.; Que, L. Oxoiron(IV) compelxes as synthons for the assembly of heterobimetallic centers such as the Fe/Mn active site of Class Ic ribonucleotide reductases. *JBIC, J. Biol. Inorg. Chem.* **2018**, *23*, 155-165.

(37) Draksharapu, A.; Rasheed, W.; Klein, J. E. M. N.; Que, L. Facile and Reversible Formation of Iron(III)–Oxo–Cerium(IV) Adducts from Nonheme Oxoiron(IV) Complexes and Cerium(III). *Angew. Chem., Int. Ed.* **2017**, *56*, 9091-9095.
(38) Connelly, N. G.; Geiger, W. E. Chemical Redox Agents for Organometallic Chemistry. *Chem. Rev.* **1996**, *96*, 877-910.
(39) Lee, J. L.; Ross, D. L.; Barman, S. K.; Ziller, J. W.; Borovik, A. S. C–H Bond Cleavage by Bioinspired Nonheme Metal Complexes. *Inorg. Chem.* **2021**, *60*, 13759-13783.
(40) Luo, J.; Rth, N. P.; Mirica, L. M. Dinuclear Co(II)Co(III) Mixed-Valence and Co(III)Co(III) Complexes with N- and O-Donor Ligands: Characterization and Water Oxidation Studies. *Inorg. Chem.* **2011**, *50*, 6152-6157.
(41) Amtawong, J.; Skielstad, B. B.; Balcells, D.; Tilley, T. D. Concerted Proton–Electron Transfer Reactivity at a Multimetallic Co_4O_4 Cubane Cluster. *Inorg. Chem.* **202**, *59*, 1553-15560.
(42) Shannon, R. D. Revised Effective Ionic Radii and Systematic Studies of Interatomic Distances in Halides and Chalcogenides. *Acta. Cryst.* **1976**, *A32*, 751-767.
(43) Gupta, R.; Lacy, D. C.; Bominaar, E. L.; Borovik, A. S.; Hendrich, M. P.; Electron Paramagnetic Resonance and Mössbauer Spectroscopy and Density Functional Theory Analysis of a High-Spin Fe^{IV}–Oxo Complex. *J. Am. Chem. Soc.* **2012**, *134*, 9775-9784.
(44) Fan, R.; Serrano-Plana, J.; Oloo, W. N.; Draksharapu, A.; Delgado, Pinar, E.; Company, A.; Martin-Diaconescu, V.; Borrell, M.; Lloret-Fillol, J.; García-España, E.; Guo, Y.; Bominaar, E. L.; Que, L.; Costas, M.; Münck, E. Spectroscopic and DFT Characterization of a Highly Reactive Nonheme Fe^{V}-Oxo Intermediate. *J. Am. Chem. Soc.* **2018**, *140*, 3916-3928.
(45) Mondal, B.; Neese, F.; Bill, E.; Ye, S. Electronic Structure Contributions of Non-Heme Oxo-Iron(V) Complexes to the Reactivity. *J. Am. Chem. Soc.* **2018**, *140*, 9531-9544.
(46) Miessler, G. L.; Tarr, D. A. In *Inorganic Chemistry*, 3rd ed.; Pearson Education, Inc.: New Jersey, 2004; pp 367-368.
(47) Gispert, J. R. Crystal Field Theory and Spin-Orbit Coupling: Energy Terms and Multiplets. In *Coordination Chemistry*; Wiley-VCH: Weinheim, 2008; pp 8.
(48) Cook, S. A.; Bogart, J. A.; Levi, N.; Weitz, A.; Moore, C. E.; Rheingold, A. L.; Ziller, J. W.; Hendrich, M. P.; Borovik, A. S. Mononuclear Complexes of a Tridentate Redox-Active Ligand with Sulfonamide Groups: Structure, Properties, and Reactivity. *Chem. Sci.* **2018,** 9, 6540-6547.
(49) Ray, M.; Hammes, B.; Yap, G. P. A.; Rheingold, A. L.; Borovik, A. S. Structural and Physical Properties of Trigonal Monopyramidal Iron(II), Co(II), Nickel(II), and Zinc(II) Complexes. *Inorg. Chem.* **1998**, *37*, 1527-1532.
(50) Lucas, R.; Zart, M. K.; Mukherjee, J.; Sorrell, T. N.; Powell, D. R.; Borovik, A. S. A Modular Approach toward Regulating the Secondary Coordination Sphere of Metal Ions: Differential Dioxygen Activation Assisted by Intramolecular Hydrogen Bonds. *J. Am. Chem. Soc.* **2006**, *128*, 15476-15489.
(51) Cho, J.; Sarangi, R.; Kang, H. Y.; Lee, J. Y.; Kubo, M.; Ogura, T.; Solomon, E. I.; Nam, W. Synthesis, Structural, and Spectroscopic Characterization and Reactivities of Mononuclear Cobalt(III)-Peroxo Complexes. *J. Am. Chem. Soc.* **2010**, *132*, 16977-16986.
(52) Lacy, D. C.; Park, Y. J.; Ziller, J. W.; Yano, J.; Borovik, A. S. Assembly and Properties of Heterobimetallic $Co^{II/III}/Ca^{II}$ Complexes with Aquo and Hydroxo Ligands. *J. Am. Chem. Soc.* **2012**, *134*, 17526-17535.
(52) Zhdankin, V. V.; Litvinov, D. N.; Koposov, A. Y.; Luu, T.; Ferguson, M. J.; McDonald, R.; Tykwinski, R. R. Preparation and Structure of 2-Iodoxybenzoate Esters: Soluble and Stable Periodinane Oxidizing Reagents. *Chem. Commun.* **2004**, *263*, 106-107.

(53) Zhdankin, V. V.; Koposov, A. Y.; Litvinov, D. N.; Ferguson, M. J.; McDonald, R.; Luu, T.; Tykwinski, R. R. Esters of 2-Iodoxybenzoic Acid: Hypervalent Iodine Oxidizing Reagents with a Pseudobenziodoxole Structure. *J. Org. Chem.* **2005**, *70*, 6484-6491.
(54) Schoenfeldt, N. J.; Ni Z.; Korinda, A. W.; Meyer R. J.; Notestein J. M. Manganese Triazacyclononane Oxidation Catalysts Grafted under Reaction Conditions on Solid Cocatalytic Supports. *J. Am. Chem. Soc.* **2011**, *133*, 18684–18695.
(55) Cao R.; Müller, P.; Lippard, S. J. Tripodal Tris-tacn and Tris-dpa Platforms for Assembling Phosphate-Templated Trimetallic Centers. *J. Am. Chem. Soc.* **2010**, *132*, 17366–17369.
(56) Bell, F. A.; Ledwith, A.; Sherrington, D. C. Cation-radicals:tris-(*p*-tribromophenyl)amminium perchlorate and hexachloroantimonate. *J. Chem. Soc. C* **1969**, 2719-2720.
(57) Eberson L.; Larsson, B. Electron Transfer Reactions in Organic Chemistry. XII. Reactions of 4-Substituted Triarylaminium Radical Cations with Nucleophiles; Polar vs. Electron Transfer Pathways. *Acta. Chemica. Scandinavica* **1987**, *B41*, 367-378.
(58) Curley, J. J.; Bergman, R. G.; Tilley, T. D. Preparation and physical properties of early-late heterobimetallic compounds featuring Ir–M bonds (M = Ti, Zr, Hf). *Dalton Trans.* **2012**, *41*, 192-200.
(59) Petasis, D. T.; Hendrich, M. P. Quantitative Interpretation of Multifrequency Multimode EPR Spectra of Metal Containing Proteins, Enzymes, and Biomimetic Complexes. *Methods Enzymol.* **2015**, *563*, 171-208.
(60) APEX2 Version 2014.11-0, Bruker AXS, Inc.; Madison, WI 2014.
(61) SAINT Version 8.34a, Bruker AXS, Inc.; Madison, WI 2013.
(62) Sheldrick, G. M. SADABS, Version 2014/5, Bruker AXS, Inc.; Madison, WI 2014.
(63) Sheldrick, G. M. SHELXTL, Version 2014/7, Bruker AXS, Inc.; Madison, WI 2014
(64) International Tables for Crystallography 1992, Vol. C., Dordrecht: Kluwer Academic Publishers.
(65) Parsons, S., Flack, H. D., Wagner, T. Acta Cryst. B69, 249-259, 2013.

Appendix A

Development of New Hybrid Ligands to Stabilize M–O_2 Species

Introduction

Dioxygen binding and activation are essential in many biological processes.[1-2] For example, the respiratory protein myoglobin contains a heme cofactor that reversibly binds dioxygen, in which a formally Fe^{III}-superoxido species is produced (Figure A.1).[3] However, the binding mode of the O_2 moiety to the metal center in these enzymes is still not fully elucidated.[4,5] Understanding the relationship between structure and function in M–O_2 species can help modulate their reactivity towards dioxygen storage and transport, or activation of inert chemical bonds.[6,7]

While the reactivity of metallocofactors is largely governed by the ligands immediately bound to the metal ion (primary coordination sphere), there are effects from the secondary coordination sphere via hydrogen bonds (H-bonds).[8] This effect is illustrated with myoglobin in which H-bonds between the distal His64 and the O-atoms of the coordinated O_2 have a stabilization effect on this crucial adduct (Figure A.1).[3]

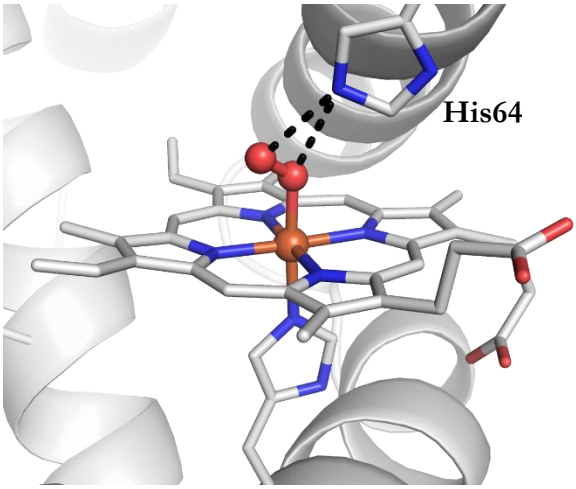

Figure A.1. The active site of oxymyoglobin, illustrating the H-bonding network in the microenvironment (PDB: 1A6M). Black dotted lines indicate H-bonds.

The Borovik Group is interested in designing ligand frameworks that incorporate intramolecular H-bonds to stabilize and study reactive metal species. Previously, a hybrid tripodal ligand – bis[(*N*-*tert*-butylureayl)-*N*-ethyl]-(6-pivalamido-2-pyridylmethyl)amine (H_5bupa) – was developed. Upon addition of dioxygen to the $[Mn^{II}H_2bupa]^-$ complex, a Mn^{III}-peroxido species was observed (Scheme A.1).[9,10] Although this species was generated and spectroscopically characterized, it proved to be too reactive to isolate. The molecular structure could not be determined through crystallographic methods, and the binding mode of the O_2^{2-} moiety was not fully elucidated.

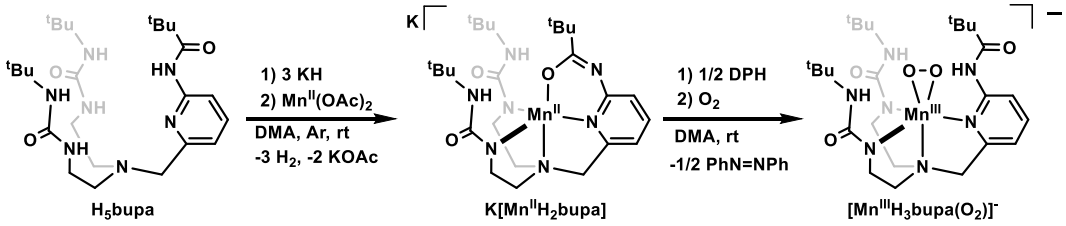

Scheme A.1. The formation of a Mn^{III}-peroxido species in the $[Mn^{III}H_3bupa(O_2)]^-$.

This appendix describes the development of two new precursor hybrid ligand frameworks, H_4pub and H_3papa (Scheme A.2). These two ligands were designed to prepare various M–O_2 adducts. Incorporation of two neutral equatorial donors is proposed to decrease the ability of the metal complex to fully activate the O–O bond upon treatment with O_2 or related reagents. In addition, stabilization is achieved by incorporating structural features (e.g. H-bonds) that aid in stabilizing these adducts so that their properties could be determined. Dioxygen reactivity and oxidation studies of an Fe^{II} complex supported by the $[Hpub]^-$ is discussed.

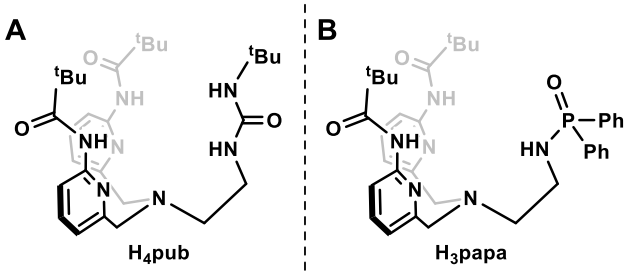

Scheme A.2. Structures of H_4pub (A) and H_3papa (B).

Results & Discussion

Ligand Synthesis. The syntheses of H_4pub and H_3papa were performed in six steps, diverging in the last step to install the desired urea or phosphinamide arm, respectively (Schemes A.3 and A.4). Ethylenediamine was protected with a *tert*-butyloxycarbonyl group to produce **1** (88 % yield). Treating pivaloylchloride with 2-amino-6-methyl-chloride yielded **2** (74 %), which was subsequently brominated with *N*-bromosuccinimide to afford **3** after purification (37 %). One equivalent of **1** and two equivalents of **3** were coupled via nucleophilic substitution to produce **4** (65 % yield). **4** was then deprotected to afford the free amine **5** (94 %).

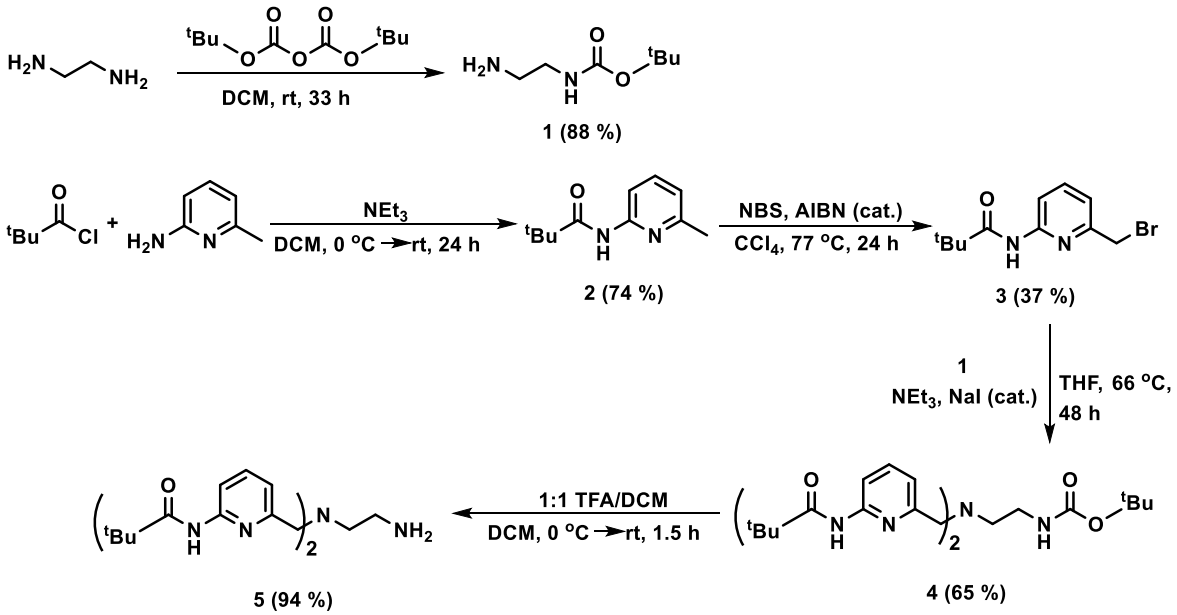

Scheme A.3. Initial five synthetic steps for precursors of H_4pub and H_3papa.

5 was reacted with *tert*-butylisocyanate to afford H_4pub (71 %). Separately, **5** was treated with diphenylphosphinic chloride to produce H_3papa (84 %).

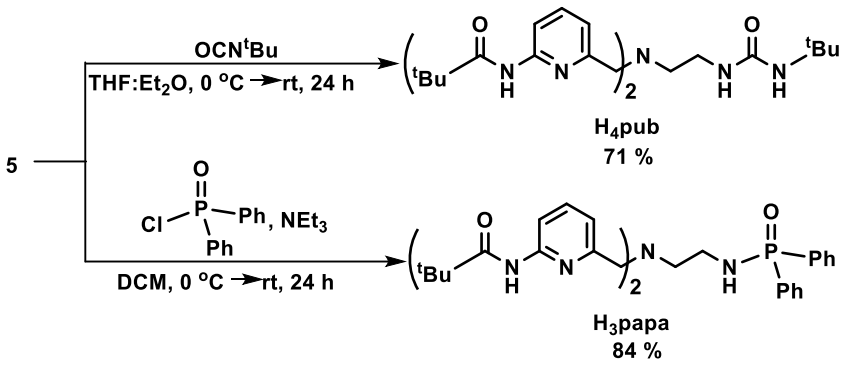

Scheme A.4. Divergent synthesis of H_4pub and H_3papa.

Complex Synthesis. Both new ligands were used to synthesize metal complexes, but obtaining molecular structures of complexes in the H_3papa precursor framework proved challenging, so the remaining of this appendix addresses coordination chemistry using H_4pub. H_4pub was treated with three equivalents of KH followed by $Fe^{II}(OAc)_2$ to produce K[Fe^{II}Hpub] in 86 % yield (Scheme A.5). Alternatively, H_4pub was treated with three equivalents of NaH followed by $Fe^{II}(OAc)_2$ and NMe_4OAc to produce NMe_4[Fe^{II}Hpub] in 70 % yield. The carboxyamide N–H proton is more acidic than the urea protons, so three equivalents of base are required to ensure deprotonation of the urea. This has previously been observed in metal complexes in $[H_2bupa]^{3-}$ and related ligand frameworks.[9-11] Recrystallization of NMe_4[Fe^{II}Hpub] provided single crystals suitable for X-ray diffraction, and its molecular structure is depicted in Figure A.2.

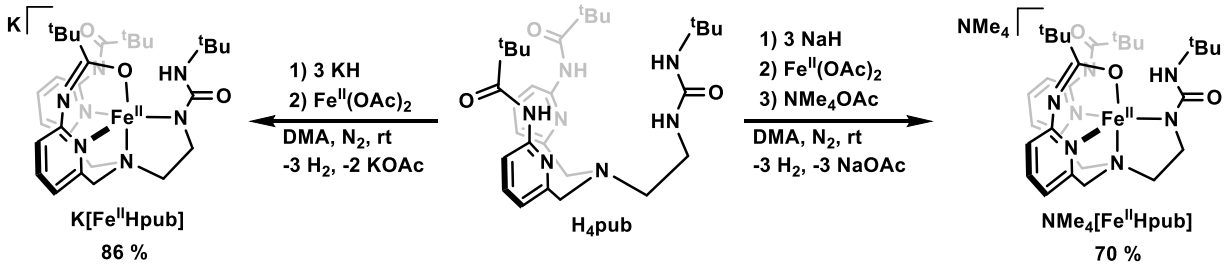

Scheme A.5. Preparation of K[Fe^{II}Hpub] and NMe_4[Fe^{II}Hpub].

Molecular Structure. The complex $[Fe^{II}Hpub]^-$ possesses a distorted trigonal bipyramidal geometry (τ_5 = 0.65). The Fe^{II} center has an N_4O primary coordination sphere with both carboxyamidepyridyl arms being deprotonated; however, only one arm coordinates to the Fe center with an Fe1–O1

bond length of 1.965 Å (the resolution is for connectivity purposes only; e.s.d's were not obtained). Moreover, the bond lengths observed in the carboxyamidato group containing O1 suggest N5–C7 is a double bond and O1–C7 is a single bond, leading to the formally anionic O1 coordination to the Fe^{II} center. The trigonal bipyramidal geometry of the Fe^{II} complex is significant: the Fe^{II} center is coordinatively unsaturated, allowing for the possibility of binding an exogenous species.

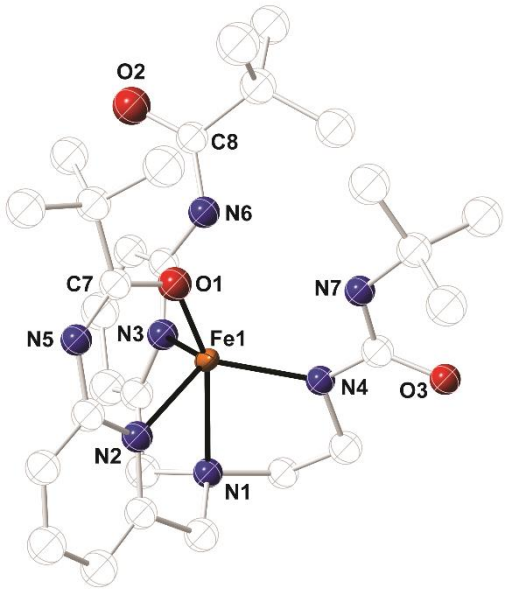

Bond Lengths/Distances (Å)	
Fe1–N1	2.269
Fe1–N2	2.167
Fe1–N3	2.115
Fe1–N4	2.029
Fe1–O1	1.965
N5–C7	1.284
O1–C7	1.295
N6–C8	1.335
O2–C8	1.260
O1–N7	3.256
Bond Angle (º)	
O1–Fe1–N1	157.48
τ_5	0.65

Figure A.2. The molecular structure of $NMe_4[Fe^{II}Hpub]$. Hydrogen atoms and non-interacting counter ions were removed for clarity. Bond lengths, distances, and bond angle of interest are included in the corresponding chart. $\tau_5 = (\beta - \alpha)/60^o$, where β = the largest bond angle of a coordination center, and α = the second largest bond angle of a coordination center. *The resolution is for connectivity purposes only, and e.s.d.'s are not obtained.

Redox Properties. A reversible one-electron redox event was observed for the complex at $E_{1/2}$ = –990 mV versus $[Fe^{III/II}Cp_2]^{+/0}$ at room temperature in DMSO (ΔE_p = 95 mV, $|i_{pa}/i_{pc}|$ = 1.41); this is assigned to the $[Fe^{III/II}Hpub]^{0/-}$ couple (Figure A.3A). While $[Fe^{II}Hpub]^-$ is electrochemically competent to reduce dioxygen by one electron to superoxide (E^o = –180 mV versus NHE),[2] this potential is significantly more positive than other Fe^{II} complexes prepared in our group with tri-

anionic ligands, suggesting that it may be less likely to fully reduce dioxygen and lead to O–O scission.

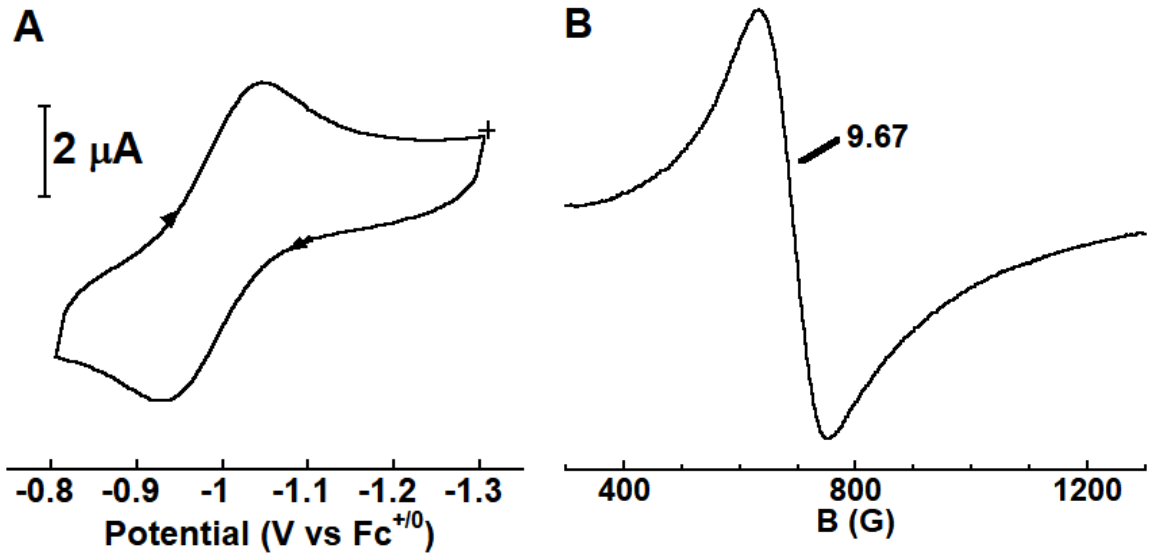

Figure A.3. (A) Cyclic voltammogram of K[Fe^{II}Hpub] collected in DMSO at a 100 mV/s scan rate with 100 mM TBAP supporting electrolyte, with ferrocene as an internal standard. (B) Parallel-mode EPR spectrum of a 10 mM solution of K[Fe^{II}Hpub] in 1:1 DMF:THF collected at 10 K.

Spectroscopic Properties. A derivative feature at g = 9.67 is observed in the parallel-mode X-band electron paramagnetic resonance (EPR) spectrum for the frozen 1:1 DMF:THF solution of K[Fe^{II}Hpub], consistent with a mononuclear Fe^{II} center with an S = 2 spin ground state (Figure A.3B). The Fe^{II} complex exhibited absorption features at λ_{max} = 493 nm (ε = 1200 M^{-1} cm^{-1}) and 929 nm (ε = 120 M^{-1} cm^{-1}) in 1:1 DMF:THF at –80 °C (Figure A.4A, black trace). The λ_{max} = 493 nm feature is assigned to be a metal-to-ligand charge transfer (MLCT) between the Fe^{II} center and the coordinated pyridine,[12] while the λ_{max} = 929 nm feature is assigned to be a d-d transition.

Reactivity with O_2. The treatment of K[Fe^{II}Hpub] with 1 equivalent of O_2 at –80 °C in 1:1 DMF:THF was monitored spectrophotometrically and showed growth of a new absorbance feature at λ_{max} = 513 nm (Figure A.4A, red trace). The reactivity of K[Fe^{II}Hpub] towards O_2 was further investigated using EPR spectroscopy. Treatment of the Fe^{II} complex with 1 equivalent of O_2 at –80 °C showed growth of a new feature at g = 17.0 in the parallel-mode spectrum (Figure A.4B). The corresponding

perpendicular-mode spectrum indicates the presence of a small amount of a rhombic signal with *g* values at 3.70, 5.19 and 8.83, attributed to a high spin Fe^{III} species ($S = 5/2$) (Figure A.4C). Treatment of K[Fe^{II}Hpub] with 20 equivalents of O_2 produced the same $g = 17.0$ signal observed in the reaction with 1 equivalent of O_2, albeit with weaker intensity (Figure A.4D). Furthermore, the rhombic high spin Fe^{III} species was also observed in the corresponding perpendicular-mode spectrum, and its features displayed increased intensity relative to the perpendicular-mode spectrum obtained from the reaction with 1 equivalent of O_2 (Figure A.4E).

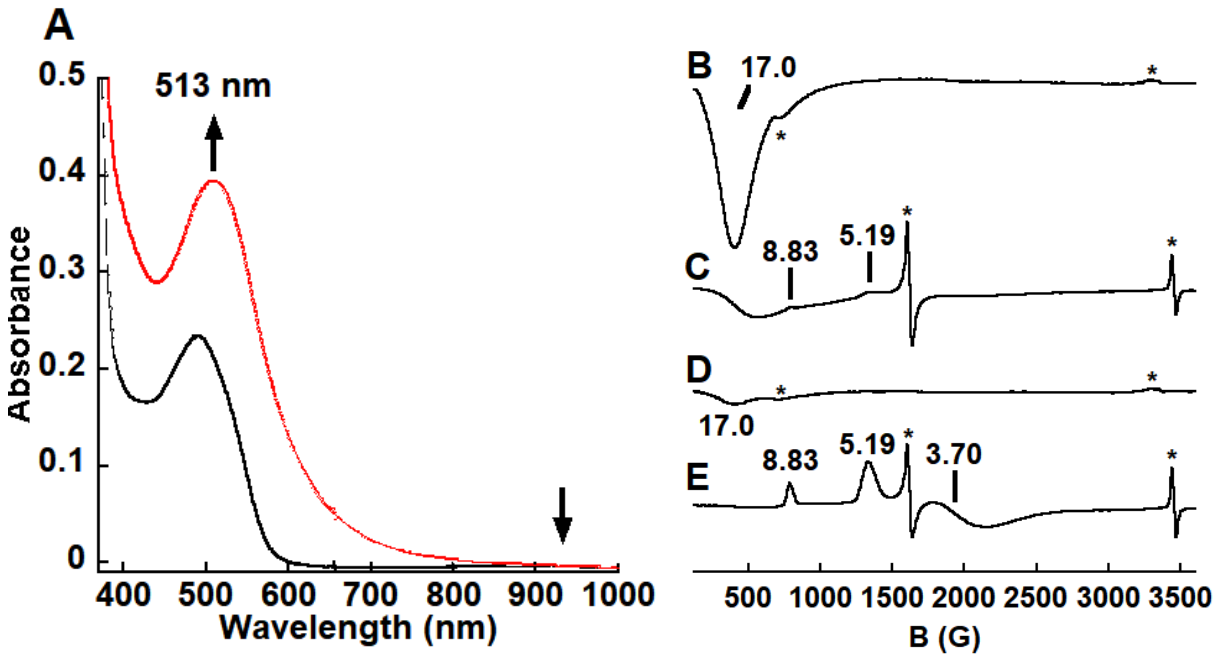

Figure A.4. (A) UV-vis spectral changes before (black) and after (red) the addition of 1 equiv. of O_2 in DMF:THF at –80 °C. Parallel- (B) and perpendicular-mode (C) EPR spectra after the addition of 1 equiv. of O_2 in DMF:THF at –80 °C. Parallel- (D) and perpendicular-mode (E) EPR spectra after the addition of 20 equiv. of O_2 in DMF:THF at –80 °C. All EPR spectra were collected at 10 K. Asterisks (*) indicate starting Fe^{II}, adventitious Fe^{III}, or radical impurities.

To further interrogate the oxidation of K[Fe^{II}Hpub] in the absence of O_2, the one-electron oxidation of the Fe^{II} complex was performed with ferrocenium: treatment of the Fe^{II} complex with 1 equivalent of $[FeCp_2]BF_4$ in 1:1 DMF:THF at –80 °C showed growth of a new intense band at λ_{max} = 513 nm (Figure A.5A, red trace): note that the absorbance spectrum of this oxidized species is

nearly identical to that obtained when dioxygen was used as the oxidant (Figure A.5B). This finding suggests that the same species is formed by both oxidative routes.

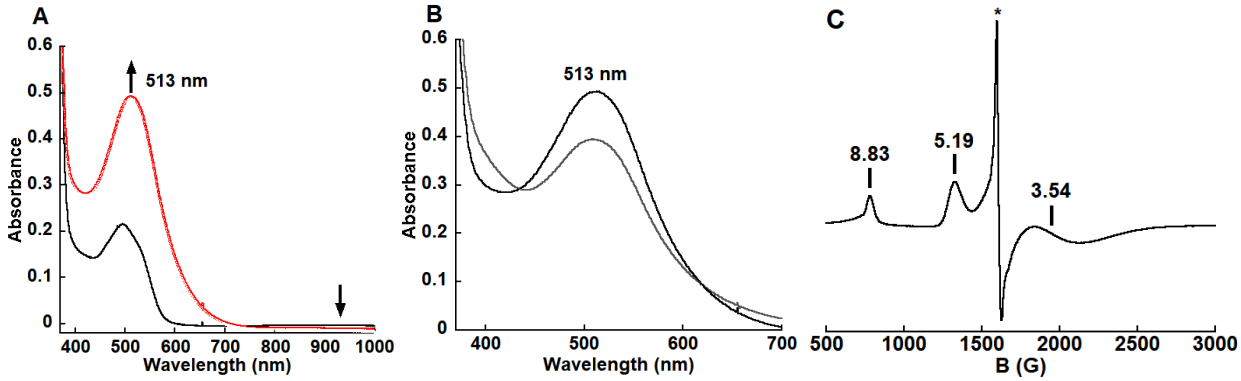

Figure A.5. (A) UV-vis spectral changes before (black) and after (red) the addition of 1 equiv. of $[FeCp_2]BF_4$ in DMF:THF at –80 °C. (B) Comparison of the products in the reactions with 1 equiv. of O_2 (grey) and $[FeCp_2]BF_4$ in DMF:THF at –80 °C (black). (C) Perpendicular-mode EPR spectrum after the addition of 1 equiv. of $[FeCp_2]BF_4$ in DMF:THF at –80 °C (collected at 10 K). Asterisks (*) indicate adventitious Fe^{III} impurities.

Further support for this idea came from EPR results. When the Fe^{II} complex was treated with 1 equivalent of $[FeCp_2]BF_4$, a high spin rhombic Fe^{III} species (g = 3.54, 5.19 and 8.83) was observed in the perpendicular-mode (Figure A.5C). This spectrum is identical to that found when the oxidation was done with 20 equivalents of O_2. Thus, the 1-electron oxidation of $K[Fe^{II}Hpub]$ by either $[FeCp_2]BF_4$ or excess O_2 is tentatively assigned as $[Fe^{III}Hpub]$. It is worth noting the species with the g = 17.0 feature in the parallel-mode was not observed in the $[FeCp_2]^+$ oxidation route, and is unstable at temperatures above –80 °C. Similarly, $[Fe^{III}Hpub]$ is unstable at temperatures above –50 °C. Bulk synthetic and spectroscopic studies to generate and characterize these species at room temperature were attempted, but spectroscopic features observed during reactivity at low temperature were not observed at room temperature.

The identity of the species with the g value of 17.0 in parallel-mode EPR spectroscopy is of continued interest. Low field parallel-mode EPR signals have been previously observed in non-heme diiron enzymes in the Fe^{II}_2 state, as well as in synthetic models.[13-17] In both enzymatic and synthetic systems, the two ferrous ions are high spin (S = 2) and are weakly ferromagnetically coupled to

produce low-field EPR signals between g ~ 15-17 in the parallel-mode, indicating an $S = 4$ ground state. Additionally, similarly low field features have been observed for high-valent mononuclear and dinuclear Fe complexes.[18-20] It would be interesting to elucidate the identity of this integer-spin species with relevance to metal/O_2-binding chemistry.

Conclusion

Metal-assisted dioxygen binding and activation are essential in many biological processes, but the nature of the initial O_2 binding to the metallocofactor is contentious due to the reactive M–O_2 adduct. In this appendix, two new hybrid tripodal ligand scaffolds, H_4pub and H_3papa, were developed. H_4pub contains two carboxyamide-pyridine donors and one urea donor, while H_4papa contains two carboxyamide-pyridine donors and one phosphinic donor. The hydrogen bond donating/accepting groups are proposed to stabilize an M–O_2(H) adduct. An Fe^{II} complex was synthesized within the $[Hpub]^-$ ligand framework, and its reactivity with dioxygen was examined. Upon treatment with excess dioxygen, the Fe^{II} complex was oxidized by one electron in what appears to be an outer-sphere redox event. The identity of an unknown integer spin species with a *g* value of 17.0 is yet to be elucidated.

Experimental

General Procedures. Organic transformations, unless otherwise noted, did not require the use of an inert atmosphere. All inorganic syntheses and manipulations were performed under a nitrogen atmosphere in a Vacuum Atmosphere Co. dry box. Solvents were sparged with argon and purified using a JC Meyer Co. solvent purification system with columns containing Q-5 and molecular sieves. All reagents, unless otherwise noted, were purchased from commercial sources and used as received. Potassium hydride (KH) or sodium hydride (NaH), as a 30% suspension in mineral oil, was filtered

and washed with diethyl ether (5 X 10 mL) and pentane (5 X 10 mL) and dried under vacuum prior to use. Triethylamine, ethylenediamine, and dimethylformamide were distilled prior to use. Ferrocenium tetrafluoroborate ($[FeCp_2]BF_4$) was synthesized according to a literature procedure.[21]

tert-Butyl-(2-aminoethyl)carbamate (1). Di-*tert*-butyl-dicarbonate (8.396 g, 38.47 mmol), dissolved in 220 mL CH_2Cl_2, was added dropwise to a solution of ethylenediamine (11.44 g, 190.3 mmol) dissolved in 30 mL CH_2Cl_2 over 9 hours. The solution stirred for 24 hours, and then was concentrated to approximately 50 mL. 150 mL saturated $NaHCO_3$ was added to the solution, and the mixture was washed with CH_2Cl_2 (3 X 100 mL). The organic layer was dried over $MgSO_4$, and then was concentrated to 5.42 g of a clear, colorless oil (88.0 %). ^{1}H NMR (500 MHz, $CDCl_3$) δ 5.55 (1H, bs, N*H*), 3.17 (2H, m, NHC*H*$_2$), 2.79 (2H, t, *J* = 5.9 Hz, NH_2CH_2), 1.47 (9H, s, C(C*H*$_3$)$_3$), 1.25 (2H, bs, N*H*$_2$)); ^{13}C NMR (500 MHz, $CDCl_3$) δ 156.3, 79.0, 43.3, 41.8, 28.4.

N-(6-Methyl-2-pyridyl)pivalamide (2). Pivaloylchloride (17.94 g, 148.8 mmol), dissolved in 110 mL CH_2Cl_2, was added dropwise to a solution of 2-amino-6-methyl-pyridine (15.67 g, 144.9 mmol) and triethylamine (15.20 g, 150.4 mmol) dissolved in 120 mL CH_2Cl_2 over 4 hours. The mixture stirred for 48 hours. Triethylammonium chloride was filtered off, and the organic layer was washed with H_2O (3 X 100 mL) and brine (2 X 100 mL). The clear yellow solution was dried over $MgSO_4$, and then was concentrated to an off-white solid *in vacuo*. The crude solid was triturated in petroleum ether in an ice bath for 15 minutes, and 20.5 g of pale yellow needles were collected (73.7 %). ^{1}H NMR (500 MHz, $CDCl_3$) δ 8.05 (1H, d, *J* = 8.3 Hz, Ar*H*), δ 7.93 (1H, bs, N*H*), 7.58 (1H, t, *J* = 7.9 Hz, Ar*H*), 6.88 (1H, d, *J* = 7.5 Hz, Ar*H*), 2.45 (3H, s, C*H*$_3$), 1.32 (9H, s, C(C*H*$_3$)$_3$); ^{13}C NMR (500 MHz, $CDCl_3$) δ 177.1, 156.7, 151.0, 138.7, 119.2, 110.7, 39.8, 27.6, 24.1.

N-(6-Bromomethyl-2-pyridyl)pivalamide (3). A solution of **2** (8.779 g, 45.66 mmol), N-bromosuccinimide (9.277 g, 52.12 mmol) and azobisisobutyronitrile (0.1258 g, 0.7661 mmol), dissolved in 120 mL CCl_4, was heated under reflux for 30 hours. Orange precipitates were filtered from a dark red solution,

which was washed with saturated $NaHCO_3$ (1 X 150 mL) and H_2O (1 X 150 mL). The organic layer was dried over $MgSO_4$ overnight, and then was concentrated to a dark red oil. The crude oil was purified by flash column chromatography (silica gel) using a 4:1 hexane/ethyl acetate eluent. The purified fractions were collected and concentrated to 4.63 g of an orange solid (37.4 %). ^{1}H NMR (500 MHz, $CDCl_3$) δ 8.18 (1H, d, *J* = 8.4 Hz, Ar*H*), 8.02 (1H, bs, N*H*), 7.68 (1H, t, *J* = 7.9 Hz, Ar*H*), 7.14 (1H, d, *J* = 7.5 Hz, Ar*H*), 4.42 (2H, s, CH_2Br), 1.32 (9H, s, C(CH_3)$_3$); ^{13}C NMR (500 MHz, $CDCl_3$) δ 177.2, 154.9, 151.4, 139.4, 119.2, 113.4, 39.9, 33.4, 27.5.

tert-Butyl-(2-bis((6-pivalamido-2-pyridyl)methyl)amino)ethyl)carbamate (4). A THF mixture (50 mL) of **1** (1.010 g, 6.307 mmol), **3** (3.478 g, 12.83 mmol), triethylamine (2.771 g, 27.43 mmol) and potassium iodide (0.2731 g, 1.645 mmol) was heated under reflux for 72 hours. The precipitates were removed from the yellow solution, which was concentrated *in vacuo* to an off-white foam. The crude product was purified by flash column chromatography (silica gel) using a 94:5:1 CH_2Cl_2/CH_3OH/NEt_3 eluent. The purified fractions were collected and concentrated to 2.22 g of a yellow solid (65.0 %). ^{1}H NMR (500 MHz, *d*$_6$-DMSO) δ 9.58 (2H, s, ArN*H*), 7.89 (2H, d, *J* = 8.1 Hz, Ar*H*), 7.72 (2H, t, *J* = 7.9 Hz, Ar*H*), 7.32 (2H, d, *J* = 7.6, Ar*H*), 6.75 (1H, t, CH_2N*H*), 3.69 (4H, s, ArCH_2), 3.1 (2H, dd, NHCH_2), 2.55 (2H, t, NCH_2), 1.36 (9H, s, OC(CH_3)$_3$), 1.22 (18H, s, C(CH_3)$_3$); ^{13}C NMR (500 MHz, *d*$_6$-DMSO) δ 177.0, 158.1, 155.6, 151.4, 138.3, 117.7, 112.3, 77.5, 69.8, 59.5, 54.0, 45.7, 28.2, 26.9.

N,N'-((((2-Aminoethyl)azanediyl)bis(methylene))bis(pyridine-6,2-diyl))bis(2,2-dimethylpropanamide) (5). Trifluoroacetic acid (12.7 g, 111 mmol), dissolved in 8.5 mL CH_2Cl_2, was added dropwise to a solution of **4** (0.8331 g, 1.541 mmol) dissolved in 5 mL CH_2Cl_2 over 15 minutes at 0 °C. The solution was warmed to room temperature and stirred for 1 hour, and the solvent was removed *in vacuo*. 4 M NaOH (25 mL) was added to basicify the orange oil until the pH reached 14. The aqueous mixture was extracted with $CHCl_3$ (10 X 25 mL). The organic layer was dried over $MgSO_4$, and then was concentrated to 0.641 g yellow solid (94.4 %). ^{1}H NMR (500 MHz, *d*$_6$-DMSO) δ 9.6

(2H, bs, ArN*H*), 7.89 (2H, d, *J* = 8.2 Hz, Ar*H*), 7.74 (2H, t, *J* = 7.9 Hz, Ar*H*), 7.32 (2H, d, *J* = 7.4, Ar*H*), 3.72 (4H, s, ArCH_2), 2.65 (2H, t, *J* = 6.5 Hz, NH_2CH_2), 2.51 (2H, t, *J* = 6.7, NCH_2), 1.22 (18H, s, C(CH_3)$_3$); ^{13}C NMR (500 MHz, d_6-DMSO) δ 177.0, 158.3, 151.4, 138.3, 117.6, 112.3, 69.8, 59.9, 57.1, 39.5, 26.9.

N,N'-((((2-(3-(tert-Butyl)ureido)ethyl)azanediyl)bis(methylene))bis(pyridine-6,2-diyl)bis(2,2-dimethylpropanamide) (H_4pub). *tert*-Butyl isocyanate (0.357 g, 3.60 mmol), dissolved in 12 mL 1:1 THF/Et_2O, was added dropwise to a solution of **5** (1.331 g, 3.020 mmol) dissolved in 12 mL 1:1 THF/Et_2O over 15 minutes at 0 °C. The solution was warmed to room temperature and stirred for 24 hours, and the solvent was removed *in vacuo*. The off-white solid was triturated in cold Et_2O, and 1.16 g of white solid was collected on a medium porosity glass frit (71.3 %). ^{1}H NMR (500 MHz, $CDCl_3$) δ 8.53 (2H, bs, ArN*H*), 8.12 (2H, d, *J* = 8.2, Ar*H*), 7.61 (2H, t, *J* = 7.9 Hz, Ar*H*), 7.01 (2H, d, *J* = 7.3 Hz, Ar*H*), 4.48 (1H, bs, CON*H*), 4.21 (1H, bs, N*H*C(CH_3)$_3$), 3.75 (4H, bs, ArCH_2), 3.18 (2H, bs, NHCH_2), 2.76 (2H, bs, NCH_2), 1.34 (18H, s, C(CH_3)$_3$), 1.29 (9H, s, NHC(CH_3)$_3$); ^{13}C NMR (500 MHz, $CDCl_3$) δ 177.6, 158.2, 151.6, 139.0, 118.9, 112.8, 65.9, 59.5, 54.0, 50.3, 40.0, 29.6, 27.5; FTIR (ATR, cm^{-1}) 3433, 3358, 3318, 3058, 2962, 2926, 2871, 1694, 1666, 1625, 1622, 1559, 1516, 1444, 1401, 1364, 1306, 1294, 1270, 1220, 1149, 991, 804. HRMS (ES+, m/z): Exact mass calculated for $C_{29}H_{46}N_7O_3$ $[M + H]^+$: 540.3662. Found: 540.3685.

N,N'-((((2-((diphenylphosphoryl)amino)ethyl)azanediyl)bis(methylene))bis(pyridine-6,2-diyl)bis(2,2-dimethylpropanamide) (H_3papa). Under an inert atmosphere, diphenylphosphinic chloride (0.5251 g, 2.219 mmol), dissolved in 100 mL CH_2Cl_2, was added dropwise to a solution of **5** (0.938 g, 2.13 mmol) and triethylamine (3.440 g, 34.06 mmol) dissolved in 1000 mL CH_2Cl_2 over 8 hours at 0 °C. The solution warmed to room temperature and stirred for 48 hours, and the solvent was removed *in vacuo*. Et_2O was added to the yellow solid, and triethylammonium chloride precipitates were filtered off. The Et_2O was removed *in vacuo*. The crude product was purified by flash column

chromatography (alumina) using a gradient CH_3OH/ethyl acetate eluent. The purified fractions were collected and concentrated to 1.15 g of yellow solid (84.1 %). ^{1}H NMR (500 MHz, $CDCl_3$) δ 8.25 (2H, bs, ArN*H*), 8.12 (2H, d, *J* = 8.3 Hz, Ar*H*), 7.75 (4H, m, Ar*H*), 7.59 (2H, t, *J* = 7.9 Hz, Ar*H*), 7.48 (2H, m, Ar*H*), 7.40 (4H, m, Ar*H*), 7.03 (2H, d, *J* = 7.5 Hz, Ar*H*), 3.88 (1H, dd, PON*H*), 3.70 (4H, s, ArC*H*$_2$), 3.02 (2H, m, NHC*H*$_2$), 2.76 (2H, t, *J* = 5.8 Hz, NC*H*$_2$CH$_2$), 1.29 (18H, s, C(C*H*$_3$)$_3$; ^{13}C NMR (500 MHz, $CDCl_3$) δ 177.5, 174.9, 157.2, 151.4, 138.9, 132.8, 132.0, 128.6, 119.0, 112.6, 59.8, 56.8, 54.9, 39.9, 27.5; ^{31}P NMR (400 MHz, $CDCl_3$) δ 24.7; FTIR (ATR, cm^{-1}) 3431, 3223 (broad), 3184, 3053, 2962, 2932, 2870, 1679, 1576, 1514, 1449, 1401, 1299, 1187, 1152, 1124, 797. HRMS (ES+, m/z): Exact mass calculated for $C_{36}H_{45}N_6O_3PNa$ $[M + Na]^+$: 663.3188. Found: 663.3206.

Potassium (N,N'-((((2-(3-(tert-Butyl)ureido)ethyl)azanediyl)bis(methylene))bis(pyridine-6,2-diyl)bis(2,2-dimethylpropanamidato)ferrate) (K[Fe^{II}Hpub]). Solid KH (47.0 mg, 1.17 mmol) was added to a solution of H_4pub (202.0 mg, 0.3742 mmol) in 3 mL anhydrous DMA. After H_2 evolution ceased, $Fe(OAc)_2$ (67.0 mg, 0.374 mmol) was added to the mixture, which stirred for an additional 3 hours. The red reaction mixture was filtered to remove KOAc precipitate (100 mg, 91 %), and the solvent was removed *in vacuo*. The red solids were redissolved in 2 mL THF, and pentane was added to precipitate orange solids, which were collected on a fine porosity glass frit and dried for one hour (203 mg, 86.0 %). FTIR (ATR, selected bands, cm^{-1}) 3393 (N-H stretch), 1637, 1621, 1577, 1563 (C=O stretches).

Tetramethylammonium (N,N'-((((2-(3-(tert-Butyl)ureido)ethyl)azanediyl)bis(methylene))bis(pyridine-6,2-diyl)bis(2,2-dimethylpropanamidato)ferrate) (NMe$_4$[Fe^{II}Hpub]). Solid NaH (15.2 mg, 0.633 mmol) was added to a solution of H_4pub (103.0 mg, 0.1908 mmol) in 3 mL anhydrous DMA. After H_2 evolution ceased, $Fe(OAc)_2$ (33.3 mg, 0.192 mmol) and NMe_4OAc (26.5 mg, 0.199 mmol) were added to the mixture, which stirred for an additional 3 hours. The red reaction mixture was filtered to remove NaOAc

precipitate (49.7 mg, 98 %). Orange solids were obtained upon vapor diffusion of Et_2O into the filtrate, and were collected on a fine porosity glass frit and dried for one hour (88.5 mg, 70.0 %). Orange crystals were obtained upon further recrystallization. FTIR (ATR, selected bands, cm^{-1}) 3392 (N-H stretch), 1630, 1585, 1563 (C=O stretches).

Physical Methods. UV-Vis spectra were collected on an Agilent UV-Vis spectrophotometer equipped with a Unisoku Unispeks cryostat in a 1 cm quartz cuvette. ^{1}H and ^{13}C NMR spectra were collected on a Bruker CRYO500 spectrometer (500 MHz); ^{31}P NMR spectra were collected on a DRX400 spectrometer (162 MHz). X-band EPR spectra (microwave frequency 9.28 GHz) were collected on a Bruker EMX spectrometer equipped with an ER041XG microwave bridge, an Oxford Instrument liquid He quartz cryostat and a dual-mode cavity (ER4116DM). Infrared spectra were collected on a Thermo Scientific Nicolet iS5 FT-IR spectrometer equipped with an iD5 ATR accessory. High resolution mass spectrometry of organic ligands was performed on a Waters Micromass LCT Premier Mass Spectrometer in positive ion electrospray mode. Cyclic voltammograms were collected using a CHI600C electrochemical analyzer in a dry box under nitrogen atmosphere. A glassy carbon, platinum wire and silver wire electrodes were used as the working, counter and reference electrodes, respectively. A Bruker SMART APEX II diffractometer was used to collect crystallographic data.

References

(1) Kovaleva, E. G.; Lipscomb, J. D. *Nat. Chem. Biol.* **2008**, *4*, 186-193.
(2) Huang, X.-Y.; Groves, J. T. *Chem. Rev.* **2018**, *118*, 2491-2553.
(3) Vojtěchovský, J.; Chu, K.; Berendzen, J.; Sweet, R. M.; Schlichting, I. *Biophys. J.* **1999**, *77*, 2153-2174.
(4) Bren, K. L.; Eisenberg, R.; Gray, H. B. *Proc. Nat. Acad. Sci. USA* **2015**, *112*, 13123-13127.
(5) Wilson, S. A.; Green, E.; Mathews, I. I.; Benfatto, M.; Hodgson, K. O.; Hedman, B.; Sarangi, R. *Proc. Nat. Acad, Sci. USA* **2013**, *110* , 16333-16338.
(6) Bollinger, J. M. Jr.; Krebs, C. *Curr. Opin. Chem. Bio.* **2007**, *11*, 151-158.
(7) Van der Donk, W.; Krebs, C.; Bollinger, J. M. Jr. *Curr. Opin. Structural Bio.* **2010**, *20*, 673-683.
(8) Shook, R. L.; Borovik, A. S. *Inorg. Chem.* **2010**, *49*, 3646-3660.
(9) Shook, R. L.; Gunderson, W. A.; Greaves, J.; Ziller, J. W.; Hendrich, M. P.; Borovik, A. S. *J. Am. Chem. Soc.* **2008**, *130*, 8888-8889.

(10) Shook, R. L.; Peterson, S. M.; Greaves, J.; Moore, C.; Rheingold, A. L.; Borovik, A. S. *J. AM. Chem. Soc.* **2011**, *133*, 5810-5817.
(11) Ng, G. K.-Y.; Ziller, J. W.; Borovik, A. S. *Inorg. Chem.* **2011**, *50*, 7922-7924.
(12) Braterman, P. S.; Song, J.-I.; Peacock, R. D. *Inorg. Chem.* **1992**, *31*, 555-559.
(13) Reem, R. C.; Solomon, E. I. *J. Am. Chem. Soc.* **1987**, *109*, 1216-1226.
(14) Fox, B. G.; Surerus, K. K.; Münck, E.; Lipscomb, J. D. *J. Biol. Chem.* **1988**, *263*, 10553-10556.
(15) Lynch, J. B.; Juarez-Garcia, C.; Münck, E.; Que, L. Jr. *J. Biol. Chem.* **1989**, *28*, 8091-8096.
(16) Borovik, A. S.; Hendrich, M. P.; T. R. Holman, Münck, E.; Papaefthymiou, V.; Que, L. Jr. *J. A. Chem. Soc.* **1990**, *112*, 6031-6038.
(17) Jang, H. G.; Hendrich, M. P.; Que, L. Jr. *Inorg. Chem.* **1993**, *32*, 911-918.
(18) Stoian, S. A.; Xue, G.; Bominaar, E. L.; Que, L. Jr.; Münck, E. *J. Am. Chem. Soc.* **2014**, *136*, 1545-1558.
(19) Weitz, A. C.; Mills, M. R.; Ryabov, A. D.; Collins, T. J.; Guo, Y.; Bominaar, E. L.; Hendrich, M. P. *Inorg. Chem.* **2019**, *58*, 2099-2108.
(20) Mbughuni, M. M.; Chakrabarti, M.; Hayden, J. A.; Bominaar, E. L.; Hendrich, M. P.; Münck, E.; Lipscomb J. D. *Proc. Nat. Acad. Sci. USA* **2010**, *107*, 16788-16793.
(21) Connelly, N. G.; Geiger, W. E. *Chem. Rev.* **1996**, *96*, 877-910.

Appendix B

Spectroscopic and Reactivity Studies of an Fe^{III}–Alkylperoxido Species

Introduction

In Appendix A, the design and complexation using the ligand precursor H_4pub were discussed (Figure B.1A). The design concept for H_4pub extends from that for H_5bupa (Figure B.1B): incorporation of two neutral pyridine donors instead of one was proposed to make the metal site even less reducing, so various M–O_2 adducts can be prepared. However, the carboxylamidate group in $[H_2bupa]^{3-}$ and $[Hpub]^{3-}$ can bind and hinder the metal site upon complexation, as evidenced in $K[Mn^{II}H_2bupa]$ (see Appendix A Scheme 1). Therefore, reduction of the carboxylamide groups in H_4pub to neopentylamine groups was envisioned to make the metal site more accessible to exogenous ligands. The resulting H-bond donating N–H groups can aid in stabilizing M–O_2 adducts so that these reactive species could be trapped. The synthesis and characterization of this new ligand framework, H_4nub (Figure B.1C), is described in this appendix. Alkylperoxido binding studies of an Fe^{II} complex supported by H_4nub is also discussed, and further studies were performed to determine its reactivity within this non-heme ligand environment.

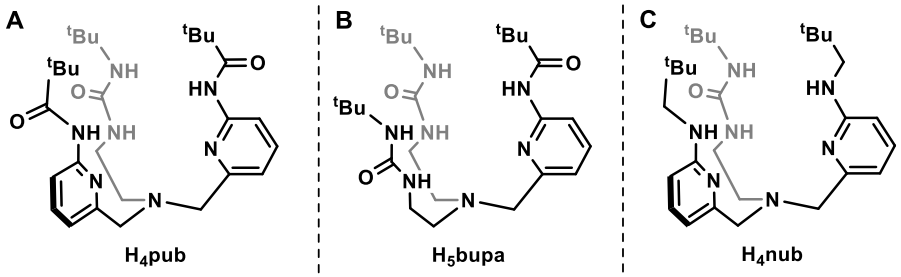

Figure B.1. Structures of H_4pub (A), H_5bupa (B), and H_4nub (C).

Results & Discussion

Ligand Synthesis. H_4nub was prepared from a convergent 7-step route (Scheme B.1). The first five steps are detailed in Appendix A (Scheme A.3) to produce the free amine **1**, which carboxyamide

groups are reduced to neopentyl amine by $LiAlH_4$ (90 %). The primary amine in **2** is then functionalized as a urea group with the addition of *tert*-butyl isocyanate to form H_4nub (83 %).

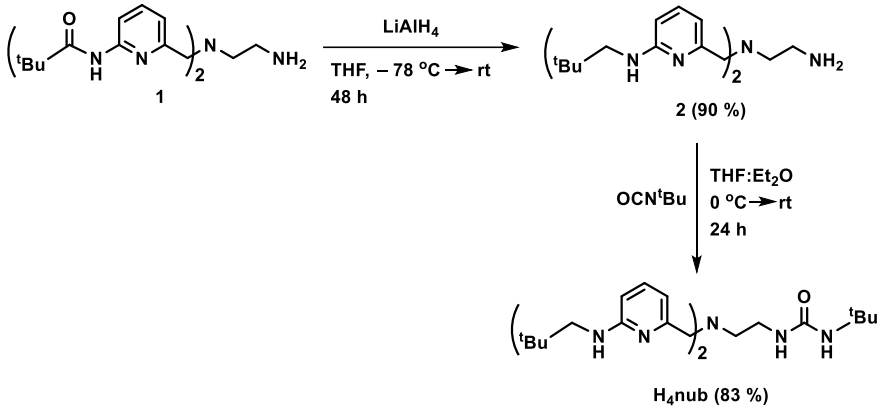

Scheme B.1. Ligand synthesis of H_4nub.

Complex Synthesis. Preparation of "[$Fe^{II}H_3$nub(OAc)]" was attempted by treating H_4nub with potassium hydride (KH) in *N,N*-dimethylacetamide (DMA), then metalating with $Fe^{II}(OAc)_2$ (Scheme B.2A). Recrystallization of the product from this reaction provided single crystals suitable for X-ray diffraction. However, the molecular structure (Figure B.2) had an empirical formula of [$Fe^{II}H_4$nub(OAc)$_2$]·DMA, which revealed the urea arm remained protonated. The complex [$Fe^{II}H_4$nub(OAc)$_2$] can be independently prepared by treating H_4nub with $Fe^{II}(OAc)_2$ in the absence of base (Scheme B.2B).

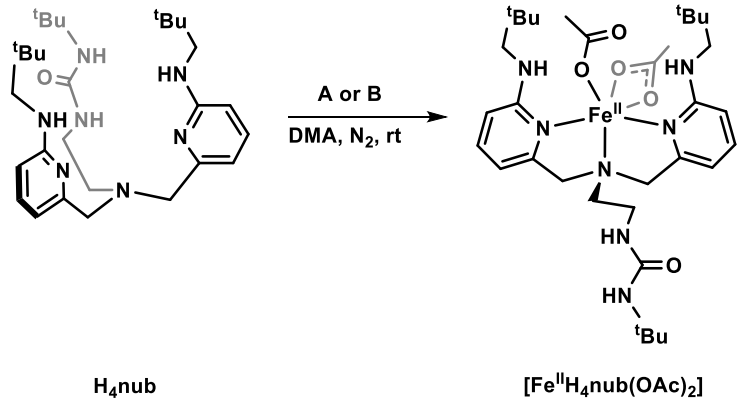

Scheme B.2. Preparation of [$Fe^{II}H_4$nub(OAc)$_2$]. A: (i) KH; (ii) $Fe^{II}(OAc)_2$. B: $Fe^{II}(OAc)_2$.

Structural Properties. The molecular structure of [$Fe^{II}H_4$nub$(OAc)_2$] revealed a mononuclear Fe ion in a distorted octahedral geometry (Figure B.2). The Fe^{II} center had an N_3O_3 primary coordination sphere with two acetate ions bound: one acetate was bound in a κ^1 fashion through O2, and the other was bound in a κ^2 fashion through O4 and O5. The H_4nub ligand binds the Fe^{II} center through the pyridine nitrogen atoms (N2 and N3) and the apical nitrogen atom (N1) in a meridional fashion (∠N2–Fe1–N3 = 155.2(1)°). The secondary amine groups in the two pyridine arms participated in weak H-bonding to the κ^1-bound acetate (N5/6–H---O2 ~ 3.1 Å). There was no indication in the solid state of H-bonding to the κ^2-bound acetate ligand. The urea arm remained protonated and unbound to the metal center.

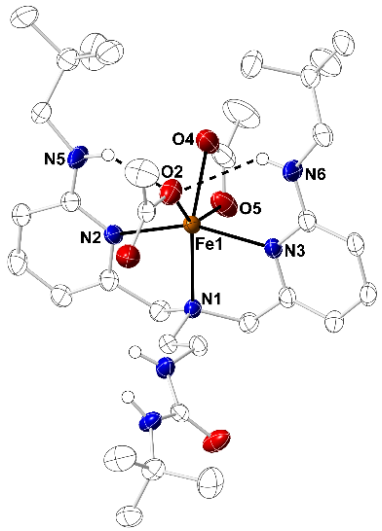

Table B.1. Selected metrical parameters for [$Fe^{II}H_4$nub$(OAc)_2$].

Bond Lengths/Distances (Å)	
Fe1–N1	2.195(3)
Fe1–N2	2.191(3)
Fe1–N3	2.197(3)
Fe1–O2	1.995(3)
Fe1–O4	2.192(4)
Fe1–O5	2.243(4)
N5–H---O2	3.096(5)
N6–H---O2	3.108(5)
Bond Angle (°)	
N2–Fe1–N3	155.2(1)

Figure B.2. The thermal ellipsoid plot of [$Fe^{II}H_4$nub$(OAc)_2$]. Ellipsoids are shown at the 50% probability level. Only urea and neopentyl amine hydrogen atoms are shown and solvent molecules are removed for clarity. Bond lengths, distances, and bond angles of interest are included in the corresponding **Table B.1**.

Electrochemical Properties. Electrochemical analysis of [$Fe^{II}H_4$nub$(OAc)_2$] exhibited an irreversible one-electron redox event at $E_{1/2}$ = – 180 mV vs $[FeCp_2]^{+/0}$ at room temperature in tetrahydrofuran (THF) (ΔE_p = 320 mV, $|i_{pa}/i_{pc}|$ = 2.1), which was tentatively assigned to the [$Fe^{III/II}$] process (Figure B.3A). This [$Fe^{III/II}$] reduction potential is more positive than other Fe^{II} complexes prepared

in our group,[1-4] suggesting that it may be less likely to reduce and cleave the O–O moiety when an O_2 exogenous ligand binds to the metal center. There was an additional, unidentified reductive event at – 700 mV vs $[FeCp_2]^{+/0}$.

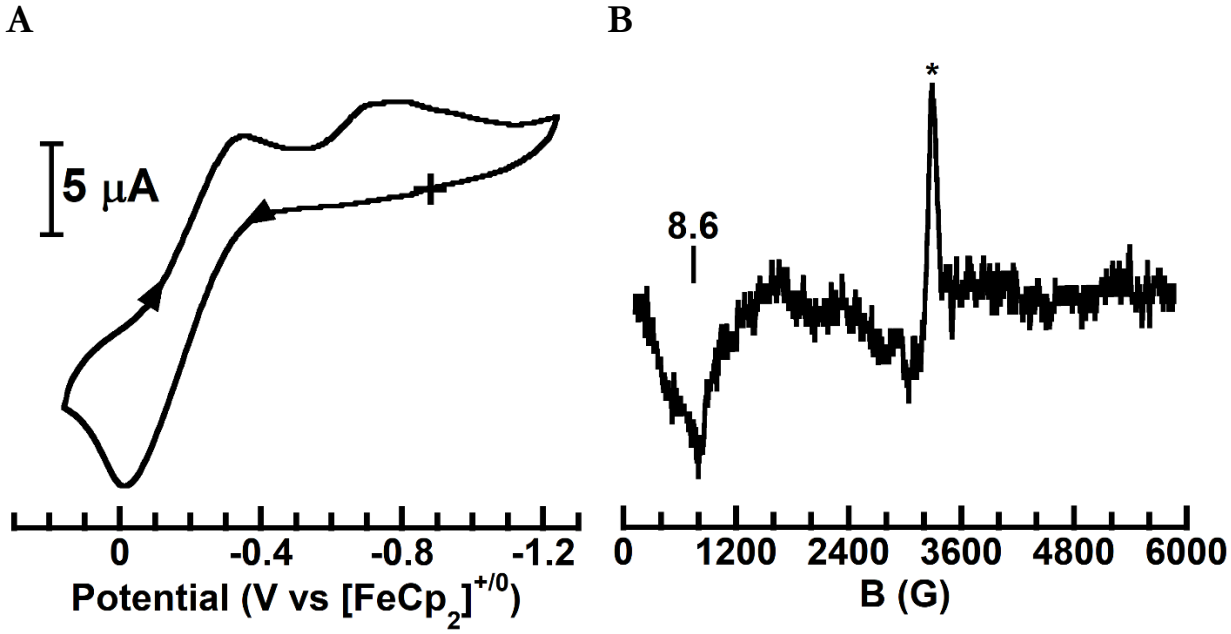

Figure B.3. (A) Cyclic voltammogram of $[Fe^{II}H_4nub(OAc)_2]$ collected in THF at 100 mV/s scan rate. (B) //-mode EPR spectrum of $[Fe^{II}H_4nub(OAc)_2]$ collected at 10 K. Asterisk (*) indicates cavity signal.

Spectroscopic Properties. A feature at g = 8.6 was observed in the parallel (//)-mode X-band electron paramagnetic resonance (EPR) spectrum for the frozen 1:1 THF:DMF (*N,N*-dimethylformamide) solution of $[Fe^{II}H_4nub(OAc)_2]$, consistent with a mononuclear Fe^{II} center with an S = 2 spin ground state (Figure B.3B). The spin state was corroborated with the room temperature solution NMR Evans' method magnetic moment of μ_{eff} = 5.13 μ_B (compared to the spin-only magnetic moment of 4.90 μ_B for an S = 2 system). The Fe^{II} complex exhibited absorption features at λ_{max} (ε_{max} (M^{-1} cm^{-1})) = 413 nm (900) and 925 nm (150) in THF at 0 °C (Figure B.4A, black). The λ_{max} = 413 nm feature is assigned to be a metal-to-ligand charge transfer (MLCT) between the Fe^{II} center and the coordinated pyridine,[5] while the λ_{max} = 925 nm feature is assigned to be a d-d transition.

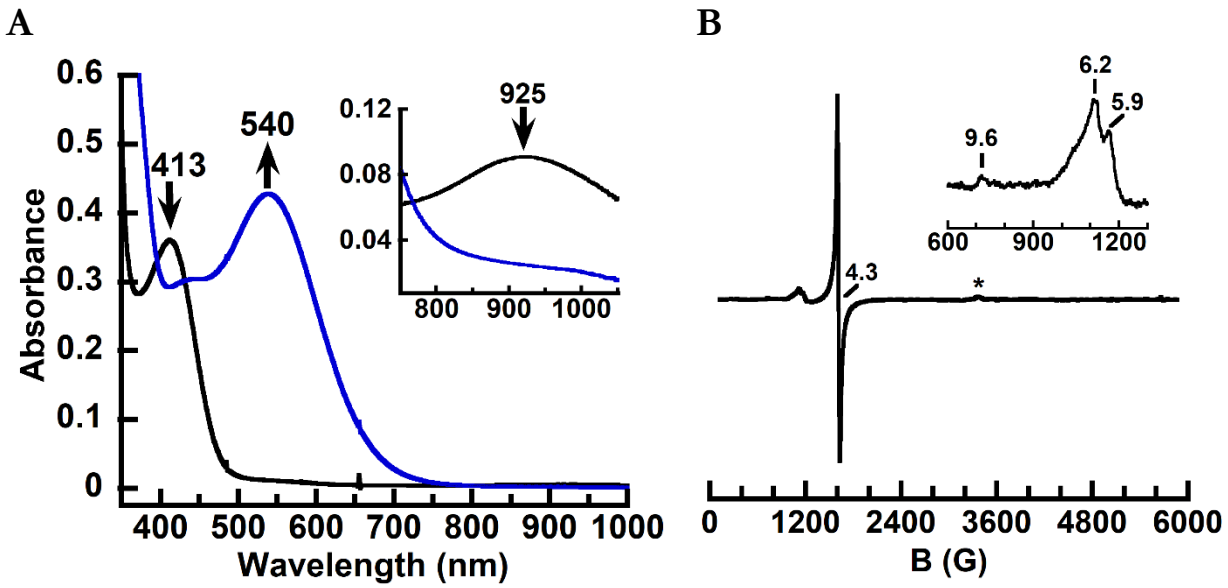

Figure B.4. (A) UV-vis spectral changes before (black) and after (blue) the addition of 1.5 equiv. of *t*BuOOH to $[Fe^{II}H_4nub(OAc)_2]$. Inset: low energy region. (B) ⊥-mode EPR spectrum (collected at 77 K) after the addition of 1.5 equiv. of *t*BuOOH to $[Fe^{II}H_4nub(OAc)_2]$. Inset: low field. Asterisk (*) indicates spectrometer cavity signal.

Generation of [Fe^{III}(OO^{t}Bu)]. Treatment of $[Fe^{II}H_4nub(OAc)_2]$ with 1.5 equivalents of *tert*-butyl hydroperoxide (*t*BuOOH) at 0 °C in THF was monitored spectrophotometrically (Figure B.4A, blue) and showed growth of new absorbance features at λ_{max} (ε_{max} ($M^{-1}\,cm^{-1}$)) = 445 nm (ca. 760) and 540 nm (ca. 1100). The lower energy feature was consistent with a ligand-to-metal charge transfer (LMCT) between an alkoxyperoxido unit and an Fe^{III} center, as illustrated in the purple form of soybean lipoxygenase-3 (λ_{max} (ε_{max} ($M^{-1}\,cm^{-1}$)) = 590 nm (1400)) and other synthetic Fe^{III}–alkoxyperoxido examples.[6-15] The reactivity of $[Fe^{II}H_4nub(OAc)_2]$ towards *t*BuOOH was further investigated using perpendicular (⊥)-mode EPR spectroscopy. Treatment of the Fe^{II} complex with 1.5 equivalents of *t*BuOOH at 0 °C showed growth of new features at g = 9.5, 6.1, 5.9 and 4.3 (Figure B.4B), which were similar to those observed in the purple lipoxygenase.[6,16] These g values are consistent with S = 5/2 (high spin Fe^{III}) systems; however, it cannot be determined at the moment if the features all belong to the same or multiple S = 5/2 Fe^{III} species.

An alternate route to generate the [Fe^{III}(OO*t*Bu)] species has been explored and monitored by optical spectroscopy (Scheme B.3). Treatment of [$Fe^{II}H_4$nub$(OAc)_2$] with 1 equivalent of ferrocenium tetrafluoroborate ([$FeCp_2$]BF_4) at 0 °C in THF (Figure B.5A, gray) showed growth of a new absorbance feature at λ_{max} (ε_{max} (M^{-1} cm^{-1})) = 495 (ca. 600). This was assigned as the singly-oxidized analog of the Fe^{II} complex, [$Fe^{III}H_4$nub$(OAc)_2$]$^+$ ([Fe^{III}]$^+$). The [Fe^{III}]$^+$ species can be reduced back to the Fe^{II} complex with the treatment of 1 equivalent of cobaltocene ([$CoCp_2$], – 1.33 V vs [$FeCp_2$]$^{+/0}$) by monitoring the loss of the 495 nm feature and the reemergence of the 413 nm feature (Figure B.5A, blue). The increased intensity of the 413 nm band was attributed to absorbance contribution from the byproducts of the oxidation-reduction reactions ([$FeCp_2$] and [$CoCp_2$]$^+$, λ_{max} = 440 and 405 nm, respectively). Addition of 1 equivalent of *t*BuOOH to [Fe^{III}]$^+$ did not result in any changes in the optical spectrum (Figure B.4B, gray); however, subsequent addition of 3 equivalents of 1,8-diazabicyclo[5.4.0]undec-7-ene (DBU) showed growth of an absorbance at λ_{max} (ε_{max} (M^{-1} cm^{-1})) = 445 nm (sh) and 540 nm (ca. 1500), which were characteristic of [Fe^{III}(OO*t*Bu)] (Scheme B3; Figure B.5B, blue). The features from this route were more intense than when the Fe^{II} complex was treated with 1.5 equivalents of *t*BuOOH (Figure B.4A). The alternate route demonstrated that addition of base was necessary to generate the characteristic features associated with the putative [Fe^{III}(OO*t*Bu)] species.

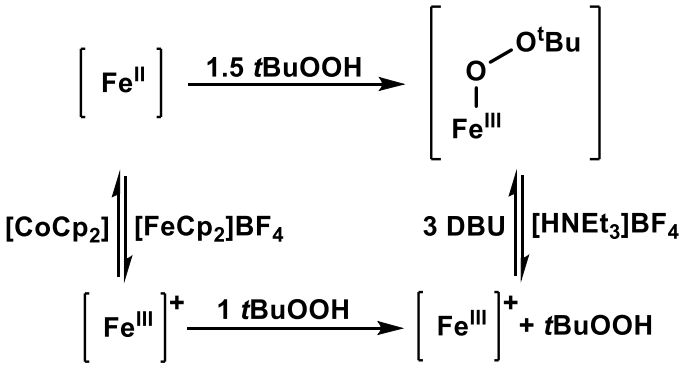

Scheme B.3. Two different routes to generate [Fe^{III}(OO*t*Bu)] from [$Fe^{II}H_4$nub$(OAc)_2$]. All manipulations were performed in THF or 1:1 THF:DMF at 0 °C.

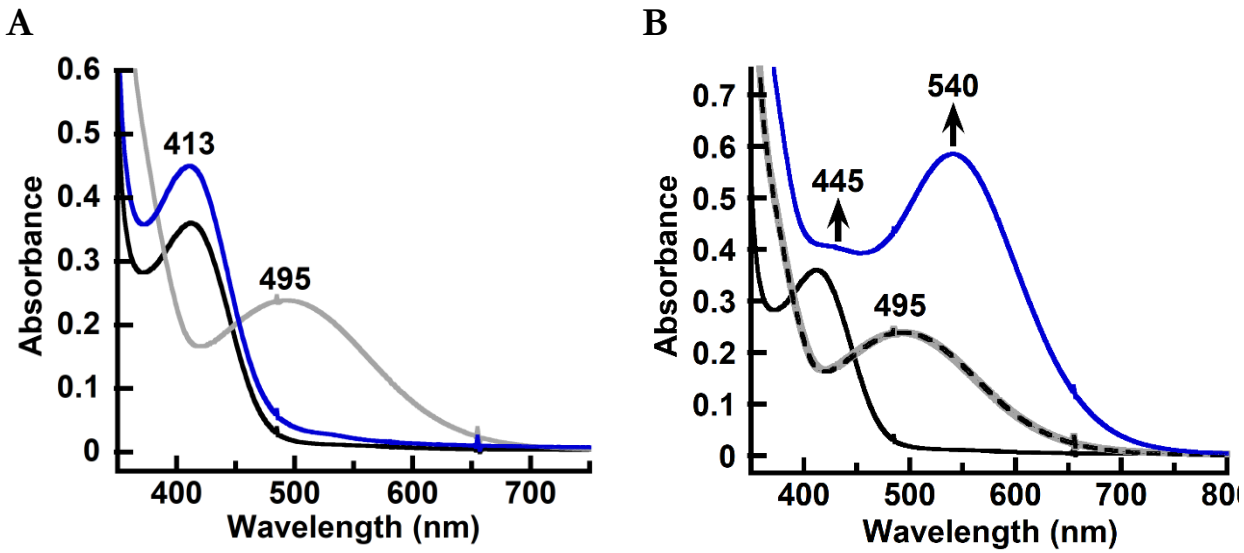

Figure B.5. (A) UV-vis spectral changes before (black) and after the additions of 1 equiv. of $[FeCp_2]BF_4$ (gray), then 1 equiv. of $[CoCp_2]$ (blue) to $[Fe^{II}H_4nub(OAc)_2]$. (B) UV-vis spectral changes before (black solid) and after the additions of 1 equiv. of $[FeCp_2]BF_4$ (black dash), 1 equiv. of *t*BuOOH (gray), then 3 equiv. of DBU (blue) to $[Fe^{II}H_4nub(OAc)_2]$.

The alternate route to generate the $[Fe^{III}(OO$*t*$Bu)]$ species has also been investigated by ⊥-mode EPR spectroscopy (Scheme B.3). Treatment of $[Fe^{II}H_4nub(OAc)_2]$ with 1 equivalent of $[FeCp_2]BF_4$ at 0 °C in THF:DMF revealed a rhombic $S = 5/2$ signal (g = 9.6, 8.0, 5.6, 4.3) that was consistent with a mononuclear high spin Fe^{III} center (Figure B.6B). This was assigned as $[Fe^{III}]^+$. Addition of 1 equivalent of *t*BuOOH to $[Fe^{III}]^+$ did not result in a significant change in the EPR spectrum (Figure B.6C), consistent with the lack of reactivity observed in the UV-vis spectrum. Subsequent addition of 3 equivalents of DBU showed the growth of an axial $S = 5/2$ signal (Figure B.6D, g = 6.2, 5.9, 2.0). An axial $S = 5/2$ signal was observed for the $[Fe^{III}(OO$*t*$Bu)]$ generated in the original route (Figure B.4B), albeit at a much lower yield. This is consistent with the lower conversion observed by UV-vis spectroscopy (Figure B.4A).

Upon generating the tentative $[Fe^{III}(OO$*t*$Bu)]$ species, addition of 1 equivalent of an acid, triethylammonium tetrafluoroborate ($[HNEt_3]BF_4$, pK_a 11), showed growth of a band at λ_{max} (ε_{max} (M^{-1} cm^{-1})) = 495 nm (ca. 600) which was characteristic of $[Fe^{III}]^+$ (Scheme B.3; Figure B.7, gray). Subsequent treatment with 3 equivalents of DBU regenerated $[Fe^{III}(OO$*t*$Bu)]$ quantitatively, as

illustrated by the reemergence of the 540 nm LMCT feature of similar intensity (Figure B.7, blue). These reversible reactions further supported that the exogenous ligand $^{-}$OO*t*Bu becomes labile upon protonation.

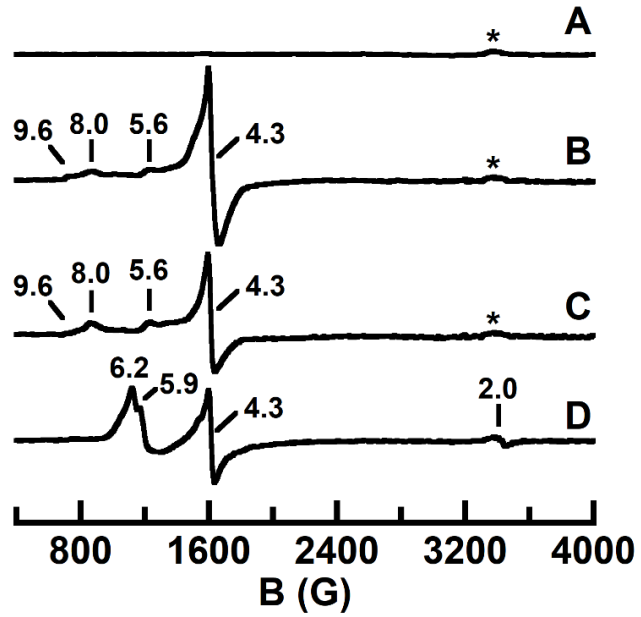

Figure B.6. ⊥-mode EPR spectral changes (collected at 77K) before (A) and after the additions of 1 equiv. of $[FeCp_2]BF_4$ (B), then 1 equiv. of *t*BuOOH (C), then 3 equiv. of DBU (D) to $[Fe^{II}H_4nub(OAc)_2]$. Asterisk (*) indicates spectrometer cavity signal.

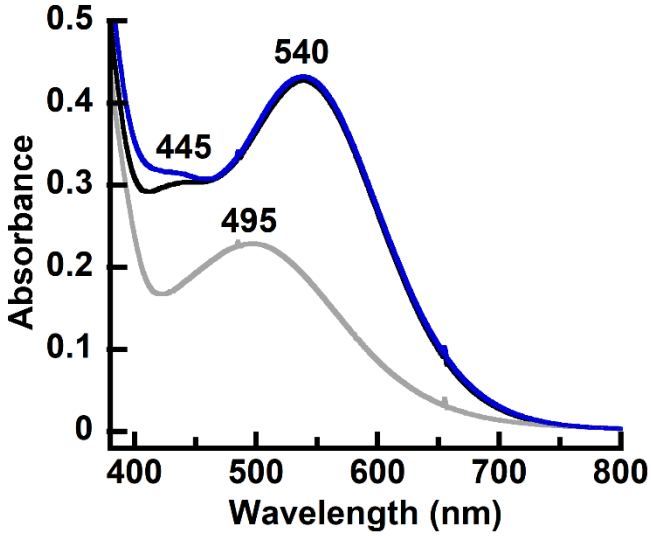

Figure B.7. UV-vis spectral changes before (black) and after the additions of 1 equiv. of $[HNEt_3]BF_4$ (gray), then 3 equiv. of DBU (blue) to $[Fe^{III}(OOtBu)]$.

Reactivity Studies. [Fe^{III}(OO*t*Bu)] was tested for reactivity such as (1) H_2O-assisted O–O bond heterolytic cleavage,[17] (2) H-atom abstraction (diphenylhydrazine (DPH), 1-hydroxy-2,2,6,6-tetramethyl-piperidine (TEMPO-H), 2,6-di-*tert*-butyl-4-methylphenol (BHT)), (3) C–H bond activation (cyclohexene), and (4) O–atom transfer (cyclooctene, triphenylphosphine, thianthrene). These reactions were monitored by UV-vis spectroscopy and gas chromatography-mass spectrometry (GC-MS), but no reactivity was observed.

Conclusion

An [Fe^{III}(OO*t*Bu)] species was proposed to be generated and stabilized in the H_4nub scaffold, demonstrating correct modulation of electronic donation with pyridine-based neutral ligands can stabilize an Fe^{III} center without further reducing the $^{-}$OO*t*Bu moiety by cleaving the O–O bond. However, further characterization is required to support this identification. The H-bond donating amine groups may participate in the stabilization of the $^{-}$OO*t*Bu unit; structural characterization is needed to validate any non-covalent interactions. Solution vibration spectroscopic methods (e.g. solution FT-IR, resonance Raman) could provide information of the O–O and Fe–O bonding, and possibly the H-bonding character of the N–H groups; however, caution must be taken in the analysis of these vibrations in solution, since solvent molecules can participate in H-bonding with the amine groups. ^{57}Fe Mössbauer spectroscopy will also be used to gain further insight into the oxidation and spin states of the iron center. X-ray absorption spectroscopy can be performed to determine the geometric structure around the Fe^{III} center.[18] Upon generating [Fe^{III}(OO*t*Bu)], it was of interest to activate the O–O bond and oxidize various organic substrates, as observed in the catalytic cycle of many oxygenases; however, no such reactivity was observed. The lack of substrate reactivity was similarly observed in several previously reported high spin Fe^{III}(OOR) systems; a

potential energy barrier to lengthen the O–O bond has been proposed, making the O–O bond activation endergonic.[8,19,20]

Experimental

General Procedures. Organic syntheses, unless otherwise noted, did not require the use of an inert atmosphere. All inorganic syntheses and manipulations were performed under a nitrogen atmosphere in a Vacuum Atmosphere Co. dry box. Solvents were sparged with argon and purified using a JC Meyer Co. solvent purification system with columns containing Q-5 and molecular sieves. All reagents, unless otherwise noted, were purchased from commercial sources and used as received. $[FeCp_2]BF_4$ and $[HNEt_3]BF_4$ were synthesized according to literature procedure.[21,22] Synthesis of the free amine **1** is detailed in Appendix A (Compound 5 in Scheme A.3, experimental section).

N^1,N^1-bis((6-(neopentylamino)pyridin-2-yl)methyl)ethane-1,2-diamine (2). $LiAlH_4$ (1.657 g, 43.66 mmol) was suspended in 85 mL anhydrous THF in a 250 mL two-neck round bottom flask with a stir bar in a glovebox under a nitrogen atmosphere. The round bottom flask was capped with a septum on one neck and a Schlenk adaptor on the other. The flask was transferred out of the glovebox onto a Schlenk line under a N_2 atmosphere. The flask was then chilled in a –78 °C cold bath for 15 minutes. The free amine **1** (1.917g, 4.351 mmol) was dissolved in 15 mL THF in a 50 mL Erlenmeyer flask and was put under an inert atmosphere by bubbling N_2 for 15 minutes. The amine solution was then added to the round bottom flask containing the $LiAlH_4$/THF suspension via cannula transfer. The mixture was allowed to stir for 2 hours at –78 °C and was then warmed up to stir at room temperature for two days. After the reaction was complete, the mixture was quenched with 60 mL DI water and then with 60 mL 1.0 M NaOH at 0 °C. Upon warming to room temperature, the insoluble material was removed via filtration. The aqueous layer was extracted four times with 150 mL $CHCl_3$, which was combined with the organic filtrate. The $CHCl_3$/THF solution was dried over

Na_2SO_4, and the solvents were removed *in vacuo* to produce a yellow oil as the free amine **2** (1.61 g, 90.0 %). ^{1}H NMR (500 MHz, $CDCl_3$, ppm): δ 7.39 (2H, t, *J* = 7.6 Hz, Ar*H*), 6.80 (2H, d, *J* = 7.2, Ar*H*), 6.25 (2H, d, *J* = 8.2 Hz, Ar*H*), 4.55 (2H, m, ArN*H*), 3.64 (4H, s, ArCH_2), 3.02 (4H, d, *J* = 6.2 Hz, ArNHCH_2), 2.76 (2H, m, NCH_2CH_2), 2.63 (2H, m, NCH_2CH_2), 0.99 (18H, s, C(CH_3)$_3$); ^{13}C NMR (500 MHz, $CDCl_3$) δ 159.1, 158.4, 137.9, 111.5, 103.7, 60.8, 57.4, 54.2, 39.8, 32.1, 27.6.

1-(2-(Bis((6-(neopentylamino)pyridin-2-yl)methyl)amino)ethyl)-3-(tert-butyl)urea (H_4nub). The free amine **2** (0.835 g, 2.02 mmol) was dissolved in a mixture of 40 mL THF and 40 mL Et_2O, and the solution was chilled in a 0 °C ice bath for 15 minutes. *tert*-Butyl isocyanate (0.203 g, 2.05 mmol) was dissolved in a mixture of 40 mL THF and 40 mL Et_2O and was added dropwise to the free amine **2** solution while stirring for 40 minutes. The reaction was then allowed to warm up to room temperature overnight, and the solvents were removed *in vacuo* to afford an off-white solid, H_4nub (840 mg, 83.0 %). ^{1}H NMR (500 MHz, $CDCl_3$, ppm): δ 7.36 (2H, t, *J* = 7.8 Hz, Ar*H*), 6.59 (2H, d, *J* = 6.9, Ar*H*), 6.27 (2H, d, *J* = 8.2 Hz, Ar*H*), 5.95 (1H, bs, C(O)N*H*CH_2), 4.82 (2H, bs, ArN*H*), 4.63 (1H, s, N*H*C(CH_3)$_3$), 3.59 (4H, s, ArCH_2), 3.18 (2H, q, *J* = 5.3 Hz, NHCH_2CH_2), 3.02 (4H, d, *J* = 3.3 Hz, ArNHCH_2), 2.63 (2H, t, *J* = 5.6 Hz, NCH_2CH_2), 1.30 (9H, s, NHC(CH_3)$_3$), 0.99 (18H, s, CH_2C(CH_3)$_3$); ^{13}C NMR (500 MHz, $CDCl_3$) δ 159.4, 158.3, 157.4, 138.1, 112.2, 104.0, 60.2, 54.2, 53.1, 50.0, 37.7, 32.2, 29.7, 27.6. FTIR (ATR, selected bands cm^{-1}) 3332, 3056, 2953, 1637, 1599, 1577, 1506, 1462, 1362, 1265, 1212, 1155, 982, 783. HRMS (ES+, m/z): Exact mass calculated for $C_{29}H_{50}N_7O$ $[M + H]^+$: 512.4077. Found: 512.4057.

1-(2-(Bis((6-(neopentylamino)pyridin-2-yl)methyl)amino)ethyl)-3-(tert-butyl)urea-bis(acetato)ferrate(II) ([$Fe^{II}H_4$nub(OAc)$_2$]). A solution of H_4nub (106 mg, 0.206 mmol) and $Fe^{II}(OAc)_2$ (40 mg, 0.23 mmol) in 2 mL anhydrous DMA was stirred for 6 hours. The yellow reaction mixture was filtered to remove excess $Fe^{II}(OAc)_2$, and the solvent was removed *in vacuo*. The yellow solids were redissolved in 4 mL THF, which was layered under pentane at -30 °C to produce yellow crystalline solids. The

solids were collected on a fine porosity glass frit and dried for an hour (116 mg, 82 %). Elemental analysis calcd. (found) for [$Fe^{II}H_4$nub$(OAc)_2$] ($C_{33}H_{55}N_7O_5Fe$): C, 57.80 (57.96); H, 8.09 (8.14); N, 14.30 (14.06) %. FTIR (ATR, selected bands cm^{-1}) 3323, 3079, 2953, 1608, 1580, 1478, 1442, 1364, 1331, 1319, 1254, 1212, 1196, 1169, 1038, 996, 775. Evans' method (CD_2Cl_2, 298 K, 500 MHz NMR), μ_{eff} = 5.13 μ_B.

Physical Methods. UV-vis spectra were collected on an Agilent UV-vis spectrophotometer equipped with a Unisoku Unispeks cryostat in a 1 cm quartz cuvette. ^1H and ^{13}C NMR spectra were collected on a Bruker CRYO500 spectrometer (500 MHz). X-band EPR spectra (microwave frequencies 9.28 and 9.62 GHz) were collected on a Bruker EMX spectrometer equipped with an ER041XG microwave bridge, an Oxford Instrument liquid He quartz cryostat and a dual-mode cavity (ER4116DM). Solid-state infrared spectra were collected on a Thermo Scientific Nicolet iS5 FT-IR spectrometer equipped with an iD5 ATR accessory. High resolution mass spectrometry of organic ligands was performed on a Waters Micromass LCT Premier Mass Spectrometer in positive ion electrospray mode.

Electrochemical Methods. Cyclic voltammograms were collected using a CHI600C electrochemical analyzer in a dry box under nitrogen atmosphere at room temperature. Tetrabutylammonium hexafluorophosphate (TBAP, 100 mM) was used as the electrolyte. A glassy carbon, platinum wire and silver wire electrodes were used as the working, counter, and reference electrodes, respectively. Cobaltocenium hexafluorophosphate ($[CoCp_2]PF_6$, – 1.33 V vs $[FeCp_2]^{+/0}$) was used as an internal standard.

Low Temperature UV-vis Spectroscopic Studies. In a typical experiment, a stock solution of [$Fe^{II}H_4$nub$(OAc)_2$] (0.40 mM) was prepared in THF in a dry box, and 3 mL of the stock solution was transferred to a 1 cm quartz cuvette with a stir bar inside. The cuvette was sealed with a rubber septum and brought out of the box. The cuvette was placed in the Agilent UV-vis

spectrophotometer equipped with a cryostat and was allowed to cool at 0 °C for at least 15 minutes. Additional reagents were often prepared at a concentration of 40 mM and were added via a gas-tight syringe. More concentrated UV-vis spectroscopic studies were performed at a concentration of 5.2 mM to monitor low intensity absorption features.

Low Temperature EPR Spectroscopic Studies. In a typical experiment, a stock solution of $[Fe^{II}H_4nub(OAc)_2]$ (24 mM) was prepared in 1:1 THF:DMF mixture in a dry box. 100 μL of the stock solution was added to a quartz EPR tube, which was sealed with a rubber septum. The tube was brought out of the box and was allowed to cool in an ice bath at 0 °C for at least 15 minutes. Additional reagents (80 mM) were added via a gas-tight syringe. When the reaction was complete (2 minutes), the tube was taken out of the ice bath, wiped dry of water molecules, and quickly frozen in liquid nitrogen. The final metal concentration in low temperature reactions was 10 mM. The $[Fe^{II}H_4nub(OAc)_2]$ sample (46 mM) was frozen immediately after it was brought out of the dry box.

X-Ray Crystallographic Methods. A Bruker SMART APEX II diffractometer was used to collect crystallographic data for $[Fe^{II}H_4nub(OAc)_2]$. A yellow crystal of approximate dimensions 0.351 x 0.242 x 0.153 mm was mounted in a cryo-loop and transferred to the diffractometer. The APEX21[23] program package was used to determine the unit-cell parameters and for data collection. The raw frame data was processed using SAINT28[24] and SADABS3[25] to yield the reflection data file. Subsequent calculations were carried out using the SHELXTL4[26] program. The structure was solved by dual space methods and refined on F2 by full-matrix least-squares techniques. The analytical scattering factors[27] for neutral atoms were used throughout the analysis.

References

(1) Mukherjee, J.; Lucas, R. L.; Zart, M. K.; Powell, D. R.; Day, V. W.; Borovik, A. S. *Inorg. Chem.* **2008**, *47*, 5780-5786.
(2) Macbeth, C. E.; Hammes, B. S.; Young, V. G. Jr.; Borovik, A. S. *Inorg. Chem.* **2001**, *40*, 4733-4741.
(3) Shook, R. L. Doctoral Dissertation, University of California-Irvine, Irvine, CA, 2009.
(4) Lau, N.; Ziller, J. W.; Borovik, A. S. *Polyhedron* **2015**, *85*, 777-782.
(5) Braterman, P. S.; Song, J. -I.; Peacock, R. D. *Inorg. Chem.* **1992**, *31*, 555-559.
(6) Skrzypczak-Jankun, E.; Bross, R. A.; Carroll, R. T.; Dunham, W. R.; Funk, M. O. Jr. *J. Am. Chem. Soc.* **2001**, *123*, 10814-10820.
(7) Wada, A.; Ogo, S.; Watanabe, Y.; Mukai, M.; Kitagawa, T.; Jitsukawa, K.; Masuda, H.; Einaga, H. *Inorg. Chem.* **1999**, *38*, 3592-3593.
(8) Lehnert, N.; Ho, R. Y. N.; Que, L. Jr.; Solomon, E. I. *J. Am. Chem. Soc.* **2001**, *123*, 12802-12816.
(9) Lehnert, N.; Ho, R. Y. N.; Que, L. Jr.; Solomon, E. I. *J. Am. Chem. Soc.* **2001**, *123*, 8271-8290.
(10) Kim, J.; Zang, Y.; Costas, M.; Harrison, R. G.; Wilkinson, E. C.; Que, L. Jr. *J. Biol. Inorg. Chem.* **2001**, *6*, 275-284.
(11) Krishnamurthy, D.; Kasper, G. D.; Namuswe, F.; Kerber, W. D.; Narducci Sarjeant, A. A.; Moënne-Loccoz, P.; Goldberg, D. P. *J. Am. Chem. Soc.* **2006**, *128*, 14222-14223.
(12) Namuswe, F.; Kasper, G. D.; Narducci Sarjeant, A. A.; Hayashi, T.; Krest, C. M.; Green, M. T.; Moënne-Loccoz, P.; Goldberg, D. P. *J. Am. Chem. Soc.* **2008**, *130*, 14189-14200.
(13) Namuswe, F.; Hayashi, T.; Jiang, Y.; Kasper, G. D.; Narducci Sarjeant, A. A.; Moënne-Loccoz, P.; Goldberg, D. P. *J. Am. Chem. Soc.* **2010**, *132*, 157-167.
(14) Hong, S.; Lee, Y.-M.; Cho, K.-B.; Seo, M. S.; Song, D.; Yoon, J.; Garcia-Serres, R.; Clémancey, M.; Ogura, T.; Shin, W.; Latour, J.-M.; Nam, W. *Chem. Sci.* **2014**, *5*, 156-162.
(15) Widger, L. R.; Jiang, Y.; McQuilken, A. C.; Yang, T.; Siegler, M. A.; Matsumura, H.; Moënne-Loccoz, P.; Kumar, D.; De Visser, S. P.; Goldberg, D. P. *Dalton Trans.* **2014**, *43*, 7522-7532.
(16) De Groot, J. J. M. C.; Veldink, G. A.; Vliegenthart, J. F. G.; Boldingh, J.; Wever, R.; Van Gelder, B. F. *Biochimica Acta.* **1975**, *377*, 71-79.
(17) Oloo, W. N.; Fielding, A. J.; Que, L. Jr. *J. Am. Chem. Soc.* **2013**, *135*, 6438-6441.
(18) Shan, X.; Rohde, J.-U.; Koehntop, K. D.; Zhou, Y.; Bukowski, M. R.; Costas, M.; Fujisawa, K.; Que, L. Jr. *Inorg. Chem.* **2007**, *46*, 8410-8417.
(19) Zang, Y.; Kim, J.; Dong, Y.; Wilkinson, E. C.; Appelman, E. H.; Que, L. Jr. *J. Am. Chem. Soc.* **1997**, *119*, 4197-4205.
(20) Chen, K.; Que, L. Jr. *J. Am. Chem. Soc.* **2001**, *123*, 6327-6337.
(21) Connelly, N. G.; Geiger, W. E. *Chem. Rev.* **1996**, *96*, 877-910.
(22) Hill, E. A. Doctoral Dissertation, University of California-Irvine, Irvine, CA, 2016.
(23) APEX2 Version 2010.3-0, Bruker AXS, Inc.; Madison, WI 2010.
(24) SAINT Version 7.68a, Bruker AXS, Inc.; Madison, WI 2009.
(25) Sheldrick, G. M. SADABS, Version 2008/1, Bruker AXS, Inc.; Madison, WI 2008. 29.
(26) Sheldrick, G. M. SHELXTL, Version 2008/4, Bruker AXS, Inc.; Madison, WI 2008.
(27) International Tables for X-Ray Crystallography 1992, Vol. C., Dordrecht: Kluwer Academic Publishers.